ESCOLA DE DOUTORAMENTO
INTERNACIONAL DA USC

Lisandra Cristina
de Castro Alves

Tese de doutoramento

Magnetic nanomaterials based on sustainable biopolymers for circular bioeconomy

Santiago de Compostela, 2022

Programa de Doutoramento en Ciencia de Materiais

TESE DE DOUTORAMENTO

MAGNETIC NANOMATERIALS BASED ON SUSTAINABLE BIOPOLYMERS FOR CIRCULAR BIOECONOMY

Lisandra Cristina de Castro Alves

ESCOLA DE DOUTORAMENTO INTERNACIONAL DA UNIVERSIDADE DE SANTIAGO DE COMPOSTELA

PROGRAMA DE DOUTORAMENTO EN CIENCIA DE MATERIAIS

SANTIAGO DE COMPOSTELA

2022

USC
UNIVERSIDADE
DE SANTIAGO
DE COMPOSTELA

USC
UNIVERSIDADE
DE SANTIAGO
DE COMPOSTELA

USC
UNIVERSIDADE
DE SANTIAGO
DE COMPOSTELA

DECLARACIÓN DO AUTOR/A DA TESE

Dna. **Lisandra Cristina de Castro Alves**

Título da tese: **Magnetic nanomaterials based on sustainable biopolymers for circular bioeconomy**

Presento a miña tese, seguindo o procedemento axeitado ao Regulamento, e declaro que:

1) A tese abarca os resultados da elaboración do meu traballo.
2) De ser o caso, na tese faise referencia ás colaboracións que tivo este traballo.
3) Confirmo que a tese non incorre en ningún tipo de plaxio doutros autores nin de traballos presentados por min para a obtención doutros títulos.
4) A tese é a versión definitiva presentada para a súa defensa e coincide a versión impresa coa presentada en formato electrónico

E comprométome a presentar o Compromiso Documental de Supervisión no caso de que o orixinal non estea na Escola.

En **Santiago de Compostela**, **11 de Xullo de 2022**.

Asdo. Lisandra C. De Castro Alves

USC
UNIVERSIDADE
DE SANTIAGO
DE COMPOSTELA

AUTORIZACIÓN DO DIRECTOR / TITOR DA TESE

Magnetic nanomaterials based on sustainable biopolymers for circular bioeconomy

D. José Rivas Rey (Director/Titor)
Dna. Yolanda Piñeiro Redondo (Directora)

INFORMA/N:

Que a presente tese, correspóndese co traballo realizado por Dna. Lisandra Cristina De Castro Alves, baixo a miña dirección/titorización, e autorizo a súa presentación, considerando que reúne os requisitos esixidos no Regulamento de Estudos de Doutoramento da USC, e que como director desta non incorre nas causas de abstención establecidas na Lei 40/2015.

De acordo co indicado no Regulamento de Estudos de Doutoramento, declara tamén que a presente tese de doutoramento é idónea para ser defendida en base á modalidade de Monográfica con reproducción de publicaciones, nos que a participación da doutoranda foi decisiva para a súa elaboración e as publicacións se axustan ao Plan de Investigación.

En Santiago de Compostela, 11 de Xullo de 2022

Asdo. Prof. José Rivas Rey
Director/Titor

Asdo. Dna Yolanda Piñeiro Redondo
Directora

USC
UNIVERSIDADE
DE SANTIAGO
DE COMPOSTELA

Á minha família,

Aos que já não estão, mas

que sempre estarão presentes

USC
UNIVERSIDADE
DE SANTIAGO
DE COMPOSTELA

USC
UNIVERSIDADE
DE SANTIAGO
DE COMPOSTELA

ACKNOWLEDGMENTS

Estas são as últimas palavras que estou a escrever e as que mais sentido e satisfação têm para mim. Durante este desafio de formação profissional, não posso deixar de lado o crescimento pessoal, os altos e os baixos, os falhos e as vitórias. Só tenho que agradecer a estas pessoas magníficas que acreditaram em mim e sempre me incentivaram para não desistir dos meus objetivos e sonhos.

De manera muy especial y sincera quiero agradecer a mis directores el Prof. José Rivas y a la Dra. Yolanda Piñeiro quien me brindó la oportunidad de realizar mi doctorado y quien con su apoyo, experiencia, conocimiento, paciencia y motivación a lo largo de los años permitió el desarrollo de este trabajo de investigación.

I want to express my deepest gratitude to Prof. Orlando Rojas for accepting me into his research group at Aalto University for such a short time. I have learnt alot from his advice and I admire his fascination for forest-science. I am also grateful to Dra. Maryam Borghei, who was with me every day helping me get around the laboratory, thank you for your enormous help, attention, and guidance in conducting my research work. I would like to thank Ling, Jannika, and Luis, who support me with their knowledge, and valuable ideas.

Também queria agradecer ao Prof. Lorenzo Pastrana por me acolher no seu grupo no INL durante esta pandemia. Obrigada por tudo e por fazer possível parte dos resultados que estão neste trabalho. Não poderia deixar de mencionar o Miguel Cerqueira que foi o meu mentor no INL e sempre disponibilizou um tempinho para mim quando eu precisava tirar dúvidas.

Quiero también agradecer a todo el personal de las unidades de rayos X, IR-RAMAN y de microscopía electrónica y confocal de las infraestructuras de Apoyo a la Investigación y al Desarrollo Tecnológico (RIAIDT-USC). En la cual quiero destacar a Bruno, Ines, Ezequiel y Maria Jose por su buen trabajo, rapidez y explicaciones. En especial, quiero dar las gracias a Raquel por su paciencia en hacer tal cual las imágenes de SEM como yo querían. Quiero también agradecer a Paloma, de la Unidad de Elementos Traza, espectroscopia y especificación (GETEE) que sin ella mucho de los resultados de adsorción no serían posible, muchas gracias por tu ayuda, amabilidad y eficiencia; a Maria del Carmen Herrero por las imágenes obtenidas con el perfilómetro en Física Aplicada y también a Ramon Silva por me ayudar con las medidas de reometría. Por último, tengo que dar las gracias a Carmen Serra del Servicio de Nanotecnoloxía e Análise de Superficies (C.A.T.I., Vigo) por sus informes de XPS super detallados y sus explicaciones que me sacaron de un gran apuro.

A mis compañeros de NANOMAG con los que he tenido el gustazo de trabajar durante estos años. Susana, solo tengo que agradecerte, di mis primeros pasos en la investigación bajo tu supervisión, te considero como mi mentora he aprendido mucho contigo, mil gracias! A Maria, Nerea, Iria y José por vuestra simpatía, ayuda y risas compartidas. En especial a Manu, Angela, Pelayo y Roman gracias por sacarme una sonrisa, por vuestra amistad, por ser como sois, ayudarme en momentos de dudas y por los momentos que hemos disfrutado juntos.

Aos meus amigos Filipa, Benni, Sie Yung, Michael, Daniel, Niti e Alejandra que apesar de estarem longe sempre demonstraram imenso carinho e fizeram com que eu seguisse em frente, obrigado por estar sempre ao meu lado! Em especial, a ti, Ana, sem ti, sem a tua ajuda, conselhos, paciência em ouvir os meus problemas eu não conseguiria terminar este trabalho.

USC
UNIVERSIDADE DE SANTIAGO DE COMPOSTELA

Não existe forma de te agradecer tudo o que fizeste por mim, obrigada pela tua amizade e que seguirá por vários anos mais.

Quero expresar o meu sincero agradecemento a ti, Alberto, a quen tiven a verdadeira bendición de coñecer durante esta viaxe. Grazas por cativarme a diario, axudarme a pasar os días máis difíciles, por levarme sempre á razón e manter os meus pés firmes na terra. Grazas pola túa amabilidade, empatía, amizade e amor. Non me podía esquecer da miña familia de Santiago, grazas por recibirme tan ben, señor Luis, Marta, Ester e Jorge.

Por último quero agradecer aos meus pais, que foram os meus primeiros mentores e amigos na minha vida, por darem-me os melhores valores, educação, compreensão e o seu amor. Obrigada por acreditarem em mim, pelo vosso apoio, sem vocês eu não teria feito este trabalho. À minha irmã, pelo seu apoio absoluto e por me ter dado a melhor prenda este ano, a de poder ser madrinha. Ao meu lindo sobrinho, Afonso, que foi a minha melhor distração durante a escrita deste trabalho, fico muito agradecida por ter visto os seus primeiros dias, choros, cólicas e "acidentes".

Finalmente, não poderia me sentir mais abençoada pela família que tenho e por todos os amigos e colegas com quem tive a sorte de cruzar, mesmo que por um curto espaço de tempo. Muito obrigada a todos!

USC
UNIVERSIDADE DE SANTIAGO DE COMPOSTELA

TABLE OF CONTENTS

TABLE OF CONTENTS **13**
LIST OF ABBREVIATIONS AND ACRONYMS **17**
LIST OF PUBLICATIONS **19**
RESUMO **21**
RESUMEN **29**
ABSTRACT **33**
MOTIVATION **37**
1. GENERAL INTRODUCTION **41**
1.1. CAUSES AND PATHWAYS OF ENVIRONMENTAL POLLUTION **41**
1.2. WATER POLLUTION AND CONTAMINANTS **41**
1.2.1. Heavy metals occurrence and characteristics *42*
1.2.2. Fungi producing toxins *44*
a. Mycotoxins: Structure and toxicity 45
b. Fungi and Mycotoxins contamination risk in drinking waters 48
1.2.3. Remediation techniques *50*
a. Heavy metals removal technologies 50
b. Mycotoxins detoxification techniques 51
c. Biosorption 52
1.2.4. Ability of biosorbents to bind heavy metals and mycotoxins *53*
1.3. BIOMASS: FUTURE RENEWABLE RESOURCE **54**
1.3.1. Lignocellulosic Biomass *54*
a. Valorisation of lignocellulosic Biomass 56
1.3.2. Aquatic biomass *57*
a. Brown seaweed: Simultaneously invasive and environmentally friendly 58
b. Sargassum species main composition 59
c. A valuable source of polysaccharides 59
1.4. THE ROLE OF BIOMASS TO A FUTURE CIRCULAR BIOECONOMY **61**
1.4.1. Fundamental concepts *61*
1.4.2. Benefits and limitations of CBE *62*
1.4.3. Industrial sectors: Economic profit and employment *63*
1.4.4. From biomass into high-added-value nanomaterials *66*
1.5. NANOTECHNOLOGY, NANOMATERIALS, AND NANOPARTICLES **66**
1.5.1. Nanomaterials *67*
a. Naturally occurring nanomaterials 68
1.5.2. Synthetic Nanoparticles *69*
1.5.3. Magnetic nanoparticles structure, properties, and applications *70*
a. Magnetite nanoparticles (Fe_3O_4 NPs) 70
b. Magnetism and magnetic technologies 71
c. Hysteresis loops 72

1.5.4. Magnetic sustainable nanomaterials for environmental remediation and other applications *74*

2. MATERIALS BASED ON THE BLUE ECONOMY CONCEPT FOR CONTAMINANTS ADSORPTION: MAGNETIC BEADS **79**

2.1. ADSORPTION DESIGN: INTRODUCTION **79**

2.1.1. Adsorption isotherm models *80*

2.1.2. Adsorption Kinetic models *82*

2.1.3. Adsorption thermodynamics *85*

2.1.4. Error function analysis *86*

2.2. DEVELOPMENT OF MAGNETIC BEADS AND EXPERIMENTAL PARAMETERS: MATERIAL AND METHODS **86**

2.2.1. Preparation method of the magnetic sodium alginate beads *86*

2.2.2. Mycotoxins experimental Assays: adsorption, desorption, and beer detoxification *88*

2.2.3. Heavy metals: batch (mono, binary, ternary) and desorption experiments *89*

2.2.4. Magnetic sodium alginate beads: Characterizations *91*

2.3. CONTAMINANTS ADSORPTION: RESULTS AND DISCUSSION **95**

2.3.1. Elimination of mycotoxins from water and beverages *95*

a. Ability of magnetic beads to adsorb mycotoxins 96

b. Recovery of mycotoxins from the magnetic beads 100

c. Mycotoxins removal from beer wort 101

2.3.2. Elimination of heavy metal ions from water: Mono, binary, and ternary systems *102*

2.3.2.1. Elimination of Cd(II) ions from water: Study and experimental parameters optimization 103

a. Optimization of experimental parameters (contacting time, adsorbent dosage, agitation speed and type) 103

b. Effect of pH on Cd(II) ions adsorption 106

c. Effect of initial concentration of Cd(II) ions 107

d. Desorption and Reusability 108

e. Adsorption performance 109

2.3.2.2. Elimination of Hg(II) ions from water in a mono and binary system 118

a. Effect of initial metal concentration 124

b. Adsorption performance 125

2.3.2.3. Elimination of a heavy metal's ternary mixture from water 142

a. Determination of optimum pH for Cd(II), Ni(II), and Hg(II) adsorption 147

b. Effect of initial concentration in the mono and ternary system 149

c. Adsorption Performance 152

2.3.3. Application of magnetic alginate beads at Industrial-scale processes *162*

2.4. CONCLUSION **163**

3. FUTURE MATERIALS FROM FOREST-BASED ECONOMY: MAGNETIC MICROFIBERS, FILMS, AND CAPSULES **167**

3.1. FUTURE CHANGES IN THE FOREST SECTOR: INTRODUCTION **167**

3.2. STUDY OF MAGNETIC MICROFIBERS PROPERTIES **169**

3.2.1. Magnetic microfibers: Material and Methods *169*
a. *In-situ* preparation of Fe_3O_4 NPs on TEMPO-oxidized cellulose nanofibers 169
b. *Ex-situ* preparation of Fe_3O_4 NPs for mixing with sodium alginate 170
c. Microfibers spinning: coagulation time and drying process 170
3.2.2. Magnetic microfibers properties: Results and discussion *172*
3.3. FABRICATION OF FLEXIBLE MAGNETIC CELLULOSE ACETATE FILMS 189
3.3.1. Magnetic cellulose acetate films: Materials and Methods *189*
a. Synthesis of Iron carbide (Fe_5C_2), hexagonal-shaped (Fe_3O_4@OA) and multicore magnetite (*m*-Fe_3O_4) NPs 189
b. Production of the magnetic cellulose acetate films 190
c. Relevant parameters for packaging methodologies 191
3.3.2. Magnetic cellulose acetate films: Results and discussion *192*
3.4. FUNCTIONAL MAGNETIC 3D BACTERIAL NANOCELLULOSE CAPSULES 204
3.4.1. Magnetic 3D BNC capsules bio-fabrication: Material and methods *204*
a. Synthesis of magnetite nanoparticles coated with polyacrylic acid (Fe_3O_4@PAA) 204
b. Magnetic 3D BNC capsules preparation and washing 205
3.4.2. Magnetic 3D BNC capsules: Results and discussion *205*
3.5. CONCLUSION 210
4. GENERAL CONCLUSION 215
5. REFERENCES 216
6. APPENDIX 241
6.1. CHARACTERIZATION METHODS 241
6.2. CHAPTER 2: APPENDIX 248
6.3. CHAPTER 3: APPENDIX 280
6.4. FIGURES RIGHTS AND PERMISSIONS 289

USC UNIVERSIDADE DE SANTIAGO DE COMPOSTELA

USC
UNIVERSIDADE
DE SANTIAGO
DE COMPOSTELA

LIST OF ABBREVIATIONS AND ACRONYMS

AC	Activated carbon
AFs	Aflatoxins
AFB_1	Aflatoxin B1
AFB_2	Aflatoxin B2
AFG_1	Aflatoxin G1
AFG_2	Aflatoxin G2
ARE	Average relative error
As	Arsenic
Au	Gold
BE	Bioeconomy
BNC	Bacterial nanocellulose
BET	Brunaer-Emmett-Teller
CA	Cellulose acetate
Ca^{2+}	Calcium ions
CBE	Circular bioeconomy
CE	Circular economy
Cd	Cadmium
Cd(II)	Cadmium ions
CNCs	Cellulose nanocrystals
CNFs	cellulose nanofibers
CNT	Carbon nanotubes
CRG	Carragenate
CTAB	Cetrimonium bromide
Cr	Chromium
CS	Chitosan
Cu	Copper
DKR	Dubinin-Kaganer-Radushkevich
DON	Deoxynivalenol
DOM	Dissolved organic matter
DLS	Dynamic light scattering
Ds	Diameter size
EABS	Sum of the absolute errors
EB	Elongation at break
EEA	European Economic Area
EFSA	European safety authority
e.g.	for example
EQS	Environmental quality standards
ERRSQ	Sum of the Square of the Errors
FAO	Food Agriculture Organization
FB	Fumonisins
FB_1	Fumonisin B1
FDA	US Food and Drug Administration
Fe	Iron
Fe_3O_4	Magnetite (iron oxide)
Fe_3O_4_com	Commercial Magnetite
Fe_5C_2	Iron carbide
FTIR	Fourier transform infrared spectroscopy
IPD	Intraparticle diffusion
G´	Storage modulus
G˝	Loss modulus
GDP	Gross domestic product
GPa	Gigapascal
GO	Graphene oxide
h	hours
HA	Humic acid
Hc	Coercive field
Hg	Mercury
Hg(II)	Mercury ions
HMF	Hydroxymethyl--furfural
HYBRID	Hybrid fractional error function
ICDD	International Centre for Diffraction data
ICP-OES	Inductively coupled plasma optical emission spectroscopy
IR	Infrared
JRC	Joint Research Centre
MAAC	magnetic alginate activated carbon beads
min	minutes
***m*-Fe_3O_4**	multicore-magnetite
MFC	Microfibrillated cellulose
MNPs	Magnetic nanoparticles
Mo	moblidenium
MPa	Megapascal
Mr	Remnant magnetization
Ms	Saturation magnetization
MSPD	Derivative of Marquadt's Percent standard deviation
MW	Molecular weight

USC UNIVERSIDADE DE SANTIAGO DE COMPOSTELA

Ni	Nickel
Ni(II)	Nickel ions
NMs	Nanomaterials
NP/NPs	Nanoparticle /Nanoparticles
OA	Oleylamine
rpm	Revolutions per minute
R_{ku}	Kurtosis
R_q	Root mean squared of the surface roughness
R_{sk}	Skewness
R_t	Total height profile
SA	Sodium alginate
SAR	Specific absorption rate
SAXS	Small-angle X-ray scattering
S_{BET}	BET surface area
SD	Standard deviation
SEM	Scanning electron microscope
SEM-EDX	Scanning Electron Microscopy - Energy Dispersive X-ray spectroscopy
SMEs	Small and medium sized companies
SPIONS	Superparamagnetic iron oxide nanoparticles
t	time
TCTC	Trichothecenes
TEA	Triethylamine
TEM	Transmission electron microscope
TGA	Thermogravimetric analysis
TOCNF	2,2,6,6-tetramethylpiperidine-1-oxyl (TEMPO)-oxidized cellulose nanofibers
TS	Tensile strength
PAA	Polyacrylic acid
Pb	Lead
Pec	Pectin
Pec_est	Esterified pectin
PDI	Polydispersity index
PFO	Pseudo-first order
PMDA	Pyromellitic dianhydride
PSO	Pseudo-second order
PTFE	Polytetrafluoroethylene
FDA	US Food and Drug Administration
V_p	Pore volume
VSM	Vibrating sample magnetometry
XPS	X-ray photoelectron spectroscopy
XRD	Powder X-ray diffraction
WFD	Water framework directive
WHO	World health organisation
WMC	Wooden multistory construction
WTP	Water treatment plants
YM	Young´s modulus
ZEN	Zearalenone
Zn	Zinc

USC UNIVERSIDADE DE SANTIAGO DE COMPOSTELA

LIST OF PUBLICATIONS

1. Puig J., **de Castro Alves L.**, García Acevedo P., Arnosa Prieto A., Yáñez-Vilar S., Teijeiro C., Piñeiro-Redondo Y., Hoppe C., Rivas J., Controlling the structure and photocatalytic properties of three—dimensional aerogels obtained by simultaneous reduction and self-assembly of BiOI/GO aqueous colloidal dispersions. NanoExpress, 2021, 2,2, doi:10.1088/2632-959X/abfd8b

2. **de Castro Alves L**., Yáñez-Vilar S., Piñeiro-Redondo Y., Rivas J., Efficient separation of Heavy Metals by Magnetic Nanostructured beads. Inorganics, 2020, 8, 40, doi:10.3390/inorganics8060040

3. González-Jartín JM., **de Castro Alves L.**, Alfonso A., Piñeiro-Redondo Y., Yañez-Vilar S., González Gómez M., Osorio Vargas Z., Sainz M., Vieytes M., Rivas J., Botana L., Magnetic nanostructures for marine and freshwater toxins removal. Chemosphere, 2020, 256, doi: 10.1016/j.chemosphere.2020.127019

4. Piñeiro-Redondo, Y.; González Gómez M.; **de Castro Alves L.**; Arnosa Prieto A.; García Acevedo P.; Seco Gudiña R.; Puig J.; Teijeiro C.; Yáñez-Vilar S.; Rivas J., Hybrid Nanostructured Magnetite Nanoparticles: From Bio-Detection and Theragnostics to Regenerative Medicine. Magnetochemistry, 2020, 6, doi: 10.3390/magnetochemistry6010004.

5. González-Jartín JM., **de Castro Alves L.**, Alfonso A., Piñeiro-Redondo Y., Yáñez-Vilar S., González Gómez M., Osorio Vargas Z., Sainz M., Vieytes M., Rivas J., Botana L., Detoxification agents based on magnetic nanostructured particles as a novel strategy for mycotoxin mitigation in food. Food chemistry, 2019,294, 60-66, doi: 10.1016/j.foodchem.

6. **de Castro Alves L.**, Yáñez-Vilar S., Piñeiro-Redondo Y., Rivas J., Novel Magnetic Nanostructured Beads for Cadmium(II) Removal. Nanomaterials (Basel). 2019;9(3):356, doi:10.3390/nano9030356.

USC
UNIVERSIDADE DE SANTIAGO DE COMPOSTELA

USC
UNIVERSIDADE
DE SANTIAGO
DE COMPOSTELA

RESUMO

O aumento da poboación mundial está a desencadear unha reacción en cadea de escaseza de recursos, demanda de enerxía e emisións de efecto invernadoiro que provoca o aquecemento global, por iso a sustentabilidade da tecnoloxía que se usa para producir calquera tipo de ben de consumo é un tema de gran relevancia. Isto fai que se precise un maior desenvolvemento de produtos a partires de materiais biodegradables ou a obtención de materiais de alto valor engadido a partires da transformación de materiais de desfeito. Cun enfoque axeitado a biomasa ou os residuos vexetais de diversas actividades industrias (procesos de transformación de alimentos vexetais, residuos de industria madeireira, etc), poden ter unha capacidade significativa para a produción de enerxía ou compostos químicos alternativas para uso industrial.

Neste cambio de paradigma, a nanotecnoloxía, que se ocupa do estudo teórico e desenvolvemento de aplicacións tecnolóxicas dos materiais no rango nanométrico, a mil millonésima parte dun metro, pode ser un aliado que dote ós materiais circulares de funcionalidades engadidas. Entre os desafíos da síntese de materiais nanoestructurados atópase o poder de controlar os tamaños, a composición e a estrutura dos materiais ou producir nanomateriais híbridos que presenten propiedades con propiedades deseñadas a priori. Diversos materiais nanoestruturados son de utilidade na protección medioambiental, tanto na fase de detección e control, como na fase de eliminación de substancias indesexables das augas residuais. A dopaxe de biopolímeros con nanomateriais de baixo custo e escaso impacto ambiental, permite obter materiais multifuncionais para unha variedade de aplicacións, incluíndo o almacenamento de enerxía, a remediación de auga e a nanocatálise.

Nesta Tese desenvólvense materias híbridos e sostibles baseados en biopolímeros dopados con nanopartículas magnéticas de baixo custo e biocompatibles, con diversas morfoloxías (esferas, fibras e filmes), dirixidas para várias aplicacións.

No primeiro capítulo ponse en contexto o problema medioambiental da contaminación das augas: vías, causas e os tipos de contaminantes da auga. Xa que a auga e un compoñente esencial da vida animal e vexetal, a contaminación das augas e un problema medioambiental de alcance planetario. Entre os distintos contaminantes producidos pola acción humana, os hidrocarburos, os fármacos, os microplasticos, os compostos fluorados ou os metais pesados son unha lista curta pero moi representativa do problema. A estes, hai que engadir as micotoxinas, contaminantes naturais producidos por algas, cianobacterias ou fungos, que estimuladas polo quecemento global, teñen una incidencia cada vez maior no medioambiente. As técnicas de uso convencional en limpeza de augas para evitar a contaminación dos recursos naturais (a precipitación química, o intercambio iónico, a filtración por membrana, a coagulación/floculación, os tratamentos electroquímicos e, finalmente, a adsorción) non bastan hoxe en dia para adsorber a cantidade e variedade de especies moleculares que se atopan disoltas nas augas e a adsorción é a preferida debido ao seu baixo custo e fácil manipulación. Actualmente, debido ao aumento da regulamentación ambiental, as empresas comezaron a adoptar esta técnica xa que non é necesario o uso de produtos químicos e o material adsorbente utilizado para o tratamento pódese afinar facilmente con varios compoñentes biocompatibles.

Se ten demostrado a capacidade de numerosos biosorbentes compostos por biomasa e residuos de algas para eliminar micotoxinas e metais pesados da auga. Estes materiais conteñen na súa superficie grupos funcionais cruciais como carboxilos, aminos, hidroxilos e fosfatos. É posible transformar a biomasa residual nunha ampla gama de compostos de alto valor engadido.

Da madeira é posible extraer tres biopolímeros importantes como son a celulosa, a hemicelulosa e a lignina mediante pretratamentos que dan como resultado o aumento do valor do produto final que pode ser utilizado na produción de biocombustibles, encimas, precursores químicos ou mesmo para desenvolver nanomateriais.

Da biomasa acuática, máis concretamente das algas pardas pola súa rica composición en polisacáridos, extráense alxinatos, fucoidanos e tamén celulosa. O alxinato é un biopolímero máis utilizado na industria, cosméticos, produtos farmacéuticos e alimentos xa que pode actuar como estabilizador, emulsionante e como axente encapsulante. Nesta tese tratáronse as necesidades de implantación de materiais de base biolóxica feitos a partir de residuos ou biomasa para unha bioeconomía circular, en base ós beneficios xerais da bioeconomia circular e o beneficio económico por sector/país e o crecemento do valor engadido por sector na UE entre 2008 e 2017.

A hibridación de materiais biopoliméricos con nanopartículas magnéticas, promete o desenvolvemento de novas aplicacións que combinan todo os beneficios da economía circular, as propiedades químicas, mecánicas e estructuráis especificas dos biopolímeros e as funcionalidades magnéticas (hipertermia magnética, manipulación magnética, detección magnética, extracción magnética, etc). En concreto as nanopartículas de magnetita (Fe_3O_4), son fáciles de producir e biocompatibles, e son o material escollido nesta Tesis Doutoral para desenvolver unha serie de materiais híbridos a partir de celulosa, lignina, alxinato sodio, quitosano, etc, en forma de esferas, fibras ou filmes magnéticos para diversas aplicacións.

No segundo capítulo está dedicado ó desenvolvemento, caracterización e uso para adsorción de contaminantes de esferas magnéticas de alxinato, comprobandose:

- A capacidade de adsorción das esferas magnéticas nanoestructuradas para adsorber micotoxinas ou metais pesados. O estudo e desenvolvemento de diferentes composicións de esferas tamén foi un punto de atención, para atopar novas características con maior eficiencia de adsorción de micotoxinas en medios acuosos e mosto de cervexa.
- Despois dunha avaliación da adsorción optimizáronse condicións experimentais como o tempo de contacto, o pH, a concentración inicial de metal, a dosificación do adsorbente, a velocidade de rotación e o tipo para a máxima adsorción de metais pesados disoltos nunha solución acuosa. Dado que as esferas con maior capacidade de adsorción de metais pesados posuían carbon comercial, a súa eficiencia comparouse con outras esferas compostas por carbono mesoporoso CMK-3 nun sistema único, binario e ternario. Conseguise elaborar un material capaz de adsorber de forma eficiente ambos contaminantes de diferentes sistemas contaminados.

As nanopartículas de magnetita foron preparadas previamente mediante procesos de síntese de química húmida (coprecipitación reversa) e serviron para a dopaxe posterior de esferas de alxinato magnético con diferentes composicións, sintetizadas mediante xelificación ionotrópica. Preparáronse diversas composisicións partindo do alxinato de sodio como biopolímero principal, engadindo quitosano, ou pectina esterificada, polas súas propiedades encapsulantes e afinidade con certas micotoxinas. Dopáronse además con diferentes materiais inorgánicos, como o óxido de grafeno, carbon comercial ou carbono mesoporoso CMK-3, e

funcionalizantes como o ácido húmico, o metabisulfito de sodio, sulfito de sodio, con diferentes capacidades de adsorción para calquera dos contaminantes.

Estruturalmente, todas as esferas presentan un tamaño de aproximadamente 2,0 mm de diámetro en condicións húmidas (en seco 1,3 mm) cunha superficie externa rugosa variable en función da composición (nas esferas L3 con carbon comercial observouse a presenza de estruturas en forma de capas). A estrutura, textura, porosidade, morfoloxía, magnetismo, perda de peso das esferas caracterizouse utilizando técnicas de gran resolución (difracción de Raios X, microscopía electrónica, analise elemental, termogravimetría, porosimetría e magnetometría) para analizar a súa capacidade de adsorción, de micotoxinas ou metais pesados, en relación as súas propiedades fisicoquímicas.

En primeiro lugar, estudouse a eficacia de adsorción de varias esferas magnéticas nun sistema multimicotoxina que contén DON, ZEN, FB1 e aflatoxinas (AFB1, AFB2, AFG1 e AFG2) de solucións acuosas e posteriormente de mosto de cervexa. Probouse a eficacia de adsorción das esferas magnéticas en condicións experimentais fixas: tempo de contacto de 180 min e dosificación de adsorbente de aproximadamente 300 mg. As esferas L1 só con alxinato sodio e Fe_3O_4 foron capaces de eliminar as micotoxinas, ZEN e aflatoxinas do 70 % ao 90 %, mentres que só se eliminou o 10% das micotoxinas DON. A adición de carbon comercial ás esferas L3 aumentou a eliminación de DON ata o 54 %. Observouse un comportamento de adsorción diferente, por exemplo nas esferas con sulfito de sodio (L5 e L6), as aflatoxinas reducíronse ao 50 %, mentres que nas esferas L8 (metabisulfito) a redución foi inferior ao 6 %. Pola contra, informouse de que unha redución do 22 % do DON e do 49 % do FB1 por esferas L8 foi o dobre que a observada polas esferas L5 e L6. A incorporación de pectina nas esferas L7 mellorou a eliminación de fumonisinas, as aflatoxinas e as micotoxinas DON reducíronse a un 26,63 %, o que foi o segundo valor máis alto informado. A substitución de esferas de carbon comercial (L3) comerciais por oxido de grafeno (L6) deu lugar a unha redución total da adsorción de micotoxinas do 70 % e do 37 %, respectivamente.

No primeiro lote de partículas (L1-L9), as micotoxinas DON foron máis adsorbidas polas esferas L3 e L7. Para conseguir unha maior redución das micotoxinas DON formulouse un novo conxunto de esferas cunha composición mixta de carbón comercial e pectina esterificada (L10-L12). No segundo conxunto de partículas observouse que un incremento de carbón comercial e pectina esterificada favoreceu a eliminación de toda a micotoxina, en especifico DON.

Tamén se observou, a mesma capacidade de eliminación de micotoxinas, utilizando 900 mg esferas ben en solución acuosa ou en mosto de cervexa. Usando 900 mg de esferas L3, eliminouse un 79 % e un 69 % de AFB1, mentres que, polas esferas L7, eliminouse un total do 62 % e un 60 % do mosto de cervexa e da auga, respectivamente. Tamén se avaliou a recuperación total de micotoxinas, revelouse unha maior taxa de recuperación no primeiro conxunto de partículas, que conteñen alxinato de sodio, como biopolímero principal, ao contrario do segundo conxunto de partículas con pectina esterificada e alxinato sodio.

En segundo termo, analizouse a eficacia de adsorción de esferas para os ións metálicos de Cd(II), Ni(II) e Hg(II) nun sistema único, binario e ternario en diversas condicións ambientais. Como resultado do primeiro estudo, seleccionouse a esfera magnética con maior potencial de adsorción para os próximos estudos de adsorción de metais pesados. A eliminación por adsorción de Cd(II) polas esferas L3 nun único sistema estudouse con parámetros experimentais optimizados previamente. Despois da avaliación da viabilidade, que permitiu seleccionar parámetros relevantes como o tempo de contacto, a dosificación do adsorbente, o pH, o tipo de axitación e a velocidade. Tamén se estudou o efecto da concentración inicial de metal, o equilibrio de adsorción, a cinética e a termodinámica do proceso de adsorción. Os resultados

mostraron que se favorece a adsorción de Cd(II) ao utilizar os seguintes parámetros experimentais: pH de 6,5, axitación magnética de 300 rpm en 1 h de tempo de contacto con só 14 mg de adsorbente.

Pola contra, observouse unha diminución da eficiencia de eliminación de Cd(II) polas esferas L3 co aumento da concentración inicial de cadmio na solución. Isto debeuse aos sitios de adsorción de saturación das esferas L3 ao longo do proceso de adsorción, o que provocou unha redución da absorción co aumento da concentración inicial de Cd(II). O mellor modelo de isoterma e cinética de adsorción determinouse coa axuda de funcións de erro calculadas na forma lineal e non lineal dos modelos. Dado que a transformación dos modelos non lineais pode levar a certos erros, como unha mala linealidade e altos coeficientes de regresión lineal. A partir dos erros calculados, concluíuse que a adsorción de equilibrio de Cd(II) foi mellor descrita polos modelos de Freundlich e Dubinin-Kaganer-Radushkevich (DKR, sigla en ingles). Estes modelos afirman que a adsorción de Cd(II) foi de natureza física, producíndose a nivel multicapa na superficie heteroxénea das esferas que á súa vez contén diferentes sitios de adsorción, afinidade e calor.

Para comprender mellor a cinética de adsorción de Cd(II) sobre as esferas L3 estudouse a taxa de adsorción e os mecanismos nas concentracións iniciais de metais de 70, 150 e 230 mg/L. Observouse que na concentración inicial máis baixa, a adsorción estaba dominada principalmente por forzas físicas, descríbese mellor polo modelo de pseudo-primeira orde (PFO sigla en ingles). Mentres tanto, nas concentracións máis altas, a adsorción describiuse como o modelo de pseudo-segunda orde (PSO, sigla en ingles) confirmado polo modelo de Elovich que afirma que se produciu a adsorción química. Unha análise posterior da cinética de adsorción mediante o modelo de difusión interpartículas (IPD, sigla en ingles) afirmou que a adsorción xeral estaba controlada principalmente pola difusión da película.

O efecto da temperatura foi outro parámetro importante avaliado na eliminación de Cd(II) da solución acuosa nas concentracións iniciais de metais de 70, 150 e 230 mg/L usando as temperaturas de 25 °C, 30 °C e 40 °C. Os valores negativos de ΔG suxeriron que a adsorción era máis espontánea a temperaturas máis altas e de natureza física.

A reciclaxe de calquera material é unha vantaxe económica importante e, como ocorre coas micotoxinas, avaliouse a recuperación de Cd(II) das esferas L3 rexeneradas como a súa reutilización para procesos posteriores de adsorción. O Cd(II) foi desorbido con éxito das esferas L3 cunha capacidade de desorción máxima do 90 % e foi posible reutilizar as esferas sucesivamente durante cinco ciclos de adsorción-desorción sen danos estruturais.

A extensión de adsorción desta esfera foi probada nun sistema binario e comparouse con outras esferas compostas de carbono mesoporoso CMK-3 (L13) e cunha esfera de control sen ningún composto activo (L16). A mesma esfera podía eliminar eficazmente o Hg(II) dun só sistema e era a que tiña maior capacidade de adsorción no sistema binario (Hg(II)-Cd(II), Hg(II)-Ni(II)). Pola contra, a adsorción de Hg(II) ións mellorou máis co aumento da temperatura, onde os valores de entalpía e entropía indicaban que a adsorción era endotérmica cunha maior aleatoriedade na interface sólido-líquido. Tamén se observou que un incremento de temperatura aumentou a mobilidade dos ións unidos fisicamente para ser liberados da superficie das esferas L13 ao medio acuoso.

Avaliouse a competencia dos ións metálicos no sistema binario e demostrouse que a adsorción de Hg(II) mellorou dalgún xeito. A principal vía de adsorción foi a presenza de grupos carboxílicos na superficie das esferas e o intercambio iónico entre os ións Hg(II) e Ca(II) da solución.

USC DE SANTIAGO DE COMPOSTELA

A capacidade de adsorción destas esferas estudouse en profundidade nun sistema ternario xa que é unha condición que se espera que se atope no medio real con máis probabilidade. A eliminación de ións metálicos Cd(II), Ni(II) e Hg(II) nun sistema mono e ternario foi probada polas esferas L3 e L13T. Este último tamén está composto por carbono CMK-3, pero foi preparado recentemente sen ningún residuo de sílice e cunha estrutura ben ordenada de canales interconectados. Ao contrario do que se mostraba no sistema binario, as esferas L13T demostraron ser un nanomaterial excepcional que adsorbía cen veces máis metais pesados en ambos os sistemas que as esferas L3. Ademais, tamén se obtivo menores capacidades de adsorción no sistema ternario debido ao efecto de competencia entre todos os ións metálicos.

No terceiro capítulo, presentase a preparación e aplicacións futuras de materiais magnéticamente porosos e morfoloxicamente diferentes (microfibras, películas e cápsulas) a base de nanofibras TEMPO de celulosa oxidada (TOCNF, sigla en ingles), nanocelulosa bacteriana (BNC, sigla en ingles) e acetato de celulosa (CA), respectivamente analizando:

- A incorporación de nanopartículas magnéticas e os cambios fisicoquímicos que se produzan a nivel de nanofibras de celulosa.
- Os efectos causados nas propiedades estruturais, mecánicas e químicas dos materiais desenvolvidos. Especificamente, estudáronse as propiedades mecánicas, das microfibras magnéticas TOCNF e os filmes de acetato de celulosa, con e sen incorporación de nanopartículas magnéticas.
- Diferentes procedementos de síntese para preparar as nanopartículas magnéticas e a súa influencia na magnetización e distribución das nanopartículas dentro das fibras de nanocelulosa/celulosa.
- No que respecta ao filmes magnéticos de CA, e para posibles futuras aplicacións de envasado de alimentos, consideráronse os aspectos de durabilidade, permeabilidade, solubilidade, resistencia mecánica e contido de humidade. Aplicáronse metodoloxías para valorar o seu uso como material de envasado: a solubilidade, o contido de humidade e cambio de cor. O efecto sobre as propiedades de resistencia mecánica foi un punto importante avaliado nos filmes (con e sen dopaxe de nanopartículas) tanto en mostras recen preparadas como en outras almacenadas durante máis de 90 días .
- Nas cápsulas magnéticas de BNC, avaliouse a magnetización e a resistencia térmica deste material tras un período de almacenamento de 0 días a 2 anos.

As microfibras magnéticas preparáronse mediante dous métodos diferentes: con dopaxe magnético *in-situ* (co-sintetizando as nanopartículas de magnetita nunha solución de TOCNF) e *ex-situ* (engadindo partículas de magnetita previamente sintetizadas), co fin de avaliar o grado de distribución e calidade das nanopartículas de magnetita no material híbrido, e atopar procedementos de síntese sinxelos e de baixo custo para a súa aplicación industrial. Analizóuse o procedemento de unión e incorporación de diferentes nanopartículas magnéticas e o seu impacto nas modificacións físico-químicas das nanofibras. Ademais, observouse unha diminución das propiedades mecánicas coa incorporación da nanopartícula nas microfibras e nos filmes de CA. Mentres tanto, a presenza de cuberta de TOCNF nalgunhas microfibras mostrou unha gran resistencia mecánica e aumento da resistencia á tracción. As propiedades mecánicas están notablemente influenciadas pola relación entre a matriz de celulosa e as nanopartículas magnéticas. As propiedades magnéticas sen embargo, vénse moi afectadas polo método de preparación. No procedemento de dopaxe *in-situ*, a formación das nanopartículas de magnetita vénse afectadas pola presencia dos compoñentes das fibras e como resultado os

cristais de magnetita son máis pequenos, de calidade cristalina baixa e magnetización moi reducida.

Preparáronse diferentes filmes magnéticos utilizando nanopartículas de carburo de ferro (Fe_5C_2), e Fe_3O_4, de diferentes tamaños. A dopaxe fíxose neste caso *ex-situ*, para garantizar a calidade magnética dos materiais, tal e como se confirmou mediante as medidas de magnetometria. Ademáis avaliouse a rugosidade dos materiais para valorar o seu uso como material de embalaxe alternativos ós derivados do petróleo. Observouse, que a dopaxe con Fe_5C_2 produce filmes menos rugosos, con menor posibilidade de anclaxe de bacterias. Ademáis a captación de humidade e o color dos filmes magnéticos co paso do tempo é algo mais elevado que nos filmes sen dopar de acetato de celulosa. En xeral, a presenza de nanopartículas actuou como unha barreira para a luz solar aumentando a opacidade dos filmes de CA.

Finalmente, preparáronse cápsulas magnéticas de BNC, nas que se incorporaron as nanopartículas magnéticas ao medio de cultivo de bacterias produtoras de BNC. Como resultado obtivéronse cápsulas magnéticas, sen alteración na morfoloxía ou tamaño, respecto ás cápsulas sen dopar, con unha resposta magnética adecuada para a súa manipulación magnética. A porosidade e estrutura interna da rede de nanocelulosa, modificouse pola presenza das nanopartículas. As cápsulas, alamacenadas durante mais de dous años en auga, mostraron resultados prometedores de resistencia térmica e conservaron as propiedades magnéticas.

O desenvolvemento e caracterización dos materiais que se presentan nesta tese demostra que a combinación de biopolímeros e nanotecnoloxía permite a obtención de materiais magnéticos de baixo impacto ambiental capaces de substituír os materiais de uso convencional obtidos do petróleo.

USC
UNIVERSIDADE DE SANTIAGO DE COMPOSTELA

USC
UNIVERSIDADE
DE SANTIAGO
DE COMPOSTELA

USC
UNIVERSIDADE
DE SANTIAGO
DE COMPOSTELA

RESUMEN

Uno de los mayores desafíos es controlar la cantidad de residuos generados durante las actividades industriales, domésticas, agrícolas y el uso de combustibles fósiles. El agua se ve fuertemente afectada por varios contaminantes como resultado de estas actividades se vuelve no apta para el consumo. Entre los diversos contaminantes, los metales pesados requieren especial atención debido a su no biodegradabilidad y acumulación incluso en concentraciones más bajas que causan efectos tanto agudos como crónicos.

La adsorción demostró ser una tecnología eficiente y rentable, especialmente en la eliminación de contaminantes de soluciones diluidas. Teniendo esto en cuenta, se están desarrollando nuevos nanomateriales ecológicos con propiedades de adsorción.

La presente Tesis doctoral se centra en el desarrollo de materiales nanoestructurados con propiedades magnéticas combinando biopolímeros naturales de origen marítima (p. ej., alginato), de origen vegetal (p. ej., pectina, celulosa, lignina) y de origen animal (p. ej., quitosano) para diseñar materiales magnéticos híbridos nanoestructurados. La idea es generar materiales biocompatibles, reutilizables y amigables con el medio ambiente, de fácil manipulación magnética para su posterior uso en diversas aplicaciones.

La Tesis doctoral se divide en tres secciones principales importantes. Inicialmente, se proporcionó información detallada sobre las causas y las vías de la contaminación ambiental, incluido los principales contaminantes del agua y una imagen detallada de las tecnologías de tratamiento del agua y cómo beneficiarse de los residuos derivados de la industria y otros. Además de esto, se abordaron conceptos básicos de magnetismo y nanomateriales magnéticos actuales desarrollados para la remediación ambiental.

En la segunda parte, se prepararon esferas magnéticas de alginato de sodio con propiedades físicas, químicas y magnéticas únicas con alto potencial para eliminar contaminantes del agua y de productos alimenticios. Este material es muy versátil con una producción rentable, y lo más importante es que se puede funcionalizar con varios compuestos para aumentar su afinidad con varios contaminantes. Se ha estudiado su viabilidad para eliminar metales pesados (cadmio, mercurio y níquel) y micotoxinas (aflatoxinas, deoxinivalenol, zearalenona y fumonisinas) de soluciones acuosas mediante el método de adsorción.

Inicialmente, se probó la eficiencia de adsorción de varias esferas magnéticas con diferente composición para la eliminación de micotoxinas de soluciones acuosas y del mosto de cerveza contaminado. Los resultados mostraron que varios parámetros como la composición del adsorbente, la dosis y el tiempo son factores importantes para una alta adsorción de micotoxinas de ambos sistemas. La máxima capacidad de adsorción se observó cuando se utilizaron esferas magnéticas de alginato con carbón activado comercial, denominadas como esferas L3. Por esta razón, se estudió la eficiencia de la misma esfera para remover metales pesados en un sistema mono, binario y ternario.

En una primera evaluación, se optimizaron varios parámetros experimentales mediante series de adsorción por lotes de iones de cadmio. Después de la evaluación de viabilidad, que permitió la selección de parámetros relevantes como tiempo de contacto, dosificación de adsorbente, pH, tipo de agitación y velocidad. Se estudió el efecto de la concentración inicial del metal, el equilibrio de adsorción, la cinética y la termodinámica del proceso de adsorción. Los resultados mostraron que la adsorción de cadmio se vio favorecida al utilizar los siguientes parámetros experimentales: pH de 6.5, agitación magnética de 300 rpm bajo 1 h de tiempo de contacto con solo 14 mg de dosis de adsorbente.

El grado de adsorción de esta esfera se probó en un sistema binario y se comparó con otras esferas compuestas de carbón mesoporoso CMK-3 (L13) y con una esfera de control sin ningún compuesto activo (L16). La misma esfera, fue capaz de remover eficientemente el mercurio de un sistema mono y tuve mayor capacidad de adsorción en el sistema binario (Hg(II)-Cd(II), Hg(II)-Ni(II)). Se evaluó la competencia de los iones metálicos en el sistema binario y se demostró que la adsorción de mercurio mejoró de alguna manera. La principal vía de adsorción fue la presencia de grupos carboxílicos en la superficie de las esferas y el intercambio iónico entre los iones Hg(II) y Ca(II) de la solución.

La capacidad de adsorción de estas esferas se estudió más a fondo en un sistema ternario, ya que es una condición que probablemente se espera encontrar en el medio ambiente. La eliminación de iones metálicos de cadmio, níquel y mercurio en un sistema mono y ternario fue testada por las esferas L3 y L13T. Esta última esfera también está compuesta por el carbón mesoporoso, CMK-3, pero se preparó recientemente sin ningún residuo de sílice y con una estructura bien ordenada de canales interconectados. Al contrario de lo que se obtuvo en el sistema binario, las esferas L13T demostraron ser un nanomaterial excepcional que adsorbe cien veces más metales pesados en ambos sistemas que las esferas L3. Además, también se obtuvieron menores capacidades de adsorción en el sistema ternario debido al efecto de competencia entre todos los iones metálicos.

En la tercera parte de esta Tesis doctoral, tres tipos de nanocelulosas/celulosa, (TEMPO, sigla en inglés)-nanofibras de celulosa oxidada (TOCNF, sigla en inglés), nanocelulosa bacteriana (BNC, sigla en inglés), y acetato de celulosa (CA, sigla en inglés) en los que se incorporaron nanopartículas magnéticas para lograr diferentes tipos de materiales porosos magnéticamente funcionales (microfibras, filmes y cápsulas). Se mostró la unión e incorporación de diferentes nanopartículas magnéticas y su impacto en las modificaciones físico-químicas de las nanofibrillas. Además, también se demostró la disminución de las propiedades mecánicas tanto de los filmes magnéticos de acetato de celulosa como de las microfibras. Mientras tanto, la cubierta de TOCNF en algunas microfibras ha mostrado una gran resistencia mecánica y una mayor resistencia a la tracción. Las propiedades mecánicas están notablemente influenciadas por la proporción de matriz de celulosa y nanopartículas magnéticas. Sin embargo, la presencia de nanopartículas incorporadas hace como una barrera para la luz solar aumentando la opacidad de los filmes de celulosa de acetato. Se informaron resultados prometedores de resistencia térmica y propiedades magnéticas conservadas en cápsulas de celulosa bacteriana almacenadas durante más de dos años.

Por lo tanto, esta Tesis doctoral proporciona una visión de caminos novedosos para la producción y aplicación de materiales magnéticos de alginato/nanocelulosa. Contribuyendo a un futuro con nanomateriales sustentables para múltiples aplicaciones, siendo una alternativa adecuada para reemplazar productos derivados del petróleo.

USC
UNIVERSIDADE DE SANTIAGO DE COMPOSTELA

USC
UNIVERSIDADE
DE SANTIAGO
DE COMPOSTELA

USC
UNIVERSIDADE
DE SANTIAGO
DE COMPOSTELA

ABSTRACT

One of the most significant challenges is to control the amount of generated waste during industrial, domestic, and agricultural activities and the use of fossil fuels. Water is heavily affected by several contaminants and becomes unsuitable for consumption due to these activities. Among the several pollutants, heavy metals require special attention due to their non-biodegradability and accumulation even at lower concentrations causing both acute and chronic effects. Adsorption proved to be an efficient and cost-effective technology, especially in removing contaminants from diluted solutions. Having this in mind, newly environmentally friendly nanomaterials with adsorptive properties are being developed.

The present PhD thesis is focused on the development of nanostructured materials with magnetic properties combining natural biopolymers of algae origin (e.g., alginate), plant origin (e.g., pectin, cellulose, lignin), and animal origin (e.g., chitosan) to design functional magnetic hybrid nanostructured materials. The idea was to come up with biocompatible, reusable, and environmentally friendly materials with easy magnetic manipulation for posterior use in several applications.

The PhD Thesis is divided into three main important sections. Initially, it is provided detailed information on the causes and pathways of environmental pollution, including the primary water contaminants and a clear picture of the water treatment technologies and how to benefit from residues derived from industry and others. Besides this, it was approached basic concepts of magnetism and current magnetic nanomaterials developed for environmental remediation.

In the second part, it was prepared magnetic alginate beads with unique physical, chemical, and magnetic properties with a high potential to remove contaminants from water and food products. This material is highly versatile with cost-effective production and, most importantly, is easily tailored with various compounds to increase their affinity to several contaminants. The feasibility of removing heavy metals (cadmium, mercury, and nickel) and mycotoxins (aflatoxins, deoxynivalenol, zearalenone, and fumonisins) from aqueous solutions has been studied by the adsorption method.

Initially, it was tested the adsorption efficiency of several magnetic beads with different compositions for mycotoxins in aqueous solutions and contaminated beer wort. The results showed that several parameters such as adsorbent composition, dosage, and time are important factors for the high adsorption of mycotoxins from both systems. The maximum adsorption capacity was observed using magnetic alginate beads with commercial activated carbon, L3 beads. For this reason, the efficiency of the same bead was studied to remove heavy metals in a single, binary, and ternary system.

In a first assessment, several experimental parameters were optimized by batch adsorption series of cadmium metal ions. After the viability assessment, which allowed the selection of relevant parameters such as contact time, adsorbent dosage, pH, agitation type, and speed. The effect of the initial metal concentration, adsorption equilibrium, the kinetics and the thermodynamic of the adsorption process was studied. The results showed that cadmium adsorption was favoured when using the following experimental parameters: pH of 6.5, magnetic agitation of 300 rpm under 1 h of contacting time with only 14 mg of adsorbent dosage.

The adsorption extent of this bead was tested in a binary system and compared with other beads composed of CMK-3 mesoporous carbon (L13) and with a control bead without

any active compound (L16). The same bead could efficiently remove mercury ions from a mono system and was the one with higher adsorption capacity in the binary system (Hg(II)-Cd(II), Hg(II)-Ni(II)). The competition of the metal ions in the binary system was assessed, and it was shown that mercury adsorption was somehow enhanced. The main adsorption route was the presence of carboxylic groups on the beads surface and ion exchange between Hg(II) and Ca(II) ions from the solution.

The adsorption capacity of these beads was further studied in a ternary system since it is a condition that is probably more expected to find in the environment. The removal of Cd(II), Ni(II), and Hg(II) metal ions in a mono and ternary system was tested by the L3 and L13T beads. The L13T bead contains a newly prepared CMK-3 carbon with no silica residues and a well-ordered structure of interconnected channels. Contrarily to what was shown in the binary system, the L13T beads proved to be an exceptional nanomaterial adsorbing a hundred times more heavy metals in both systems than the L3 beads. Furthermore, it was also obtained lower adsorption capacities in the ternary system due to the competition effect between all metal ions.

In the third part of this PhD Thesis, three types of nanocelluloses/cellulose (TEMPO)-oxidized cellulose nanofibers (TOCNF), bacterial nanocellulose (BNC), and cellulose acetate (CA) were used and incorporated magnetic nanoparticles to achieve different types of magnetically functional porous materials (microfibers, films, and capsules). It was shown the binding and incorporation of different magnetic nanoparticles and their impact on the nanofibrils physicochemical properties. Furthermore, it was also shown the decreased mechanical properties of both magnetic cellulose acetate films and microfibers. Meanwhile, the TOCNF shell on some microfibers has shown great mechanical strength and increasing tensile strength. The mechanical properties are remarkedly influenced by the ratio of cellulose matrix and magnetic nanoparticles. However, the presence of nanoparticles acted as a barrier to sunlight, increasing the opacity of the cellulose acetate films. Promising results of thermal resistance and conserved magnetic properties were reported by bacterial nanocellulose capsules stored for over two years.

Thus, this PhD Thesis provides an insight into novel pathways for the production and application of magnetic alginate/nanocellulose materials contributing to a future with sustainable nanomaterials for several applications, being a suitable alternative´ to replace the petroleum-based product.

USC
UNIVERSIDADE DE SANTIAGO DE COMPOSTELA

USC
UNIVERSIDADE
DE SANTIAGO
DE COMPOSTELA

USC
UNIVERSIDADE
DE SANTIAGO
DE COMPOSTELA

MOTIVATION

Nowadays, society is facing many challenges concerning the increase in pollution, energy demand, food availability, and many others. The need of manufacturing large amounts of products using large quantities of fuel, chemicals, and other materials from fossil resources to meet the world population's requirements is causing serious environmental problems. Global warming caused by greenhouse gas emissions, is modifying the climate patterns, augmenting the negative effect of persistent toxic compounds in a large variety of ecosystems and human life. Therefore, it is required to develop new sustainable routes to replace fossil resources with renewable ones, and recover and reuse biodegradable waste.

In this regard, the circular bioeconomy appears as a sustainable model of production and consumption that can help us do much more with much less. It can help us to limit our overall demand for resources per capita and ensure enough resources for future generations.

Circular economy seeks to reduce material losses and bringing residues into a new material loop. The idea is to successfully recover residual waste and develop sustainable materials with added value.

In this context, the use of Forest and Ocean biomass (in particular, cellulose and sodium alginate) offer an alternative to fossil resources for developing green materials with diverse applications, and are being tested, due to their capability and affinity to eliminate contaminants such as heavy metals, toxins, and organic pollutants from water and food products.

Coupling nanomaterials with biopolymers, to create efficient and sustainable products may produce high added value products. Specifically, incorporating magnetic nanoparticles provides an easy separation procedure for magnetic hybrids after post-treatment, reducing energy consumption during and after the treatments. On top of this, all the recovering processes, production of the magnetic biobased materials, and cleaning treatments are contributing to a more sustainable circular bioeconomy.

Thesis objectives

Having in mind the above framework, the main objective of the present work was to develop morphologically different magnetic nanomaterials with biodegradable polymers extracted from Forest or Ocean residual biomass for environmental remediation and other applications. The capability and affinity of some of these materials was investigated to remove heavy metal ions and mycotoxins from water solutions and food products. Aside from this, it was also studied the incorporation effect of magnetic nanoparticles in the different materials. In order to achieve this general objective, this work was divided into two main parts with the following specific objectives.

Specific objectives regarding the mycotoxins and heavy metal ions adsorption process using the magnetic sodium alginate beads

1. Test the magnetic nanostructure sodium alginate beads adsorption capacity to adsorb either mycotoxins or heavy metals.
2. Use different compositions to find new features and efficiencies in the mycotoxins biosorption from water or beer wort.
3. Investigate the best experimental conditions, including contact time, pH, initial concentration, adsorbent dosage, rotating speed, and heavy metal adsorption type.

4. The beads' efficiency composed of two different carbons to adsorb in a mono, binary, and ternary system (Cd(II), Hg(II), and Ni(II) metal ions).
5. To characterize the magnetic sodium alginate beads using VSM, SEM, TEM, RAMAN, XRD, FTIR, and XPS techniques.

Specific objectives regarding the materials (microfibers, films, and capsules) made of cellulose or nanocellulose

1. The binding and incorporation of magnetic nanoparticles within the cellulose network.
2. Mechanical properties of the developed materials (microfibers and films) with and without the incorporation of magnetic nanoparticles.
3. Influence of the nanoparticle's synthesis method in the magnetization and nanocellulose fibrils coordination and structure.
4. Study of colour change, solubility, and mechanical resistance of films with and without nanoparticles.
5. Assessment of magnetization, thermal resistance, and morphology of bacterial nanocellulose capsules after 2 years stored.
6. Study the physicochemical, mechanical, morphological, and magnetic properties using VSM, SEM, FTIR, XRD, confocal microscope, RAMAN, TEM, profilometer, rheometric, and colorimetry techniques.

USC UNIVERSIDADE DE SANTIAGO DE COMPOSTELA

Chapter 1

USC
UNIVERSIDADE
DE SANTIAGO
DE COMPOSTELA

USC
UNIVERSIDADE
DE SANTIAGO
DE COMPOSTELA

1. General Introduction

1.1. Causes and pathways of environmental pollution

Environmental pollution can be defined as the presence of an undesired agent that can harm either the environment or human health. Pollutants can take many forms due to both natural and human activities. The whole process of pollution can be represented as a causal chain, starting from the source, transportation through many routes, and finally, the resultant effect from the direct contact with the pollutant. Most pollutants are of human origin and are derived from industry, transportation, domestic activities, waste disposal, agriculture, or energy production [1]. Also, natural resources are a significant source of pollution. Rocks are composed of various minerals, and some are found in relatively high concentrations, such as uranium, thorium, and potassium, which are naturally radioactive. For example, the natural decay of uranium 238 ends up forming radon-222, the most common radionuclide found in building materials [2]. Heavy metal ions accumulate in soils and sediments from ore-bearing rocks [3]. For instance, arsenic is one of the most found metals in Earth's crust, transformed into highly volatile and soluble species released into groundwaters [4].

From a global perspective, anthropogenic activities play an important role in diffusing heavy metal ions and other pollutants into the hydrosphere, pedosphere, and atmosphere [4]. Despite the increasing efforts to reduce pollution, it is still insufficient to balance the enormous amount of contaminants released to the environment by human activities. The lack of good practices such as poor sanitation, inadequate wastewater management, and contaminated water effluents [1] have enormous consequences on a global scale. The impact fostered by climate change can be seen in biodiversity loss, changes in the nitrogen and phosphorus cycles, ocean acidification, aerosols, and chemical pollution [5–7]. Once released into the environment, pollutants are transported through different pathways, often moving from one medium to another while undergoing chemical modifications.

Atmospheric transport is recognized as the primary method of global distribution and entrance into the food chain. Although some pollutants reside mainly in the soil, a small portion volatilizes to the atmosphere. During transportation, these pollutants are attached to the atmosphere and transferred back to the ground through wet and dry deposition [8]. The transport of pollutants in water can occur by particulate organic matter binding or, depending on the pollutant solubility, dissolved into the media. Discharged into surface waters, by spillage or leakage, and in groundwaters, by runoff of agricultural chemicals (such as pesticides, fertilizers, insecticides, and herbicides). In soils, pollutants after deposition from either the atmosphere or through the deliberated transport processes become bioaccumulated in the vegetation and available to animals. Thus, the food chain becomes the primary human exposure pathway for most global pollutants [8].

1.2. Water pollution and contaminants

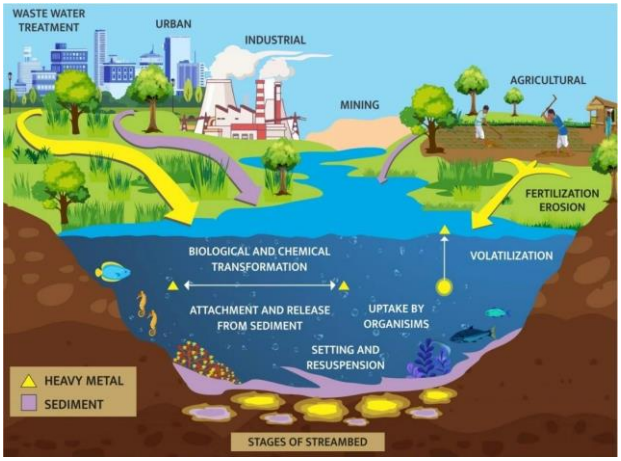
Water is one of life's most critical essential elements. Unfortunately, due to the increase in population and industrialization, water reservoirs are being overexploited and becoming a worldwide serious problem. It is already well known how pollutants enter water bodies, which typically happens by the improper disposal of hazardous materials and chemicals from industrial companies' oil tankers, the direct disposal of garbage due to incorrect human habits, or inadequate agriculture practices. The nature of pollutants varies according to the source. In

agriculture, the excessive use of fertilizers, pesticides, and herbicides at wrong times of the year can contribute to their transportation on rainy days or by excessive water irrigation, delivering a cocktail of pollutants to nearby water streams. As a result of the runoff, direct or unintentional dumping of contaminants, carrying a high concentration of chemicals, nutrients, heavy metal ions, pathogens, and plastics are washed into streams, rivers, lakes, creeks, and, from there, to the ocean. The nutrient enrichment and the increasing temperature due to the carbon dioxide emissions cause the overgrowth of harmful algae blooms that produce toxins responsible for mass mortality of aquatic and vertebrate populations [9].

Plastics, deposited for many years in the oceans, are disintegrated into tiny particles by exposure to environmental factors, mainly sun radiation and mechanical erosion from the ocean waves [10]. Microplastics are a secondary product formed by the degradation of larger plastics but are also present in care products and cosmetics (such as toothpaste, shower gel, peeling) that inevitably end up drained into the sewage system [11]. Since the microplastics range size is below 500 µm, the wastewater treatment plants are not well prepared and equipped to remove these tiny particles. Eventually, they end up in the natural cycle of water being ingested by many fish and shellfish species [11, 12].

Also, pharmaceuticals can enter into water bodies and bioaccumulate, affecting abiotic and biotic systems [13]. Finally, heavy metal ions were listed as one of the most priority contaminants in the EU legislation [14]. Heavy metal ions are known to be naturally occurring elements and also the product of anthropogenic activities which are introduced into water by several processes. Metal ions can be carried out for several miles from the source as gaseous or particulate matter. Due to their chemical reactivity and non-degradable state, metals have been shown to cause acute and, as well, chronic poisoning in humans and animals through their bioaccumulation in the food chain [15, 16]. Water decontamination is a crucial process that should be rapidly addressed to prevent and eliminate those contaminants to guarantee potable drinking water for the next generations.

1.2.1. Heavy metals occurrence and characteristics



USC UNIVERSIDADE DE SANTIAGO DE COMPOSTELA

Figure 1.1 Sources of heavy metals in water (Reproduced with permission from reference [17], *U.S. Geological Survey*).

As shown in Table 1.1, cadmium (Cd), copper (Cu), and lead (Pb) are the most abundant heavy metal ions present in rivers observed in different countries. However, mercury (Hg), arsenic

(As), nickel (Ni), cadmium (Cd), and chrome (Cr), although being in moderate concentrations, cause high toxicity. The remaining contaminant metals, such as iron (Fe), zinc (Zn), and copper (Cu), can be beneficial for plant growth and development when found in limited amounts [18]. Rivers are the primary source of drinking water, and their quality is assessed and extensively studied to limit the contamination concentrations to a minimum and prevent harmful effects, as shown in Figure 1.1.

The European water framework directive (European WFD) is the most significant mark in the European Union (EU) on water legislation, which has the aim of intensifying the monitoring of pollutants in ecosystems and the contaminant's control release in water [14]. The directive of 2008 (Directive 2008/105/EC, 2008 [19] updated in 2013 (Directive 2013/39/EU, 2013 [20] identified new priority substances/classes (PSs) and old environmental quality standards (EQS) were revised. The Directive 2013/39/EU included a list of 45 PSs (41 organic substances or classes and four metals, namely Cd, Hg, Pb, and Ni) and other pollutants (n=8) with EQS to be defined or revised. The directive calls attention to the monitorization of these compounds in surface waters within the EU, which pose serious environmental hazards.

Table 1.1. Sources and heavy metals found in rivers from several countries

Sources	Heavy metals	Location	References
Industrial waste	Cd, Pb, Zn, Cu	Latvia	[21]
Mining	As, Cu, Pb, Hg, Mo	Chile	[22]
Agricultural activities (fertilizers and pesticide use), airborne sources (vehicle emissions) and sewage sludge	Cd, Cu, Pb, Zn	Thohoyandou (South Africa)	[23]
Agriculture, industrial (cork, paper, textile production) and Metallurgical activities	Zn, Cu, Pb, Cr	Portugal	[24]
Pharmaceutical and textile waste	Cd, Ni, Fe	India	[25]

Table 1.2 shows three of the most priority metals listed by the European-WFD and their respective legal concentrations by the EU standards, the health effects by exposure, and main contamination sources.

- **Cadmium** is used in industrial processes as an anti-corrosive agent, stabilizer in PVC products, or the fabrication of nickel-cadmium batteries [26]. The legal EU benchmark for Cd in drinking water or surface and groundwaters is 0.05 mg/L [27]. Long-term exposure at levels above the maximum contaminant level (MCL), Cd can cause the chronic potential to kidney failure skeletal and blood damage [27].

- **Mercury** is a highly volatile toxic metal in the atmosphere as vapor form. The primary sources of Hg contamination are fossil fuel burning, erosion of natural sources, and agricultural waste (such as pesticides) [8]. The toxicity of Hg depends on which elemental form, inorganic or organic Hg compounds, are found. After deposition into the water, Hg is methylated into methylmercury by sulfur and iron-reducing bacteria living in the water bodies [28]. Methylmercury bioaccumulates in aquatic organisms, namely shellfish and fish, which may impact human health. The consumption of contaminated food by several forms of Hg above (0.05 mg/L EU standard) can lead to serious neurological effects, gastrointestinal disorders, or even death [16].

- **Nickel**, among the three metals, exists at deficient levels in the environment. It is used to produce alloys and superalloys, such as pipes and household fittings [29]. The primary source of nickel contamination in drinking water is leaching from pipes. If nickel uptake is too significant (>> 0.04 mg/L EU standard), there are higher chances of cancer development, whereas, in small quantities, it can result in hair loss, hypersensitivity, and skin irritations [16].

Removal of these heavy metals from any water bodies is crucial for the wellbeing of the environment, animals and human population.

Table 1.2. Sources, potential damage and EU standard limits of cadmium, mercury and nickel metal ions.

Metal contaminant	EU standards (mg/L)	Health effects by exposure beyond the desirable limit	Sources	References
Cadmium	0.05	Kidney damage	Discharge from metal refineries; runoff from waste batteries and paints	[27]
Mercury	0.05	Abortion, congenital malformation and gastrointestinal disorders	Erosion of natural deposits; Agricultural waste; Burning fossil	[30]
Nickel	0.04	Hair loss, skin irritation, hypersensitivity, and cancer	Corrosion and leaching from pipes	[31], [29]

1.2.2. Fungi producing toxins

Fungi are a kingdom of multicellular eukaryotic organisms that are important in the nutrient cycling of an ecosystem. Fungi multiplication occurs due to specific environmental conditions such as temperature, moisture, and nutrient availability [32]. Different types of fungi, belonging principally to five genera (*Fusarium*, *Penicillium*, *Aspergillus*, *Alternaria*, and *Cladosporium*) under favourable environmental conditions proliferate and may produce secondary metabolites [33], as shown in Figure 1.2.

Mycotoxins are considered secondary metabolites of fungi with no significance for their growth and development. Furthermore, it is believed to play a role in eliminating other

microorganisms in the same environment [33]. Commonly, fungi enter the food chain through contaminated food (feed crops) and water. The cereal crops can be infested by natural phenomena (mycotoxins) or direct human action (pesticides, fertilizers). The cereals become infested prior to and during harvest or during unsuitable storage conditions (high humidity and temperature). Also, fungi can be leached or released from agricultural sites, soil, or air to contaminate surface waters.

Once water is contaminated, fungi can reach tap water at homes or hospitals due to insufficient disinfection by water treatment plants (WTP). In WTP, fungi attach to the pipes system as biofilms since they reside on the surface top waters. In the end, water can be contaminated again by fungi biofilms and end up as tap water, posing severe human health problems [33].

a. Mycotoxins: Structure and toxicity

Mycotoxins are secondary metabolites with low molecular weight produced by fungi causing significant injuries to humans and animals. Mycotoxins contamination can occur during pre-harvesting when the crops are growing or during post-harvesting processes, namely processing, packaging, distribution, and storage [34–36]. Generally, improper storage of crops or cereals under intense temperatures and humidity for extended periods favours mould growth and mycotoxins contamination. Nowadays, there are more than 400 types of mycotoxins, 20 of which are naturally present in food and feed at significant levels. Most are thermally and chemically stable during food processing, cooking, boiling, roasting, and pasteurization. Contaminated feed consumed by animals delivers contaminated products such as eggs or meat for human consumption [36].

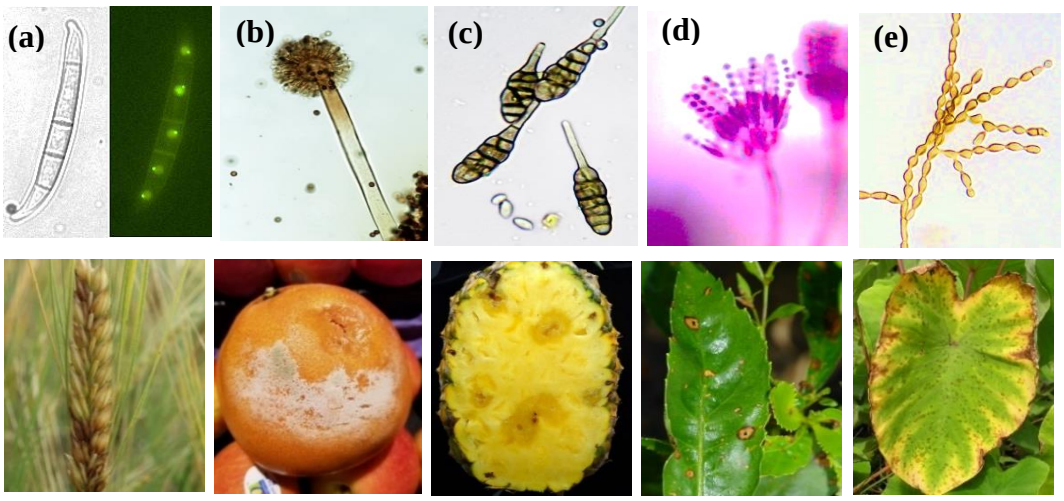


Figure 1.2. Fungi spores of a) *Fusarium*, b) *Aspergillus*, c) *Penicillium*, d) *Alternaria* and e) *Cladosporium* with respective contamination products (CC permissions in Appendix)

USC UNIVERSIDADE DE SANTIAGO DE COMPOSTELA

It was reported by several studies the effect of consuming toxin-contaminated food, specifically *trichothecenes*, that causes protein synthesis inhibition and chromosomal changes [37], [38]. There is a significant risk of developing Alimentary toxic Aleukia (ATA) illness, which is a haemorrhagic syndrome that resulted in the death of thousands of people during the

second world war [33]. Nowadays, national and international public governmental health authorities, namely, US Food and Drug Administration (FDA), the world health organization (WHO), Food Agriculture Organization (FAO), and the European safety authority (EFSA), are alerting about the effects of mycotoxins contamination in food and feed. Currently, 100 countries have established limits and strict regulatory guidelines for major mycotoxins classes in food and feed [39].

Table 1.3 shows a small set of mycotoxins that are of practical relevance for beverages and fruit juices contamination with the respective Eu regulatory limits in food and feed. In the EU regulation (EC) No 1881/2006 it was established the maximum levels for deoxynivalenol (DON), zearalenone (ZEN), fumonisin B1 (FB1), and aflatoxins (AFs) [40]. These mycotoxins are mainly produced by several fungi species of *Fusarium* and *Aspergillus* genus contaminating mostly cereal grains and beer. Expressly, beer brewed from malted barley and other cereals turn out infested by several Fusarium mycotoxins in beer industries [41,42]. Due to their characteristics, mycotoxins can be transferred from grains to malt and finally to beer because of their water solubility (FB and DON) and high thermal stability (AFs, DON, and ZEN) [43].

The EU established the maximum limits for aflatoxins in food and feed. More precisely, the mycotoxins AFB1 with 0.1-12 µg/Kg in food and 5-20 µg/Kg in feed. AFB1 has a more significant degree of epoxidation, being, therefore, the most toxic mycotoxins of all. Besides, the metabolites obtained by biotransformation are excreted in bile, urine, milk, and eggs [44], [45]. On the other hand, the EU regulatory limits for FB1 is not strict with 200-4000 µg/Kg concentration limit in food and 5000-60.000 µg/Kg in feed, possibly due to the lower adsorption of AFB1 compared to other mycotoxins, and it is often excreted as parent form [46].

Table 1.3. Major mycotoxins involved in the contamination of fruit juice and beverages and EU range limits

Produced Mycotoxins	Genus and Fungi species	Products contaminated	Limits for food (µg/Kg)[a]	Limit values for feed (µg/Kg)[a]	References
DON	*Fusarium graminearum, F. cerealis* and *F.culmorum*	Plant-based beverages, beer, cereals grains	200-1.750	900-12.000	[40,47,48]
ZEN	*Fusarium graminearu, F. verticillioides, F. cerealis, F.culmorum* and *F. equiseti*	Cereal grains, beer, wine	20-400	100-3.000	[40,47,49]
FB1	*Fusarium proliferatum, F. verticillioides* and *F. nygamai*	Beer, cereals and sorghum	200-4.000	5.000-60.000	[40,47,50,51]
AFB1 AFB2 AFG1 AFG2	*Aspergillus parasiticus, A. falvus, A. Repens, A. Ruber, A. Tamarii and A. oryzae*	Fruits (orange), juices (apple, grape) and cereal grains	0.1-12 (AFB1) 4-15 (sum of all AFs)	5-20 [b](AFB1)	[40,52,53]

[a] Limits values for feed and food [54]
[b] There are general limits for the AFB1, however for the remain mycotoxins the legal limits are only recommendations.

USC UNIVERSIDADE DE SANTIAGO DE COMPOSTELA

The mycotoxins functions are not clearly established. To evaluate their occurrence, toxicity, and chemical behaviour, it is essential to conduct safety and efficacy assessments that will help reduce contamination, setting maximum levels in food and feed. Figure 1.3 shows the chemical structure of the mycotoxins, DON, ZEN, AFs (B1, B2, G1, G2), and FB1.

- **DON** belongs to the *trichothecenes* family (TCTC) mycotoxins mainly produced by *Fusarium graminearum* [55]. Furthermore, it is known as vomitoxin since it induces strong vomiting effects after consumption being transported into the brain, where it runs dopamine receptors. Structurally DON is a polar organic compound containing three free hydroxyl groups (-OH), which are associated with its toxicity (Figure 1.3a). One of DON's most important physicochemical properties is its ability to tolerate temperatures up to 350 °C without reduction [56].

- **ZEN** is a non-steroidal mycotoxin produced by *Fusarium* species, mainly *F. graminearum* and *F. culmorum*. Its production is favoured by high humidity and low temperature conditions. Usually, ZEN contamination occurs simultaneously with DON and less often with AFs. Structurally, ZEN contains fourteen-membered lactone combined with 1,3-dihydroxybenzene reminding an estrogenic molecule with a similar hormone-like effect in cells (Figure 1.3b) [57]. It was demonstrated that ZEN functional groups, namely, hydroxyl, ketone, or lactone, form hydrogen bonds with the polar lipid side of membranes. As a result, the *Van der Waals* interaction changes due to modifying its hydrophobic parts. After diffusion into cells, ZEN undergoes biotransformation, causing estrogenic effects in humans and animals [58].

- **Fumonisins** (FBs) are a group of 25 similar mycotoxins produced by *Fusarium* species, mainly *F. proliferatum* and *F. verticillioides* which regularly contaminate maize and other crops. Over 28 fumonisins were isolated and classified into four groups (A, B, C, and P). Only fumonisins type B are relevant due to their toxicity and occurrence, being FB1 the most commonly found with 70-80 % of the total FBs in food and feed [51]. FB1 commonly contaminates maize and can cause pulmonary edema and leukoencephalomalacia (LEM) [59,60]. Structurally, FB1 is a long chain of amino polyols with two tricarballylic acid side chains (Figure 1.3c).

- **AFs** are a group of about 18 compounds structurally related produced by *Aspergillus* species, namely *A. parasiticus* and *A. flavus*, which are generally present in soil and organic materials [61,62]. The production of these species is favoured in warm and humid areas, mainly found in tropical regions. There are four main AFs, *A. flavus* produces only AFs (B1 and B2) while *A. parasiticus* can produce all (F1, F2, G1, and G2) [39]. AFs have been subjected to much research and are considered the most studied mycotoxins [35]. It can contaminate various food products such as cereals (maize, rice, barley, and oats), nuts, almonds, milk, and many others [39]. Chemically, AFs belong to the class of organic compounds known as difurocoumarolactones. Their structure consists of a bifuran ring or a six-membered lactone ring in AFB (1,2) and AFG (1,2), respectively (Figure 1.3d). Due to their chemical reactivity and behaviour, AFs have few systematic studies beyond the ones associated with structure elucidation [63]. However, it was reported that AFB1 reacted with hydroxyl groups under the catalytic stimulus of a strong acid [63]. AFs can be highly toxic and are related to acute

and chronic carcinogenicity in humans and animals. AFs can be bio-transformed mostly in the liver into more toxic species through hydroxylation, demethylation, and epoxidation [41].

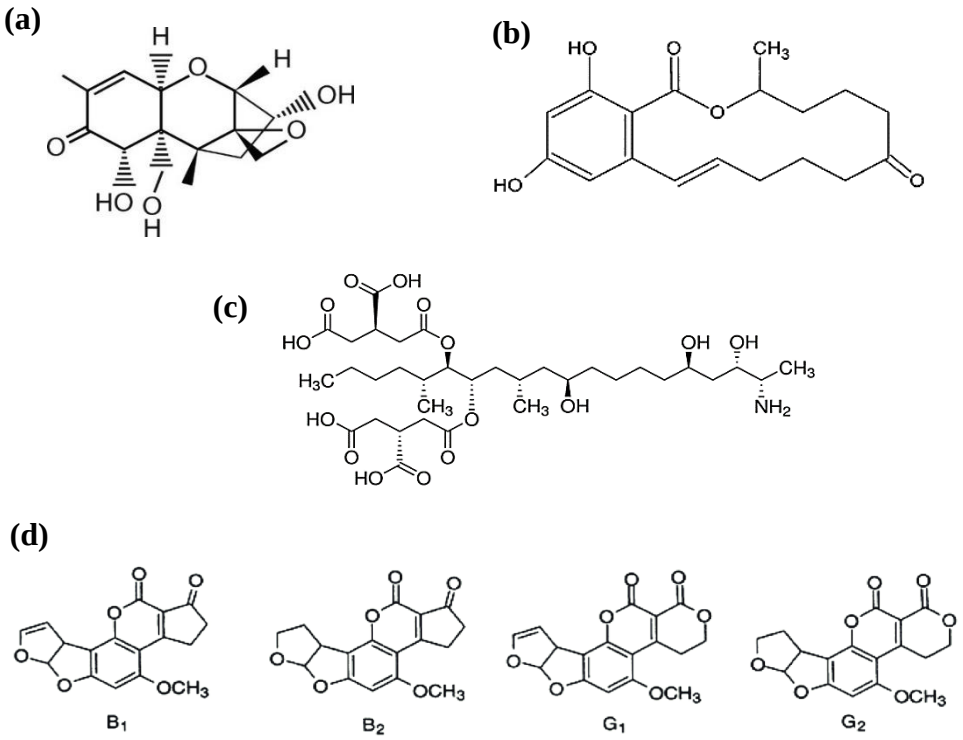


Figure 1.3. Chemical structure of Deoxynivalenol (a), Zearalenone (b), Fumonisin B1 (c) and Aflatoxins B1, B2, G1 and G2 (d)

b. Fungi and Mycotoxins contamination risk in drinking waters

Drinking water sources contain several biological pollutants, such as bacteria, viruses, and fungi. It was reported that the presence of fungi in drinking water changes its taste and odour [64,65]. Several fungi species were isolated from different water sources, such as surface water, tap water, groundwater, water from WTP, water consumed in schools, and municipal water supply systems [64,66–70]. The most common found fungi species are *Cladosporium*, *Penicillium*, *Aspergillus*, *Alternaria*, *Fusarium*, *Trichoderma* and *Curvular ia.* The detection of all fungi was primarily found in surface waters than in groundwaters [64], being *Aspergillus* the predominant species in all water sources [71]. Another class of agents is produced by such fungi, namely the mycotoxins. In the past, AFB2 and AFG2 mycotoxins have been detected in water storage tanks and, most recently, the presence of ZEN in surface water, groundwater, and wastewater [72, 73].

Mycotoxins are known for being genotoxic to humans or animals when exposed to or ingest contaminated food. Also, they are known to cause hypoestrogenism and physiological alterations of the reproductive tract [74]. Figure 1.4, shows a diagram with the primary sources affected by fungi proliferation and the chain production/effect of mycotoxins.

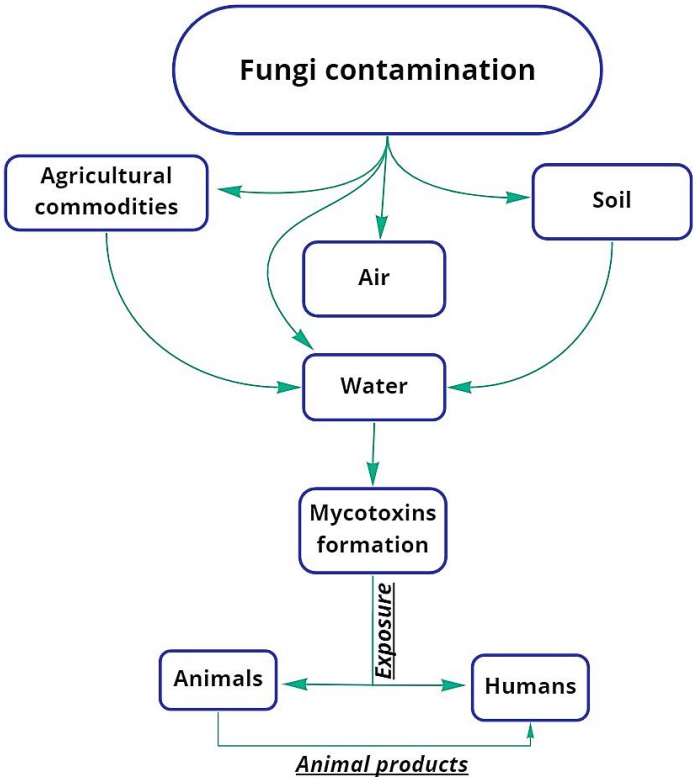


Figure 1.4. Diagram with primary sources and exposure routes of humans and animals to fungi and mycotoxins (Adapted with permission from reference [33]. Copyright (2021) *Springer Nature*)

The fungi outbreak poses severe problems to agriculture with the infestation of food products. Fungi can directly enter the three most important natural resources (water, soil, and air) and spread continuously from one natural resource to another through several processes (runoff, spillage, leaching, and spraying). Inhalation of fungi through aerosols is a concerning problem since water is being employed massively in farm irrigation, car washing facilities, etc [33].

Mycotoxins grow under specific and optimum environmental conditions of humidity and temperature, which are the most important factors that favour mould growth [75]. Besides, food such as feed and cereals can be infested during poor storage or during harvest or processing, and animals are then exposed to mycotoxins by contaminated feed, entering finally in this way into the food chain of humans. Food and water contamination by mycotoxins are real and not entirely regulated by the administrative bodies for which new detection and remediation measurements should be undertaken in time to avoid mass propagation.

USC UNIVERSIDADE DE SANTIAGO DE COMPOSTELA

1.2.3. Remediation techniques

Over the years, various techniques have been developed and applied to control and remove contaminants from water or food. Different water remediation methods such as physical, chemical, electrochemical, or biological approaches are employed to prevent the contamination of natural resources and increase drinking water quality [76]. Heavy metals removal techniques and mycotoxins detoxification strategies from aqueous media have challenges. However, each method has the same inherent limitations and advantages to reduce contaminants from water.

a. Heavy metals removal technologies

Environmental degradation, caused mainly by industrialization, has moved the public concern towards the need to implement efficient environmental remediation techniques. Current technologies to remove heavy metals from water present some limitations that should be taken into account. Especially high operation costs, solid wastes generated through the cleaning processes, chemical, and physical properties of heavy metals, and how efficient the treatment is before effluent discharge [77]:

- **Chemical precipitation** is one of the most widely used processes for heavy metal removal by industries due to its simplicity. In this precipitation process, chemicals react with heavy metals forming insoluble residues in the form of hydroxides, sulphides, carbonates, and phosphates. Once the heavy metals precipitates are formed, they can be separated from water by sedimentation, filtration, or changing significant parameters such as pH, temperature, ion charge, etc. [78]. In addition, the produced sludge must be managed as hazardous waste due to the high concentration of contaminants, increasing the cost of using this treatment process [77].

- **Ion-exchange** is based on a reversible interchange of ions from the liquid (water) to the solid (resin) phase. In this process ion exchange resins are used on the zeta potential (ζ) since they can adsorb positive and negative charge ions from the solution, releasing other ions with the same charge in equal amounts. The positive charge in cationic resins such as hydrogen or sodium ions is exchanged with positive metal ions. Similarly, negative ions in the resins, such as hydroxyl and chloride ions, are exchanged by negative charge ions such as nitrates, sulphates, and dissolved organic matter (DOC). Ion exchangers can only be used at low concentrated metal solutions because they eventually become exhausted and must be regenerated by proper solutions [77, 78].

- **Membrane filtration** is a membrane separation method for mechanical and chemical separation of particles or macromolecules [78]. Depending on the particle's size to separate, membranes can be classified as ultrafiltration, nanofiltration, microfiltration, and reverse osmosis. This technique has been extensively used for removing organic compounds, suspended solids, and inorganics contaminants such as heavy metals. Even though any additives are not required in the process, these membranes are expensive, difficult to install, and are susceptible to fouling, scaling, or even degradation [79].

- **Coagulation and flocculation** are based on the collision of insoluble particles and dissolved organic matter to form larger aggregates that can be removed or separated by

filtration, straining, or floatation. The mechanism relies on the zeta potential (ζ) measurement to define the electrostatic interaction between the contaminants and the coagulant-flocculant agents [80]. The coagulant agents, such as aluminium sulphate, lime, and ferric salts, destabilize the suspended particles by microfiltration. These particles are then aggregated by flocculation, allowing subsequent removal in other stages. The main drawbacks of this technique are the application of chemicals that remain on the solid phase [78].

- **Electrochemical treatments** can remove or recover heavy metals after precipitation using a weakly acidic or neutralized catholyte (hydroxides). This method has several disadvantages since it requires the use of a large number of chemicals to reduce heavy metals. Furthermore, huge amounts of sludge are produced during the process, and metal precipitation can be very slow, contributing to long-term exposure of toxic waste to the environment [81]. Electrochemical wastewater treatments involve electro-deposition, electro-coagulation, electro-flotation, and electro-oxidation [82].

- **Adsorption** is the adhesion of ions, atoms, or molecules from a gas, liquid, or solid to a surface. The accumulation of any particle can occur at the interface between the surface and the bulk phase, in which mass transfer can bind either by physical or chemical interactions. This method is the most widely used due to its low cost, eco-friendly and easy handling, for which it was the selected approach in this thesis, being later discussed [83, 84].

b. Mycotoxins detoxification techniques

Mycotoxins are secondary metabolites of fungi, with a broad spectrum of toxicity even at low concentrations. Some of them present potential carcinogenic, mutagenic, and genotoxic mechanisms [85], and due to their physical and chemical stability, degradation is a complex challenge. Fungi growth and mycotoxins formation are controlled by environmental conditions, agricultural and manufacturing practices. In this sense, the temperature and humidity of the storage facilities can be decreased to avoid the development of fungi and further mycotoxins formation. Different strategies have been used over the years to reduce the impact of mycotoxins in agricultural products.

Conventional strategies include appropriated grain handling processes such as sorting, separation, immersion, and washing. Sorting and separation are crucial to remove mouldy grains or products, reducing mycotoxins formation and propagation. In addition, floating and washing allow the contaminated grains to float since they have a lower density than the healthier ones, which are easier to separate and discard [86–89].

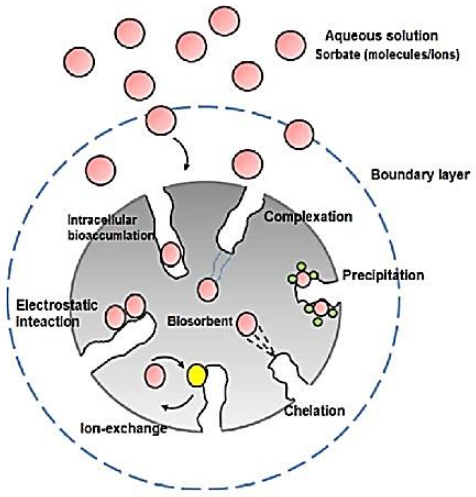
However, most of these strategies do not successfully destroy these contaminants. Novel strategies were implemented in the food industry, such as cold plasma, ozone processing, irradiation, and biological methods [90–93]. These techniques revealed little or no adverse effect on cereal grains' quality and nutritional value. However, the economic expenses of the procedure have an impact on the final prices of the products. Other approaches to mitigate the impact of mycotoxins in livestock health, limiting their binding in the gastrointestinal are adsorbents composed of aluminosilicates, activated carbon, and other minerals [94]. Some studies showed that incorporating magnetic nanoparticles to certain adsorbents could successfully remove mycotoxins [42, 95]. Nanotechnology has gained quite a lot of interest

over the years due to the development of new functional nanomaterials with detoxification capabilities.

c. Biosorption

In general, all of the above-discussed processes are expensive, and it is required further use of chemicals resulting in the production of large volumes of waste. For this reason, companies have adapted cost-efficient treatment techniques with excellent cleaning capabilities due to increased environmental awareness. Biosorption is a method that involves physical and chemical processes in which an adsorbate (heavy metals, mycotoxins), when dissolved in a liquid phase (water or other solvents), can adhere to a solid phase (biosorbent or adsorbent). This method is quite promising since it uses biomass as raw material that is abundantly found in nature or as waste from agriculture or food industries processes. Furthermore, it is possible to treat large volumes of water due to the processing speed and the possibility of removing several pollutants simultaneously. In addition to that, is not required the use of chemicals, there is no generation of large volumes of waste, and the selectivity and efficacy of the biosorbent to bind several contaminants can be tuned.

The biosorption efficiency for several water pollutants depends on specific features of the biosorbent, such as surface area, textural properties, solubility, molecular size, chemical composition, and hydrophobicity. Therefore, to be chemically versatile, the structural components of the biosorbent should contain numerous functional groups (i.e., hydroxyl, carboxyl, amino, thiol, etc.) to enable the adsorption of the water pollutants through several sorption mechanisms. Figure 1.5 shows the different interactions between the contaminant and the biosorbent surface. The adsorbate can interact via aggregation, electrostatic interaction, ion exchange, precipitation, and complexation. The biosorption process continues until equilibrium is achieved between the amount of bounded adsorbate species onto the biosorbent surface and the remaining present species present in solution [96].



USC UNIVERSIDADE DE SANTIAGO DE COMPOSTELA

Figure 1.5. Biosorption mechanisms (Reproduced with permission from reference [96]. Copyright (2021) Elsevier)

1.2.4. Ability of biosorbents to bind heavy metals and mycotoxins

Biosorbents can be composed of diverse substrates of biological origin such as microorganisms (i.e., bacteria, fungi, yeast), algae, industrial (i.e., activated sludge, brewery spent grain, fruit pulp, bark, sawdust, wood chips, moss, etc.) and agricultural waste (i.e., bark, stem, leaves, roots, straw, chaff, husk). The removal of heavy metals and mycotoxins from water using biosorbents has been addressed with different approaches, as shown in Table 1.4.

Table 1.4. Heavy metal and mycotoxins removal by different biosorbents.

Heavy metals removal				
Type of Biosorbent	Biosorbents	Heavy metals	Metal uptake (mg/g)[a]	References
Algae	*Sargassum natans*	Cd	135	[97]
Algae	*Ascophyllum nodosum*	Co	100	[98]
Plant	*Dendrocalamus membranaceus* Munro	Pb Cd	381.7 278.6	[99]
Bacteria	*Bacillus subtilis*	Cu	152	[100]
Mycotoxins removal				
Type of Biosorbent	Biosorbents	Mycotoxins	Adsorption index (%)[b]	References
Marine Algae	*Lithothamnium calcareum*	AFB1	77.6	[101]
Plant	*Myriophyllum spicatum L.*	AFs	95.97	[102]
Agricultural/natural waste	Almond shell	AFB1 ZEN FB1 DON	40 24 40 0	[99]
	Olive tree leave	ZEN AFB1 DON FB1	58 13 6 0	[103]

[a],[b] the metal uptake and mycotoxins adsorption were performed at pH=3

Biosorbents from algae biomass (seaweed) showed a high ability to bind heavy metals due to specific functional groups such as carboxyl, amines, hydroxyl, and phosphate [104]. Meanwhile, marine algae (*Lithothamnium calcareum*) in *in-vitro* absorption studies revealed a successful removal efficiency of AFB1 by 77.6 %, preventing aflatoxicosis in broiler chickens [101]. Also, plants have a great potential to act as biosorbents due to carboxylic and phenolic functional groups in their structural components, namely, cellulose, lignin, and hemicellulose [105]. A porous biosorbent was developed using lignocellulosic biomass extracted from *Dendrocalamus membranaceus* Munro (bamboo) to remove Cd and Pb. The adsorption capacity was remarkable (Cd=278.6 mg/g; Pb=381.7 mg/g) due to the content of carboxyl groups present in the biosorbent, which increased the adsorption capacity for both metals [99].

In another experiment, *Myriophyllum spicatum* waste was used in *in-vitro* studies to observe the reduction of multi-mycotoxins. This plant that is often used as animal feed reveals to absorb over 95.97 % of AFs [102]. Among the microorganisms, the bacteria *subtilis* also showed excellent metal-binding properties with specific activity to adsorb Cu with an adsorption capacity of 152 mg/g [100]. Bacteria have the advantage of having a high percentage of cell wall material which may enhance their adsorption properties [106]. The natural waste from agricultural activities is a raw material that can be safely used to absorb multi-mycotoxins simultaneously from aqueous mediums. Almond shell and olive tree leaves reduced more than 60 % of the total mycotoxins in solution with different binding affinities. The almond shell decreased approximately 40 % of AFB1 in solution while the olive tree leaves reduced 13 %. An additional trend revealed the reduction of ZEN, where the olive tree leaves and the almond shell decreased approximately 58 % and 24 %, respectively.

This highlights the crucial importance of choosing the biosorbent type based on the structural composition and the main functional groups to maximise its affinity to mycotoxins and heavy metals.

1.3. Biomass: Future renewable resource

Biomass is a renewable resource that is abundantly available in nature. It is comprised of forest, agricultural crops or waste, wood, aquatic plants, livestock residue, and municipal or industrial waste. Over the years, biomass has emerged as a great sustainable resource and an alternative for energy production due to reducing gas emissions to the atmosphere. Also, it can provide a new source of economic growth by transforming the residual biomass into a wide range of compounds with high added value.

1.3.1. Lignocellulosic Biomass

Forests are the most important terrestrial ecosystem on Earth and the source of the largest resource of solid biomass. Lignocellulose is a dry plant biomass compound produced through photosynthesis comprising of about 70 % of the plant cell walls [107]. It is the most abundant organic resource used worldwide due to its properties and accessibility, being the source of neutral carbon used to produce biofuels.

Its structure is composed of a small fraction of pectin, proteins, waxes, or lipids and a large polysaccharide fraction formed by three biopolymers such as cellulose, hemicellulose, and lignin, as shown in Figure 1.6. Lignocellulosic biomass is mainly composed of cellulose (40- 50 %), hemicellulose (25-35 %), and lignin (15-20 %) [108].

USC
UNIVERSIDADE DE SANTIAGO DE COMPOSTELA

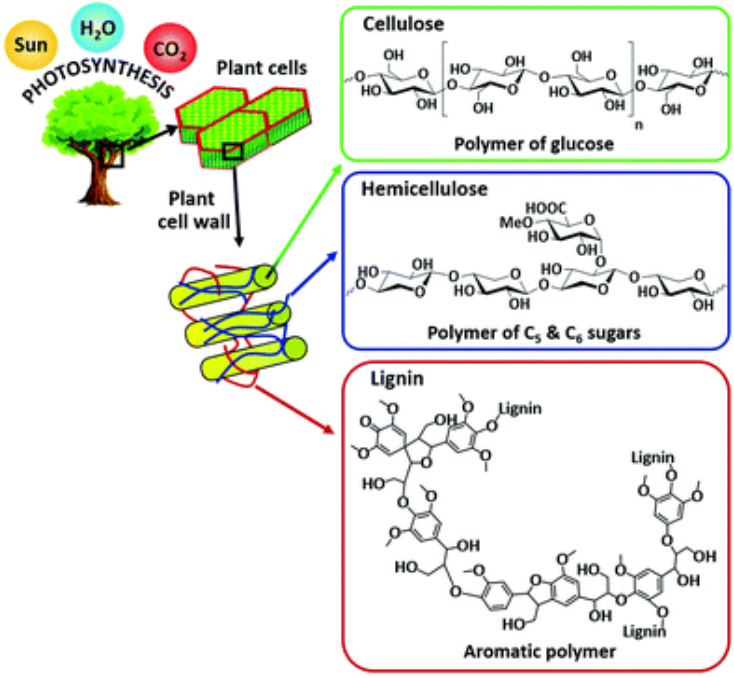


Figure 1.6. Chemical structure of the major components of lignocellulosic biomass: Cellulose, hemicellulose and lignin (Reproduced with permission from reference [109]. Copyright (2021) *Elsevier*)

- **Cellulose** is the main component of plant cell walls with a well-ordered structure of D-glucose subunits linked by (1,4)-glycosidic bonds [110]. The long linear chain structure is linked by hydrogen and *Van der Waals* forces causing the packed-type structure of the cellulose microfibrils. Besides, it can be comprised of crystalline and amorphous forms.

- **Hemicellulose** is the second most abundant component of lignocellulose biomass, composed of short lateral chains of sugars. Compared with cellulose, hemicellulose contains more soluble molecules. Moreover, it serves as an interface between the cellulose and lignin through hydrogen bonding between the -CH_2OH groups of cellulose and the oxygens of its glycosidic bonds [111]. As for the composition, its structure depends on the biomass source, however, usually, it consists of pentoses (xylose, arabinose, and rhamnose), hexoses (glucose, mannose, and galactose), and uronic acids [110]. The presence of pentoses and hexoses turns hemicellulose into a renewable and sustainable source in the production of biofuel and chemical products [112].

- **Lignin** is an aromatic polymer with a large molecular structure with phenolic monomers linked by ether (alkyl-aryl, alkyl-alkyl, and aryl-aryl) and carbon bonds. This polymer provides structural support, impermeability, and resistance against physical and biological agents. All components are bound through non-covalent bonds and covalent cross-linkages [110].

a. Valorisation of lignocellulosic Biomass

The complex and rich structure of lignocellulose has contributed to the development of new techniques allowing its transformation into new materials and products with high added value. For instance, the hydroxymethylfurfural (HMF) molecule is formed from hemicellulose and cellulose, and both are also used to produce biofuels through the fermentation process [113]. In addition, lignin produces phenolic compounds or other intermediates of chemical interest [114]. In this context, to enhance the valorisation of lignocellulose, these components must be break down, as shown in Figure 1.7, by specific pretreatments.

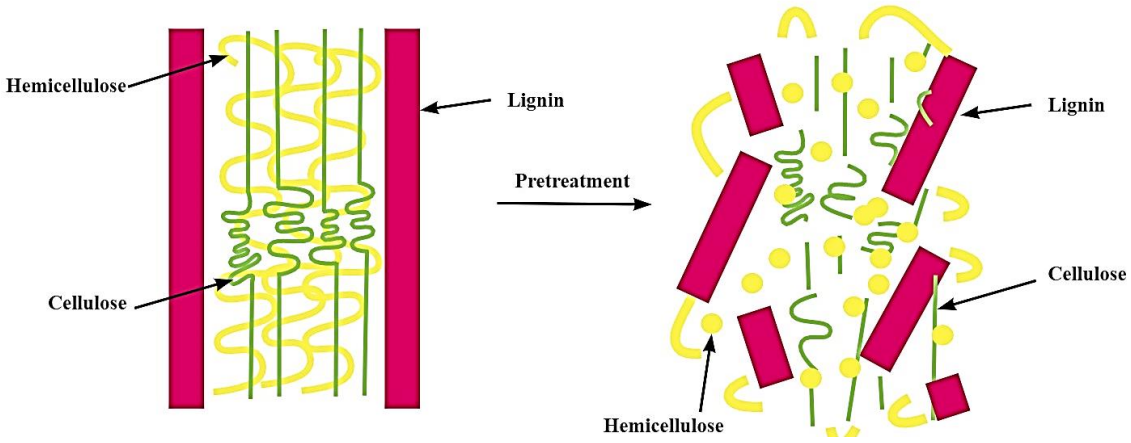


Figure 1.7. Scheme of the breakdown of the lignocellulosic structure by pretreatment (Adapted with permission from reference [110]. Copyright (2021) *American Chemical Society*)

However, it is required to make a previous assessment of the composition of the distinct components of lignocellulose to select the best pretreatment to be applied. First, it is crucial to consider the cellulose crystallinity since the more crystalline parts are more difficult to be hydrolysed [115]. The specific surface area is an essential factor affecting the enzymatic hydrolysis of lignocellulosic biomass. The process only occurs when the pore volume of the substrate is large enough to enhance the coupling of different enzymes since pore volume is linearly correlated to the rate of enzymatic hydrolysis [116]. The lignin that gives the lignocellulosic material's rigidity aspect turns its hydrolysis more difficult [115]. Finally, removing the hemicellulose, which acts as a physical barrier, the pore size increases, allowing a fast hydrolysis of the biomass [117].

The lignocellulosic biomass pretreatment methods can be classified as chemical (alkali, dilute acid, ionic liquids, and organic solvents), physical (milling, extrusion, and sonication), physicochemical (steam pretreatment, hydrothermolysis, and wet oxidation), and as biological (fungi, bacteria, and microbial consortia), as shown in Figure 1.8. These methods improve the formation of sugars, avoid the degradation of hemicellulose and cellulose, avoid the appearance of by-products that inhibit the processes of hydrolysis and fermentation, generate small quantities of waste, reduce the use of reagents, and must be cost-effective [118].

The pretreatments are essential for the depolymerization of the lignocellulose structural components that, once finished, allow the obtention of different products for a wide variety of

applications [119]. In addition, the different added value products that pass through the pretreatment processes provide more economical and environmental benefits than the ones that have not been treated, providing new opportunities in the industry and energy sector [120].

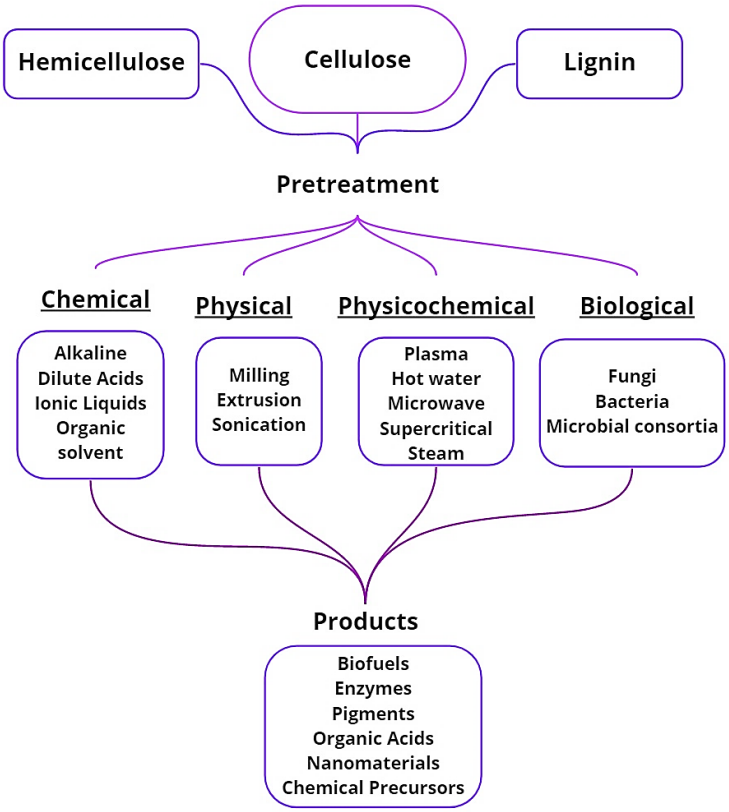


Figure 1.8. Diagram of the lignocellulosic pretreatments and resulting products (Adapted with permission from reference [119]. Copyright (2021) *Elsevier*)

1.3.2. Aquatic biomass

Aquatic biomass is composed of aquatic plants and diverse species of micro and macroalgae. Macroalgae are seaweeds of several meters in length that grow either in fresh or saltwater. These multicellular plants are classified into three main taxonomic groups, namely *phylum Chlorophyta* (green algae), *phylum Rhodophyta* (red algae), and *phylum Ochrophyta* (brown algae), being distinguished by their characteristic pigmentation and morphology [121, 122]. In contrast, microalgae are photosynthetic unicellular microorganisms living in the water column of surface waters. Therefore, they can be classified as eukaryotic microorganisms and prokaryotic cyanobacteria that can perform photosynthesis and fixate atmospheric N_2 [123].

These algae are good candidates to produce biofuels and chemicals due to their photosynthesis efficiency. High growth rates are an excellent advantage for producing large quantities of algae biomass. Besides this, their composition contains different types of carbohydrates, proteins, lipids, and inorganic compounds, with critical functional groups

(oxygens, phosphorus, sulphur, and nitrogen) for the biosorption of heavy metals, fungi, and mycotoxins [124, 125].

a. Brown seaweed: Simultaneously invasive and environmentally friendly

The brown seaweed macroalgae are the most studied and exploited algae. They are used in diverse applications, specifically in agriculture as fertilizer or animal feed, and in the industry to produce phycocolloids [122].

Sargassum is a genus of brown algae mostly found in high concentrations in tropical and subtropical marine environments. The bloom of these algae is usually associated with a high concentration of nutrients present in water due to fertilizers usage, deforestation, and agricultural waste discharges. Some *sargassum* species, namely *Sargassum fluitans* and *Sargassum natans*, remain pelagic through the beginning of their life cycle, reproducing sexually, and when maturation is reached, they reproduce asexually by fragmentation which can result in substantial floating seaweed mats on the Ocean [126, 127]. The excessive growth of these floating species poses a significant environmental concern and economic losses [128], as is represented in Figure 1.9.

From an economic perspective, when close to the shore, these *sargassum* floating mats can reduce tourism or even affect local fishing activities. As for an environmental concern, marine ecosystems are negatively affected by reducing sunlight, dissolved oxygen, and changes in water temperature. In addition, due to the persistence and decomposition of *sargassum* algae on the shore, eutrophication increases due to the dissolved organic matter. For diverse aquatic species, *sargassum* floating mats is a feeding area, a temporary habitat since it provides juvenile fishes with food and protection against predators [129]. It is undoubtedly that *sargassum* in the shore presents several problems, but on the other hand, it can represent an economic opportunity if its removal procedure is well managed without impacting on the aquatic biodiversity and the beach coasts. Recently, it was suggested as a prevention measure to collect the *sargassum* before it reaches the shore at about 50 to 500 meters from the coast [130].

Given this, the environmental impacts would be reduced, and alternatives of valorisation for the collected algae would be promoted to equilibrate the costs of the removal process. These macroalgae have several uses in health, food, agricultural industries, biofuels production, or as bioremediation agents for several pollutants [131].

USC
UNIVERSIDADE DE SANTIAGO DE COMPOSTELA

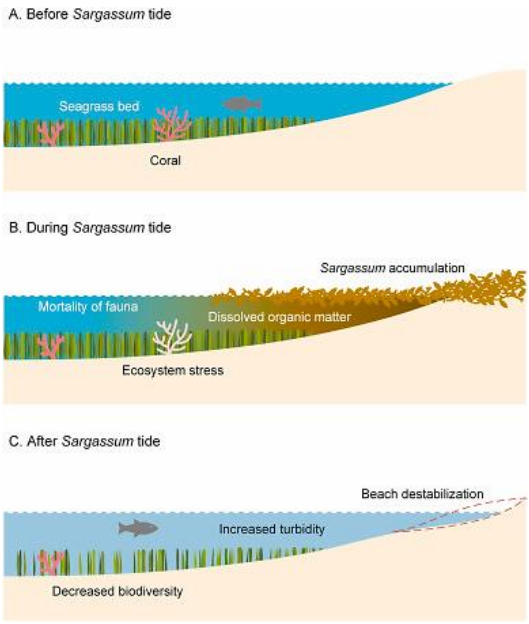


Figure 1.9. Environmental effects of *sargassum* algae, before arrival on shore (A), during (B) and after (C) (Reproduced with permission from reference [132]**. Copyright (2021) *Elsevier*)**

b. Sargassum species main composition

Seaweeds are typically composed of high amounts of carbohydrates and medium/low amounts of proteins, lipids, minerals, and ashes. However, the composition may vary depending on the seasonal change, for instance, in the summer is produced more sugars while in the spring, more proteins, and minerals [133].

In general, it was reported that the *sargassum* species, *S. fluitans* and *S. natans* have about 34 to 47 % of dry ash content, 3 to 17 % of proteins, 1 to 5 % of lipids, 7 to 38 % of minerals, and about 78 % of carbohydrates, correspondents to dry weight. In addition, these brown seaweeds contain a small fraction of fucoxanthin, flavonoids, and phenolics that have antioxidant activity [134].

Among carbohydrates, polysaccharides account for about 30 to 50 % of the dry weight present in the cell walls as alginate, fucoidan, and cellulose. At the same time, laminarin and mannitol are present as carbon sources [135]. The hydrolysis of the source polysaccharides (laminarin and mannitol) results in the formation of glucose which is the primary source of chemical energy used for cell functions.

Alginate is the most important and the main structural polymer of brown seaweeds responsible for their stability and flexibility [136]. All components of the brown seaweed are used to produce several daily food products such as salt, emulsifiers, and vitamins [133].

USC UNIVERSIDADE DE SANTIAGO DE COMPOSTELA

c. A valuable source of polysaccharides

The numerous applications of brown algae are mainly due to their rich composition in polysaccharides such as alginates, fucoidans, and cellulose. The quantity and quality of each

component depend on a few factors discussed previously, such as the algae species, the harvesting season, type, and age of the algae tissues [137].

Alginate and fucoidans are the most abundant, representing up to 40 and 10 % of dry matter of brown seaweeds, respectively [138]. Both have the potential to bind heavy metals by ion exchange due to the presence of carboxyl and sulphate groups on their structure [125], as shown in Figures 1.10a and 1.10c.

Like plants, brown algae produce cellulose, but it only accounts for a small portion of the cell wall ranging between 1 to 5 % of the dry weight [139]. These polysaccharides are extremely important to ensure the algae subsistence in nature but also individually, they can be extracted and used in several applications fomenting therefore industry.

The pretreatment methods (mechanical, thermal, chemical, and biological) are employed to brown seaweed. The chemical pretreatment reveals to be the most promising technique used for the extraction of polysaccharides from brown algae since it allows, through some technical updates, the increase of the extraction yield, diminished operating time, and use of high temperatures and solvents. These new measures help contribute to a more sustainable valorisation of brown seaweed by reducing the extraction costs of its components.

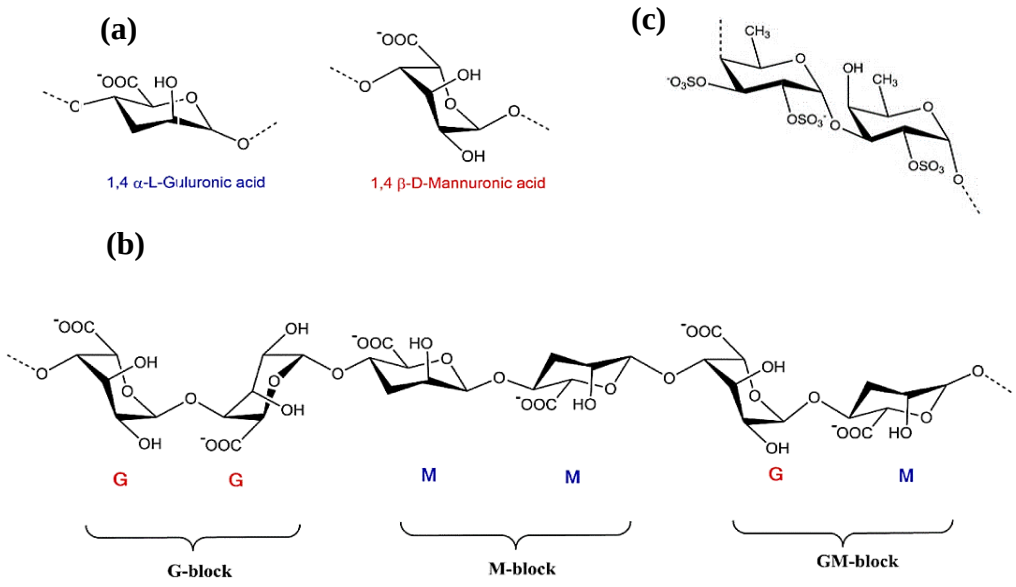


Figure 1.10. Chemical structure of alginate and fucoidan. (a) Alginate monomers; (b) block distribution of alginate monomers and fucoidan structure (c) [140,141] **(CC BY 4.0)**

Among the three polysaccharides, alginate is the most widely used in the industry of pharmaceuticals, cosmetics, food, and medical technology due to its physical, chemical, and rheological properties [142]. In addition, it can behave as a stabilizer for aqueous dispersions, as an emulsifier because of its viscosity and gelling characteristics. At the structural level, alginates are comprised of unbranched binary copolymers of 1,4-β-D-mannuronic acid (M) and 1,4-α-L-guluronic acid (G) monomers covalently linked in different blocks (M-M, G-G, and M-G) as shown in Figure 1.10b.

The M/G ratio varies between species of algae and has an important effect on the physicochemical properties of alginates. Metal beads coated with sodium alginate extracted from *Laminaria digitata* have shown superior adsorption capacity for Cd, Cu, and Cr heavy metals than uncoated beads [143].

Alginates are usually extracted in the form of sodium alginate by ion-exchange procedures adding either acids or calcium salts. In brief, adding acids causes alginic acid to separate as a gel being posteriorly extracted by sodium carbonate, which converts alginic acid to sodium alginate. By the second method, sodium alginate is extracted using calcium salts to form soluble calcium alginate fibrils, then converted to sodium alginate by acid precipitation and neutralisation reaction. The use of sodium alginate is expanding in the development of biomaterials as it can form colloidal systems [144, 145].

1.4. The role of biomass to a future circular Bioeconomy

Humans produce huge amounts of waste from several sectors, particularly from agriculture, forestry, and ocean activities [146,147]. Among the several causes is the increase in global population that consequently requires a high demand for energy, food, and other daily products. During the pursuit of accomplishing all the population's needs, industries start to lack and apply improper management measures that result in waste accumulation or improper disposal or discharge into the environment. In recent years, the scientific community has raised concerns about the environmental impacts of waste and greenhouse production on climate change [148].

To minimize pollution, new technologies are under development to process waste and use renewable resources as a sustainable way of reusing and producing products of commercial interest.

Biorefineries are presented as a potential solution to the existing waste disposal problems since it converts any biomass (waste, wood, feed, etc.) to energy and other by-products such as chemicals, materials, and fuels [149].

This approach has been identified as the second generation of waste valorisation due to the reuse techniques to produce higher-value products. Also, this valorisation approach is a promising pathway to achieve an efficient circular bioeconomy (CBE) with reducing human-induced environmental problems, developing new materials, generating job opportunities, and the competent use of resources [150].

1.4.1. Fundamental concepts

To achieve economic sustainability, first, it is essential to know some important differences and the relationship between circular economy (CE) and bioeconomy (BE) concepts. The circular economy relies on the reuse and recycling initiatives maximizing the use of a product or materials indefinitely. Oppositely, the linear economy approach relies on collecting, extracting, and processing raw materials into new products that are thrown away after use [151]. On the other hand, BE is a foundation for a future in which societies rely on renewable and sustainable resources to meet needs for energy, chemicals, and raw materials, replacing today's use of non-renewable resources [151, 152].

In order to produce new added-value products such as food, feed, bioenergy, and biobased materials. Both CE and BE concepts, explained by the researchers Carus and Dammer [153], "have similar targets, but none is fully part of the other nor embedded in the other." Therefore,

it is important to bind both CE and BE concepts following three key objectives to achieve a CBE.

The first is the use of by-products of biomass and residues, as the unique resource to drive value and increase economic productivity. Secondly is the efficient use of biomass in a circular chain to avoid the use of raw materials and transform it into a material to achieve economic value and generation of job opportunities. Lastly, the third objective is to create a more sustainable and resource-efficient society. Both CE and CBE reduce the use of fossil fuels in this aspect.

The CE concept improves resource efficiency and the utilization of recycled materials to minimize the demand for fossil carbon. In contrast, the BE concept substitutes fossil carbon with renewable carbon from biomass. Thus, the backbone of a strong CBE is sustainable utilization, supporting education and innovation capacity.

1.4.2. Benefits and limitations of CBE

CBE arises from the need for a more sustainable and resource-efficient world, and it offers a variety of societal, economic, and environmental benefits, as seen in Figure 1.11.

Socially, CBE enables the economic growth of innovative businesses dedicated to developing biobased products. Furthermore, it allows the creation of new job opportunities, specifically in rural, coastal, and small industrial regions, thereby fixing the population in such areas avoiding their depopulation. Professional training is provided to have high-skilled professionals in diverse areas in emerging countries promoting social equity [119].

In the long term, economic growth is attained by the efficient use of raw materials obtained from by-products as a result of the improved waste management measures of reuse and recycling. These positive practices change the attitude at various organisational levels leading to a sustainable future with more conscience towards major environmental issues such as food, water, and energy [151].

From an environmental perspective, CBE enacts a sustainable management of natural resources, maintaining an equilibrium in the ecosystem and species biodiversity. Environmental sustainability is enhanced by productivity and simultaneously by the reduction of pollution attained by the right investments that are essential to keep ecosystem health and the correct management of environmental risks [154].

The key for a CBE model is the efficient valorisation of biomass and its value optimization (social, environmental, and economic aspects) to balance with the high costs of waste management practices [155]. One of the main challenges to establish a CBE is the urgent transfer of knowledge to industries on how to upgrade their technology to make a profit from biomass or residues. Cultural barriers in a company's management culture and the lack of consumer interest and consciousness to the current environmental problems are often more problematic and pertinent than any technological misunderstanding or policy makers [156].

Therefore, to achieve an effective CBE, the key goals are the mobilization of investment and politics for science, technology, knowledge transfer, and social innovation.

USC UNIVERSIDADE DE SANTIAGO DE COMPOSTELA

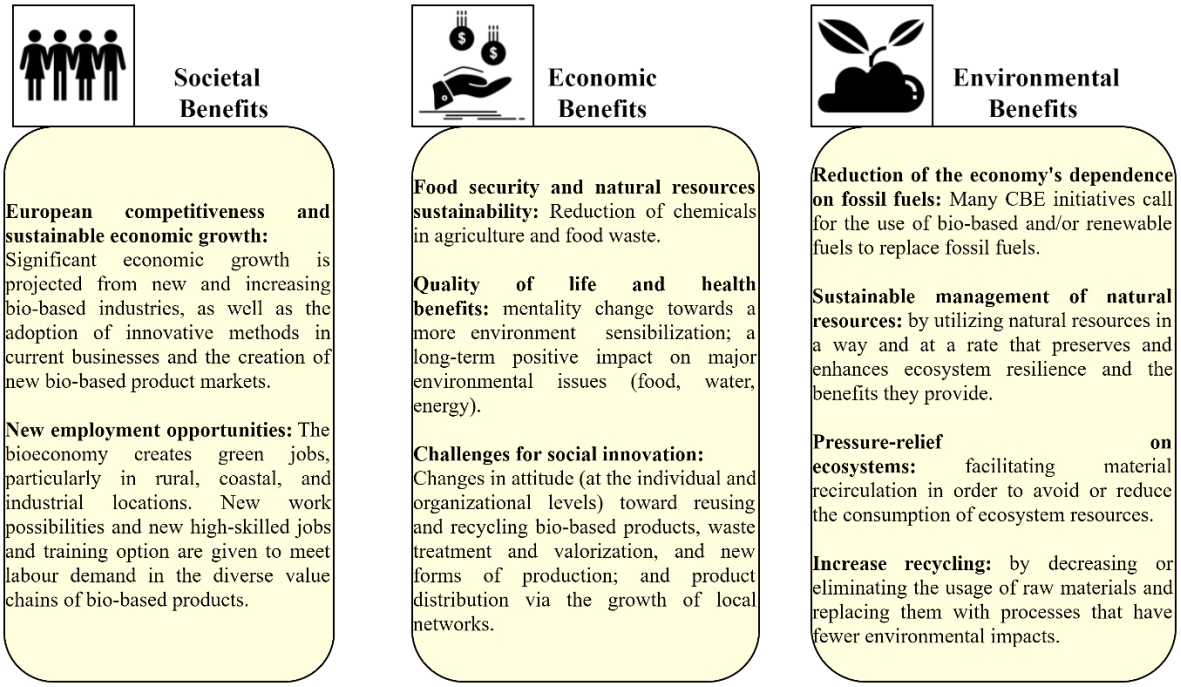


Figure 1.11. Societal, economic, and environmental benefits of CBE approach (Adapted with permission from reference [151]. Copyright (2021) *Elsevier)*

1.4.3. Industrial sectors: Economic profit and employment

Biomass is a substitute for fossil fuels, in which the economic value must be extracted and transformed. Europe has traced a plan that focuses on three main objectives to achieve a CBE. The first objective is focused on developing new markets and competitiveness in different industrial sectors through the use of biomass to improve resource efficiency [157].

Bioeconomy is linked to various primary resources (forestry, agriculture, fishing, and aquaculture) and sectors (energy, chemicals, food, tourism, and industrial materials production). The primary forestry resource plays a crucial role in bioeconomy.

Forest provides renewable materials (wood and non-wood), bioenergy, and chemicals to ensure the needs of the upcoming population growth [158]. However, to ensure a sustainable use of the forest-based sector, industries cannot rely only on the forest natural resource. One alternative is to use mixed feedstock (agriculture, Ocean, and forest) from biorefineries to avoid the overexploitation of forests [159]. Safeguarding a sustainable development and use of resources is necessary for a successful forest bioeconomy. In the 20th century, the only profit obtained from the forest sector was from wood, pulp, and paper products.

Nowadays, and in the long term, the forest-based sector is increasing towards the production of bioenergy, bio-textiles, biochemicals, intelligent packaging, bioenergy, etc. It is turning out as a leading sector in the sustainable development of bioeconomy [158]. In part due to the demand for forest goods, bioeconomy is increasing and the economic opportunities for the sector. Also, it is being requested for carbon sequestration and other ecosystem services

such as social and human welfare. However, in Europe, the forest bioeconomy is complex since it requires specific policy objectives to be accomplished.

Most people associate Ocean only with fishing, but there is more than meets the eye. Blue bioeconomy is a revolutionary field of innovation transforming aquatic biomass into energy, smart food, feed, pharmaceuticals, packaging, biomaterials, etc. Also, the aquatic sector has a high potential to contribute to the increase of the EU economy by providing more jobs, more public health conditions. Meanwhile, it supports the sustainable development and protects the environment [160]. However, a lot of progress must be made, starting from the public awareness to food loss and the utilization of food scraps (such as fish, meat, etc.) by companies as a resource rather than waste, where additional value can be taken from.

Iceland is an example of optimal utilization of all codfish parts, 75 % to 80 % of each cod caught is used for value creation which is high compared to other countries [161]. Collaboration of research facilities and industries has created an important new value stream from what has been thrown away. Fish skins are used to make high fashion textiles, snacks for human consumption, and even medical products for skin regeneration [162]. Also, biorefineries by processing fish frames are obtaining bioactive compounds. These are posteriorly used in food supplements, cosmetic products, fertilizers, or as feed to microorganisms that produce biodegradable plastics [163]. New products made in biorefineries cascading from higher to lower value-added products can also apply to the algae sector.

Algae play an important role in carbon neutrality, Ocean acidification, and water quality, absorbing CO_2, nitrogen, and phosphorus. In addition, algae biomass has increased over the years in the bio-based economy. In the last few years, algae demand has been rising for the production of various high-value products (e.g., cosmetics and pharmaceuticals) and its utilization in bio-based applications (bioenergy and biomaterials) as its normal use in agriculture, fertilizer, and feed [160].

Algae production has increased worldwide from 10.5 wet weight (MT) in 2000 to 31.2 MT in 2016, with an estimated market value of 1.073 million dollars. In Europe, algae production remained constant, with the EU contributing with 0.2 % and the European Economic Area (EEA) with 0.8 % of the global production [160, 164]. Over 17.000 people are currently employed in the EU algae sector, with an estimated income of about €1.5 billion-plus €240 million redirected for research. In total, the sector in the EU englobes 560 companies and more than 300 research groups [164].

Apart from the two mentioned sectors above (Forest and Fishing/Aquaculture) that contribute to a sustainable and increased bioeconomy. Figure 1.12a shows the other sectors, including food, agriculture, bio-based electricity, and bio-based chemicals, pharmaceuticals, plastics, and rubber (excl. biofuels) that provide added value to the EU bioeconomy. The bio-based sectors that contributed the most to the EU bioeconomy in 2017 were food, agriculture, and bio-based chemicals, with a share of 45.19 %, 36.26 %, and 11.71 %, respectively. All three sectors have a turnover in the EU-28 of over €2 million (Joint Research Centre (JRC) [165]).

USC UNIVERSIDADE DE SANTIAGO DE COMPOSTELA

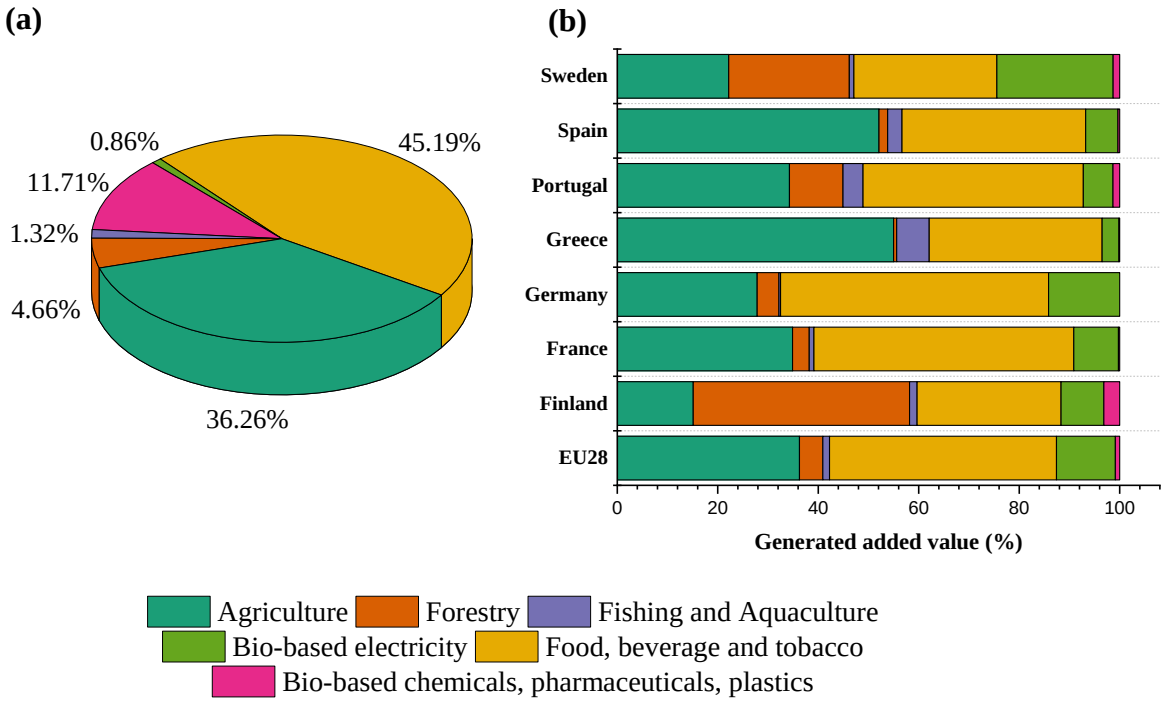


Figure 1.12. Value added in the bioeconomy by sectors from EU28 (a) and the share of value added generated by sector per country in 2017 (b) [165].

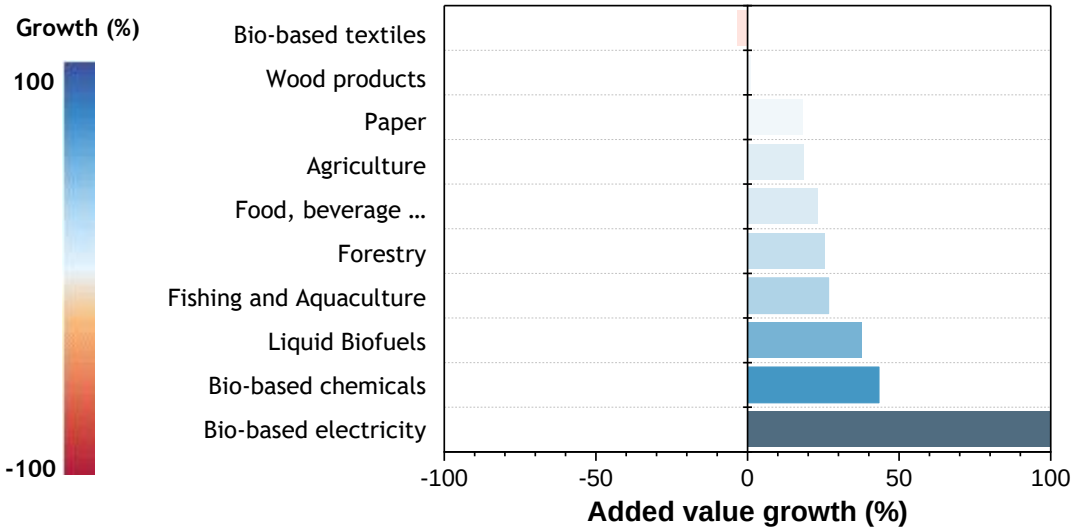


Figure 1.13. Value added growth per sector between 2008 and 2017 from EU28 [165].

USC UNIVERSIDADE DE SANTIAGO DE COMPOSTELA

Figure 1.12b, shows the variation of generated added value per sector in different countries. Southern European countries, including France, are the main contributors in primary production sectors (agriculture, food, fishing, and aquaculture).

On the other hand, the Nordic countries (Finland and Sweden) are considered the top contributors in the forest sector. Finland and Sweden hold great potential for implementing circular bioeconomy in large multinational companies, while small and medium-sized companies (SMEs) are evolving with sustainable business models [166]. These countries have extensive forest areas, and in recent years, wooden multistorey construction (WMC) has been a new business opportunity leading to the evolution of the forest bioeconomy [167].

Figure 1.13 shows the evolution of the added value growth of several sectors between 2008 and 2017 in EU28. Bio-based electricity accounts for the highest growth, while bio-based textiles report the lowest added value in that time range. Overall, the trend is positive since almost all sectors have an added value growth of above 10%. Biological resources are progressively being used in new ways, generating a new biotechnology industrial sector.

Biotechnology in agriculture, industrial processes, and production control have increased significantly over the past few years. Biotechnology, along with nanotechnology, and material technology, creates an optimistic view in developing new products and services [168].

1.4.4. From biomass into high-added-value nanomaterials

Biomass can be upgraded into added value nanomaterials due to the versatility that physicochemical properties in the nanoscale impart to materials. The growth of the Forest and Blue bioeconomy is partially driven by the active role of nanotechnology in developing sustainable nanostructures and nanodevices from renewable resources [169]. For instance, nanocarbons and hybrid nanocomposites are excellent materials with several potential applications in medicine (fabrication of sensors), energy storage, and supercapacitor electrodes. The high carbon content derived from biomass allows the production of these nanosized architectures [170].

Currently, companies rely even more on transforming waste (bamboo chopsticks) or wood-based lignin biomass into carbon anode materials for lithium-ion batteries. These materials have similar properties as graphite, have more attractive prices and are environmentally sustainable [171].

Nanoparticles are also added to specific types of biomass (algae). Silver nanoparticles increase algae growth rate and lipid production for biofuel generation [172]. Biofuels are harvested from the algae continuously without damaging the algae cell walls. Metal nano-catalysts are also being explored for biogasification of wet algae biomass, saving energy costs [173].

Given this, nanotechnology has numerous roles in improving the efficiency, reliability, and the potential benefits of biomass for a circular bioeconomy.

1.5. Nanotechnology, Nanomaterials, and Nanoparticles

Nanotechnology is a field of basic and applied science that deals with substances or objects in the size range between 1-100 nanometers (nm) [174]. To put the nanoscale in perspective, Figure 1.14 shows the range length differences of several biological and macroscopic elements. For example, red blood cells have around 10 µm diameter while our DNA has only 2 nm. Today, it is also possible to have man-made structures with nanometer-sized dimensions, such as transistors which are the core component in computers, graphene, carbon nanotubes, nanowires, and nanoparticles, all having one or more dimensions smaller than 100 nm [174]. Thus, industry

is putting a lot of effort into synthesizing, controlling, and functionalizing nanoparticles to obtain nanomaterials with outstanding properties.

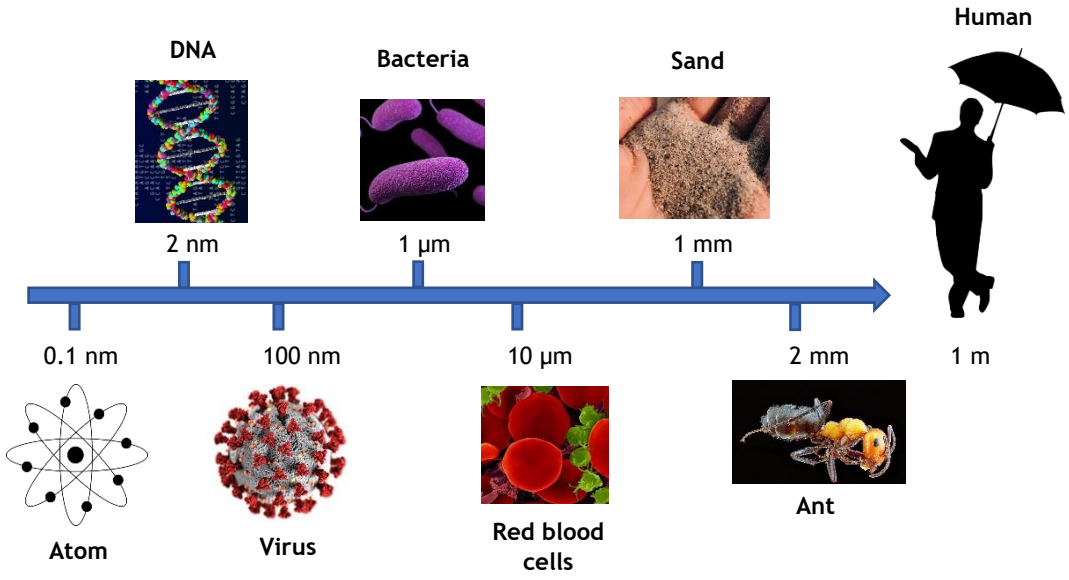


Figure 1.14. Scale comparison from nano to the macroscopic size (CC permissions in Appendix).

1.5.1. Nanomaterials

Nanomaterials (NMs) have a large ratio of surface area to volume ratio, which is responsible for the dominant contribution of surface properties on their overall performance. Surface and size effects, are behind their specific behaviour that comprise higher catalytic activity (large proportion of surface-active sites with chemical reactivity). Nowadays, there is a growing interest in NMs due to their enhanced catalytic activity, superparamagnetic response, localized plasmon resonance, or size dependent fluorescent responses, among others [175]. These properties are important in several areas such as bioenergy, electronics, pharmaceuticals, ionic liquids, polymers, among others. The NMs classification is based on the number of dimensions, as shown in Figure 1.15. The nanostructure materials are classified as [176]:

- **Zero-dimensional (0D) NMs** are basically nanoparticles, including nanospheres, nanoclusters, or quantum dots, whose size ranges are between 1-100 nm.

- **One-dimensional (1D) NMs** have two dimensions at the nanoscale (x, y), while the other dimension is above the nanoscale. Here is included needle-shaped NMs, such as nanowires, nanofibers, nanotubes, and nanorods.

- **Two-dimensional (2D) NMs** have only one dimension (x) at the nanoscale. These 2D nanostructures exhibit thin-layer-like structures, namely nanolayers, nanofilms, and nanocoatings. Due to their structure, these 2D-NMs present a wide range of unique physicochemical properties in magnetism, electrical conductivity, and catalysis.

- **Three-dimensional (3D) NMs**, are not restricted to the nanoscale in any dimension. These 3D nanostructures can be composed by the self-assembly of low dimensional NMs (0D, 1D, or 2D). It can include nanowires, nanoplates, polycrystals, or even small-sized nanoparticles that are interconnected, resulting in the formation of interfaces. The spatial arrangement of the interconnect networks (0D, 1D, or 2D) in the 3D-NMs can enhance specific properties to diverse applications.

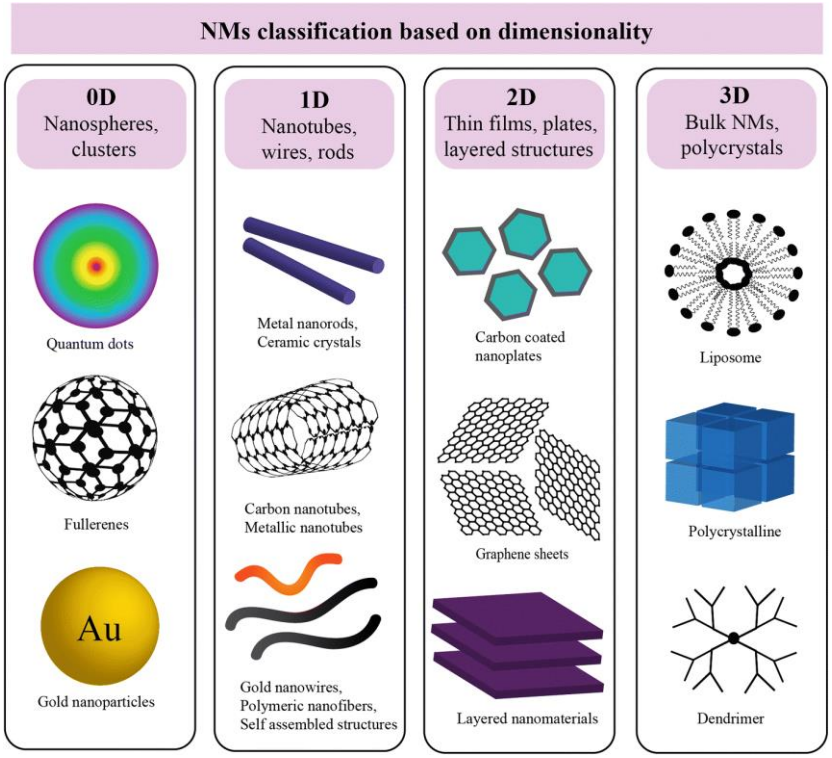


Figure 1.15. Dimensionalities of Nanomaterials (Reproduced with permission from the reference [177] under CC BY 4.0)

a. Naturally occurring nanomaterials

Recently, naturally occurring nanomaterials or artificially produced from natural resources are gaining much attention due to their physical, chemical, and biological properties. For instance, nanocellulose, originally extracted through several mechanisms from cellulose, has been used to replace blood vessels, soft tissue, or even to develop medical biomaterials [178]. Also, it has been used for energy storage devices to improve electrochemical performance [179].

Nanocellulose refers to three sets of nanomaterials: cellulose nanofibrils (CNFs), cellulose nanocrystals (CNCs), and bacterial nanocellulose (BNC). The three vary in shape, size, cellulose source, surface chemistry, and extraction method [180]. Such nanomaterials have numerous applications, especially in medicine, agriculture, and cosmetics, due to their biocompatibility, biodegradability, and robust mechanical properties.

From aquatic plants and animals, it is also possible to obtain nanostructures and transform them from 1D to 3D nanomaterials. For example, chitin is an abundant polysaccharide present in crabs and shrimps in the form of chitin nanofibrils. It is widely used as a smart nanocarrier for cargo release and as a biostimulant for agriculture and most recently as 3D nanostructures for environmental and biomedical remediation [181].

Alginate is another type of polysaccharide present in brown algae that have been explored in different forms (fibre, beads, hydrogel, and as 3D printed material). Furthermore, it is also used in combination with organic or inorganic nanoparticles in drug delivery, water remediation, or other industrial applications [182].

1.5.2. Synthetic Nanoparticles

In the last years, synthetic nanoparticles of different types have been used as an advanced ingredient to improve the mechanical or chemical performance of products or materials in a wide variety of sectors such as, automotive, cosmetic, health and electronic industries. Most recently, they are being used in nanomedicine, environmental protection, and biofuel and bioenergy production. Nanoparticles are classified according to their morphology, size, chemical, and physical characteristics. They are generally divided into organic, inorganic, and carbon-based [183].

- **Organic nanoparticles**, Liposomes, dendrimers, carbon nanomaterials, and polymeric micelles are examples of organic nanoparticles. The liposomes, micelles, or polymers are widely used in drug delivery systems since they are sensitive to heat and electromagnetic radiation. In addition to that, they can be used as target drug delivery being injected into specific parts of the body [184].

- **Inorganic nanoparticles** are also attractive due to their physical (e.g., optical, magnetic) and chemical (easy functionalization, stability) properties [185]. Usually, inorganic nanoparticles are categorized as metal and oxide-based nanoparticles.

- **Metal-based nanoparticles** are basically nanoparticles synthesized from metals, namely aluminium (Al), gold (Au), silver (Ag), iron (Fe), or zinc (Zn). These nanoparticles can have low sizes ranging from 10 to 100 nm, high surface area to volume ratio, pore size, spherical or cylindrical morphology as crystalline and amorphous structures. They are sensitive under light, heat, or humidity environmental conditions.

- **Metal oxide-based nanoparticles** are synthesized to increase the reactivity of the corresponding metal. For instance, iron nanoparticles in the presence of oxygen can be oxidized into antiferromagnetic oxide (α-Fe_2O_3), known as hematite which is widely used due to its photocatalytic activity [186]. Commonly synthesized oxides are aluminium oxide (Al_2O_3), cerium oxide (CeO_2), magnetite (Fe_3O_4), titanium oxide (TiO_2), and silica oxide (SiO_2). Fe_3O_4 NPs have a superparamagnetic behaviour being used in magnetic, biomedicine application, while TiO_2 NPs are ideally used in water splitting and catalytic applications [187].

USC UNIVERSIDADE DE SANTIAGO DE COMPOSTELA

- **Carbon-based nanoparticles** are entirely made of carbon and are classified as fullerenes, graphene, carbon nanotubes (CNT), carbon nanofibers, and activated carbon [187].

1.5.3. Magnetic nanoparticles structure, properties, and applications

Magnetic materials at the nanometre scale exhibit interesting physical properties such as giant magnetoresistance, large coercive forces, tunnelling magnetoresistance, and superparamagnetism [188–190]. Furthermore, because of the exclusive properties and small size, magnetic nanoparticles (MNPs) can be used in several technological, medical, and environmental applications such as magnetic ink, data storage, magnetic resonance imaging, biotechnology, and environmental applications [191–193]. However, for a successful application, the MNPs must be developed following processes to achieve good compatibility, stability, and size with the surrounding media. For example, in biomedicine, more precisely for *in-vitro* assays, optimum particle size is required around 10-20 nm because otherwise large aggregates will be formed and eliminated from the bloodstream by the immune system [194]. MNPs must be in the superparamagnetic regime to avoid the formation of agglomerates and their further elimination from the body. In hyperthermia, the activation of magnetic nanoparticles by an alternating magnetic field is a new technique in cancer therapy [195]. The heat generated by an alternating magnetic field of low frequency is utilized to kill cancerous cells. The size, functionalization, surface charge, and morphology are important properties to enhance their heating efficiency to be used as hyperthermia agents.

Furthermore, magnetic nanoparticles are also widely used as adsorbents for environmental remediation of organic and inorganic pollutants. Most recently, biosensors are being developed with the incorporation of magnetic nanoparticles to enhance their stability and sensitivity for the early detection of environmental analytes. The main types of magnetic nanoparticles are composed of three metals, namely iron, cobalt, and nickel. The iron magnetic nanoparticles exist in the form of pure and iron oxide, such as γ-Fe_2O_3 (maghemite), α-Fe_2O_3 (hematite), Fe_3O_4 (magnetite), FeO (wüstite), and α-FeOOH (goethite). Meanwhile, cobalt and nickel nanoparticles exist in the pure form and in their correspondent oxides (Co_3O_4, CoO) and NiO, respectively [196]. Among the magnetic nanoparticles, magnetite is by far the most widely used and employed, especially in biomedical applications. In contrast, the nanoparticles of nickel and cobalt are of little interest due to their toxicity and susceptibility to oxidation [197].

a. Magnetite nanoparticles (Fe_3O_4 NPs)

Fe_3O_4 is a natural mineral and the most magnetic present all over the Earth. Its structure follows an inverse spinel pattern with alternate octahedral and octahedral-tetrahedral layers. The iron ions within the matrix occupies different positions. The Fe^{2+} and Fe^{3+} species are equally distributed in the octahedral positions and are hexacoordinated by oxygens. At the same time, only the Fe^{3+} species are tetracoordinate by oxygens occupying the tetrahedral positions. Thus, the final chemical formula $Fe^{3+[}Fe^{2+}Fe^{3+]}O_4$, allows the representation of octahedral sites (with brackets) and tetrahedral sites (without brackets). In addition, Fe_3O_4 has a centred cubic pattern structure with a crystal lattice parameter (a) equal to 8.396 Å and the presence of eight units within each magnetite unit cell [198].

Many procedures are used to synthesize Fe_3O_4 NPs according to their application, such as co-precipitation, solvothermal, and thermal decomposition methods [199]. Among the various synthesis methods, co-precipitation is the more convenient method to synthesize Fe_3O_4 NPs since it only requires an aqueous solution of iron salts (Fe^{2+}/Fe^{3+}), a base, and an inert atmosphere at room temperature. During the process no toxic solvents are produced and temperatures below 100 ºC are used. In addition, the method is used at an industrial scale since it is easily scaled up, reproducible and eco-friendly [198, 200]. In this thesis, the reverse-coprecipitation method was used and optimized.

On the contrary, to the standard co-precipitation method, in the reverse co-precipitation method, a solution of dissolved Fe salts is added dropwise into an alkaline solution (e.g., ammonium hydroxide, NH_4OH). As a result, the pH value gradually decreases causing a posterior reduction in the mean crystalline and particle size compared to the standard co-precipitation method [201]. Due to their magnetic properties, Fe_3O_4 NPs can be applied in several research fields: catalysis, biosensing, bioimaging, and biomedicine.

b. Magnetism and magnetic technologies

Among the technologies aimed at separating the contaminants from the drinking water and industrial wastewater, magnetic technology, applicable in packed beds and fluidized beds, is an innovative technology that can lead to high selectivity and specificity of pollutants removal.

Magnetism origin lies in electrons' spin and orbital motion and the type of interaction between the electrons. Normally, magnetic materials respond to an externally applied magnetic field due to the interaction with their magnetic moment. Based on the response of materials to an external magnetic field, there are five basic types of magnetism related to the magnetic behaviour of materials, namely: diamagnetism, paramagnetism, ferromagnetism, antiferromagnetism, and ferrimagnetism. The direction in which the magnetic moments are aligned to each other (parallel, antiparallel, and in exceptional cases, in spiral (helical) arrays, or randomly) is important to tell the type of magnetism. In addition, the magnetic susceptibility (χ) measures the ability of a material to be magnetized under the action of magnetic stimulation [202]. Figure1.16 shows the different orientation moments of five types of materials following each magnetization under and without an applied external magnetic field.

- **Diamagnetic materials** have a weak magnetic susceptibility ($\chi<0$), in the absence of a magnetic field, the material atoms have no net magnetic moment. However, under an applied magnetic field, the electrons spinning motion produces magnetization in the opposite direction of the applied field. Silver, lead, pyrolytic carbon are examples of diamagnetic particles [203, 202].

- **Paramagnetic materials** have unpaired electrons with a random distribution of magnetic moments and a zero net magnetization throughout all material. However, when a field is applied, the moments align up, giving a positive magnetic moment in the direction of the magnetic field. Even though the magnetic susceptibility is positive, these materials do not retain any magnetic properties when an external field is removed. Paramagnetic materials include palladium, molybdenum, tungsten, lithium, and tantalum [204].

- **Ferromagnetic materials** possess a large and positive magnetic susceptibility to an external magnetic field, giving them "magnetic memory." Their strong magnetic properties are partly due to the presence of magnetic domains with a large number of aligned atom moments. As a result of an applied field, the domains become parallelly aligned, producing a strong net magnetization. Contrarily, the domains become randomly distributed with a net magnetism equal to zero in the absence of a magnetic field. For a better situation, one typical example of a ferromagnetic material would be a magnet onto a refrigerator. The magnet stays magnetically attached because the refrigerator door is composed of ferromagnetic material. Iron, nickel, and cobalt are good examples of ferromagnetic materials.

- **Antiferromagnetic materials** are not attracted to magnets due to the cancellation of the magnetic moments of neighbouring atoms, which are arranged anti-parallelly. These materials have the particularity of becoming paramagnetic when heated to a specific temperature, which is known as *Néel* temperature [205]. One of the most known antiferromagnetic materials is hematite and other transition metal oxides.

- **Ferrimagnetic materials** have opposing moments, similar to that of antiferromagnetism, however, the opposing moments are unequal, so a spontaneous magnetization remains. Magnetite is one example of a ferrimagnetic material [205].

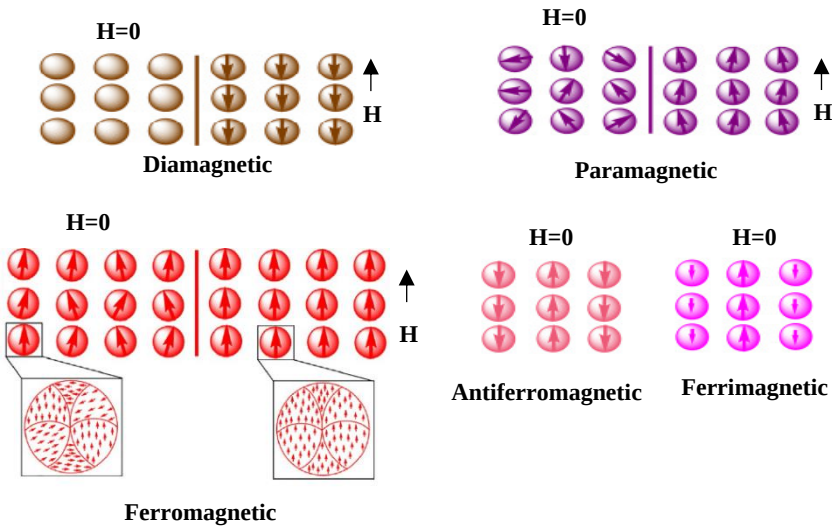


Figure 1.16. Magnetic dipoles disposition of different types of magnetic materials (Adapted with permission from reference [206] Copyright (2022) Elsevier).

c. Hysteresis loops

Magnetic hysteresis occurs when an external magnetic field is applied to a ferromagnetic or ferrimagnetic material (e.g., iron or magnetite). The magnetic hysteresis loop represents the magnetization (M) versus the applied magnetic field (H) of a ferro- and ferri-magnetic material.

Figure 1.17 shows a typical hysteresis loop and a number of primary magnetic properties associated with each material, such as are the saturation magnetization (M_s), remanence (M_r),

and coercive force (H_c). The saturation magnetization (M_s) is the maximum magnetic moment per unit volume for a magnetic material, and all magnetic moments are aligned along the applied magnetic field. However, when the applied magnetic field is cancelled, some residual magnetization remains being called the remanent magnetization (M_r). Lastly, the coercive field (H_c) is the resistance of a magnetic material and the magnetic field that has to be applied to demagnetize it [202].

As shown in Figure 1.17, the shape and size of the hysteresis loop depend on the magnetic nature of the material. Therefore, one material is selected based on its magnetization hysteresis loop profile for a particular application. For example, ferromagnetic materials can be classified into soft and hard ferromagnetic materials. Both are distinguished by the H_c and M_s values. Soft ferromagnetic materials usually have a low coercive value of around 10 Oe and a M_s of 100 emu/g. This leads to a narrow hysteresis loop, which is normally seen in permalloy or FeSi alloys. On the other hand, hard-ferromagnetic materials present a high coercivity, large hysteresis loop area, with H_c values larger than 350 Oe and M_s under 100 emu/g. Hard- ferromagnetic materials are also known as permanent magnets and have several applications in industry producing magnetic sensors, recording media, synchrotrons, and others [207].

Unlike ferromagnetic materials, both paramagnetic and diamagnetic materials do not form any hysteresis loop since they cannot retain any residual magnetization after the external magnetic field is removed. Therefore, apart from the analysis of the magnetization profile, it is possible to obtain information about the magnetic moment distribution.

Superparamagnetism is a type of magnetism related to sufficiently small nanoparticles. In very small magnetic nanoparticles, the magnetization can randomly flip direction under the influence of temperature.

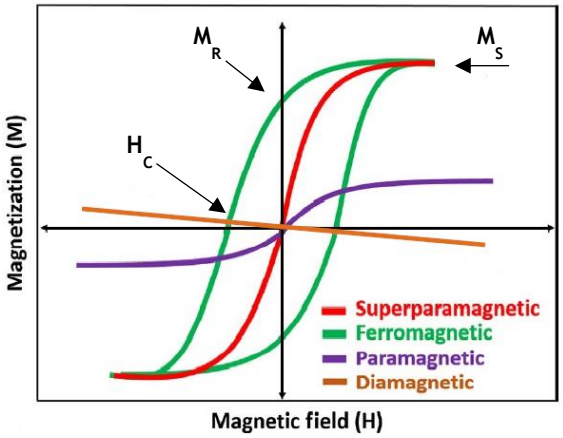


Figure 1.17. Hysteresis loop of ferromagnetic, paramagnetic, superparamagnetic and diamagnetic particles (Adapted with permission from reference [206]. Copyright (2022) *Elsevier*)

Figure 1.18 shows the particle size and the domain type variation when measuring the hysteresis loop of a material. It is already known that ferromagnetic materials have a large hysteresis loop. However, when a ferromagnetic particle size increases, the magnetic moment also increases, increasing its magnetization to a maximum saturation value, revealing a thinner hysteresis loop. Conversely, when the particle size is smaller, the hysteresis loop widens until a specific nanoparticle size, often called critical diameter size (D_s). After the critical size is

reached, the hysteresis loop starts to narrow with decreasing size till the superparamagnetic region/size is achieved. In this region, the nanoparticles hysteresis curve retains the sigmoidal shape typically found in a ferromagnetic material but, in contrast, loses the hysteresis loop.

Due to their magnetic properties, superparamagnetic materials have gained a lot of interest over the years, especially in biomedicine technologies such as drug delivery, anticancer magnetic hyperthermia, or ferrofluids. Among the several nanoparticles, superparamagnetic iron oxide nanoparticles (SPIONS), in particular magnetite and maghemite, exhibit outstanding magnetic properties and appropriate size plus biodegradability, making them attractive for several fields [208].

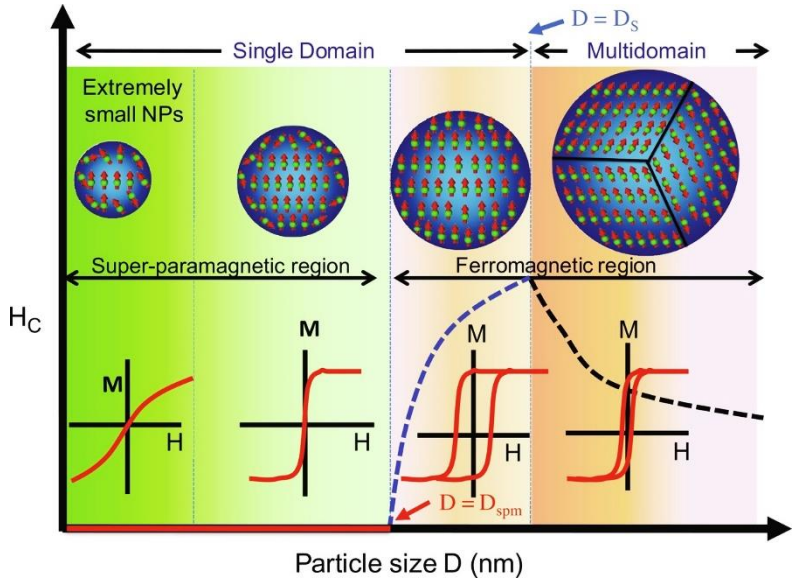


Figure 1.18. Size-dependent magnetic domain structures (Reproduced with permission from reference [209]. Copyright (2021) *Elsevier*)

1.5.4. Magnetic sustainable nanomaterials for environmental remediation and other applications

In the last few years, magnetic nanomaterials have been developed for environmental remediation and other applications due to their easy recovery, reusability, and cost-effective production.

Fe_3O_4 NPs are widely used and employed as adsorbents due to their very high magnetization making them more suitable and efficient in responding to an applied magnetic field resulting in a fast separation from any aqueous media [210]. In addition, these NPs can be easily functionalized to tune their affinity towards the removal of several contaminants present in drinking water ranging from metals to organic molecules. The functionalization also prevents their fast oxidation and aggregation caused by anisotropic attraction. Besides the actual surface modification, Fe_3O_4 NPs can also be dispersed into a polymeric matrix fomenting the development of biocompatible magnetic materials with several morphologies and valuable properties in the biomedical (anti-inflammatory effects of bacterial cellulose), and electronical fields (calcinated lignin fibres present electroconductive properties). For this reason, the design is a critical aspect to take into account in order to achieve a highly functional magnetic material.

Given this, several researchers have developed magnetic nanocomposites of macroscopic size with different combinations of several biodegradable and biocompatible compounds. Besides this, they have numerous advantageous biocompatible features, such as cost-effective production, easy handling, and fast separation under an external magnetic force. Bio-based magnetic nanocomposites, due to their size, shape, exceptional surface/volume ratio, porosity, and dispersibility in water, have high selectivity to several contaminants allowing optimal mass transport and good contact.

It was reported that alginate-based composites with either Fe_3O_4 or γ-Fe_2O_3 NPs could efficiently adsorb methylene blue or malachite green from water [210]. Another research studied the removal efficiency of metal ions from water in a single and ternary system using magnetic alginate beads composed of activated carbon. These beads revealed higher adsorption at the single system with a removal efficiency of approximately 80 % [211]. In recent studies, Fe_3O_4 has been incorporated into biomass-based materials, specifically to plant biomass to remove contaminants from water (e.g., heavy metals, fungi, and mycotoxins) [212]. In combination with magnetic nanoparticles, cellulose was used to develop recyclable catalysts, transparent films for magneto-optical applications, and as an oil-adsorbent [213, 214].

Cellulose-based magnetic materials are typically prepared by confining the ion oxides into the cellulose matrix [215]. Recently, magnetic cellulose-based materials from olive solid waste were developed and showed excellent removal efficiency of methylene blue from wastewater [216]. The cellulose was converted to nanocrystalline cellulose to easily incorporate and disperse the iron metal ions due to its high porosity and large number of reactive functional groups [217].

Recent studies also indicated cellulose nanofibrils and lignin as a sustainable alternative to the high demand of renewable resources with the development of carbon microfibers and their potential integration in small portable and wearable electronics [218]. In addition, cellulose acetate derived from cellulose through acetylation, in combination with lithium perchlorate ($LiClO_4$) demonstrated to be a great biodegradable polyelectrolyte to use in supercapacitors [219] and also a sustainable biopolymer to be used in bio-packaging [220].

Aside from cellulose derivatives and cellulose extracted either from waste or directly from forest biomass, bacterial nanocellulose is a natural cellulose nanofiber synthesized by bacteria. Nowadays, bacterial nanocellulose is widely popular because of its unique porosity, 3D morphology, elasticity, crystallinity, lightweight, non-toxicity, and biodegradability. Fe_3O_4 NPs were also incorporated into the bacterial nanocellulose structure, resulting in new products with potential for biomedical applications such as wound tissue regeneration or as adsorbent for heavy metals ions [210]. Magnetic bacterial nanocellulose structures showed great potential as adsorbent for Pb^{2+}, Mn^{2+}, and Cr^{3+} with maximum adsorption capacities of 65 mg/g, 33 mg/g, and 25 mg/g, respectively [221]. Another study successfully prepared a magnetic bacterial nanocellulose structure with activated carbon for the adsorption of Pb^{2+} and methyl orange (MO) from aqueous solutions [222].

Furthermore, it is proven that magnetic materials made from sustainable resources are gaining even more attention due to the current circumstances and the need to think outside the box.

USC UNIVERSIDADE DE SANTIAGO DE COMPOSTELA

USC
UNIVERSIDADE
DE SANTIAGO
DE COMPOSTELA

Chapter 2

The results presented in this chapter are related to the following publications (the editorial authorizations for the use of these publications are in the Appendix 6.4):

1. González-Jartín JM. [a], **de Castro Alves L. [b]**, Alfonso A.[a], Piñeiro-Redondo Y.[b], Yáñez-Vilar S. [b], González Gómez M.[b], Osorio Vargas Z.b, Sainz M.[c], Vieytes M. [d], Rivas J. b, Botana L. [a], Detoxification agents based on magnetic nanostructured particles as a novel strategy for mycotoxin mitigation in food. *Food chemistry* (2019), 294, 60-66. (I.F: 6.5, Q1) https://doi.org/10.1016/j.foodchem.2019.05.013

[a] Department of Pharmacology, Facultad de Veterinaria, University of Santiago de Compostela, 27002 Lugo, Spain
[b] Department of Applied Physics, Universidad de Santiago de Compostela, Faculty of Physics, 15782 Santiago de Compostela, Spain
[c] Department of Vegetal Production and Engineering Projects, Facultad de Veterinaria, University of Santiago de Compostela, 27002 Lugo, Spain
[d] Department of Physiology, Facultad de Veterinaria, University of Santiago de Compostela, 27002 Lugo, Spain

The main contribution of the PhD student to this study are explicitly indicated below:
Experimental: Development, synthesis and characterization of the particles (L1-L9).
Manuscript: Reviewing and editing the original draft (methods and characterization).

2. **de Castro Alves L.**, Yáñez-Vilar S., Piñeiro-Redondo Y., Rivas J., Novel Magnetic Nanostructured Beads for Cadmium(II) Removal. *Nanomaterials*. (2019), 9(3):356. (I.F: 4.3, Q1) https://doi.org/10.3390/nano9030356

Department of Applied Physics, Universidad de Santiago de Compostela, Faculty of Physics, 15782 Santiago de Compostela, Spain.

The main contribution of the PhD student to this study are explicitly indicated below:
Experimental: Development, synthesis and characterization of particles, experimental conceptualization, investigation, data acquisition and analysis.
Manuscript: Preparation of the paper and writing the initial draft (all sections).

3. **de Castro Alves L.**, Yáñez-Vilar S., Piñeiro-Redondo Y., Rivas J., Efficient separation of Heavy Metals by Magnetic Nanostructured beads. *Inorganics* (2020) 8, 40. (I.F: 4.4, Q2) https://doi.org/10.3390/inorganics8060040

Department of Applied Physics, Universidad de Santiago de Compostela, Faculty of Physics, 15782 Santiago de Compostela, Spain. The main contribution of the PhD student to this study are explicitly indicated below:
Experimental: Development, synthesis and characterization of particles, experimental conceptualization, investigation, data acquisition and analysis.
Manuscript: Preparation of the paper and writing the initial draft (all sections).

USC
UNIVERSIDADE
DE SANTIAGO
DE COMPOSTELA

2. Materials based on the Blue economy concept for contaminants adsorption: magnetic beads

2.1. Adsorption design: Introduction

Human activities and climate change play a crucial role in the water quality and scarcity by the overexploitation and contamination of natural water sources. These environmental stresses result in an irregular distribution of freshwater with a destabilization of water supplies [223, 224] from groundwater, reservoirs, lakes, and rainwater. The type and origin of pollutants vary from one-point source to another, and different measurements need to be undertaken. The water quality is determined by applying various treatment techniques involving flocculation, sedimentation, reverse osmosis, ozonization, chlorination, adsorption, etc. Among all techniques involved in the cleaning process, adsorption has been found as the most cost-effective and suitable treatment employed in industries to treat water or wastewater from different contaminants. Secondary sludges or intermediate products are not generated by adsorption, and few chemicals are used.

Over the years, adsorption technology has contributed immensely to the global drinking water supply. Substantial efforts are devoted to innovative adsorption technologies at the research level seeking efficiency increments and selectivity. The high impact of innovative adsorption technologies at the laboratory scale, scaling up pilot experiments in a natural environment is still challenging. Thus, a better understanding of the equilibrium adsorption capacity, pollutant uptake rate, and thermodynamics conditions, the type and use of an adsorbent are essential for the optimization of large-scale water treatments.

Batch experiments are a facile process that can be rapidly used to assess the efficiency of an adsorbent and is frequently used to sequestrate contaminants from water and wastewaters [225]. The batch system study consists of a batch container with an adsorbent in the presence of an adsorbate dissolved in a solution. The system is intentionally mixed, for a specific interval of time, with optimized experimental conditions such as temperature, adsorbent dosage, agitation speed, temperature, and pH, so the system attains an adsorption equilibrium. The time required to achieve equilibrium between the adsorbate and adsorbent is extremely dependent on the conditions mentioned above [226]. The chemical and physicochemical properties of the adsorbent are also crucial since it is one key parameter that governs adsorption. A precise understanding of the basic properties of one adsorbent allows the maximization of its use in both fixed-bed and batch mode systems.

Moreover, experimental studies demonstrate that an adsorbent is more effective in a single system than in a mixed one because of the adsorption competition between the adsorbates in the solution [227]. This behaviour can be analysed in terms of adsorption models accounting for several experimental conditions at constant temperature (adsorption isotherms) or various experimental conditions at different contact time (adsorption kinetics). The use of isotherm and kinetic models in water treatment provides the rate and efficiency of an adsorbent to remove a contaminant, besides the thermodynamic nature of the adsorption system and the mechanism that is taking place. Therefore, batch adsorption models are suitable to provide reliable predictions of the adsorption capacity of an adsorbate at large-scale water treatment process. Most importantly, the procedure can quickly assess an adsorbent's efficiency in removing target contaminants from aqueous solutions.

Thus, in the present chapter, batch adsorption studies were performed to remove mycotoxins and metals in a mono, binary, and ternary system, using magnetic alginate beads

with various compositions. It was demonstrated the physical, chemical, and magnetic properties of the particles and their adsorption capacity were described using isotherm, kinetic, and diffusion models.

2.1.1. Adsorption isotherm models

In general, adsorption isotherm describes the mobility of a substance from an aqueous media to a solid phase at constant conditions of temperature and pH. The equilibrium is only established when a dynamic balance is reached between the adsorbed substance onto the adsorbent surface and the remaining ones in the solution. A set of isotherm models have been developed to describe the different adsorption processes, such as Langmuir, Freundlich, Temkin, or Dubinin- Kaganer- Radushkevich (DKR) isotherms, that take into account the specific details of the adsorbent properties and the adsorbed species.

- **Langmuir isotherm model**

The Langmuir isotherm assumes monolayer and homogeneous adsorption onto a surface containing a finite number of adsorption sites that possess an equal affinity for the adsorbate. Once a site is filled, no further adsorption can occur in that site, indicating that the surface can reach a saturation point where the maximum surface adsorption will be achieved. The isotherm is expressed by the following non-linear equation (1):

$$q_e = \frac{q_m K_L C_e}{1+K_L C_e} \quad (1)$$

The linear form of the Langmuir isotherm is given by equation (2):

$$\frac{C_e}{q_e} = \frac{1}{K_L q_m} + \frac{C_e}{q_m} \quad (2)$$

where, q_e (mg/g), is the amount adsorbed. C_e (mg/L), is the adsorbate concentration in solution, both at equilibrium. K_L (L/mg), is the Langmuir adsorption constant and q_m (mg/g), is the maximum adsorption capacity for monolayer formation on the adsorbent. The adsorption equilibrium data was plotted as C_e/q_e against C_e. Out of the four different linearized Langmuir isotherm equations (not shown), type 1 and type 2 are the most commonly used due to the minimized deviations from the fitted equation resulting in the best error distribution [228]. For this reason, the type-1 Langmuir linear equation was used in this thesis. Hereby, a fundamental characteristic of Langmuir isotherm regarding dimensionless constant known as separation factor, R_L, defined by Weber and Chakraborti in 1974 [229], can be represented as:

$$R_L = \frac{1}{1+K_L C_0} \quad (3)$$

where, C_0 (mg/mL), is the adsorbate initial concentration. The R_L value is important since it defines if the isotherm is linear (R_L= 1), unfavourable (R_L> 1) or favourable (0 < R_L < 1) [230].

USC DE SANTIAGO DE COMPOSTELA

- **Freundlich isotherm model**

The Freundlich isotherm assumes that the adsorption takes place on a heterogeneous multilayer surface with no limited degree of adsorption sites, and the energy is non-uniformly distributed. The isotherm is represented by the non-linear equation (4) [231]:

$$q_e = K_F C_e^{1/n} \quad (4)$$

The linear form of the Freundlich isotherm is given by equation (5):

$$\log q_e = \log K_F + \frac{1}{n} log C_e \quad (5)$$

where, K_F and n, indicate the adsorption capacity and the adsorption linearity, respectively. The equilibrium data for the adsorption is plotted as $\log q_e$ against $\log C_e$. The two constants, K_F and n are calculated from the curve. Deviation of n constant from unity indicates a nonlinear adsorption that takes place on heterogeneous surfaces [232]. If n value is equal to unity (n=1), adsorption is linear. If (n>1) adsorption is favourable and is a physical process. Adsorption is considered to fit the Freundlich approach when exponent *n* takes values within the range 1–10 [233].

- **Temkin isotherm model**

The Temkin isotherm model contains a factor that explicitly considers the interactions of adsorbent-adsorbate and the adsorption process. The model assumes that the heat of adsorption (ΔH_{ads}) of adsorbate present in the surface layer decreases linearly as a result of increased surface coverage [234]. Also, the equation reveals a uniform distribution of binding energies. The quantity adsorbed, q_e, was plotted against lnC_e, and the constants were determined from the slope and intercept. The model is represented by the following non-linear equation (6) [235].

$$q_e = \mathrm{bt} \ln(K_T C_e) \quad (6)$$

where, b_T (J/mol), is the constant related to the adsorption heat and K_T (L/g), is the Temkin isotherm equilibrium binding constant. However, is commonly used the rearranged linear form of the Temkin isotherm equation, represented by equation (7):

$$q_e = \frac{RT}{b_T} \ln K_T + \frac{RT}{b_T} ln\, C_e \quad (7)$$

where, R, (8.314 J/molK), is the universal gas constant and T (K), is the absolute temperature.

- **Dubinin-Kaganer-Radushkevich (DKR) isotherm model**

The DKR isotherm model assumes that the adsorption curve depends on the adsorbent's porous structure and that adsorption adopts a multilayer pore filling character, where electrostatic interactions (*Van der Waals* forces) are the main physical forces during the process [236]. The non-linear equation form is expressed as:

$$q_e = q_m \exp(-\beta \varepsilon^2) \quad (8)$$

where, q_m (mg/g), is the adsorption capacity (maximum theoretical adsorption capacity for the formation of a monolayer). β, is the DKR constant representing mean adsorption energy (mol^2/kJ^2) and ε, is the Polanyi potential, which can be calculated through equation (9):

$$\varepsilon = \mathrm{RT}\ln(1 + \frac{1}{C_e}) \quad (9)$$

The linear form of this model is described as:

$$\ln q_e = \ln q_m - \beta\varepsilon^2 \quad (10)$$

Furthermore, the E value describes the type of adsorption, if the value is under 1-8 kJ/mol or within 8-16 kJ/mol, the adsorption process is physical (electrostatic interactions) or chemical (covalent interactions), respectively. The value of E can be calculated using equation (11) [230]:

$$E = \frac{1}{\sqrt{2\beta}} \quad (11)$$

2.1.2. Adsorption Kinetic models

Adsorption kinetics models describe the adsorption over time at constant concentration and determined adsorbent dosage, pH, and temperature conditions. During adsorption, there are two main processes involved, physisorption and chemisorption. Physisorption or physical process results from weak attraction forces, namely, *Van der Waals*. Meanwhile, chemisorption or chemical processes result from strong bonding forces between the adsorbate and the adsorbent with the transfer of electrons [237]. Adsorption kinetics was studied in terms of pseudo first-order, pseudo second-order, Elovich kinetic models, and the interparticle diffusion model.

- **Pseudo first-order (PFO) model**

The Pseudo first-order model (PFO) describes a physical adsorption where the adsorption rate constant, k_1, usually decreases with the increasing initial adsorbate concentration, due to the saturation of the adsorption sites [237]. If the PFO equation does not fit well the whole range of time and initial adsorbate concentrations, the adsorption process follows a much more complex mechanism [238]. The non-linear form is described by equation (12):

$$q_t = q_e^{(1-e^{-k_1 t})} \quad (12)$$

while, in its he linear form it is expressed by equation (13):

$$\log(q_e - q_t) = \log q_e - \frac{k_1}{2.303} t \quad (13)$$

The constant of adsorption capacity (q_t) at time, t, can be calculated using the following equation:

$$q_t = \frac{(C_0 - C_t)V}{\mathrm{m}} \quad (14)$$

USC UNIVERSIDADE DE SANTIAGO DE COMPOSTELA

where, q_t and q_e represents the amount of solute adsorbed (mg/g) at any time (minutes) and at equilibrium, respectively. C_0 (mg/L) is the initial concentration of metal ions. C_t (mg/L) is the concentration of metal ions at time *t*. V(L) is the volume of solution and m (g) is the mass of adsorbent. k_1 (min^{-1}) represents the adsorption constant of PFO and *t* (minutes) is the contact time. If $\log(q_e - q_t)$ plotted versus *t* follows a linear relationship, the system follows the kinetic model and the constant k_1 is determined by the slope of the plot.

- **Pseudo second-order (PSO) model**

The PSO kinetic model is characteristic of a chemical adsorption (chemisorption). The model depends on the applied experimental conditions, such as, initial adsorbate concentration, pH, temperature and agitation rate [238]. The adsorption rate constant, k_2, usually decreases with the increasing initial adsorbate concentration. Thus, the higher the initial adsorbate concentration, longer time is needed to achieve an equilibrium and in turn k_2 value decreases. The non-linear form of this chemisorption model is described by the following equation (15):

$$q_t = \frac{k_2 q_e^2 t}{1 + k_2 q_e t} \tag{15}$$

and its linear form is expressed by equation (16):

$$\frac{t}{q_t} = \frac{1}{k_2 q_e^2} + \frac{1}{q_e} t \tag{16}$$

where, k_2(mg/g min^{-1}) is the pseudo-second order rate constant; q_e(mg/g) is the amount of metal ions adsorbed at equilibrium and $h = k_2 q_e^2$ (mg/g min) is the initial PSO adsorption rate. If t/q_t plotted versus *t* follows a linear relationship, the system follows the PSO kinetics model and k_2 and q_e can be determined from the intercept and slope of the plot, respectively [239].

- **Elovich model**

The Elovich model assumes that adsorption is a chemisorption process and predicts the mass and surface diffusion, activation, and deactivation energy of a system [240]. In this model, the solute's adsorption rate decreases exponentially as the amount of adsorbed solute increases (289). The non-linear form is described by the following equation (17):

$$q_t = \frac{1}{\beta} ln(1 + \alpha\beta t) \tag{17}$$

The model can be expressed mathematically in the linear form by the following equation (18):

$$q_t = \frac{1}{\beta}\ln(\alpha\beta) + \frac{1}{\beta}\ln t \tag{18}$$

USC UNIVERSIDADE DE SANTIAGO

where, α (mg/g min) represent the initial rate of adsorption and β (mg/g min) is correlated to the surface saturation and activation energy required for chemisorption.

- **Intraparticle diffusion (IPD) model**

In addition to adsorption, diffusion is a key mechanism governing the whole procedure, and for this reason, mass transport models have been included as a fundamental step of new adsorption approaches. The adsorption process using the diffusion model is based on the following steps [241]:

1. Bulk solution transport is the adsorbate diffusion within the liquid solution far from the external boundary layer of the particle.
2. Step 1- Film diffusion occurs in a nearby liquid region (liquid film) close to the external adsorbent surface, where the adsorbate diffuses through, and some interactions with the adsorbent material begin to happen at the surface (external diffusion).
3. Step 2 – Pore diffusion from the film to the internal pores.
4. Step 3- Surface reaction, the adsorptive binding to the adsorbent's internal surface.

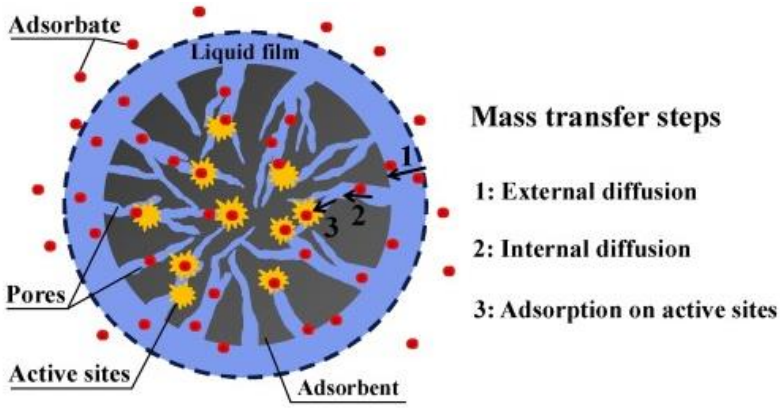


Figure 2.1. Adsorption transport processes onto the internal surface of a porous adsorbent (Reproduced with permission from reference [242]. Copyright (2022) *Elsevier*).

Figure 2.1 shows the transport of an adsorbate during the adsorption process. Step 1 and 2 are transport steps, while step 3 is the adsorption of the adsorbate on the adsorbent active sites.

In step 1, the interactions with the surface atoms of the adsorbent can be done by chemisorption (strong adsorbate-adsorbent interactions or covalent bonds), or by physisorption (weak adsorbate-adsorbent interactions similar to the *Van der Waals* forces). In the latter case, desorption can occur due to weak interactions.

In step 2, the adsorbate attached to the surface of the adsorbent is ultimately diffused into the pores and is adsorbed (step 3). The determining step of adsorption is recognized by the slowest interactions (low-rate constants) and hence the kinetics of the adsorption process. When step 1 is the slowest determining step, adsorption occurs through film diffusion (with chemical or physical interactions), and when step 2 is the lowest, internal diffusion occurs [243].

Weber and Morris [244] developed a kinetic model representing the time-dependent intraparticle diffusion of components. This model is the third most common for liquid adsorption kinetics in environmental remediation after the PFO and PSO models. It assumes that the adsorption process can be controlled by one or more of the following steps such as film diffusion, pore diffusion, and adsorption onto the active sites of the adsorbent [245]. Besides

this, it assumes that in batch adsorption experiments, the adsorbate diffuses into the interior of the adsorbent, being a dynamic process dependent on the square root of time ($t^{1/2}$), and the intercept (C) is associated with the boundary layer. This model is given by the following equation (19):

$$q_t = k_{id} t^{1/2} + C \quad (19)$$

where, k_{id} (mg/g min$^{1/2}$) is the intraparticle diffusion constant and C (mg/g) is the initial adsorption constant and is related as well to the thickness of the boundary layer [246]. The greater the value of C, the greater the boundary layer thickness [247].

Raji and Pakizeh [248] found that a higher adsorptive concentration in solution increases either the IPD rate constant and the boundary layer effect. If q_t plotted against $t^{1/2}$ gives a straight line, the sorption is diffusion controlled. However, if the represented experimental data shows multiple linear plots, the sorption process is controlled by more than one adsorption processes (step 1, 2 and 3 mentioned above).

2.1.3. Adsorption thermodynamics

The thermodynamic properties of adsorbate molecules onto an adsorbent from an aqueous solution reveal if the adsorption process follows physisorption or chemisorption. In physisorption, weak *Van der Waals* attraction forces attract the adsorbate molecules to the adsorbent surface, and the process is reversible, requiring no activation energy [249]. On the contrary, chemisorption occurs by forming chemical bonds between the adsorbent surface and adsorbate molecules, being of irreversible nature [250]. The thermodynamic parameters infer the type and mechanism of the adsorption process. The Gibbs energy, ΔG, is calculated using equation (20):

$$\Delta G = -RTlnK_d \quad (20)$$

A negative Gibbs energy value indicates the spontaneous nature of the adsorption process [251]. The distribution constant, K_d, can be expressed and calculated following the equation (21):

$$K_d = \frac{C_{Ae}}{C_e} \quad (21)$$

where, $C_{Ae}(mg/L)$ and $C_e(mg/L)$ are the concentration of solute adsorbed at equilibrium and the solute concentration in solution at equilibrium, respectively. T (K) is the absolute temperature. The relationship of (ΔG) with enthalpy change (ΔH) and entropy change (ΔS) of adsorption is expressed as:

$$\Delta G = \Delta H - T\Delta S \quad (22)$$

which, substituting equation (20) into equation (22) results in:

$$lnK_d = \frac{\Delta S}{R} - \frac{\Delta H}{RT} \quad (23)$$

the values of (ΔH) and (ΔS) are determined from the slope and intercept of the linear plot of (lnK_d) versus ($1/T$). A positive or negative value of (ΔH) indicates that the adsorption is an endothermic or exothermic process, respectively. Entropy changes reveal whether a particular

reaction is faster or slower than another. The negative sign in ΔS indicates desorption direction and a positive value indicates adsorption. Negative ΔG, shows the feasibility of a spontaneous adsorption process, while a positive ΔG value reveals that the adsorption process is not spontaneous [252].

2.1.4. Error function analysis

Linear regression has been used to verify the theoretical assumptions of various models by the best fitting relationship between adsorbate and adsorbent. The accuracy of the fitting is only assessed by the coefficient of determination (R^2), where the values of R^2close to unity are considered a best fit. The adsorption isotherm was solved in Origin 2018, and the model's constants were calculated from the slope and intercept of the linear regression curves. However, the transformation of the nonlinear regression to the linear regression of the isotherm models produces bias errors (poor linearity). For this reason, to avoid these errors, the nonlinear regression method was used to determine the adsorption constants. This employed process of using the nonlinear regression instead of the linear regression has been recommended by several researchers [253–255].

The software MATLAB (Math Works Inc. Release r2020b, Perpetual License number 40903113, Universidad de Santiago de Compostela, Spain) was used to fit the experimental data to nonlinear equation models using the function (*lsqcurvefit*), which solves the curve-fitting data in the least-square method. Several error functions were used for the kinetic and isotherm equations. In each case, parameters were determined by minimizing well-known error functions to calculate the error deviation between the experimental and predicted equilibrium adsorption data of the linear and nonlinear models mentioned above. The following six statistical error functions were used: Sum of the Square of the Errors (ERRSQ), Composite Fractional Error Function (HYBRID), Derivative of Marquardt's Percent Standard Deviation (MPSD), Sum of the Absolute Errors (EABS), Average Relative Error (ARE) and the Chi-square test ($\chi 2$) (Appendix 6.2.1).

The $\chi 2$ value at a confidence level of 0.05 for the different experiments was selected from the $\chi 2$ distribution table (Table A1.4). Also, a significance level of 0.05 was selected since it assumed a 5% risk of concluding that a difference exists within our experimental data. The errors ARE and MSPD were chosen as the most representative of being dimensionless, but only the MSPD error and chi-square were presented on the result tables for brevity. Furthermore, the MATLAB codes can be consulted in Appendix 6.2.1.

2.2. Development of magnetic beads and experimental parameters: Material and Methods

2.2.1. Preparation method of the magnetic sodium alginate beads

USC UNIVERSIDADE DE SANTIAGO DE COMPOSTELA

First, Fe_3O_4 NPs were synthesized by the reverse coprecipitation method [256]. In this procedure, 15 mL of 1.0 M $FeCl_3 \cdot 6H_2O$ and 0.5 M $FeSO_4 \cdot 7H_2O$ were mixed until total dissolution. This mixture was added dropwise into an ammonium hydroxide (NH_4OH) solution (20 mL, 3.5 M) at 60 °C and stirred mechanically for 30 min.

The NPs obtained were washed several times with distilled water and re-dispersed in 150 mL of water. Afterward, magnetic alginate beads were prepared using $CaCl_2$ as a cross-linking agent. Firstly, 2.0 g of sodium alginate ($NaC_6H_7O_6$) was weighted using a Mettler AT100 analytical balance, which was subsequently added to the previously prepared Fe_3O_4 NPs solution. Finally, different active components were added, as shown in Table 2.1 with relevant information on the quantities reported in Appendix (Table A1.1).

Activated carbon, humic acid, pectin, chitosan, nanocellulose, sodium alginate, and several of the chosen components are known to have outstanding adsorption properties for several contaminants due to their physicochemical properties, biocompatibility, non-toxicity, and biodegradability. The obtained suspension was mixed for 4 h, then added dropwise into a bath of 0.13 M $CaCl_2$ under a continuous constant speed of about 450 rpm using a New Era NE-300 syringe pump (Biogen, Madrid, Spain).

Magnetic alginate beads were instantly formed and left in the solution bath for hardening for 30 min, as shown in Figure 2. 2. The beads were then cleaned with distilled water. Afterward, the washed magnetic beads were reserved in distilled water (pH=6.5) and dried overnight at 60 °C for storing purposes.

The precursors and dried magnetic beads were characterized by scanning electron microscope (SEM), Small-angle X-ray scattering (SAXS), Fourier-transform infrared spectroscopy (FTIR), X-ray powder diffraction (XRD), Thermogravimetric analysis (TGA), Vibrating-sample magnetometer (VSM), Confocal Raman microscopy, X-ray photoelectron spectroscopy (XPS) or Brunauer-Emmett-Teller (BET) surface area analysis to assess their physicochemical properties and gain insights into the adsorption mechanism of toxins and heavy metal ions. Some of the characterization data are reported in Appendix 6.1.

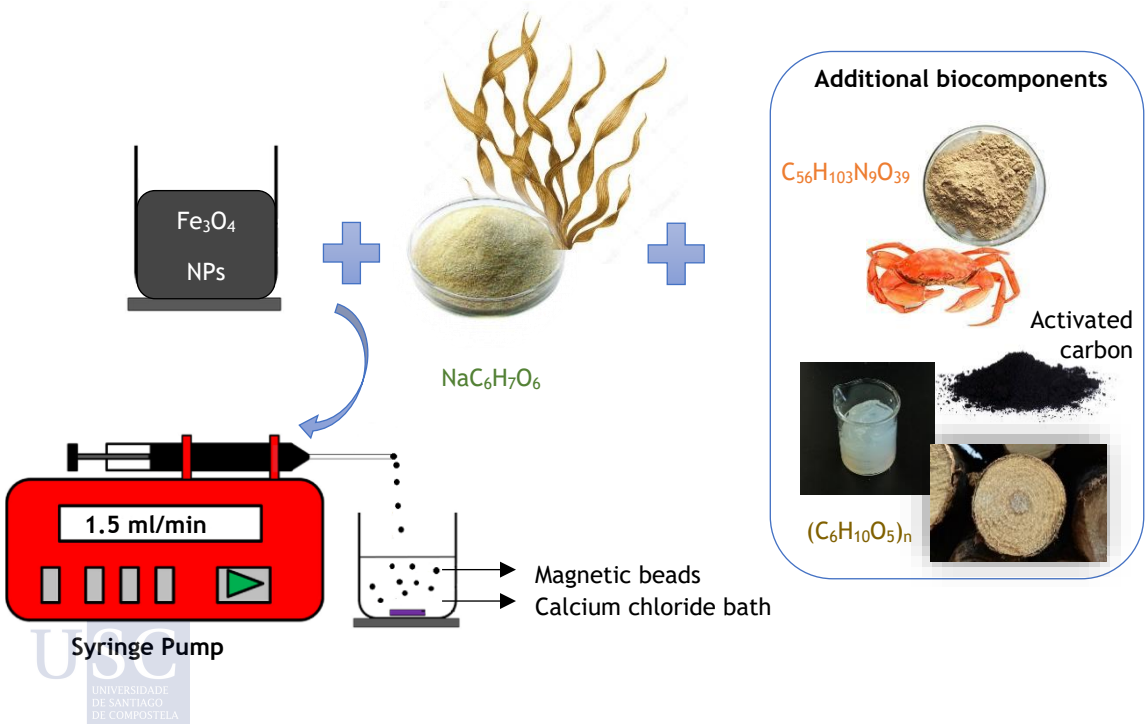


Figure 2.2. Synthesis procedure of the magnetic alginate bead using sodium alginate ($NaC_6H_7O_6$) and additional biocomponents such as chitosan ($C_{56}H_{103}N_9O_{39}$), activated carbon and cellulose ($(C_6H_{10}O_5)_n$).

Table 2.1. Magnetic beads composition and use in the distinct experiments.

Particle	Composition*	Experimental studies section
L1	Fe_3O_4_com@$NaC_6H_7O_6$	2.3.1
L2	Fe_3O_4@CRG@CS@NaC_6H7O_6	2.3.1
L3	Fe_3O_4@$NaC_6H_7O_6$@AC_com	2.3.1; 2.3.2.1-3
L4	Fe_3O_4@$NaC_6H_7O_6$@Na_2SO_3	2.3.1
L5	Fe_3O_4@$NaC_6H_7O_6$@Na_2SO_3	2.3.1
L6	Fe_3O_4@$NaC_6H_7O_6$@GO	2.3.1
L7	Fe_3O_4@$NaC_6H_7O_6$@Pec	2.3.1
L8	Fe_3O_4@$NaC_6H_7O_6$@$Na_2S_2O_5$	2.3.1
L9	Fe_3O_4@$NaC_6H_7O_6$@HA	2.3.1
L10	Fe_3O_4@$NaC_6H_7O_6$@Pec_est@AC_com	2.3.1
L11	Fe_3O_4@$NaC_6H_7O_6$@Pec_est@AC_com	2.3.1
L12	Fe_3O_4@$NaC_6H_7O_6$@Pec_est@AC_com	2.3.1
L13	Fe_3O_4@$NaC_6H_7O_6$@CMK-3	2.3.1; 2.3.2.2;2.3.2.3
L14	Fe_3O_4@$NaC_6H_7O_6$@TOCNF	2.3.1
L15	Fe_3O_4@$NaC_6H_7O_6$@CMK-3@TOCNF	2.3.1
L16	Fe_3O_4@$NaC_6H_7O_6$	2.3.2.2

*Fe_3O_4_com = commercial magnetite; CS = chitosan, CRG = carragenate; AC_com = commercial activated carbon; GO = graphene oxide; Pec = pectin; HA = humic acid; Pec_est = esterified pectin; CMK-3 = type of mesoporous carbon; TOCNF = TEMPO-mediated oxidized cellulose nanofibers.

2.2.2. Mycotoxins experimental Assays: adsorption, desorption, and beer detoxification

Adsorption assays

The mycotoxins adsorption capacity of the different developed beads was evaluated by preparing standard solutions with well-defined concentrations of a mixture of toxins: DON at 12.5 µg/L, ZEN at 50 µg/L, FB1 at 50 µg/L and aflatoxins (B1, B2, G1, and G2) at 1.75 µg/L.

The absorption efficiency was assessed in triplicate using a fixed volume of the mycotoxins mixture solution equal to 2 mL, and it was used between 300 mg of beads. One control aliquot of 120 µl was taken from each solution before the adsorption experiment (addition of the particles). The experiment was left under agitating (250 rpm) at ambient temperature.

The effect of contacting time was evaluated by taking out aliquots at 30, 90, and 180 min. Also, a control test was submitted to the same procedure to assess toxins losses during the experiment. At the end of the experiment, the particles were removed magnetically from the solutions by applying an external magnet (neodymium iron boron (NdFeB). The removed aliquots (100 µl) were filtered and evaporated.

A mixture of acetonitilewater-acetic water (49/50/1 v/v/v) was added before analysing the mycotoxins present by ultra-performance liquid chromatography-tandem mass spectrometer (UHPLC-MS/MS). The adsorption percentage and adsorption capacity (q_e) were computed using equation (24) and equation (25), respectively.

$$Adsorption\ (\%) = \frac{(C_0 - C_{eq}) * 100}{C_0} \quad (24)$$

$$q_e = \frac{(C_0 - C_{eq}) * V}{m} \quad (25)$$

where, C_0 (µg/L) and C_{eq} (µg/L) are the initial concentration and the residual number of mycotoxins at equilibrium time, respectively. The term q_e (µg/mg), is the quantity of mycotoxins adsorbed per unit of adsorbent. In this study q_e was transformed in ng/mg multiplying by a factor of 1x10^3 or in ng/g multiplying by a factor of 1x10^6. V (L) is the volume of the solution and m (mg) is the mass of adsorbent.

Desorption and recuperation

After the adsorption experiment, mycotoxins were extracted from the particles employing 0.5 mL of acetonitrile/water/acetic acid solution (79/20/1, v/v/v) under vortex agitation for 5 min and sonication for 3 min at 50-60 Hz [42, 253]. The particles were extracted magnetically, and the solutions were subsequently filtered before toxin analysis by UPHLC-MS/MS. The percentage of mycotoxins extracted was calculated using equation (26):

$$Extraction\ (\%) = \frac{(C_{extraction} * V_{extraction})}{(C_0 - C_{eq}) * V} * 100 \quad (26)$$

where, $C_{extraction}$ is the mycotoxin concentration measured in the extract, $V_{extraction}$ is the volume of the extraction solution (mL), C_0 and C_{eq} are in (ng/mL) and V is the volume of the adsorption assay (mL).

Beer detoxification

The mycotoxins concentration in beer worth was measured following the protocol described (275). For this study, wort was contaminated with DON, ZEN and FB1 at known concentrations of 50 µg/L and 3 µg/L of aflatoxins (B1, B2, G1 and G2). The adsorbent dosage was tested using 200, 450 and 900 mg of beads per treatment. The incubation was performed for 180 min under agitation at 250 rpm. Controls were kept without particles to establish the initial amount of toxin. After the incubation, particles were magnetically removed from wort and both treated and control samples, were analysed by UPHLC-MS/MS.

2.2.3. Heavy metals: batch (mono, binary, ternary) and desorption experiments

Mono, Binary and Ternary batch experiments

The adsorption efficiency of the magnetic beads for metal ions in a mono system was tested. It was firstly studied and optimized certain experimental parameters for a greater Cd(II) ions removal from aqueous solutions by the L3 beads. Adsorbent dosage, time of contact, pH, speed and type of agitation were optimized in batch experiments before studying the effect of the initial metal concentrations. The effect of the batch parameters was investigated by changing adsorbent dosage (3.0, 8.0, 14 mg), contact time (5, 10, 15, 20, 30, 60 min), agitation speed (150, 250, 300, 500 rpm) in both agitation types (orbital, magnetic) using a Cd(II) ions

concentration of 10 mg/L at room temperature. These optimized parameters were then used to study the pH effect (3-9) on Cd(II) adsorption, adjusting the pH with 0.1 M HCl and 0.05 M NaCl using a pH meter Milwaukee pH51 waterproof. In the final batch experiment, the effect of the initial Cd (II) concentration (10, 25, 70, 100, 125, 150, 170, 200, 250 mg/L) was studied keeping all the previous optimized parameters unchanged. The competitive state of Hg(II) ions in the presence of Ni(II) and Cd(II) ions was investigated using the magnetic beads (L3, L13 and L16). The binary experiments were conducted to measure the adsorption capacity of Hg(II) ions (with initial concentrations from 10 to 230 mg/L), in the presence of Cd(II) or Ni(II) ions with a constant concentration of 130 mg/L. In order to studied and compare the competitive state of Hg(II) ions (with Cd(II) or Ni(II) ions presence), a mono Hg(II) ions adsorption experiment was carried out using all three adsorbents. Both experiments were conducted for 6 h, the 20 mL solutions were magnetically agitated at a constant speed of 300 rpm with a pH of 4.5 using 14 mg of adsorbent (L3, L13 and L16). As in the binary adsorption, the same experimental procedure and conditions were used in the ternary experiment. It was performed a mono and ternary study to compare the adsorption efficiency of L3 and L13 to remove Hg(II), Cd(II) and Ni(II) ions with initial concentrations ranging from 10 to 250 mg/L. The metal precursors used to prepare the metal solutions in all systems were: cadmium chloride hemi(pentahydrate) ($CdCl_2 \cdot 21/2H_2O$), nickel chloride hexahydrate ($NiCl_2 \cdot 6H_2O$), and mercury chloride ($HgCl_2$). The batch experiments were carried out at room temperature. The metal ions concentration was measured by inductively coupled plasma optical emission spectrophotometry (ICP-OES) (Appendix 6.1). The adsorption capacity, q_e, and adsorption/removal percentage using equations (1 and 2).

Desorption and beads reusability

In the desorption experiment, was studied the reusability of the L3 beads by repetitive adsorption and desorption cycles of Cd(II) metal ions using 0.01 M and 0.1 M HCl solution, as the desorption solution. It was performed five cycles of adsorption-desorption containing five replicates. In the adsorption procedure it was used 14 mg of adsorbent which was subsequently added to a previously prepared solution of 10 mg/L Cd(II) and left agitating magnetically (300 rpm) for 1 h. Afterwards, the beads were magnetically separated from solution and washed with distilled water. The desorption procedure was carried out by adding the cleaned and dried beads to 20 mL solutions of 0.01 M and 0.1 M HCl. The desorption efficiency or reusability was assessed for using the ultrasonic and magnetic agitation, where the solutions were left agitating for 30 min. The $q_{desorption}$ (mg/g) of Cd(II) was calculated directly from the amount of Cd(II) adsorbed and amount of Cd(II) ions desorbed using equation (27):

$$q(desorption) = \frac{(m_{adsorb} - m_{desorb})V}{m} \quad (27)$$

Where, m_{adsorb} and m_{desorb} are the adsorbed and desorbed amount of metal ions (mg/g), respectively. V(L) is the volume of desorption solution and m (g) the mass of the beads used. The desorption percentage was calculated using equation (28):

$$\%\, Desorption = \frac{m_{desorb}}{m_{adsorb}}\, x\, 100 \quad (28)$$

Competitive evaluation ratio

The interactive effect of Cd(II), Hg(II) and Ni(II) was investigated in the ternary system. For that, an evaluation ratio was introduced to assess the type of adsorption competition between each metal ion in the system and combined (276). The evaluation ratio is expressed by equation (29):

$$E = \frac{Q'_e}{Q_e} \quad (29)$$

where E, is the evaluation ratio. Q'_e (mg/g) is the amount of metal ions adsorbed in a ternary system and Q_e (mg/g) is the amount of metal ions adsorbed in the mono-metal system. If the evaluation ratio, E > 1, the presence of other metal ions has enhanced the adsorption of other metal ions in solution (synergism effect). When E = 1, this means that the presence of other metal ions would not influence the adsorption of another metal ion, and when E < 1, the presence of another metal ion would suppress the adsorption of one another (antagonism effect).

2.2.4. Magnetic sodium alginate beads: Characterizations

The magnetic beads were fully characterized before any experimental study to assess their structural and textural properties, magnetic behaviour, and morphology. Firstly, the morphology of the synthesized Fe_3O_4 NPs was studied by TEM, and the particle size was further analysed by distribution size histogram, as shown in Figures 2.3.a and 2.3.b.

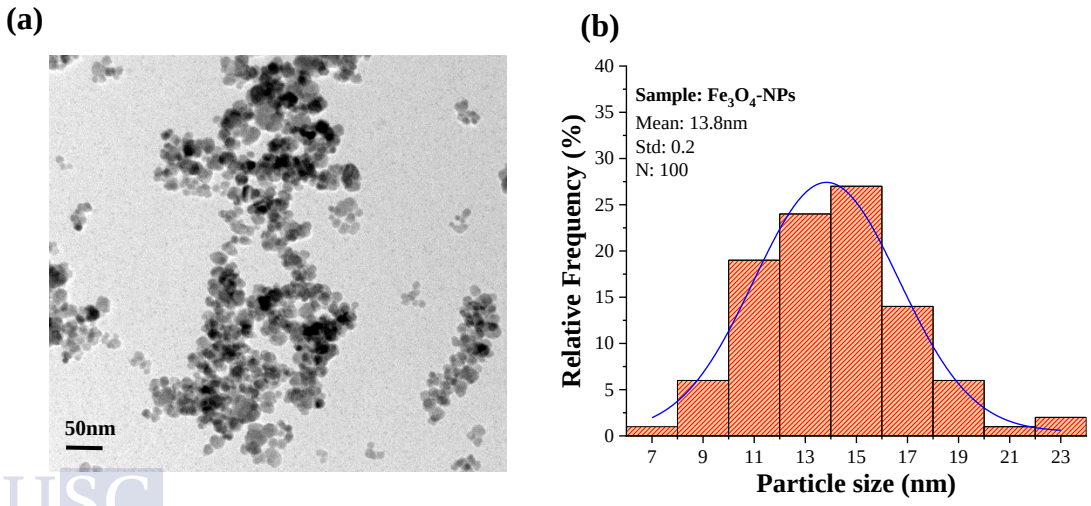


Figure 2.3. TEM micrograph of Fe_3O_4 NPs (a) and the respective particle size distribution histogram (b) fitted with a Gaussian curve (blue line).

The TEM micrograph of the Fe_3O_4 NPs reveals that the particles are nearly spherical and uniformly distributed with small agglomerations. The histogram with the Gaussian distribution

shows that the particles size ranges from 9 to 19 nm, presenting an average size of 13.8 nm. Smaller particles of approximately 7 nm were also observed, probably due to the vigorous mechanical agitation. The relative frequency distribution showed that most of the particles are in the range size of 11 to 15 nm. These results agree with the value obtained by dynamic light scattering (DLS) (Table A1.2). Also, the average crystalline size of the nanoparticle (L) was determined from X-Ray diffractograms using the Scherrer equation (30) [258]:

$$L = \frac{K\lambda}{\beta cos\theta} \tag{30}$$

where, K is a constant related to crystallite shape usually equal to 0.9, λ (nm) is the X-ray wavelength, and β (radians) is the peak width of the diffraction peak profile at half maximum height. The value of ɵ (radians) corresponds to the Bragg angle.

The crystalline size calculated from the X-ray diffractogram of the Fe_3O_4 NPs (Figure 2.4.a) reveals a crystallite size of about 10.68 nm, which is in accordance with the results obtained from TEM analysis. Furthermore, the hydrodynamic size of the final precursors after sodium alginate and biocomponents addition was characterized by DLS revealing high polydispersity index (PDI) ranging from 0.200 to 0.700, which can be ascribed to agglomeration provoked by the addition of the highly viscous sodium alginate (Table A1.2). The particles surface is negatively charged with a zeta potential value ranging from -30 to -70 mV because of the carboxylic and carbonyl functional groups of sodium alginate.

Figure 2.4 shows the X-ray diffractogram and FTIR spectrum of the synthesized Fe_3O_4 NPs, sodium alginate, and two magnetic beads, L3 and L16, for comparison purposes. In the X-ray diffraction pattern of the dried beads, L3 and L16, five peaks can be observed at 2θ = 30.1, 35.8, 43.1, 57.2, and 63.1° with the following indexing planes (022), (113), (044), (115), and (044), that correspond to the magnetite crystalline phase (ICDD: 98-015-8743) which are embedded into the porous structure of the beads. Besides, it is clearly evidenced by the equal relative frequency and peak location in the diffractogram of the embedded Fe_3O_4 NPs.

In the IR spectrum of the magnetic beads, five intense peaks at 3228, 1585, 1288, 1076, and 588 cm^{-1} are observed. The broad peak at 3229 cm^{-1} and the intense peak at 1076 cm^{-1} are attributed to the -OH and $-CO^-$ stretching vibration bands of sodium alginate, respectively [259]. Moreover, the peaks that appear at 1585 and 1288 cm^{-1} are assigned to asymmetric and symmetric stretching vibrations of carboxyl groups of sodium alginate, respectively [260]. The last band detected at 588 cm^{-1} is important since it corresponds to the stretching vibration of Fe-O bonds in the Fe_3O_4 NPs [261]. Despite the different compositions of both beads, no significant structural and chemical surface topography differences are observed.

USC UNIVERSIDADE DE SANTIAGO DE COMPOSTELA

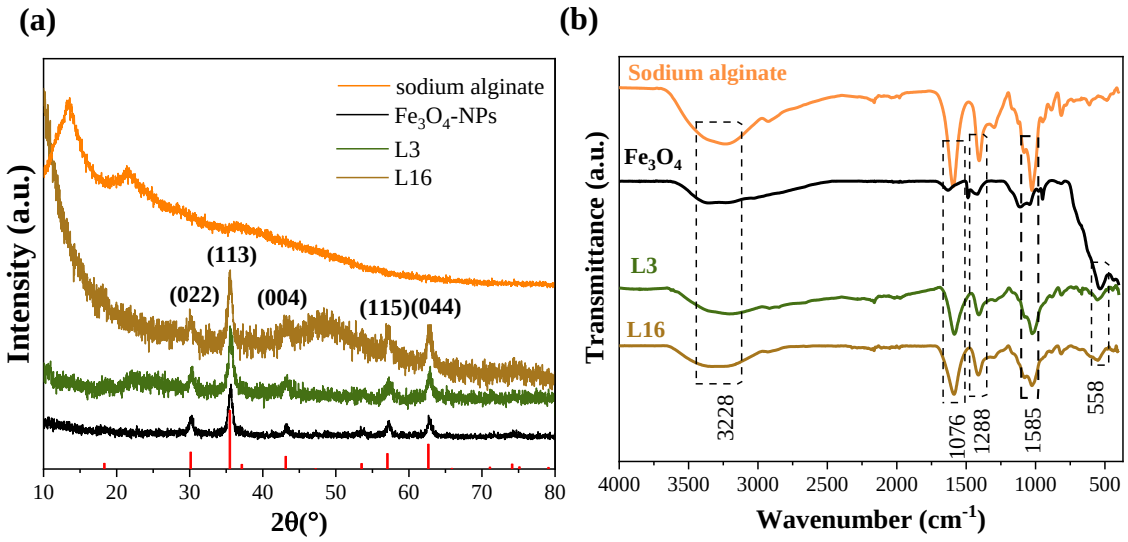


Figure 2.4. X-ray diffractogram (a) and IR spectrum (b) of sodium alginate, Fe_3O_4 NPs, L3 and L16 beads.

Figure 2.5 shows the SEM micrographs of the external surface and cross-section of the magnetic beads L1, L3, and L16. All beads present a spherical morphology with an external rough surface with some observed cracks commonly formed during the drying process (Figure 2.5 a, d, g). Internally (Figures 2.5b,e,h), it can be observed small white spots randomly distributed, which is an indication of the Fe_3O_4 NPs presence within the structure of the beads.

Also, the internal structure and distribution differ among the beads, where L3 beads possess a more porous layer-like internal structure mainly because of the precursor (commercial AC) compared to beads, L1, and L16. Figure 2.5c shows a digital image of the beads in the humid state and after drying (overnight, 60 °C), shown in Figure 2.5f. It is clearly seen that the beads decreased in size from approximately 2.0 mm to 1.3 mm after drying, as shown in Figure 2.5i. Also, it was noticed the black colour which arises from the presence of the Fe_3O_4 NPs.

USC UNIVERSIDADE DE SANTIAGO DE COMPOSTELA

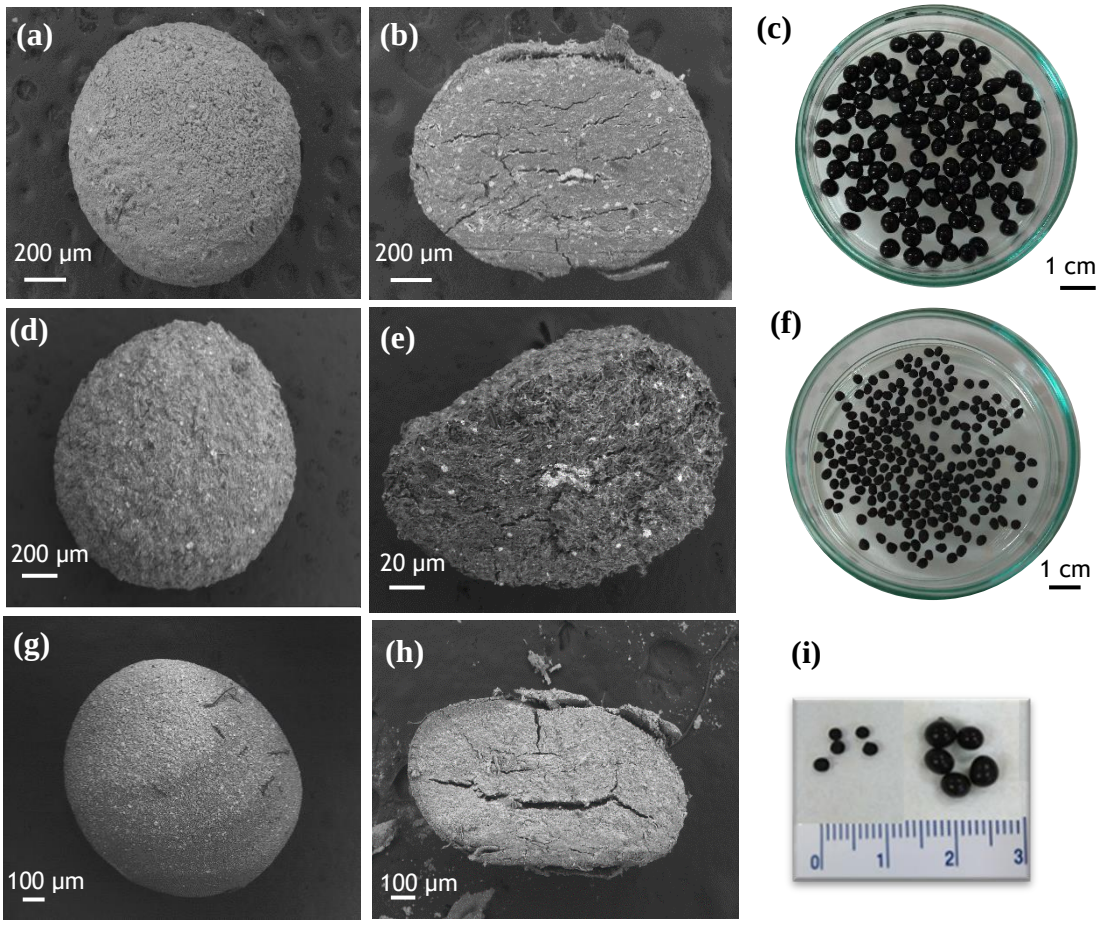


Figure 2.5. SEM micrographs of the surface morphology of several magnetic beads: (a, d, g) external surface and cross-section (b, e, h) of the beads L1, L3, and L16, respectively. Digital images of (c) humid beads, (f) after dried and (i) size comparison of both humid and dry beads.

The magnetization of the synthesized Fe_3O_4 NPs, L3, and L16 beads, are presented in Figure 2.6.a. The magnetization was normalized to the amount of magnetic mass content of the samples obtained by TGA analysis, and the percentage of magnetic content was 86.40, 23.25, and 26.38 % for Fe_3O_4 NPs, L3, and L16 beads, respectively (Table A1.3).

The saturation magnetization (*Ms*) of Fe_3O_4 NPs showed a value of 59.29 emu/g Fe_3O_4, while in L3 and L16 beads, a value of 38.02 and 57.94 emu/g Fe_3O_4 was obtained, respectively. The magnetization of the beads is slightly lower than native Fe_3O_4 NPs, but negligible coercivity and absent remanence are observed, indicating the superparamagnetic behaviour of the Fe_3O_4 NPs embedded in the polymer matrix was preserved. This characteristic prevents magnetic aggregation and subsequent flocculation in the absence of an external magnetic field which is the main advantage for their fast and instantaneous separation from solution and subsequent use in the industry either in the dry or humid state, as shown in Figure 2.6.b

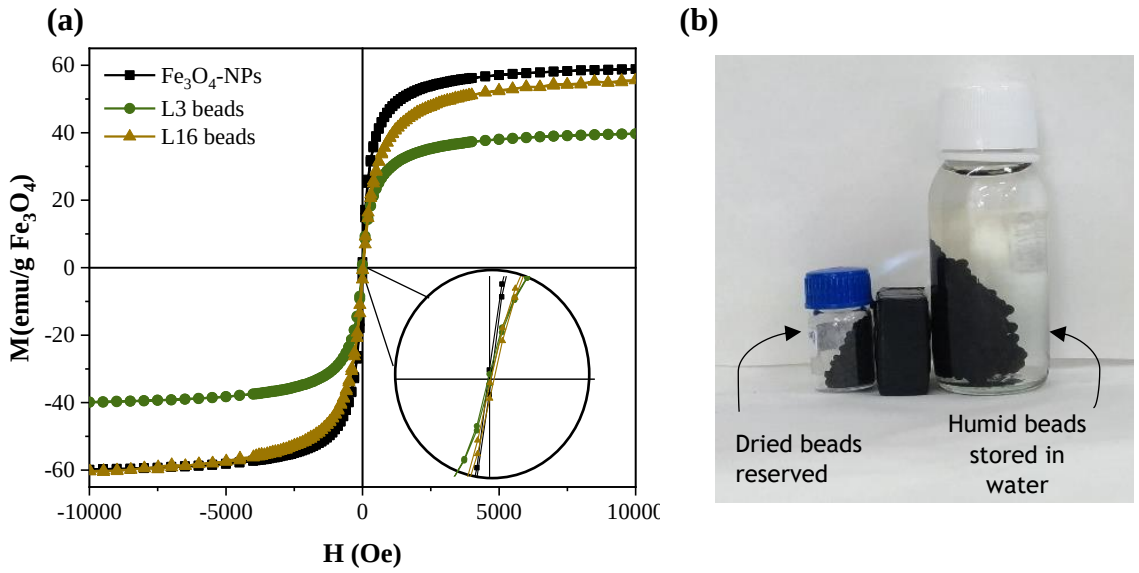


Figure 2.6. Magnetization curve of Fe_3O_4 NPs and of the beads L3 and L16 at 25°C (a) with amplification of the hysteresis cycle. Digital image of dried and humid beads reserved under an external magnetic force (b), respectively.

2.3. Contaminants adsorption: Results and discussion

The magnetic alginate beads are prepared by a cost-effective method and are easily tailored with various compounds to increase their capacity to remove different contaminants. In this work, it was studied the feasibility of these beads in removing heavy metal ions (Cd(II), Hg(II), Ni(II)), and mycotoxins (AFs, DON, ZEA, and FB) from aqueous solutions using the adsorption method.

Firstly, it was assessed the adsorption efficiency and reusability of several magnetic beads based on their composition for mycotoxins in an aqueous solution, and posteriorly, an optimization experiment of adsorbent dosage to remove mycotoxins from contaminated beer wort was performed.

Secondly, the adsorption capacity to remove heavy metal ions from solution was studied in a mono, binary, and ternary system. For this, the most efficient beads were used, and several assays were performed, such as parameters optimization, removal efficiency, and desorption/recyclability. The adsorption mechanism was studied using isotherm, kinetic, diffusion, and thermodynamic models.

2.3.1. Elimination of mycotoxins from water and beverages

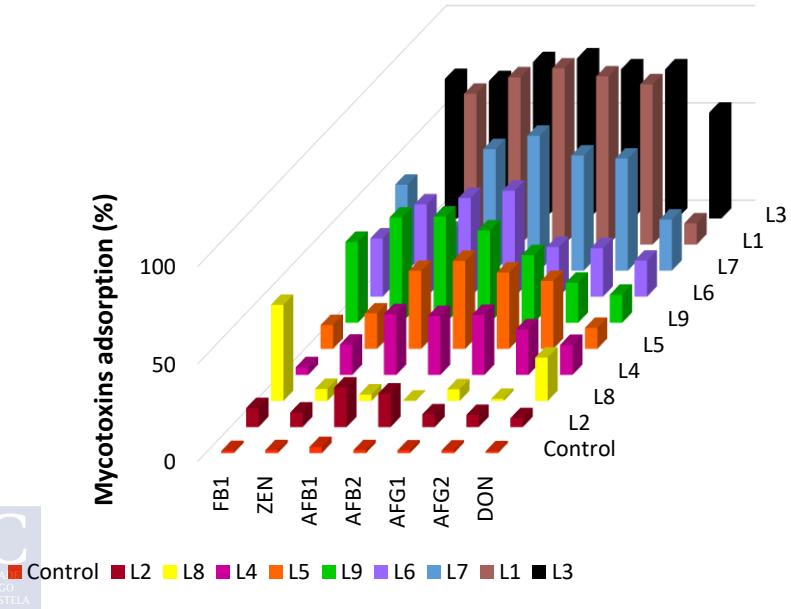
The experimental work involving the adsorption and desorption tests of mycotoxins was carried out by the group of Veterinary Faculty (Department of Pharmacology) from the University of Santiago de Compostela (USC), Lugo. The publication was also part of the PhD thesis of Jesús M. González-Jartín [54] which was supervised by the Prof. Luis Botana. The magnetic beads and nanoparticles used in the experiments were developed by Lisandra Cristina de Castro Alves, and are an experimental part present in this Thesis.

a. Ability of magnetic beads to adsorb mycotoxins

The particles were developed to meet one crucial criterion the simultaneous binding of a set of different mycotoxins. Frequently multi-mycotoxins are encountered in food such as cereals and feedstuff. Therefore, decontamination protocols often use the addition of mycotoxins binders to the feedstock, preventing the adsorption of mycotoxins in an animal's digestive tract [262].

For this reason, a set of magnetic particles (1.5 mm diameter in the dried state) was developed, integrating a set of effective mycotoxins binders into a polymeric matrix to provide a large surface-to-volume area, mass transfer behaviour between the components and target mycotoxins. Mycotoxins binders, such as humic acid, activated carbon, sodium metabisulfite, sodium sulfite, and CMK-3 mesoporous carbon, were chosen due to their affinity to bind certain mycotoxins. Therefore, it was studied their adsorption efficiency to remove a multi-mycotoxin system containing DON, ZEN, FB1, and aflatoxins (AFB1, AFB2, AFG1, and AFG2) from aqueous solutions and from beer wort with known concentrations ranging from 1.75 µg/L in aflatoxins to 50 µg/L in FB1 and ZEN toxins [263, 264] which are above the legal limits found in beer.

Firstly, the adsorption capacity of the magnetic beads was tested in fixed environmental conditions: contacting time of 180 min and adsorbent dosage of approximately 300 mg. The capability of each type of bead to remove the mycotoxins from the solution is shown in Figure 2.7. The differences and affinities of each particle to certain mycotoxins are clearly seen.The L1 beads containing only sodium alginate and magnetic nanoparticles were revealed to be able to remove ZEN and aflatoxins from 60 to 80 %, whereas DON and FB1 adsorption was below 10 %. The addition of commercial activated carbon (L3 beads) increased the removal of DON and FB1 from 54 % and 71 %, respectively. But the adsorption of the remaining mycotoxins was lower than the results observed by the L1 beads.



USC UNIVERSIDADE DE SANTIAGO DE COMPOSTELA

Figure 2.7. Mycotoxins adsorption (%) from aqueous solution by magnetic beads L1 to L9. (Adapted with permission from reference [42]. Copyright (2021) *Elsevier*)

Activated carbon is one of the components with the most significant potential due to its large surface area and excellent adsorption capacity. In various studies, it was used as general toxins adsorbing agent for various digestive diseases [265]. The use of activated carbon showed reduced aflatoxicosis in goats [266] and milk cows [267]. Also, it was proven its capability to bind ZEN and DON from contaminated feed inhibiting its bioaccessibility [268].

The composition of the beads led to different results. For instance, beads with sodium sulfite (L4 and L5) reduced more than 50 % of aflatoxins. The higher concentration of sodium alginate present in L5 (SA, 53 wt%) enhanced a greater adsorption capacity of 20.32 ng/g compared to L4 (SA, 37 wt%), which was equal to 13.09 ng/g (Table A1.5). The decrease in the aflatoxins elimination was even more evident with the addition of sodium metabisulfite (L8). However, 22 % of DON and 49 % of FB1 were adsorbed by the L8 beads, which was twice than L5 and L6 beads.

Early studies indicate that the reduction of DON in contaminated cereal grains could be done by sodium metabisulfite ($Na_2S_2O_5$) through the formation of less toxic sulfonated DON derivatives called (DONS1, DONS2, and DONS3) [269, 270]. Incorporating pectin (L7 beads) enhanced a higher elimination of aflatoxins, fumonisins, and DON mycotoxins compared to L2, L4, L5, L6, and L9 beads.

DON reduction of 26.23 % was the second-highest reported value. Pectin is present in various peel fruits and is an excellent adsorbent of heavy metals [271–273]. In one recent study, durian peel was used for mycotoxins decontamination of feed, being effective in adsorbing AFB1, ZEN, and ochratoxin A (OTA) [273]. L9 beads with humic acid eliminated 54 % of ZEN and revealed an adsorption capacity of 495 ng/g. Replacing commercial activated carbon (L3) with graphene oxide (L6) resulted in mycotoxins adsorption reduction from 70 % in L3 to 37 % in L6. Both humic acid (HA) and graphene oxide (GO) contain a unique structure with the potential to capture several substances.

HA, is the most common form of organic carbon in the environment. Like activated carbon, it has a strong affinity to various substances, such as heavy metals, minerals, and mycotoxins [274–276]. Its structure contains hydroxyl and phenol functional groups that react with mycotoxins, releasing hydrogen radicals upon reaction with reactive oxygen species to form more stable carboxylic acids, carboxyl, or phenyl radicals [277].

GO structure is composed of a basal plane and edges enriched with various oxygen functional groups (carbonyl, hydroxyl, carboxyl, and epoxide groups) and as HA has the potential to capture heavy metal ions (arsenic, strontium, selenium, cadmium), polycyclic aromatics, antibiotics, organic dyes and mycotoxins [278–285]. The basal plane of GO sheets can bind mycotoxins onto the aromatic rings and edges (Figure 2.8b) and GO defects by hydrogen bonding. A study has demonstrated that a combination of GO with magnetic nanoparticles (MGO) accelerated the adsorption of fusarium through the hydroxyl groups with iron ions in palm kernel cake [286].

USC UNIVERSIDADE DE SANTIAGO DE COMPOSTELA

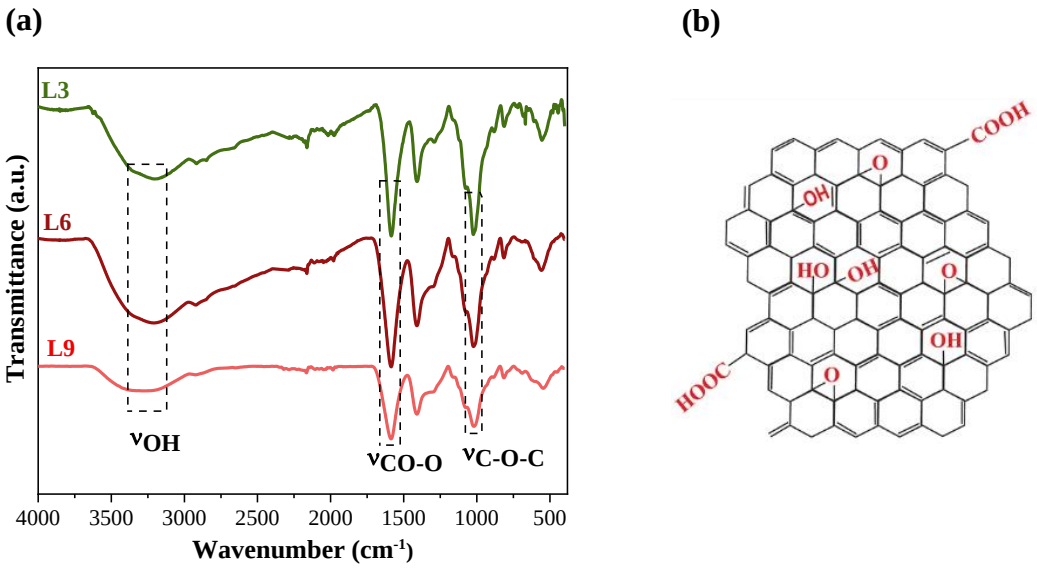


Figure 2.8. IR spectra of the beads L3, L6, and L9 (a) and chemical structure of GO (b), Adapted with permission from reference [287]. Copyright (2022), *Spring Nature*).

Among all beads, the ones that adsorbed a more significant number of mycotoxins were L3, L6, and L9, with total adsorption capacities of 598, 407, and 495 ng/g, respectively (Table A1.5).

Figure 2.8a shows the IR spectra of all beads that reveal the presence of those main functional groups responsible for higher adsorption of mycotoxins. However, L3 particles composed of sodium alginate and commercial activated carbon showed the best performance since more than 50% of all mycotoxins were eliminated from the solution.

In the first batch of particles (L1-L9), DON mycotoxin was most reduced by the L3 with commercial activated carbon and the L7 bead with pectin. For this reason, a new set of beads was formulated combining commercial activated and esterified pectin (L10-L12) since DON is extremely difficult to remove. Besides this, new compositions using CMK-3 mesoporous carbon (L13) and modified TEMPO-oxidized cellulose nanofiber (TOCNF) (L14-L15) beads were prepared, and the adsorption capacity is shown in Figure 2.9.

USC UNIVERSIDADE DE SANTIAGO DE COMPOSTELA

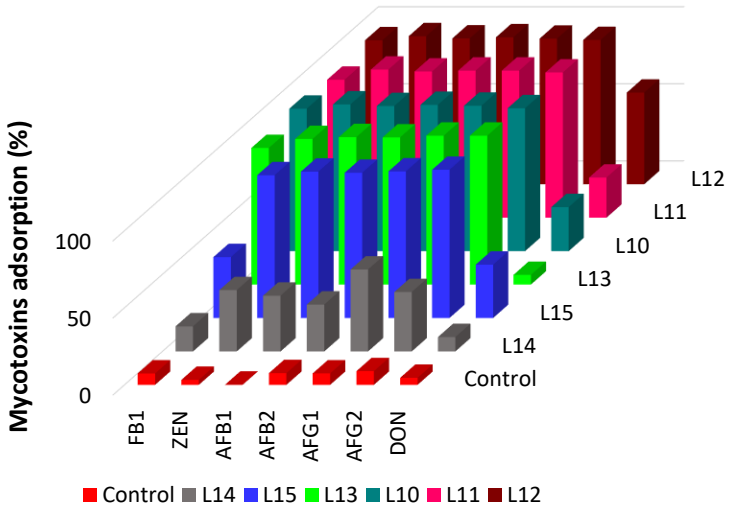


Figure 2.9. Mycotoxins adsorption (%) from aqueous solution by magnetic beads L10 to L15.

The L10-L12 beads were prepared using different proportions of esterified pectin with respect to commercial activated carbon.

Esterified pectin was selected due to the large presence of carbonyl groups, an important functional group in binding mycotoxins. It was observed that by incrementing the concentration of added esterified pectin for bead L11 (Pec_est, 26 wt%), it was observed a slight increase in the elimination of the mycotoxin ZEN and aflatoxins. However, the relation of weight percentage of commercial activated carbon (20 wt%) to esterified pectin (15 wt%) in L10 beads proved to be an optimum composition in eliminating approximately 28.54 % and 92.38 % of DON and FB1, respectively (Table A1.5). A further increase in the added weight percentage of activated carbon to 27 % in L12 beads was revealed to increase the removal efficiency of DON to 59.5 % and FB1 to 93.44 %. Additionally, a similar elimination of over 90 % was obtained for aflatoxins and ZEN.

As a result of the concentration increment of AC a higher elimination of all mycotoxins in specific DON was favoured. CMK-3 mesoporous carbon belongs to the class of ordered mesoporous carbons, which are widely known for their large surface area, good stability, and conductivity being used in the fabrication of electrochemical sensors [288–290]. It was reported [291] that the development of a MIP sensor with Au-NPs deposited on the surface of a boron-ordered mesoporous carbon for the detection of ZEN mycotoxin. Not only could the sensor give an accurate and early detection of ZEN in food, but it also increased the sensitivity and selectivity for other substances [291].

Based on the adsorbing properties, CMK-3 mesoporous carbon was incorporated into the L13 beads in combination with sodium alginate. L13 beads were able to adsorb over 88 % to 97 % of FB1, ZEN, and aflatoxins, while DON removal efficiency by L3 was below 80 %. Although L13 beads had a great affinity for FB1, ZEN, and the remaining aflatoxins, L3 beads could adsorb approximately 54 % of DON, in contrast to the L13 beads, where it was only adsorbed 6.29 %. For this reason, beads (L10-L12) containing commercial AC and esterified pectin are an excellent candidate for eliminating all mycotoxins and DON.

TOCNF cellulose was another natural polymer incorporated (L14 and L15). Cellulosic materials are known for their adsorption capacities for heavy metals and, most recently, for mycotoxins [288, 289]. The removal efficiency of L14 beads with TOCNF and sodium alginate was under 40 % in all mycotoxins except for AFG1, which was above 50 %.

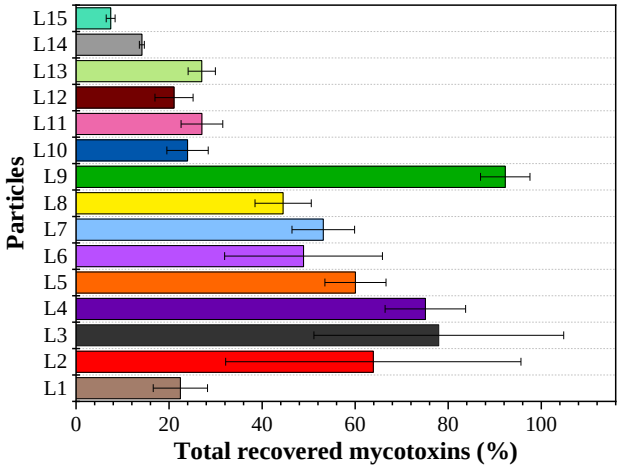
The addition of CMK-3 mesoporous carbon in L15 beads increased the removal efficiency to over 90 % except in DON and FB1. The incorporation of TOCNF in L15 beads and CMK-3 favoured DON adsorption from 6.29 % (L13) to 34.6 % (L15). The CMK-3 morphology (tunnels interconnected) may have allowed the fast binding of the mycotoxins to the active functional groups of the remaining components.

b. Recovery of mycotoxins from the magnetic beads

Mycotoxins' detoxification or desorption from any particle is extremely important at the industrial level. The mycotoxins can be recovered from the particles without damaging their structure, allowing their use in subsequent cleaning cycles to reduce production costs.

Figure 2.10 shows the percentage of total recovered mycotoxins from all beads. A maximum total recovery of mycotoxins was observed in the following order L9 (92 %)>L3 (77.87 %)>L4 (75.09 %)> L2 (63.90 %). The L9 (humic acid) and L3 (commercial AC) beads allowed a large percentage of recovered toxins, whereas from the beads, L1 (commercial Fe_3O_4 NPs and sodium alginate) it was only recovered 22.43 % of mycotoxins being the lowest value reported from the first set of particles (L1 to L9).

From all mycotoxins, the one that was most intensively recovered from this set of particles was AFB1 mycotoxin, and the least recovered was the DON mycotoxin. On the contrary, in the second set of particles (L10-L15), the most intensively recovered mycotoxin with approximately 7 % to 49 % was FB1, while the least recovered was AFB2. However, the second set of particles reported a total recovery rate below 30 %. Again, the composition of the particles is a crucial factor in adsorption and desorption of mycotoxins.



USC UNIVERSIDADE DE SANTIAGO DE COMPOSTELA

Figure 2.9. Total mycotoxins recovered from the studied magnetic beads.

c. Mycotoxins removal from beer wort

The efficacy of the magnetic beads to adsorb mycotoxins from beer was also tested. Considering the performance obtained in DON absorption by L3 (commercial AC and sodium alginate) and L7 (pectin) beads in an aqueous medium, both were selected for beer detoxification.

Figure 2.10 shows the percentage of mycotoxins absorbed by the adsorbent dosage used. The adsorption of mycotoxins increases when the adsorbent dosage increases from 200 to 900 mg. For instance, 900 mg of L3 beads adsorb 50 % of FB1 and 81 % of AFB1, and when used 450 mg, FB1 and AFB1 are reduced to 31% and 79 %, with 200 mg to 7 % and 69 %, respectively. Similar results were observed in bead L7.

Adsorbent dosages of L3 and L7 in water (300 mg) and in beer wort (200-900 mg) yield different removal efficiencies. In water using only 300 mg of adsorbent, the removal efficiency was as great compared to 900 mg of particles used in the beer wort experiments. In this context, AFB1 was eliminated by L3 in 79 % of wort and 80 % of water, while in the case of L7, 62% and 60 % of toxins were reduced, respectively.

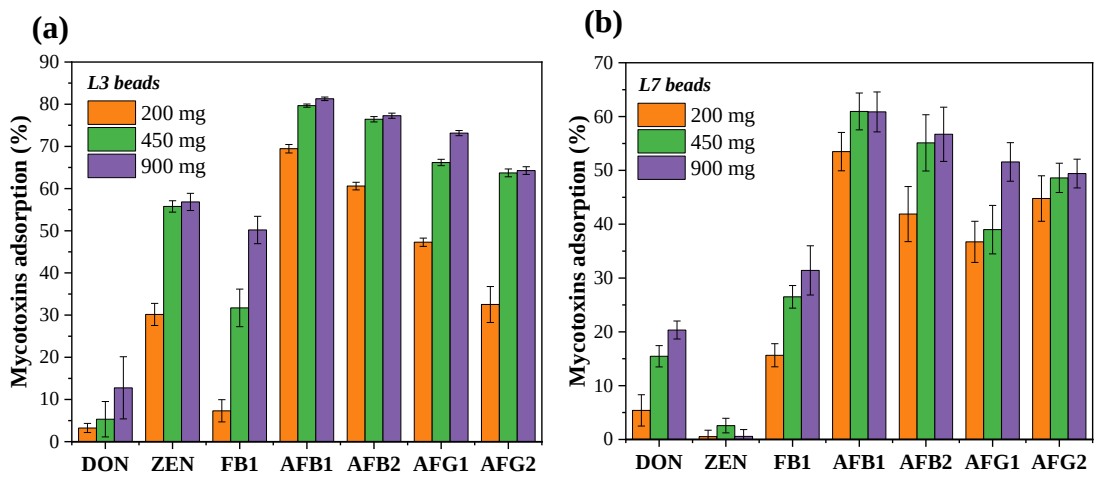


Figure 2.10. Mycotoxins adsorbed (%) from wort using different dosage of the beads L3 (a) and L7 (b).

The L3 beads have been recognized as a strong adsorbent to reduce all mycotoxins except the DON mycotoxin, which was best reduced by the L7 bead. The main structural features of pectin are linear chains of linked α-D-galacturonic acid residues partially esterified, as shown in Figure 2.11a. The esterification of pectin might have enhanced the binding of DON by covalent bonds. Meanwhile, the alginate chemical structure of linear chain (1-4) of (1–4)-linked residues of β-D-mannuronic acid and α-L-guluronic acid in different proportions and sequential arrangements enhanced the binding of the remaining mycotoxins, as shown in Figure 2.11b.

USC UNIVERSIDADE DE SANTIAGO DE COMPOSTELA

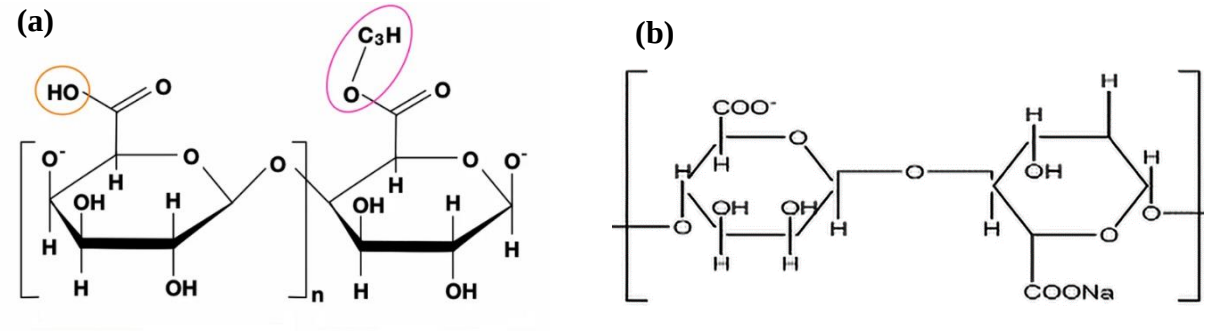


Figure 2.11. Chemical structure of esterified pectin (a) and sodium alginate (b) (Reproduced with permission from reference [294, 295]. Copyright (2022) Springer Nature).

2.3.2. Elimination of heavy metal ions from water: Mono, binary, and ternary systems

Table 2.2 illustrates a brief summarized description of the heavy metal ions experimental studies and particles used in a mono, binary, and ternary system. The elimination of heavy metals was firstly tested in a mono system using one particle (L3) to adsorbed Cd(II) ions from the solution to optimize several experimental parameters (contact time, pH, adsorbent dosage, type, and rotation speed) and test the adsorption capacity of this bead to remove efficiently Cd(II) ions under optimized conditions.

The reusability and recycling of this particle was tested over five successive cycles of adsorption and desorption since a material's reusability reduces costs and generates less waste. In the last experiment studies, it was assessed the adsorption process onto the bead, changing the time (kinetic, diffusion), temperature (thermodynamics), and initial metal concentration (isotherm).

Secondly, in the binary system, it was tested the adsorption capacity and efficiency of three beads namely, L3 (commercial AC), L13 (CMK-3 mesoporous carbon), and L16 (Control) to remove Hg(II) ions from the solution. Similar to the mono study of Cd(II) ions, the adsorption process of Hg(II) ions was evaluated by the isotherm, kinetic, diffusion, and thermodynamic models. The ions competition and adsorption mechanism between Hg(II)-Cd(II) and Hg(II)-Ni(II) ions was assessed by analysing the contaminated beads used in the different treatments by FTIR and XPS.

Finally, a new CMK-3 mesoporous carbon was synthesized at the ternary system to prepare the bead, L13T, and the L3 bead was used again. The adsorption capacity, efficiency, and the effect of the initial metal concentration of these two beads was assessed at the mono and ternary systems under optimized pH conditions to remove Cd(II), Hg(II), and Ni(II) ions from solution. The metal ions competition was calculated using the evaluation ratio (eq. 29), isotherm adsorption models were applied to know more information about the adsorption process, and the adsorption mechanism was evaluated by XPS and FTIR on the contaminated beads at the mono and ternary systems.

USC UNIVERSIDADE DE SANTIAGO DE COMPOSTELA

Table 2.2. Description of heavy metal ions experimental studies and particles used in the different systems/sections (mono, binary, and ternary system).

	Mono	Binary	Ternary
Metal ions	Cd(II)	Hg(II) Hg(II)-Ni(II) Hg(II)-Cd(II)	Cd(II) Hg(II) Ni(II) Cd(II)+Hg(II)+Ni(II)
Particles	L3	L3 L13 L16	L3 L13T
Experimental studies	1. Parameters optimization (contact time, pH, type and rotation speed, adsorbent dosage). 2. Adsorption capacity and removal efficiency. 3. Desorption and Recycling. 4. Isotherm, kinetic, diffusion, and thermodynamic models.	1. Adsorption capacity and removal efficiency of Hg(II). 2. Kinetic, diffusion and thermodynamic models for Hg(II) ions adsorption. 3. Ions competition at the binary system. 4. Adsorption mechanism.	1. Adsorption capacity and removal efficiency of each metal ions. 2. pH optimization. 3. Isotherm models. 4. Competition evaluation. 5. Adsorption mechanism.
Section	**(1)**	**(2)**	**(3)**

2.3.2.1. Elimination of Cd(II) ions from water: Study and experimental parameters optimization

a. Optimization of experimental parameters (contacting time, adsorbent dosage, agitation speed and type)

The elimination of Cd(II) ions from aqueous solutions was studied following a similar approach as in the mycotoxins study using L3 (commercial AC) beads, which showed an optimal performance for mycotoxins removal as an adsorbent candidate.

Cadmium is one of the highest priority metals listed by European-WFD due to its toxicological concern and non-biodegradability at low concentrations [296, 297]. For this reason, cadmium was selected as the first heavy metal ion to test the adsorption efficiency of the magnetic L3 beads. In the research article [298] published with these results, the beads were first named as magnetic alginate activated carbon (MAAC) beads. To maintain a cohesive and easy follow-up of the thesis results, they were renamed as L3 beads.

Several experimental parameters were optimized before studying the effect of Cd(II) ions initial concentrations and pH, namely contacting time, adsorbent dosage, agitation speed, and type. The time interval that adsorbate and adsorbent are maintained in contact is an important parameter for a designed adsorption process. For this aim, 20 mL of Cd(II) ions solution (10 mg/L) and 8 mg of adsorbent, at (pH=5.64), were kept under orbital or magnetic agitation for distinct times to measure subsequent aliquots of metal removal at an agitation speed of 250 rpm. The effect of the contacting time on the removal efficiency of Cd(II) by the L3 beads at different times is shown in Figure 2.12a. Independently of the contacting time, magnetic

agitation is more efficient than orbital mixing in metal removal. After 10 minutes, it was observed a Cd(II) removal of approximately 18 % in the magnetic agitation, while about 3.6 % of Cd(II) removal was observed in the orbital case. This initial adsorption indicates a favourable effect of stirring, which allowed easy adsorption and penetration onto the surface sites of the L3 beads. As the time proceeds, Cd(II) ions accumulate on the absorbents surface, and the removal percentage constantly increases. After 1 h, approximately 39 % and 19 % of Cd(II) are removed in the magnetic and orbital agitation, respectively.

Even though the adsorption equilibrium was not attained after 1 h of contacting time, this period of time (1 h) was used in the subsequent experiments. Usually, the extent of adsorption increases during an initial stage and then becomes slower at a later stage until a plateau is achieved. However, for this study, 1 h of contacting time seemed a key parameter for cost-effective wastewater treatment applications [299]. Generally, higher equilibrium times for Cd(II) adsorption are required by other adsorbent materials, i.e., carbonaceous materials often need 72 h [300] to reach equilibrium, and activated carbon usually takes 3-5 days [301, 302]. Other studies stated that equilibrium of Cd(II) ions adsorption was attained within 1 h for different initial concentrations [303–305]. Despite this, it was performed a complementary study to the initial experiment with contacting times of 90, 120, 240, and 360 min using magnetic agitation to evaluate if the removal efficiency of Cd(II) ions would change over time.

Figure 2.12b shows that the removal efficiency of Cd(II) by the L3 beads was approximately 20 % and 41 %, with a contacting time of 90 and 360 min, respectively. In comparison with the initial experiment, where the removal efficiency of Cd(II) ions was 38 % within 1 h in the complementary study with 6 h contacting time, the removal efficiency was around 40 %. This result corroborates the premise of taking 1 h of contacting time to have a proper removal of Cd(II) ions from water. In addition, the result fulfils the objective of this study, which was to use the L3 beads at the lowest contacting time with a fair Cd(II) ions removal from water for their posterior use at an industrial scale, avoiding high energy consumption during the cleaning processes.

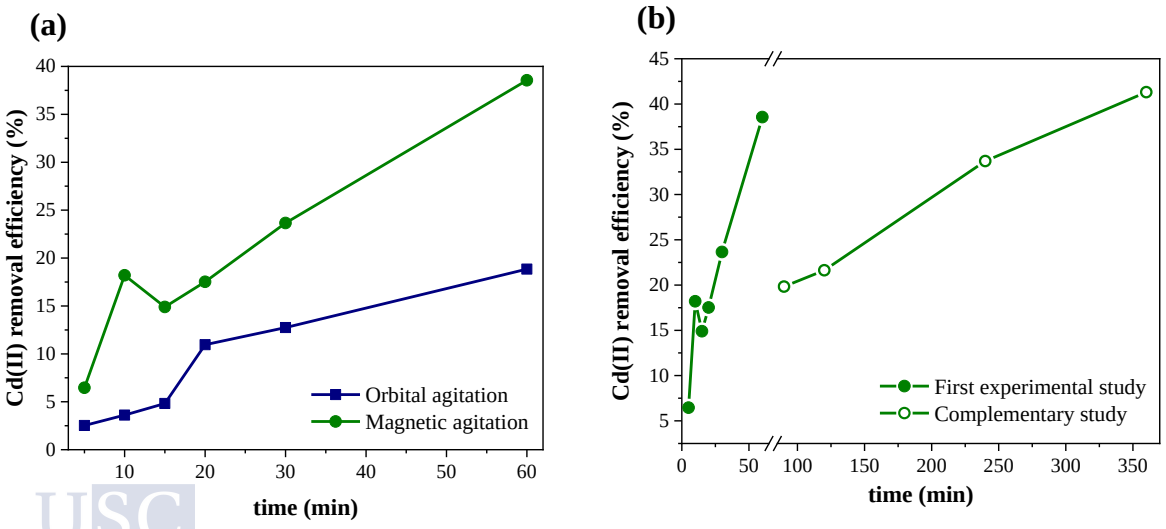


Figure 2.12 Cd(II) ions removal efficiency (%) as a function of time in the orbital and magnetic agitation (a). Complementary study of contacting time with magnetic agitation (b) (Adapted from reference [298] under CC BY 4.0).

The influence of the rotating speed was another parameter studied on the adsorption process under a magnetic and orbital agitation from 150 to 500 rpm for 60 min using 8 mg of adsorbent. The results in Figure 2.13a show that the removal efficiency of Cd(II) increased with the agitation speed in both orbital and magnetic agitations.

A maximum Cd(II) removal of 60 % was observed in the magnetic agitation at 300 rpm. In contrast, the removal percentage of Cd(II) ions remains lower than 40 % throughout the adsorption process in the orbital agitation. These results suggest that, for the above-described experimental setup conditions, the optimum agitation speed is 300 rpm using the magnetic agitation, and it will be the fixed parameter.

Magnetic agitation of the L3 beads has shown to be generally more efficient than orbital agitation. One of the reasons for this result is that the magnetic agitation is provoked by an external rotating magnetic field that equally affects all the magnetic beads in the solution. This is of crucial industrial importance since magnetic agitation can be much more easily implemented than orbital agitation for large wastewater reservoirs.

Moreover, the influence between adsorbent and adsorbed materials on the removal procedure was assessed by keeping constant all the experimental parameters (contacting time of 1 h, agitation speed of 300 rpm) while varying the mass of L3 beads between 2 and 14 mg. This adsorbent dose range was selected as a criterion for successfully applying this material to industrial uses to reduce costs using minimum adsorbent dosages.

Figure 2.13b, illustrates the adsorption capacity of Cd(II) ions for increasing amounts of adsorbent, which follows an increasing trend reaching a maximum at 14 mg in both magnetic and orbital agitation. This result indicates that an increment of available surface sites for metal loading allows for a larger loading metal capacity. However, the loading saturation capacity was not achieved for the used adsorbent dosages, partly due to the chosen equilibrium time (1 h). A maximum Cd(II) removal efficiency of approximately 60 % and 40 % was observed at the magnetic and orbital agitation, respectively. Therefore, according to these results, the adsorbent dose was fixed to 14 mg using magnetic agitation.

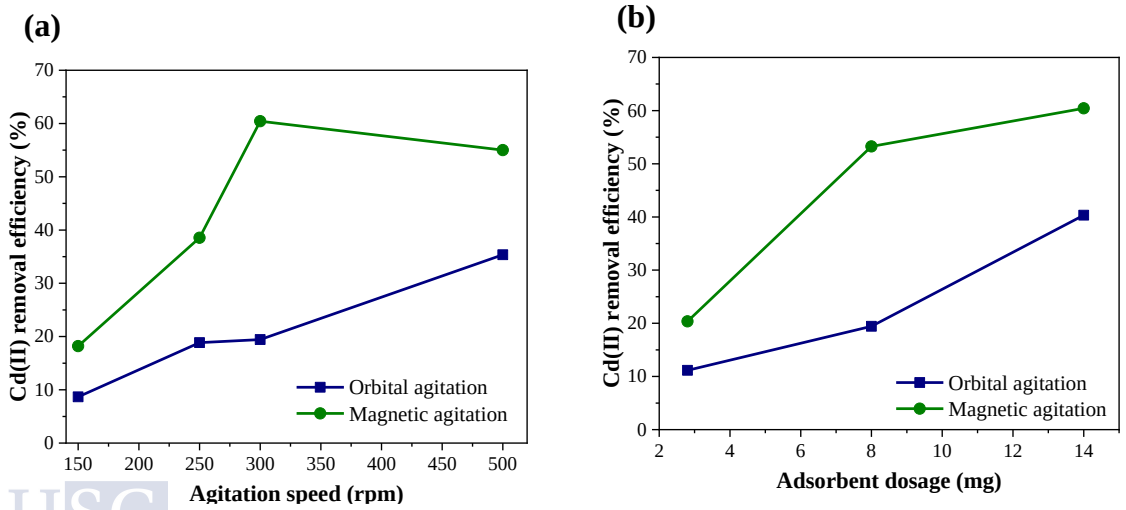


Figure 2.13. Cd(II) ions removal efficiency (%) as a function of agitation speed (a) and adsorbent dosage (b) in the orbital and magnetic agitation (Adapted from reference [298] under CC BY 4.0).

b. Effect of pH on Cd(II) ions adsorption

The solution pH is one of the most important parameters able to govern metal adsorption since it acts on the protonation of the binding sites of the adsorbent and consequently strongly affects the adsorption capacity. The influence of pH ranging from 3 to 9 on Cd(II) ions uptake capacity by the L3 beads was studied using the optimized parameters of the previous studies, which are magnetic agitation at 300 rpm, using 14 mg of dried L3 beads for 1 h.

As observed in Figure 2.14, Cd(II) removal percentage increases from pH of 3 to 6, followed by a steep decrease with a minimum removal and adsorbed metal around pH=6.5. It must be highlighted that for pH values over 6.5, precipitation, ion exchange, and formation of metal hydroxides such as $Cd(OH)_2$ and $Cd(OH)_3^-$ may become significant and influence the Cd(II) ions removal process. These conditions often lead to incorrect adsorption capacity values once metal precipitation does not produce a stabilized form of the heavy metal ions [303–305].

The lower removal percentage of Cd(II) ions at pH of 3 is due to the low number of deprotonated sites, which is attributed to an insufficient number of sites for the adsorption of Cd(II) ions [306, 307]. Moreover, the presence of excess H^+ and H_3O^+ ions in the solution competes with Cd(II) ions for the available sites. The removal percentage of Cd(II) ions on L3 beads increased with the increase of pH, attaining a maximum of approximately 47 % and adsorption capacity of 7 mg/g at pH 6, as shown in Figure 2.14. At higher pH ranges, lesser competing H^+ and H_3O^+ ions and negatively charged groups are available on the surface of the adsorbent, which enhances the adsorption of metal ions through attractive electrostatic forces [308–310].

Adsorption of Cd(II) depends on the nature of the adsorbent surface, as it is revealed in a study using cork powder [301] as adsorbent. A higher adsorption capacity was attained at pH of 6, as in another study where it was used rice husk [305]. Therefore, pH value of 6 was fixed for the following batch experiments.

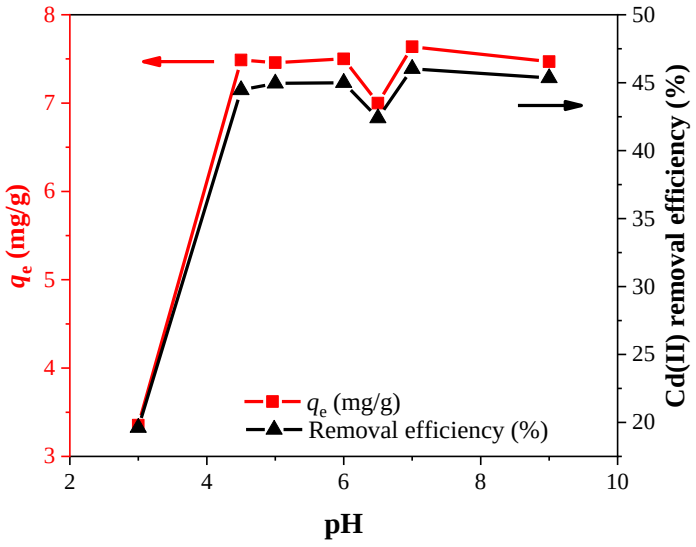


Figure 2.14. Influence of pH on adsorption capacity (q_e (mg/g)) and removal efficiency (%) of cadmium ions by L3 beads.

c. Effect of initial concentration of Cd(II) ions

The effect of Cd(II) initial concentration was studied from 10 to 250 mg/L at previously optimized conditions (magnetic agitation at 300 rpm, using 14 mg of L3 beads during 1 h at pH=6).

Figure 2.15 shows that the adsorption capacity increased by increasing the Cd(II) initial concentration, reaching its maximum adsorption of 68.77 mg/g at 150 mg/L. The increasing initial Cd(II) concentration enhances the adsorption uptake of Cd(II) ions and its interaction with the L3 beads due to the produced driving forces by the concentration gradient [305]. Afterward, a slight and constant decrease in the adsorption capacity is observed, resulting in adsorption equilibrium from the initial concentration of 150 to 250 mg/L. Conversely, the removal efficiency of Cd(II) ions by the L3 beads decreases with increasing initial Cd(II) concentration in the solution. This may be due to the saturation adsorption sites of the L3 beads throughout the adsorption process, leading to a reduction in the equilibrium uptake process for increasing Cd(II) initial concentration.

To prove this, the external and internal surface of the beads after Cd(II) adsorption were analysed by SEM-EDX (Figures A1.3 and A1.4). This technique provides quantitative information on the structure of Cd(II) metal ions in the L3 beads. The beads used in the initial concentration of 10 and 250 mg/L were analysed for comparative purposes. Before the analysis, the beads were cleaned with water and dried at room temperature. In the diagrams (Figures A1.4c and A1.4d), it was reported an apparent increase of the Cd(II) metal ions at the initial concentration of 250 mg/L, either on the surface of the L3 bead (Figure A1.4c) or internally (Figure A1.4d). At the lowest concentration, due to the ratio of pore sites available to the adsorptive concentration in solution, the metal ions diffuse into the internal structure of the L3 beads. As a result, the resistance and competition were lower, so a higher weight percentage of Cd(II) ions was reported inside than outside of the beads at the concentration of 10 mg/L (Figures A1.4a and A1.4b). The opposite trend was found at the highest concentration, the metal ions over-saturated the surface pores of the L3 beads inhibiting the diffusion of the metal ions towards the internal pores of the beads.

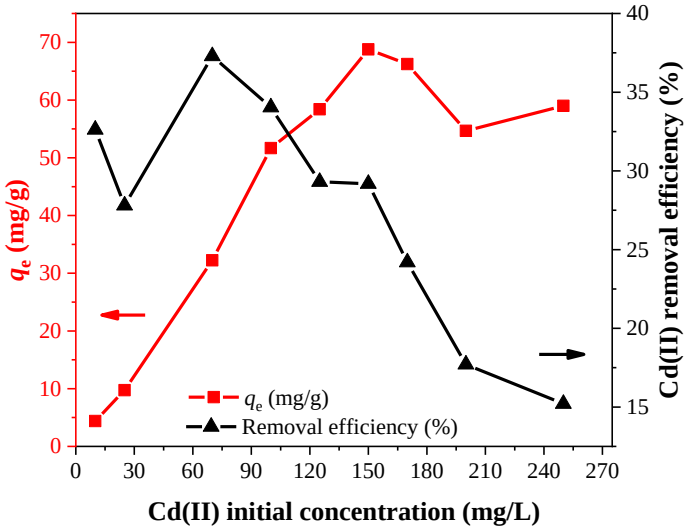


Figure 2.15. Effect of Cd(II) initial concentrations on adsorption capacity (q_e (mg/g)) and removal efficiency (%) by L3 beads.

d. Desorption and Reusability

Recycling any adsorbent is an important economic advantage for cleaning procedures, and the recovery of heavy metals from the regenerated adsorbent is of economic profit. Therefore, the possibility of re-using the L3 beads over five successive adsorption and desorption cycles was evaluated using HCl as a desorbent solution. The desorption efficiency of Cd(II) ions from L3 beads over five cycles is shown in Figure 2.16a.

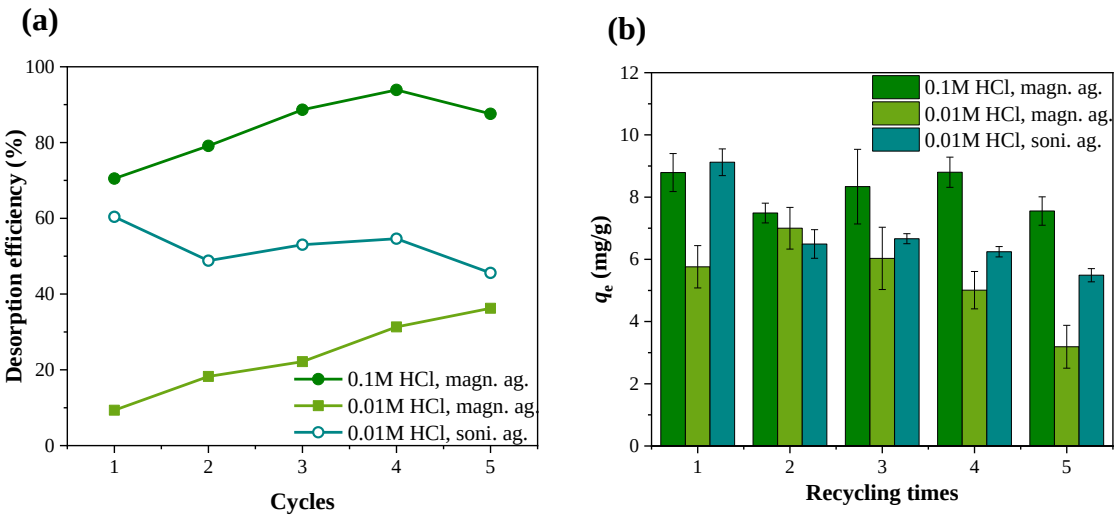


Figure 2.16. Desorption efficiency (%) of cadmium ions (a) and recycling cycles (b) of L3 beads using different concentrations of desorbent and agitation type.

Two types of desorption agitation were tested, ultrasonic and magnetic, using 0.1 M and 0.01 M HCl. It has been considered that ultrasonication promotes a great recovery of heavy metals from granular activated carbon and magnetic hybrid materials [311, 312]. Given this, ultrasonic agitation was selected and compared to the magnetic agitation, which was the optimum parameter used in the previous experiments. The desorption efficiency using magnetic agitation seems to increase over the cycles compared to the ultrasonication agitation.

In the first approach to desorb Cd(II) ions, a concentration of 0.01 M HCl was chosen in the ultrasonic and magnetic agitation. It was noted that during the desorption process using the ultrasonication agitation a gradual disintegration of the L3 beads was observed. The ultrasonic adsorption initially had 60 % desorption efficiency in the first cycle compared to 20 % using the magnetic agitation. Over time, the efficiency declined because of the particle's disintegration.

In a second approach, once the particle structure was completely intact using only 0.01 M HCl at the magnetic agitation, and the desorption efficiency was gradually increasing over the cycles. A concentration of 0.1 M HCl was selected to perform the second study. HCl was chosen as the only desorbent agent since, in several studies, it has proven to be more effective in desorbing Cd(II) and other heavy metal ions than the carbonate salts and chelators [313–315]. For this reason, a HCl concentration of 0.1M was selected to perform the second study.

Figure 2.16a shows the influence of using different concentrations of HCl on the desorption efficiency of Cd(II) ions from the L3 beads. The desorption efficiency using 0.1 M

HCl was slow from the cycles (1 to 3), reaching its maximum at the 4th cycle with approximately 90 % of Cd(II) ions desorbed. However, the desorption efficiency decreased after the 5th cycle, but not significantly. The reusability of any adsorbent avoids the adsorption process's cost and reduces environmental pollution. Therefore, the regeneration of L3 beads allows their use in water treatment.

The L3 beads reusability was examined, and the results are shown in Figure 2.16b. After the first adsorption-desorption cycle, it was observed a loss in uptake capacity in both ultrasonication and magnetic agitation using 0.01 M HCl. In contrast, the regeneration of the L3 beads when it was used the 0.1 M HCl showed a constant uptake capacity but slightly lower than in the first cycle. These results suggest that continuous adsorption resulted in internal pore saturation and, consequently, decreased adsorption capacity.

Thus, it can be said that these beads have the potential to be reused for up to four cycles. Moreover, it was found that using large concentrations of a desorbing agent (0.1 M HCl) under magnetic agitation, the adsorbent structure was preserved, and its capacity for Cd(II) ions desorption was approximately 90 %.

e. Adsorption performance

Adsorption isotherm models

The adsorption equilibrium was studied following the linear and nonlinear fittings of the Langmuir, Freundlich, Temkin, and DKR models using the optimized parameters defined in precedent sections: magnetic agitation with a rotating speed of 300 rpm, 14 mg of L3 beads, contacting time of 1 h, pH = 6, over a Cd(II) concentration range of 10-250 mg/L.

The fitting of experimental Cd(II) adsorption by L3 beads to the linear fitting of Langmuir (eq. 2), Freundlich (eq. 5), Temkin (eq. 7), and DKR (eq.10) models was performed to obtain the model parameters (compiled in Table 2.4) and shown in Figure 2.17. The maximum adsorption capacity (q_{max}) obtained by the Langmuir adsorption isotherm equation was 94.34 mg/g, which was compared with other adsorbents in the literature, as shown in Table 2.3.

The L3 beads proved to be the most efficient material in removing Cd(II) ions from water in just 1 h of contacting time with 14 mg of adsorbent. The values of RL indicate the type of isotherm, if it is irreversible (RL = 0), if it is favourable (0 < RL < 1), linear (RL = 1) or unfavourable (RL > 1). The RL values were found to be less than 1 and greater than 0 (Table 2.4) under the chosen experimental conditions, revealing the Cd(II) adsorption by L3 beads was a favourable phenomenon. The results obtained fitting to the Freundlich isotherm model indicate that the adsorption intensity of Cd(II) (1/n)= 0.79 and n= 1.26 onto the L3 beads was favourable under the experimental conditions.

Based on the linear plot obtained from the Temkin model, the calculated b_t=130.52 J/mol and K_T = 0.169 L/g, indicate that adsorption is a physical process for the experimental conditions. Furthermore, the energy of Cd(II) adsorption by L3 beads was E =1.581 kJ/mol, which was obtained through the DKR model, which suggests that adsorption of metal ions of Cd(II) was by physisorption with a maximum monolayer adsorption capacity of q_m = 47.68 mg/g.

USC UNIVERSIDADE DE SANTIAGO DE COMPOSTELA

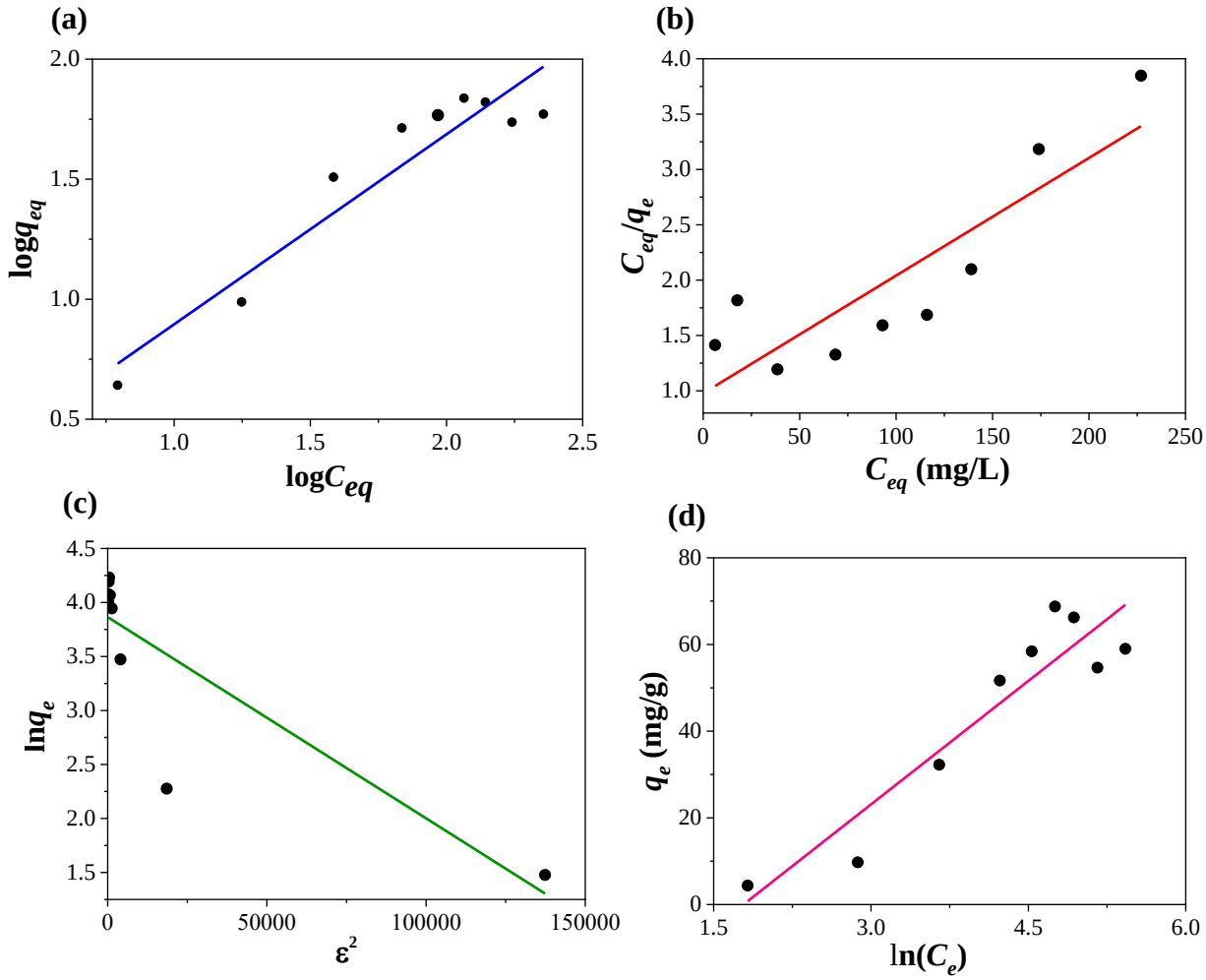


Figure 2.17. Linear isotherm models: Freundlich (a), Langmuir (b), Temkin (c) and DKR (d) describing adsorption of Cd(II) ions onto L3 beads (Adapted from reference [298] under CC BY 4.0).

USC
UNIVERSIDADE DE SANTIAGO DE COMPOSTELA

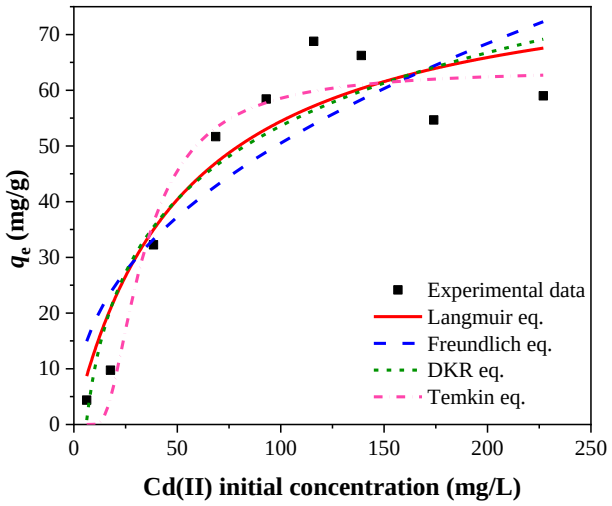
Table 2.3. Comparison of adsorption capacity of several adsorbents for the removal of Cd(II) ions from aqueous solutions.

Particles	q_{max} (mg/g)	Reaction time (h)	Experimental conditions*	Reference
Biochar derived from grape (GPR) and apple (APR)	GPR= 57 APR= 49	2	D =0.05; C_0 =0-200; pH=5	[316]
Olive stone	11.72	3	D =0.25; C_0 =200	[317]
Powdered activated carbon impregnated alginate beads (ABPAC)	89.6	24	D =1.0; C_0 =10-600	[318]
Leucaena leucocephala activated carbon	70.42	2.6	D =0.5; C_0 = 10-50; pH=7; T(50 °C)	[319]
Magnetite/carbon nanocomposites	76.67		D =1.0; C_0 =10-150; pH=6; T(25 °C)	[320]
Ca-alginate from *Laminaria digitata*	141.98	24	D = 1.0; pH=4.5; T(25 °C)	[321]
L3 beads	**94.34**	**1**	**D =0.014; C_0 = 10-250; pH=6; T(25 °C)**	**Present study**

***D: dosage (g/L); C_0: initial concentration (mg/L)**

In addition, the nonlinear regression of the adsorption models was performed to obtain a more precise estimate of the parameters and test the validity of the linear fitting since linearization of the original equations can violate models' assumptions/theories [322].

Figure 2.18 shows the experimental data of Cd(II) fitting to the nonlinear and linear Langmuir (eq. 1), Freundlich (eq. 4), DKR (eq. 6) and Temkin (eq. 8) models equation against the Cd(II) initial concentration.



USC UNIVERSIDADE DE SANTIAGO DE COMPOSTELA

Figure 2.18. Nonlinear isotherm models and experimental data representation of Cd(II) adsorption capacity, $q_e(mg/g)$, against the initial Cd(II) initial concentration, $C_e(mg/L)$.

The Langmuir isotherm parameters obtained from the nonlinear regression do not differ substantially from those from the linear regression, see Table 2.4. The adsorption capacity is 83.45 mg/g with a Langmuir constant (K_L=0.0129 L/mg) which is slightly higher than the one reported in the linear regression. On the other hand, the Freundlich constant value of 6.71 $mg^{1-(1/n)}L^{1/n}g^{-1}$ obtained from the nonlinear model is 6 times higher than in the linearized model. The results are in accordance with the linear regression results, stating that the adsorption intensity was favourable with $(1/n)$=0.439 and n=2.28.

K_T is related to the equilibrium of binding energy calculated through the Temkin model and it was lower in the nonlinear than in the linear Temkin model. Regarding the nonlinear fitting of the DKR model, the calculated adsorption energy was lower than 8 $kJmol^{-1}$ indicating the physical nature of Cd(II) adsorption which is in concordance with the linear fitting [323]. Conversely, the adsorption capacity for the formation of a monolayer (q_m=63.75 mg/g) and mean adsorption energy (β =0.347) of Cd(II) was higher compared to the linear fitting.

Selection of the best adsorption isotherm model using error functions

As stated previously, transforming the nonlinear isotherm equations to the linear forms may produce certain errors, such as poor linearity despite and higher linear R^2. Nonetheless, it is important to apply error functions to assess the accuracy of a fitted model to the experimental data. The calculated error functions with the respective constants in both linear and nonlinear fitting of the models Langmuir, Freundlich, Temkin, and DKR are shown in Table 2.4.

The linear Freundlich model reported more minor errors than the linear Langmuir model. The error functions suggest the nonlinear fitting of the Freundlich isotherm to be discarded since the χ^2 value of 28.46 is much higher than the tabular χ^2 of 15.507. The tabular χ^2 value at 0.05 confidence level with (n−1) degrees of freedom is equal to 15.507 (n is the 9 concentrations of this study) (Table 2.4). Even though, the nonlinear fitting of the Langmuir isotherm χ^2values are below the tabular χ^2. The model does not describe so well the Cd(II) equilibrium adsorption as the linear Freundlich model due to the higher fittingness demonstrated with the calculated error functions.

In this study, the Freundlich model better described the adsorption equilibrium. The model states that during adsorption, physical bonds were produced, which is an indicative of a multilayer adsorption with non-uniform distribution of adsorption heat and affinity through the heterogeneous surface of the adsorbent [225, 308]. The Freundlich model gives more accurate results than the Langmuir isotherm for various heterogeneous adsorption systems [225]. In several studies, the Freundlich isotherm showed a strong linear relationship for Cd(II) adsorption using SBA-15 nanoporous silica [324], biochar from residues [317], activated carbon impregnated alginate beads [222], and powdered activated carbon from *Leucaena leucocephala* biomass [320]. Conversely, the linear Langmuir model better described the adsorption equilibrium of Cd(II) on microwaved olive stone activated carbon [318].

The Temkin model linear and nonlinear fitting suggests that the model does not describe the Cd(II) adsorption so well onto the L3 beads and should be discarded. The MSPD error and the χ^2values are higher, and the last is much above the tabular χ^2 of 15.507. On the other hand, the linearization improved the DKR model fittingness, reporting a χ^2 value of 4.84.

The metal ions adsorption by an adsorbent is influenced by several factors, such as the metal ion size, number of active groups, pore size present on the surface of the adsorbent, and the experimental conditions used in the adsorption process (pH, concentration, contacting time, agitation type, and rotating speed). In this study, Cd(II) adsorption was better described by the

Freundlich and DKR isotherm models. The adsorption of Cd(II) was a physical process occurring at a multilayer level with different sites affinity and adsorption heat onto the heterogeneous surface of the L3 beads.

Table 2.4. Linear and nonlinear parameters of the Isothermal models, Langmuir, Freundlich, Temkin and DKR with respective errors of Cd(II) adsorption by L3 beads.

Langmuir Model						
	R_L	q_m (mg/g)	K_L (L/mg)	R^2	MSPD	χ^2
Linear fitting	0.325	94.34	0.010	0.753	0.513	0.960
Nonlinear fitting	0.268	83.45	0.019	0.884	2.363	14.60
Freundlich Model						
	1/*n*	n	K_F ($mg^{1-(1/n)}L^{1/n}g^{-1}$)	R^2	MSPD	χ^2
Linear fitting	0.79	1.26	1.27	0.900	0.074	0.096
Nonlinear fitting	0.439	2.28	6.71	0.775	8.062	28.46
Temkin Model						
	b_T (J mol)	K_T (L/g)	R^2	MSPD	χ^2	
Linear fitting	130.52	0.169	0.870	429.4	2043.3	
Nonlinear fitting	18.99	0.168	0.870	2.075	30.25	
DKR Model						
	E (kJ/mol)	β (mol^2/kJ^2)	q_m (mg/g)	R^2	MSPD	χ^2
Linear fitting	1.58	-2.00E-05	47.680	0.733	11.980	4.84
Nonlinear fitting	1.20E-03	0.347	63.75	0.948	8.929	2.12E+55

USC DE SANTIAGO DE COMPOSTELA

Study of thermodynamic adsorption

The effect of temperature on the removal of Cd(II) from aqueous solutions was studied using 14 mg of adsorbent dosage (L3 beads) with optimum pH 6.0, magnetic agitation with 300 rpm, over a range of Cd(II) concentrations of 70, 150 and 230 mg/L. The experiments were carried out at different temperatures of 25 ºC (298 K), 30 ºC (303 K), and 40 ºC (313K).

Adsorption of Cd(II) ions by L3 bead increased when the temperature was increased from 298 to 313 K as shown in Figure 2.19a. The removal efficiency was most favoured when it was used a Cd(II) initial concentration of 70 mg/L and least favoured at 150 and 230 mg/L. Using equation (22), the enthalpy of the process was calculated for the different conditions. The process was endothermic (ΔH=24.095 kJ/mol) with high bonding strength at the concentration of 230 mg/L, while smaller ΔH= 8.269 kJ/mol was obtained at the initial concentration of 150 mg/L indicating weaker bonding strength.

Typically, ΔH values ranging from 4 to 40 kJ/mol indicate that a physical adsorption process is taking place, while from 40 to 800 kJ/mol states that adsorption is driven by chemical interactions [253, 325]. In this context, the ΔH values calculated indicated the possibility of physical adsorption, where an increase of temperature led to an increase of Cd(II) adsorption, thus ruling out the possibility of chemisorption. The entropy calculated using equation (22) had as well positive values, showing that the L3 beads affinity increases the randomness at the solid-solution interface during the adsorption of Cd(II) ions. ΔG was calculated using equation (20) for different conditions, and the results are plotted in Figure 2.19.b. Negative values of ΔG (-15 to -19 kJ/mol) imply that Cd(II) adsorption onto the L3 beads is spontaneous. Moreover, a temperature increase from 298 to 313 K, produces a decrease of the Gibbs free energy from (- 12 to -15 kJ/mol), suggesting that adsorption occurs spontaneously at high temperatures [326] which is consistent with the higher adsorption capacity. The feasibility of adsorption seems to be correlated with the initial concentrations of Cd(II) ions.

As can be observed in Figure 2.19.b, at the initial concentration of 70 mg/L, ΔG presents the lowest reported negative values ranging from -14.529 to -15.687 kJ/mol over the temperature range. Meanwhile, incrementing Cd(II) initial concentration, ΔG tends to become less negative which is translated into a lower spontaneity of the process. This behaviour can be attributed to a saturation effect of the available surface pores sites. For low Cd(II) ions concentration, more adsorption sites are available resulting in a favourable and more spontaneous adsorption, whereas for solutions with high Cd(II) ions concentration, the adsorption sites are limited or more occupied, and therefore the adsorption is less favoured. The latter case can even contribute to some extent to adsorption-desorption processes.

Similar results were reported by several authors for Cd(II) ions adsorption on biochar [317], on different crop straw biochar [326], and alginate-calcium carbonate composite beads [327]. Thus, all these results, using different adsorbents, confirm that besides temperature, the contaminant concentration has a crucial influence on the adsorption performance.

USC UNIVERSIDADE DE SANTIAGO DE COMPOSTELA

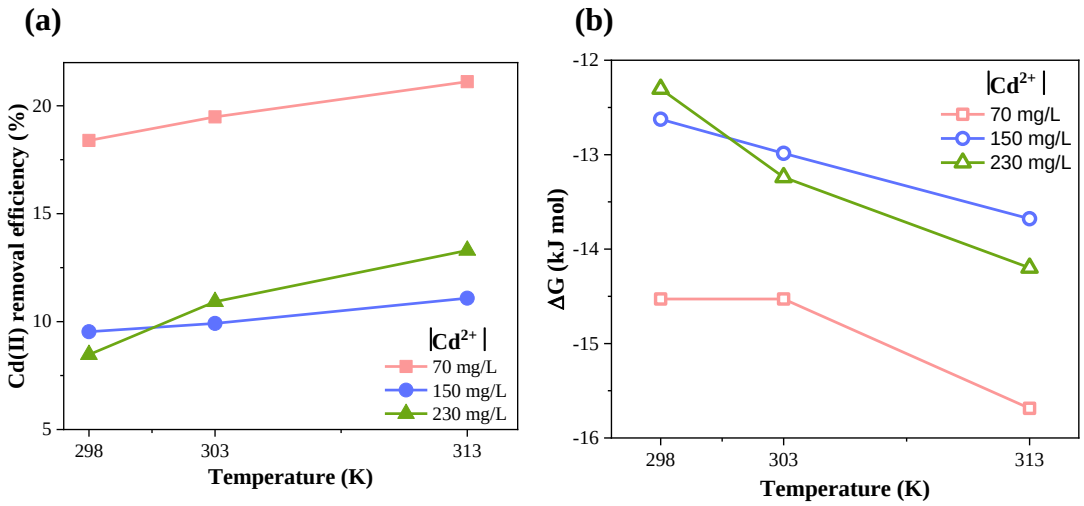


Figure 2.19. Removal efficiency (%) of Cd(II) ions (a) and free Gibbs energy, $\Delta G\ (kJ/mol)$ (b), as a function of temperature (K) at the initial concentrations of 70, 150, and 230 mg/L, respectively.

Adsorption kinetic models: selection based on error analysis

Adsorption kinetics studies were performed to gain insights into the adsorption rate and mechanism, which are crucially important for water treatment purposes. The adsorption kinetics of Cd(II) ions on the L3 beads was analysed in terms of the pseudo first order (PFO), pseudo second-order (PSO), and Elovich models for a set of experimental conditions (pH=6.0, magnetic agitation of 300 rpm, Cd(II) initial concentrations of (70,150, and 230 mg/L), room temperature (25 ºC), 14 mg of L3 beads, under contacting time of (10, 20, 30, 40, and 60 min).The calculated parameters obtained from fitting the experimental data to the nonlinear and linear models are reported in Table A1.7 and the plotted models are shown in Figure A1.5.

Figure 2.20a. shows the computed $q_e(calc)$ values obtained from fitting the experimental data to the linear and nonlinear PFO and PSO models with the experimental $q_e(exp)$ values obtained at concentrations of 70, 150, and 230 mg/L. The PFO nonlinear model was the one with similar $q_e(calc)$= 19.28, 16.83, and 31.93 mg/g values to the experimental adsorption capacity ones, $q_e(exp) = 16.6, 18.25, 31.01$ mg/g obtained at the initial Cd(II) concentrations of 70, 150, and 230 mg/L, respectively. Besides this, the obtained χ^2 in all range of concentrations, as shown in Figure 2.20b, are below the tabular $\chi^2 = 5.99$ inferring that the experimental data is in good agreement with the nonlinear fitting and not with the linear one.

Also, the experimental data fitted well the linear and nonlinear PSO model due to the lower χ^2 values obtained in all initial concentrations. It seems that at the initial concentration of 70 mg/L, physisorption domains mainly Cd(II) adsorption, whereas with increasing initial concentration, chemisorption also occurs.

Figure 2.20c, shows the parameters of Elovich obtained from linear and nonlinear fitting the initial adsorption, α (g/mg min) and surface coverage, β (mg/g min).The adsorption of Cd(II) seems to be initially faster, but when initial concentration increases, adsorption slows down, resulting in high surface coverage. This is compatible with a saturation of adsorption sites at large concentrations, high surface coverage and slow adsorption rates.

Figure 2.20d shows that linearization of the model increases the associated errors. The parameters of Elovich obtained from nonlinear regression fitting show a high binding rate of

Cd(II) ions (α=1.106 mg/g min) at the concentration of 150 mg/L with a relatively low surface coverage of β =0.133 g/mg min. The initial adsorption rate (α= 0.423 g/mg min) was initially faster and high observed by the low surface coverage at 70 mg/L (β=0.059 mg/g min), whereas at 230 mg/L the binding of adsorption was low (α=0.237 g/mg min) reported by the high surface coverage (β= 250.760 mg/g min).

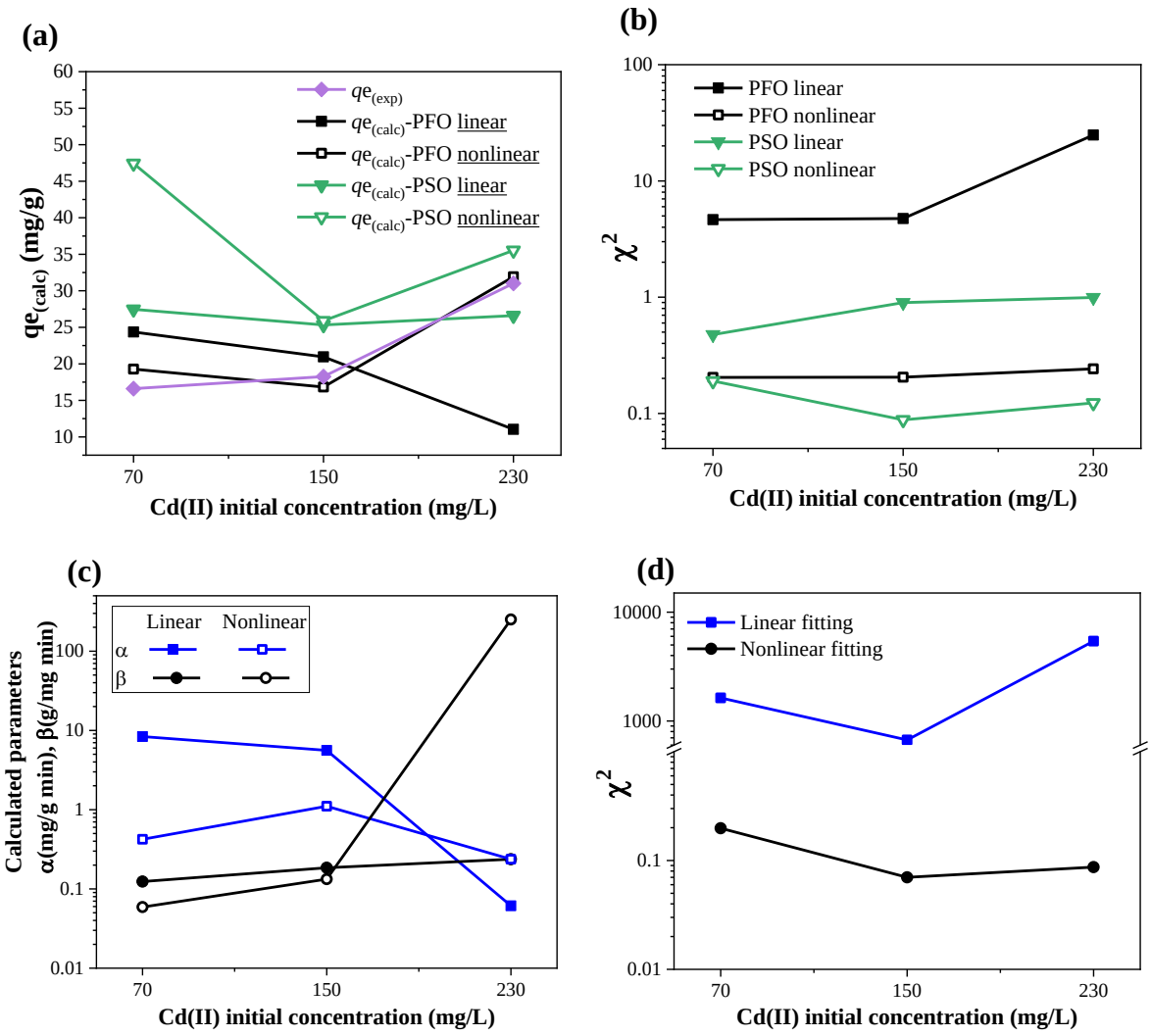


Figure 2.20. Representation of the calculated linear and nonlinear $q_e(calc)$ values of the models PFO and PSO models with the obtained experimental, $q_e(exp)$ values (a) and calculated error, χ^2 (b) against the Cd(II) initial concentration, respectively. Calculated parameters, α (g/mg min) and β (mg/g min) of the linear and nonlinear Elovich model fitting (c) with respective χ^2 (d) against the Cd(II) initial concentration, respectively.

Comparing all models, it seems that all kinetic models can describe Cd(II) adsorption in general. At the initial concentration of 70 mg/L, the $q_e(calc)$ obtained at the PFO nonlinear model was very similar to the $q_e(exp)$ and smaller errors were obtained at the Elovich and PSO linear models at this concentration. It is believed that adsorption occurred mainly by physisorption at this initial concentration, which is best described by the PFO model. Whereas

at higher concentrations, the adsorption is better described by the PSO model, which is assured by the Elovich model, which states that chemisorption occurred.

It was reported in similar studies that the PSO kinetic model also explained better the Cd(II) ions adsorption by powdered activated carbon from *Leucaena leucocephala* biomass [320]. In another research, even though the authors explanations are not based on the error functions to select the best model. The results revealed that both the PSO and Elovich models are the preferred models to explain the kinetics of Cd(II) adsorption onto two types of carbons [317].

Interparticle diffusion model

From Cd(II) adsorption experiments onto L3 beads, the parameters of *Weber and Morris* intraparticle diffusion model were computed and plotted in Figure 2.21.

Figure 2.21a, shows the presence of multi-linear regions, which may indicate that the adsorption process is not only controlled by a single intraparticle diffusion step but by more than one process. The diffusion rate increased from the first step to the last step, as stated by the high K_{id} values shown in Table A6.2 and represented in Figure 2.21b.

Film diffusion of cd(II) (k_{id1}) ions from solution to the L3 beads surface was slow compared to the adsorption of Cd(II) ions through pore diffusion (k_{id2}). Pore diffusion was initially the predominant process of Cd(II) adsorption, but as the initial concentration increases, Cd(II) diffusion through the pores of the L3 bead decreases abruptly, as observed in Figure 2.21b.

On the other hand, film diffusion increases from the initial concentration of 70 to 150 mg/L and decreases slightly at the initial concentration of 230 mg/L. The decreasing trend observed in both diffusion processes with increased initial concentration may indicate surface saturation of the L3 beads, as indicated by the high values obtained of the thickness of the boundary layer in the film (C_{i1}= 24.42 mg/g) and pore (C_{i2}=24.78 mg/g) diffusion at the initial concentration of 230 mg/L (Figure 2.21.b). This also indicates that the system approached equilibrium above $t^{1/2}$ of 6.32.

Thus, a slow first adsorption stage with film diffusion of Cd(II) ions from the bulk solution to L3 beads surface was accompanied by lower rates of k_{id1} with increasing initial concentrations implying that film diffusion was the main responsible of Cd(II) ions adsorption since it consumed more time due to the slow diffusion of the ions. Meanwhile, the second stage, with Cd(II) ions pore diffusion, was accompanied by higher k_{id} rates since a combination effect of film diffusion and surface reaction control occurred at the initial concentration of 70 and 150 mg/L reported by the negative boundary layer values obtained -15.72 and -4.21 mg/g, respectively.

USC UNIVERSIDADE DE SANTIAGO DE COMPOSTELA

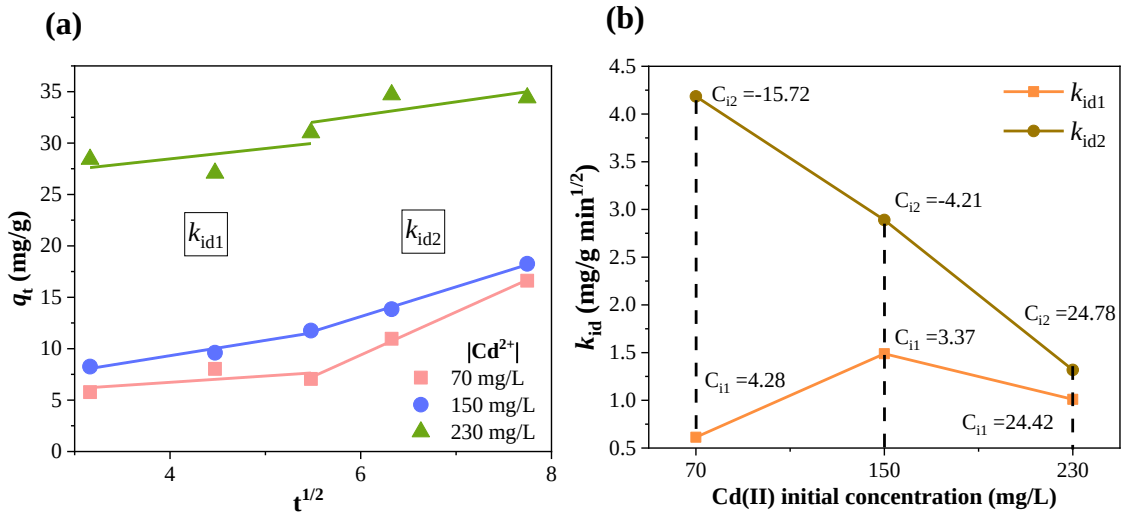


Figure 2.21 Intraparticle diffusion model of Cd(II) ions adsorption onto L3 beads (a) and representation of the intraparticle diffusion constant (k_{id}) and thickness of boundary layer (C_i) in both steps of film (1) and pore (2) diffusion.

2.3.2.2. Elimination of Hg(II) ions from water in a mono and binary system

Mercury is known as one of the most toxic heavy metals due to its persistence, bioaccumulation, and biotoxicity [328]. Consumption of water levels with more than 0.01 mg/L of mercury causes neuronal disorder and damages the cardiovascular system (390). Furthermore, mercury removal from water is quite challenging because it can be present in three different redox states (0, +1, and +2) and is capable of forming complexes with chlorine or other anions [329]. For this reason, mercury was the chosen metal ion for this study, given its difficulty in being adsorbed from the environment.

Taking advantage of the well-known adsorption abilities of carbon as good adsorbent for a wide variety of contaminant species, two forms of different carbons were added to the adsorbing alginate beads, namely, commercial AC and mesoporous carbon. To this end, the adsorption efficiency of two beads composed of commercial AC (L3) and CMK-3 mesoporous carbon (L13) was investigated using a control bead (L16) composed of Fe_3O_4 NPs and sodium alginate.

Ordered mesoporous carbons (OMCs) are gaining much attention over the years due to their structure of micropores (<10 nm) which allows a controlled diffusion of many species into the pores. CMK-3 mesoporous carbon has been widely applied in adsorption [330–332] and catalysis procedures [333]. It can be used as an optimum CO_2 adsorbent prepared from industrial coal ash [334] and NOx removal at low temperatures [335].

In this study, the CMK-3 carbon was synthesized using silica SBA-15 as template, the synthesis method is described in Appendix A6.2.4. The morphology of all precursors (SBA-15, CMK-3 carbon, and commercial AC) was characterized by SEM and TEM microscopy, as shown in Figure 2.22.

USC UNIVERSIDADE DE SANTIAGO DE COMPOSTELA

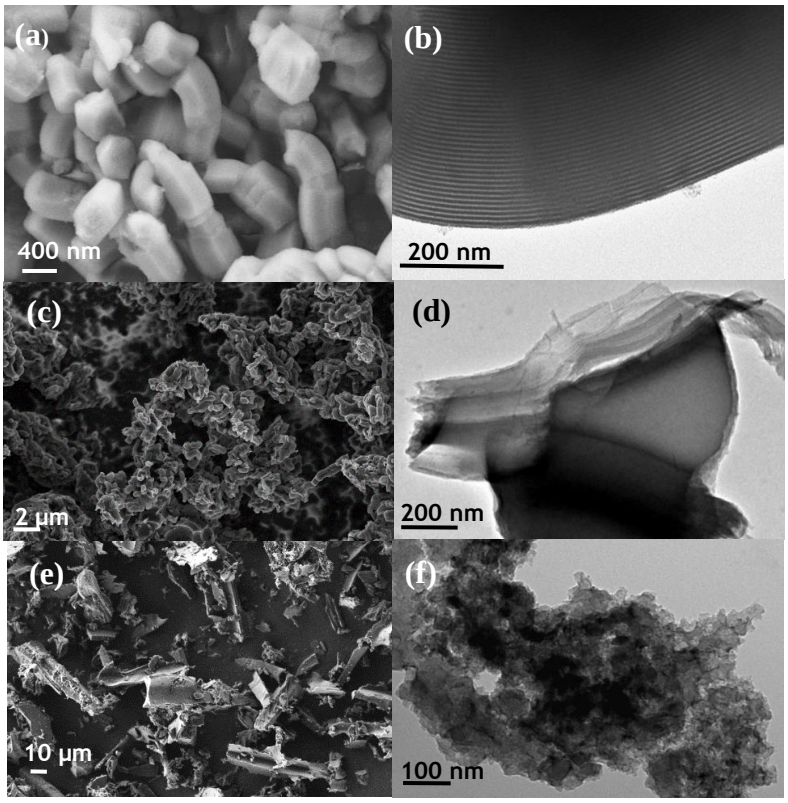


Figure 2.22. SEM and TEM micrographs of SBA-15 (a, b); CMK-3 mesoporous carbon (c, d) and commercial activated carbon (e, f), respectively.

Figure 2.22a shows the SEM images of the SBA-15 mesoporous silica developed revealed a rod-like morphology and hexagonal shape. Furthermore, in Figure 2.22c, the image of the CMK-3 carbon obtained from the SBA-15 calcination, preserved the shape of its correspondent precursor. The porous structure of SBA-15 mesoporous silica and CMK-3 carbon can be also seen in the TEM images in Figure 2.22b and 2.22d, respectively.

The SBA-15 structure was more well-ordered following an assembly of channels than the CMK-3 carbon. On the other side, in Figures 2.22e and 2.22f it is shown that the structure of commercial AC is formed by heterogeneous layers with sizes around 40 to 320 µm. EDX analysis of Fe, O, and C on the beads surface and cross-section were analysed by SEM, as shown in Figure 2.23. All components seem to be homogeneously distributed in the L3 and L13 beads surface (Figures 2.23a and 2.23b). At the same time, in the cross-section, a higher presence of C agglomerates is visible in red colour spots (Figure 2.23b) together with green spots corresponding to iron coming from Fe_3O_4 NPs at the L3 bead.

Meanwhile, in the L13 bead, carbon is almost undistinguished with few visible agglomerates either on the surface or cross-section. Iron agglomerates are clearly more visible on both surfaces. In the L16 bead, the only present elements are heterogeneously distributed with iron concentrated in specific areas of the beads surface and internal structure.

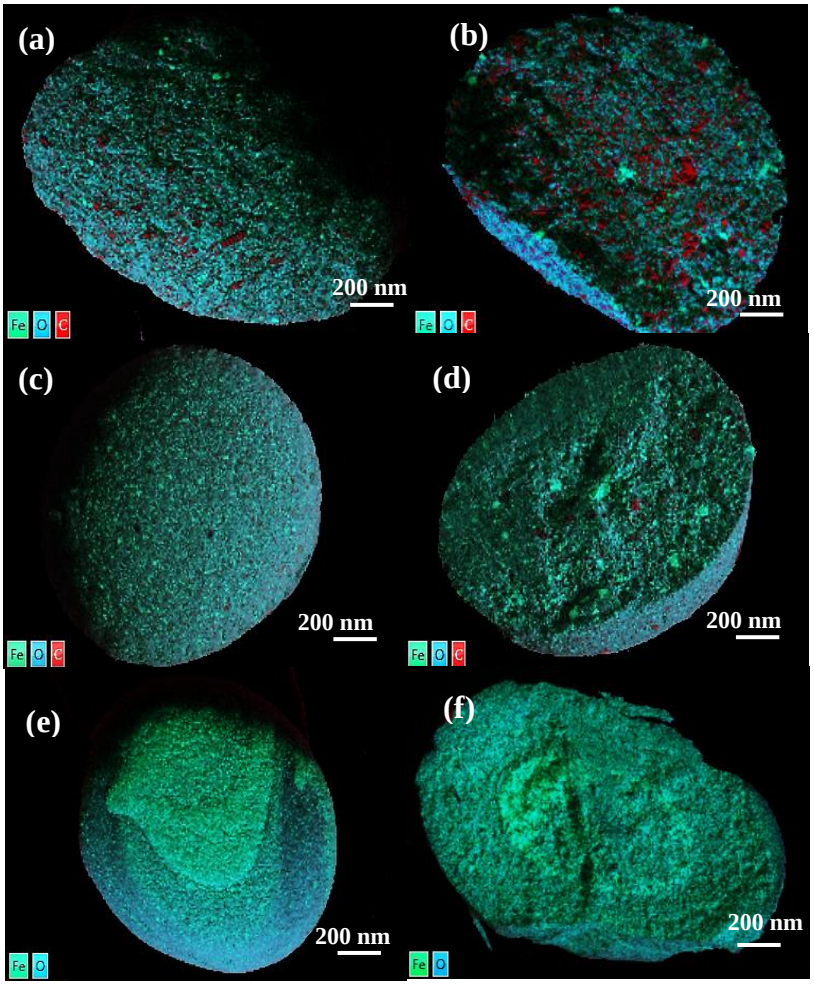


Figure 2.23. SEM images with elemental mapping (Fe, O, C) of the surface and cross-section of L3 (a, b), L13 (c, d) and L16 (e, f) magnetic beads, respectively.

USC
UNIVERSIDADE DE SANTIAGO DE COMPOSTELA

Figure 2.24.a shows the Raman spectrums of CMK-3 carbon and commercial AC. Both spectrums show two distinctive peaks at approximately 1346 cm^{-1} and 1594 cm^{-1}, which are characteristic of polycrystalline graphite, referred as D peak (disordered induced phonon mode, sp^3), and of a single graphite crystal referred as G peak (graphite lattice mode, E_{2g} sp^2), respectively. The D band corresponds to the structural defects of carbon during carbonization while the G band indicates the stretching vibrations bond of C-C.

The ratio between D and G band (ID/IG) is used to measure the degree of in-plane defects of the carbon materials and the crystalline dimension [336]. It is reported that the commercial graphite exhibits an ID/IG ratio value of 0.366 [336]. The ID/IG ratio for the commercial AC and CMK-3 carbon are 0.832 and 0.837, respectively.

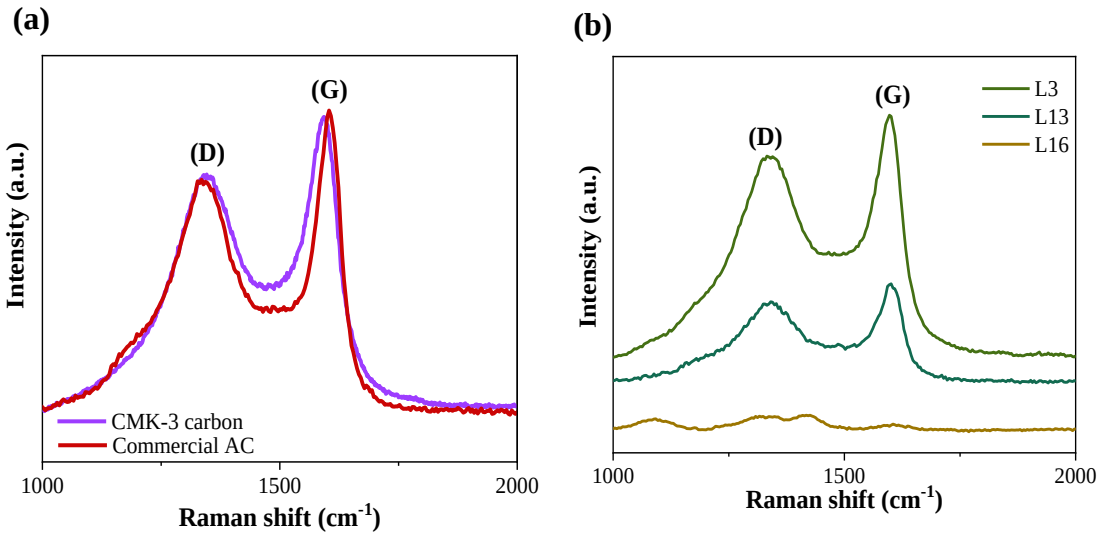


Figure 2.24. Raman spectra of the precursors commercial AC and CMK-3 mesoporous carbon (a) and of the beads L3, L13, and L16 (b).

The ID/IG values for commercial AC and CMK-3 carbon are much higher than that of pure graphite, which indicates that both carbons have a low graphitization.

However, the CMK-3 carbon has higher crystallinity than the commercial AC because of the higher ID/IG ratio, which is characteristic of a nanocrystalline carbon. Figure 2.24b shows the Raman spectra of the corresponding beads, L3 (commercial AC), L13 (CMK-3 mesoporous carbon), and L16 (control bead with only sodium alginate and Fe_3O_4 NPs).

The ID/IG ratio of the beads L3 and L13 are similar to the precursors with values of 0.832 and 0.845, respectively. The spectra of the L16 beads have no peak since no carbon component is present. A wide XPS survey scan was used to identify and quantify the elemental composition of both precursors and beads.

In the survey scan of the precursors (Figure 2.25a), the carbon signal is significant due to the pure carbon nature of the samples. In both were also detected as major elements (O, N, F) and minor ones (S, P). The elements of Cl and Si were also detected in the CMK-3 carbon, and the latter element is probably residue of the SBA-15 template that wasn't completely removed during the cleaning treatment with hydrofluoric acid. The O/C ratio calculated indicates that the commercial AC contains more polar oxygen surface functional groups than the CMK-3

carbon. High-resolution scans of C1s and O1s for both carbons are shown in Figures 2.25c and 2.25d, respectively.

As shown in Figure 2.25c, C1s peak in both carbons deconvoluted into four main peaks. The strongest is attributed to the graphitic carbon (C-sp^2), followed by carbon forming (C-H), (C-C) in sp^3 configuration (284.8 eV), by phenolic, alcohol, or ether groups in (286.1/286.6 eV), and carbonyl or carboxyl groups in (288-289 eV). In commercial AC, the last peak was located at 289 eV which is generated by carboxyl groups while in the CMK-3 carbon it was located at 288.45 eV, which is typical of carbonyl groups. Besides this, the corresponding bond generated by alcohols/ethers was relatively higher (11.1 %) in CMK-3 carbon than at the commercial AC (10.4 %).

Figure 2.25d shows that the O1s peak deconvoluted into two peaks located at approximately 531-532 eV which are assigned to C-O-C or C-OH and around 532.5-533.6 eV, which are attributed to C=O or O-C=O. Higher presence of oxygens in C-OH (60.28 %) and O- C=O (66.03 %) was found in commercial AC and CMK-3 carbon, respectively.

Figure 2.25b shows the survey scan of the beads L3, L13, and L16. The beads contain the same major elements (F, N, C, O, S) as the precursor with the addition of newer ones (Na, Ca, Fe) due to the addition of sodium alginate and Fe_3O_4 NPs to the beads. The ratio O/C was higher for the L13 (0.65) than for the L3 and L16 (0.61 and 0.58), revealing their high polarity.

USC UNIVERSIDADE DE SANTIAGO DE COMPOSTELA

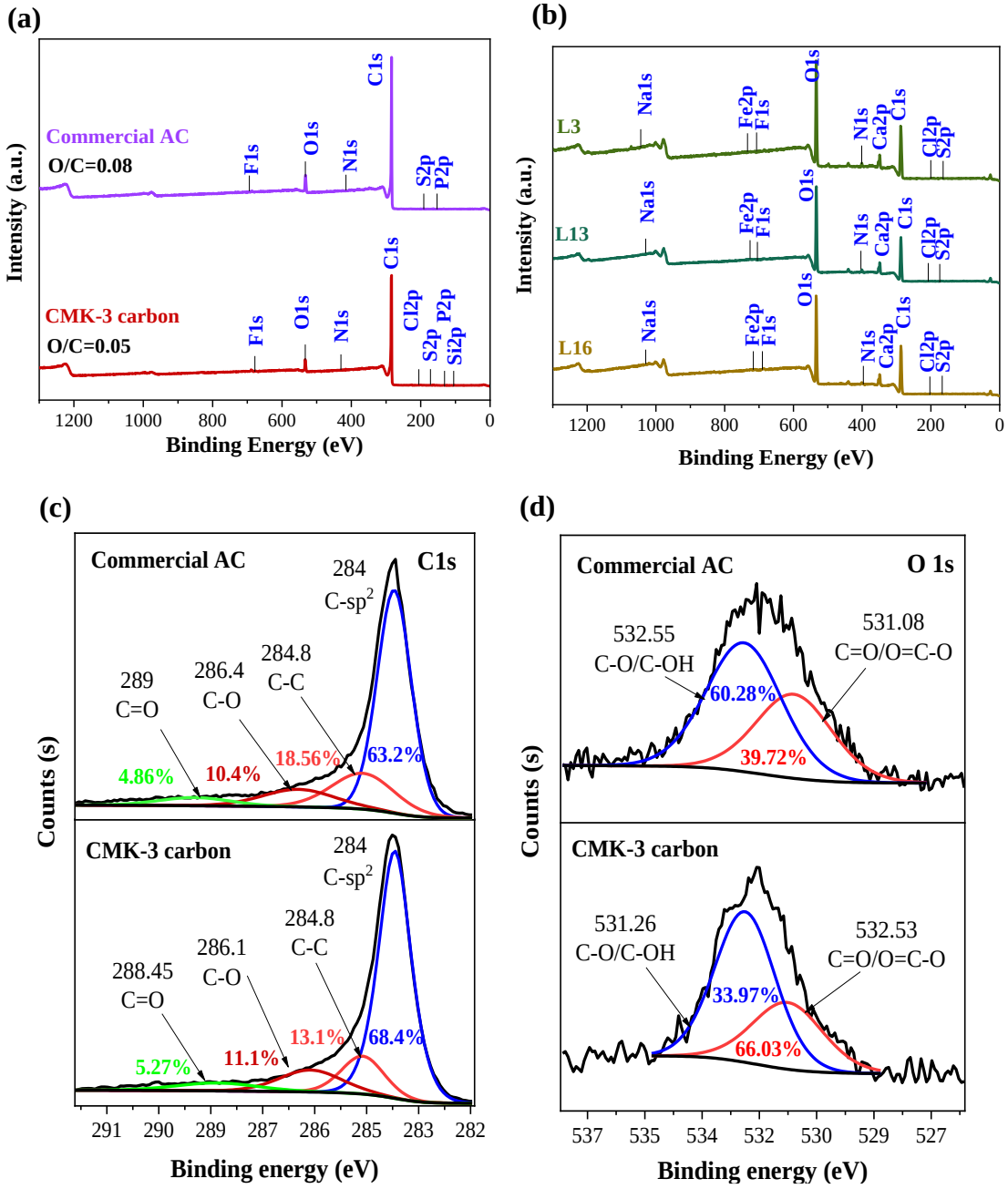


Figure 2.25 XPS survey scan of the carbons (a) and the respective beads (b). High resolution analysis of C1s and O1s of both carbons (c, d), respectively.

a. Effect of initial metal concentration

The adsorption capacity of Hg(II) ions by L3, L13, and L16 was studied at the initial metal concentrations of 10, 70, 150, 200, and 230 mg/L with a pH solution of 4.5. The experiment was conducted for over 6 h, with 14 mg of adsorbent under magnetic agitation of 300 at room temperature. Figure 2.26a shows that the adsorption capacity increased with the initial metal concentration, reaching a maximum adsorption at 150 mg/L, followed by a steep decline at the initial concentration of 200 mg/L, that afterward rises again. L3 had the greatest adsorption capacity from all beads, followed by L13 and L16.

Figure 2.26b, shows that the removal efficiency of Hg(II) decreased with increasing metal concentration, as expected. The removal efficiency of Hg(II) ions decreased from 40 % to 15 % at L3, from 15 % to 6 % at L13, and from 25 % to 4 % at L16 over the concentration range. As previously stated, the oversaturation of the adsorption sites over the initial concentrations leads to a reduction of adsorption efficiency.

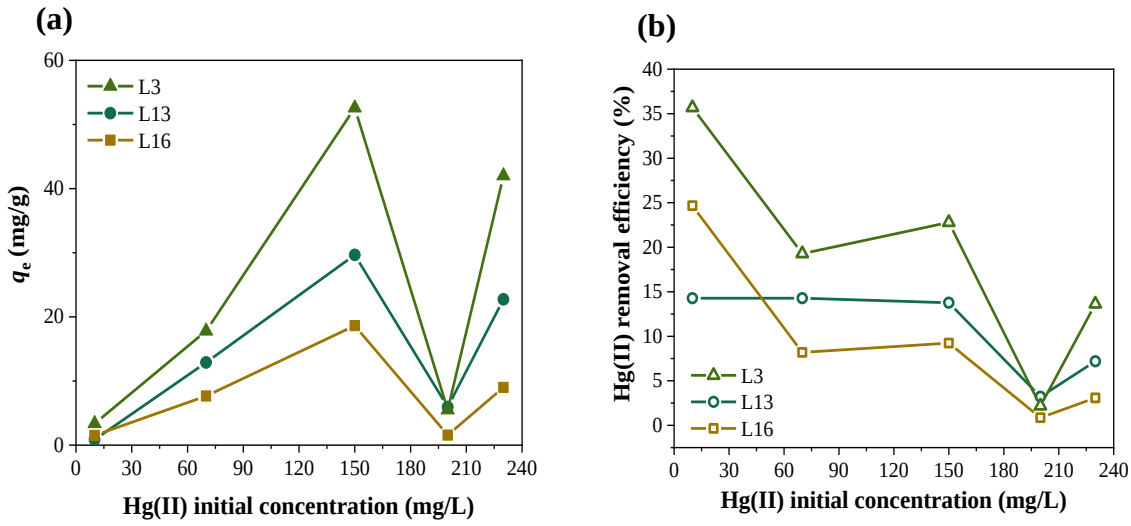


Figure 2.26. Hg(II) ions adsorption capacity (a) and removal efficiency (b) by L3, L13, and L16 beads.

SEM-EDX determined the quantitative presence of Hg(II) ions on the beads surface and cross-section in all concentrations (from 10 to 230 mg/L). Figure 2.27, shows the quantitative results (weight %) of Hg(II) ions in the surface and cross-section of the beads L3, L13, and L16. At the initial concentration of 10 mg/L, a higher percentage of Hg(II) ions at the surface was observed compared to the cross-section at L13 and L16 beads.

As the initial concentration increases (150 mg/L), the inner sites become occupied, and a balanced increment of Hg(II) ions in both surface and cross-section is observed at the L3 beads. At higher metal concentration (200 and 230 mg/L), where a steep decrease in the adsorption capacity of all beads is observed, a saturation of Hg(II) is observed at the surface.

The adsorption capacity of the beads decreases with increasing initial concentration because the ions remain oversaturated in the surface, blocking the available sites from diffusing into the internal structure of the beads. For this reason, a peak of maximum adsorption was observed at the initial concentration of 150 mg/L since the ratio between the available sites and ions concentration was optimum to achieve a great Hg(II) ions adsorption.

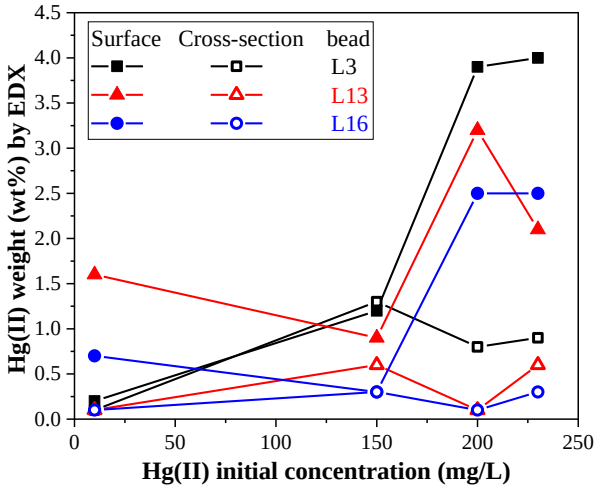


Figure 2.27. Representation of EDX quantitative analysis of Hg(II) ions on the surface and cross-section in the L3, L13, and L16 used in the adsorption experiment.

b. Adsorption performance

Effect of temperature on Hg(II) ions adsorption

The removal efficiency of Hg(II) ions by L3, L13, and L16 beads was studied as a function of temperature from 293 to 313 K. Batch experiments were carried out, with Hg(II) initial concentration of 70 and 150 mg/L, an optimum pH of 4.5 with 14 mg of adsorbent under magnetic agitation for 1 h. The thermodynamic parameters were calculated from equations (20) and (22).

The removal efficiency of Hg(II) for all tested beads at the different concentrations and temperatures is shown in Figures 2.28a and 2.28b. The removal efficiency of Hg(II) ions is generally higher for L3 beads compared to the L13 and L16 and is considerably enhanced with increasing temperature. For L3 beads, the higher removal efficiency was reached at 310 K of approximately 12 % and 7 % at the initial Hg(II) concentration of 70 and 150 mg/L, meanwhile for L13 beads, only 4 % of Hg(II) ions were removed at 298 K and 310 K in both initial concentrations.

On the contrary, L16 beads obtained a maximum removal efficiency of 8 % at the initial concentration of 150 mg/L (293 K). In contrast, at the initial concentration of 70 mg/L, only 2 % of Hg(II) ions were removed at 298 K. In general, changes in both temperature and initial concentration have a clear impact on the removal efficiency of Hg(II) by L3 beads, which is higher with increasing temperature and lower with an increase Hg(II) initial concentration. Temperature seems to have a higher impact than the initial concentrations on the L13 beads adsorption efficacy for Hg(II) ions, whereas both parameters influence Hg(II) removal efficiency by L16 beads.

Figures 2.28c and 2.28d shows negative values of ΔG in both concentrations for L3 beads indicating that adsorption was spontaneous, and all values are between -20 to 0 kJ/mol, which is an indication of a physical adsorption process [313, 322]. The negative values of ΔG increase from the temperature of 293 K to 310 K, but then decrease at 313 K. At this range of temperature (293-310K) more driving forces were present and were higher in the initial concentration of 70

mg/L, resulting in higher removal efficiency of Hg(II) at this concentration. The positive values of ΔH (17.63 and 163.44 kJ/mol) at 70 and 150 mg/L, respectively, indicate that the adsorption was endothermic, where at the last bonding strength was higher. Also, positive values of ΔS (0.0099 and 0.566 kJ/mol) indicate a randomness increase at the solid-solution interface of Hg(II) onto the L3 beads surface at the initial concentration of 70 and 150 mg/L, respectively.

As in bead L3, the adsorption of Hg(II) ions by L13 beads was an spontaneous reaction ($\Delta G < 0$), endothermic (ΔH=47.11 and 15.15 kJ/mol) and entropy (ΔS= 0.186 and 0.081 kJ/mol) was high at initial concentration of 70 and 150 mg/L, respectively. It has been discussed that L16 bead adsorption was affected by both temperature and concentration. This impact is clearly observed by the ΔH (2.81 and -71.83 kJ/mol) and ΔS (0.0352 and -0.208 kJ/mol) at the initial concentration of 70 and 150 mg/L, respectively. The negative values of ΔH and ΔS suggest that the process was exothermic and lower disorder occurred in the liquid-solid phase during Hg(II) adsorption. In addition, a further increase of ΔG values by increasing temperature shows that high temperatures do not favour adsorption at the initial concentration of 150 mg/L, as shown in Figure 2.28d.

It is believed that due to the increased molecule interaction at higher temperatures, a bond rupture occurred, resulting in Hg(II) ions released from the L16 beads surface. A similar result was reported using GO/Fe_3O_4-Si-Pr-SH to remove Hg(II) ions from water [337]. Lower ΔG and ΔH values at the L16 beads may be due to the lack of an active compound in its composition.

USC
UNIVERSIDADE DE SANTIAGO DE COMPOSTELA

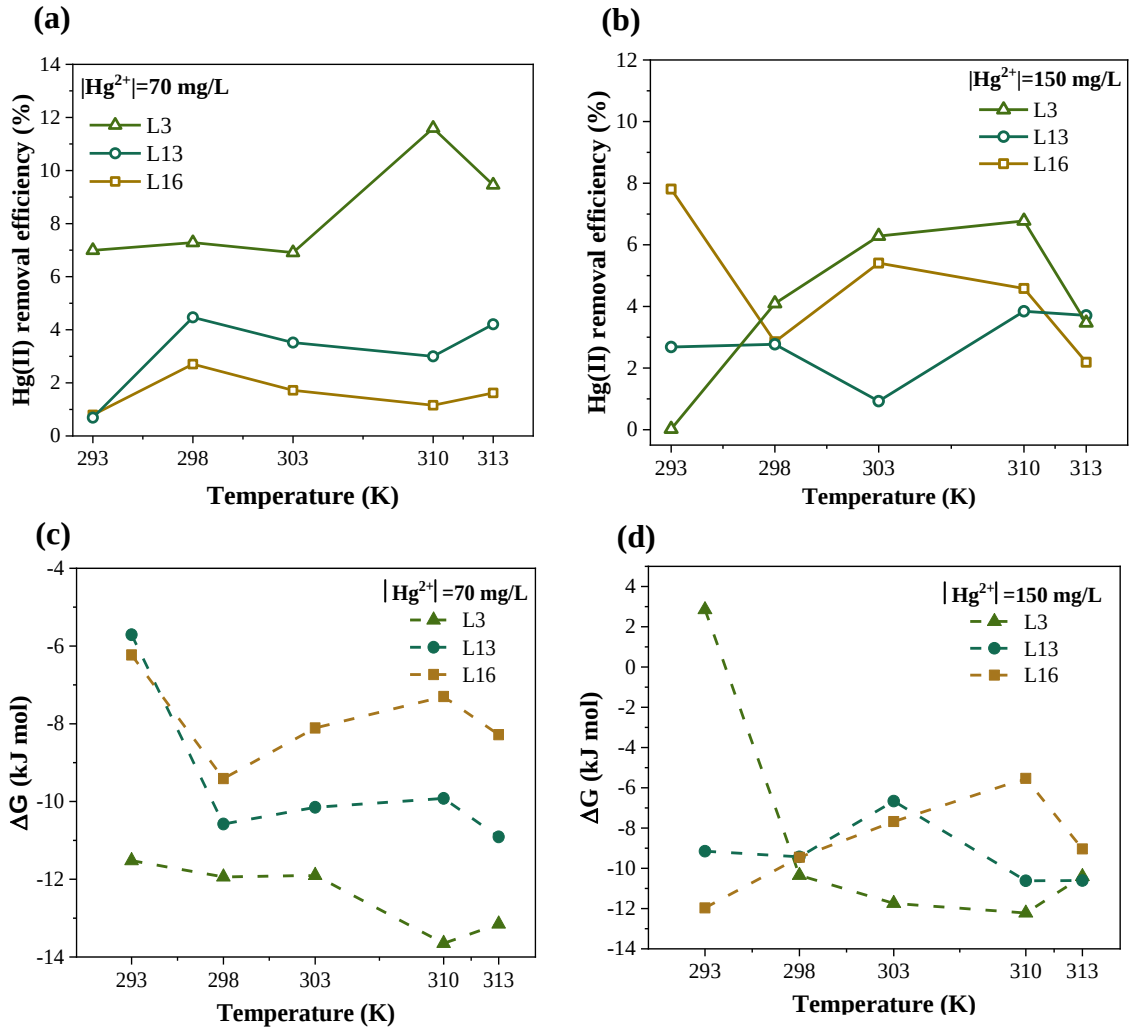


Figure 2.28. Hg(II) ions removal efficiency and ΔG calculated at the initial concentration of 70 mg/L (a, c) and 150 mg/L (b, d) against temperature, respectively by L3, L13, and L16 beads.

Adsorption kinetic and diffusion models: PFO, PSO, Elovich, and IPD

The adsorption dynamics of Hg(II) ions was analysed by fitting the experimental data to PFO, PSO, Elovich, and IPD kinetic models using different experimental conditions: 14 mg of adsorbent, metal solutions with concentrations of 70, 150, and 230 mg/L with pH of 4.5, contact time of 16, 28, 40, 120, 240, and 360 min and magnetic agitation at 300 rpm.

Figures 2.29a,c,e shows the computed $q_e(calc)$ values obtained from fitting the experimental data to the linear and nonlinear PFO and PSO models with the experimental $q_e(exp)$ values obtained at concentrations of 70, 150, 230 mg/L for the beads, L3, L13, and L16, respectively (Figures A1.6-A1.8 are the initial plotted models). Physisorption seems to be occurring at the initial Hg(II) concentrations of 70 and 230 mg/L at the L3 and L16 beads, whereas at the initial concentration of 150 mg/L chemisorption is the main process.

On the contrary, in L13 bead, Hg(II) ions adsorption was mainly done by chemisorption in all initial concentrations. This can be corroborated by the calculated, χ^2 error shown in Figures 2.29b,d,f and reported in Table A6.1.8-A2.0. Lower χ^2 values are obtained at the experimental

data of Hg(II) adsorption in L3 and L16 beads when fitted to the nonlinear PFO model at the initial concentrations of 70 mg/L and 230 mg/L, whereas at the initial concentration of 150 mg/L were better fitted with the nonlinear PSO model. Concerning the associated errors of the experimental data obtained in the bead L13, the nonlinear PSO model reported the lowest errors in all ranges of initial concentrations.

Figures 2.30a, c, e shows the calculated adsorption rate constants (k_1 and k_2) and the initial adsorption rate (h) over the initial Hg(II) concentrations at the beads L3, L13, and L16, respectively. Both rate constants (k_1 and k_2) and initial adsorption rate (h) constant decrease with increased initial Hg(II) concentration at the L3 bead. Meanwhile, in L13 bead, k_2 and h increase with the initial Hg(II) concentration. The adsorption of Hg(II) ions by the L3 bead was slow but the process was more efficient with higher removal of Hg(II) from solution than the values reported in the L13 bead (shown in Figure 2.26).

The calculated k_1 and k_2 rate constants at the L16 bead did not change considerably with increase initial Hg(II) concentration. In all particles the linearization of the experimental data to the Elovich model resulted in χ^2 values much higher than the tabular χ^2 of 5.99, as reported in Table A6.1.8-A2.0, and for this reason were excluded. It is believed that a fast adsorption occurred at the lowest and highest initial Hg(II) concentration, which was accompanied by an increase in the surface coverage.

Figures 2.30b,d,f, shows the parameters α and β calculated from the experimental data fitted to the nonlinear Elovich model since the linear fitting was excluded. In L3 bead, α and β decreased with increasing initial Hg(II) concentration. However, at the initial concentration of 150 mg/L it was reported the highest binding rate of Hg(II), α= 45.92 mg/g min with a surface coverage of β =0.148 g/mg min. These results corroborate that at this initial concentration, chemisorption was indeed the primary adsorption process of Hg(II) ions.

On the other hand, both surface coverage and adsorption rate increased with the initial Hg(II) concentrations at the L13 bead. It is known that the Elovich model is more suitable for adsorbates with heterogeneous adsorbing systems with chemical adsorption processes [338]. For this reason, this increment of both parameters is due to the surface heterogeneity with different energy affinities [339]. The EDX quantitative analysis of Hg(II) ions at the L13 bead revealed a saturation of the ions at the surface than in the cross-section. Curiously, a saturation of Hg(II) ions at the bead surface was independent of the initial concentration. In fact, at the initial concentration of 150 mg/L was reported a higher diffusion of Hg(II) inside the L13 bead structure than that at the other concentrations. The ratio of pore availability and metal ions at this concentration allowed a fast diffusion of the Hg(II) ions. Also, at the L16 beads, the initial adsorption increases with an increased initial Hg(II) concentration, but the surface coverage decreases and reveals higher values at the initial concentration of 70 mg/L.

USC
UNIVERSIDADE DE SANTIAGO DE COMPOSTELA

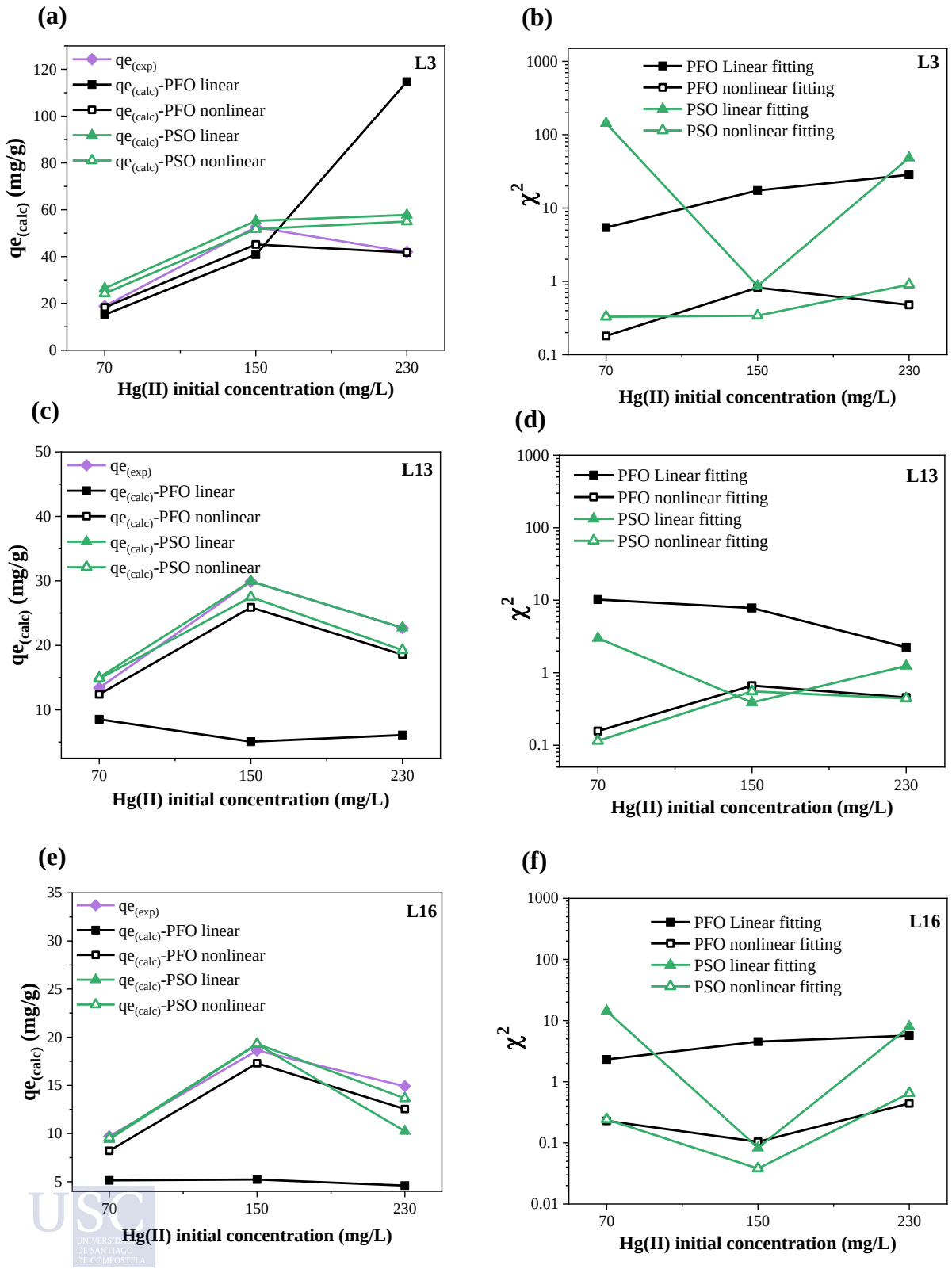


Figure 2.29. Representation of the calculated linear and nonlinear $q_e(calc)$ values of the PFO and PSO models with the obtained experimental, $q_e(exp)$ values (a, c, e) and calculated error function, χ^2 (b, d, e) against the Hg(II) initial concentration at the beads L3, L13, and L16,respectively.

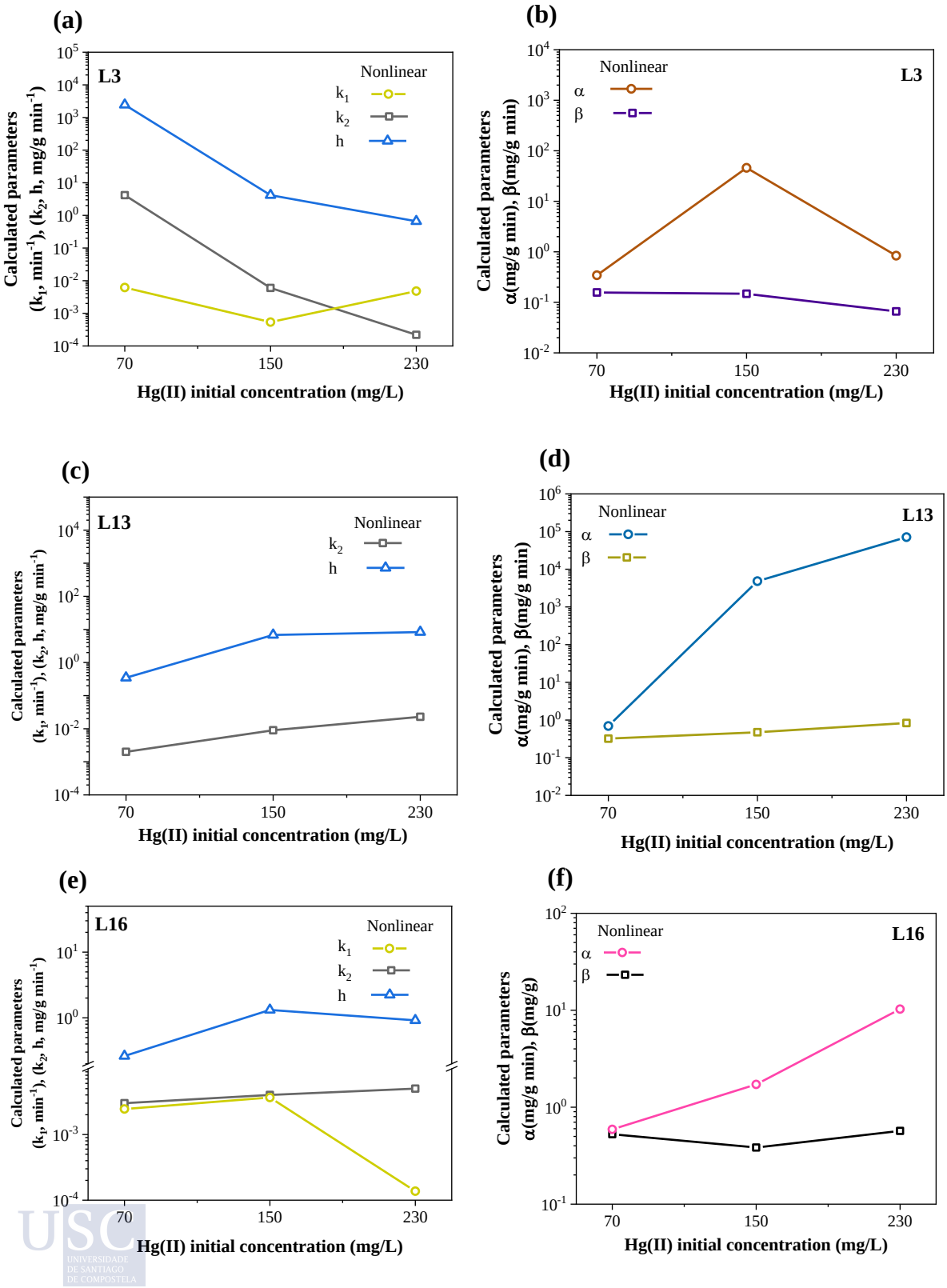


Figure 2.30. Calculated parameters, k_1 (min^{-1}), k_2 and h (mg/g min^{-1}) (a, c, e) and α (g/mg min), β (mg/g min) of the nonlinear Elovich model fitting (b, d, f) per bead L3, L13, and L16, respectively.

The parameters of the *Weber and Morris* intraparticle diffusion model for Hg(II) ions adsorption onto the L3, L13, and L16 beads were calculated and plotted in Figure 2.31.

Figures 2.31a, c, e illustrate the presence of two straight lines not intercepting the origin, indicating that Hg(II) ions adsorption was controlled by more than one process [340]. The first line ranged from 4-10 $min^{1/2}$ contact time and the second from 10 to 19 $min^{1/2}$. The deviation of the straight lines is attributed to the difference in mass transfer at the initial and final adsorption steps. The results indicate a rapid first adsorption stage with surface and film diffusion of Hg(II) ions from the solution to the beads.

Figures 2.31b,d,f demonstrates and compares the rate adsorption constants (k_{id1}, k_{id2}) trend over the initial Hg(II) concentrations at the different beads. Film diffusion, k_{id1}, in bead L3 was more pronounced (faster) than in beads L13 and L16, and increases with increase initial Hg(II) concentrations, as illustrated in Figure 2.31b. k_{iD1} values of 1.034, 1.332, and 5.228 mg/g $min^{1/2}$ with the respective boundary layer thickness values **(**C_{i1}) of 0.83, 28.62, and -16.42 mg/g at the initial concentrations of 70, 150, and 230 mg/L, respectively.

Oppositely, in Figure 3.31d, film diffusion of Hg(II) ions onto L13 beads surface over the initial concentration range was slow (k_{id1} (70, 150, 230 mg/L)=0.833, 0.870, and -0.176 mg/g $min^{1/2}$) with increase boundary layer thickness (C_{i1} (70, 150, 230 mg/L)=1.62, 18.34, and 18.49 mg/g $min^{1/2}$). The pore size and morphology of the CMK-3 carbon might be one of the reasons for Hg(II) ions saturation on the L13 beads surface, since the same pattern occurred at the L16 beads, as shown in Figure 2.31f.

Intraparticle or pore diffusion seems to be the dominant adsorption process with slower rates of k_{id2} in all beads. The slow diffusion of Hg(II) ions is attributed to their diffusion from the beads surface into the mesopores/micropores internal structure with an important increase in the boundary layer thickness (C_{i2}). It was observed a slower rate of adsorption in the beads order of L13> L3> L16.

The composition of the beads plays a crucial role in adsorption. Thus, the diffusion of Hg(II) ions onto the L3, L13, and L16 beads was accompanied by film and interparticle diffusion, where the interparticle diffusion was the main controlling step.

USC UNIVERSIDADE DE SANTIAGO DE COMPOSTELA

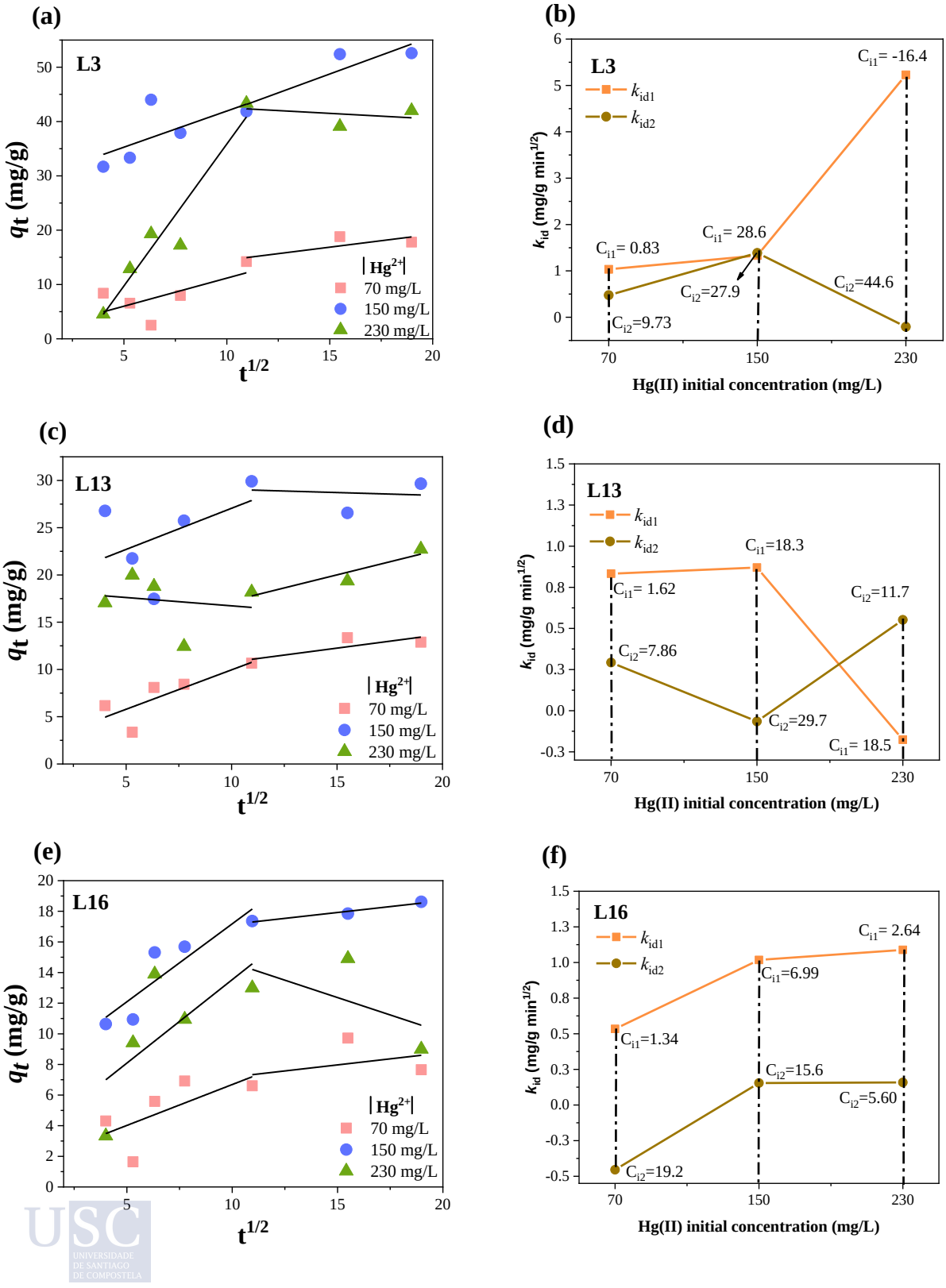


Figure 2.31. Plotted IPD model (a, c, e) and computed rate adsorption (k_{id1}, k_{id2}) and boundary layer thickness (C_{i1} , C_{i2}) (b, d, f) parameters of Hg(II) adsorption by L3, L13, and L16 beads, respectively.

Competitive state of Hg(II) ions in a binary system

The competitive state of Hg(II) ions in the presence of Ni(II) or Cd(II) metal ions was investigated. The batch experiments were conducted with initial Hg(II) concentration from 10 to 230 mg/L with 130 mg/L of Cd(II) or Ni(II) in solution (pH 4.5). To the binary solutions, 14 mg of adsorbent (L3, L13, and L16) was added, and the adsorption has undergone for 6 h under magnetic agitation at a constant speed of 300 rpm.

The results of the competitive adsorption of Hg(II) in a binary system with Ni(II) and Cd(II) at the L3, L13, and L16 are shown in Figures 2.32a,b,c.The adsorption of Hg(II) ions in a binary system exhibit an antagonistic, synergistic, and non-interaction behaviour. In general, the presence of either Cd(II) or Ni(II) caused a decrease in the Hg(II) ions adsorption in all beads, compared to its adsorption in the mono system.

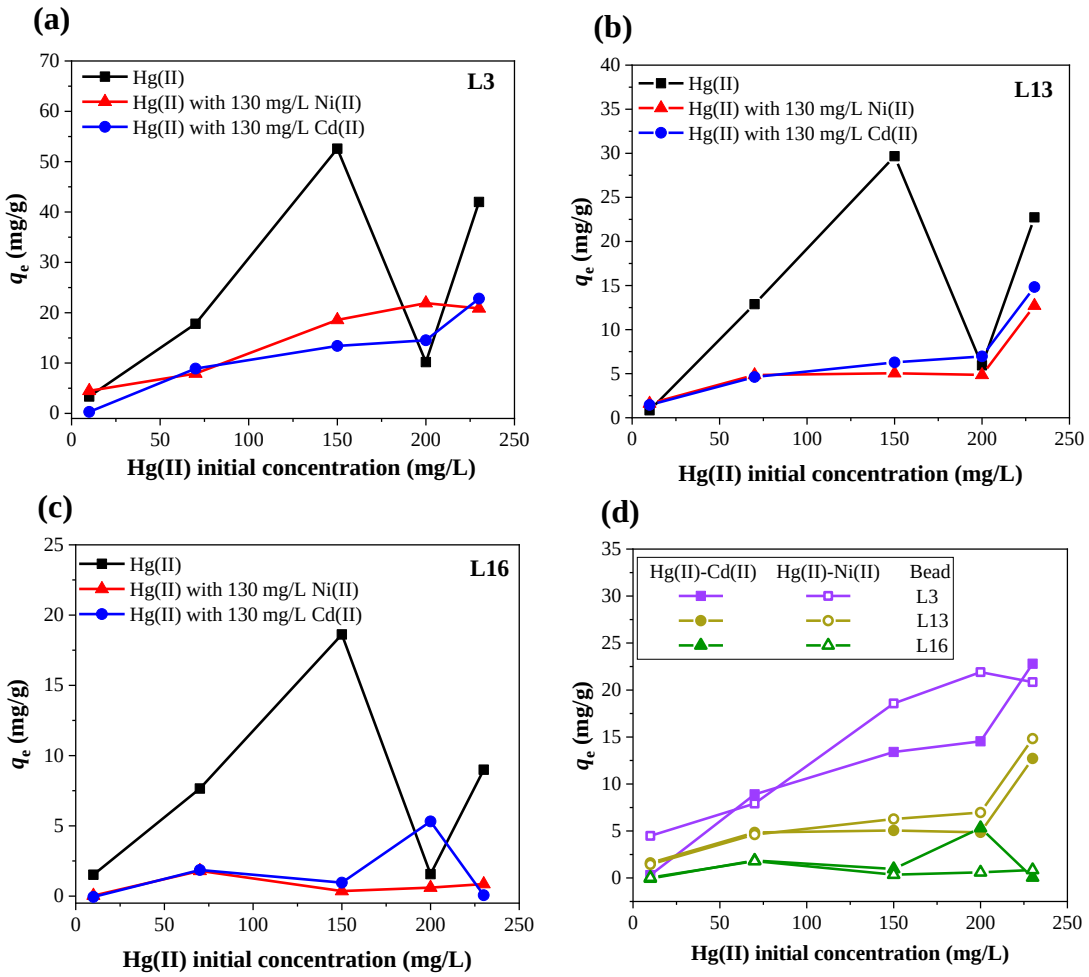


Figure 2.32. Adsorption of Hg(II) in a mono and binary system (Hg(II)-Ni(II); Hg(II)-Cd(II)) by the magnetic beads L3 (a), L13 (b) and L16 (c), respectively. Adsorption capacity of all beads in the binary system (d).

The extent of Hg(II) ions adsorption in the mono or binary system was higher in the L3 beads, as shown in Figure 2.32d. In addition, it was only observed a synergistic effect between Hg(II) and Ni(II) at this bead at the initial concentrations of 10, 150, and 200 mg/L. The effect

was more pronounced at the initial concentration of 200 mg/L since it was reported higher adsorption of Hg(II) ions in the binary system Hg(II)-Ni(II) than in the mono system.

The same feature was also observed in the other two beads, L13 and L16, at the initial concentration of 200 mg/L, but in this case, Cd(II) ions favoured Hg(II) adsorption. Possibly at this concentration, the mass transfer of Hg(II) towards the active sites of the beads was enhanced due to more driving forces.

To ascertain the possible changes on the functional groups before and after adsorption of Hg(II) in both mono and binary systems, FTIR analysis was performed on the beads, as shown in Figure 2.33. Similar bands are observed in all beads. The characteristic peak at around 3200 cm^{-1} is attributed to adsorbed water (-OH). After adsorption, the peak intensity becomes stronger due to the adsorbed water or humidity.

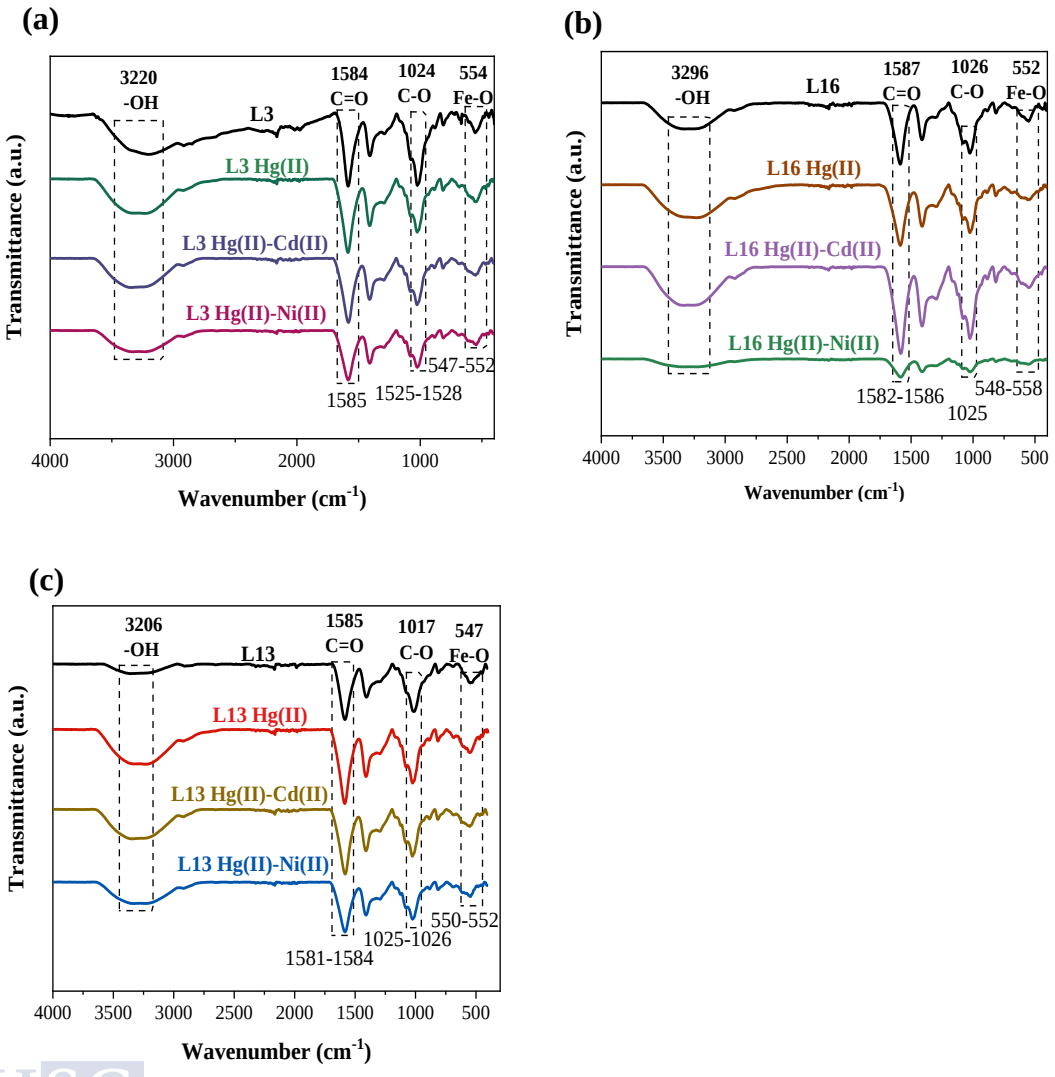


Figure 2.33. FTIR spectra before and after adsorption in a mono and binary system by L3 (a), L13 (b) and L16 (c) beads, respectively.

The C=O and C-O peaks shifted after adsorption, which might be caused by the reaction of these functional groups with the metal ions. The highest shift was observed in the C-O bond with diminished peak intensity at the beads L3 and L13. The peak shifts from 1024 cm^{-1} to 1025-1028 cm^{-1} at the L3 bead and from 1017 cm^{-1} to 1025-1026 cm^{-1} at the L13 bead. Even though the difference after adsorption is more visible at the bond C-O, the C=O bond was also involved in the adsorption process. Both bands were highly involved in the binary system Hg(II)-Ni(II), possibly forming a new bond between Ni(II) and COOH group, resulting in a decrease in the relative amount of COOH. This is highly evidenced in the L16 beads. The same applies to the Fe-O bond in Fe_3O_4. The extent of adsorption by the L16 beads was way inferior to L3 and L13 because of the low composition of oxygen functional groups, which are one of the main elements for greater metal adsorption.

To further compare and analyse the competition behaviour of the metal ions in the beads, L3 and L13, an XPS analysis was performed. Figure 2.34 illustrates the high-resolution spectra of the final forms of Cd, Ni, and Hg after adsorption in the different systems.

After adsorption of Hg, two peaks are shown at 101.5-105.5 eV (L3) and at 101.35-105.25 eV (L13), as shown in Figures 2.34a and 2.34b. These peaks are attributed to Hg 4f7/2 and 4f5/2 at both beads, respectively, and it is suggested that the adsorbed Hg is in the form of either $HgCl_2$, HgS_2, or HgO. The XPS does not determine these chemical states because the binding energies overlap in the region of ~101.5 eV (408). In addition, both binding energies in L13 were weaker, suggesting that Hg(II) ions were less adsorbed by this bead. Accordingly, to each calculated peak area of Hg 4f7/2 and Hg 4f5/2, the relative peak area of Hg 4f7/2 and Hg 4f5/2 was 40.49 %/30.67 % in the L3 beads, whereas in L13 was 35.9 %/27.21 %, respectively.

In the binary system at the L3 beads, the intensity and relative peak area decreased even more since Hg(II) ions suffered a suppression to some extent in the presence of other metal ions. The binding energies of Hg 4f7/2 and Hg 4f5/2 increased in the binary system of Hg(II)- Ni(II), similar to the qualitative analysis done by FTIR (Figure 2.33a), which evidence the synergetic behaviour between both metal ions. Conversely, no corresponding bind peaks of Hg 4f7/2 and Hg 4f5/2 are detected in the binary systems Hg(II)-Ni(II), Hg(II)-Cd(II) at the L13 bead. The concentration of Hg(II) ions was so low, being below instruments detection limit (0.1 At%).

Figure 2.34c shows the detections of two peaks for Cd, namely Cd 3d3/2 and Cd 3d5/2. Both peaks appeared at 412.61 and 405.87 eV in the L3 beads and at 412.46 and 405.72 eV in the L13 beads, respectively. This analysis suggests that Cd is mainly in the form of cadmium fluoride (CdF_2) since at the database the assigned binding energy for this Cd specie is at 405.80 eV. Comparing the binding energies, Cd(II) ions were clearly more adsorbed by the L3 beads, and in Figure 2.34d, it is observed that also Ni(II) is more adsorbed by this bead. Two peaks of Ni (Ni 2p3/2 and Ni 2p) are shown, the second one only appears when Ni is in the oxidized form [341]. The binding energy of Ni 2p3/2 was 856.12 and 8556.75 eV at L13 and L3 beads, respectively. Both binding energies indicate that most likely Ni is found as nickel hydroxide ($Ni(OH)_2$). Not only by the position of the binding energies but also due to the shape of the spectrum that matches a typical spectrum of $Ni(OH)_2$. Oxides present two double peaks at lower energy regions, while hydroxides present only one, which is the case.

USC UNIVERSIDADE DE SANTIAGO DE COMPOSTELA

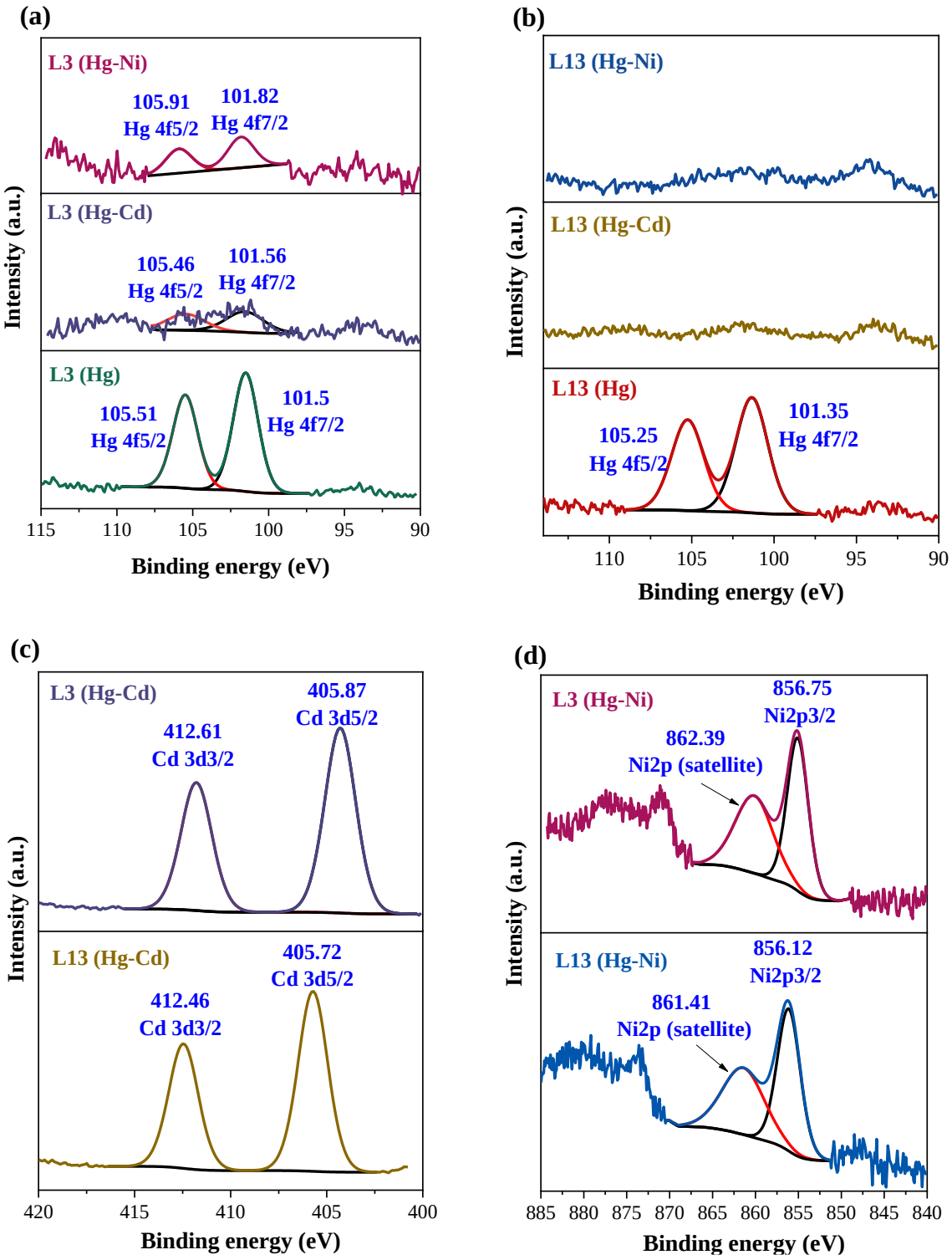


Figure 2.34. High-resolution spectra of the Hg(II), Ni(II) and Cd(II) present on the beads L3 and L13 after mono and binary adsorption.

USC UNIVERSIDADE DE SANTIAGO DE COMPOSTELA

Cd was the most adsorbed of all metal ions. The higher adsorption capacity of both beads for Cd(II) should be attributed to the hydration-free energies. The hydration-free energy of nickel (-2.16 kJ/mol) is higher than cadmium (-1.979 kJ/mol), which would require more energy to remove those water molecules [342]. For this reason, Cd(II) ions likelihood of bonding to the surface of the beads is high due to the lower energy needed to reduce the water molecules in its hydration shell. The lower affinity of both beads for Hg may be due to its high atomic radius and as well of the presence of the uncharged species of Hg ($HgCl_2$). A similar adsorption study with tetravalent manganese feroxyhyte proved to be a very efficient adsorbent with high adsorption capacity in the order of Cd>Ni>Hg [342].

Figure 2.35 shows the elemental mapping of the beads surface and cross-section after adsorption in the binary system to observe how distributed the metal ions are along the surface area. In the binary system, Hg(II)-Ni(II), Hg(II) ions remain mostly on the surface of the L3 bead (Figure 2.35b), while Hg(II) ions entered the internal structure of the L13 bead (Figure 2.35e). Also, at the binary system, Hg(II)-Cd(II), Hg(II) diffused onto the internal structure of the L13 beads (Figure 2.35h) and remained on the L3 bead surface.

Hg(II) ions are clearly more distinguished in the L3 bead in both surface and cross-section, while in the L13 bead is more noticed at the cross-section.

USC UNIVERSIDADE DE SANTIAGO DE COMPOSTELA

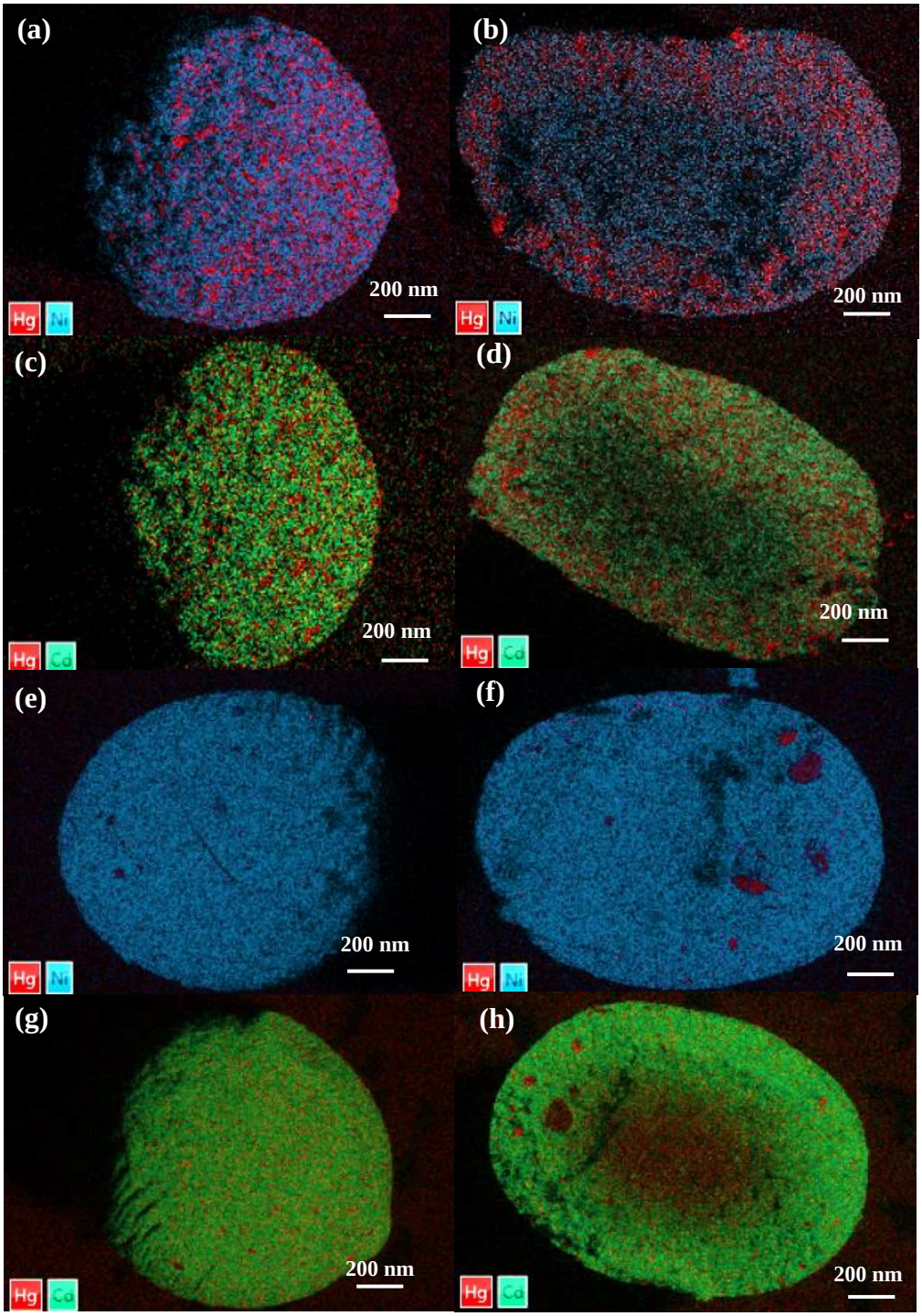


Figure 2.35. Elemental mapping of the beads L3, L13 surface at the binary system Hg(II)-Ni(II) (a, e) and cross section (b, f), respectively. Elemental mapping of the beads L3, L13 surface at the binary system Hg(II)-Cd(II) (c, g) and cross section (d, h), respectively.

USC DE SANTIAGO DE COMPOSTELA

Adsorption mechanism

The chemical state of the beads surface was further analysed after metal adsorption by XPS. Figure 2.36 shows an XPS survey scan of both beads in the mono and binary system. The peaks of C1s, O1s, Ca2p, Fe2p, N1s, and F1s remain after metal adsorption, whereas S2p and Cl2p peaks intensity decrease at L3 beads (Figure 2.36a). On the contrary, after metal adsorption by L13 beads, the only peaks that remain after adsorption in the mono and binary system were C1s, O1s, Ca2p, and Fe2p (Figure 2.36b). Furthermore, both peaks of N1s and S2p intensity increased only at the binary system of Hg(II)-Ni(II).

From this survey and as previously observed by FTIR (Figure 2.33), the presence of -OH and C=O bonds on the surface of both beads may have been the effective sites for metal ion adsorption. It is believed that the formation of new bonds is attributed to the O atoms. For this reason, any changes in O1s before and after adsorption was further analysed by XPS high-resolution scan. The results of the deconvoluted peaks are shown in Figures 2.37a and 2.37c for L3 bead and in Figures 2.37b and 2.37d for L13 bead, respectively.

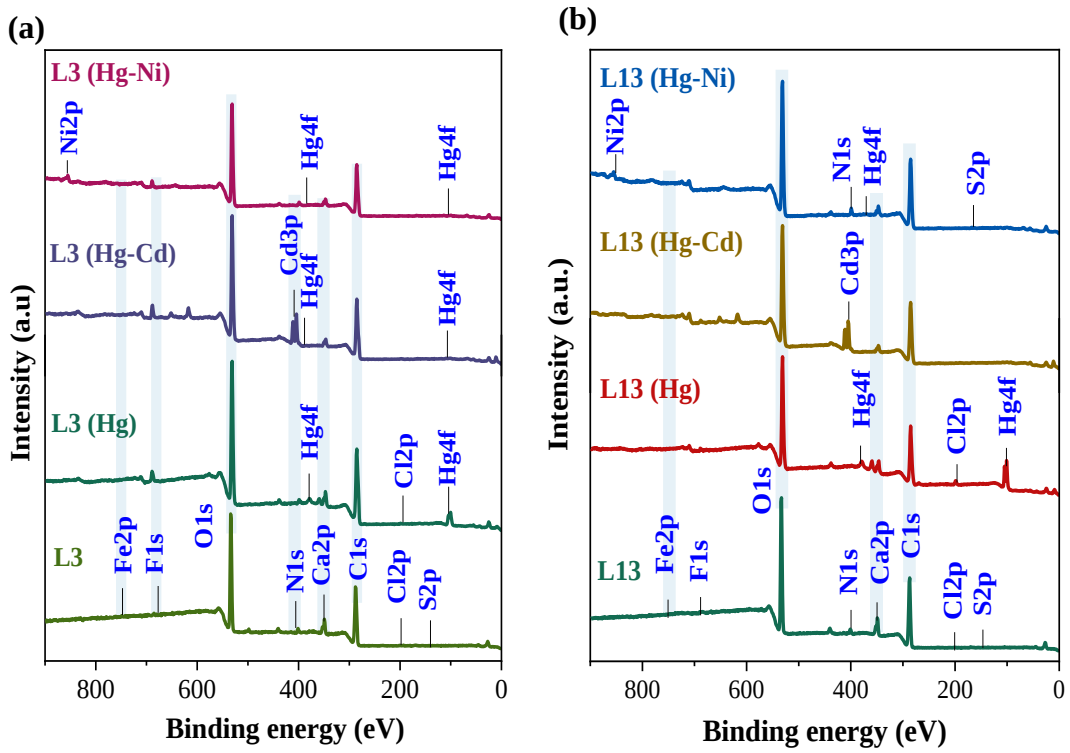


Figure 2.36 XPS survey scan before and after metal ions adsorption by L3 (a) and L13 (b) beads.

The O1s spectra for both beads are divided into three peaks at approximately 534, 532, and 531 eV, which are assigned to -OH, C=O, and metal oxides (O-M) species, respectively. The L3 beads contained more double bonded oxygen functional groups (C=O), whereas L13 had more hydroxyl (-OH) groups and metal oxides species. The corresponding relative content of the -OH peak decreased from 30.3 % to 10.2 %, and the binding energy from 534.71 to 534.42 eV in the mono adsorption of Hg(II) ions by the L3 beads. At the same time, the position of the characteristic peak of metal oxides after Hg(II) adsorption shifted from 531.2 to 531.9 eV, and the relative peak area increased from 14.7 % to 37.4 %. This indicates that Hg(II)

ions adsorption consumed a lot of O-H bonds to form new bonds of Hg-O at the surface of the L3 beads. Contrarily, at the L13 beads, the consumption of -OH groups by Hg(II) adsorption was lesser. The content of -OH decreased from 33.7 % to 29.5 %, with the respective binding energies of 533.4 to 533.63 eV. However, it was observed an increment of C=O bonds from 46.2 % to 53.1 %, and also was accompanied by a decrease of formed metal oxides from 20.0 % to 17.3%. It is believed that during Hg(II) ions adsorption by L13 beads, some complexes were formed, dislocating oxygen ions to form double or single bonds with carbon.

In the binary system, Hg(II)-Cd(II), the opposite was observed, C=O double bonds decreased from 46.2 % to 35.1 % and -OH increased from 33.73 % to 49.45 %. The adsorption in a competitive state between both metals favoured the rupture of C=O double bonds to form C-O bonds, being possibly one of the mechanisms of metal ion adsorption. The same was observed at the L3 bead, although the relative peak area decreased of C=O from 55.1 % to 30.1 %. In addition, an increase of -OH and C-O was observed from 30.2 % to 60.6 % and from 38.8 % to 39.3 %, respectively (Tables A2.0 and A2.1).

A similar trend was observed in the binary system, Hg(II)-Ni(II), with an increment of - OH and further decrease of C=O bonds but with the formation of metal oxides on the L13 surface. This corroborates with the XPS results of Ni(II) adsorption, which was in the form of $Ni(OH)_2$. In L3 beads, an increment of metal oxides was also observed, and -OH groups were slightly formed in this system than in the Hg(II)-Cd(II) (60.6 %). The competitive state of Ni(II) and Hg(II) at the L3 beads is not high as in the L13 bead, as observed in the competitive results commented earlier. Therefore, -OH groups are less consumed, C=O bonds are broken down, and C-O bonds are formed due to the synergistic interaction between both metals. It is believed that the higher adsorption capacity of L3 beads may be due to the higher content of C=O bonds, as extensively reported in the literature [343, 344].

USC
UNIVERSIDADE DE SANTIAGO DE COMPOSTELA

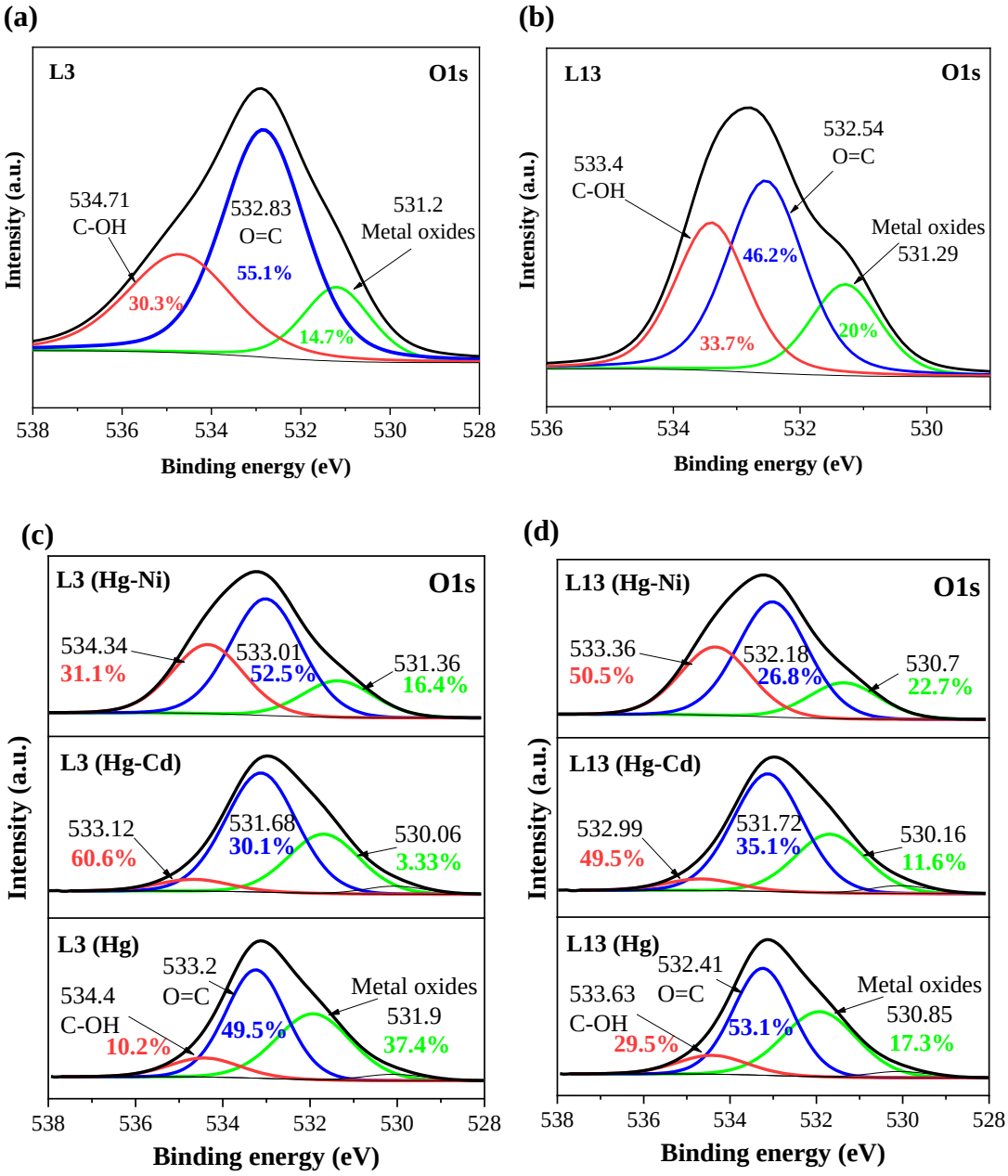


Figure 2.37. High-resolution scan of O1s before (a, b) and after metal adsorption (c, d) by L3 and L13 beads, respectively.

Through these results, it was revealed that one of the adsorption mechanisms of Hg(II) ions onto the L3 and L13 beads was by complexation, but it was also observed metal ions adsorption via ion exchange with Ca(II) ions [345,346], as shown in Figure 2.38b. Since Ca(II) ions are ionically cross-linked with the guluronic groups of alginate chains during the beads formation, it is presumably that, to a certain degree, ion exchange may be one mechanism influencing Hg(II) ions adsorption.

In the survey scan, Ca1s peak was less intense from the mono to the binary adsorption systems. The elemental composition of the beads surfaces also revealed a decrease in the atomic percentage of this element through adsorption (Table A2.2). To further assess Ca(II) ions

release, its concentration was analysed in all initial Hg(II) concentration (10, 70, 150, 200, and 230 mg/L) and the pH of the solutions after Hg(II) adsorption in the mono system was measured.

Figure 2.38a illustrates the release of Ca(II) ions with Hg(II) ions adsorption by the L3 and L13 beads. Ca(II) ions were more released during Hg(II) adsorption in the L13 than at the L3 beads. Changes in the amount of Ca(II) ions released into the solution were reported at the initial concentration of 10 mg/L before and after adsorption, confirming a predominant exchange of Ca(II) with H^+ at the L3 beads (Table A2.3). As the initial Hg(II) concentrations increase, the exchange of Ca(II) with Hg(II) is more consistent, as shown by the release increment of Ca(II) ions into solution compared with the initial values. However in the L13 bead it was observed a higher rate of ion exchange between Ca(II) and Hg(II) in all concentrations compared with the L3 bead. One reason for this is the higher number of hydroxyl groups on the L13 surface, as shown in the XPS results. The formation of hydroxyl groups may be one of the primordial factors for the Hg(II) ions adsorption capacity decline and the slight increase of the solutions pH (Table A2.3) after adsorption. A similar study using three commercial raw activated carbons for the removal of Hg(II) from aqueous medium, stated that the predominat factor causing the decline in adsorption capacity of Hg(II) was due to the formation of -OH groups [328]. The increasing trend in pH during Hg(II) ions adsorption could also be due to the release of ionic species which initially were bound to the beads [347].

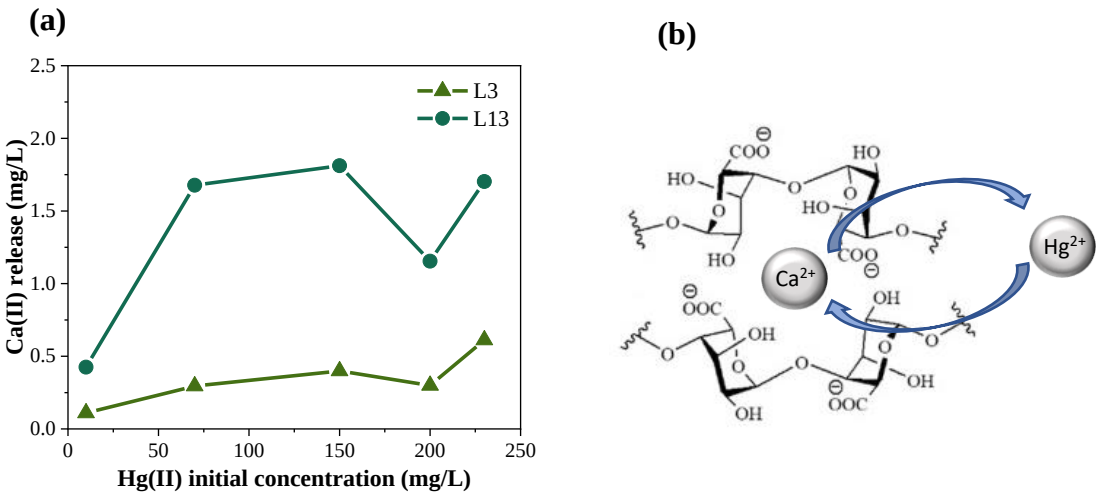


Figure 2.38. Calcium ions release during Hg(II) adsorption in the mono system by L3 and L13 beads (a), adsorption explanatory mechanism (b)(Reproduced with permission from reference [348]. Copyright (2022) *Elsevier*).

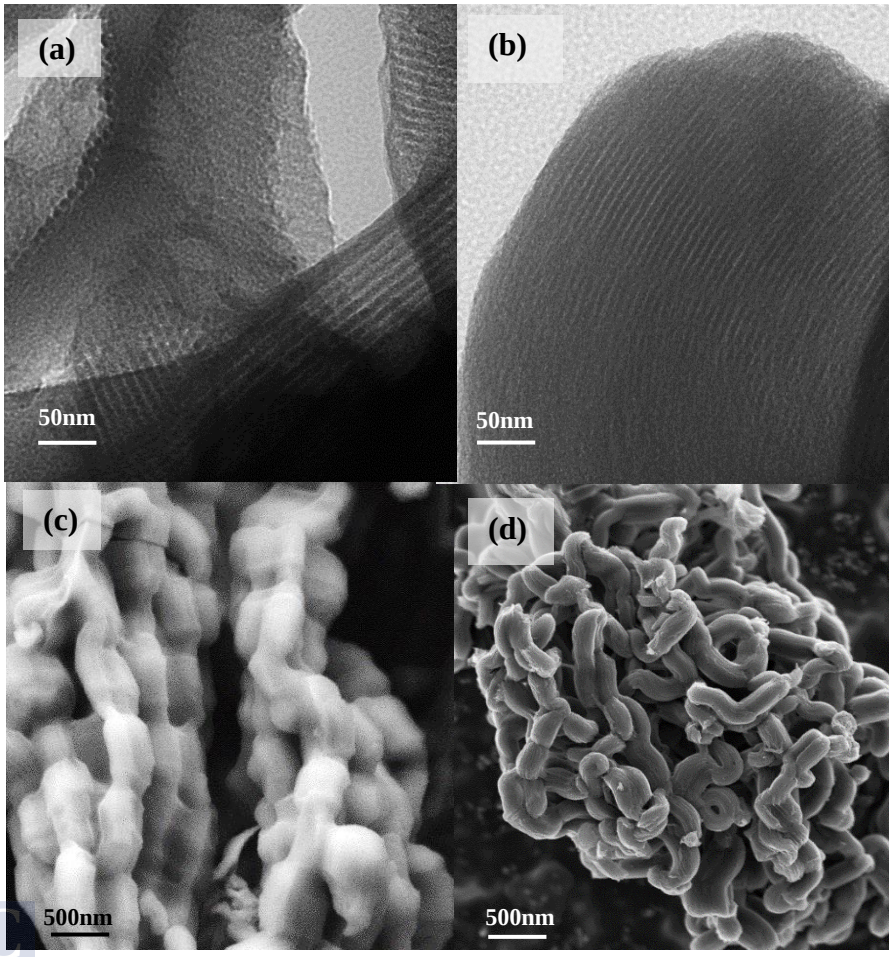
2.3.2.3. Elimination of a heavy metal's ternary mixture from water

Removal of heavy metals from mixed systems are very important since wastewaters contain more than one metal competing with each other for adsorption sites. Besides the current adsorption studies of individual metals, it is important to study the effect of one metal in the adsorption of other metals in a mixture system. This would allow a better prediction of metal adsorption in a real environment and optimize future experimental studies. Several heavy metals are released in the environment from natural or anthropogenic sources. Among all

metals, Cd, Ni, and Hg were recognized as priority substances to be removed from drinking water (Decision No. 2455/2001/EC).

For this reason, and due to their toxicity, these metals were chosen to perform the ternary experiments. To follow up with the binary study, the same particles L3 and L13 were chosen for the adsorption experiments. However, since it was observed silica residues in the CMK-3 carbon used in the binary study. A new batch of CMK-3 carbon was prepared resulting in the development of the L13T bead used in the ternary study ("T" states to the ternary system).

The morphology of both CMK-3 carbon ("B" states to carbon used in the binary experiment, "T" to the carbon used in the ternary experiments) was observed by TEM and SEM, as shown in Figure 2.39. It can be seen that the morphology of both carbons consists of nanosized nanorods or nanochannels, confirmed by the SEM images (Figure 2.39c and 2.39d). However, it was confirmed by TEM (Figure 2.39b) that well-ordered hexagonal channels were formed in the CMK-3 (T). Meanwhile, in the CMK-3 (B), the original mesoporous structure of the SBA-15 was not preserved since it can be observed the formation of nanoparticles and not well-ordered channels.



USC UNIVERSIDADE DE SANTIAGO DE COMPOSTELA

Figure 2.39. TEM (a, b) and SEM (c, d) images of the CMK-3 carbon used in the binary and ternary experiments, respectively.

Futhermore a XPS survey spectra with the fitted C1s and O1s spectra of CMK-3 (B, T) are illustrated in Figure 2.4. It was confirmed by the XPS survey spectrum of CMK-3 (T) the

presence of the elements C, O, P, N, F, Cl, and S with no sign of silica residue. In addition, the higher O/C ratio calculated revealed a higher presence of oxygen functional groups at the CMK- 3 (T) surface than at the CMK-3 (B). The deconvolution of the C1s spectrum for CMK- 3(T), reveals higher bonding energies in all peaks than CMK-3 (B). It was shown the presence of four peaks at 284, 284.6, 286.3, and 288.95 eV which correspond to the sp^2 graphitic, C-C, C-O, and C=O bond, respectively. A higher proportion of C-C bonds was found at the CMK-3 (B) carbon with a relative area of 68.4%, while at the CMK-3 (T) carbon was only 66.9%.

This confirms that the surface of CMK-3 (T) carbon is mainly based on oxygen-containing functional groups. The O1s high-resolution spectrum also confirms that 72 % and 33.9 % of oxygen is single bonded to carbon in CMK-3 (T), and CMK-3 (B), respectively.

USC
UNIVERSIDADE DE SANTIAGO DE COMPOSTELA

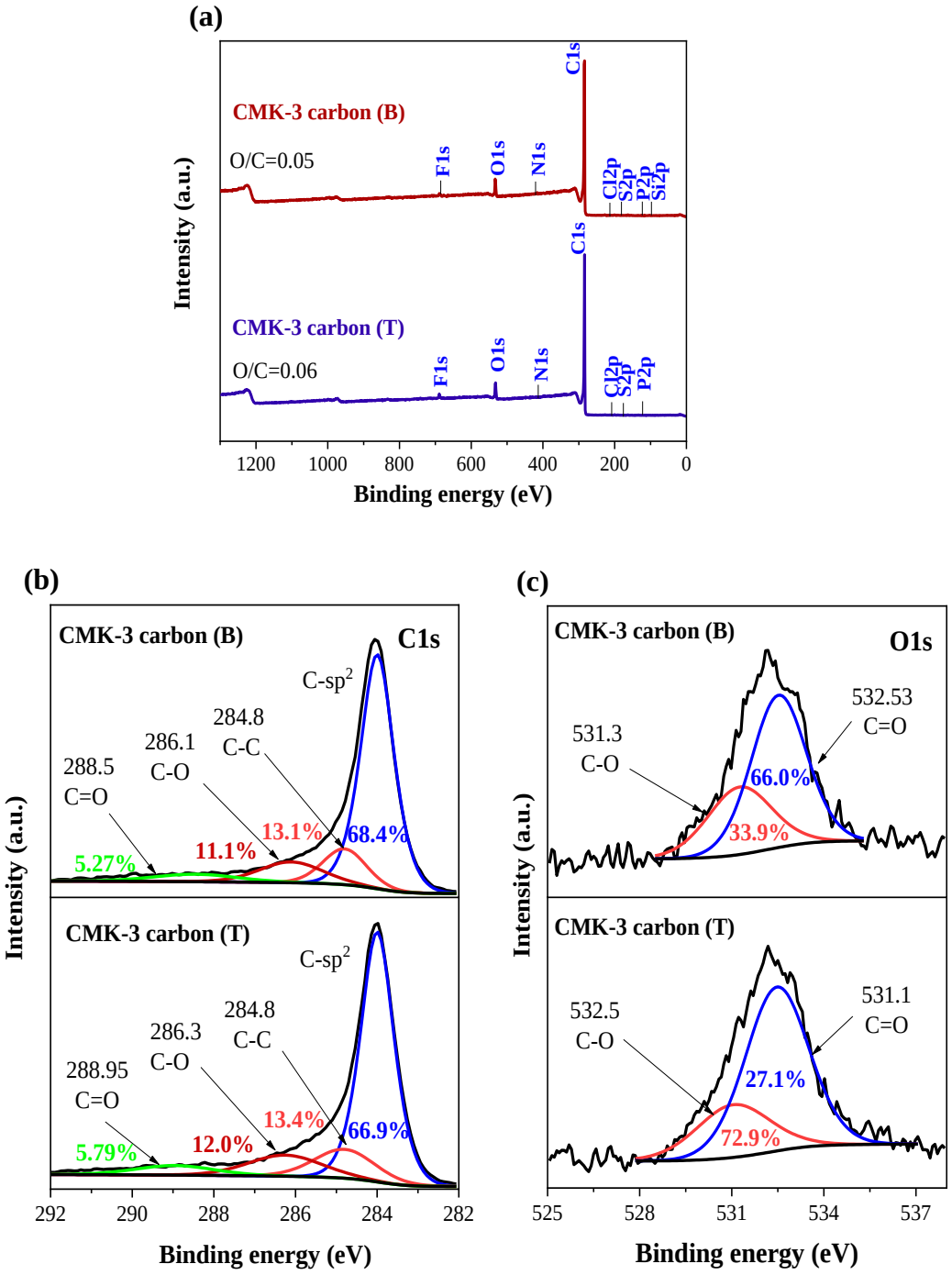


Figure 2.4. XPS survey scan (a) and high-resolution spectra of C1s (b) and O1s (c) of CMK-3 (B) and CMK-3 (T).

The surface morphology of both beads, L13 and L13T, was analysed by SEM. Figure 2.41 shows the difference between both beads.

The L13 bead has a homogeneous spherical surface with no apparent agglomerates of magnetite or carbon. On the other side, in the L13T is observed the presence of steep porous valleys along the beads surface, which is due to the newly synthesized mesoporous carbon,

CMK-3 (T). The characteristic observed channels of the CMK-3 mesoporous carbon remained preserved in the L13T beads. At the same time, in the L13, sodium alginate and the presence of Fe_3O_4 NPs seems to have clogged or collapsed the carbon channels during the synthesis procedure.

XPS determined the chemical surface composition and high-resolution C1s spectra of both beads is shown in Figure 2.42. It was also observed the presence of carbonyl, carboxyl, and carbon single bonds to oxygen. Similarly, to the respective carbons, more C-O (34.7%) and -COO- (17.7%) were found at the L13T. Meanwhile, the surface of the L13 beads was mainly composed of C=O bonds (58.1%).

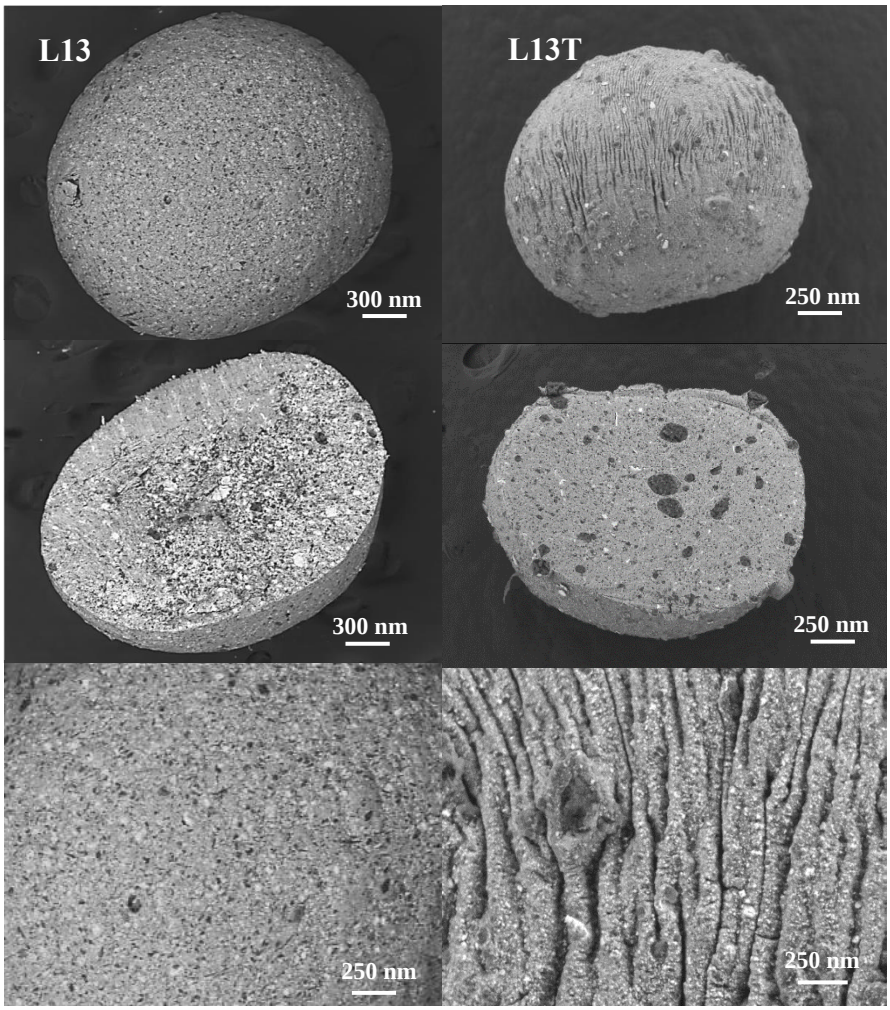


Figure 2.41. SEM images of the surface, cross-section and surface zoom of the synthesized beads used in the binary (L13) and ternary (L13T) system.

USC UNIVERSIDADE DE SANTIAGO DE COMPOSTELA

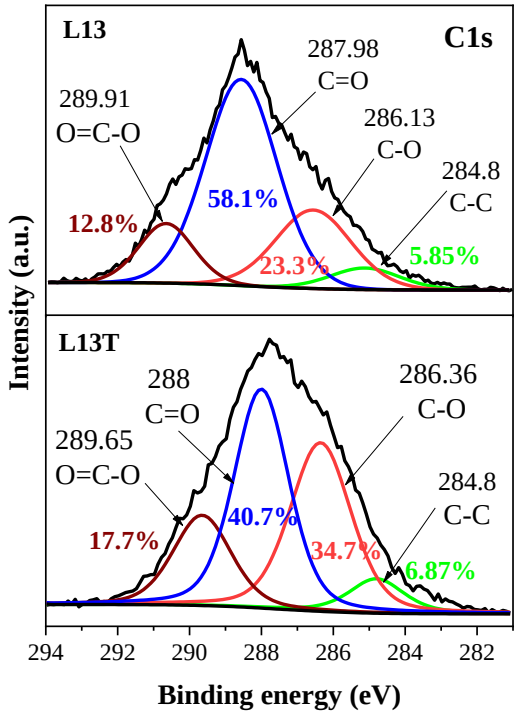


Figure 2.42. XPS high resolution spectra of C1s in L13 (binary) and L13T (ternary study).

a. Determination of optimum pH for Cd(II), Ni(II), and Hg(II) adsorption

The influence of pH on Cd(II), Ni(II), and Hg(II) adsorption capacity by L3 and L13T beads was studied at a pH range of 2-9 with initial metal concentration of 10 mg/L. The experiment was carried out under magnetic agitation with a stirring velocity of 300 rpm at room temperature (~ 25 °C) for 6 h.

Figures 2.43a and 2.43b show the pH effect on the adsorption capacity and removal efficiency of all three metal ions by the L3 bead, respectively. In the acidic pH range, cadmium ions compete with H^+ ions for binding on available surface sites therefore higher adsorption was observed in the pH range of 2 to 4.5. On the other side, the amount of Ni(II) ions adsorbed per unit of adsorbent increases continuously reaching its maximum uptake at the pH value of 9.0 with over 60 % of metal ions adsorbed. However, Ni(II) precipitated at pH values above 8.0 and hinder the adsorption process [349].

Hg(II) ions adsorption increased at the pH values of 2.5 to 4.5 with a removal efficiency of over 50 %, while in higher pH values (from 4.5 to 6.5) the removal efficiency decrease to 35 %. An increase in the adsorption capacity of Hg(II) may have resulted from the decreased electrostatic repulsion between the positively charged Hg(II) and the surface of L3 beads due to the decreased surface charge density when the solution pH was increased. It was important to study the effect of each metal individually in solution to know at which pH value lays the maximum adsorption capacity of all three metals by the L3 beads to proceed to the ternary study.

The pH used in the ternary system experiment was selected based on the intermediate pH where the removal efficiency was considered high for all metals. Based on this, the pH of 4.5 was selected to be used in posterior experiments (mono and ternary).

USC UNIVERSIDADE DE SANTIAGO DE COMPOSTELA

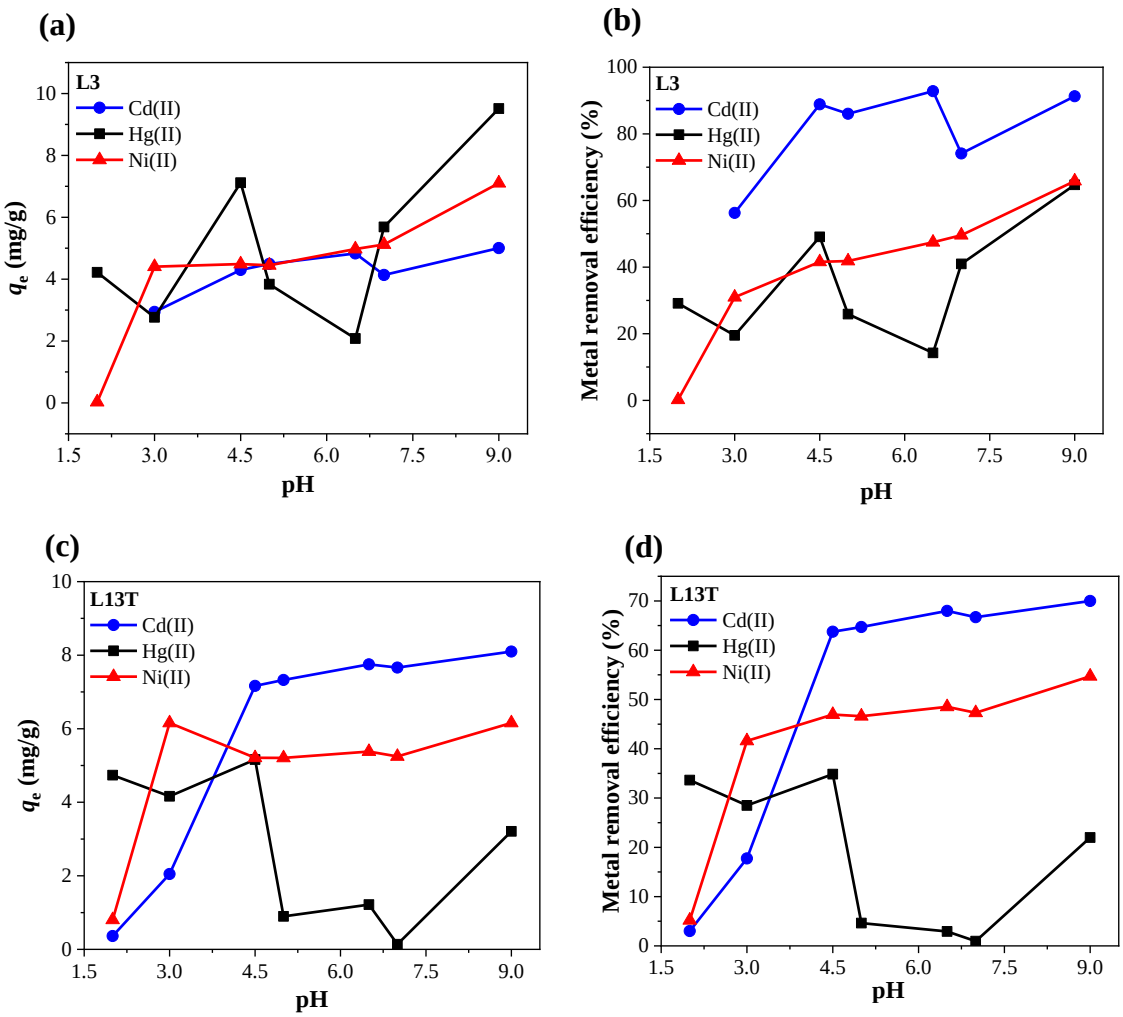


Figure 2.43. Adsorption capacity (a, c) and removal efficiency (b, d) as a function of pH of Cd(II), Hg(II) and Ni(II) by L3 and L13T beads, respectively.

The adsorption capacity and removal efficiency as a function of pH is similar in both beads. The adsorption of Cd(II) and Ni(II) ions attained equilibrium with the increased pH value. At pH value greater than 4.0 deprotonation of functional groups like carboxylic groups (-COOH) may have occurred. Resulting in more negatively charged active sites on the L13T surface.

Above the pH value of 7.0, an increment on the adsorption capacity and removal efficiency was observed due to precipitation of metal hydroxides [350]. The removal of Hg(II) ions reached a maximum at the pH of 4.5 with 35 % of metal ions removed. Above this pH value, the removal of Hg(II) ions suffered a step decrease and later a small increase, which may also be due to formed metal hydroxides or other Hg species.

The same pH selection as in the L3 beads was undertaken and the pH value of 4.5 was selected for further mono and ternary adsorption studies of Hg(II), Cd(II) and Ni(II) by the L13T beads. In both beads, Cd(II) was the most adsorbed metal ion followed by Ni(II) and Hg(II) ions.

b. Effect of initial concentration in the mono and ternary system

The effect of the initial metal concentration was performed in a mono and ternary system. For this study it was prepared aqueous solutions of the following initial metal concentrations (10, 70, 150, 200, and 250 mg/L) with a pH value of 4.5 previously optimized. The experiment was carried out with 14 mg of adsorbent (L3 and L13T beads) under magnetic agitation with stirring velocity of 300 rpm at room temperature. The adsorption capacity was calculated based on the content of carbon present in each bead (34.3 % AC commercial in L3 beads and 7.69 % CMK-3 (T) in the L13T beads).

Figures 2.44a and 2.44b show the adsorption capacity of both beads in the mono and ternary system, respectively.

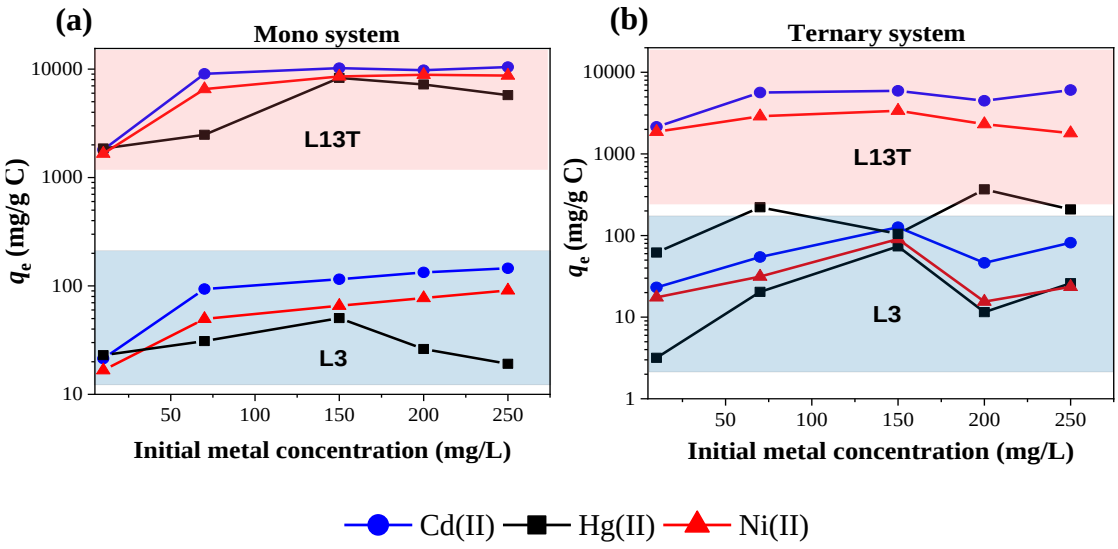


Figure 2.44. Adsorption capacity (mg/g C) in the mono (a) and ternary system (b) of Cd(II), Ni(II) and Hg(II) by L3 and L13T beads.

It is clearly seen that the adsorption capacity of the L13T beads is hundred times higher than the L3 beads for all tested metal ions in both systems. Again, the most adsorbed metal ions were Cd(II), then Ni(II) and lastly Hg(II) in both systems and particles.

The adsorption capacity in the ternary system decreased slightly, indicating higher competition between the metal ions for available binding sites. At this system, was also observed a maximum adsorption capacity of Cd(II), Ni(II) and Hg(II) at the initial concentration of 150 mg/L by L3 beads. The same behaviour was observed at the binary system using the same bead. Adsorption equilibrium was attained faster for Ni(II) and Cd(II) ions than for Hg(II) ions at the L13T, whereas no equilibrium was achieved at the L3 bead at the ternary system.

The difference between the adsorption capacity of both beads is tremendous, concerning the carbon content in their composition. The L13T exhibited higher adsorption capacity due to the new synthesized CMK-3 (T) carbon. The many attractive features of mesoporous carbons are well known, such as higher specific surface area, high pore volume, easy surface modification and higher adsorption capacity for various contaminants, dyes and molecules [351,352]. These last results are more expected than the previous obtained at the binary system due to the physical characteristics of the mesoporous carbons. Given this, the surface area and

porosity were determined to compare the quality impact of both CMK-3 mesoporous carbons and respective beads.

Table 2.6 shows the textural parameters (surface area (S_{BET}) and pore volume (V_p) of the carbons, SBA-15, and magnetic beads. The surface area of the SBA-15, CMK-3 (B) and CMK- 3 (T) was 716, 201 and 940 m^2/g, respectively. The CMK-3 (B) has a sharp decrease in surface area compared to the SBA-15 silica, which was the used template to prepare both carbons. Experimental errors might have occurred during the pyrolysis treatment which may have induced the collapse of the mesoporous channels and during the cleaning procedure of the silica template [353]. Resulting in the sharp decrease of S_{BET} value for the CMK-3 (B) carbon.

Meanwhile, CMK-3 (T) carbon had a remarkably higher surface area than the SBA-15 silica. This indicates that well-ordered carbon channels were formed during the carbonization process with higher degree of microporosity. The higher total pore volume of 0.75 cm^3/g by this carbon compared to the pore volume of the SBA-15 and CMK-3 (B) is the confirmation of a success formed mesoporous carbon with the presence of micropores in its porous structures.

Regarding the surface area of the commercial AC, it was surprisingly as high as the CMK-3 (T) carbon and the pore volume was only slightly lower. As for the beads, the surface area and the pore volume increased in the order of L3>L13T>L13.

Figure 2.45, shows the N_2 adsorption-desorption isotherm curves. The N_2 adsorption-desorption curve of commercial AC and L13 beads correspond to a type II isotherm with a H3 hysteresis loop, as shown in Figure 2.45a. This type of isotherm and hysteresis loop is frequently found in nonporous powders or microporous structures with non-rigid aggregates of plate like-particles. The isotherm curve shows further adsorption above the relative pressure (p/p_0) of 0.8, which is relative to the filling of interparticle voids. This result is in accordance with the SEM image of the commercial AC (Figure 2.22e).

Figure 2.45b shows the N_2 adsorption isotherm of SBA-15, which has a type IV isotherm with H1 hysteresis indicating uniform cylindrical pores [331].

Table 2.6. Textural parameters of carbons and respective magnetic beads: commercial AC, SBA-15, CMK-3 (B, T), L3, L13 and L13T.

Carbons and particles	S_{BET} (m^2/g)	V_P (cm^3/g)
Commercial AC	849	0.65
SBA-15	716	0.73
CMK-3 (B)	201	0.095
CMK-3 (T)	940	0.75
L3	107	0.10
L13	0.148	0.0008
L13T	40.48	0.037

USC UNIVERSIDADE DE SANTIAGO DE COMPOSTELA

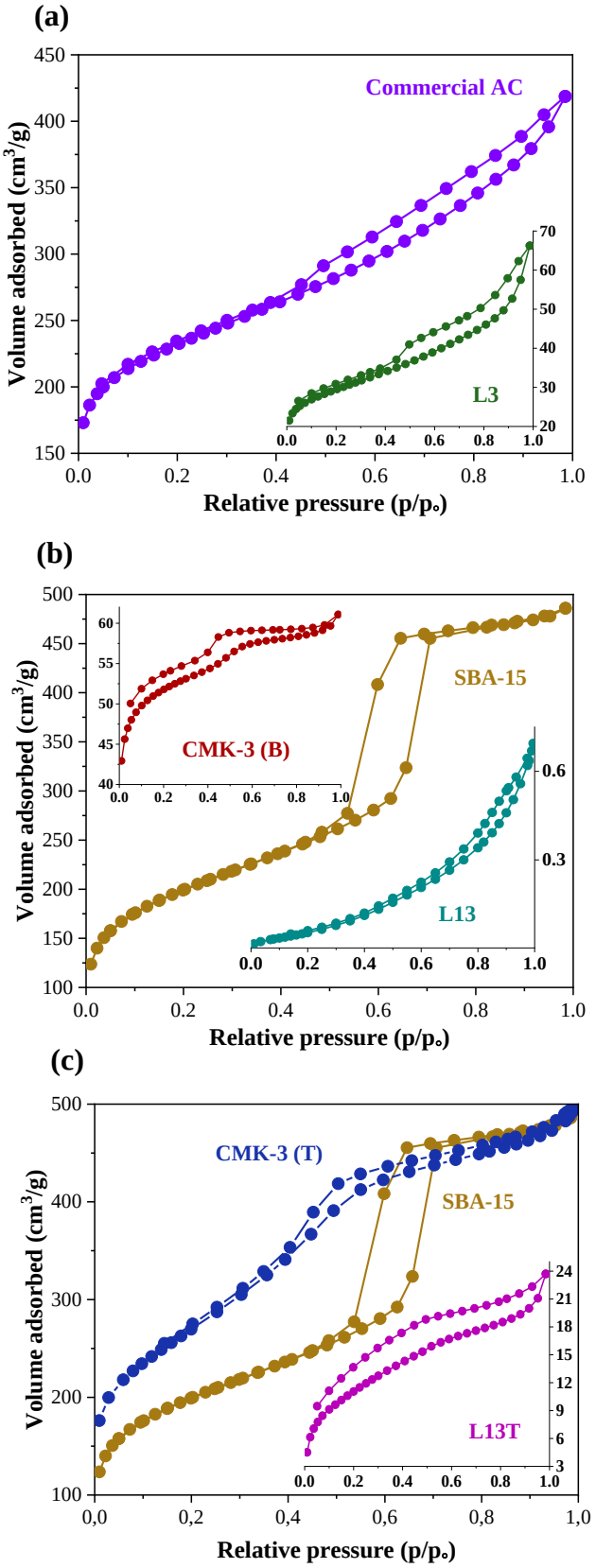


Figure 2.45. Nitrogen Adsorption-desorption isotherms of commercial AC/L3 (a), CMK-3/SBA-15/L13 (b) and CMK-3 (T)/SBA-15/L13T.

Meanwhile, the CMK-3 (B) and L13 beads have a type IV and type III isotherm, and it was only observed a hysteresis loop at the CMK-3 (B) of type H4. The observed type III in the L13B bead is a direct indication of weak adsorbate-adsorbent interactions and the type IV in the CMK-3 (B) is only formed by wedge-shaped pores revealing that the carbon has a slight microporosity character. The CMK-3 (T) carbon and respective L13T exhibit a pore filling step in the relative pressure range (p/p_0) between 0.4 and 0.8 due to the mesopores filling, as shown in Figure 2.45c. Both the shape and the presence of hysteresis loop indicates that the CMK-3 (T) and L13T have a type IV isotherm and H3 hysteresis loop.

c. Adsorption Performance

Metal ions competition at the ternary system

Table 2.7 shows the calculated evaluation ratios of the metal ions in the ternary system, either individually or in a competitive state. In the L3 beads, the evaluation ratio of the sum of all three metal ions at the concentration of 200 mg/L was E<1 and in the remaining concentrations, E>1. At the concentration of 200 mg/L, an antagonism conflict between all metal ions was present.

Analysing individually the interaction of each metal ion in the ternary system at the L3 bead, Hg(II) ions were the least suppressed ions in initial concentrations above 70 mg/L in the L3 bead. Hg(II) ions benefit from an enhancement effect, partly due to the increased electrostatic repulsion among the cations that would limit the adsorption of the metal ions [354]. Meanwhile at the initial concentration of 10 mg/L, Hg(II) ions were most suppressed while the adsorption of Cd(II) ions was favoured by the presence of Ni(II) and Hg(II) ions (E>1).

Cd(II) ions in general were the most adsorbed metal ions, yet at the concentrations of 200 and 250 mg/L its adsorption was highly suppressed, after Ni(II) ions. On the contrary, Hg(II) ions adsorption was highly enhanced. It is reported a greater improvement in the Cd(II) and Ni(II) metal ions adsorption at the initial concentrations of 10, 70, and 150 mg/L. The total sum of the evaluation ratio, was E>1, revealing a synergistic effect between all metal ions, meanwhile at the initial concentration of 200 mg/L, E<1, revealing an antagonistic effect at the L3 bead.

The competitive state between all metal ions was more pronounced in the L13T beads. One possible reason for this was the higher adsorption capacity of the L13T beads for the metal ions, leading to a higher degree of suppression. The antagonism effect (E<1) was evident for initial concentrations above 150 mg/L. Cd(II) ions were the most favoured adsorbed metal ions over all initial concentrations, followed by Ni(II) and lastly by Hg(II) ions. As in the L3 beads, Cd(II) and Ni(II) ions were most suppressed in concentrations above 200 mg/L, contrarily Hg(II) ions were suppressed at the initial concentration of 150 mg/L. Hg(II) ions besides being the most suppressed metal ion, its adsorption was slightly enhanced in the presence of Cd(II) and Ni(II) ions at the highest initial concentrations.

The different compositions of the L3 and L13T beads is another cause for the differences observed in the competition between the metal ions. The beads L13T are composed of large channels which may have favoured the adsorption of all metal ions but as well a higher competition by the available sites (either on the surface and internally). A quantitative analysis by SEM-EDX was performed to the surface and cross-section of the beads used in the ternary adsorption.

Table 2.7. Evaluation ratio of the metal ions in the ternary system (individually and in competition) adsorbed by the L3 and L13T, respectively.

Solution concentration (mg/L)			10	70	150	200	250
Adsorbent	**Metal ions**	**Adsorption system**	**Evaluation ratios**				
L3	Cd (II)	Ternary	1.08	0.58	1.10	0.35	0.56
	Hg (II)	Ternary	0.14	0.66	1.46	0.44	1.36
	Ni (II)	Ternary	1.05	0.63	1.38	0.20	0.26
	$\sum_{i=1}^{n=3} E(Cd(II) - Hg(II) - Ni(II))$		2.27	1.87	3.94	0.99	2.18
L13T	Cd (II)	Ternary	1.19	0.63	0.58	0.46	0.58
	Hg (II)	Ternary	0.03	0.09	0.01	0.05	0.04
	Ni (II)	Ternary	1.12	0.44	0.40	0.26	0.21
	$\sum_{i=1}^{n=3} E(Cd(II) - Hg(II) - Ni(II))$		2.35	1.16	0.99	0.77	0.82

Figures 2.46a and 2.46b show an increase of metal ions presence with increasing initial metal concentrations in the surface and cross-section of the L3 and L13T beads. It was observed a higher presence of metal ions inside the structure of the beads than externally. The adsorption capacity followed the order of Cd(II)>Ni(II)>Hg(II). On the other side, a lower presence of metal ions in the L13T beads was observed in both surface and cross-section. Contrary to what was observed in the L3 bead, and in the L13T, the metal ions remained mostly at the surface rather than internally.

Figures 2.47a,b,c,d shows the distribution of the metal ions by elemental mapping in the surface and cross-section of the L3 and L13T beads used in the ternary adsorption. All metal ions are heterogeneously distributed over the surface of both beads and Ni(II) (orange colour) seems to be more present at the cross-section in both beads. On the other hand, Hg(II) (blue colour) ions remain mostly on the surface of the L3 bead. These results confirm the selectivity of the beads for certain metal ions according to their composition. A XPS analysis was performed to better understand the chemical state of the metal ions on the beads surface after adsorption in the mono and ternary system.

Figure 2.48 shows the high-resolution XPS spectra of Cd(II), Hg(II), and Ni(II) in L3 and L13T beads at the mono and ternary system.

USC UNIVERSIDADE DE SANTIAGO DE COMPOSTELA

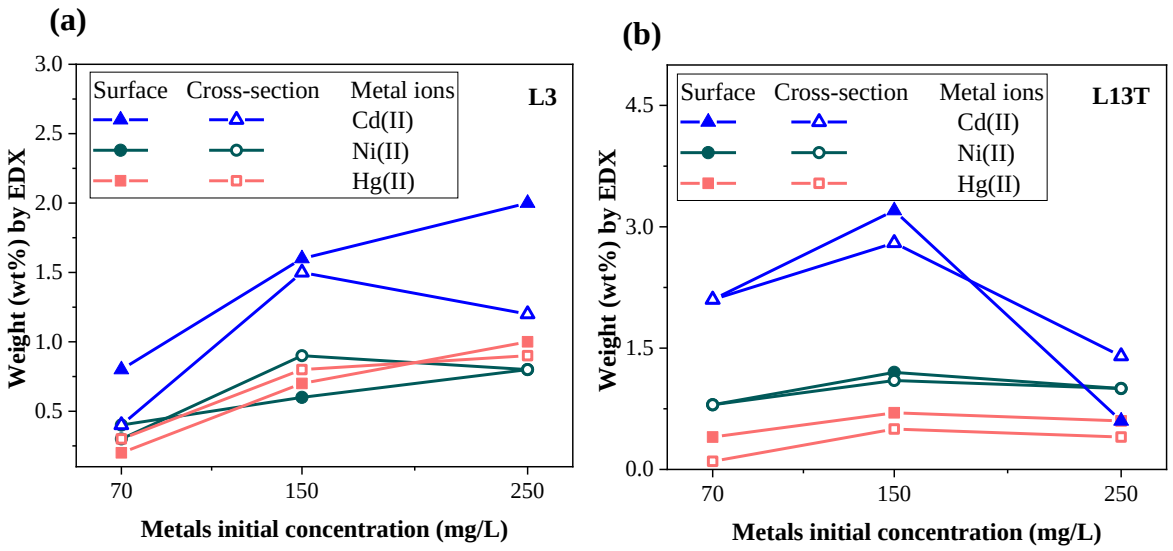


Figure 2.46. Representation of EDX quantitative analysis of Cd(II), Ni(II), and Hg(II) ions on the surface and cross-section in beads L3 (a) and L13T (b) used at the ternary system.

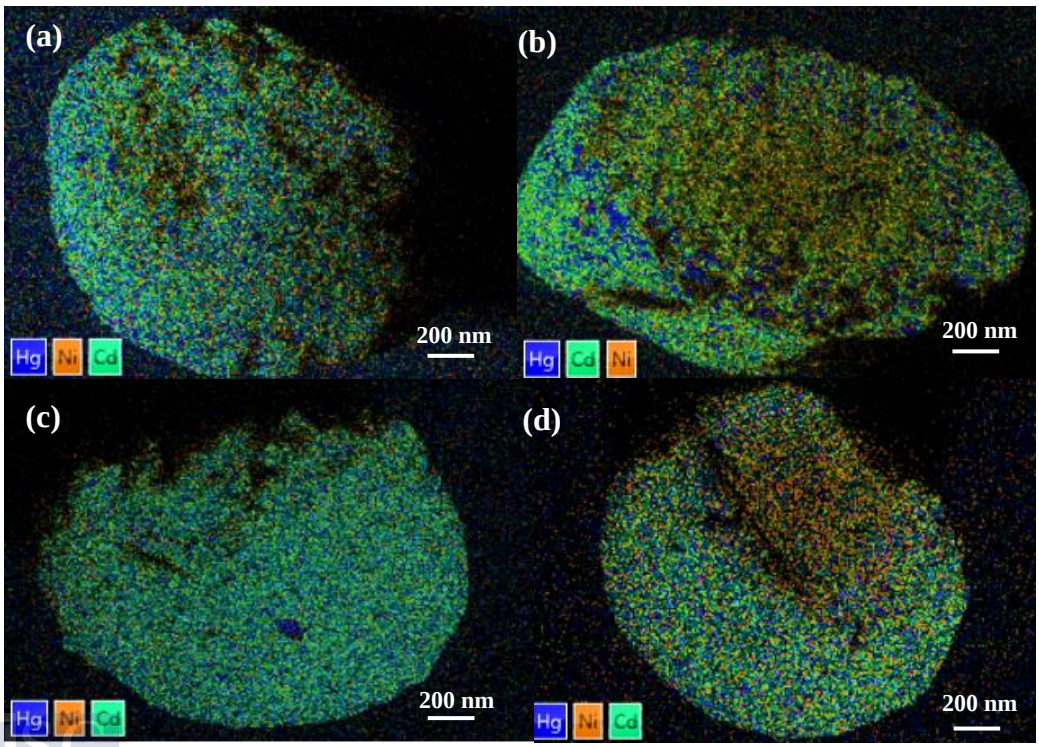


Figure 2.47. Elemental mapping of the beads surface and cross-section, L3 (a, b) and L13T (c, d) at the ternary system (Hg(II)-Ni(II)-Cd(II)), respectively.

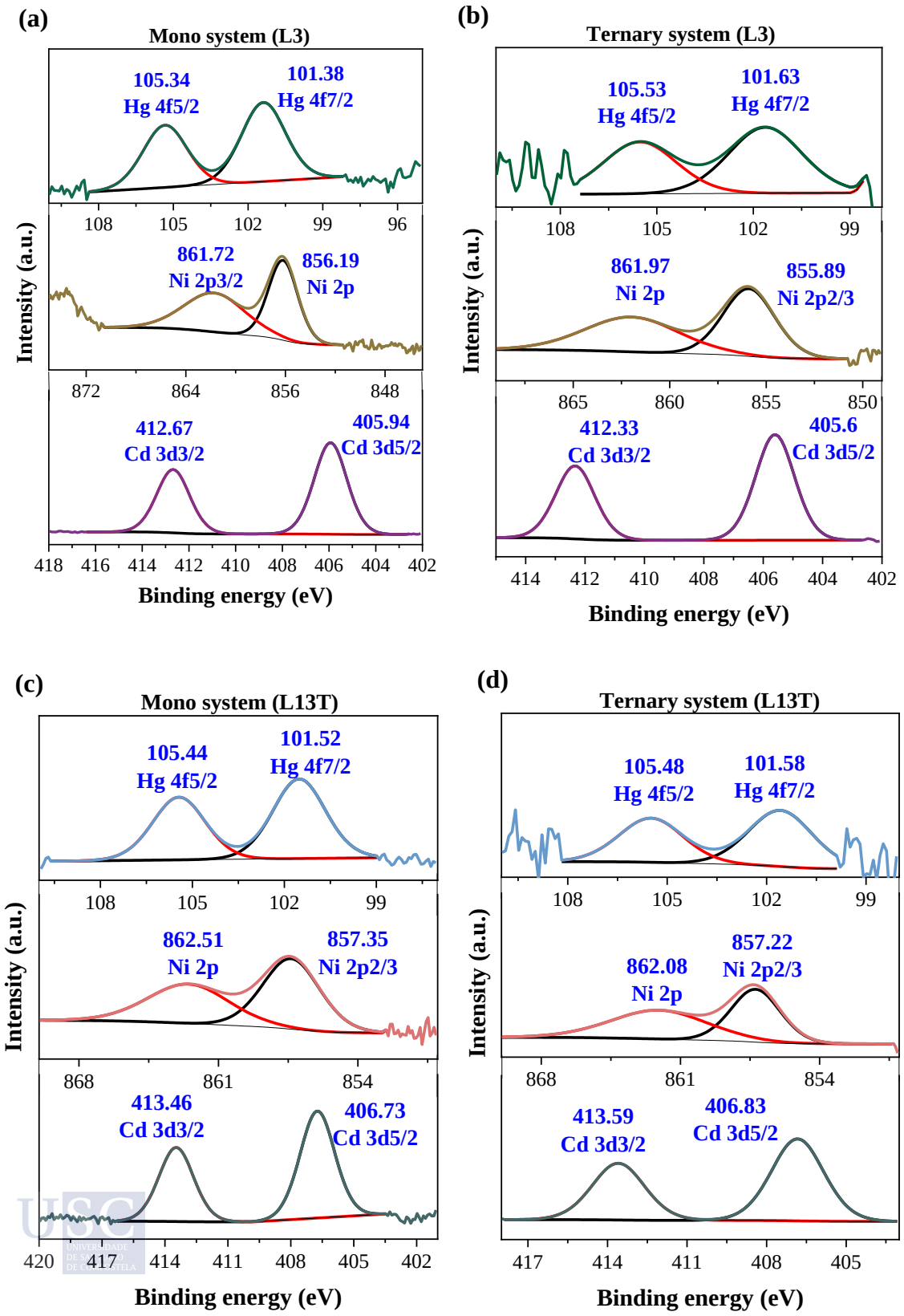


Figure 2.48. High-resolution spectra of the Hg(II), Ni(II) and Cd(II) present on the beads L3 and L13T surface after mono (a, c) and ternary (b, d) adsorption, respectively.

The corresponding peaks of Cd(II) and Ni(II) ions in the L3 beads shifted to lower binding energies from the mono to the ternary system, indicating a certain competition between the metal ions, as shown in Figures 2.48a and 2.48b. Meanwhile, the corresponding Hg peak, Hg 7f7/2 shifted from 101.38 (mono system) to 101.63 eV (ternary system). This suggests that Hg(II) ions adsorption was favoured due to the presence of Cd(II) and Ni(II) ions, as discussed previously.

It was also reported high binding energies for Hg(II) and Cd(II) at the ternary system in L13T bead, as shown in Figure 2.48d. In the calculated evaluation ratios, it was observed that Cd(II) in the L13T beads was the most favoured metal ion, and that Hg(II) ions, even though were highly suppressed, their adsorption was more enhanced. Both results are correlated, showing that metal ion competition can have a double response of adsorption enhancement or suppression.

As in the binary system, the binding energies of the detected peaks for Cd, Ni, and Hg suggest that the metal ions are mainly in the form of CdF_2, $Ni(OH)_2$, and Hg as $HgCl_2$, HgS_2, or HgO, respectively.

Linear or nonlinear isotherm models: selection of best model fitting

The experimental data of Cd(II), Hg(II), and Ni(II) ions adsorption by L3 and L13T beads in the mono and ternary systems were fitted to the nonlinear and linear Langmuir, Freundlich, Temkin, and DKR models, where the calculated parameters are listed in Tables A2.4-A2.7 and plotted in Figures 2.49 and 2.5 (Figures A1.9-A2.2 initial plotted models).

To select the model that best describes the adsorption experimental data, error functions for each model were calculated, but only χ^2 errors are displayed in the graphics.

Figure 2.49 compares the results of both linear and nonlinear fitting of the experimental data to the Langmuir and Freundlich models. The linear Freundlich model better described the adsorption of all metal ions by the L3 beads in both adsorption systems due to the low χ^2 values. A very small chi-square test means the calculated data fitted very well with the experimental data. However, lower χ^2 values in the linear Freundlich model were reported in the mono than in the ternary system, as shown in Figures 2.49c and 2.49d, this might be due to the competition state of all metals in the ternary system.

On the other hand, the metal ions adsorption by the L13T bead in the mono and ternary system was quite different. Lower χ^2 error values were computed for Ni(II) and Hg(II) in the linear Freundlich model, while for Cd(II) in the linear Langmuir model in the mono adsorption system. Meanwhile, in the ternary system, Ni(II) and Cd(II) ions adsorption was better described by the linear Freundlich model and Hg(II) by both nonlinear Langmuir and Freundlich models. In the case of Hg(II) ions adsorption, transformations of the nonlinear equation to the linear form produced poor linearity despite the high linear regression coefficients obtained in the linear models.

Thus, the adsorption of all metal ions in the mono and ternary system by L3 beads was non-uniform due to the heterogeneous surface and different adsorption heat sites distribution (Freundlich model). Contrarily, in the L13T beads, both Ni(II) and Hg(II) were adsorbed in multilayers at heterogeneous sites, and Cd(II) was uniformly distributed at a monolayer in the mono system. In the ternary system, all metal ions were adsorbed in multilayers, but Hg(II) ions were also adsorbed in a monolayer at the L13T beads since both models Freundlich and Langmuir described well its adsorption.

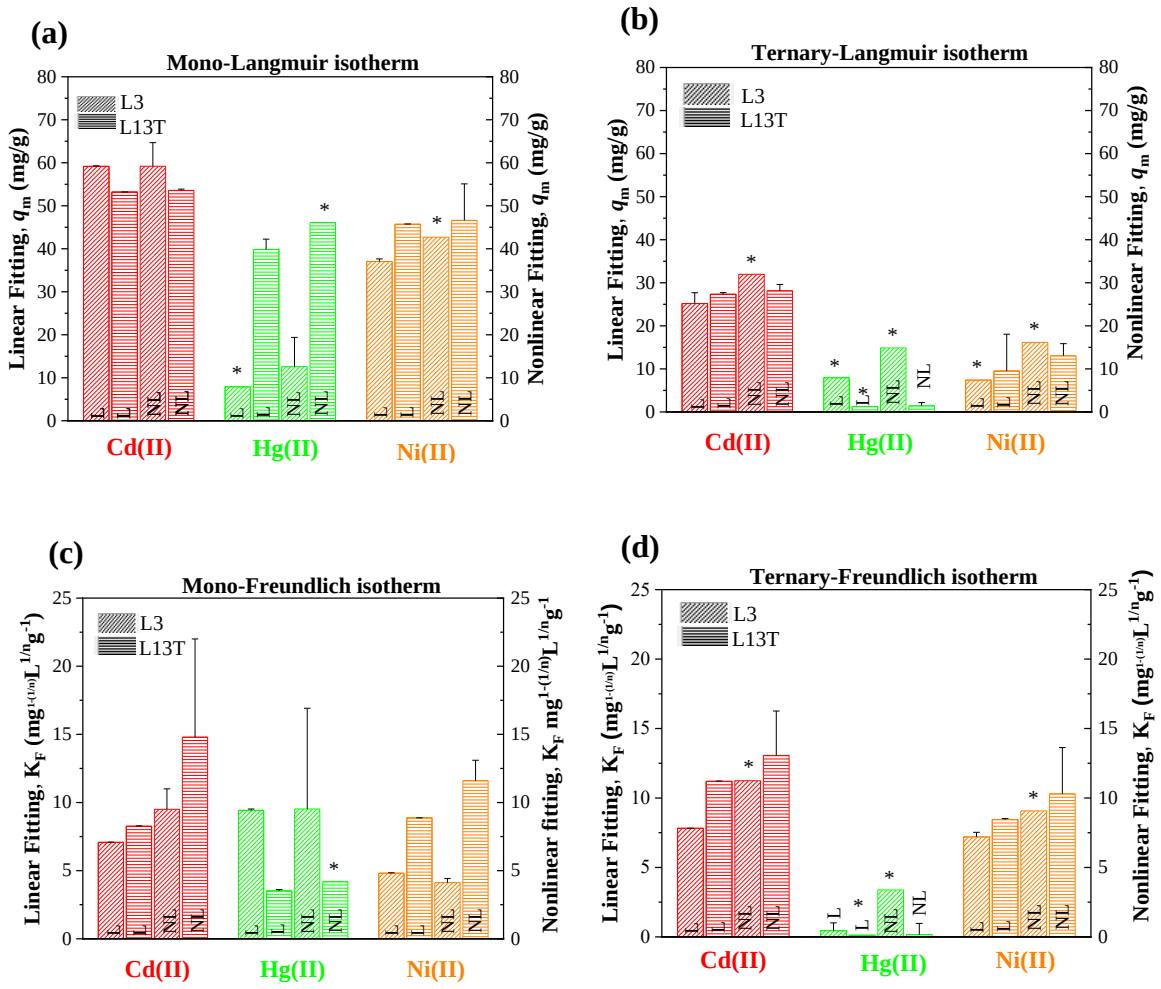


Figure 2.49. Linear and nonlinear fitting of the experimental adsorption data of the metals ions Cd(II), Hg(II), and Ni(II) (mono and ternary system) to the Langmuir (a, b) and Freundlich models (c, d), respectively. (* sign is referred to χ^2 higher than tabular χ^2 of 9.488)

Furthermore, both beads reveal different adsorption capacities from one metal ion to another. The maximum adsorption capacity (K_F, $mg^{1-(1/n)}L^{1/n}g^{-1}$) of L3 beads in the mono system follow the order of Hg(9.43)>Cd(7.09)> Ni(4.82), whereas at the ternary system follow Cd(7.82)>Ni(7.16)>Hg(0.45).

Ni(II) and Cd(II) ions adsorption was higher at the ternary than at the mono system, whereas Hg(II) ions adsorption occurred in the opposite way. The Freundlich exponent, n (Tables A2.4-A2.7) is satisfactory within 1-10. The n value was favourable for Cd(II) (n=3.78), Ni(II) (n=9.59) and Hg(II) (n=1.58) ions under ternary conditions. However, under the mono system, the reported n values for Cd(II), Ni(II), and Hg(II) were 2.52, 2.79, and 28.09, respectively. These results confirm the XPS analysis that Hg(II) ions adsorption was more favoured in a ternary system since, n, is closer to the unit.

The maximum adsorption capacity of L13T beads in the mono system follows the order of Ni(8.87)>Cd(8.45)>Hg(3.51), and in the ternary system Cd(11.15)>Ni(8.45)>Hg(0.12). The adsorption of Ni(II) and Hg(II) ions by the L13T was higher in the mono system than in the

ternary system. The opposite trend was observed for Cd(II), where the K_F, value was higher in the ternary system. The Freundlich exponent for Cd(II), Ni(II), and Hg(II) ions were 2.69, 2.32, and 3.13, respectively. The values reveal that the adsorption was a favourable physical process at the mono system. However, in the ternary system the adsorption for nickel was not so favoured having a n value of 21.83.

Figure 2.5 compares the results of both linear and nonlinear fitting of the experimental data to the Temkin and DKR models. The linearization in the Temkin model was discarded in both beads and systems since it increased the χ^2 errors. The heat release (b_T, J/mol) calculated in nonlinear Temkin model for the beads L3 and L13T revealed that all metal ions adsorption was exothermic since $b_T > 0$ [355]. However, it required more binding energy in the ternary system than in the mono system for Cd(II) and Ni(II) ions adsorption due to the high Temkin binding constant (K_T, L/g) reported. The opposite was observed in the Hg(II) ions adsorption by the beads L3 and L13T. Contrarily to what was reported at the Temkin model, the linearization of the DKR model proved to lower the χ^2 error except in Hg(II) and Ni(II) adsorption at the ternary system. The adsorption energy (E, kJ/mol) was lower than 8 kJ/mol in both systems and particles, which indicated that physical forces occurred more during adsorption than chemical forces.

Overall, the metal ions were more adsorbed at the mono than at the ternary system demonstrating that competition for available sites at the beads occurred. The bead L13T adsorbed more efficiently Cd(II) and Ni(II) in both systems and not so well Hg(II). In contrast, Hg(II) ions were more adsorbed by the L3 beads. L13T is more porous than the L3 bead, and for this reason, Hg(II) ions adsorption was not favoured since during the process desorption might have occurred, or Hg(II) ions were expelled from the pore sites due to the influence of Cd(II) and Ni(II) ions. A similar behaviour occurred using immobilized *Microcystis aeruginosa* cyanobacterium into sodium alginate to eliminate Hg(II), Cd(II), and Pb(II) from aqueous solutions [356].

USC
UNIVERSIDADE DE SANTIAGO DE COMPOSTELA

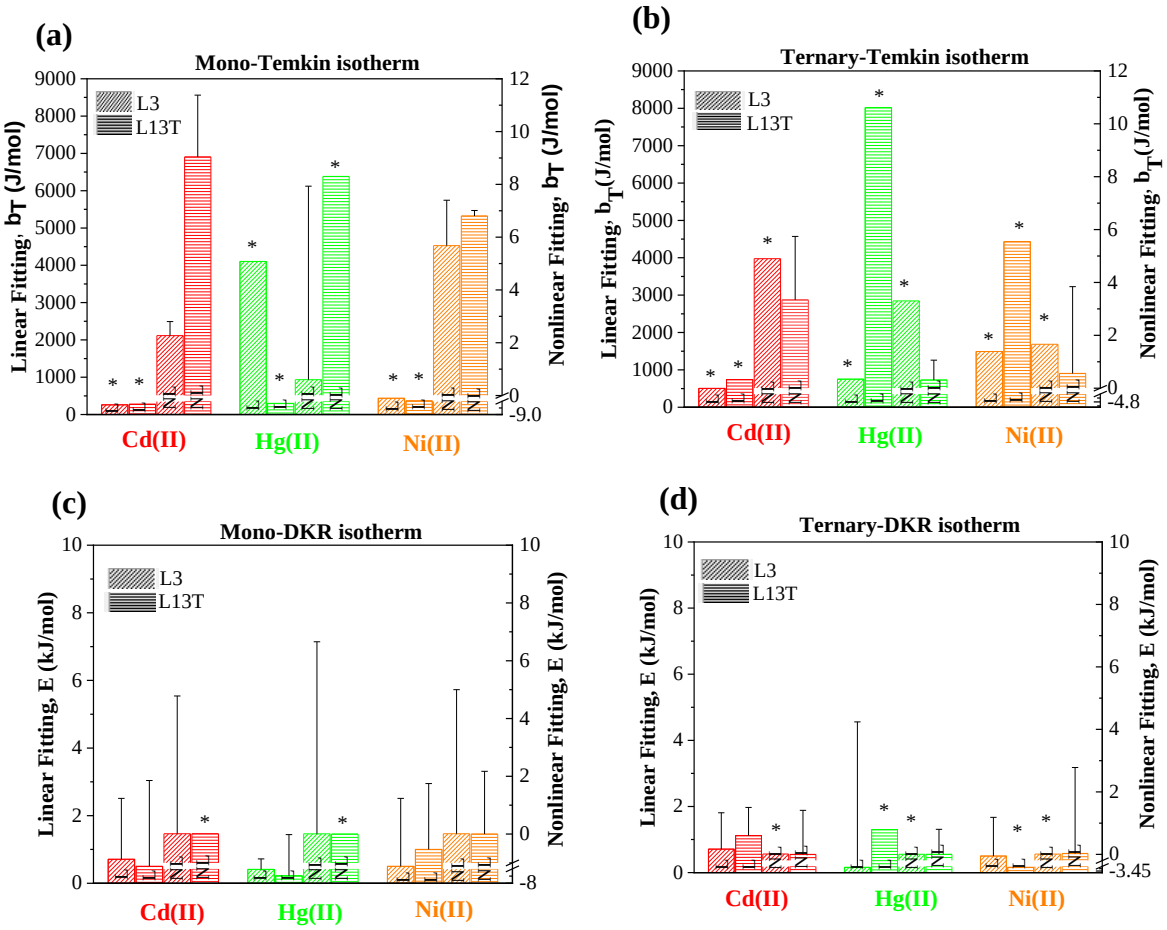


Figure 2.5. Linear and nonlinear fitting of the experimental adsorption data of the metals ions Cd(II), Hg(II), and Ni(II) (mono and ternary system) to the Temkin (a, b) and DKR models (c, d), respectively. (* sign is referred to χ^2 higher than tabular χ^2 of 9.488)

Adsorption mechanism at the ternary system

The adsorption mechanism and changes in the functional groups before and after adsorption of Cd(II), Hg(II), and Ni(II) at the mono and ternary system were analysed by FTIR.

Figures 2.51a and 2.51 show the adsorption comparison at the different systems by the beads L3 and L13T, respectively. After adsorption, the intensity of the vibrational peaks corresponding to the functional groups of C=O, C-O decreased, and the same applies to the Fe-O bond. New bonds were formed during adsorption resulting in the decrease of COOH groups present at the beads. However, both particles exhibited a slight shift and a higher peak intensity after Hg(II) adsorption. This indicates that the beads suffered structural changes with the formation of molecular bonds during Hg(II) adsorption [357].

Both bonds of C-O and C=O suffered the highest shift at the beads L13T. The peak C-O shifted from 1017 cm^{-1} to 1022-1027 cm^{-1}, and the C=O bond shifted from 1587 cm^{-1} to 1579-1583 cm^{-1}, respectively. These bonds are more highly involved in adsorption at the L13T beads. In the spectra of Cd(II) and Ni(II) ions in both beads, the peak intensity of both bonds was highly reduced, evidencing their involvement in these metals adsorption. Around 552 and 554

cm^{-1} it was detected the stretching vibration of Fe-O in Fe_3O_4 NPs at L3 and L13T beads, respectively. After adsorption, the bond intensity was less prominent and detectable, which may indicate some displacement of oxygen groups.

XPS analysis was performed to compare and analyse chemical state changes in the surface of the L3 and L13T beads before and after adsorption. On the surface of both beads, oxygen is the most predominant element. Therefore, the changes in O1s in the ternary system were further analysed. The deconvoluted peak results for L3 and L13T are shown in Figures 2.52a and 2.52b, respectively.

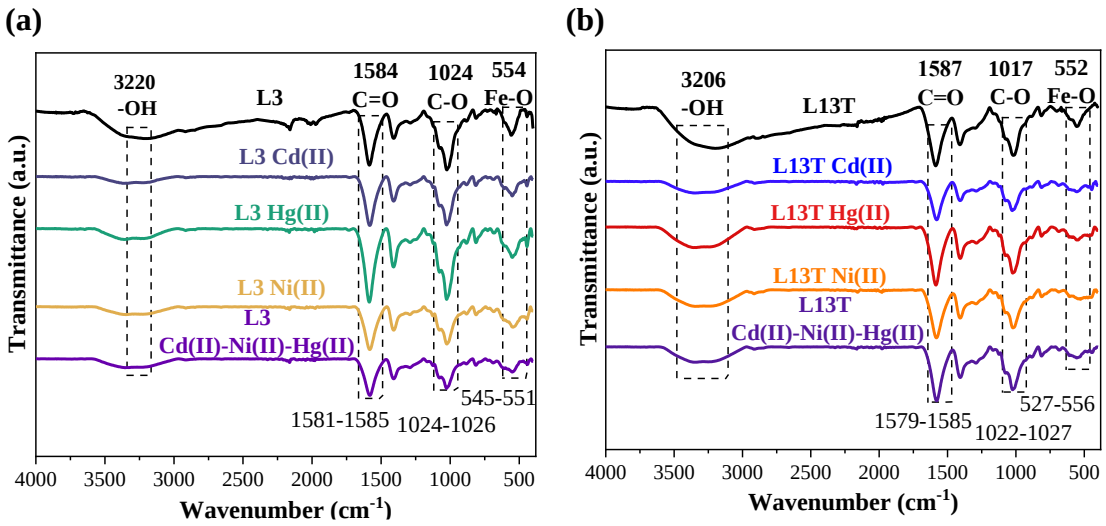


Figure 2.51. FTIR spectra before and after adsorption in a mono and ternary system by L3 (a) and L13T (b) beads.

USC
UNIVERSIDADE DE SANTIAGO DE COMPOSTELA

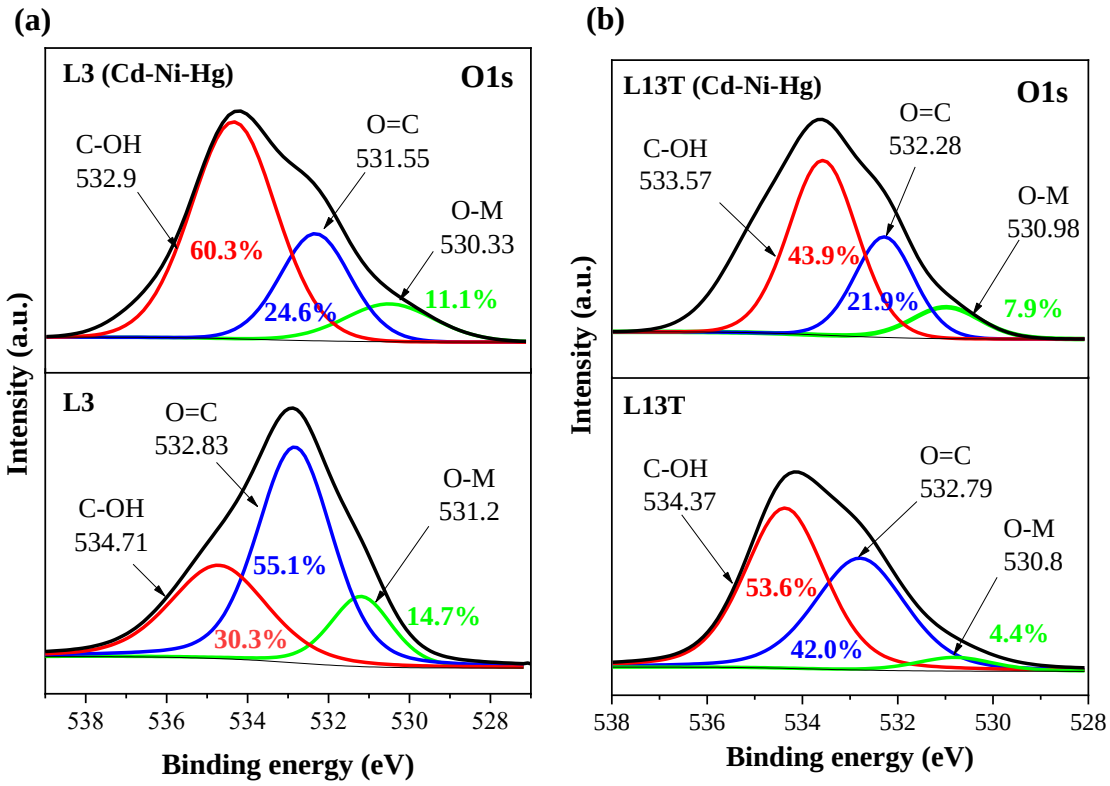


Figure 2.52. XPS high resolution spectra of O1s in L3 (a) and L13T (b) before and after ternary adsorption.

The high-resolution spectra of O1s in both beads were divided into three peaks which are assigned to C=O, C-O, and O-M (metal oxides, M=metal) bonds. There is a shift of the O1s peaks to lower binding energies at the ternary system in the L3 and L13T beads. This is attributed to the formation of new bonds between the metal ions and the oxygen functional groups present at the beads surface. In addition, the relative content of C=O at the L3 and L13T beads decreased from 55.1 % and 42.0 % to 24.6 % and 21.9 %, respectively. However, there is an increase in the C-O bond at the L3 bead from 30.3 % to 60.3 %, after metal adsorption, the C=O double bond broke, and it was converted into a C-O bond or M-O bond.

Meanwhile, the C-OH bond at the L13T decreased from 53.6 % to 43.9 %. The ratio of C=O/C-O decreases from 1.8 and 0.78 to 0.41 and 0.50 at the L3 and L13T beads, respectively. This indicates that on both beads surfaces, the C=O bond is the main adsorption site for the metal ions but is more pronounced at the L3 beads. Furthermore, a higher conversion of covalent to ionic bonds was observed at the L13T beads, which explains the higher binding energy of O-M and relative content of 4.4 % -7.9 %.

The adsorption mechanism onto mesoporous carbons is challenging, and it can be a combination of electrostatic attraction, ions exchange, surface precipitation, and chemical interaction between the metal ions and the functional groups. The high adsorption ability of the L13T is due to the presence of carboxyl groups at the channels entrance and inside the mesopores of the CMK-3 (T) mesoporous carbon [358]. It is believed that the metal ions entered inside the beads structure forming ionic bonds with oxygen from C=O, explaining the lower ratio calculated at the beads surface. Besides oxygen, it is also involved in the adsorption of S2p[1], N1s, and F1s bonds.

High-resolution XPS analysis was performed on the bonds at the mono and ternary system, as shown in Table A2.8. Both beads observed high binding energies for $S2p^1$ during Hg(II) ions adsorption. The peaks were located at 169.07 and 169.52 eV with a relative content of 46.2 % and 70.6 % at the L3 and L13T beads, respectively. The peaks are assigned to metal sufates, which indicates that Hg(II) ions formed more ionic bonds with sulfur in the L13T than in L3 beads.

During Cd(II) ions adsorption, the binding energy assigned to organic fluorides considerably increased with respect to the other metal ions in both beads. Meanwhile, Ni interacts with the nitrogen of the amino groups, proven by the high binding energies reported at the N1s high-resolution spectrum of both beads.

Thus, the metal adsorption by the beads L3 and L13T seem to be a combination of various processes, which was mainly done by complexation, ion exchange, physisorption, and chemisorption.

2.3.3. Application of magnetic alginate beads at Industrial-scale processes

Over the different experimental studies, adsorption capacity and efficiency of the different beads were studied in several systems (mono, binary, and ternary). The results reported good adsorption capacity, selectivity, and magnetic properties to the different metal ions.

The L3 magnetic beads (containing AC commercial) had an adsorption capacity for Cd(II) ions of approximately 68.77 mg/g and 145 mg/g C over 1 h and 6 h of contacting time, respectively. Meanwhile, in bead L13T (high quality CMK-3 carbon) was equal to 10439 mg/g C (6 h contacting time). Even in a ternary competing system, it yielded good adsorption capacity values for Cd(II) ions of approximately 126.5 and 6062 mg/g C by L3 and L13T beads, respectively. These results for Cd(II) adsorption are way above reported ones in the literature, as shown in Table 2.3.

Besides Cd(II), also Hg(II) ions were efficiently removed from aqueous solutions but to a lower extent. In the mono adsorption, L3 beads revealed an adsorption capacity of 55 and 50.5 mg/g C (binary and ternary experiments, respectively), whereas L13 of 30 mg/g and L13T of 8866 mg/g C. In the ternary adsorption, it was equal to 25.9 and 367.8 mg/g C at the L3 and L13T beads, respectively. In addition to Cd(II) and Hg(II) adsorption, Ni(II) ions were also adsorbed by L3 and L13T beads and was the second metal ion most adsorbed after Cd(II) ions in both mono and ternary systems.

One of the primary challenges of treating wastewaters is to efficiently remove several mixture contaminants or select a specific one due to their toxicity. These results demonstrate that it is possible to design particles to target one contaminant or several in a mixture. For this reason, it is important to optimize the particle properties (functional groups, porosity, and biocompatibility) and experimental parameters to achieve maximum.

The experimental adsorption data in all experiments were explained by fitting to adsorption isotherm (Langmuir, Freundlich, Temkin, and DKR) models and the experimental dynamics over time to the kinetic (PFO, PSO, and Elovich) and diffusion model (IPD). Freundlich was the isotherm model that best fitted the experimental data of the different metal ions (Cd(II), Ni(II), and Hg(II) in almost all of the studies. This model assumes that adsorption took place on a heterogeneous multilayer surface with different energy of the adsorptive site, which states that the studied particles are robust and porous.

Furthermore, it was also stated by the Temkin and DKR models that adsorption was an exothermic process with mainly physical forces occurring. Physisorption (PFO model) mainly

occurred at initial Hg(II) concentrations of 70 and 230 mg/L, whereas at 150 mg/L, chemisorption (PSO model) was the main process occurring at the L3 beads. On the contrary, chemisorption occurred in all ranges of initial Hg(II) concentrations at the L13 beads. A similar trend appeared in Cd(II) ions adsorption, where at lower initial concentrations, physisorption dominated, while at higher initial concentrations, adsorption occurred mainly by chemisorption at the L3 beads.

The beads are a complex system where several processes inevitably happen simultaneously, such as chemisorption, physisorption, complexation, and ion exchange. This set of properties makes the magnetic alginate beads able to remove a large variety of pollutants from contaminated waters. In addition, they can be magnetically separated, which is a promising methodology for environmental purification since no residue is produced during treatment and large wastewaters can be treated quickly.

The use of these beads at an industrial scale gain even more insight due to their biocompatibility, no toxicity, cost-effective development process, and reusability in several treatments without structural damage, improving any industry's economic profit.

2.4. Conclusion

In this chapter, the development of magnetic alginate beads with different compositions is presented with their ability to remove mycotoxins and heavy metal ions from aqueous solutions or food. The removal of mycotoxins highly depends on the composition of the beads.

The magnetic L3 beads composed of sodium alginate and commercial AC adsorbed more than 50% of all mycotoxins present in an aqueous solution. Meanwhile, the beads L12 composed of sodium alginate with a high concentration of commercial AC and esterified pectin revealed great affinity to the DON mycotoxins (59.5 % removal).

In order to obtain maximum adsorption of mycotoxins from either aqueous solutions or beer wort, the adsorbate dosage and contact time had to be optimized. It was revealed that by increasing the L3 beads dosage from 200,450 and 900 mg, the removal efficiency of the FB1 mycotoxins was 7 %, 31 %, and 50 %, respectively. Besides mycotoxins, it was also tested the efficiency of these beads in removing heavy metals from mono, binary, and ternary systems analysing the thermodynamic parameters and kinetic details of the adsorption process.

In the first study of mono metal (Cd(II)) removal by L3 beads, batch adsorption experiments were undertaken to optimize several experimental parameters. The effect of contacting time, pH, rotation speed, and agitation type were fully discussed. A higher removal efficiency of Cd(II) was shown when the L3 beads were submitted to magnetic agitation at 300 rpm for 1 h. At pH 6, the experimental data of Cd(II) isotherm and kinetic adsorption fitted well the Freundlich model. It is believed that adsorption at lower initial metal concentrations fitted the PFO model, whereas at higher initial concentrations by the PSO and Elovich model. The adsorption occurred at a multilayer level onto the heterogeneous surface by physical and chemical forces. The adsorption rate was mainly controlled by film diffusion with increased boundary layer thickness. The L3 beads have the potential to be reused for up to four cycles without structural damage, with 90 % of Cd (II) recovered from the bead.

In a binary metal study, it was demonstrated the adsorption capacity of L3, L13 (sodium alginate, low quality CMK-3 mesoporous carbon, and Fe_3O_4 NPs), and L16 (sodium alginate and Fe_3O_4 NPs) beads for a combination of (Hg(II)-Cd(II)) and (Hg(II)-Ni(II)) metal ions, compared to the mono Hg(II) removal. It was revealed a maximum of Hg(II) ions removal

efficiency of 35 %, 15 %, and 25 % by the L3, L13, and L16 beads at the initial concentration of 150 mg/L, respectively.

The removal of Hg(II) ions decreased with increasing temperature. The adsorption happened by chemisorption in all initial concentrations by the L13 beads, which is characteristic of the PSO model. Meanwhile, the PFO model (physisorption) described the adsorption of Hg(II) by L3 and L16 beads at lower initial concentrations, whereas the PSO model described the adsorption at higher initial concentrations better. In addition, it was demonstrated that the main step involved in the Hg(II) ions adsorption onto the L3, L13, and L16 beads were film and interparticle diffusion, where the interparticle diffusion was the main controlling step.

Lastly, the adsorption capacity of the beads was studied in a ternary system of Cd(II), Ni(II), and Hg(II). For this, a high-quality CMK-3 mesoporous carbon, with ordered channels was prepared and fully characterized by BET, SEM, TEM, and XPS analysis, and used in the composition of the L13T beads. The adsorption capacity of the L13T was a hundred times higher than bead L3 and bead L13 (a low-quality equivalent with poor CMK-3 carbon used in the binary study).

In both binary and ternary systems, Cd(II) was the most adsorbed of all metal ions, followed by Ni(II) and Hg(II) ions. The likelihood of Cd(II) ions to be adsorbed was attributed to the lower hydration free energy compared to Ni(II), and Hg(II) ions were less adsorbed because of their high atomic radius. A lower adsorption capacity of all metal ions was verified in both binary and ternary systems due to the competition between the metal ions for the available sites. In the binary system, it was observed a synergistic effect between Ni(II) and Hg(II) ions at the L3 beads and in L13 and L16 between Cd(II) and Hg(II). Cd(II) and Ni(II) ions were more supressed at higher initial metal concentrations, meanwhile Hg(II) ions adsorption was highly enhanced. The competition between all metal ions was more pronounced at the L13T beads and Cd(II) ions were the most favoured adsorbed metal ion, followed by Ni(II) and Hg(II) ions.

The adsorption mechanism in both systems, binary and ternary, was similar, the metal bonding was mainly done through oxygen groups on the surface of the beads. The C=O bond was involved in the adsorption process. It was also demonstrated that in the binary and ternary system, the binding energies of the metal ions of Cd(II), Ni(II), and Hg(II) obtained were assigned to CdF_2, $Ni(OH)_2$, and $HgCl_2$ or HgO. The adsorption of the metal ions seems to be a combination of various processes, such as ion exchange, chemisorption, physisorption, and complexation, where some mechanisms are more present than others.

These results indicate that the proposed magnetic hybrid beads provided a low-cost candidate for removing and recovering metal ions from contaminated aqueous mediums.

USC
UNIVERSIDADE DE SANTIAGO DE COMPOSTELA

Chapter 3

USC
UNIVERSIDADE
DE SANTIAGO
DE COMPOSTELA

USC
UNIVERSIDADE
DE SANTIAGO
DE COMPOSTELA

3. Future materials from forest-based economy: magnetic microfibers, films, and capsules

3.1. Future changes in the Forest sector: Introduction

Biobased materials applications are estimated to increase worldwide due to the need for a more sustainable future with zero carbon emissions and reduced use of fossil fuels. Cellulose is a promising alternative since it is the most abundant natural biopolymer on Earth, existing in cell walls of plants being as well secreted by bacteria, tunicates, and algae (Figure 3.1a) [220,359]. Structurally, cellulose is composed of D-glucopyranose units linked by β(1→4) glycosidic bonds. The intermolecular hydrogen bonds of the cellulose network are the cause of its crystallinity and unique three-dimensional arrangement into nanofibrils from 2-20 nm diameters (Figure 3.1b).

Nanofibrils, owing to the hierarchical structure of cellulose, can be customized in terms of morphology and size, enabling outstanding and unique mechanical, thermal, optic, and ionic properties. Wood is often modified to take advantage of these cellulose fibrils within the cell wall. Pretreatment methods (chemical, physical or physicochemical) break down the cellulose fibres into smaller fibrils to produce lightweight, strong, and tailorable nanocellulosic materials. TEMPO (2,2,6,6-Tetramethylpiperidine-1-oxyl radical)-mediated oxidation is one of the possible chemical methods that convert native cellulose into individual nanofibrils with charged carboxylate groups (-COO), usually referred to as TOCNF.

Nanocellulose is a term that describes the distinct types of nano- and micro-sized cellulose fibrils, namely cellulose nanocrystals (CNC), nanofibrils (CNF), and microfibrillated cellulose (MFC), respectively [360–363]. Although cellulose is mainly used in the pulp and paper industry, it has been exploited for high-performance materials, i.e., bioplastics production for food packaging (Figure 3.1c). Bioplastic production is growing fast, with similar performance qualities and characteristics to the oil-based ones [364]. Another important feature is their biodegradability which allows them to degrade in the environment without posing any risk to the environment.

Besides this, a growing market is expected to produce bioplastics and nanopapers, porous membranes, and aerogels, contributing to a more sustainable circular economy. Nanocellulose can also be integrated with carbon materials and metallic or magnetic nanoparticles to generate hybrid nanocomposites with incremented features [365]. Small iron oxides NPs, in specific magnetite (Fe_3O_4), show high stability, superparamagnetism, low toxicity, and biocompatibility. Fe_3O_4 NPs are versatile nanostructures with efficient performance in magnetic resonance imaging, drug delivery, and adsorption of contaminants present in wastewater [366]. Magnetic nanocellulosic materials contain both excellent properties from nanocellulose, from magnetic nanoparticles and hybrid materials are developed with excellent mechanical properties, biodegradability [367], and fast separation or recovery from water matrices under an external magnetic field.

Therefore, in the present chapter Fe_3O_4 NPs were incorporated into different types of cellulose matrix, namely TOCNF, cellulose acetate (CA), and bacterial nanocellulose (BNC). The materials were prepared in the form of microfibers, films, and capsules. Herein we demonstrated the interaction between the NPs and the cellulose matrix and their effect on the mechanical, morphology, magnetic and structural properties of the hybrid cellulosic materials in several future applications.

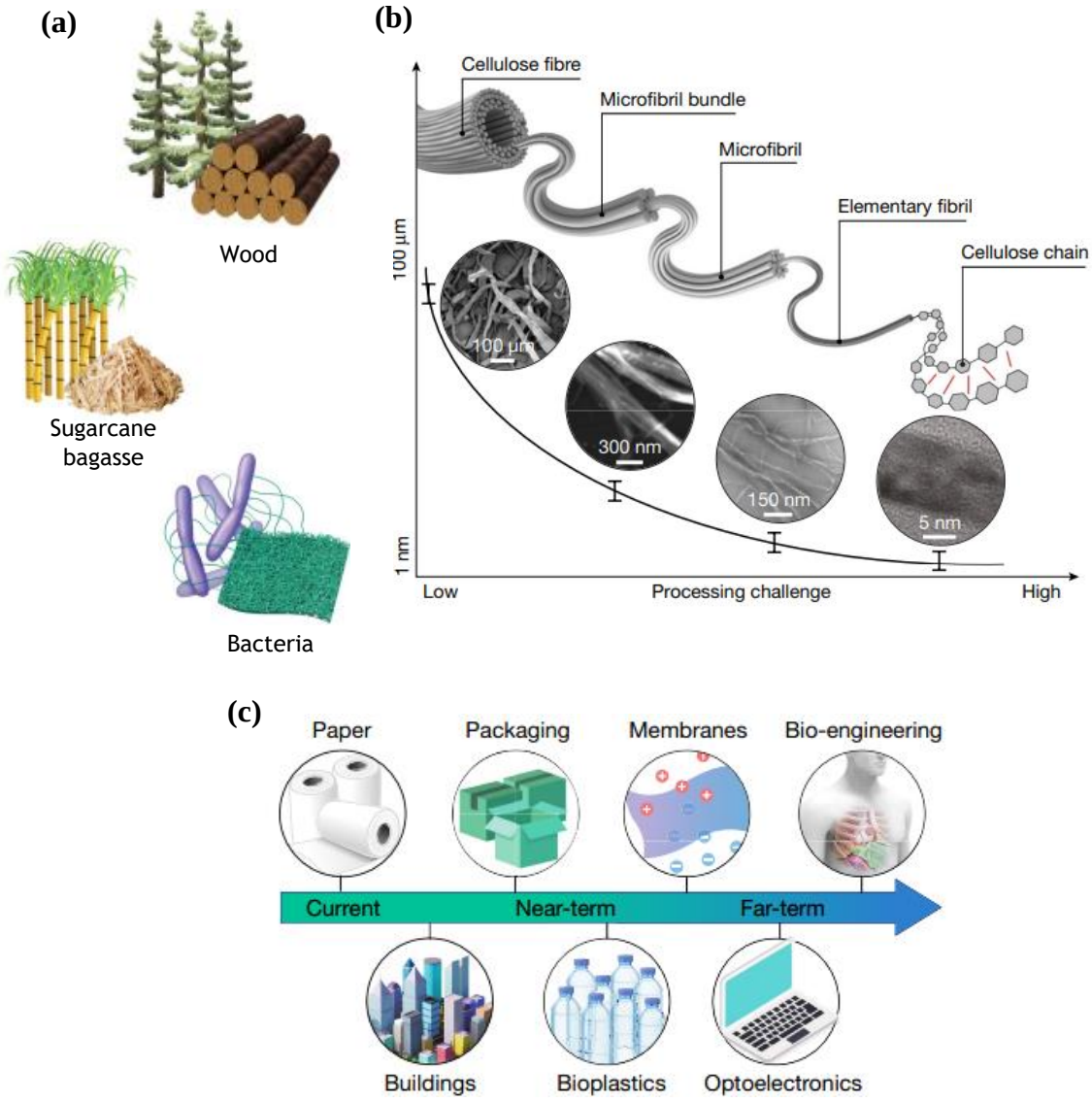


Figure 3.1. Sources of nanocellulose (a) Description of hierarchical structure of cellulose and its break down into microfibrils and nanofibrils (b). Future and on-going materials obtain from nanocellulose including paper, packaging and bio-engineering (c). (Reproduced with permission from reference [220]**. Copyright (2022)** ***Nature*****).**

USC UNIVERSIDADE DE SANTIAGO DE COMPOSTELA

3.2. Study of magnetic microfibers properties

Hybrid inorganic-organic nanocomposites have unique properties and potential advantages arising from both components. The inorganic component can favour high thermal stability, refractive index, and hardness, whereas the organic part attributes flexibility and low weight to the material. However, several challenges attributed to the interactions between the components at the interface are correlated to the size, distribution, morphology, and dispersion of the inorganic NPs fillers.

NPs tend to agglomerate, reducing the interfacial area and interactions with the organic polymer. Even in some cases, it can result in the deterioration of the final material. An innovative approach to avoid these drawbacks and achieve a homogeneous dispersion is the *in- situ* synthesis of inorganic nanoparticles in the polymeric matrix using the co-precipitation method. This method involves mixing the precursors with a nonreactive solvent and the polymer, forming nucleated NPs that grow inside the polymeric matrix. As a result of the binding effect of the polymer functional groups, the NPs have controlled size, homogeneous morphology, and reduced agglomeration [368]. However, unreacted precursors or byproducts present might be one limitation altering the properties of the hybrid nanocomposite. Another approach is to use the *ex-situ* method, mixing the pre-synthesized cleaned NPs in the polymeric matrix. However, this method is less used since it can cause an inhomogeneous dispersion of NPs within the polymeric matrix.

In this work, it was studied the synthesis procedure of Fe_3O_4 NPs by co-precipitation, using both *in-situ* (TOCNF and alginate matrix) and *ex-situ* (alginate matrix) methods to prepare magnetic microfibers of different morphology (core, core@shell). It was assessed the effect of the magnetic nanoparticles (MNPs) synthesized *in-situ* on the nanofibrils level of nanocellulose and the impact of the method chosen on the mechanical, magnetic, and morphological properties of the developed magnetic microfibers (core, core@shell). In addition, it was also prepared core magnetic microfibers with different NPs concentrations to observe their impact on the mechanical strength and magnetization of these materials.

3.2.1. Magnetic microfibers: Material and Methods

a. *In-situ* preparation of Fe_3O_4 NPs on TEMPO-oxidized cellulose nanofibers

Fe_3O_4 NPs were synthesized *in-situ* within a TOCNF solution. Briefly, 0.08 M $FeCl_3.6H_2O$ and 0.048 M $FeSO_4.7H_2O$ were added to a 250 mL aqueous suspension of TOCNF with approximately 20 wt % composition, based on total dry mass (TOCNF initial dry weight of 1.23 %). Ferrous ion was added in slight excess of the magnetite stoichiometric molar ratio (Fe^{3+}/Fe^{2+} = 6:1) in order to account for the possible oxidation of Fe^{2+} during the TOCNF impregnation. After the complete impregnation of the TOCNF (T) solution with the iron salts, the aqueous suspension was heated to 80 °C for 30 min under mechanical stirring and N_2 flow.

Afterward, 15 mL NH_4OH (25 wt %) was added dropwise, and the reaction was left under agitation for 30 min. Finally, the reaction was stopped and left to cool down to room temperature. The solution was then cleaned with water and ethanol several times, being referred to as T/Fe25. To prepare the magnetic solutions, 5.4 g of sodium alginate (SA) was added to 250 g of T/Fe25 and left agitating for 4 h at room temperature, labelled as SA/T/Fe25. Furthermore, it was also prepared solutions with Fe_3O_4 concentrations of 5, 10, 25 wt % using

as a precipitating agent NaOH (25 wt %). The magnetic solutions containing the given concentration of Fe_3O_4 NPs were therein referred to as SA/T/Fe5, SA/T/Fe10, SA/T/Fe25N, respectively.

b. *Ex-situ* preparation of Fe_3O_4 NPs for mixing with sodium alginate

Fe_3O_4 NPs were synthesized under the same reaction conditions as above but in the absence of TOCNF. To the pre-synthesized NPs redispersed in 250 mL milli-Q water it was added 5.4 g of sodium alginate and left agitating for 4 h at room temperature. The magnetic solution was labelled as SA/Fe25. In addition to the magnetic solutions, it was also prepared reference solutions without NPs (R-SA/T and R-SA) for comparison purposes.

Table 3.1 shows the compiled composition of each magnetic solution prepared. All dopes were fully characterized by TEM, SEM, TGA, DLS, and VSM (Appendix 6.1).

Table 3.1. Solutions composition and parameters.

Solutions	Sodium Alginate (SA) (%)	TOCNF (T) (%)	Fe_3O_4 NPs (%)	Precipitating agent
SA/T/Fe25	55	20	25	NH_4OH
SA/Fe25	75	-	25	NH_4OH
SA/T/Fe25N	55	20	25	NaOH
SA/T/Fe10	65	20	10	NaOH
SA/T/Fe5	75	20	5	NaOH
R-SA/T	80	20	-	-
R-SA	100	-	-	-

c. Microfibers spinning: coagulation time and drying process

The solutions in Table 3.1 were degassed (3 min at 2500 rpm) via a planetary centrifugal mixer (THINKY ARE-250) previously to the spinning. The homogenous solutions were then loaded into a 20 mL plastic syringe connected to a plastic tube (44.5 cm length and 6mm inner diameter) which ended in a coaxial needle with an inner diameter of 1.2 mm, outer diameter of 2.1 mm, and a length of 3.7 cm. The needle was then immersed in a coagulation bath (1 M $CaCl_2$), as shown in Figure 3.2a. The spinning rate was fixed at 10 mL/min, and microfibers were formed. The microfibers remained in the coagulation bath for 20 min for strong cross-linking.

Afterward, two washing steps were carried out by immersing the microfibers in water for 5 min and later for 1 h. The microfibers were then collected and dried in the air under restricted shrinkage (by fixing both ends), as shown in Figure 3.2b. The drying process varied with the microfibers type, microfibers with a TOCNF shell (TOCNF 2 % dry weight) took around 2h30min to dry, while microfibers without a shell took approximately 1 h.

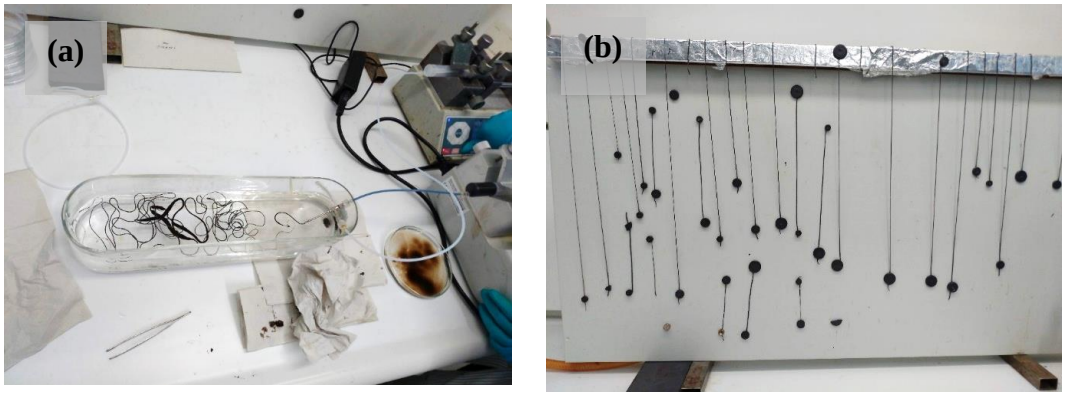


Figure 3.2. Spinning procedure (a) and the drying set-up (b) of the magnetic microfibers

The reference and the magnetic microfibers obtained after the spinning procedure, according to the composition of their mixture and the absence or presence of a TOCNF shell, were labelled as shown in Table 3.2. In addition, the texture, topography, and morphology of the microfibers were characterized by TGA, VSM, SEM-EDX, and confocal laser optical profilometry (Appendix section 6.1).

Mechanical characterization was another measurement to assess the microfibers response to an applied force. As a result, the tensile stress, $\sigma(\varepsilon)$, as calculated by dividing the maximum force to rupture, $F(\varepsilon)$, by the cross-section area, A_0, the microfibers and films. The result is expressed in megapascals (MPa), and the equation (1) is as follows [369]:

$$\sigma(\varepsilon) = \frac{F(\varepsilon)}{A_0} \quad (1)$$

The strain, ε, is related to the microfiber length and was calculated using equation (2):

$$\varepsilon(t) = \frac{L(t) - L_0}{L_0} \quad (2)$$

Where, L_0, is the original length of the material and L, is the length of the material at time t. The strain result is usually presented in percentage for better representation (since is a ratio of lengths, strain has no units).

Young's modulus, E, evaluates the elasticity of a material and the capacity to resist deformation. E, and was calculated from the slope of the elastic region according to equation (3). A higher Youngs´s modulus is correlated to a higher resistance of the material against deformation [370].

$$E = \frac{\Delta\sigma_\varepsilon}{\Delta\varepsilon} \quad (3)$$

USC DE SANTIAGO DE COMPOSTELA

Table 3.2. Type of microfibers prepared

Solution	Label solution	Microfibers (F) type	
		Core (N)	Core@shell[*1] (TS)
SA/T/Fe25	F1	F1N	F1@TS
SA/Fe25	F2	F2N	F2@TS
SA/T	RF1	RF1N	RF1@TS
SA	RF2	RF2N	RF2@TS
SA/T/Fe25N	F3	F3N	-
SA/T/Fe10	F4	F4N	-
SA/T/Fe5	F5	F5N	-

[*1] shell of TOCNF with 2 wt % dry solid content

3.2.2. Magnetic microfibers properties: Results and discussion

Fe_3O_4 NPs with concentrations of (25, 10, 5 %) were prepared using two different precipitating agents (NH_4OH and NaOH) to examine the magnetic behaviour and interaction of the nanoparticles with TOCNF. The TEM images shown in Figure 3.3 illustrate the structure of the Fe_3O_4 NPs with different concentrations loaded on TOCNF.

In Figure 3.3a, TOCNF presents a web-like structure of many nanofibrils entangled with a broad width size distribution from 10 nm to 80 nm. This heterogenous size distribution and aggregation of the nanofibrils is likely due to the intense mechanical treatment previously performed. In the remaining TEM images (Figures 3.3b-3.3f), with higher amplification, the presence of Fe_3O_4 NPs is clearly distinguished within the structure of the nanofibrils, revealing a significant degree of integration of both phases in the material. Moreover, no particular differences in the NPs sizes are observed regarding the precipitating agent used (NH_4OH or NaOH). The size distribution of the NPs in the magnetic solution SA/T/Fe25 (Figure 3.3b) presented a diameter size of 7.29 nm, as shown in the size distribution histogram in Figure 3.3g.

The Fe_3O_4 NPs synthesized using NaOH in the magnetic solution SA/T/Fe25N (Figure 3.3c) presented an average diameter size of 7.51 nm, as shown in the size distribution histogram in Figure 3.3h. In addition, the most remarkable fact is that the presence of TOCNF, used in the *in-situ* synthesis, could stabilize and control the NPs size and aggregation. NPs prepared in-situ in the presence of TOCNF reveal a diameter size from 7 to 9 nm (Figures 3.3b-3.3e) while in its absence present around an average diameter size of about 13 nm, as shown in the size distribution histogram in Figure 3.3i of the magnetic solution, SA/Fe25.

USC UNIVERSIDADE DE SANTIAGO DE COMPOSTELA

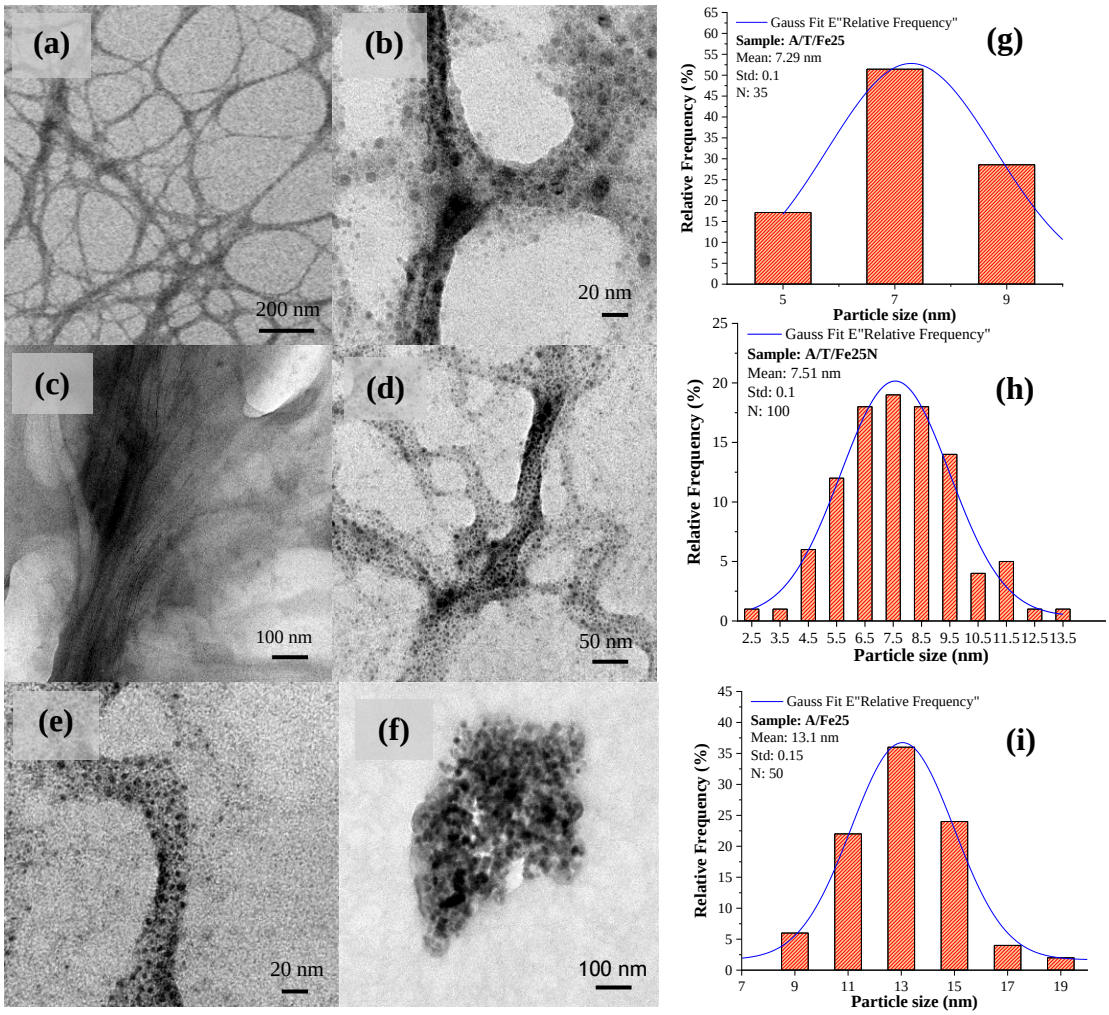


Figure 3.3. TEM images of TOCNF (a), SA/T/Fe25 (b), SA/T/Fe25N (c), SA/T/Fe10 (d), SA/T/Fe5 (e) and SA/Fe25 (f). Size distribution histogram of F_3O_4 NPs present in the magnetic solutions SA/T/Fe25 (g), SA/T/Fe25N (h), and SA/Fe25 (i).

The TEM image of the magnetic solution SA/Fe25 (Figure 3.3f), synthesized without TOCNF, reveals the extent of NPs aggregation and width size distribution. This corroborates that the presence of carboxyl groups in TOCNF enhances the ability of CNF to stabilize NPs, as previously seen in other studies [371]. However, although NPS prepared in the presence of TOCNF were smaller, individual NPs remained as part of the supernatant, indicating that not all were integrated within the nanofibers surface or inner structure.

Before spinning, no detachment of the MNPs was observed when the magnetic solutions were exposed to an external magnetic force. The freshly prepared microfibers revealed a homogenous structure to the naked eye and a great magnetic attraction, as shown in Figures 3.4a and 3.4b, respectively.

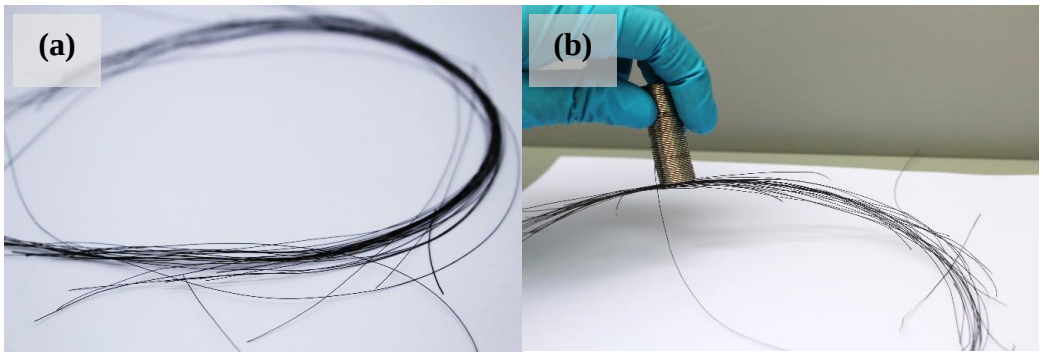


Figure 3.4. Digital photos of the magnetic microfibers (a) and under an external magnetic force (b).

The structural and textural properties of the magnetic solutions and microfibers were examined by XRD and FTIR. The FTIR spectra of both microfibers and TOCNF can be seen in Figure 3.5a. The TOCNF spectrum reveals peaks at 3300 and 2888 cm^{-1}, which are attributed to the -OH functional group and -CH_2 stretching vibrations of cellulose [372]. The vibrational band at 1604 cm^{-1} is attributed to the -C=O, while the vibrational peaks observed at 1044 and 850 cm^{-1} are referred to as C-O-C and β-glycosidic linkage vibration, respectively [372, 373].

As observed from the IR spectrum of TOCNF, the microfibers have all vibration peaks associated with nanocellulose.

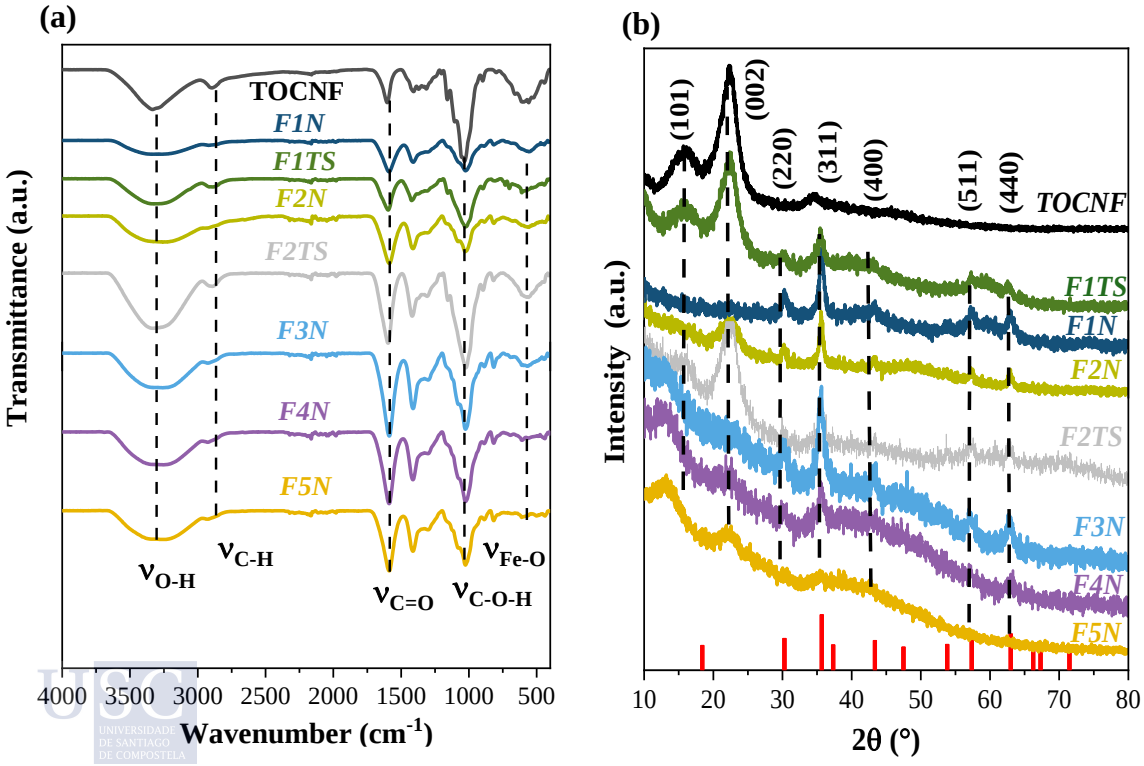


Figure 3.5. Infrared (a) spectra and X-ray (b) diffractogram of the microfibers, the latter containing the respective magnetite diffraction standard pattern (red columns).

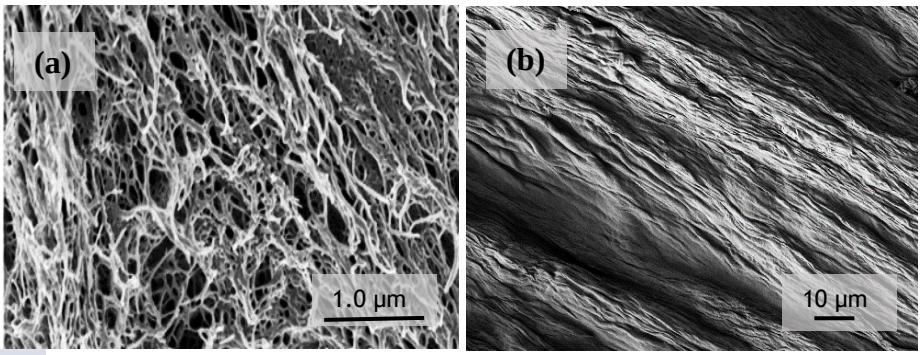
The peak corresponding to Fe-O, initially at 565 cm^{-1}, appears shifted to 595 cm^{-1} and slightly widened due to the effect of binding with the cellulose nanofibers. In the case of microfibers F4N and F5N, the Fe-O peak is negligible due to the low concentration of Fe_3O_4 NPs present (10, 5 %) in comparison to TOCNF (20 %), respectively. However, in the IR spectra of the magnetic solutions (without alginate), the peak Fe-O is noticeable (Figure A2.3b). The diffraction spectra of both magnetic microfibers and TOCNF are shown in Figure 3.5b.

Two diffraction peaks are observed at 2Θ=16.0° and 22.3° in the X-ray diffractogram of TOCNF correspond to the diffraction planes (101) and (002) diffraction cellulose crystals respectively [374]. These peaks are also present in the diffractogram of the magnetic microfibers, revealing the presence of cellulose crystals with different intensities.

For instance, the main peak at 22.3° is more visible in those microfibers with a TOCNF shell, while in the remaining microfibers, a shallow broader peak is observed. The same pattern can be observed in the diffractogram of the magnetic solutions with and without sodium alginate (Figures A2.3a and A2.3b). This implies that the preparation process and the incorporation of Fe_3O_4 NPs do not influence the crystal structure of TOCNF present in the magnetic microfibers. Moreover, the diffractogram of the magnetic microfibers shows diffraction peaks at 2Θ= 30.1, 35.2, 43.2, 57.3, and 62.6° corresponding to the (220), (311), (400), (511), and (440) crystallographic planes of Fe_3O_4 (ICDD: 98-015-8743) with a relative intensity that correlates to the content of Fe_3O_4 NPs in the magnetic microfibers.

However, the diffraction peaks of Fe_3O_4 in the magnetic microfiber F2@TS have median relative intensity, whereas, in the microfibers F3N, F4N and F5N have low intensity becoming almost negligible in the last two, revealing the low crystalline quality and small size of the formed NPs. One possible explanation for this was the lack of homogeneity in some microfibers and the formation of agglomerates during the synthesis of the F3N, F4N, and F5N nanoparticles due to inhomogeneous TOCNF solution.

The nanofibrils of TOCNF tend to aggregate during the drying process, as can be observed in the SEM image of TOCNF in Figure 3.6a, showing an agglomerated matrix of isolated fibrils. However, after the spinning procedure, a strong cross-linking between the Ca(II) cations (from the coagulation bath) with the TOCNF nanofibrils resulted in the formation of dense and ridge sheets at the microfibers with a TOCNF shell.



USC UNIVERSIDADE

Figure 3.6. SEM image of TOCNF (a) and higher magnification SEM image of microfiber with TOCNF shell (b).

The SEM image of Figure 3.6b shows a substantial cross-linking of TOCNF nanofibrils that led to a densely packed microfiber with a rough surface. SEM-EDX was used to analyse the surface and cross-section of the microfibers to gain more insight into the magnetic nanoparticle's distribution within the cellulose nanofibrils of TOCNF.

The presence of TOCNF in the core and shell of the microfibres modified the structure of the materials. The SEM images in Figures 3.7a,b,e,f illustrate the surface morphology of the microfibers F1N and F1@TS (shell of TOCNF) with the respective cross-section and their elemental analysis Figure 3.7c,d,g,h. The surface morphology of both microfibers is quite similar based on porosity due to the presence of TOCNF in the core and shell.

In contrast, when comparing the SEM images of F2N (with no TOCNF) and F2@TS in Figures 3.8a,b,c,d the surface of the first microfiber is smoother and more homogeneous than the second microfiber, which reveals a rougher and more porous surface. In several studies, TOCNF has been incorporated to enhance the porosity of materials [371, 372].

For this reason, the apparent morphological differences observed between F1N and F2N microfibers are explained. The high magnification SEM images of the surface mapping and elemental analysis (Figure A2.5) reveal a higher surface content of Fe on the microfibers F1N and F2N than in the F1@TS and F2@TS microfibers. This indicates that TOCNF was uniformly arranged around the magnetic solutions in the F1@TS and F2@TS microfibers. The cross-section SEM images revealed that all microfibers have a spherical shape, and some deformation is observed due to the microfibers cryo-cutting procedure in liquid N_2.

The elemental analysis of the cross-sections revealed a heterogeneous dispersion with a higher presence of Fe in the inner structure and C on the outer surface of F1N than in F2N microfiber, while both elements are well distinguished and separated in the core@shell microfibers. The same analysis was undertaken on the microfibers with different concentrations of Fe_3O_4 NPs (25, 10, 5 wt %), namely F3N, F4N, and F5N, respectively, as shown in Figure 3.9.

USC UNIVERSIDADE DE SANTIAGO DE COMPOSTELA

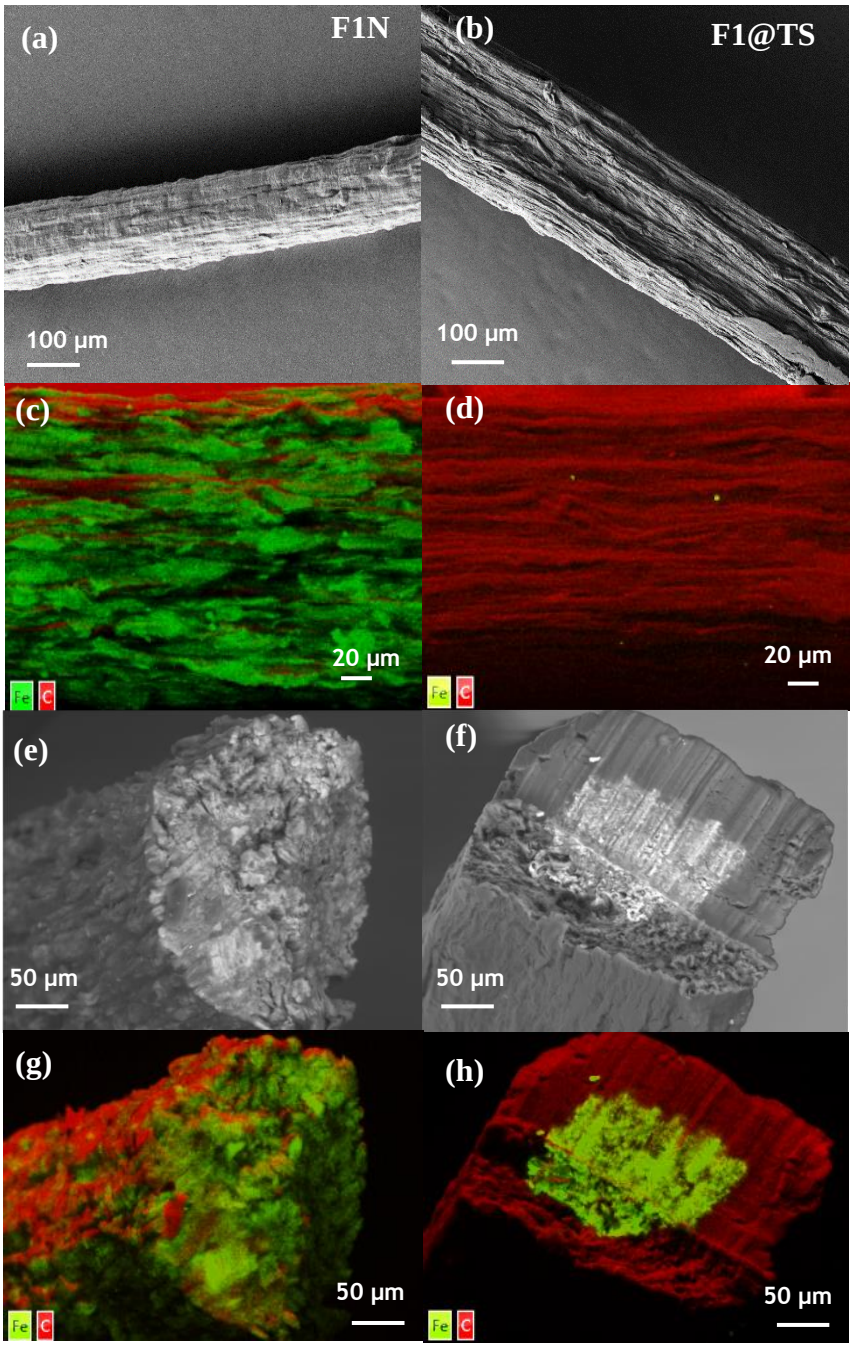


Figure 3.7. SEM images (a, b, e, f) and elemental mapping (c, d, g, h) of the surface and cross-section of the microfibers F1N and F1@TS, respectively.

USC
UNIVERSIDADE DE SANTIAGO DE COMPOSTELA

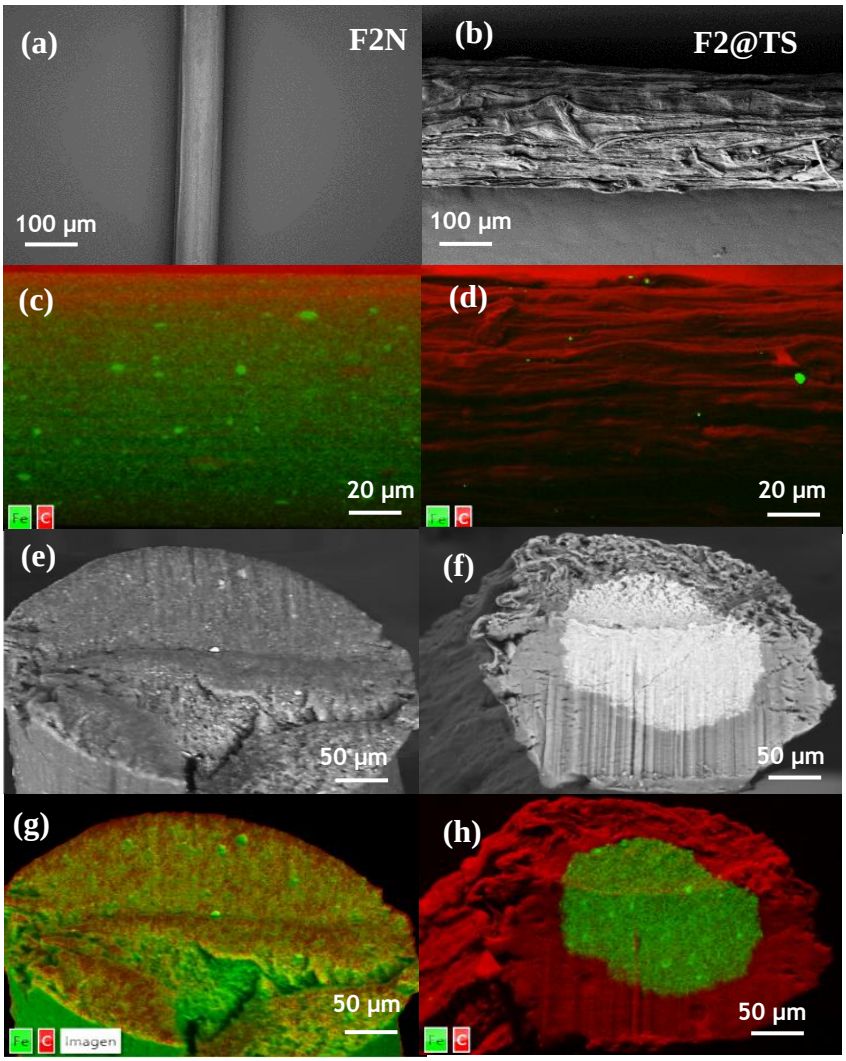


Figure 3.8. SEM images (a, b, e, f) and elemental mapping (c, d, g, h) of the surface and cross-section of the microfibers F2N and F2@TS.

The images obtained from the elemental mapping analysis illustrated a decrease in the presence of Fe (related to the Fe_3O_4 NPs presence) on the surface and cross-section corresponding to microfibers F3N, F4N, and F5N, whose respective iron weight percentages were determined by EDX analysis revealed was 3.7, 0.8, 0.4 % (Figure A2.6). It was not observed any irregularity or modification on the surface of the microfibers due to the different content of MNPs.

USC
UNIVERSIDADE DE SANTIAGO DE COMPOSTELA

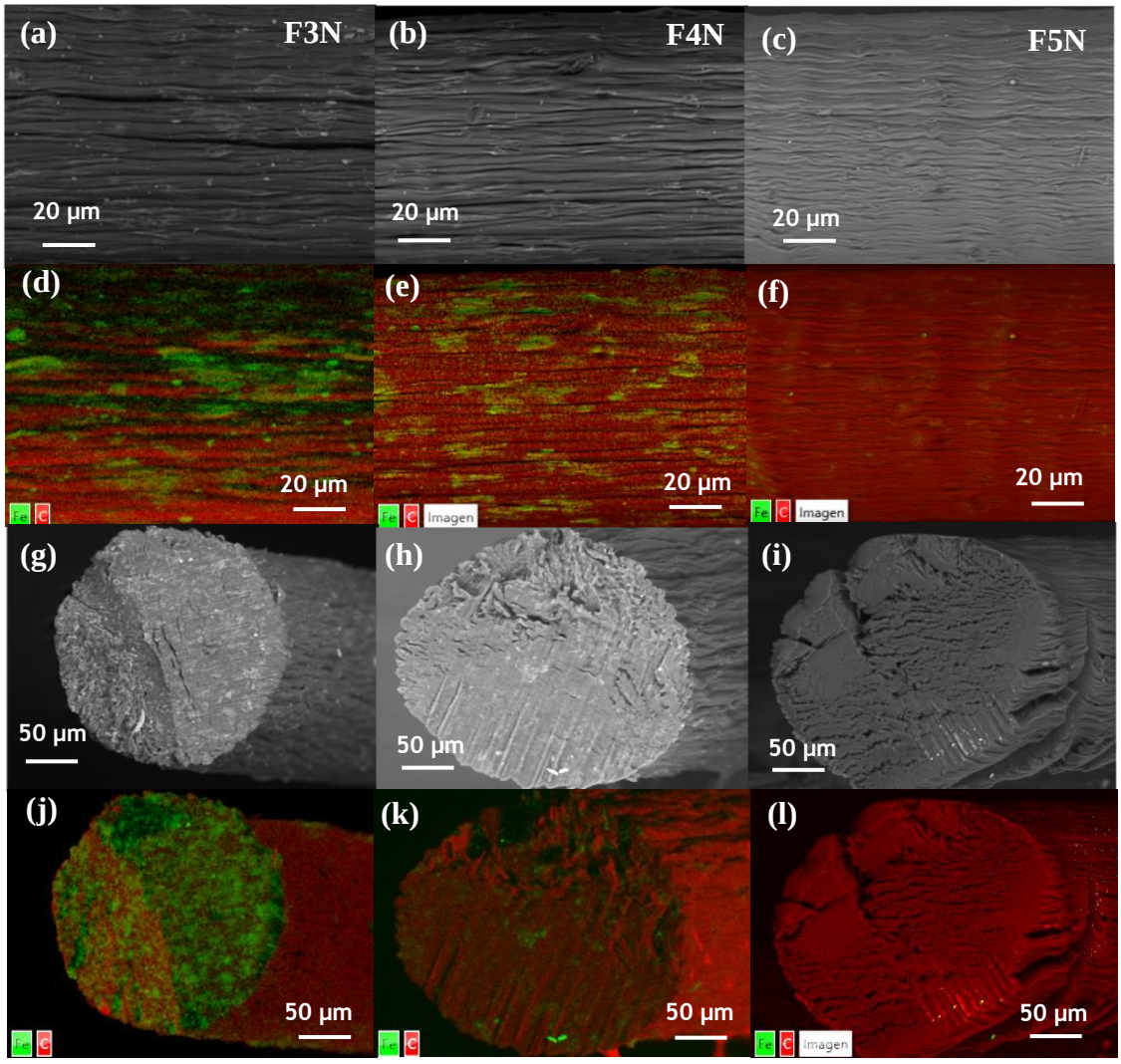


Figure 3.9. SEM images of surface (a, b, c) and cross-sections (g, h, i) with respective elemental mapping of the surface (d, e, f) and cross-sections (j, k, l) of the microfibers F3N, F4N and F5N, respectively.

With the help of an optical profilometer, different surface topography features have been determined from 2D surface measurements (Figure 4.0) performed on the microfibers (F1N, F1@TS, F2N, and F2@TS). Areas of about 0.8 mm^2 from different locations of the samples were scanned, and height variations were recorded. The height and the roughness of the profile were determined by ISO 4287:1997.

Figure 4.0 shows that the topography of simple (F1N, F2N) and core@shell (F1@TS, F2@TS) magnetic microfibres is appreciated by a colour pallet, and some of the roughness parameters calculated for this study are presented in Table 3.3.

USC UNIVERSIDADE DE SANTIAGO DE COMPOSTELA

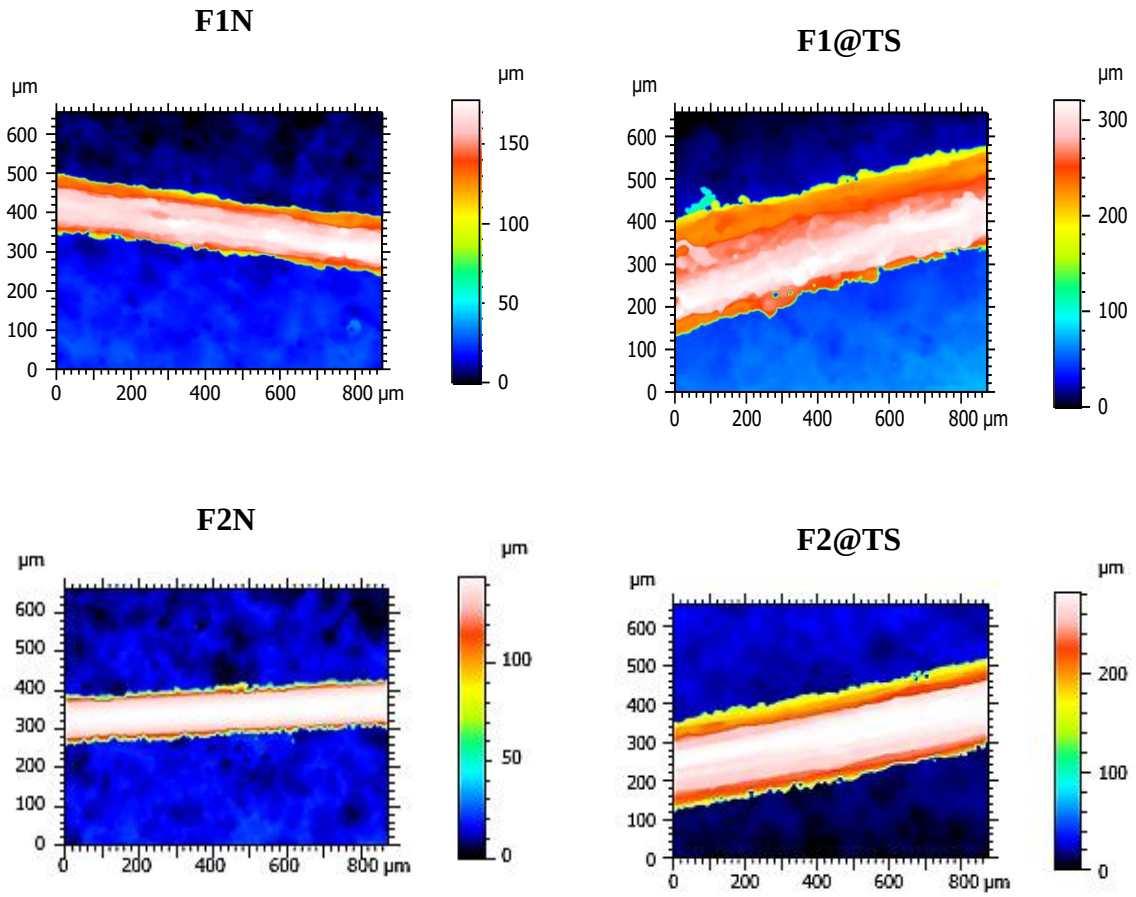


Figure 4.0. Topography images of the microfibers F1N, F1@TS (TOCNF shell), F2N and F2@TS (TOCNF shell).

The total height of the profile, R_t, is calculated as the sum of the maximum peak height and valley depth within the evaluation length. In addition, the root mean squared of the surface roughness, R_q, is calculated as the standard deviation of the height distribution over the evaluation length [376].

Table 3.3, shows R_t and R_q compiled values for core and core@shell microfibers, and showed that the microfibers with a TOCNF shell, as expected, presented a larger thickness than the ones without a TOCNF shell. This result, is a further confirmation, together with the SEM characterization, that the spinning procedure used to produce core@shell microfibers is a facile and successful way to obtain complex microfibers.

More specifically, the height profiles and 3D images in Figure 4.1, show that core@shell microfibers double their dimensions compared to single microfibers.

USC
UNIVERSIDADE DE SANTIAGO DE COMPOSTELA

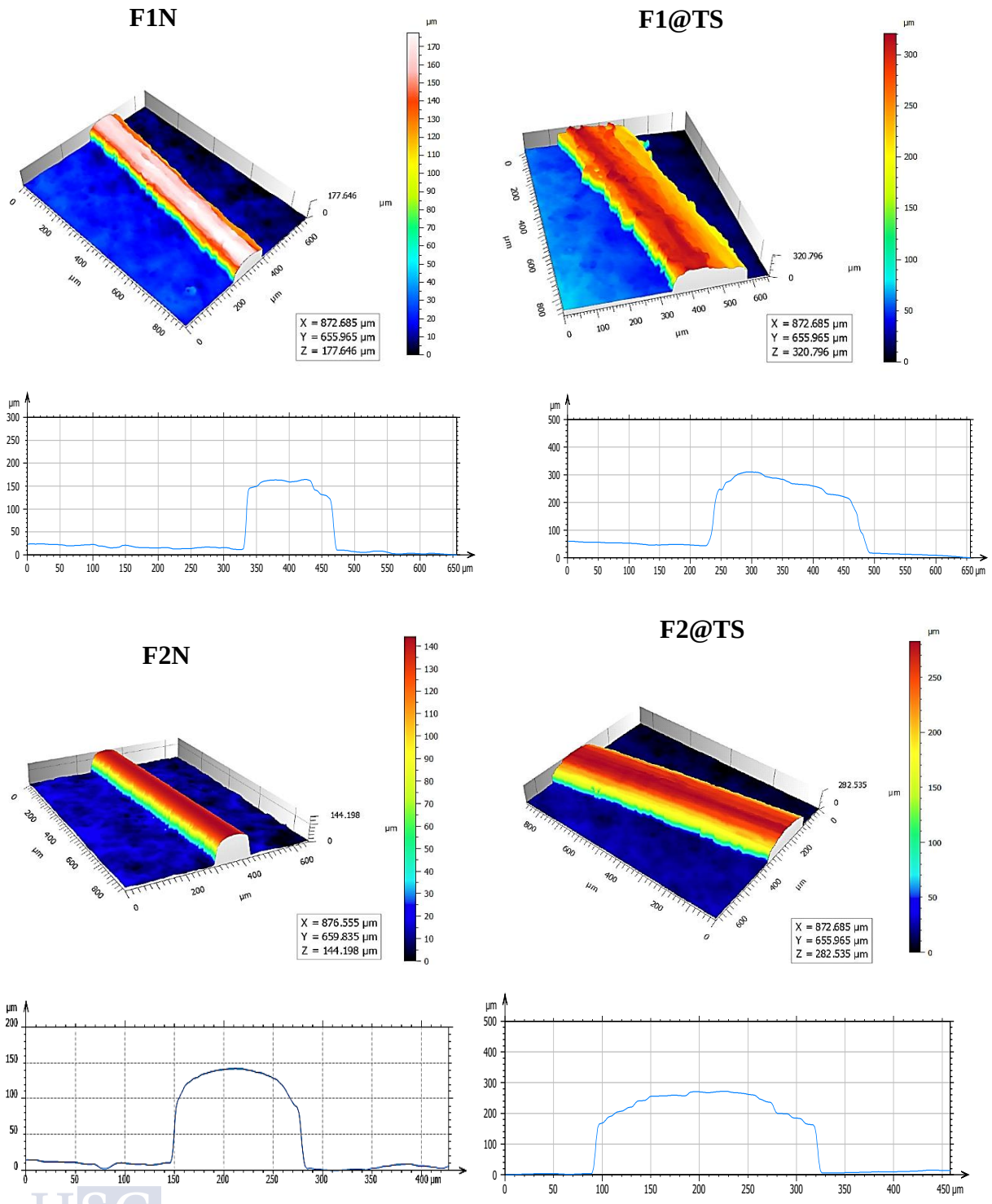


Figure 4.1. Roughness 3D images and respective height profile of the microfibers F1N, F1@TS, F2N and F2@TS.

The roughness of the microfibres defined by R_q shows that the addition of a TOCNF shell nearly doubles the roughness of both microfibres compositions. In addition, the skewness (R_{sk}) and kurtosis (R_{ku}) have been also determined to obtain additional textural information about the height distribution and the geometry of the peaks and valleys [377].

The microfibers F1N, F1@TS and F2N have negative values of R_{sk} which reveal a surface with deeper valleys than peaks, while the opposite is observed on the F2@TS microfiber. It seems that the microfibers with *in-situ* Fe_3O_4 NPs (F1N and F1@TS) have an even height distribution compared to the microfibers F2N and F2@TS. The analysis of R_{ku}, reveals the peaks or valleys geometry of the samples and shows that when a TOCNF shell is incorporated (F1@TS and F2@TS), the height distribution of the microfibers becomes more even or uniform (R_{ku}<3), while in the microfibers F1N and F2N the surface is sharper (R_{ku}>3).

Besides surface topography and morphology, the thermal behaviour of a material is a crucial factor in determining its thermal stability under conditions of high temperature, which is usually estimated by weight loss [378]. TGA is a reliable technique used to determine the thermal behaviour, weight loss, and thermal degradation of materials with temperature [379]. Figures 4.2a and 4.2b shows the TGA curves of the reference microfibers (RF1, RF2, RF1@TS, and RF2@TS) and of the magnetic microfibers (F1N, F1@TS, F2N and F2@TS), respectively.

Table 3.3. Profile roughness parameters of the microfibers.

Microfibers	R_t (µm)	R_q (µm)	R_{ku} (µm)	R_{sk} (µm)
F1N	120.44	27.34	3.31	-0.277
F1@TS	162.08	43.37	2.45	-0.356
F2N	64.30	9.97	3.84	-0.619
F2@TS	122.9	16.22	2.67	0.286

The thermal degradation in the oxidative atmosphere of the microfibers exhibits a three-stage decomposition. The first one (from 37 to 250 °C) corresponds to the microfibers water loss and other volatile components. The main weight loss in the second stage was between 250- 450 °C. In microfibers F1N and F1@TS, the weight loss at this stage is attributed to the complex degradation of glycoside chains present in the structure of alginate-nanocellulose: depolymerization, dehydration, and decomposition of the glycosidic units [380].

USC UNIVERSIDADE DE SANTIAGO DE COMPOSTELA

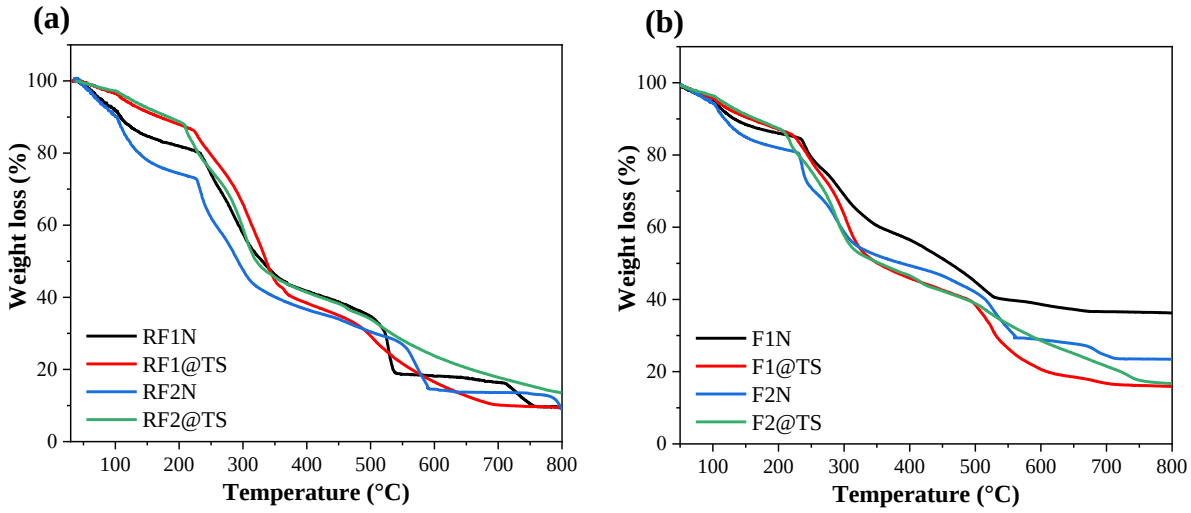


Figure 4.2. TGA curves of the reference microfibers (a) (without MNPs) and the magnetic microfibers (b) F1N, F1@TS, F2N and F2@TS.

On the other hand, in the F2N and F2@TS microfibers, which are only composed of Fe_3O_4 and sodium alginate, the weight loss was caused by the alginate breaking backbone, and above 300 °C, the material decarboxylated and formed CO_2. It was noted great thermal stability of the magnetic microfibers compared to the reference microfibers after being heated at 800 °C. Also, the influence of the *in-situ* synthesis of Fe_3O_4 NPs onto TOCNF against its absence on the thermal stability of the microfibers was clearly enhanced. The total weight loss reported was 35.8, 15.7, 23.45, and 16.69 % for F1N, F1@TS, F2N, and F2@TS, respectively (Table A3.0).

The microfibers F1N and F1@TS (*in-situ* Fe_3O_4 NPs) had higher thermal stability than the F2N and F2@TS microfibers due to the strong interactions between the Fe_3O_4 NPs and TOCNF. Similar interactions and thermal stability were observed in other studies incorporating metal oxides onto BNC nanocomposites [366, 378]. The incorporation of MNPs into nanocellulose can open a window of opportunities to develop nanomaterials for ferromagnetic applications, such as magnetic resonance imaging (MRI) [360].

The magnetization of the microfibers and magnetic solutions was determined with a vibrating sample magnetometer from -10 kOe to 10 kOe at room temperature. To avoid errors in the magnetic determination due to heterogeneous magnetic content within the chosen microfiber's samples, all magnetic solutions and microfibers were milled. Posteriorly the solid magnetic content was determined with precision by TGA, and the magnetization results were normalized to the amount of solid magnetic content.

The magnetization parameters, reported in Tables A3.1 and A3.2, and the magnetization curves of the milled and not milled samples are shown in Figure 4.3. The milled samples are more homogeneous resulting in a more precise determination of the microfibers magnetization. It was observed a decrease in the saturation magnetization (M_s) of the microfibers compared to the respective magnetic solutions and also revealed a lower magnetization of the magnetic solution, SA/T/Fe25, compared to the Fe_3O_4 NPs prepared *ex-situ* (Fe25). A further reduction was as well observed when comparing the magnetic solutions with and without sodium alginate presence.

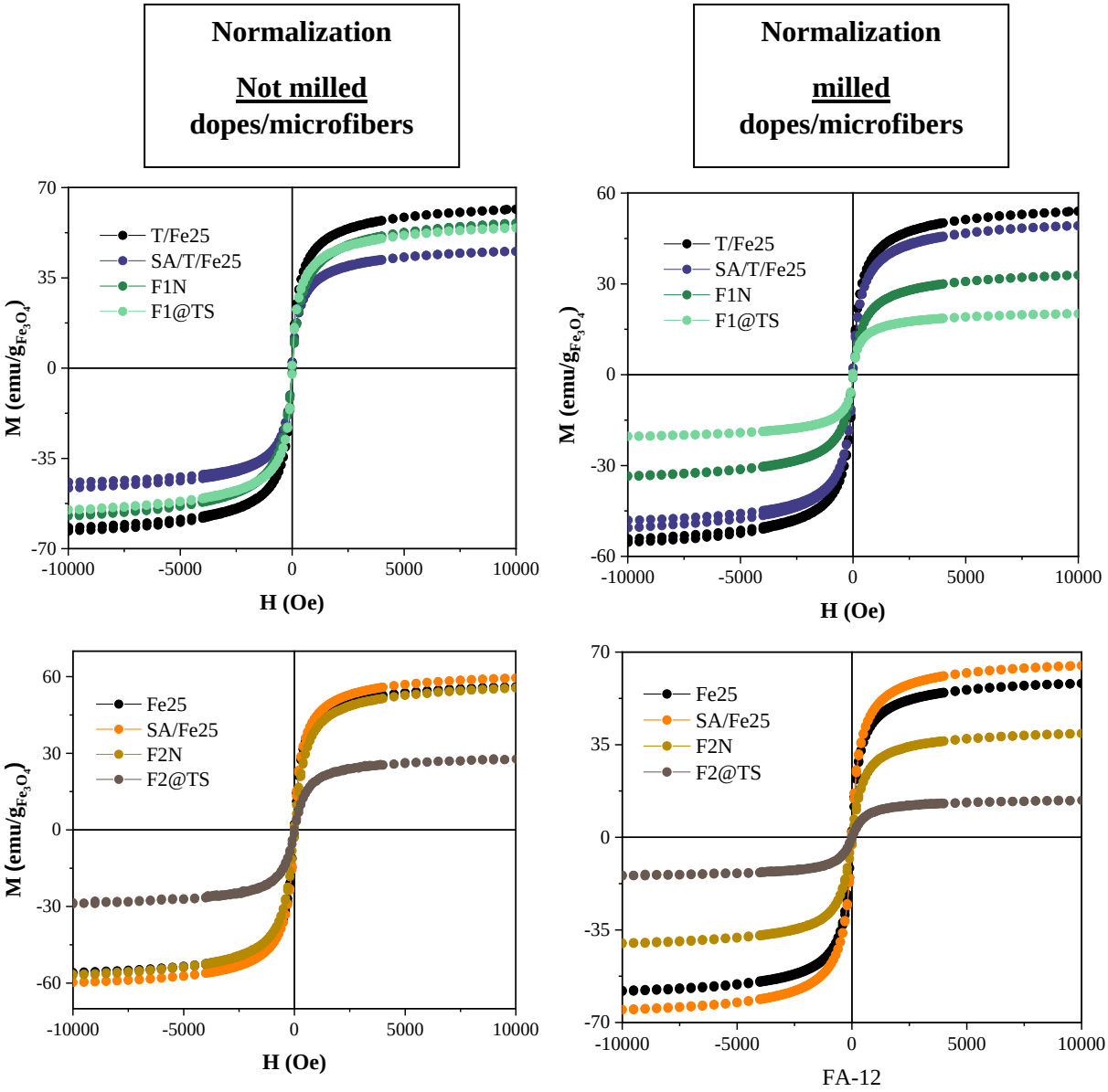


Figure 4.3. Magnetization curves normalized with the magnetic solid content of the magnetic solutions and microfibers (milled and not milled).

The reduction in magnetization observed in Fe_3O_4 NPs bonded to TOCNF and sodium alginate for the different samples is in concordance with previous studies that reflect similar variations and attribute it to the effect of the encapsulation of MNPs either by sodium alginate or nanocellulose [381–383]. Another important fact to state is the negligible remnant and coercive magnetization values obtained in the *in-situ* magnetic solutions and respective microfibers confirming their superparamagnetic behaviour.

Due to the small size of the precipitated Fe_3O_4 NPs, as shown previously in the TEM images above. The magnetic behaviour of the microfibers F3N, F4N, and F5N with different concentrations of Fe_3O_4 NPs (25, 15, and 5 %) were also studied and shown in Figure 4.4. In this particular case, it was shown a reduction of the magnetization for those samples with smaller amounts of Fe_3O_4 NPs. The microfibers F1N and F3N have the same ratio of Fe_3O_4 NPs, but both have distinct magnetism. The only difference was the chosen precipitating agent

used in the synthesis, where the NPs in F1N were prepared with NH_4OH and the ones in F3N with NaOH.

In previous studies, it was stated that the M_s of a sample is larger when the particle size of Fe_3O_4 NPs is increased [384, 385]. Contrarily, in this study, the NPs with higher M_s have a smaller size (F1N). This result could be attributed to the surface spin of Fe_3O_4 NPs caused by the polymer modification and the use of NH_4OH (a weak base), which produced a smaller number of Fe_3O_4 cores with higher crystallinity. Furthermore, as observed in X-ray diffractogram, the peak intensity of Fe_3O_4 in the microfibers F3N, F4N, and F5N was low, which led us to believe, that pure Fe_3O_4 NPs were not formed, therefore explaining this low magnetization observed.

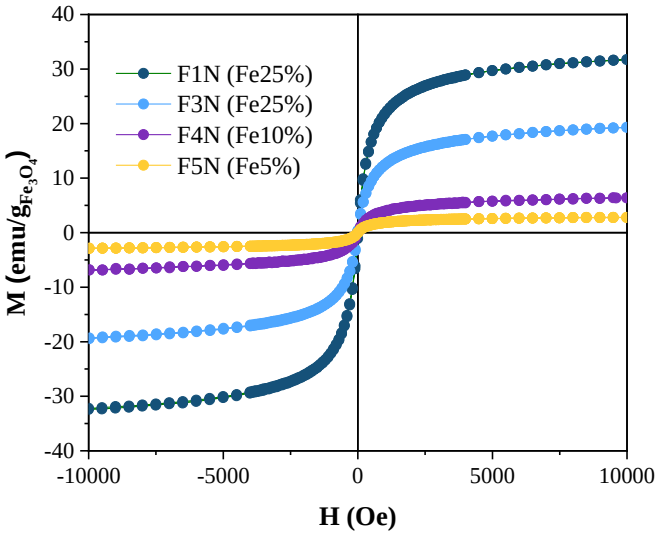


Figure 4.4. Magnetization curves of the microfiber F1N, F3N, F4N and F5N (normalized milled values).

Tensile measurements were carried out to investigate the effect of the biopolymer's composition (sodium alginate, TOCNF), the configuration (core, core@shell), and the Fe_3O_4 NPs content on the mechanical properties of the microfibers. Tensile stress (σ)-strain (ε) curves and Young's modulus of the reference and magnetic microfibers are shown in Figure 4.5.

USC UNIVERSIDADE DE SANTIAGO DE COMPOSTELA

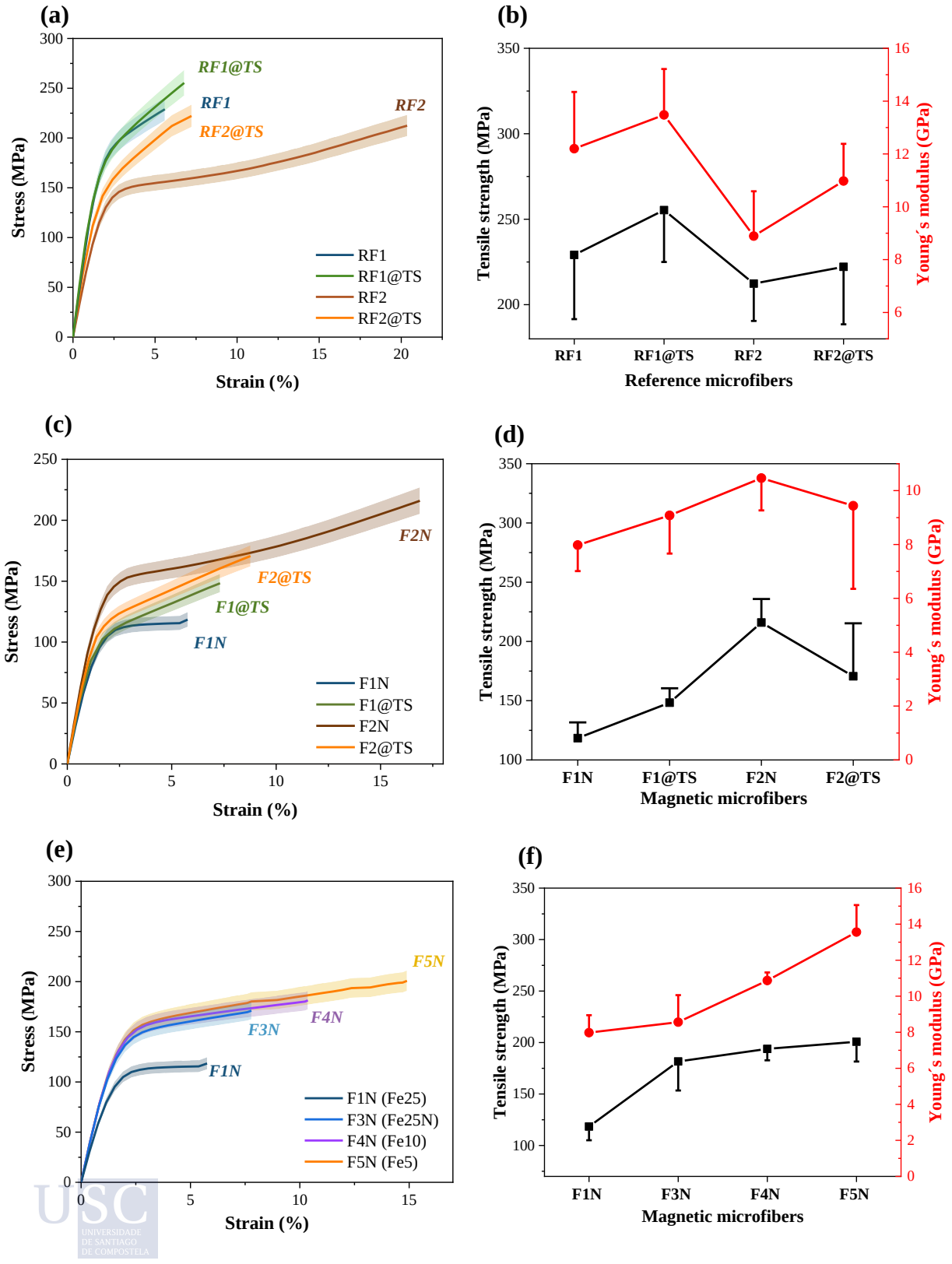


Figure 4.5. Stress–strain curves of reference (a) and magnetic microfibers (c, e) (standard deviations are highlighted around the curves). Tensile strength and young's modulus of reference (b) and magnetic microfibers (d, f).

The reference microfibers, with no inclusion of Fe_3O_4 NPs, present tensile strength ranging from 210 to 255 (MPa), Young's modulus from 10 to 13 (GPa), and a strain at break from 6 to 19 %, which are reportedly higher than the ones obtained for the magnetic microfibers, as illustrated in Figures 4.5a,b,c,d.

This behaviour is in accordance with a general rule of microstructural robustness in nanocomposites, where the presence of NPs imparts points of fragility within the microstructure of composite materials [386]. On the other hand, the composition of the biopolymeric matrix in undoped or doped materials has a crucial role in strengthening the robustness of the structure in a non-predictable way, depending on the specific chemical compatibility established among all the nanocomposite components [387].

The core reference microfibers were prepared using only SA (RF2) or a mixture of SA/TOCNF (RF1) and to the core@shell microfibers (RF1@TS, RF2@TS) was added a TOCNF shell. The tensile stress (σ)-strain (ε) curves and Young's modulus of the reference microfibres prepared with SA (RF2, RF2@TS) are weaker than those containing TOCNF (RF1, RF1@TS) as part of the core mixture, which enhances the mechanical stability of the reference microfibres and decreases the strain at break. This observation is in concordance with some results reported in literature where alginate films remarkably improved their mechanical and swelling properties when doped with nanocellulose and resulted in a flexible, strong material for wound dressing and drug delivery [360, 366]. The inclusion of MNPs on both core and core@shell microfibers produces a general decrease in their mechanical properties compared to the reference microfibers, as shown in Figures 4.5c and 4.5d.

However, it has to be highlighted that the best performing microfibers are the ones carrying only sodium alginate as biopolymer in the core (F2N and F2@TS), contrary to what was expected from the results obtained in the reference microfibers. The tensile strength of F2N almost doubles that of F1N, σ_{F2N}=216 (MPa) >σ_{F1N}=118 (MPa), and the addition of a TOCNF shell has a contradictory role, increasing the quality of F1N, $\sigma_{F1@TS}$=148 (MPa), but decreasing the quality of the alginate core F2N, $\sigma_{F2@TS}$=171 (MPa). The same behaviour was observed at the Young's modulus where magnetically doped sodium alginate core microfibres showed higher results E_{F2N}=10 GPa> $E_{F2@TS}$=9 GPa≈ $E_{F1@TS}$=9 GPa> E_{F1N}=8 GPa.

The incorporation of Fe_3O_4 NPs, decreases the toughness, tensile strength, and Young's modulus but the strain at break slightly increases for the magnetic microfibers with TOCNF shell, F1@TS, and F2@TS, respectively. This evident decrease may be explained by the lack of strong covalent/hydrogen bonds occurring between the NPs and -OH groups of cellulose and sodium alginate, which explains the decreased toughness and chain mobility, therefore reducing the strength of the microfibers, as contrarily reported elsewhere [366]. Adding TOCNF or MNPs imparts new functionalities to the hybrid microfibers, compensating mainly for the loss of mechanical quality, turning it into an optimum material for, i.e., magnetic remote control and magnetic hyperthermia or electric conduction.

The effect of mechanical weakening when adding NPs to the nanocomposite is evidenced in Figures 4.5e and 4.5f, where the microfibers with the same biopolymeric composition (SA + TOCNF) are prepared with different concentrations of Fe_3O_4 NPs. By increasing the content of Fe_3O_4 NPs from 5 to 25 %, the Young's modulus and tensile strength of the microfibers decrease from 14 to 9 GPa and from 201 to 118 MPa, respectively (Table A3.2). Also, the strain at break and toughness decreases from 18 to 8 % and from 23 to 15 %, respectively.

This decrement can be explained by the weak interactions between the NPs and TOCNF/alginate and a diminished number of crosslinking points within the biopolymer

network interrupted by the presence of the NPs thus limiting the formation of a robust network. Nonetheless, there is an improvement in the mechanical properties of microfiber F3N compared to the microfiber, F1N, where the main difference between both is the reducing agent, NaOH, and NH_4OH, respectively used to synthesize the NPs. More studies are needed to explain this behaviour and the optimum concentration of Fe_3O_4 NPs to improve the mechanical requirements for specific applications.

USC
UNIVERSIDADE
DE SANTIAGO
DE COMPOSTELA

3.3. Fabrication of flexible magnetic cellulose acetate films

Biodegradable polymeric materials are being developed to replace non-biodegradable synthetic polymers (e.g., plastics) more cost-effectively, providing both economic and environmental advantages to society. Cellulose, a natural biopolymer, is being used in its derivative form to produce biodegradable food packaging films [388] and anti-counterfeiting tags [389]. Cellulose acetate is an insoluble biodegradable, nontoxic polymer with antimicrobial properties and mechanical strength among the cellulose derivatives.

Cellulose acetate is widely used in a broad field of applications, among them in fabricating biodegradable films with high toughness, heat resistance, and optical properties for food packaging. In literature, it has been reported that incorporating customized NPs, increases the thermal stability of films [390] and provides counterfeit identification abilities [391] for tagging products.

In this work, different MNPs were incorporated into cellulose acetate matrix to produce magnetic films with various magnetic performances for food packaging and tagging applications. To this end, MNPs with different compositions, morphology, size, and the magnetic response were prepared, such as iron carbide (Fe_5C_2), hexagonal and multicore-Fe_3O_4 NPs. The chosen NPs are great candidates for achieving interactions by ionic and covalent bonds with the -OH and -C=O groups present in the cellulose acetate chain, ensuring a suitable bonding among organic and inorganic components. Besides this, Fe_3O_4 NPs have excellent superparamagnetic behaviour, high chemical stability, and low toxicity. Meanwhile, Fe_5C_2 NPs have excellent magnetic stability [392], where the presence of carbon atoms enhances an excellent chemical inertness and mechanical strength for their use in metallic alloys and hard coatings [393].

3.3.1. Magnetic cellulose acetate films: Materials and Methods

a. Synthesis of Iron carbide (Fe_5C_2), hexagonal-shaped (Fe_3O_4@OA) and multicore magnetite (*m*-Fe_3O_4) NPs

Fe_5C_2 NPs were prepared according to the method described [394] . Briefly, 7.0 g of octadecylamine, 0.8 g of cetrimonium bromide (CTAB), and 2 mL of oleylamine (OA) were mechanically stirred and heated to 180 °C under Ar flow. Afterwards, 0.2 mL of $Fe(CO)_5C_2$ (1.5 mmol) was added. The reaction was left agitating for 10 min at 180 °C, and then the temperature increased to 350 °C and was kept agitating for 30 min (M1). It was kept agitating for 60 min (M2) in another procedure. Both solutions were left to cool down and washed with ethanol and hexane to remove any octadecylamine excess. The Fe_5C_2 NPs, were labelled as M1 and M2 and redispersed in hexane until further use.

MNPs coated with oleic acid (Fe_3O_4@OA) were also prepared following the method described [395]. Briefly, 0.70 g of acetylacetonate was added to a previous mixture of 1.10 g and 10.4 g of oleic acid and benzyl ether, respectively. The solution was mechanically stirred for 1 h at 25 °C and then at 300 °C for 30 min. After cooling, a previously prepared solution of toluene and hexane was added, to precipitate the hexagonal shaped Fe_3O_4, which was labelled as M3. NPs were washed by centrifugation using chloroform.

Lastly, the multicore magnetite (*m*- Fe_3O_4) NPs were prepared by the solvothermal method, as described [396], with minor modifications. It was added to 30 mL ethylene glycol (EG), 1.5 g $FeCl_3.6H_2O$, 1.0 g polyvinylpyrrolidone (PVP 40), and 2.0 g of sodium acetate anhydrous (NaAc). The mixture was stirred for 2 h and autoclaved for 8 h at 200 °C. The

product solution was cleaned with ethanol, and the synthesized *m*-Fe_3O_4 NPs were dried at 60 ºC previously to their use. These NPs were named M4. All NPs were fully characterized by FTIR, XRD, TGA, TEM, SEM, and VSM (Appendix 6.1).

b. Production of the magnetic cellulose acetate films

The magnetic cellulose acetate (CA) films were prepared by the solvent casting method. Firstly, 8 g of cellulose acetate (Mn~50.000) was added to 100 mL of acetone. Then, 0.4 g of pyromellitic dianhydride (PMDA, purity ≥ 97 %) was added to 40 mL of the previously prepared CA solution.

At this stage, the agitation speed is increased (500 rpm) for a faster PMDA dissolution, and once the mixture has been homogenized, the rate is decreased (150 rpm) to avoid the formation of air bubbles. CA Solutions were prepared with MNPs (Fe_5C_2, hexagonal Fe_3O_4, and *m*-Fe_3O_4) concentrations ranging from 0.005 to 0.2 %. After complete dissolution and dispersion of NPs, 20 µL of triethylamine (TEA, purity ≥ 99 %) was added to each solution and stirred for 1-2 min. The final magnetic solution was poured into a petri-dish with different diameters (D_1= 13.5 cm and D_2= 9 cm) and covered with parafilm. After 24 h, the parafilm was removed, and the films were left to dry for approximately 48 h before their removal from the petri-dish.

The magnetic films were labelled after the NPs and respective concentrations, as shown in Table 3.4. The topography, magnetic behaviour, mechanical strength, colour change, and solubility in water were some of the parameters analysed.

Table 3.4. Films composition and parameters

Concentration MNPs (%)	Film-M1 (Fe_5C_2)	Film-M2 (Fe_5C_2)	Film-M3 (hexagonal Fe_3O_4)	Film-M4 (*m*-Fe_3O_4)
0.005	-	FM2Fe0.005	-	-
0.02	FM1Fe0.02	FM2Fe0.02	FM3Fe0.02	FM4Fe0.02
0.1	FM1Fe0.1	FM2Fe0.1	FM3Fe0.1	FM4Fe0.1
0.2	-	FM2Fe0.2	-	-

USC UNIVERSIDADE DE SANTIAGO DE COMPOSTELA

c. Relevant parameters for packaging methodologies

Moisture content and water solubility

The sensitivity of the films to water was analysed through the determination of moisture content (MC) and water solubility. MC refers to the weight of water contained in a material. It is essential to consider this parameter to ensure the quality of food products before consumption because moisture content can affect the shelf life, physical and chemical aspects of food stored for an extended period.

Therefore, an accurate determination of the MC is a key parameter used in many industries to ensure product quality. In this study, the MC of the magnetic films was determined by the following method [397]. Briefly, five replicates of approximately 50 mg of each film were cut and acclimatized at a relative humidity of 55 % for 24 h. Afterward the films replicates were weighted, posteriorly dried at 105 °C for 24 h, and finally weighted to calculate MC using the following equation (4):

$$Moisture\ content\ (\%) = \left(\frac{M_i - M_f}{M_i}\right) * 100 \quad (4)$$

where, M_i and M_f are the masses of initial (before dried, acclimatized) and dried films (mg), respectively.

The same replicates used in the moisture content experiment were used in the solubility experiment to see if films have good water insolubility, which is a requirement for most food packaging applications [398]. The solubility of the magnetic films was determined by immersing the five dried replicates (S_i) in 50 mL of water for 24 h under magnetic agitation (700 rpm) at 20 ºC. In the end, the remaining insolubilized film replicates were dried at 105 °C for 24 h and weighed (S_f) to determine the dry matter that was not solubilized in water. The percentage of water solubility of the films was calculated following the equation (5):

$$Solubility\ (\%) = \left(\frac{S_i - S_f}{S_i}\right) * 100 \quad (5)$$

Opacity and colour

The CIElab scale was used to determine the colour parameters (L*, a*, b*). In this sense, L* indicates the lightness (which ranges from black to white) and a* (reveals the difference in green (-a*) and red (+a*)) and b* (difference between blue (-b*) and yellow (+b*)) are the chromatic parameters [399]. The colour parameters were obtained by using a Minolta colorimeter in three replicates of each film. The films were superposed on a white standard background, and a set of colour coordinates were given for each replicate. The total difference value (ΔE) was determined following the equation (6):

$$\Delta E = (\Delta L^2 + \Delta a^2 + \Delta b^2)^{0.5} \quad (6)$$

USC UNIVERSIDADE DE SANTIAGO DE COMPOSTELA

where, $\Delta L = L_{standard} - L_{sample}$; $\Delta a = a_{standard} - a_{sample}$; $\Delta b = b_{standard} - b_{sample}$. The standard values used were the ones from the control films. The opacity percentage was also determined according to the Hunterlab method [400], following the equation (7):

$$Opacity\ (\%) = \frac{Y_b}{Y_w} * 100 \quad (7)$$

Where, Y is the CIE tristimulus value of the film on a black standard (Y_b) and on a white standard (Y_w). It was taken three measurements per film.

3.3.2. Magnetic cellulose acetate films: Results and discussion

The TEM images of the synthesized magnetic nanoparticles are shown in Figure 4.6. Fe_5C_2 NPs with different mean sizes are presented in Figures 4.6a (M1) and 4.6b (M2), and Fe_3O_4 NPs with hexagonal (M3) and multicore configuration (M4) in Figure 4.6c and 4.6d, respectively.

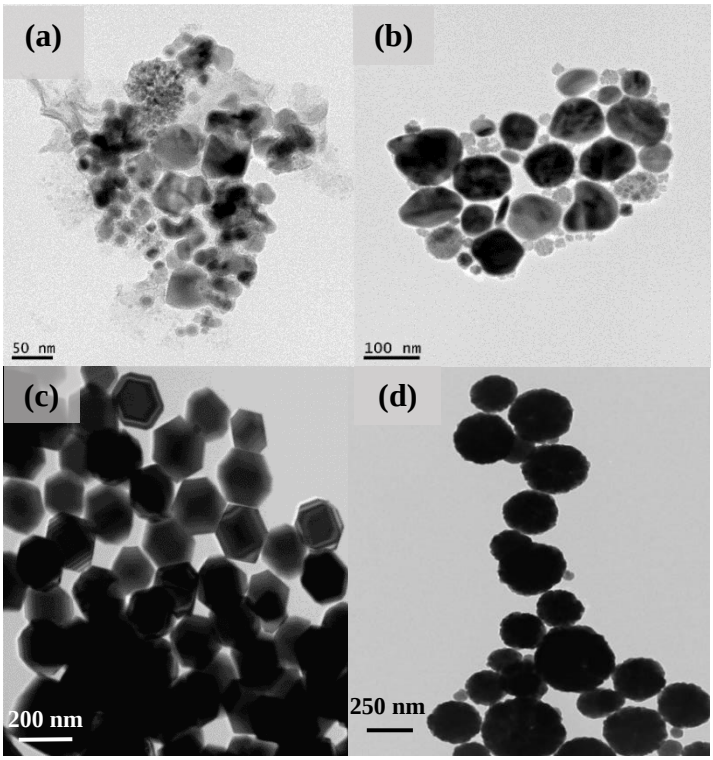


Figure 4.6. TEM images of MNPs: (a) Fe_5C_2 (M1), (b) Fe_5C_2 (M2), (c) hexagonal Fe_3O_4 (M3) and (d) multicore Fe_3O_4 (M4), respectively

The magnetic Fe_5C_2 NPs reveal a broad size distribution and heterogeneous morphology. Moreover, is clearly visible a higher heterogeneity in the as-synthesized Fe_5C_2 NPs (M1) with a size distribution around 50 nm. Meanwhile, the Fe_5C_2 (M2), with a mean diameter of around 100 nm, presents a spherical-like shape due to the longer synthesized reaction time [394]. The TEM image (Figure 4.6c) revealed a hexagonal like-structure of the as-synthesized Fe_3O_4 NPs with and uniform diameter of 140 nm. The TEM image (Figure 4.6d) of the multicore-Fe_3O_4 NPs revealed that each nanoparticle consists of many magnetic cores with a final spherical structure and size diameter of approximately 250 nm. The structural and textural properties of

the NPs were analysed by XRD and FTIR. The diffraction and infrared spectra are shown in Figure 4.7.

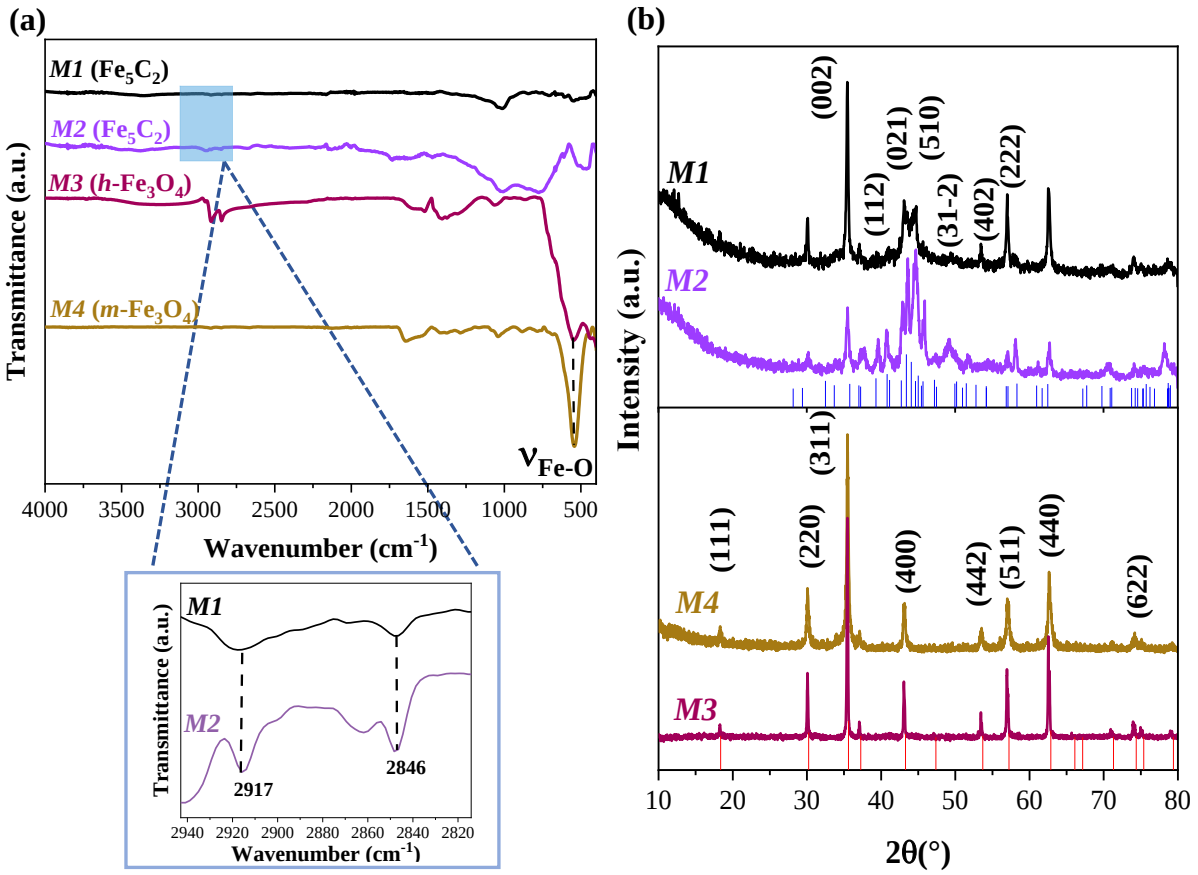


Figure 4.7. FTIR (a) spectra and XRD (b) diffractograms of the MNPs: Fe_5C_2 (M1), Fe_5C_2 (M2), hexagon-Fe_3O_4 (M3) and multicore-Fe_3O_4 (M4), the latter with the standard diffraction patterns of Fe_5C_2 (blue columns) and F_3O_4 (red columns) NPs. Inset: Zoom-in of the 2900-2850 cm^{-1} spectral region from M1 and M2 NPs.

The FTIR spectra of both Fe_5C_2 NPs, M1 and M2, show the presence of adsorption bands at 2846 and 2938 cm^{-1}, which are attributed to asymmetric and symmetric stretch vibration, - CH_2, respectively. These peaks are characteristic of Fe_5C_2 NPs. Furthermore, it is not observed that the corresponding adsorption band of Fe-O at 558 cm^{-1}, and 633 cm^{-1} of Fe_3O_4 and γ-Fe_2O_3, respectively [401,402], confirming that Fe_5C_2 is the only magnetic phase in the sample. On the other side, the mentioned band at 558 cm^{-1} is observed at the nanoparticles M3 and M4.

The diffraction patterns of Fe_3O_4 (M3 and M4) and Fe_5C_2 NPs (M1 and M2) are compared, respectively. In the XRD diffractogram of the Fe_5C_2 NPs, it is observed diffraction peaks located at 2Θ= 35.4, 39.3, 43.2, 44.7, 49.1, 53.2, and 56.1° being indexed to (002), (112), (021), (510), (31.2), (402) and (222) planes. The crystalline structure of the NPs M1 and M2 is consistent with Fe_5C_2 NPs (ICDD: 98-004-3194) [403]. The XRD pattern of both M3 and M4 NPs present diffraction peaks located at 2Θ= 18.3, 30.1, 35.6, 43, 53.7, 57.2, 62.7, and 74.2°, which correspond to the planes (111), (220), (311), (400), (442), (511), (440) and (622) of Fe_3O_4 in a face-centred cubic (ICDD: 98-015-8743), respectively.

These nanoparticles were incorporated into a cellulose acetate matrix in different amounts and homogeneously distributed within the hybrid films, which were prepared by the casting method. Therefore, a set of magnetic films were obtained with other Fe concentrations of 0.02, 0.1 wt % using the NPs M1, M3, and M4, and M2 with Fe concentration of 0.005, 0.02, 0.1, and 0.2 wt %, respectively.

Morphological observations of a selected set of magnetic films and a control film are shown in Figure 4.8. Generally, the MNPs appear as agglomerates onto the polymeric matrices compared to the CTRL film. The surface of the magnetic films, FM1Fe0.2, and FM4Fe0.1, present a more uniform dispersion of nanoparticles than the ones prepared with the NPs M2 and M3. These may be due to the magnetic properties of the NPs and the interaction with cellulose acetate. Moreover, it has to be highlighted that the structural integrity of all films has no observable holes, which is a requirement in packaging uses, preventing the crossing of large moieties from the exterior to the internal area of any product protecting it against contamination.

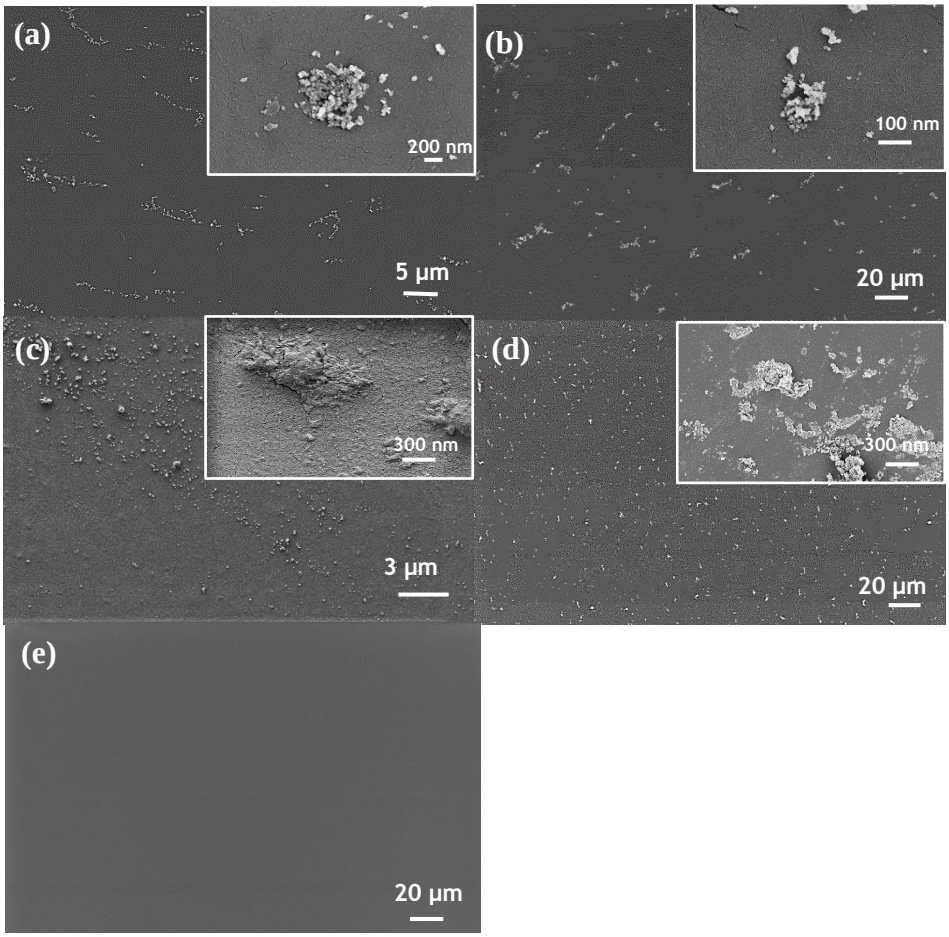


Figure 4.8. SEM images of the films with different content of nanoparticles; (a) FM1Fe0.1 (Fe_5C_2), (b) FM2Fe0.2 (Fe_5C_2), (c) FM3Fe0.2 (*h*-Fe_3O_4), (d) FM4Fe0.1 (*m*-Fe_3O_4) and (e) control film without nanoparticles. Zoom inset SEM images included of each film.

Figure 4.9, shows the magnetic behaviour of the bare NPs and respective films measured at 300 K. The hysteresis loops in Figure 4.9a and 4.9b, shows that Fe_5C_2 NPs (M1 and M2) have ferromagnetic behaviour with a saturation magnetization of M_s=104.3 emu/g_{Fe3O4} and M_s=109 emu/g_{Fe3O4} and a coercive magnetization of H_{coer}=307.6 Oe and H_{coer}=280.4 Oe, respectively (Table A3.3). The obtained M_s values are slightly higher than reported values, M_s=90 emu/g [404] and M_s=95 emu/g [405] for nanoparticles with a diameter size below 100 nm.

The synthesized hexagonal Fe_3O_4 (M3) NPs possess a magnetic behaviour of a soft ferromagnetic material with high saturation magnetization (M_s=90 emu/g_{Fe3O4}) and low coercivity (H_{coer}=84 Oe) values, as shown in Figure 4.9c. Meanwhile, the magnetization saturation value of the multicore Fe_3O_4 (M4) NPs was M_s=95 emu/g_{Fe3O4}, which is way above of that reported in the literature of a bulk sample of Fe_3O_4 (M_s=92 emu/g) [395]. This result implies the occurrence of experimental errors during the determination of either the magnetic solid content by TGA or during the adjustments of the calculated magnetic parameters. Besides this, the NPs M4 have a low coercivity (H_{coer}=6.6 Oe) and low remanence (M_{rem}=9.3 emu/g_{Fe3O4}) values displaying weak ferromagnetism.

Attending the different magnetic behaviour observed, these NPs were chosen and incorporated into CA. Magnetic CA films were developed with the same magnetic print as the starting NPs, which facilitates design methods to implement magnetic anti-counterfeiting tags with magnetic performance designed under demand.

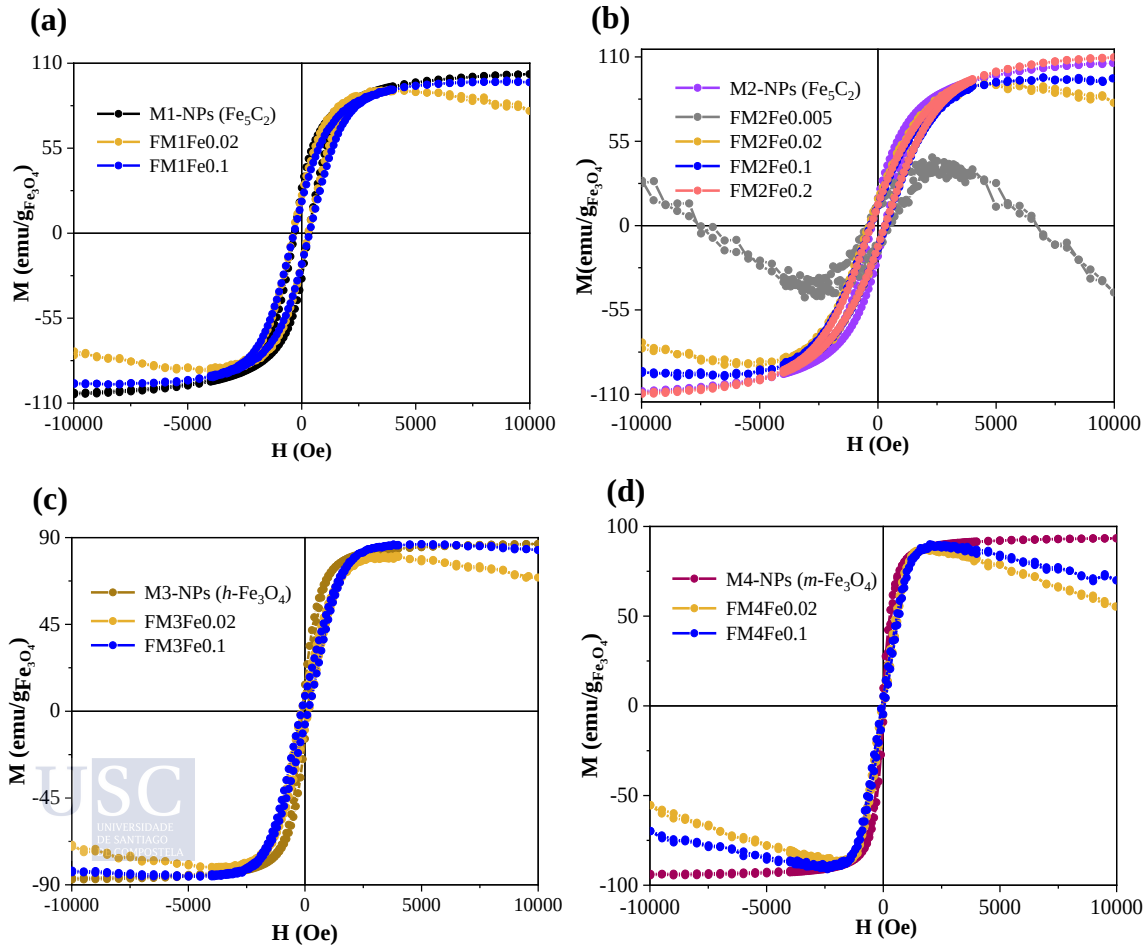


Figure 4.9. Magnetization cycles of both nanoparticles (a) M1, (b) M2, (c) M3, (d) M4 and respective films with distinct nanoparticles concentrations.

In addition, it can be observed a slight decrease in the M_s of hybrid films with a low content of MNPs, being especially intense in the case of FM2Fe0.005 in Figure 4.9b. This behaviour can be ascribed to the diamagnetic contribution of the CA layer (Figure A2.7), which becomes evident in weakly magnetized films.

Attending to their magnetic properties and the homogeneity of the MNPs distribution over the CA matrix, the films FM1Fe0.1 and FM4Fe0.1, with a magnetic content of 0.1 %, were chosen as suitable candidates. To further understand the effect of the casting solvent and the NPs incorporation on the morphology and structural properties of the magnetic CA films, rheological studies were conducted under a solvent trap to avoid acetone evaporation.

Figure 5.0a illustrates the storage (G′) and loss (G″) modulus as a function of shear stress (%) for the magnetic and control CA solutions, determined by dynamic stress sweep measurements.

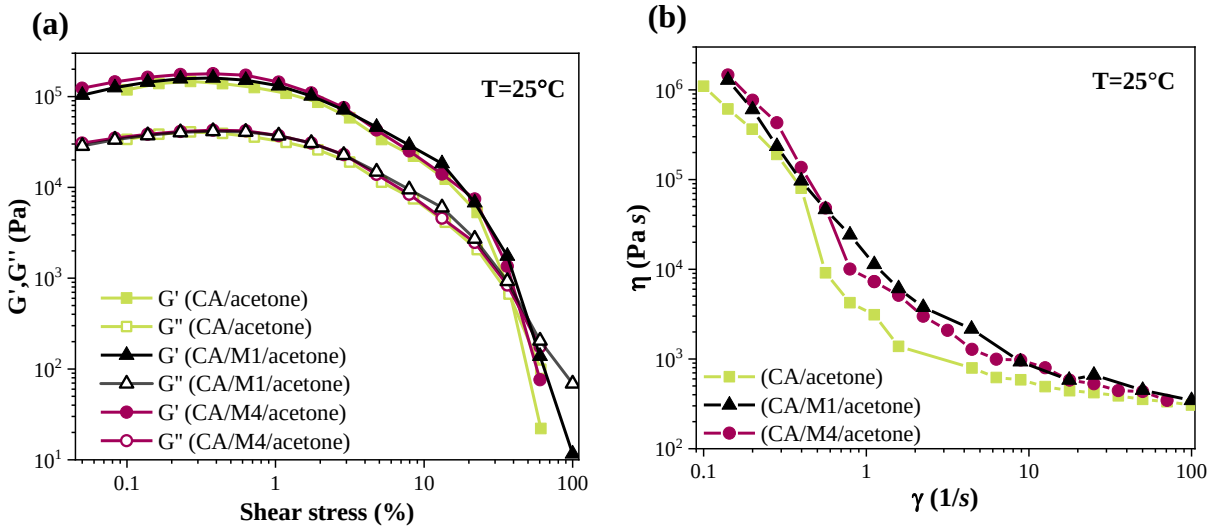


Figure 5.0. Rheological measurements, G′ and G″ as a function of shear stress (%) (a) and viscosity plot (b) versus shear rate for CA solutions with and without MNPs, respectively.

The CA solutions exhibit similar stress complex modulus (G′ and G″). At low applied shear stress, both G′ and G″ are nearly constant, indicating that the CA solutions are in the linear viscoelastic (LVE) region. This region shows the operational range where stress can be applied without destroying the structure of a sample and evaluates its viscoelastic character. In all CA solutions in this regime, the storage modulus (G′) is always higher than the loss modulus (G″), stating that all samples show a gel-like structure and can be designated as solid viscoelastic material [406]. However, applying large shear stress, the interaction bonds in the gel network start to break down, and a gradual decrease of G is observed because deformation energy is converted into friction heat. Furthermore, the effect of the NPs is observed on the displacement of the flow or crossover point (G′=G″) towards higher stress values compared to one of the native CA solutions.

The crossover point (G′=G″) is achieved when the gel-like character (G′>G″) changes to a liquid state (G″>G′) [407]. In this study, CA solutions containing MNPs (M1, M4) present a crossover point of 49.89 and 43.81 %, which is higher than the crossover point value of 38.9 % observed for the CA control solution. This is an indication of the higher resistance of the

magnetic CA solution against an applied force resulting in later internal structure breakdown, causing the solution to flow later than the CA solution [407].

The steady flow curves in terms of viscosity as a function of shear rate are described in log-log representation in Figure 5.0b. The viscosity measurements were performed at 25 °C in the linear viscoelastic regime of the samples. The CA solutions with NPs are more viscous than the control in the low and medium shear rate (γ<20 s^{-1}). The M1 NPs effect in the viscosity shifting towards higher stress values is more pronounced than the one observed by the M4 NPs. This fact may indicate better dispersion of the M1 NPs compared to the M4 NPs. Similar results were observed in another study, where the addition of Rich Rice Straw Nanofibers (RSNF) to a CA solution resulted in a significant increase in its viscosity and nanofibers dispersibility within the cellulose network [408]. The same trend was observed with the addition of cellulose nanofibrils (CNF) to a CA solution, where good interaction between CNF and CA macromolecules [409] was observed.

The structure, topography, and textural properties of the dried magnetic films were also studied. The FTIR spectra of CA and CA film mixtures with (0.1 %) magnetic NPs are shown in Figure 5.1a. The broad absorption peak at 3472 cm^{-1} present in control and magnetic films is attributed to the stretching intermolecular hydrogen bonds of hydroxyl groups (-OH) due to moisture in the samples. Also, stretching vibration bands in control film can be observed at 2945, 1736, and 1028 cm^{-1}, which are attributed to the functional groups -CH, -C=O, and - C=OH, respectively. The vibrational deformation band (-CH_2) and the anti-symmetric stretching vibration (-C-O-C-) characteristic of the ester group of pure CA are located at the wavenumber 1431 and 1220 cm^{-1}, respectively [410].

All mentioned bands are also observed in the CA magnetic films but with lower intensity and broader shape than the control films due to complexation effects [219,411]. Neither Fe-O characteristic in FM4Fe0.1 band nor the characteristic band of Fe_5C_2 NPs in the FM1Fe0.1 film can be perceived due to the deficient concentration of MNPs present in both films.

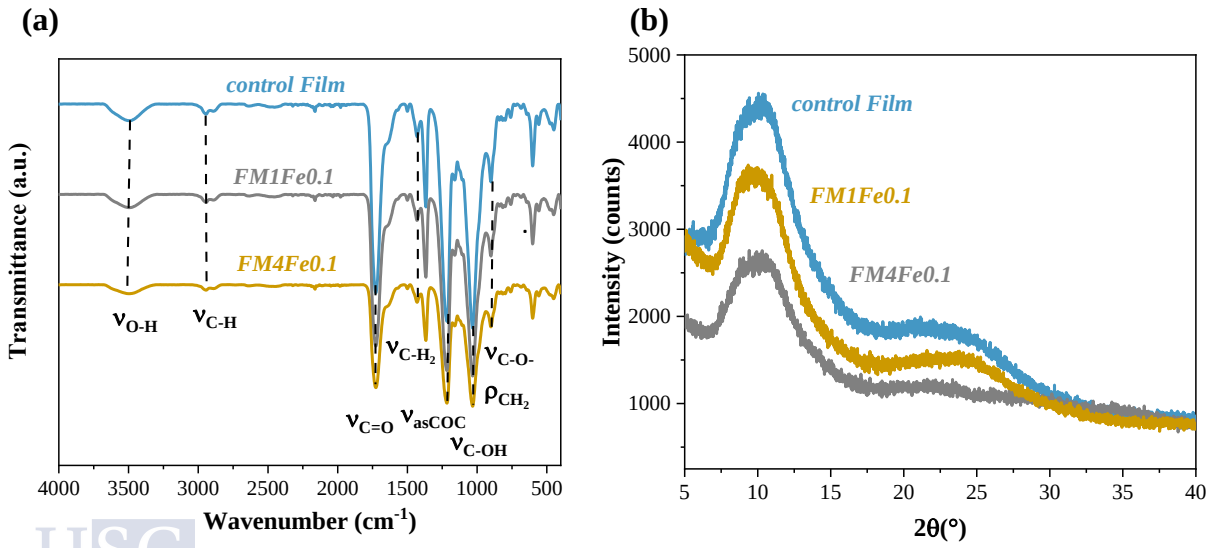


Figure 5.1. FTIR spectrum (a) and XRD (b) diffractogram of magnetic cellulose acetate films: FM1Fe0.1 (0.1 wt.% Fe_5C_2 NPs), FM4Fe0.1 (0.1 wt.% Fe_3O_4 NPs) and control film.

The XRD diffractogram of the control and magnetic CA films is shown in Figure 5.1b. The diffractogram of the control film reveals two intense peaks centred at 2Θ=10.2 and 22.8 °, corresponding to the semi-crystalline structure of CA, which become less prominent after the addition of the MNPs in the magnetic CA films. Although XRD infers that cellulose films maintain their structural features when doped with MNPs, the reduction in peak intensity does not allow to distinguish the structural presence of MNPs in the films. No reflection peak corresponding to Fe_3O_4 or Fe_5C_2 can be distinguished in the diffractogram, for which alternative tools were used to gain insight into the hybrid material structure.

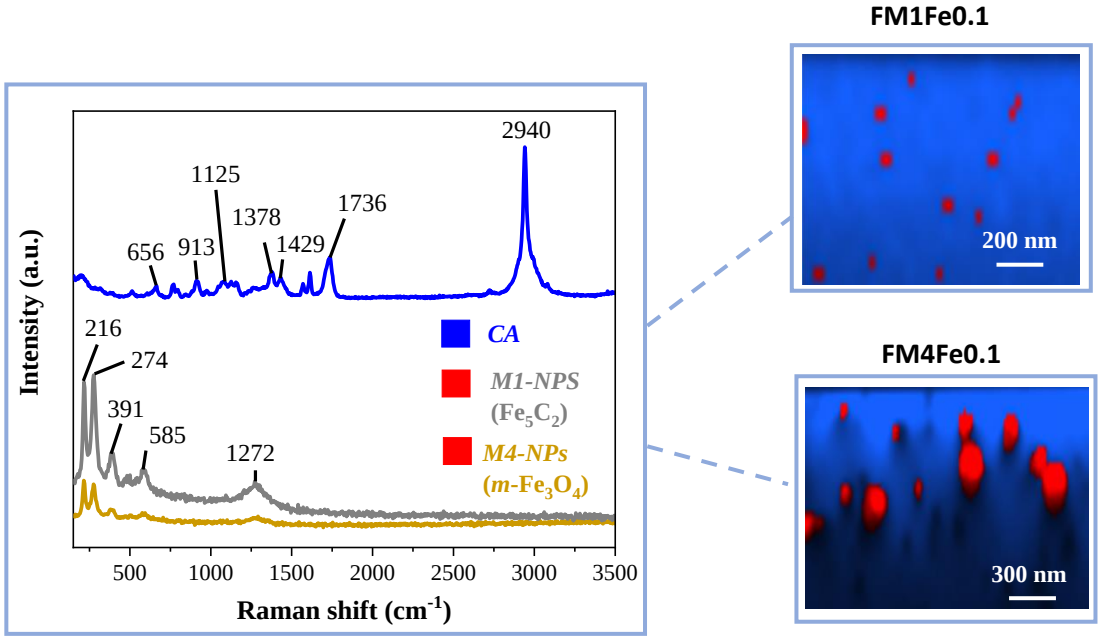


Figure 5.2. Confocal Raman spectroscopy of magnetic CA films, FM1Fe0.1 and FM4Fe0.1 with respective image of the CA component highlighted in blue colour and in red the NPs.

Confocal Raman spectroscopy was performed on the magnetic CA films (FM1Fe0.1 and FM4Fe0.1), showing a Raman spectrum for each component (CA and NPs), as shown in Figure 5.2. In the M1 NPs (Fe_5C_2) spectrum present in the film FM1Fe0.1, a peak at 1272 cm^{-1} is observed, corresponding to a D band commonly found in carbon materials. The surface of the as-synthesized Fe_5C_2 NPs may have suffered structural defects explaining the more dominant Fe_3O_4 NPs phase observed in the Raman spectrum of these NPs.

Characteristic peaks of Fe_3O_4 NPs are located at 391 and 585 cm^{-1}, which corresponds to the vibration modes of the Fe-O band [412]. These peaks are also observed at the M4-NPs (*m*-Fe_3O_4), confirming the formation of Fe_3O_4 NPs. The fundamental cellulose bands have been noticed in the Raman spectrum of CA in Figure 5.2. Characteristic bands were present at 1125 and 2940 cm^{-1}, which are attributed to the stretching C-H and the asymmetric stretching vibration of C-O-C glycosidic linkage, respectively. The peaks located at 1378, 1429, and 1736cm^{-1} are attributed to asymmetric and symmetric vibrations of -CH and of the (C=O) group present in the ($COCH_3$) groups of cellulose. The remaining signals at 656 and 913 cm^{-1} can be associated with C-OH and C-H bonds, respectively [413].

The confocal images of the films show the distribution of the NPs (red) over the CA network (blue). The dispersion of the NPs is more homogenous at the film FM1Fe0.1 than at

the film FM4Fe0.1. In addition, the surface topography was further evaluated by a 3D optical profilometer. Figure 5.3 is represented a 2D and 3D surface image of the magnetic CA films over a scanned area of 0.8 mm^2. The roughness parameters were determined by ISO 4287:1997, and some are present in Table 3.5.

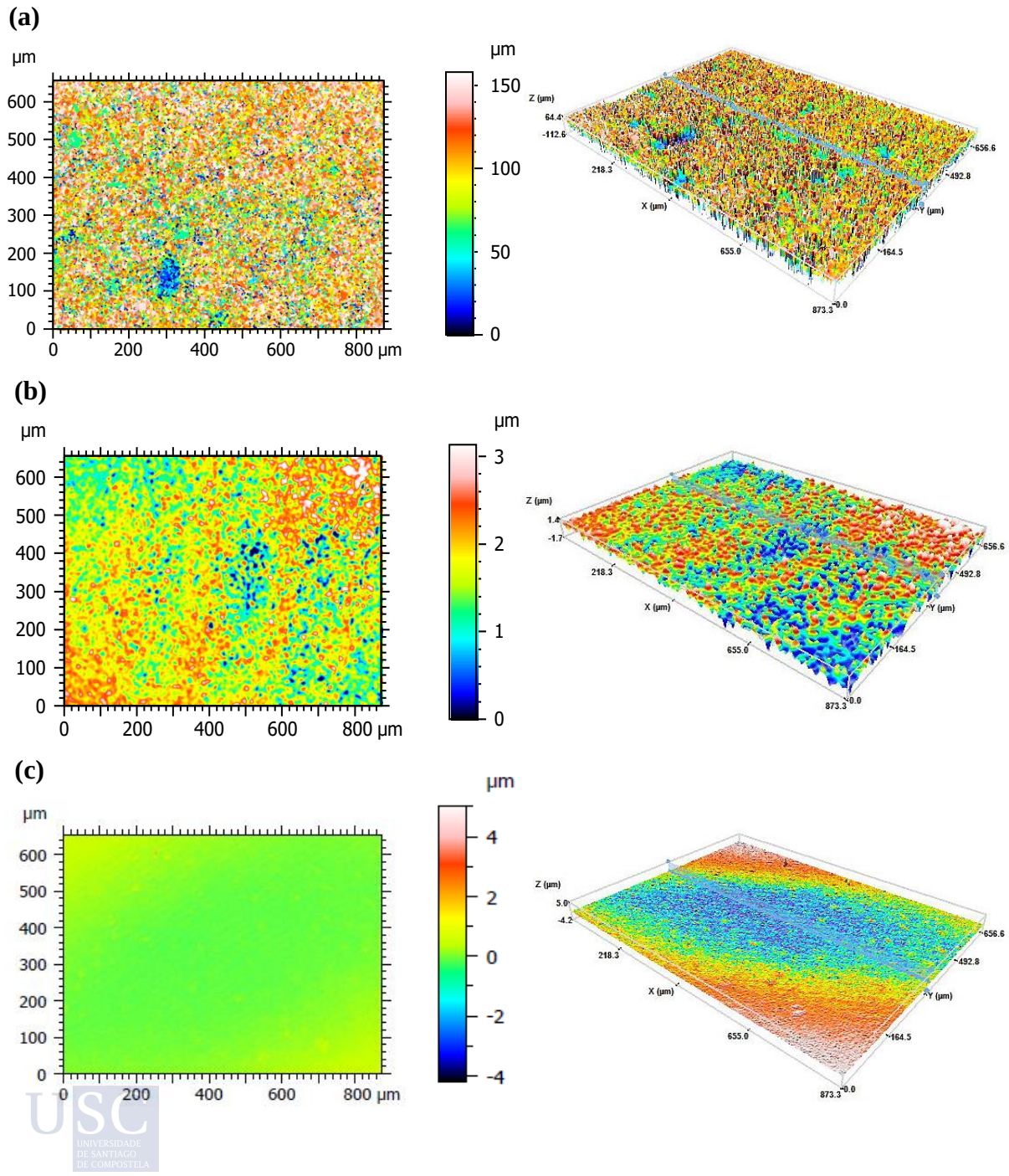


Figure 5.3. Topography images of the magnetic CA films: FM1Fe0.1 (a), FM4Fe0.1 (b) and the control (c) with respective 3D profile images (right).

The total height of the profile (R_t) and root mean squared of the surface roughness (R_q)of the magnetic CA films is much higher than the control film. FM1Fe0.1 film was wider and rough with R_t=157.01 µm and R_q=39.3 µm than FM4Fe0.1 film, which reported the following values R_t=1.85 µm and R_q=0.33 µm.

In the 2D and 3D topography images the difference between both films is clearly visible. The film area analysed on FM1Fe0.1 reveals higher variations (peaks and valleys) than in FM4Fe0.1 and control film. Skewness (R_{sk}) and kurtosis (R_{ku}) were evaluated to quantify different features of the topography and surface distribution of the films.

Negative values of $R_{sk} < 0$ reveal that all films surface have deeper valleys than peaks, and the surface is sharper (R_{ku}>3). The films, FM1Fe0.1 and FM4Fe0.1 have values of (R_{sk}, R_{ku}) equal to (-0.90, 2.99 µm) and (-0.66, 3.49 µm), respectively. The film FM1Fe0.1 has fewer valleys than FM4Fe0.1, and the surface is less sharp. Perhaps the M1 (Fe_5C_2) NPs were more homogeneously dispersed in the cellulose network than M4 (*m*-Fe_3O_4) NPs.

Roughening of surface materials increases the available area for bacterial adhesion, and once optimized, it can minimize surface contamination [414]. In addition to this, some factors must be considered when choosing packaging materials, such as durability, permeability, solubility, cost-effective production, and biodegradability. Therefore, other than the roughness of the films, also the mechanical strength, water solubility and moisture content were determined to evaluate the suitability of the magnetic films for packaging applications.

Table 3.5. Roughness parameters of CA films.

Films	R_t (µm)	R_q (µm)	R_{ku} (µm)	R_{sk} (µm)
FM1Fe0.1	157.1	39.3	2.99	-0.90
FM4Fe0.1	1.85	0.33	3.49	-0.66
control	0.346	0.041	3.20	-0.21

Table 3.6 reports the MC and water solubility of freshly made magnetic and CTRL CA films. Solubility and MC are important packaging parameters to determine the films biodegradability when used as packaging or tagging materials. Preservation of goods from external toxic compounds (toxins, bacteria, viruses) depends crucially on the ability of the material to prevent moisture penetration.

Conventionally used plastics derived from oil derivatives, for instance, low-density polyethylene (LDPE) in one study was used to develop plastic packaging films for pistachio storage to prevent aflatoxins contamination revealed to have a MC value of 8.1 % and insolubility in water [415]. On the other side, a compostable film based on sugar palm (*arenga pinnata*) starch for food packaging revealed a MC of approximately 6.5 % (using sorbitol as plasticizer) and a solubility of around 20 to 30 % (depending on the plasticizer concentration) [416]. Even though non-biodegradable polymers such as LDPE provide a strong resistance against microbial attack, they persist in the environment for several years after their disposal. In this regard, films from biopolymers or polysaccharides present a potential alternative to mitigate the above disadvantages of petroleum-based plastics.

For this reason, it was assessed the NPs influence on the films hydrophilicity in aqueous media. Firstly, all films were conditioned (25 ºC at 65 % RH), cut into 50 mg pieces, and dried to determine the MC gravimetrically. Afterward, it was tested the solubility of the film pieces by analysing the content of dry matter solubilized after 24 h of immersion in water at approximately 20 ºC. Doing so, it was found that the solubility of the films in water is low compared to other studies where pectin-based films were completely soluble in water, meanwhile, chitosan films had a water solubility value of 88 %, respectively [417, 418].

Cellulose acetate films are known to have low moisture uptake and solubility compared to other films because of the low OH- groups present in their structure and are known to be most suitable for several food applications due to their water insolubility to provide water resistance and boost shelf-life of food products. The addition of MNPs causes a further decrease in the hydrophilic properties of the magnetic CA films compared to the control film. The film FM1Fe0.1 had lower solubility than the film FM4Fe0.1, probably due to the homogeneous dispersion of the NPs on the CA network, as stated above.

Table 3.6. Values of moisture content and water solubility of the magnetic CA and control films (storage time 0days).

Films	Moisture content (%)	Solubility (%)
FM1Fe0.1	6.3	2.23
FM4Fe0.1	6.85	2.53
control	7.11	2.59

These results reveal that the incorporation of NPs can influence the moisture content of the films. Similar behaviour was observed in chitosan/cellulose acetate films with CeO_2 NPs for wound dressing [419]. So far, no reported literature research studies MNPs behaviour onto CA films. However, the results indicate that in the presence of MNPs, MC and water solubility of magnetic CA films decrease, providing additional benefits to the overall performance of the magnetic films.

The effects of the storage time on the opacity, colour, and mechanical properties of the CA films were also studied. Opacity is an important parameter used to measure the light intensity passing through a material controlling the incidence of light on packaged food offering a barrier against oxidative processes. Figure 5.4 shows digital photos of the same films right after preparation (0 days) and after (90 days). Visually, the films with NPs are darker in colour than the control, and no additional difference is observed. Table 3.7, the opacity and colour parameters are compiled to provide quantitative information about the visual influence of the MNPs in CA films.

USC UNIVERSIDADE DE SANTIAGO DE COMPOSTELA

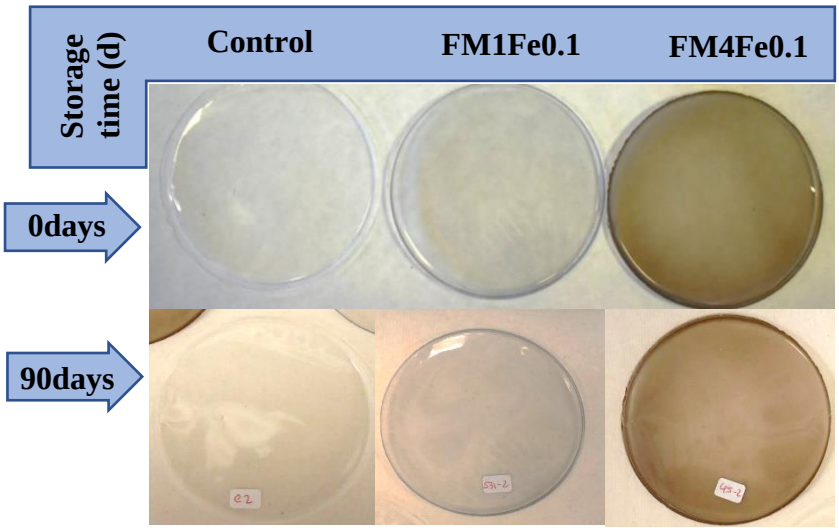


Figure 5.4. Digital photos of the control and magnetic cellulose acetate films stored at 0 and after 90 days.

The results show that the films opacity increased after 90 days, reporting higher opacity values in the magnetic CA films. In addition, the a* values of the magnetic CA films suggest a more reddish colour and yellower appearance (b*) than the CTRL film. On the contrary, the addition of MNPs decreased the lightness (L*) value. The NPs acted as a barrier reducing the light that passes through the film and consequently increased opacity. The calculated total difference value, ΔE, shows clear differences between the magnetic CA films. The film FM4Fe0.1 is more opaque, reddish, and yellower than FM1Fe0.1 film, as shown in Figure 5.4. Both films have the same magnetic content (0.1 wt.%), and these differences can be attributed to the different composition, size, and shape of the MNPs that act as light barriers (iron Fe_3O_4 and Fe_5C_2 NPs).

The mechanical properties of the magnetic CA films, such as tensile strength (TS), elongation at break (EB), and Young's modulus (YM), were also affected by the presence of the MNPs, as shown in Table 3.7. The results show that for freshly prepared samples, TS and EB values slightly decrease for the magnetic CA films, while YM values increase compared to the CTRL film.

USC UNIVERSIDADE DE SANTIAGO DE COMPOSTELA

Table 3.7. Values of opacity, colour parameters, total difference value (ΔE) and mechanical properties of the control and magnetic cellulose acetate films

Film	Storage time (days)	Opacity (%)	Colour parameters (L*, a*, b*)	ΔE	TS (MPa)	EB (%)	YM (GPa)
FM1Fe0.1	0 90	9.96±0.7 10.43±0.1	(91.3, 0.22, 2.48) (86.2, 0.23, 2.43)	3.94±0.2 8.46±0.3	52.3±7.1 47.24±5.0	3.53 ±0.9 2.10±0.3	24.5 ±1.9 26.5±0.2
FM4Fe0.1	0 90	13.1±0.9 17.6±3.0	(74.5; 2.98; 6.27) (63.0; 4.58; 7.8)	21.22±4.3 32.44±1.9	51.9±5.8 53.34±6.1	2.94± 0.3 3.15± 0.5	24.5± 3.7 24.3± 4.0
control	0 90	8.83±0.1 9.26±0.4	(95.2; 0.20; 2.10) (94.7; 0.20; 2.31)	0 0	55.5±4.5 50±3.2	7.76± 0.6 4.72±0.2	23.23 ±5.7 20.9±4.1

However, after 90 days, it is observed a decrease in the TS and EB for both control and FM1Fe0.1 film, while the opposite happens for FM4Fe0.1 film. This indicates that Fe_3O_4 NPs incorporated on the FM4Fe0.1 film seem to have favoured a slower film deterioration after 90 days compared to Fe_5C_2 NPs added to the FM1Fe0.1 film. Generally, hydrogen bonds established between the nanoparticles and the cellulose network are attributed to higher TS values, decreased brittleness, and stiffness of doped films [420].

Furthermore, the incorporation of MNPs slightly reduces the mechanical properties of the films, as, over time, acetic acid has been reported to be released, causing the rupture of hydrogen bonds between both polymer and NPs, leading to a brittleness material [421]. In future studies, the optimization of magnetic CA films would require a deeper analysis of the effect of the plasticizer concentration and solvent type on the mechanical properties of the doped films.

USC UNIVERSIDADE DE SANTIAGO DE COMPOSTELA

3.4. Functional magnetic 3D bacterial nanocellulose capsules

Nanocellulosic materials are gaining increasing interest for their inherent properties and in meeting the current environmental problems. Alternatively, to the conventional nanocellulosic materials obtained from plants, bacterial nanocellulose (BNC) is another type of nanocellulose of microbial origin, being a potential source for the development of new materials. BNC is one of the purest forms of nanocellulose and presents the highest crystallinity, water absorbency, mechanical strength, moldability, and biological affinity over plant celluloses [422, 423].

For this reason, BNC is used in a wide range of applications, from scaffolds for regenerative medicine (e.g., dental implants, cartilage growth, nerve regeneration, and skin repair) to carbon based-nanocomposites for energy applications (e.g., sensors, electrically conductive and catalytic materials) [422, 424, 425]. Furthermore, structured materials with controlled 3D morphology can be shaped due to their specific interfacial affinity in air-water. 3D BNC capsules are generated by the liquid marble strategy. In short, upon pipetting the bacterial culture media on a hydrophobic bed of polytetrafluoroethylene (PTFE) powder, the formed liquid marbles stabilized in the shape of beads and after incubation in the capsular morphology. Furthermore, the possibility of encapsulating various types of cargo (e.g., MOFs, enzymes, and nanoparticles) has been reported to increase the functionality of these bio- fabricated capsules [426].

In this study, magnetic BNC capsules were produced via pipetting (controlled volume) of a previous mixed bacterial precultured media with Fe_3O_4 NPs coated with polyacrylic acid (Fe_3O_4@PAA). PAA is a water-soluble polymer with high binding capacity and reactive functional groups, which allows a strong binding between the iron oxide and biomolecules, being very attractive and used for biomedical applications [427]. For this reason, the functionalized Fe_3O_4@PAA were used to produce 3D magnetic BNC capsules with different NPs content to study their effect on the cellulose nanofibrils and how time plus storage conditions can impact the magnetic behaviour of freshly prepared magnetic BNC capsules and after 2 years storage.

3.4.1. Magnetic 3D BNC capsules bio-fabrication: Material and methods

a. Synthesis of magnetite nanoparticles coated with polyacrylic acid (Fe_3O_4@PAA)

Fe_3O_4@PAA NPs were prepared through the co-precipitation method [428]. Briefly, 5.5 g $FeCl_3.6H_2O$ and 3.5 g $FeSO_4.7H_2O$ were dissolved in 80 mL Milli-Q water under N_2 atmosphere. After reaching the temperature of 60 ºC, 0.49 g PAA (MW: 5000 g/mol) was added to the system and left agitating for 30 min. Afterward, 10 mL NH_4OH (25 %) was quickly added and left mixing again for more 30 min. The solution was left to cool down and was then washed with water and acetone. The MNPs were redispersed in water, labelled as F6, and characterized by TEM, TGA, and VSM (Appendix 6.1).

USC UNIVERSIDADE DE SANTIAGO DE COMPOSTELA

b. Magnetic 3D BNC capsules preparation and washing

BNC was produced by the bacteria strain *Gluconacetobacter medellinensis* (ID: 13488), which was originally isolated from fruit vinegar in Colombia [429]. The bacteria were grown on a medium consisting of 20 g/L glucose, 5 g/L peptone, 5 g/L yeast extract, and 2.5 g/L sodium phosphate dibasic at pH 4.5 adjusted with citric acid. The culture media was previously sterilized by autoclave for 120 min at 120 ºC.

Afterward, 100 mL of sterilized culture media was inoculated with 1 mL culture stock and was left to grow one day previously to the preparation of the capsules. On the preparation day, 10 mL of sterilized culture media in different batches were prepared, adding 100 µl, 500 µl, and 1 mL of Fe_3O_4@PAA NPs. The final solution (bacterial culture media plus MNPs) was cast via pipetting a fixed volume of 30 µl on a bed of PTFE (35 µm average particle size) powder to equilibrate the air-medium interface. The formed liquid marbles were covered with PTFE powder to prevent aggregation and maintain an ideal environment for BNC production by the bacteria. The preparation was carried out inside a small container with saturated humidity (wet cotton inside) and then closed for incubation to avoid culture medium evaporation.

After 2 days of incubation, bio- fabricated magnetic BNC capsules were formed, washed with 0.1 M NaOH overnight, followed by washing and storing using deionized water. The NPs, BNC and capsules were fully characterized by SEM, TEM, TGA, XRD, FTIR and VSM (Appendix 6.1).



Figure 5.5. Preparation set-up of magnetic BNC capsules.

3.4.2. Magnetic 3D BNC capsules: Results and discussion

The morphology and size distribution of the Fe_3O_4@PAA NPs (F6 NPs) was analysed by TEM, and illustrated in Figure 5.6. The TEM image shows an ensemble of nearly spherical particles (Figure 5.6.a) and heterogeneous size distribution with an average size diameter of 11 nm, (Figure 5.6b). This small size is a requirement that grants the superparamagnetic behaviour ensuring a homogeneous dispersion of F6 NPs in the culture medium to facilitate their integration within the nanocellulose network.

USC UNIVERSIDADE DE SANTIAGO DE COMPOSTELA

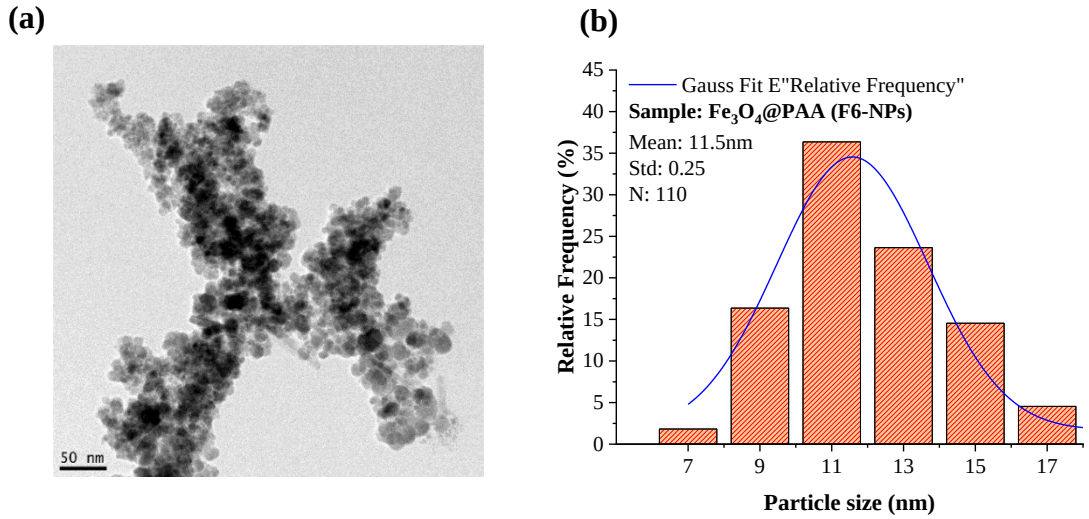


Figure 5.6. TEM image (a) and size histogram distribution (b) of Fe_3O_4@PAA (F6 NPs), respectively.

Figure 5.7a shows the magnetic BNC capsules produced. The incorporation of F6 NPs into the BNC capsule's structure is clearly observed by the black side colour resulting in the NPs incorporation within the nanocellulose network. As expected, the capsules with higher NPs concentration are attracted with higher intensity when an external magnetic field is applied, as observed in Figure 5.7b. The magnetic capsules were kept in water for almost two years. As it can be seen in Figure 5.7.c, no evident signs of ageing were observed: the entire capsule preserved its integrity, and the MNPs remained unaltered with no signs of oxidation affecting their magnetic performance and intense magnetic attraction.

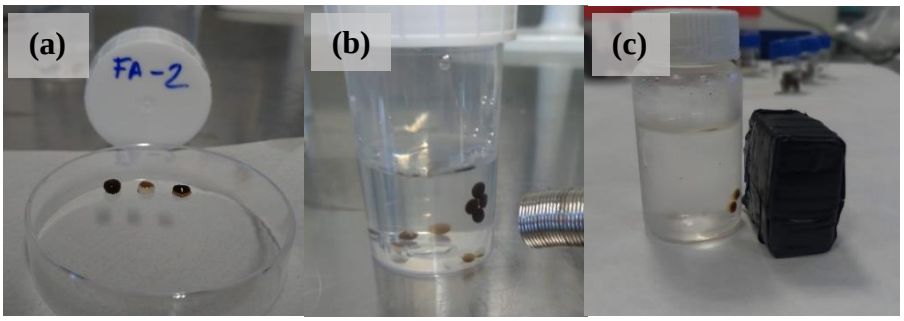


Figure 5.7. Magnetic BNC capsules (a) under an external magnetic field at the first day of synthesis (b) and after 2 years (c).

USC UNIVERSIDADE DE SANTIAGO

To gain insights into the structural and textural properties of the native and magnetic BNC capsules, a set of characterizations were performed. First, the FTIR spectrum of native BNC showed typical vibrations peaks of cellulose, located at 3343, 2914, 1054, and around 1300 cm^{-1}, which are attributed to -OH stretching, -CH bending, and -CO stretching bonds, as shown in Figure 5.8a [430]. Similar peaks were also observed in the magnetic BNC capsule (CF6)

spectrum, with an additional peak found at 558 cm^{-1} corresponding to Fe-O bonds. This peak was initially located at 552 cm^{-1} but shifted to 558 cm^{-1} due to the binding of cellulose fibrils with Fe_3O_4 NPs.

The XRD diffraction pattern of BNC, CF6 magnetic capsules, and the respective F6 NPs is shown in Figure 5.8b The diffractogram of BNC shows two peaks located at 16 and 23°, which correspond to the planes (110) and (002) of two coexisting crystalline phases, Iα (triclinic) and Iβ (monoclinic), respectively [431, 432]. These peaks can also be observed in the diffractogram of CF6 (magnetic capsules) together with the Fe_3O_4 planes (220), (311), (111), (442), (511), and (440), thus confirming the presence of Fe_3O_4 NPs and preservation of the crystalline phase of cellulose.

The microstructure, morphology, and spatial distribution of the F6 NPs onto the BNC network, were analysed by SEM and are shown in Figure 5.9. As observed, the native structure of BNC in Figure 5.9d presents a compact network of fine nanofibrils organized in a random arrangement, forming a highly porous matrix with a wide range of pore dimensions (from several nm to several µm), allowing water retention. The nanofibrils produced had an average diameter of 30 nm and a length of several microns.

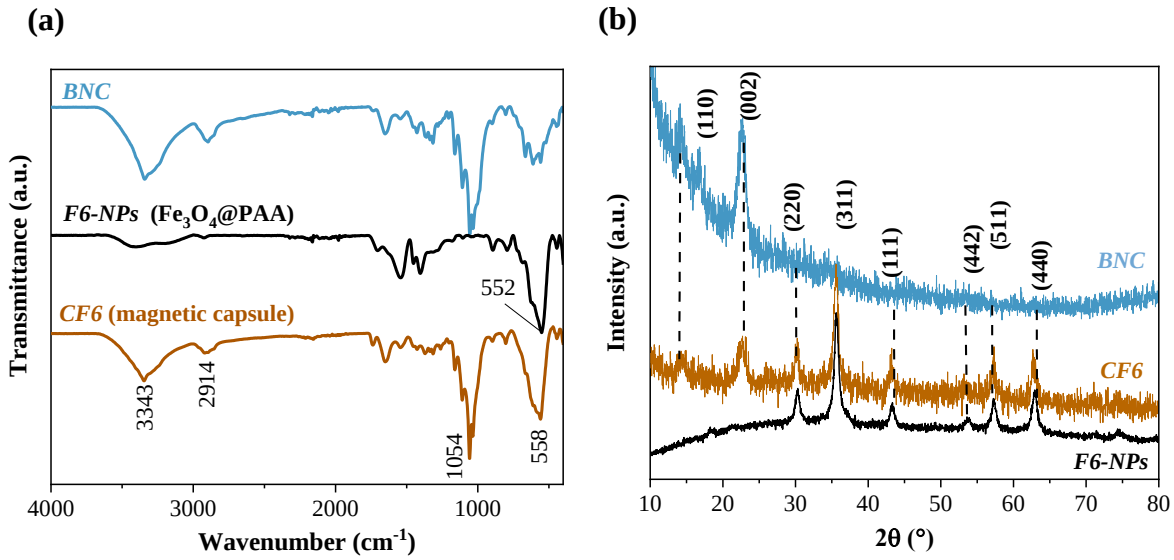


Figure 5.8. FTIR (a) spectra and XRD (b) diffractogram of BNC, F6 NPs and CF6 capsule, respectively.

The MNPs bound to BNC fibrils' surface and inside the BNC matrix formed aggregates of about 200 nm, as can be observed in the SEM images. Compared to the pure BNC capsules network (Figure 5.9d), the magnetic BNC capsules present a network with dense knots where magnetic nanoparticles appear aggregated. Moreover, the magnetic BNC network pattern is more heterogeneous and less regular than that of pure BNC, resulting from the MNPs that partially obstruct the porous structure and the nanofibrils surface, as shown in Figure 5.9a. On the other hand, the network of BNC doped with medium (5 wt.%) and low (1 wt.%) NPs content remains less disrupted by the presence of NPs that remained dispersed and attached to the fibrils surface, as shown in Figures 5.9b and 5.9c.

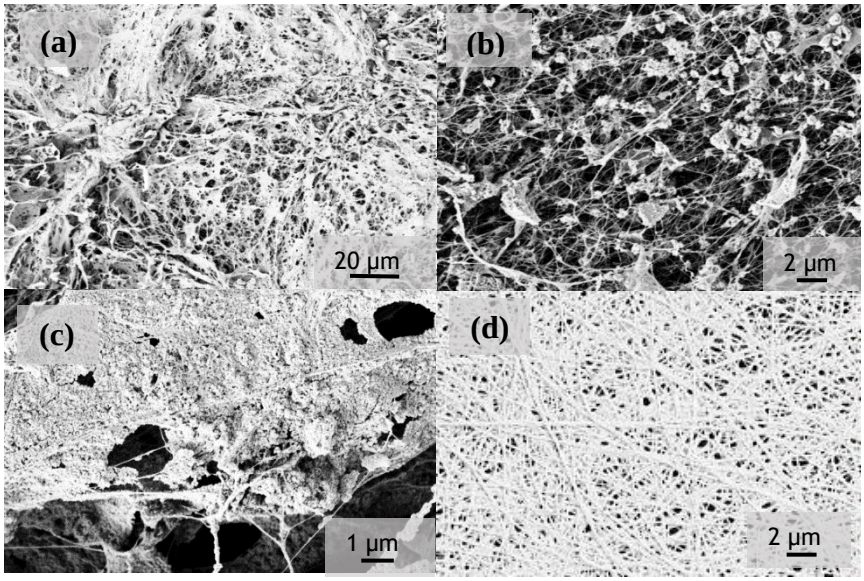


Figure 5.9. SEM micrographs of the BNC capsules with 1% (a), 5% (b) and 10% (c) of F6 NPs and (d) control without nanoparticles

This loss of regularity by the presence of NPs has been observed in similar microstructures reported in the literature [433, 434]. However, the formation of BNC capsules with magnetic NPs has not yet been reported. The embedment of Fe_3O_4 NPs on one side of the BNC capsules can be observed clearly in Figure 6.0. The confocal microscope images taken from different samples of magnetic capsules that were stored for two years also confirm the material integrity. Storing the magnetic capsules in water did not cause any sign of oxidation and eventual magnetic degradation, as the magnetic characterization of the samples confirms.

Magnetization measurements of the magnetic capsule's storage in the water right after synthesis (0 h) and after two years (2 y) were compared to the magnetization of the F6 NPs used to produce the capsules, as shown in Figure 6.1a. The magnetization curve revealed that the magnetic performance of both capsules remains unaltered given the period and storage conditions.

USC
UNIVERSIDADE DE SANTIAGO DE COMPOSTELA

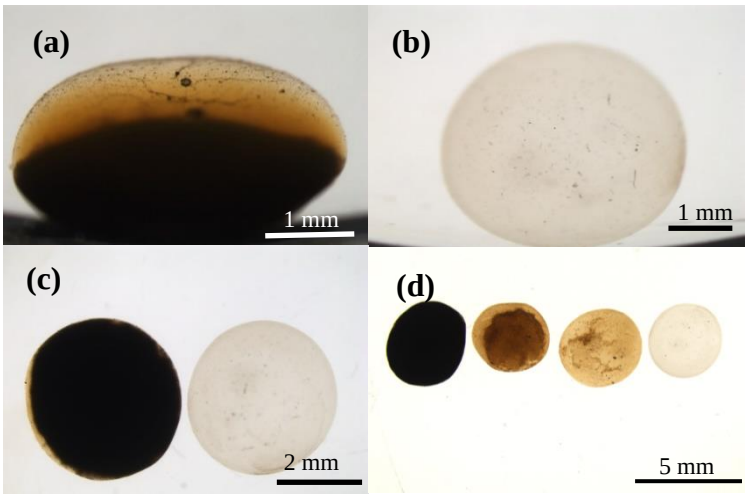


Figure 6.0. Confocal microscope images of the magnetic BNC capsules after 2 years stored (a) F6 NPs (10 wt.%), (b) control capsules, (c) upper perspective of both capsules and (d) all magnetic BNC capsules with distinct NPs concentration

The magnetic response of the NPs revealed a hysteresis loop with saturation magnetization, magnetic remanence, and coercivity of M_s=58.39 emu/g_{Fe3O4}, M_{rem}= 1.63 emu/g_{Fe3O4}, and H_{co}= 10.7 Oe at room temperature (Table A3.4), respectively. The negligible remanence and coercivity indicate the superparamagnetic behaviour of the F6 NPs and the capsules (0 h and 2 y). However, the M_s slightly decreased from 57.0 to 54.43 emu/g_{Fe3O4} at the magnetic BNC (0 h) and BNC (2 y) capsules, respectively. These results show that the magnetic BNC capsules maintain the superparamagnetism of the starting nanoparticle after two years stored, demonstrating its ability to be magnetically functional for long periods. This feature is important for the potential commercialization of the magnetic capsules as a biomedical tool capable of magnetically delivering encapsulated cargos (biological moieties) for long periods.

In addition, BNC is also known to act as a great thermal stabilizer for hydrogel composites [435]. The efficiency of the magnetic BNC capsules (2 y) to dissipate heat for hyperthermia purposes was analysed by raising the temperature through an induced magnetic field of 30 mT under a fixed frequency of 293 kHz. The heat dissipation results of three magnetic BNC capsules (2 y) dispersed in 1 mL water are shown in Figure 6.1b. The respective specific absorption rate (SAR) values were determined by the temperature-time curves using the equation mentioned (Appendix 6.1).

USC UNIVERSIDADE DE SANTIAGO DE COMPOSTELA

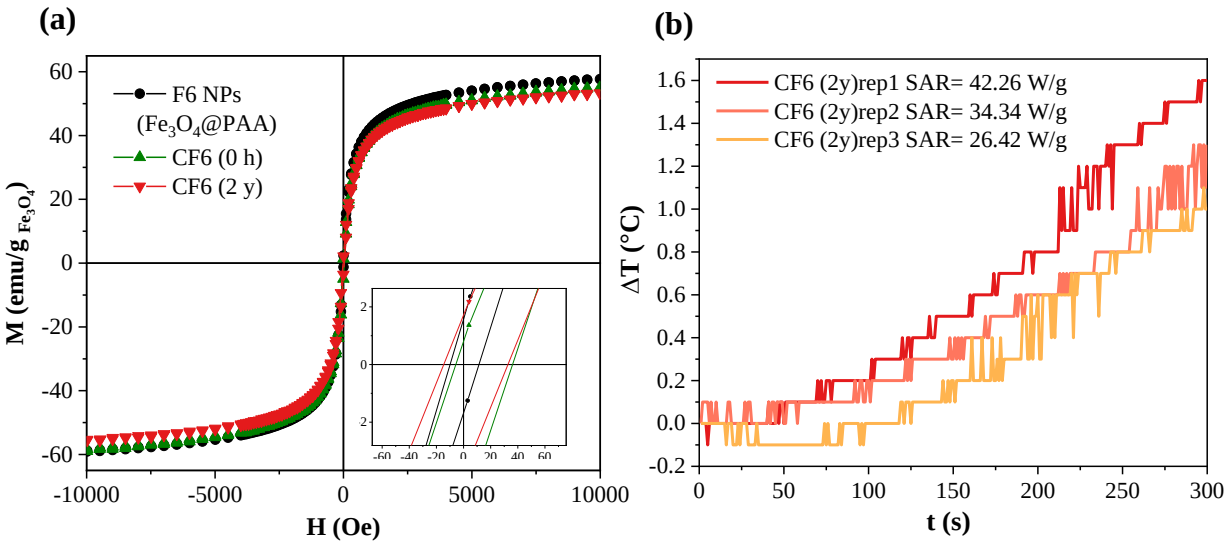


Figure 6.1. Magnetization (a) comparison curve between F6-NPs and magnetic BNC capsules of (0h) and (2 y), respectively; Temperature evolution of three replicates of CF6 (2 y) capsules with 10 wt % of F6-NPs (b) at fixed frequency of 293 kHz and an induced magnetic field of 30 mT, respectively.

Magnetic NPs are physically anchored in the BNC network of the capsules, and the heat released by magnetic hyperthermia tests is limited to *Néel* relaxation. As observed in Figure 6.1b the temperature increment is small ($\Delta T<2$ ºC), and heat diffusion appears to present noise (in the form of "jumps"). In addition, due to the low concentration of NPs, the effect of magnetic inter-particle dipolar interaction is not expected to alter the performance of SAR values [436].

The main contribution to the thermal response of magnetic BNC capsules can be ascribed to the BNC thermal stability, provoking a low heat dissipation. It has been shown in several studies that the addition of BNC in composite materials improves their thermal properties due to synergistic interactions [435, 437]. This allows the fabrication of innovative materials with outstanding properties on temperature sensitivity.

Several studies must be performed to fully understand the effect of Fe_3O_4 NPs in the complex network of BNC and incorporate different cargos to tailor magnetic hyperthermia responses in an under-demand way for specific applications.

3.5. Conclusion

In this chapter it was demonstrated the successfully incorporation of MNPs into a cellulose matrix of TOCNF, cellulose acetate, and BNC to develop functional nanocellulosic magnetic materials with different morphology (microfibers, films, and capsules). In the case of the microfibers, not all NPs were efficiently incorporated to the material, since dispersed NPs were observed in the solution. On the contrary to what was observed in the BNC capsules, the MNPs were strongly attached to the nanocellulose fibrils for over two years without oxidation.

The presence of NPs influenced the mechanical properties of the hybrid materials, specifically the mechanical strength of the microfibers and CA films. The limited interactions between the NPs and TOCNF/sodium alginate caused a discontinuous network. Overtime, in the case of the films, acetic acid was released, breaking hydrogen bonds between the CA matrix and the MNPs, leading to a more brittle material. However, in one film (FM4Fe0.1), the NPs seem to have slowed the deterioration of the film after 90 days stored, increasing its TS and EB.

NPs acted as light barriers, consequently increasing the opacity of the films. The homogenous dispersion of the NPs into the CA network enhanced a low MC and water solubility of the films. The type of NPs and synthesis method played an important role in the mechanical and magnetic properties of the microfibers and films. Microfiber, F1N, revealed a higher magnetization than F3N, since both MNPs were prepared with different reducing agents. However, a mechanical improvement of the F3N microfiber was observed compared to the F1N. Even though the MNPs reduced the mechanical strength, the EB was enhanced, turning the microfibers an optimum material for e.g., remote controls. Concerning the synthesized MNPs, in the remaining microfiber F3N, F4N, and F5N, pure Fe_3O_4 NPs were not formed explaining the reduced magnetization.

On the other hand, the magnetization of the magnetic CA films and BNC capsules was similar to the bulk NPs. Also, it was demonstrated that the NPs integrated within the BNC capsules maintained the superparamagnetic behaviour of the original NPs even at lower concentrations. BNC also proved to be thermally stable when used in magnetic hyperthermia experiments since it released heat in the form of small warm-up jumps. Future studies must be done to fully understand the effect of different MNPs and other components in the morphology, structural and mechanical properties of these nanocellulosic materials.

USC
UNIVERSIDADE DE SANTIAGO DE COMPOSTELA

USC
UNIVERSIDADE
DE SANTIAGO
DE COMPOSTELA

Chapter 4

USC
UNIVERSIDADE
DE SANTIAGO
DE COMPOSTELA

USC
UNIVERSIDADE
DE SANTIAGO
DE COMPOSTELA

4. General Conclusion

In this thesis, sodium alginate and nanocellulose were utilized as the main biopolymeric network to develop sustainable magnetic materials with different architectures. The overall aim was to investigate the adsorption efficiency in several mediums and give a better understanding of how the presence of MNPs would affect materials properties.

The production of the magnetic sodium alginate beads was straightforward with a very simple, rapid, and cost-effective procedure, which also allows to control the beads size and functionalities. These beads are versatile since they can adsorb either mycotoxins or heavy metals from aqueous solutions.

Chapter 2 demonstrated the development of various magnetic alginate beads with different active compounds and their efficiency in adsorbing mycotoxins and heavy metal ions by performing batch adsorption studies. Some beads proved to be more efficient than others or had more affinity for certain mycotoxins in aqueous media and in beer wort. The composition of the beads was a crucial point affecting their efficiency in the mycotoxin's adsorption. The same beads proved to be very efficient in removing Cd(II), Hg(II), and Ni(II) ions from a mono, binary and ternary system under optimized experimental parameters.

In a competitive system, the metal ions competed for the available adsorption sites on the beads surface, decreasing their adsorption capacity. It was also demonstrated that the composition and specific functional groups on the beads are important for achieving an overall fair metals adsorption. Considering their advantageous production process and functionalities, these beads have a huge potential to fulfil the requirements of specific industries and for their use in water treatment technologies or other fields. However, it would be interesting to carry out ecotoxicity studies to see if the cleaned media poses any risk to living organisms.

Chapter 3 showed the development of functional materials with different morphologies produced from nanocellulose and cellulose derivatives. It was also demonstrated the successful incorporation of MNPs into the nanofibrils of the cellulose matrix. It was observed the reduced mechanical strength with NPs incorporation in both films and microfibers. However, an improvement of the EB was observed in one magnetic microfiber compared to the reference microfibers. Also, in one magnetic CA film, the incorporation of Fe_3O_4 NPs slower the deterioration of the film by increasing its opacity acting as light barrier. In addition, the MNPs provided additional advantages of MC and solubility performance to the films. The magnetic BNC capsules were thermally resistance in part due to the low content of NPs and also is one of the characteristic properties of BNC. This material is unique, since the MNPs encapsulated into the BNC matrix for 2 years did not suffer oxidation and magnetization remained unchanged compared to the BNC capsules (0 h) and respective NPs.

For future studies, it is suggested to use different magnetic nanoparticles for the preparation of magnetic microfibers, the ratio of nanoparticles to nanocellulose, and study the posterior effect on the mechanical properties and their potential use for specific fields. In the case of the magnetic cellulosic films, it would be suggested the optimization of the plasticizer agent concentration and explore several environmental conditions that affect the storing and magnetization of the films. Lastly, for future prepared BNC capsules, it would be beneficial to determine the best incubation period to obtain a magnetic capsule able to encapsulate active cargo and, through magnetic hyperthermia, be gradually dispersed in the area of interest.

5. References

1. Briggs, D. Environmental pollution and the global burden of disease. *British Medical Bulletin* **68**, 1–24 (2003).
2. Missimer, T. M. *et al.* Natural Radiation in the Rocks, Soils, and Groundwater of Southern Florida with a Discussion on Potential Health Impacts. *Int. J. Environ. Res. Public Health* **16**, (2019).
3. Ermakov, V. V. *et al.* Impact of natural and man-made factors on migration of heavy metals in the Ardon River basin (North Ossetia). *J. Soils Sediments* **16**, 1253–1266 (2016).
4. Masuda, H. Arsenic cycling in the Earth's crust and hydrosphere: interaction between naturally occurring arsenic and human activities. *Prog. Earth Planet. Sci.* **5**, 1–11 (2018).
5. Diamond, M. L. *et al.* Exploring the planetary boundary for chemical pollution. *Environ. Int.* **78**, 8–15 (2015).
6. Rockström, J. *et al.* Planetary boundaries: Exploring the safe operating space for humanity. *Ecol. Soc.* **14**, (2009).
7. Rockström, J. *et al.* A safe operating space for humanity. *Nat.* **461**, 472–475 (2009).
8. Travis, C.*et al*. Global chemical pollution. *Environ. Sci. Technol.* **25**, 814–819 (1991).
9. El Nemr, A. Impact, monitoring and management of environmental pollution. *Pollut. Sci.* (2011).
10. Waldschläger, K. *et al*. The way of microplastic through the environment – Application of the source-pathway-receptor model (review). *Sci. Total Environ.* **713**, 136584 (2020).
11. Andrady, A. L. The plastic in microplastics: A review. *Mar. Pollut. Bull.* **119**, 12–22 (2017).
12. Avio, C. *et al*. Plastics and microplastics in the oceans: From emerging pollutants to emerged threat. *Mar. Environ. Res.* **128**, 2–11 (2017).
13. Kadam, A., *et al*. A. Pharmaceutical Waste Management An Overview. *Indian J. Pharm. Pract.* **9**, 2–8 (2016).
14. Gorito, A.*et al.* A review on the application of constructed wetlands for the removal of priority substances and contaminants of emerging concern listed in recently launched EU legislation. *Environ. Pollut.* **227**, 428–443 (2017).
15. Vhahangwele, M. *et al*. Environmental Contamination by Heavy Metals. Chapter, in: Hosam M. *et al*.(ed.), Heavy Metals, *IntechOpen* (2018).
16. Mahurpawar Govt, M. Effects of heavy metals on human health. *Int. J. Res.* **3**, 1–7 (2015).
17. Meade, R. H. Contaminants in the Mississippi River, 1987-92. *US Geol. Surv. Circ.* **1133**, 140 (1995).
18. Alloway, B. *et al*. Heavy Metals and Metalloids as Micronutrients for Plants and Animals. Chapter Heavy Metals in Soils. *Environ. Pollut.* **22**, 195–209 (2013)
19. EU. Directive 2008/105/EC of the European Parliament and of the Council of 16 December 2008 on environmental quality standards in the field of water policy, amending and subsequently repealing Council Directives 82/176/EEC, 83/513/EEC, 84/156/EEC, 84/491/EEC. *Off. J. Eur. Union* **l**, 348 84–97 (2008).
20. EU. Directive 2013/39/EU of the European Parliament and of the Council of 12 August 2013 amending Directives 2000/60/ECand 2008/105/EC as regards priority substances in the field of water policy. *Off. J. Eur. Union* **226**, 1–17 (2013).

21. Klavinš, M. *et al.* Heavy metals in rivers of Latvia. *Sci. Total Environ.* **262**, 175–183 (2000).
22. Pizarro, J. *et al*. Heavy metals in northern Chilean rivers: Spatial variation and temporal trends. *J. Hazard. Mater.* **181**, 747–754 (2010).
23. Okonkwo, J. O.*et al*. Physico-chemical characteristics and pollution levels of heavy metals in the rivers in Thohoyandou, South Africa. *J. Hydrol.* **308**, 122–127 (2005).
24. Fernandes, C. *et al*. Heavy metals in water, sediment and tissues of Liza saliens from Esmoriz–Paramos lagoon, Portugal. *Springer* **136**, 267–275 (2008).
25. Lokhande, R. S. *et al*.Toxicity Study of Heavy Metals Pollutants in Waste Water Effluent Samples Collected from Taloja Industrial Estate of Mumbai, India. *Resour. Environ.* **1**, 13–19 (2011).
26. Järup, L. Hazards of heavy metal contamination. *Br. Med. Bull.* **68**, 167–182 (2003).
27. United States Environmental Protection Agency. Groundwater and driking water : national primary and drinking regulations. *US EPA* (2020).
28. Chen, C. Y. *et al.* The influence of nutrient loading on methylmercury availability in Long Island estuaries. *Environ. Pollut.* **268**, 115510 (2021).
29. World Health Organization. Nickel in drinking-water. Background document for development of WHO Guidelines for drinking-water quality No.WHO/SDE/WSH/07.08/55, World Health Organization (2005).
30. Sankhla, M. S. *et al*. Heavy Metals Contamination in Water and their Hazardous Effect on Human Health-A Review. *Int. J. Curr. Microbiol. Appl. Sci.* **5**, 759–766 (2016).
31. Peters, Adam, *et al.* Assessing the Extent of Environmental Risks From Nickel in European Freshwaters: A Critical Reflection of the European Commission's Current Approach. *Environ. Toxicol. Chem.* (2022).
32. Sanchis, V.*et al*. Environmental conditions affecting mycotoxins. *Mycotoxins Food* 174–189 (2004).
33. Al-Gabr, H. M. *et al.* Fungi Contamination of Drinking Water. *Rev. Environ. Contam. Toxicol.* **228**, 121–139 (2014).
34. Bhatnagar, D., *et al.* Understanding the genetics of regulation of aflatoxin production and Aspergillus flavus development. *Mycopathologia* **162**, 155–166 (2006).
35. Pereira, V. L. *et al.* Mycotoxins in cereals and related foodstuffs: A review on occurrence and recent methods of analysis. *Trends Food Sci. Technol.* **36**, 96–136 (2014).
36. Alshannaq, A. *et al.* Occurrence, Toxicity, and Analysis of Major Mycotoxins in Food. *Int. J. Environ. Res. Public Heal.* **14**, 632 (2017).
37. Fernández-Cruz, M. L. *et al.* Mycotoxins in fruits and their processed products: Analysis, occurrence and health implications. *J. Adv. Res.* **1**, 113–122 (2010).
38. Savazzini, F. *et al.* Real-time PCR for detection and quantification of the biocontrol agent Trichoderma atroviride strain SC1 in soil. *J. Microbiol. Methods* **73**, 185–194 (2008).
39. Bennett, J. W. *et al.* Mycotoxins. *Clin. Microbiol. Rev.* **16**, 497–516 (2003).
40. EU commission regulation. Amending Annex I to Directive 2002/32/EC of the European Parliament and of the Council as regards maximum levels for nitrite, melamine, Ambrosia spp. and carry-over of certain coccidiostats and histomonostats. **8**, 1–18 (2011).
41. Peters, J. *et al.* Mycotoxin profiling of 1000 beer samples with a special focus on

craft beer. *PLoS One* **12**, e0185887 (2017).
42. González-Jartín, J. M. *et al.* Detoxification agents based on magnetic nanostructured particles as a novel strategy for mycotoxin mitigation in food. *Food Chem.* **294**, 60–66 (2019).
43. Rodríguez-Carrasco, Y. *et al.* Occurrence of Fusarium mycotoxins and their dietary intake through beer consumption by the European population. *Food Chem.* **178**, 149–155 (2015).
44. Opinion of the scientific panel on contaminants in the food chain related to the potential increase of consumer health risk by a possible increase of the existing maximum levels for aflatoxins in almonds, hazelnuts and pistachios and derived prod. *EFSA Journal* **5**, 1–127 (2007).
45. Fink-Gremmels, J. Mycotoxins: Their implications for human and animal health. *Vet. Q.* **21**, 115–120 (1999).
46. Knutsen, H. K. *et al.* Risks for animal health related to the presence of fumonisins, their modified forms and hidden forms in feed. *EFSA J.* **16**, e05242 (2018).
47. Pascari, X. *et al.* Mycotoxins and beer. Impact of beer production process on mycotoxin contamination. A review. *Food Res. Int.* **103**, 121–129 (2018).
48. Kuzdraliński, A. et al. Deoxynivalenol and zearalenone occurence in beers analysed by an enzyme-linked immunosorbent assay method. *Food Control* **29**, 22–24 (2013).
49. Zhang, B. *et al.* Simultaneous Analysis of 20 Mycotoxins in Grapes and Wines from Hexi Corridor Region (China): Based on a QuEChERS¯UHPLC¯MS/MS Method. *Molecules* **23**, (2018).
50. Liu, Y. et al. A review of postharvest approaches to reduce fungal and mycotoxin contamination of foods. *Compr. Rev. Food Sci. Food Saf.* **19**, 1521–1560 (2020).
51. Rheeder, J. P. *et al.* Production of Fumonisin Analogs by Fusarium Species. *Appl. Environ. Microbiol.* **68**, 2101 (2002).
52. Probst, C. *et al.* Diversity of aflatoxin-producing fungi and their impact on food safety in sub-Saharan Africa. *Int. J. Food Microbiol.* **174**, 113–122 (2014).
53. Kumar, P. et al. Aflatoxins: A global concern for food safety, human health and their management. *Front. Microbiol.* **7**, (2017).
54. González Jartín, J. M. The application of the nanotechnology in the elimination of phycotoxins and mycotoxins and implementation of mass spectrometry for their detection (PhD thesis) *Universidade de Santiago de compostela* (2020).
55. Kushiro, M. Effects of milling and cooking processes on the deoxynivalenol content in wheat. *Int. J. Mol. Sci.* **9**, 2127–2145 (2008).
56. Sobrova, P. *et al.* Deoxynivalenol and its toxicity. *Interdiscip. Toxicol.* **3**, 94–99 (2010).
57. FILEK, Maria, *et al.* Occurrence and physiology of zearalenone as a new plant hormone. In: Sociology, organic farming, climate change and soil science. *Springer*, 419-435 (2010).
58. Gzyl-Malcher, B. *et al.* Manganese protects wheat from the mycotoxin zearalenone and its derivatives. *Sci. Reports* 9, 1–12 (2019).
59. Gelderblom, W. C. A. *et al.* Fumonisins - novel mycotoxins with cancer-promoting activity produced by Fusarium moniliforme. *Appl. Environ. Microbiol.* **54**, 1806–1811 (1988).
60. Yazar, S. *et al.* Fumonisins, trichothecenes and zearalenone in cereals. *Int. J. Mol. Sci.* **9**, 2062–2090 (2008).
61. Wilson, D. *et al.* Biology and ecology of mycotoxigenic Aspergillus species as related to economic and health concerns. *Springer* **504**, 3–17 (2002).

62. Liu, Y. *et al.* Global burden of aflatoxin-induced hepatocellular carcinoma: a risk assessment. *Environ. Health Perspect.* **118**, 818–824 (2010).
63. Dhanasekaran, D. *et al.* Aflatoxins and Aflatoxicosis in Human and Animals. *Aflatoxins - Biochem. Mol. Biol.* (2011).
64. Pereira, V. J. *et al.* Assessment of the presence and dynamics of fungi in drinking water sources using cultural and molecular methods. *Water Res.* **44**, 4850–4859 (2010).
65. Gonçalves, A. B. *et al.* Survey and significance of filamentous fungi from tap water. *Int. J. Hyg. Environ. Health* **209**, 257–264 (2006).
66. Grabińska-Łoniewska, A. et al. Occurrence of fungi in water distribution system. *Polish J. Environ. Stud.* **16**, 539–547 (2007).
67. Nasser, L. A. Incidence of Terrestrial Fungi in Drinking Water Collected from Different Schools in Riyadh Region, Saudi Arabia. *Pakistan J. Biol. Sci.* **7**, 1927–1932 (2004).
68. Sammon, N. B. *et al.* Incidence and distribution of microfungi in a treated municipal water supply system in sub-tropical Australia. *Int. J. Environ. Res. Public Health* **7**, 1597–1611 (2010).
69. Anaissie, E. J. *et al.* Pathogenic molds (including Aspergillus species) in hospital water distribution systems: A 3-year prospective study and clinical implications for patients with hematologic malignancies. *Blood* **101**, 2542–2546 (2003).
70. Hageskal, G., Knutsen, A. K., Gaustad, P., De Hoog, G. S. and Skaar, I. Diversity and significance of mold species in Norwegian drinking water. *Appl. Environ. Microbiol.* **72**, 7586–7593 (2006).
71. Arvanitidou, M. *et al.* High level of recovery of fungi from water and dialysate in haemodialysis units. *J. Hosp. Infect.* **45**, 225–230 (2000).
72. Gromadzka, K. *et al.* Occurrence of estrogenic mycotoxin - Zearalenone in aqueous environmental samples with various NOM content. *Water Res.* **43**, 1051–1059 (2009).
73. Paterson, R. R. M. *et al.* Natural occurrence of aflatoxins and Aspergillus flavus (Link) in water. *Lett. Appl. Microbiol.* **25**, 435–436 (1997).
74. Abid-Essefi, S. *et al.* Cytotoxicity, inhibition of DNA and protein syntheses and oxidative damage in cultured cells exposed to zearalenone. *Toxicol. In Vitro* **18**, 467–474 (2004).
75. Gebremeskel, A. F. et al. Prevalence and controlling mechanisms of mycotoxin. *Cogent food and agriculture* **5**, 1658978 (2019).
76. Bhattacharya, S. et al. Water Remediation. *Springer* (2018).
77. Cheremisinoff, P. N. Handbook of water and wastewater treatment technology. Routledge. *Routledge* (2019).
78. Gunatilake SK. Methods of Removing Heavy Metals from Industrial Wastewater. *J. Multidiscip. Eng. Sci. Stud.* **1**, 2912–1309 (2015).
79. Ayoob, S., et al. Conceptual overview on sustainable technologies for the defluoridation of drinking water. *Critical reviews in environmental science and technology* **38**, 401–470 (2008).
80. López-Maldonado, E. A. et al. Coagulation-flocculation mechanisms in wastewater treatment plants through zeta potential measurements. *J. Hazard. Mater.* **279**, 1–10 (2014).
81. Aziz, H. A. *et al.* Heavy metals (Cd, Pb, Zn, Ni, Cu and Cr(III)) removal from water in Malaysia: Post treatment by high quality limestone. *Bioresour. Technol.* **99**, 1578–1583 (2008).
82. Shim, H. Y. *et al.* Application of Electrocoagulation and Electrolysis on the

Precipitation of Heavy Metals and Particulate Solids in Washwater from the Soil Washing. *J. Agric. Chem. Environ.* **03**, 130–138 (2014).
83. Demirbas, A. Heavy metal adsorption onto agro-based waste materials: A review. *J. Hazard. Mater.* **157**, 220–229 (2008).
84. Pintor, A. M. A. *et al.* Use of cork powder and granules for the adsorption of pollutants: A review. *Water Res.* **46**, 3152–3166 (2012).
85. Zain, M. E. Impact of mycotoxins on humans and animals. *J. Saudi Chem. Soc.* **15**, 129–144 (2011).
86. Fandohan, P. *et al.* Fate of aflatoxins and fumonisins during the processing of maize into food products in Benin. *Int. J. Food Microbiol.* **98**, 249–259 (2005).
87. Beretta, B. *et al.* Patulin in apple-based foods: occurrence and safety evaluation. *Food Addit. Contam.* **17**, 399–406 (2000).
88. Van der Westhuizen, L. *et al.* Optimising sorting and washing of home-grown maize to reduce fumonisin contamination under laboratory-controlled conditions. *Food Control* **22**, 396–400 (2011).
89. Mousavi Khaneghah, A. et al. Aflatoxins in cereals: State of the art. *J. Food Saf.* **38**, e12532 (2018).
90. Ismail, A. *et al.* Aflatoxin in foodstuffs: Occurrence and recent advances in decontamination. *Food Res. Int.* **113**, 74–85 (2018).
91. Aziz, N.et al. Control of Fusarium moulds and fumonisin B1 in seeds by gamma-irradiation. *Food Control* **18**, 1337–1342 (2007).
92. Savi, G. D. *et al.* Ozone treatment efficiency on Fusarium graminearum and deoxynivalenol degradation and its effects on whole wheat grains (Triticum aestivum L.) quality and germination. *J. Stored Prod. Res.* **59**, 245–253 (2014).
93. Mir, S. A. et al. Understanding the Role of Plasma Technology in Food Industry. *Food Bioprocess Technol.* **9**, 734–750 (2016).
94. Jard, G. *et al*. Review of mycotoxin reduction in food and feed: from prevention in the field to detoxification by adsorption or transformation. *Food Addit. Contam. Part A. Chem. Anal. Control. Expo. Risk Assess.* **28**, 1590–1609 (2011).
95. Çelik, K. The efficacy of mycotoxin-detoxifying and biotransforming agents in animal nutrition. *Nanomycotoxicology*, 271-284 (2020).
96. Abdel Maksoud, M. I. A. *et al.* Insight on water remediation application using magnetic nanomaterials and biosorbents. *Coord. Chem. Rev.* **403**, 213096 (2020).
97. Holan, Z. R. et al. Biosorption of cadmium by biomass of marine algae. *Biotechnol. Bioeng.* **41**, 819–825 (1993).
98. Kuyucak, N. *et al.* Accumulation of cobalt by marine alga. *Biotechnol. Bioeng.* **33**, 809–814 (1989).
99. Zhong, L. X., Peng, X. W., Yang, D. and Sun, R. C. Adsorption of heavy metals by a porous bioadsorbent from lignocellulosic biomass reconstructed in an ionic liquid. *J. Agric. Food Chem.* **60**, 5621–5628 (2012).
100. Mattuschka, B.et al. Biosorption of metals by a waste biomass. *J. Chem. Technol. Biotechnol.* **58**, 57–63 (1993).
101. Perali, C. *et al.* Lithothamnium calcareum (Pallas) Areschoug seaweed adsorbs aflatoxin B1 in vitro and improves broiler chicken's performance. *Mycotoxin Res.* **36**, 371–379 (2020).
102. Bočarov-Stančić, A. *et al.* In vitro removing of mycotoxins by using different inorganic adsorbents and organic waste materials from Serbia. *Food Feed Res.* **45**, 87–96 (2018).
103. Greco, D. *et al.* Comparative efficacy of agricultural by-products in sequestering mycotoxins. *J. Sci. Food Agric.* **99**, 1623–1634 (2019).

104. Costa, C. S. D. *et al.* Equilibrium study of binary mixture biosorption of Cr(III) and Zn(II) by dealginated seaweed waste: investigation of adsorption mechanisms using X-ray photoelectron spectroscopy analysis. *Environ. Sci. Pollut. Res.* **26**, 28470–28480 (2019).
105. Abdi, O. *et al.* A review study of biosorption of heavy metals and comparison between different biosorbents. *J. Mater. Environ. Sci* **6**, 1386–1399 (2015).
106. Ramachandra, T., Ahalya, N. and Kanamadi, R. Biosorption: Techniques and Mechanisms. *CES TR* **110**, (2006).
107. Sánchez, C. Lignocellulosic residues: biodegradation and bioconversion by fungi. *Biotechnol. Adv.* **27**, 185–194 (2009).
108. Palma, V. *et al.* Microwaves and heterogeneous catalysis: A review on selected catalytic processes. *Catalysts* **10**, (2020).
109. Sudarsanam, P. *et al.* Advances in porous and nanoscale catalysts for viable biomass conversion. *Chem. Soc. Rev.* **48**, 2366–2421 (2019).
110. Kumar, P.*et al.* Methods for Pretreatment of Lignocellulosic Biomass for Efficient Hydrolysis and Biofuel Production. *Ind. Eng. Chem. Res.* **48**, 3713-3729 (2009).
111. Gírio, F. M. *et al.* Hemicelluloses for fuel ethanol: A review. *Bioresour. Technol.* **101**, 4775–4800 (2010).
112. Luo, Y. *et al.* The production of furfural directly from hemicellulose in lignocellulosic biomass: A review. *Catal. Today* **319**, 14–24 (2019).
113. Alonso, D. M. et al. Bimetallic catalysts for upgrading of biomass to fuels and chemicals. *Chem. Soc. Rev.* **41**, 8075–8098 (2012).
114. Upton, B. M. *et al.* Strategies for the conversion of lignin to high-value polymeric materials: Review and perspective. *Chem. Rev.* **116**, 2275–2306 (2016).
115. Kumar, R. *et al.* Does change in accessibility with conversion depend on both the substrate and pretreatment technology? *Bioresour. Technol.* **100**, 4193–4202 (2009).
116. Grethlein, H. E. The effect of pore size distribution on the rate of enzymatic hydrolysis of cellulosic substrates. *Bio/Technology* **3**, 155–160 (1985).
117. Chandra, R. P. *et al.* Substrate pretreatment: The key to effective enzymatic hydrolysis of lignocellulosics. *Adv. Biochem. Eng. Biotechnol.* **108**, 67–93 (2007).
118. Taherzadeh, M. J. *et al.* Pretreatment of Lignocellulosic Wastes to Improve Ethanol and Biogas Production: A Review. *Int. J. Mol. Sci.* **9**, 1621 (2008).
119. Batista Meneses, D. *et al.* Pretreatment methods of lignocellulosic wastes into value-added products: recent advances and possibilities. *Biomass Convers. Biorefinery* **12**, 547–564 (2020).
120. Fedorova, E. *et al.* Balancing Socio-Efficiency and Resilience of Energy Provisioning on a Regional Level, Case Oulun Energia in Finland. *Clean Technol.* **1**, 273–293 (2019).
121. Anastopoulos, I. *et al*. Progress in batch biosorption of heavy metals onto algae. *J. Mol. Liq.* **209**, 77–86 (2015).
122. Pereira, L. Macroalgae. *Encyclopedia* **1**, 177–188 (2021).
123. Vale, M. A. *et al*. CO_2 capture using microalgae. *Adv. Carbon Capture* 381–405 (2020).
124. Kulik, M. M. The potential for using cyanobacteria (blue-green algae) and algae in the biological control of plant pathogenic bacteria and fungi. *Eur. J. Plant Pathol.* **101**, 585–599 (1995).
125. Ivánová, D., Kavuliďová, J., Horváthová, H. and Kaduková, J. Determination of the Functional Groups in Algae Parachlorella Kessleri by Potentiometric Titrations. *Nov. Biotechnol. Chim.* **11**, 93–99 (2012).

126. Su, L. *et al*. Analyses of the genetic structure of Sargassum horneri in the Yellow Sea: implications of the temporal and spatial relations among floating and benthic populations. *J. Appl. Phycol.* **30**, 1417–1424 (2018).
127. Van Hees, D. H. *et al.* Cast adrift: Physiology and dispersal of benthic Sargassum spinuligerum in surface rafts. *Limnol. Oceanogr.* **64**, 526–540 (2019).
128. Wang, M. *et al.* Remote Sensing of Sargassum Biomass, Nutrients, and Pigments. *Geophys. Res. Lett.* **45**, 12.359-12.367 (2018).
129. David Wells, R. J. *et al*. Spatial and temporal patterns of habitat use by fishes associated with sargassum mats in the northwestern Gulf of Mexico. *Bull. Mar. Sci.* **74**, 81–99 (2004).
130. Monroy-Velázquez, L. V. *et al.* Motile macrofauna associated with pelagic Sargassum in a Mexican reef lagoon. *J. Environ. Manage.* **252**, 109650 (2019).
131. Wang, M. *et al.* The great Atlantic Sargassum belt. *Science (80-.).* **364**, 83–87 (2019).
132. Amador-Castro, F. *et al*. Valorization of pelagic sargassum biomass into sustainable applications: Current trends and challenges. *J. Environ. Manage.* **283**, 112013 (2021).
133. Jard, G. *et al.* French Brittany macroalgae screening: Composition and methane potential for potential alternative sources of energy and products. *Bioresour. Technol.* **144**, 492–498 (2013).
134. Peinado, I. *et al*. Chemical composition, antioxidant activity and sensory evaluation of five different species of brown edible seaweeds. *Food Res. Int.* **66**, 36–44 (2014).
135. Jung, K. A. *et al.* Potentials of macroalgae as feedstocks for biorefinery. *Bioresour. Technol.* **135**, 182–190 (2013).
136. Horn, S. J. Seaweed Biofuels: Production of biogas and bioethano from brown macroalgae. *J. Appl. Phycol.* **24**, 1295-1301 (2009).
137. Rinaudo, M. Biomaterials based on a natural polysaccharide: alginate. *TIP* **17**, 92–96 (2014).
138. Kleinübing, S. J. *et al.* Extraction of alginate biopolymer present in marine alga sargassum filipendula and bioadsorption of metallic ions. *Mater. Res.* **16**, 481–488 (2013).
139. Abasalizadeh, F. *et al.* Alginate-based hydrogels as drug delivery vehicles in cancer treatment and their applications in wound dressing and 3D bioprinting. *J. Biol. Eng.* **14**, 89–103 (2020).
140. Kang, H. K.et al. The effects of marine carbohydrates and glycosylated compounds on human health. *Int. J. Mol. Sci.* **16**, 6018–6056 (2015).
141. Abasalizadeh, F. *et al.* Alginate-based hydrogels as drug delivery vehicles in cancer treatment and their applications in wound dressing and 3D bioprinting. *J. Biol. Eng.* **14**, 1–22 (2020).
142. Stephen, Alistair M., and Glyn O. Phillips. Food Polysaccharides and Their Applications.*CRC Press*, (2016).
143. Papageorgiou, S. K., Kouvelos, E. P. and Katsaros, F. K. Calcium alginate beads from Laminaria digitata for the removal of Cu^{+2} and Cd^{+2} from dilute aqueous metal solutions. *Desalination* **224**, 293–306 (2008).
144. Augst, A. D., Kong, H. J., and Mooney, D. J. Alginate hydrogels as biomaterials. *Macromol. biosci.* **6**, 623-633 (2006).
145. Jönsson, M., Allahgholi, L., Sardari, R. R. R., Hreggviosson, G. O. and Karlsson, E. N. Extraction and modification of macroalgal polysaccharides for current and next-generation applications. *Molecules* **25,** 930 (2020).

146. Baiano, A. Recovery of biomolecules from food wastes - A review. *Molecules*. **19**, 14821–14842 (2014).
147. Bilgen, S. and Sarıkaya, İ. Utilization of forestry and agricultural wastes. *Energy Sources A: Recovery, Util. Environ. Eff.* **38**, 3484–3490 (2016).
148. Pandey, Aviyan. FOOD wastage: causes, impacts and solutions. *Science Heritage Journal* (*GWS*) 5, 17-20 (2021).
149. Sheldon, R. A. Green chemistry, catalysis and valorization of waste biomass. *J. Mol. Catal. A Chem.* **422**, 3–12 (2016).
150. Nishimura, H. *et al.* Production of ethanol from a mixture of waste paper and kitchen waste via a process of successive liquefaction, presaccharification, and simultaneous saccharification and fermentation. *Waste Manag.* **67**, 86–94 (2017).
151. Brandão, A. S. *et al*. Circular bioeconomy strategies: From scientific research to commercially viable products. *J. Clean. Prod.* **295**, 126407 (2021).
152. Ramcilovic-Suominen, S., & Pülzl, H. Sustainable development–a 'selling point'of the emerging EU bioeconomy policy framework? *J. Clean. Prod.* **172**, 4170-4180 (2018).
153. Carus, M. and Dammer, L. The Circular Bioeconomy - Concepts, Opportunities, and Limitations. *Ind. Biotechnol.* **14**, 83–91 (2018).
154. Morganti, P. Bionanotechnology to save the environment: plant and fishery's biomass as alternative to petrol (2019).
155. Stegmann, P., Londo, M. and Junginger, M. The circular bioeconomy: Its elements and role in European bioeconomy clusters. *Resour. Conserv. Recycl. X* **6**, 100029 (2020).
156. Sherwood, J. The significance of biomass in a circular economy. *Bioresour. Technol.* **300**, 122755 (2020).
157. Schmidt, O. *et al*. The bio-economy concept and knowledge base in a public goods and farmer perspective. *BAE* **1**, 47–63 (2012).
158. Wolfslehner, B. *et al.* Forest bioeconomy-a new scope for sustainability indicators. From science to policy 4 (2016).
159. de Arano, I. M. *et al*. A forest-based circular bioeconomy for southern Europe: visions, opportunities and challenges (2018).
160. EC. The EU Blue Economy Report. *Publications Office of the European Union. Luxembourg* (2019).
161. Saviolidis, N. M. *et al.* Realising blue growth in the fishing industry in Iceland and Norway: Industry perceptions on drivers and barriers to blue growth investments and policy implications. *Mar. Policy* **117**, 103967 (2020).
162. Jónsson, Á. and Viðarsson Auðlindir Og Afurðir, J. R. By-products from whitefish processing (2016).
163. Ahuja, I., Dauksas, E., Remme, J. F., Richardsen, R. and Løes, A. K. Fish and fish waste-based fertilizers in organic farming – With status in Norway: A review. *Waste Manag.* **115**, 95–112 (2020).
164. Camia, A. *et al.* Biomass production, supply, uses and flows in the European Union: First results from an integrated assessment (2018).
165. Joint Research Centre (JRC). Jobs and Wealth in the EU Bioeconom. *Data-Modelling platform of resource economics* (2018).
166. D'Amato, D., Veijonaho, S. and Toppinen, A. Towards sustainability? Forest-based circular bioeconomy business models in Finnish SMEs. *For. Policy Econ.* **110**, 101848 (2020).
167. Toppinen, A., Röhr, A., Pätäri, S., Lähtinen, K. and Toivonen, R. The future of wooden multistory construction in the forest bioeconomy – A Delphi study from

Finland and Sweden. *J. For. Econ.* **31**, 3–10 (2018).
168. Johnson, F. X. Industrial Biotechnology and Biomass Utilisation: Prospects and Challenges for the Developing World. (2009).
169. Kagan, C. R. *et al.* Nano Day: Celebrating the Next Decade of Nanoscience and Nanotechnology. *ACS Nano* **10**, 9093–9103 (2016).
170. Karahan, H. E. *et al.* Biomass-derived nanocarbon materials for biological applications: challenges and prospects. *J. Mater. Chem. B* **8**, 9668–9678 (2020).
171. Selva, M. Nanotechnologies for the sustainable valorization of biowastes. *Curr. Opin. Green Sustain. Chem.* **24**, 38–41 (2020).
172. Steele, J. M., Grady, N. K., Nordlander, P. and Halas, N. J. Plasmon hybridization in complex nanostructures. *Springer Ser. Opt. Sci.* **131**, 183–196 (2007).
173. Khan, Nida, Kumarasamy Sudhakar, and Rizalman Mamat. Role of biofuels in energy transition, green economy and carbon neutrality. *Sustainability*, 12374 (2021)
174. Moon, R. J., Frihart, C. R. and Wegner, T. Nanotechnology applications in the forest products industry. *For. Prod. J.* **56**, 4–10 (2006).
175. Contreras, J. E., Rodriguez, E. A. and Taha-Tijerina, J. Nanotechnology applications for electrical transformers—A review. *Electr. Power Syst. Res.* **143**, 573–584 (2017).
176. Tiwari, J. N., Tiwari, R. N. and Kim, K. S. Zero-dimensional, one-dimensional, two-dimensional and three-dimensional nanostructured materials for advanced electrochemical energy devices. *Prog. Mater. Sci.* **57**, 724–803 (2012).
177. Poh, T. Y. *et al.* Inhaled nanomaterials and the respiratory microbiome: clinical, immunological and toxicological perspectives. *Part. Fibre Toxicol.* **15**, 1–16 (2018).
178. Chen, C. and Hu, L. Nanocellulose toward Advanced Energy Storage Devices: Structure and Electrochemistry. *Acc. Chem. Res.* **51**, 3154–3165 (2018).
179. Lin, N. and Dufresne, A. Nanocellulose in biomedicine: Current status and future prospect. *Eur. Polym. J.* **59**, 302–325 (2014).
180. Mokhena, T. C. and John, M. J. Cellulose nanomaterials: new generation materials for solving global issues. *Cellul.* **27**, 1149–1194 (2019).
181. Nekvapil, F. *et al.* From Blue Bioeconomy toward Circular Economy through High-Sensitivity Analytical Research on Waste Blue Crab Shells. *ACS Sustain. Chem. Eng.* **7**, 16820–16827 (2019).
182. Ahmad Raus, R., Wan Nawawi, W. M. F. and Nasaruddin, R. R. Alginate and alginate composites for biomedical applications. *Asian J. Pharm. Sci.* **16**, 280–306 (2021).
183. Karmakar, N. *et al*. A review on the classification, characterisation, synthesis of nanoparticles and their application. *IOP Conf. Ser. Mater. Sci. Eng.* **263**, 032019 (2017).
184. Khan, I., Saeed, K. and Khan, I. Nanoparticles: Properties, applications and toxicities. *Arab. J. Chem.* **12**, 908–931 (2019).
185. Hulteen, J. C. *et al.* Nanosphere lithography: Size-tunable silver nanoparticle and surface cluster arrays. *J. Phys. Chem. B* **103**, 3854–3863 (1999).
186. Meijer, J. M. and Rossi, L. Preparation, properties, and applications of magnetic hematite microparticles. *Soft Matter* **17**, 2354–2368 (2021).
187. Bhaviripudi, S. *et al.* CVD synthesis of single-walled carbon nanotubes from gold nanoparticle catalysts. *J. Am. Chem. Soc.* **129**, 1516–1517 (2007).
188. Hernández-Mínguez, A. *et al.* Quantum magnetic deflagration in Mn12 acetate. *Phys. Rev. Lett.* **95**, 217205 (2005).

189. Aharoni, A. Relaxation time of superparamagnetic particles with cubic anisotropy. *Phys. Rev. B* **7**, 1103–1107 (1973).
190. Batlle, X. and Labarta, A. Finite-size effects in fine particles: magnetic and transport properties. *J. Phys. D. Appl. Phys.* **35**, 201 (2002).
191. Ziolo, R. F. *et al.* Matrix-Mediated Synthesis of Nanocrystalline γ-Fe_2O_3: A New Optically Transparent Magnetic Material. *Science (80-.).* **257**, 219–223 (1992).
192. Zhu, J. *et al.* Magnetic nanocomposites for environmental remediation. *Adv. Powder Technol.* **24**, 459–467 (2013).
193. Piñeiro, Y., Vargas, Z., Rivas, J. and Lopez-Quintela, M. A. Iron Oxide Based Nanoparticles for Magnetic Hyperthermia Strategies in Biological Applications. *Eur. J. Inorg. Chem.* **2015**, 4495–4509 (2015).
194. Lu, A. H., Salabas, E. L. and Schüth, F. Magnetic Nanoparticles: Synthesis, Protection, Functionalization, and Application. *Angew. Chemie Int. Ed.* **46**, 1222–1244 (2007).
195. Fatima, H., Charinpanitkul, T. and Kim, K. S. Fundamentals to Apply Magnetic Nanoparticles for Hyperthermia Therapy. *Nanomater.* **11**, 1203 (2021).
196. Gubin, S. P., Koksharov, Y. A., Khomutov, G. B. and Yurkov, G. Y. Magnetic nanoparticles: Preparation, structure and properties. *Usp. Khim.* **74**, 539–574 (2005).
197. Merbach, A., Helm, L. and Tóth, É. The Chemistry of Contrast Agents in Medical Magnetic Resonance Imaging: Second Edition. *John Wiley and Sons* (2013).
198. Blaney, L. Magnetite (Fe_3O_4): Properties, Synthesis, and Applications. *Lehigh Preserve*. **15**, 5 (2007)
199. Wu, W., He, Q. and Jiang, C. Magnetic Iron Oxide Nanoparticles: Synthesis and Surface Functionalization Strategies. *Nanoscale Res. Lett.* **3**, 397 (2008).
200. Aliramaji, S., Zamanian, A. and Sohrabijam, Z. Characterization and Synthesis of Magnetite Nanoparticles by Innovative Sonochemical Method. *Procedia Mater. Sci.* **11**, 265–269 (2015).
201. Aono, H. *et al.* Synthesis of fine magnetite powder using reverse coprecipitation method and its heating properties by applying AC magnetic field. *Mater. Res. Bull.* **40**, 1126–1135 (2005).
202. Kumari, M. Magnetic Properties of Iron-Oxide Nanoparticles and Methods for Their Characterization (PhD Thesis) *Indian Institute of Technology* (2015).
203. Montazer, M. and Harifi, T. Magnetic nanofinishes for textiles. *Nanofinishing Text. Mater.* 225–240 (2018).
204. Leslie-Pelecky, D. L. and Rieke, R. D. Magnetic properties of nanostructured materials. *Chem. Mater.* **8**, 1770–1783 (1996).
205. Eschweiler, Z. T. Superparamagnetic nanoparticle technology and analysis of water, water-treatment, health-risks of contaminates water, and a proposed solution (PhD Thesis). *Western Reserve University* (2017).
206. Tapeinos, C. Magnetic Nanoparticles and Their Bioapplications. *Smart Nanoparticles Biomed.* 131–142 (2018).
207. Sort Vinas, J. Magnetic hardening induced by ferromagnetic-antiferromagnetic coupling (PhD Thesis). *Universitat Autònoma de Barcelona* (2002).
208. Straczek, T. *et al.* Dynamics of Superparamagnetic Iron Oxide Nanoparticles with Various Polymeric Coatings. *Mater.* **12**, 1793 (2019).
209. Mohapatra, J. and Liu, J. P. Rare-Earth-Free Permanent Magnets: The Past and Future. *Handbook of Magnetic Materials* **27,** 1–57 (2018).
210. Tummino, M. L. *et al.* The "Lab4treat" Outreach Experience: Preparation of Sustainable Magnetic Nanomaterials for Remediation of Model Wastewater. *Mol.*

26, 3361 (2021).
211. de Castro Alves, L., Yáñez-Vilar, S., Piñeiro-Redondo, Y. and Rivas, J. Efficient Separation of Heavy Metals by Magnetic Nanostructured Beads. *Inorganics* **8**, 40 (2020).
212. Huang, X., Zhan, X., Wen, C., Xu, F. and Luo, L. Amino-functionalized magnetic bacterial cellulose/activated carbon composite for Pb^{2+} and methyl orange sorption from aqueous solution. *J. Mater. Sci. Technol.* **34**, 855–863 (2018).
213. Xia, T., Ma, Q., Hu, T. and Su, X. A novel magnetic/photoluminescence bifunctional nanohybrid for the determination of trypsin. *Talanta* **170**, 286–290 (2017).
214. Nypelö, Tiina, et al. Magneto-responsive hybrid materials based on cellulose nanocrystals. *Cellulose* **21,** 2557-25668 (2014).
215. Wu, W. B., Gong, Y. J., Zhou, X. F. and Dai, H. Q. Preparation and properties of magnetic cellulose fiber composites. *BioResources* **6**, 3396–3409 (2011).
216. Jodeh, S. *et al.* Magnetic nanocellulose from olive industry solid waste for the effective removal of methylene blue from wastewater. *Environ. Sci. Pollut. Res. Int.* **25**, 22060–22074 (2018).
217. Schyrr, B. *et al.* Biosensors based on porous cellulose nanocrystal-poly(vinyl alcohol) scaffolds. *ACS Appl. Mater. Interfaces* **6**, 12674–12683 (2014).
218. Wang, L. et al. Mesoporous Carbon Microfibers for Electroactive Materials Derived from Lignocellulose Nanofibrils. *ACS Sustain. Chem. Eng*. **8**, 8549–8561 (2020).
219. Selvakumar, M. and Krishna Bhat, D. $LiClO_4$ doped cellulose acetate as biodegradable polymer electrolyte for supercapacitors. *J. Appl. Polym. Sci.* **110**, 594–602 (2008).
220. Li, T. et al. Developing fibrillated cellulose as a sustainable technological material. *Nat.* **590**, 47–56 (2021).
221. Zhu, H. *et al.* Biosynthesis of spherical Fe_3O_4/bacterial cellulose nanocomposites as adsorbents for heavy metal ions. *Carbohydr. Polym.* **86**, 1558–1564 (2011).
222. Huang, X., Zhan, X., Wen, C., Xu, F. and Luo, L. Amino-functionalized magnetic bacterial cellulose/activated carbon composite for Pb^{2+} and methyl orange sorption from aqueous solution. *J. Mater. Sci. Technol.* **34**, 855–863 (2018).
223. Omorogie, M. O., Babalola, J. O., Unuabonah, E. I. and Gong, J. R. Kinetics and thermodynamics of heavy metal ions sequestration onto novel Nauclea diderrichii seed biomass. *Bioresour. Technol.* **118**, 576–579 (2012).
224. Onda, K., Lobuglio, J. and Bartram, J. Global Access to Safe Water: Accounting for Water Quality and the Resulting Impact on MDG Progress. *Int. J. Environ. Res. Public Heal.* **9**, 880–894 (2012).
225. Mckay, Gordon. Use of Adsorbents for the Removal of Pollutants from Wastewater. *CRC press* (1995).
226. Cucarella, V. and Renman, G. Phosphorus Sorption Capacity of Filter Materials Used for On-site Wastewater Treatment Determined in Batch Experiments–A Comparative Study. *J. Environ. Qual.* **38**, 381–392 (2009).
227. Michalak, I., Chojnacka, K. and Witek-Krowiak, A. State of the art for the biosorption process - A review. *Appl. Biochem. Biotechnol.* **170**, 1389–1416 (2013).
228. Shahmohammadi-Kalalagh, S., Babazadeh, H. and Nazemi, A. Comparison of linear and nonlinear forms of isotherm models for Zn(II) and Cu(II) sorption on a kaolinite. *Arab. J. Geosci.* **8**, 397–402 (2015).
229. Weber, T. W. and Chakravorti, R. K. Pore and solid diffusion models for fixed-

bed adsorbers. *AIChE J.* **20**, 228–238 (1974).
230. Nworie, F. S., Nwabue, F. I., Oti, W., Mbam, E. and Nwali, B. U. Removal of methylene blue from aqueous solution using activated rice husk biochar: Adsorption isotherms, kinetics and error analysis. *J. Chil. Chem. Soc.* **64**, 4365–4376 (2019).
231. Ghahremani, D., Mobasherpour, I. and Mirhosseini, S. A. Sorption thermodynamic and kinetic studies of Lead removal from aqueous solutions by nano Tricalcium phosphate. *Bull. la Société R. des Sci. Liège*, 96–112 (2017).
232. Shahwan, T. and Erten, H. N. Thermodynamic parameters of Cs+ sorption on natural clays. *J. Radioanal. Nucl. Chem.* **253**, 115–120 (2002).
233. García-Calzón, J. A. and Díaz-García, M. E. Characterization of binding sites in molecularly imprinted polymers. *Sensors Actuators B. Chem.* **123**, 1180–1194 (2007).
234. Ayawei, N., Ebelegi, A. N. and Wankasi, D. Modelling and Interpretation of Adsorption Isotherms. *J. Chem.* **2017**, (2017).
235. Mehta, N., Gehlot, G., Verma, S. and Sharma, S. Adsorption Isotherm Studies in the Removal of Malachite Green Dye from Aqueous Solution by Using Coal Fly Ash. *Int. J. Chem. Stud. IJCS* **3**, 42–44 (2015).
236. Salam, N. A., Ugbe, F. A. and Ugbe, A. V. I. Optimization and sorption isotherms analysis of anionic dye eosin yellow decontamination by goethite adsorbents. *Acta Sci. Malaysia* **4**, 75–81 (2020).
237. William Kajjumba, G., Emik, S., Öngen, A., Kurtulus Özcan, H. and Aydın, S. Modelling of Adsorption Kinetic Processes—Errors, Theory and Application. *Adv. Sorption Process Appl.* 1-19 (2018)
238. Sen Gupta, S. and Bhattacharyya, K. G. Kinetics of adsorption of metal ions on inorganic materials: A review. *Adv. Colloid Interface Sci.* **162**, 39–58 (2011).
239. J, K. Modeling of Experimental Adsorption Isotherm Data for Chlorothalonil by Nairobi River Sediment. *Mod. Chem. Appl.* **05**, (2017).
240. Chien, S. H. and Clayton, W. R. Application of Elovich Equation to the Kinetics of Phosphate Release and Sorption in Soils. *Soil Sci. Soc. Am. J.* **44**, 265–268 (1980).
241. Tan, K. L. and Hameed, B. H. Insight into the adsorption kinetics models for the removal of contaminants from aqueous solutions. *J. Taiwan Inst. Chem. Eng.* **74**, 25–48 (2017).
242. Wang, J. and Guo, X. Adsorption kinetic models: Physical meanings, applications, and solving methods. *J. Hazard. Mater.* **390**, 122156 (2020).
243. Sen Gupta, S. and Bhattacharyya, K. G. Kinetics of adsorption of metal ions on inorganic materials: A review. *Adv. Colloid Interface Sci.* **162**, 39–58 (2011).
244. Weber, W. J. and Morris, J. C. Kinetics of Adsorption on Carbon from Solution. *J. Sanit. Eng. Div.* **89**, 31–59 (1963).
245. Fierro, V., Torné-Fernández, V., Montané, D. and Celzard, A. Adsorption of phenol onto activated carbons having different textural and surface properties. *Microporous Mesoporous Mater.* **111**, 276–284 (2008).
246. Asuquo, E., Martin, A., Nzerem, P., Siperstein, F. and Fan, X. Adsorption of Cd(II) and Pb(II) ions from aqueous solutions using mesoporous activated carbon adsorbent: Equilibrium, kinetics and characterisation studies. *J. Environ. Chem. Eng.* **5**, 679–698 (2017).
247. Singh, S. K., Townsend, T. G., Mazyck, D. and Boyer, T. H. Equilibrium and intra-particle diffusion of stabilized landfill leachate onto micro- and meso-porous activated carbon. *Water Res.* **46**, 491–499 (2012).

248. Raji, F. and Pakizeh, M. Kinetic and thermodynamic studies of Hg(II) adsorption onto MCM-41 modified by $ZnCl_2$. *Appl. Surf. Sci.* **301**, 568–575 (2014).
249. Sahmoune, M. N. Evaluation of thermodynamic parameters for adsorption of heavy metals by green adsorbents. *Environ. Chem. Lett. 2018 172* **17**, 697–704 (2018).
250. Aksakal, O. and Ucun, H. Equilibrium, kinetic and thermodynamic studies of the biosorption of textile dye (Reactive Red 195) onto Pinus sylvestris L. *J. Hazard. Mater.* **181**, 666–672 (2010).
251. Din, M. I., Hussain, Z., Mirza, M. L., Shah, A. T. and Athar, M. M. Adsorption Optimization of Lead (II) Using Saccharum Bengalense as a Non-Conventional Low Cost Biosorbent: Isotherm and Thermodynamics Modeling. *Int. J. Phytoremediation* **16**, 889–908 (2014).
252. M. Hamzaoui, B. Bestani, N. B. The use of linear and nonlinear methods for adsorption isotherm optimization of basic green 4-dye onto sawdust-based activated carbon. *J. Mater. Environ. Sci.* **9**, 1110–1118 (2018).
253. Foo, K. Y. and Hameed, B. H. An overview of dye removal via activated carbon adsorption process. *Desalin. Water Treat.* **19**, 255–274 (2010).
254. Jasper, E. E. *et al*., Nonlinear regression analysis of the sorption of crystal violet and methylene blue from aqueous solutions onto an agro-waste derived activated carbon. *Appl. Water Sci. 2020 106* **10**, 1–11 (2020).
255. López-Luna, J. *et al.* Linear and nonlinear kinetic and isotherm adsorption models for arsenic removal by manganese ferrite nanoparticles. *SN Appl. Sci.* **1**, 1–19 (2019).
256. Hammouda, S. Ben, Adhoum, N. and Monser, L. Synthesis of magnetic alginate beads based on Fe_3O_4 nanoparticles for the removal of 3-methylindole from aqueous solution using Fenton process. *J. Hazard. Mater.* **294**, 128–136 (2015).
257. Malachová, A., Sulyok, M., Beltrán, E., Berthiller, F. and Krska, R. Optimization and validation of a quantitative liquid chromatography–tandem mass spectrometric method covering 295 bacterial and fungal metabolites including all regulated mycotoxins in four model food matrices. *J. Chromatogr. A* **1362**, 145–156 (2014).
258. Monshi, A., Foroughi, M. R. and Monshi, M. R. Modified Scherrer Equation to Estimate More Accurately Nano-Crystallite Size Using XRD. *World J. Nano Sci. Eng.* **02**, 154–160 (2012).
259. Daemi, H. and Barikani, M. Synthesis and characterization of calcium alginate nanoparticles, sodium homopolymannuronate salt and its calcium nanoparticles. *Sci. Iran.* **19**, 2023–2028 (2012).
260. Jiang, N., Xu, Y., Dai, Y., Luo, W. and Dai, L. Polyaniline nanofibers assembled on alginate microsphere for Cu^{2+} and Pb^{2+} uptake. *J. Hazard. Mater.* **215**–**216**, 17–24 (2012).
261. Li, Z., Sun, Q. and Gao, M. Preparation of Water-Soluble Magnetite Nanocrystals from Hydrated Ferric Salts in 2-Pyrrolidone: Mechanism Leading to Fe_3O_4. *Angew. Chemie* **117**, 125–128 (2005).
262. Whitlow, L. Evaluation of mycotoxin binders. *Proc. 4th Mid-Atlantic Nutr.* 132–143 (2006).
263. Peters, J. et al. Mycotoxin profiling of 1000 beer samples with a special focus on craft beer. PLoS One 12, e0185887 (2017).
264. Pascari, X., Ramos, A. J., Marín, S. and Sanchís, V. Mycotoxins and beer. Impact of beer production process on mycotoxin contamination. A review. *Food Res. Int.* **103**, 121–129 (2018).
265. Radostits, O. M. The Merck veterinary manual. *The Canadian Veterinary Journal*

41, 334 (2000).
266. Hatch, R. C., Clark, J. D., Jain, A. V. and Weiss, R. Induced acute aflatoxicosis in goats: treatment with activated charcoal or dual combinations of oxytetracycline, stanozolol, and activated charcoal. *Am. J. Vet. Res.* **43**, 644–648 (1982).
267. Galvano, F. *et al.* Reduction of carryover of aflatoxin from cow feed to milk by addition of activated carbons. *J. Food Prot.* **59**, 551–554 (1996).
268. Avantaggiato, G., Havenaar, R. and Visconti, A. Assessment of the multi-mycotoxin-binding efficacy of a carbon/aluminosilicate-based product in an in vitro gastrointestinal model. *J. Agric. Food Chem.* **55**, 4810–4819 (2007).
269. Bahrenthien, L. *et al.* Detoxifying deoxynivalenol (DON)-contaminated feedstuff: consequences of sodium sulphite (SoS) treatment on performance and blood parameters in fattening pigs. *Mycotoxin Res.* **36**, 213–223 (2020).
270. Schwartz, H. E. *et al.* Characterization of three deoxynivalenol sulfonates formed by reaction of deoxynivalenol with sulfur reagents. *J. Agric. Food Chem.* **61**, 8941–8948 (2013).
271. Lazim, Z. M. *et al.* Utilization of durian peel as potential adsorbent for bisphenol a removal in aquoeus solution. *J. Teknol.* **74**, 109–115 (2015).
272. Merry Mitan, N., Saifulazwan Ramlan, M., Zainul Hakim Nawawi, M. and Hafizuddin Mohd Gazali, M. Performance of binders in briquetting of durian peel as a solid biofuel. *Mater. Today.* **5**, 21753–21758 (2018).
273. Adunphatcharaphon, S. *et al.* The Effectiveness of Durian Peel as a Multi-Mycotoxin Adsorbent. *Toxins* **12**, 108 (2020).
274. Čežíková, J., Kozler, J., Madronová, L., Novák, J. and Janoš, P. Humic acids from coals of the North-Bohemian coal field: II. Metal-binding capacity under static conditions. *React. Funct. Polym.* **47**, 111–118 (2001).
275. Moura, M. N., Martín, M. J. and Burguillo, F. J. A comparative study of the adsorption of humic acid, fulvic acid and phenol onto Bacillus subtilis and activated sludge. *J. Hazard. Mater.* **149**, 42–48 (2007).
276. Arafat, R. Y., Khan, S. H. and Saima. Evaluation of Humic Acid as an Aflatoxin Binder in Broiler Chickens. *Ann. Anim. Sci.* **17**, 241 (2017).
277. Haus, M., Žatko, D., Vašková, J. and Vaško, L. The effect of humic acid in chronicdeoxynivalenol intoxication. *Environ. Sci. Pollut. Res.* **28**, 1612–1618 (2020).
278. Bytesnikova, Z., Adam, V. and Richtera, L. Graphene oxide as a novel tool for mycotoxin removal. *Food Control* **121**, 107611 (2021).
279. Qi, Y., Yang, M., Xu, W., He, S. and Men, Y. Natural polysaccharides-modified graphene oxide for adsorption of organic dyes from aqueous solutions. *J. Colloid Interface Sci.* **486**, 84–96 (2017).
280. Nam, S. W. *et al.* Adsorption characteristics of diclofenac and sulfamethoxazole to graphene oxide in aqueous solution. *Chemosphere* **136**, 20–26 (2015).
281. Wang, J., Chen, Z. and Chen, B. Adsorption of polycyclic aromatic hydrocarbons by graphene and graphene oxide nanosheets. *Environ. Sci. Technol.* **48**, 4817–4825 (2014).
282. Ghorbani, M., Shams, A., Seyedin, O. and Afshar Lahoori, N. Magnetic ethylene diamine-functionalized graphene oxide as novel sorbent for removal of lead and cadmium ions from wastewater samples. *Environ. Sci. Pollut. Res.* **25**, 5655–5667 (2017).
283. Koudelkova, Z. *et al.* Electrochemical Evaluation of Selenium (IV) Removal from Its Aqueous Solutions by Unmodified and Modified Graphene Oxide. *Mol.* **24**, 1063 (2019).

284. Wen, T., Wu, X., Tan, X., Wang, X. and Xu, A. One-pot synthesis of water-swellable Mg-Al layered double hydroxides and graphene oxide nanocomposites for efficient removal of As(V) from aqueous solutions. *ACS Appl. Mater. Interfaces* **5**, 3304–3311 (2013).
285. Wen, T. *et al.* Efficient capture of strontium from aqueous solutions using graphene oxide–hydroxyapatite nanocomposites. *Dalt. Trans.* **43**, 7464–7472 (2014).
286. Pirouz, A. A. *et al.* The use of innovative and efficient nanocomposite (magnetic graphene oxide) for the reduction on of Fusarium mycotoxins in palm kernel cake. *Sci. Reports* **7**, 1–9 (2017).
287. Priyadarsini, S., Mohanty, S., Mukherjee, · Sumit, Basu, S. and Mishra, M. Graphene and graphene oxide as nanomaterials for medicine and biology application. *J. Nanostructure Chem.* **8**, 123–137 (2018).
288. Yang, Y., Cao, Y., Wang, X., Fang, G. and Wang, S. Prussian blue mediated amplification combined with signal enhancement of ordered mesoporous carbon for ultrasensitive and specific quantification of metolcarb by a three-dimensional molecularly imprinted electrochemical sensor. *Biosens. Bioelectron.* **64**, 247–254 (2015).
289. Xu, B., Yang, L., Zhao, F. and Zeng, B. A novel electrochemical quercetin sensorbased on Pd/MoS2-ionic liquid functionalized ordered mesoporous carbon. *Electrochim. Acta* **247**, 657–665 (2017).
290. Fang, G., Liu, G., Yang, Y. and Wang, S. Quartz crystal microbalance sensor based on molecularly imprinted polymer membrane and three-dimensional Au nanoparticles@mesoporous carbon CMK-3 functional composite for ultrasensitive and specific determination of citrinin. *Sensors Actuators B Chem.* **230**, 272–280 (2016).
291. Hu, X., Wang, C., Zhang, M., Zhao, F. and Zeng, B. Ionic liquid assisted molecular self-assemble and molecular imprinting on gold nanoparticles decorated boron-doped ordered mesoporous carbon for the detection of zearalenone. *Talanta* **217**, 121032 (2020).
292. Solís-Cruz, B. *et al.* Evaluation of Chitosan and Cellulosic Polymers as Binding Adsorbent Materials to Prevent Aflatoxin B1, Fumonisin B1, Ochratoxin, Trichothecene, Deoxynivalenol, and Zearalenone Mycotoxicoses Through an In Vitro Gastrointestinal Model for Poultry. *Polym.* **9**, 529 (2017).
293. Hokkanen, S., Bhatnagar, A. and Sillanpää, M. A review on modification methods to cellulose-based adsorbents to improve adsorption capacity. *Water Res.* **91**, 156–173 (2016).
294. Tamilisai, R., Palanisamy, P. N., Selvasekarapandian, S. and Maheshwari, T. Sodium alginate incorporated with magnesium nitrate as a novel solid biopolymer electrolyte for magnesium-ion batteries. *J. Mater. Sci. Mater. Electron.* **32**, 22270–22285 (2021).
295. Blanco-Pérez, F. *et al.* The Dietary Fiber Pectin: Health Benefits and Potential for the Treatment of Allergies by Modulation of Gut Microbiota. *Curr. Allergy Asthma Rep.* **21**, 1–19 (2021).
296. Waalkes, M. P. Cadmium carcinogenesis in review. *J. Inorg. Biochem.* **79**, 241–244 (2000).
297. Amin, N. U., Hussain, A., Alamzeb, S. and Begum, S. Accumulation of heavy metals in edible parts of vegetables irrigated with waste water and their daily intake to adults and children, District Mardan, Pakistan. *Food Chem.* **136**, 1515–1523 (2013).

298. Alves, L. de C., Yáñez-Vilar, S., Piñeiro-Redondo, Y. and Rivas, J. Novel Magnetic Nanostructured Beads for Cadmium(II) Removal. *Nanomater.* **9**, 356 (2019).
299. Kadirvelu, K. and Namasivayam, C. Activated carbon from coconut coirpith as metal adsorbent: adsorption of Cd(II) from aqueous solution. *Adv. Environ. Res.* **7**, 471–478 (2003).
300. Hanzlík, J., Jehlička, J., Šebek, O., Weishauptová, Z. and Machovič, V. Multi-component adsorption of Ag(I), Cd(II) and Cu(II) by natural carbonaceous materials. *Water Res.* **38**, 2178–2184 (2004).
301. Krika, F., Azzouz, N. and Ncibi, M. C. Adsorptive removal of cadmium from aqueous solution by cork biomass: Equilibrium, dynamic and thermodynamic studies. *Arab. J. Chem.* **9**, S1077–S1083 (2016).
302. Leyva-Ramos, R., Rangel-Mendez, J. R., Mendoza-Barron, J., Fuentes-Rubio, L. and Guerrero-Coronado, R. M. Adsorption of cadmium(II) from aqueous solution onto activated carbon. *Water Sci. Technol.* **35**, 205–211 (1997).
303. Namasivayam, C. and Ranganathan, K. Removal of Cd(II) from wastewater by adsorption on "waste" Fe(III)Cr(III) hydroxide. *Water Res.* **29**, 1737–1744 (1995).
304. Ajmal, M., Ali Khan Rao, R., Anwar, S., Ahmad, J. and Ahmad, R. Adsorption studies on rice husk: removal and recovery of Cd(II) from wastewater. *Bioresour. Technol.* **86**, 147–149 (2003).
305. Senthil Kumar, P., Ramakrishnan, K., Dinesh Kirupha, S. and Sivanesan, S. Thermodynamic and kinetic studies of cadmium adsorption from aqueous solution onto rice husk. *Brazilian J. Chem. Eng.* **27**, 347–355 (2010).
306. Dutta, A., Diao, Y., Jain, R., Rene, E. R. and Dutta, S. Adsorption of Cadmium from Aqueous Solutions onto Coffee Grounds and Wheat Straw: Equilibrium and Kinetic Study. *J. Environ. Eng.* **142**, C4015014 (2015).
307. Dhir, B. and Kumar, R. Adsorption of Heavy Metals by Salvinia Biomass and Agricultural Residues. *Int. J. Environ. Res.* **4**, 427–432 (2010).
308. Foo, K. Y. and Hameed, B. H. Insights into the modeling of adsorption isotherm systems. *Chem. Eng. J.* **156**, 2–10 (2010).
309. Luef, E., Prey, T. and Kubicek, C. P. Biosorption of zinc by fungal mycelial wastes. *Appl. Microbiol. Biotechnol.* **34**, 688–692 (1991).
310. Aldor, I., Fourest, E. and Volesky, B. Desorption of cadmium from algal biosorbent. *Can. J. Chem. Eng.* **73**, 516–522 (1995).
311. Hong, H. Y., Moed, N. M., Ku, Y. and Lee, H. Y. Ultrasonic Regeneration Studies on Activated Carbon Loaded with Isopropyl Alcohol. *Appl. Sci.* **10**, 7596 (2020).
312. Elwakeel, K. Z., Hamza, M. F. and Guibal, E. Effect of agitation mode (mechanical, ultrasound and microwave) on uranium sorption using amine- and dithizone-functionalized magnetic chitosan hybrid materials. *Chem. Eng. J.* **411**, 128553 (2021).
313. Xie, J. *et al.* A Reusable Biosorbent Using Ca-Alginate Immobilized Providencia vermicola for Pd(II) Recovery from Acidic Solution. *Water, Air, Soil Pollut.* **231**, 1–12 (2020).
314. Alqadami, A. A., Khan, M. A., Siddiqui, M. R., Alothman, Z. A. and Sumbul, S. A facile approach to develop industrial waste encapsulated cryogenic alginate beads to sequester toxic bivalent heavy metals. *J. King Saud Univ. - Sci.* **32**, 1444–1450 (2020).
315. Lata, S., Singh, P. K. and Samadder, S. R. Regeneration of adsorbents and recovery of heavy metals: a review. *Int. J. Environ. Sci. Technol.* **12**, 1461–1478 (2015).
316. Desta, M. B. Batch sorption experiments: Langmuir and freundlich isotherm

studies for the adsorption of textile metal ions onto teff straw (eragrostis tef) agricultural waste. *J. Thermodyn.* **1**, (2013).
317. Hamzenejad Taghlidabad, R., Sepehr, E., Khodaverdiloo, H., Samadi, A. and Rasouli-Sadaghiani, M. H. Characterization of cadmium adsorption on two cost-effective biochars for water treatment. *Arab. J. Geosci.* **13**, 1–10 (2020).
318. Alslaibi, T. M., Abustan, I., Ahmad, M. A. and Foul, A. A. Cadmium removal from aqueous solution using microwaved olive stone activated carbon. *J. Environ. Chem. Eng.* **1**, 589–599 (2013).
319. Sigdel, A. *et al.* Concurrent removal of cadmium and benzene from aqueous solution by powdered activated carbon impregnated alginate beads. *Catena* **148**, 101–107 (2017).
320. Wan Ibrahim, W. M. H., Mohamad Amini, M. H., Sulaiman, N. S. and Kadir, W. R. A. Powdered activated carbon prepared from Leucaena leucocephala biomass for cadmium removal in water purification process. *Arab J. Basic Appl. Sci.* **26**, 30–40 (2019).
321. Andelescu, A., Nistor, M. A., Muntean, S. G. and Rădulescu-Grad, M. E. Adsorption studies on copper, cadmium, and zinc ion removal from aqueous solution using magnetite/carbon nanocomposites. *Sep. Sci. Technol.* **53**, 2352–2364 (2018).
322. Papageorgiou, S. K., Kouvelos, E. P. and Katsaros, F. K. Calcium alginate beads from Laminaria digitata for the removal of Cu^{+2} and Cd^{+2} from dilute aqueous metal solutions. *Desalination* **224**, 293–306 (2008).
323. Nagy, B. *et al.* Linear and nonlinear regression analysis for heavy metals removal using Agaricus bisporus macrofungus. *Arab. J. Chem.* **10**, S3569–S3579 (2017).
324. Zhai, Q.-Z. and Li, X.-D. Efficient removal of cadmium(II) with SBA-15 nanoporous silica: studies on equilibrium, isotherm, kinetics and thermodynamics. *Appl. Water Sci.* **9**, 1–11 (2019).
325. Tapan, K. S., Karmaker, S., Ichikawa, H. and Fukumori, Y. Mechanisms and kinetics of trisodium 2-hydroxy-1,1′-azonaphthalene-3,4′,6-trisulfonate adsorption onto chitosan. *J. Colloid Interface Sci.* **286**, 433–439 (2005).
326. Sun, J., Lian, F., Liu, Z., Zhu, L. and Song, Z. Biochars derived from various crop straws: Characterization and Cd(II) removal potential. *Ecotoxicol. Environ. Saf.* **106**, 226–231 (2014).
327. Mahmood, Z. *et al.* Adsorption studies of cadmium ions on alginate–calcium carbonate composite beads. *Appl. Water Sci.* **7**, 915–921 (2017).
328. Guo, Y., Wang, Z., Zhou, X. and Bai, R. Removal of mercury (II) from aqueous solution with three commercial raw activated carbons. *Res. Chem. Intermed.* **43**, 2273–2297 (2017).
329. David W. Mazyck, A. M. H. and H. B. Aqueous Phase Mercury Removal: Strategies for a Secure Future Water Supply. *De Clercq J.*, (2009).
330. Barczak, M. *et al.* Ordered mesoporous carbons as effective sorbents for removal of heavy metal ions. *Microporous Mesoporous Mater.* **211**, 162–173 (2015).
331. Jeong, Y. *et al.* Development of modified mesoporous carbon (CMK-3) for improved adsorption of bisphenol-A. *Chemosphere* **238**, 124559 (2020).
332. Ezzeddine, Z., Batonneau-Gener, I., Pouilloux, Y. and Hamad, H. Removal of methylene blue by mesoporous CMK-3: Kinetics, isotherms and thermodynamics. *J. Mol. Liq.* **223**, 763–770 (2016).
333. Hu, L., Dang, S., Yang, X. and Dai, J. Synthesis of recyclable catalyst–sorbent Fe/CMK-3 for dry oxidation of phenol. *Microporous Mesoporous Mater.* **147**, 188–193 (2012).

334. Chandrasekar, G., Son, W. J. and Ahn, W. S. Synthesis of mesoporous materials SBA-15 and CMK-3 from fly ash and their application for CO_2 adsorption. *J. Porous Mater.* **16**, 545–551 (2008).
335. Wu, R. *et al.* Adsorption performance of CMK-3 and C-FDU-15 in NO removal at low temperature. *J. Environ. Sci.* **87**, 289–298 (2020).
336. Saikia, D. *et al.* A comparative study of ordered mesoporous carbons with different pore structures as anode materials for lithium-ion batteries. *RSC Adv.* **5**, 42922–42930 (2015).
337. Mohammadnia, E., Hadavifar, M. and Veisi, H. Kinetics and thermodynamics of mercury adsorption onto thiolated graphene oxide nanoparticles. *Polyhedron* **173**, 114139 (2019).
338. Wu, F. C., Tseng, R. L. and Juang, R. S. Characteristics of Elovich equation used for the analysis of adsorption kinetics in dye-chitosan systems. *Chem. Eng. J.* **150**, 366–373 (2009).
339. Pintor, A. M. A., Vieira, B. R. C., Santos, S. C. R., Boaventura, R. A. R. and Botelho, C. M. S. Arsenate and arsenite adsorption onto iron-coated cork granulates. *Sci. Total Environ.* **642**, 1075–1089 (2018).
340. Boparai, H. K., Joseph, M. and O'Carroll, D. M. Kinetics and thermodynamics of cadmium ion removal by adsorption onto nano zerovalent iron particles. *J. Hazard. Mater.* **186**, 458–465 (2011).
341. Grosvenor, A. P., Biesinger, M. C., Smart, R. S. C. and McIntyre, N. S. New interpretations of XPS spectra of nickel metal and oxides. *Surf. Sci.* **600**, 1771–1779 (2006).
342. Kokkinos, E., Soukakos, K., Kostoglou, M. and Mitrakas, M. Cadmium, mercury, and nickel adsorption by tetravalent manganese feroxyhyte: selectivity, kinetic modeling, and thermodynamic study. *Environ. Sci. Pollut. Res.* **25**, 12263–12273 (2017).
343. Liu, Y. *et al.* Study on Adsorption Properties of Modified Corn Cob Activated Carbon for Mercury Ion. *Energies* **14**, 4483 (2021).
344. Wang, Z. *et al.* The selective adsorption performance and mechanism of multiwall magnetic carbon nanotubes for heavy metals in wastewater. *Sci. Reports* **11**, 1–13 (2021).
345. Cataldo, S., Gianguzza, A., Pettignano, A. and Villaescusa, I. Mercury(II) removal from aqueous solution by sorption onto alginate, pectate and polygalacturonate calcium gel beads. A kinetic and speciation-based equilibrium study. *React. Funct. Polym.* **73**, 207–217 (2013).
346. Crist, R. H., Oberholser, K., Shank, N. and Nguyen, M. Nature of Bonding between Metallic Ions and Algal Cell Walls. *Environ. Sci. Technol.* **15**, 1212–1217 (1981).
347. Schiewer, S. and Volesky, B. Modeling of the proton-metal ion exchange in biosorption. *Environ. Sci. Technol.* **29**, 3049–3058 (1995).
348. Sutirman, Z. A., Sanagi, M. M. and Wan Aini, W. I. Alginate-based adsorbents for removal of metal ions and radionuclides from aqueous solutions: A review. *Int. J. Biol. Macromol.* **174**, 216–228 (2021).
349. Jacob, J. J., Varalakshmi, R., Gargi, S., Jayasri, M. A. and Suthindhiran, K. Removal of Cr (III) and Ni (II) from tannery effluent using calcium carbonate coated bacterial magnetosomes. *NPJ Clean Water* **1**, (2018).
350. Deshmukh, P. D., Khadse, G. K., Shinde, V. M. and Labhasetwar, P. Cadmium Removal from Aqueous Solutions Using Dried Banana Peels as An Adsorbent: Kinetics and Equilibrium Modeling. *J. Bioremediation Biodegrad.* **8**, 1–7 (2017).
351. Goscianska, J., Marciniak, M. and Pietrzak, R. Mesoporous carbons modified with

lanthanum(III) chloride for methyl orange adsorption. *Chem. Eng. J.* **247**, 258–264 (2014).
352. Guo, R., Guo, J., Yu, F. and Gang, D. D. Synthesis and surface functional group modifications of ordered mesoporous carbons for resorcinol removal. *Microporous Mesoporous Mater.* **175**, 141–146 (2013).
353. Zhang, D. *et al.* Fabrication of nitrogen doped ordered mesoporous carbon derived from glucosamine with hybrid capacitive behaviors. *Carbon Lett.* **23**, 9–16 (2017).
354. Mahamadi, C. and Nharingo, T. Competitive adsorption of Pb^{2+}, Cd^{2+} and Zn^{2+} ions onto Eichhornia crassipes in binary and ternary systems. *Bioresour. Technol.* **101**, 859–864 (2010).
355. Batool, F., Akbar, J., Iqbal, S., Noreen, S. and Bukhari, S. N. A. Study of Isothermal, Kinetic, and Thermodynamic Parameters for Adsorption of Cadmium: An Overview of Linear and Nonlinear Approach and Error Analysis. *Bioinorg. Chem. Appl.* **2018**, (2018).
356. Chen, J. Z., Tao, X. C., Xu, J., Zhang, T. and Liu, Z. L. Biosorption of lead, cadmium and mercury by immobilized Microcystis aeruginosa in a column. *Process Biochem.* **40**, 3675–3679 (2005).
357. Norman Jones, R., Ramsay, D. A. and Keir, D. S. The Intensities of Carbonyl Bands in the Infrared Spectra of Steroids. *J. Am. Chem. Soc.* **74**, 80–88 (1952).
358. Rahman, M. M. *et al.* Mesoporous Carbon: A Versatile Material for Scientific Applications. *Int. J. Mol. Sci.* **22**, 4498 (2021).
359. Carvalho, J. P. F., Silva, A. C. Q., Silvestre, A. J. D., Freire, C. S. R. and Vilela, C. Spherical Cellulose Micro and Nanoparticles: A Review of Recent Developments and Applications. *Nanomater.* **11**, 2744 (2021).
360. Patil, T. V. *et al.* Nanocellulose, a versatile platform: From the delivery of active molecules to tissue engineering applications. *Bioact. Mater.* **9**, 566–589 (2022).
361. Amiralian, N. *et al.* High aspect ratio nanocellulose from an extremophile spinifex grass by controlled acid hydrolysis. *Cellulose* **24**, 3753–3766 (2017).
362. Pennells, J., Godwin, I. D., Amiralian, N. and Martin, D. J. Trends in the production of cellulose nanofibers from non-wood sources. *Cellulose* **27**, 575–593 (2020).
363. Kępa, K. *et al.* Evaluation of properties and specific energy consumption of spinifex-derived lignocellulose fibers produced using different mechanical processes. *Cellulose* **26**, 6555–6569 (2019).
364. Kakadellis, S. and Harris, Z. M. Don't scrap the waste: The need for broader system boundaries in bioplastic food packaging life-cycle assessment – A critical review. *J. Clean. Prod.* **274**, 122831 (2020).
365. Du, X., Zhang, Z., Liu, W. and Deng, Y. Nanocellulose-based conductive materials and their emerging applications in energy devices - A review. *Nano Energy* **35**, 299–320 (2017).
366. Oprea, M. and Mihaela Panaitescu, D. Nanocellulose Hybrids with Metal Oxides Nanoparticles for Biomedical Applications. *Mol.* **25**, 4045 (2020).
367. Moon, R. J., Martini, A., Nairn, J., Simonsen, J. and Youngblood, J. Cellulose nanomaterials review: structure, properties and nanocomposites. *Chem. Soc. Rev.* **40**, 3941–3994 (2011).
368. Leong, W. L. *et al.* Non-Volatile Organic Memory Applications Enabled by In Situ Synthesis of Gold Nanoparticles in a Self-Assembled Block Copolymer. *Adv. Mater.* **20**, 2325–2331 (2008).
369. Cook, J. G. Handbook of textile fibres: man-made fibres. *Woodhead publishing* (1984).

370. Fourné, F. Synthetic fibers : machines and equipment, manufacture, properties : handbook for plant engineering, machine design, and operation. *Hanser* (1999).
371. Uddin, K. M. A. *et al.* Silver nanoparticle synthesis mediated by carboxylated cellulose nanocrystals. *Green Mater.* **2**, 183–192 (2014).
372. Otenda, B. V. *et al.* Cellulose Nanofibrils from Sugarcane Bagasse as a Reinforcing Element in Polyvinyl Alcohol Composite Films for Food Packaging. *J. Nat. Fibers* (2020)
373. Johar, N., Ahmad, I. and Dufresne, A. Extraction, preparation and characterization of cellulose fibres and nanocrystals from rice husk. *Ind. Crops Prod.* **37**, 93–99 (2012).
374. Xu, J. *et al.* High-strength, transparent and superhydrophobic nanocellulose/nanochitin membranes fabricated via crosslinking of nanofibers and coating F-SiO2 suspensions. *Carbohydr. Polym.* **247**, 116694 (2020).
375. Ho, H. Van, Tripathi, G., Gwon, J., Lee, S. Y. and Lee, B. T. Novel TOCNF reinforced injectable alginate/β-tricalcium phosphate microspheres for bone regeneration. *Mater. Des.* **194**, 108892 (2020).
376. Nicolas-Silvente, A. I. *et al.* Influence of the Titanium Implant Surface Treatment on the Surface Roughness and Chemical Composition. *Mater.* **13**, 314 (2020).
377. Talibouya Ba, E. C. *et al.* Investigation of the effects of skewness Rsk and kurtosis Rku on tribological behavior in a pin-on-disc test of surfaces machined by conventional milling and turning processes. *Mater. Res.* **24**, (2021).
378. Wahid, F. *et al.* A facile construction of bacterial cellulose/ZnO nanocomposite films and their photocatalytic and antibacterial properties. *Int. J. Biol. Macromol.* **132**, 692–700 (2019).
379. Muşat, V., Təbəcaru, A., Vasile, B. Ş. and Surdu, V. A. Size-dependent photoluminescence of zinc oxide quantum dots through organosilane functionalization. *RSC Adv.* **4**, 63128–63136 (2014).
380. Siqueira, P. *et al.* Three-Dimensional Stable Alginate-Nanocellulose Gels for Biomedical Applications: Towards Tunable Mechanical Properties and Cell Growing. *Nanomater.* **9**, 78 (2019).
381. Elrhman, H. M. A. Synthesis and characterization of core-shell magnetite nanoparticles with modified nano-cellulose for removal of radioactive ions from aqueous solutions. *Results Mater.* **8**, 100138 (2020).
382. Denizot, B. *et al.* Phosphorylcholine Coating of Iron Oxide Nanoparticles. *J. Colloid Interface Sci.* **209**, 66–71 (1999).
383. Bedê, P. M., Da Silva, M. H. P., Da Silva Figueiredo, A. B. H. and Finotelli, P. V. Nanostructured magnetic alginate composites for biomedical applications. *Polímeros* **27**, 267–272 (2017).
384. Yazid, N. A. and Joon, Y. C. Co-precipitation synthesis of magnetic nanoparticles for efficient removal of heavy metal from synthetic wastewater. *AIP Conf. Proc.* **2124** (2019).
385. Wei, Y. *et al.* Synthesis of Fe_3O_4 Nanoparticles and their Magnetic Properties. *Procedia Eng.* **27**, 632–637 (2012).
386. Zare, Y. Study of nanoparticles aggregation/agglomeration in polymer particulate nanocomposites by mechanical properties. *Compos. Part A Appl. Sci. Manuf.* **84**, 158–164 (2016).
387. Liu, H. and Brinson, L. C. Reinforcing efficiency of nanoparticles: A simple comparison for polymer nanocomposites. *Compos. Sci. Technol.* **68**, 1502–1512 (2008).
388. Soon, J. M. and Manning, L. Developing anti-counterfeiting measures: The role of

smart packaging. *Food Res. Int.* **123**, 135–143 (2019).
389. Dong, B. *et al.* Screen-printed nanoparticles as anti-counterfeiting tags. *Nanotechnology* **27**, 095702 (2016).
390. Jalajerdi, R., Gholamian, F., Shafie, H., Moraveji, A. and Ghanbari, D. Thermal and Magnetic Characteristics of Cellulose Acetate- Fe_3O_4. *J. Nanostructures* **1**, 105–109 (2011).
391. Raymond M. Robertson and David Nyy. Tagged cellulose ester films (2015).
392. Yu, J. *et al.* Iron carbide nanoparticles: an innovative nanoplatform for biomedical applications. *Nanoscale Horiz.* **2**, 81–88 (2017).
393. Yang, C., Zhao, H., Hou, Y. and Ma, D. Fe 5C 2 nanoparticles: A facile bromide-induced synthesis and as an active phase for Fischer-Tropsch synthesis. *J. Am. Chem. Soc.* **134**, 15814–15821 (2012).
394. Huang, G. *et al.* Highly magnetic iron carbide nanoparticles as effective T2 contrast agents. *Nanoscale* **6**, 726–730 (2014).
395. Kim, D. *et al.* Synthesis of uniform ferrimagnetic magnetite nanocubes. *J. Am. Chem. Soc.* **131**, 454–455 (2009).
396. Zhu, M. and Diao, G. Synthesis of porous Fe_3O_4 nanospheres and its application for the catalytic degradation of xylenol orange. *J. Phys. Chem. C* **115**, 18923–18934 (2011).
397. Costa, M. J. *et al.* Use of wheat bran arabinoxylans in chitosan-based films: Effect on physicochemical properties. *Ind. Crops Prod.* **66**, 305 (2015).
398. Gilbert, M. Cellulose Plastics. *Brydson's Plast. Mater. Eighth Ed.* 617–630 (2017).
399. Ly, B. C. K., Dyer, E. B., Feig, J. L., Chien, A. L. and Del Bino, S. Research Techniques Made Simple: Cutaneous Colorimetry: A Reliable Technique for Objective Skin Color Measurement. *J. Invest. Dermatol.* **140**, 3-12.e1 (2020).
400. Cheng, N., Barbano, D. M. and Drake, M. A. Hunter versus CIE color measurement systems for analysis of milk-based beverages. *J. Dairy Sci.* **101**, 4891–4905 (2018).
401. Parikh, S. J., Goyne, K. W., Margenot, A. J., Mukome, F. N. D. and Calderón, F. J. Soil Chemical Insights Provided through Vibrational Spectroscopy. *Adv. Agron.* **126**, 1–148 (2014).
402. Xuan, S. *et al.* Preparation of water-soluble magnetite nanocrystals through hydrothermal approach. *J. Magn. Magn. Mater.* **308**, 210–213 (2007).
403. Liu, Y. *et al.* Preparation of low carbon olefins on a core–shell K–Fe_5C_2@ZSM-5 catalyst by Fischer–Tropsch synthesis. *RSC Adv.* **10**, 26451–26459 (2020).
404. Ahmadpoor, F., Shojaosadati, S. A., Delavari, H. H., Christiansen, G. and Saber, R. Synthesis of Fe_5C_2@SiO_2 core@shell nanoparticles as a potential candidate for biomedical application. *Mater. Res. Express* **5**, 055038 (2018).
405. Yang, Z. *et al.* Modulating the phases of iron carbide nanoparticles: from a perspective of interfering with the carbon penetration of Fe@Fe_3O_4 by selectively adsorbed halide ions. *Chem. Sci.* **8**, 473–481 (2016).
406. Ferry, J. D. Viscoelastic properties of polymers. *John Wiley and Sons* (1980).
407. Mezger, T. The Rheology Handbook. *Pigment Resin Technol.* **38**, 790–797 (2009).
408. Hassan, M. *et al.* Nanocomposite Film Based on Cellulose Acetate and Lignin-Rich Rice Straw Nanofibers. *Mater.* **12**, 595 (2019).
409. Cindradewi, A. W. *et al.* Preparation and Characterization of Cellulose Acetate Film Reinforced with Cellulose Nanofibril. *Polym.* **13**, 2990 (2021).
410. Nishikawa, K. *et al.* Mechanical strength and ionic conductivity of polymer electrolyte membranes prepared from cellulose acetate-lithium perchlorate. *IOP Conf. Ser. Mater. Sci. Eng.* **223**, 012052 (2017).

411. Ramesh, S., Shanti, R. and Morris, E. Plasticizing effect of 1-allyl-3-methylimidazolium chloride in cellulose acetate-based polymer electrolytes. *Carbohydr. Polym.* **87**, 2624–2629 (2012).
412. Huang, C. *et al.* Magnetic micelles as a potential platform for dual targeted drug delivery in cancer therapy. *Int. J. Pharm.* **429**, 113–122 (2012).
413. Sánchez-Márquez, J. A. *et al.* Membrane made of cellulose acetate with polyacrylic acid reinforced with carbon nanotubes and its applicability for chromium removal. *Int. J. Polym. Sci.* **2015**, (2015).
414. Gharechahi, M. *et al.* Effect of Surface Roughness and Materials Composition. *J. Biomater. Nanobiotechnol.* **3**, 541–546 (2012).
415. Shakerardekani, A. and Karim, R. Effect of different types of plastic packaging films on the moisture and aflatoxin contents of pistachio nuts during storage. *J. Food Sci. Technol.* **50**, 409–411 (2013).
416. Sanyang, M. L., Sapuan, S. M., Jawaid, M., Ishak, M. R. and Sahari, J. Effect of plasticizer type and concentration on physical properties of biodegradable films based on sugar palm (arenga pinnata) starch for food packaging. *J. Food Sci. Technol.* **53**, 326–336 (2016).
417. Sady, S., Błaszczyk, A., Kozak, W., Boryło, P. and Szindler, M. Quality assessment of innovative chitosan-based biopolymers for edible food packaging applications. *Food Packag. Shelf Life* **30**, 100756 (2021).
418. Luna-Sosa, B. *et al.* Pectin-Based Films Loaded with Hydroponic Nopal Mucilages: Development and Physicochemical Characterization. *Coatings* **10**, 467 (2020).
419. Kalaycıoğlu, Z. *et al.* Antibacterial nano cerium oxide/chitosan/cellulose acetate composite films as potential wound dressing. *Eur. Polym. J.* **133**, 109777 (2020).
420. Yadollahi M. *et al.* How properties of cellulose acetate films are affected by conditions of iodine-catalyzed acetylation and type of pulp. *Cellulose* **26**, 6119–6132 (2019).
421. Richardson, E., Truffa Giachet, M., Schilling, M. and Learner, T. Assessing the physical stability of archival cellulose acetate films by monitoring plasticizer loss. *Polym. Degrad. Stab.* **107**, 231–236 (2014).
422. Hu, W., Chen, S., Yang, J., Li, Z. and Wang, H. Functionalized bacterial cellulose derivatives and nanocomposites. *Carbohydr. Polym.* **101**, 1043–1060 (2014).
423. Foresti, M. L., Vázquez, A. and Boury, B. Applications of bacterial cellulose as precursor of carbon and composites with metal oxide, metal sulfide and metal nanoparticles: A review of recent advances. *Carbohydr. Polym.* **157**, 447–467 (2017).
424. Poddar, M. K. and Dikshit, P. K. Recent development in bacterial cellulose production and synthesis of cellulose based conductive polymer nanocomposites. *Nano Sel.* **2**, 1605–1628 (2021).
425. Cherng, J. H. *et al.* Bacterial Cellulose as a Potential Bio-Scaffold for Effective Re-Epithelialization Therapy. *Pharm.* **13**, 1592 (2021).
426. Kuah, Y. *et al.* An ionic liquid process for mercury removal from natural gas. *Dalt. Trans.* **44**, 8617–8624 (2015).
427. Xu, Y., Zhuang, L., Lin, H., Shen, H. and Li, J. W. Preparation and characterization of polyacrylic acid coated magnetite nanoparticles functionalized with amino acids. *Thin Solid Films* **544**, 368–373 (2013).
428. Sanchez, L. M., Martin, D. A., Alvarez, V. A. and Gonzalez, J. S. Polyacrylic acid-coated iron oxide magnetic nanoparticles: The polymer molecular weight influence. *Colloids Surfaces A Physicochem. Eng. Asp.* **543**, 28–37 (2018).

429. Castro, C. *et al.* Gluconacetobacter medellinensis sp. nov., cellulose- and non-cellulose-producing acetic acid bacteria isolated from vinegar. *Int. J. Syst. Evol. Microbiol.* **63**, 1119–1125 (2013).
430. Halib, N., Amin, M. C. I. M. and Ahmad, I. Physicochemical Properties and Characterization of Nata de Coco from Local Food Industries as a Source of Cellulose. *Sains Malaysiana* **41**, 205–211 (2012).
431. Tsouko, E. *et al.* Bacterial cellulose production from industrial waste and by-product streams. *Int. J. Mol. Sci.* **16**, 14832–14849 (2015).
432. Kennedy, J. F. and Shimizu, J. Cellulosic polymers—blends and composites. *Polym. Int.* **37**, 84–84 (1995).
433. Teixeira, S. R. Z. *et al.* Biosynthesis and Functionalization of Bacterial Cellulose Membranes with Cerium Nitrate and Silver Nanoparticles. *Mater. Res.* **22**, 20190054 (2019).
434. Khalid, A. *et al.* Bacterial cellulose–TiO_2 nanocomposites promote healing and tissue regeneration in burn mice model. *RSC Adv.* **7**, 47662–47668 (2017).
435. Pa'e, N., Salehudin, M. H., Hassan, N. D., Marsin, A. M. and Muhamad, I. I. Thermal Behavior of Bacterial Cellulose Based Hydrogels with Other Composites and Related Instrumental Analysis. A *reference Series; Md.I.H. Mondal (ed.) Springer*, 763-787 (2018).
436. Piñeiro-Redondo, Y. *et al.* The influence of colloidal parameters on the specific power absorption of PAA-coated magnetite nanoparticles. *Nanoscale Res. Lett.* **6**, 1–7 (2011).
437. Nainggolan, H., Gea, S., Bilotti, E., Peijs, T. and Hutagalung, S. D. Mechanical and thermal properties of bacterial-cellulose-fibre-reinforced Mater-Bi® bionanocomposite. *Beilstein J. Nanotechnol.* **4**, 325–329 (2013).

USC UNIVERSIDADE DE SANTIAGO DE COMPOSTELA

Chapter 6

USC
UNIVERSIDADE
DE SANTIAGO
DE COMPOSTELA

USC
UNIVERSIDADE
DE SANTIAGO
DE COMPOSTELA

6. Appendix

6.1. Characterization methods

1. X-ray powder diffraction (XRD)

The samples (beads, microfibers and films) previously milled, were measured on Philips type powder diffractometer fitted with Philips "PW1710" control unit, vertical Philips "PW1820/00" and FR590 Enraf Nonius generator. The instrument was equipped with a graphite diffracted beam monochromator and copper radiation source ($\lambda(K_{\alpha 1})$=1.5406Å), operating at 40 kV and 30 mA. The X-Ray powder diffraction pattern (XRPD) has been collected by measuring the scintillation response to Cu Kα radiation versus the 2 Θ value over a 2 Θ range of 10-80, with a step size of 0.02° and counting time of 2 s per step. To perform the mathematical analysis of the obtained diffractograms, it was used the "HighScore Plus, Version 3.0d" software.

2. Small-angle X-ray scattering (SAXS)

The structural studies were performed by X-ray diffraction (XRD) using a Philips diffractometer (Panalytical, Callo End, UK) equipped with Cu Kα radiation (λ = 1.5406 Å) and a detector type CPAD PIXcel3. The diffractograms were obtained by using a step size of 0.02° and a counting time of 2 s per step from 0.5° to 2.5° (2 Θ). Samples were milled previously to the analysis, and the diffractograms were obtained using the "HighScore Plus, Version 3.0d" software.

3. Fourier-transform infrared spectroscopy (FTIR)

The Fourier transform infrared spectra (FTIR) were recorded on a Varian FT-IR 670 (Varian, Palo Alto, CA, USA) spectrophotometer in the range 400–4000 cm^{-1}. The infrared equipment is equipped with an ATR diamant, PIKE model GladiATR. The samples were registered in the range of 400-4000 cm^{-1} with 64 scans and a resolution of 4 cm^{-1}.

4. Confocal Raman microscopy

The Raman spectrums were obtained from an WITec Raman confocal microscope (model= ALPHA300R+) with a Zeiss 50x Epiplan-Neofluar objective, a 1024 pixels back-illuminated CCD detector and a 532 nm diode laser with a power of 0.2 mW. The film samples were measured using an excitation of 0.3 s integration and 450 scans.

5. Thermogravimetric analysis (TGA)

The thermogravimetric analysis (TGA) was recorded using a Perkin Elmer Pyris (Perkin, Waltham, MA, USA) for the beads and films while a Perkin Elmer TGA 8000 (Perkin, Waltham, MA, USA) was used for the microfibers and BNC capsules. The analyses were performed using a temperature range from 50 to 850 °C, approximately 20 mg of sample at 10 °C/min (magnetic beads), 25 °C/min (magnetic CA films) and 20°C/min (microfibers and capsules) under oxygen flow (20 mL/min).

6. Vibrating-sample magnetometer (VSM)

Magnetic properties were assessed by measuring the magnetization curve using a vibrating sample magnetometer (VSM) (DMS, Massachuset, MA, USA) with an applied field between -10.000 and 10.000 Oe at room temperature. Approximately, 3 mg of sample was used for the analyses and the magnetization results were normalized to the amount of magnetic mass content of the respective sample which was obtained by TGA.

7. Dynamic light scattering (DLS) particle size and Zeta Potential

Previously to the measurements, diluted solutions of the particles were prepared. The mean particle size, polydispersity (PDI) index and zeta potential were performed with at least 3 replicates at 25 °C using a NanoZS (Malvern Instruments, Malvern, UK) with an angle detection of 173°.

8. Transmission electron microscopy (TEM)

The morphology of the NPs and carbons (chapter 2) were characterized by transmission electron microscopy (TEM) using a JEOL JEM-1011 microscope (JEOL, Tokyo, Japan) operating at 100 kV and a high-resolution ZEISS libra 200 FE OMEGA microscope with EDX operating at 200 kV. Previously to the measurements a diluted solution of each particle was prepared. A drop of the diluted particle solution (approximately 10 µl) was deposited onto a copper grid with a thin layer of carbon film (Formvar films) and was left to dry under a white light bulb.

9. Scanning electron microscopy (SEM)

The morphology and topography of the magnetic materials were characterized using a ZEISS EVO LS15 microscope equipped with a BSD (backscattered electron detector) and a SE (secondary electron detector). The equipment was operating at 20 kV under variable pressure conditions.

It was also used for high resolution images of the FESEM ZEISS Ultra plus microscope. The high-resolution microscope was used to perform an energy-dispersive X-ray spectroscopy (EDS) analysis using the detector EDS (model INCA-X act, OXFORD) to determine the composition of the particles surface. An area in the sample was selected generating a spectrum and a table that shows the semiquantitative relationship in weight and in atoms of the present elements all normalized to 100 %.

The results were acquired at the operating conditions of 20 kV and a working distance of 8.5 mm. Being the optimal conditions for capturing and collecting more counts for a more precise analysis. Previously to the measurements, the samples were assembled onto aluminium stubs using conductive double-sided adhesive carbon tabs (Pro SciTech).

USC DE SANTIAGO DE COMPOSTELA

10. Hyperthermia

Magnetic hyperthermia characterization was performed to the BNC capsules using a homemade magnetic radio-frequency (RF) power generator operating at a fixed frequency (293 kHz) and an induced magnetic field (B=30 mT). The samples preparation was done by weighing a small quantity of magnetic material (3 mg) inside a cylindrical Teflon. The sample holder was then placed inside a thermally isolated cylindrical Dewar

glass under high vacuum conditions (10^{-6} mbar). Measurements were recorded (temperature increase versus time) with a fibre-optic thermometer (Neoptix) during 5 min of applied magnetic field. The BNC capsules were dispersed in water for the measurements. The specific adsorption rate (SAR) [1] was calculated using equation (1):

$$SAR = C * \frac{\Delta T}{\Delta t} \quad (1)$$

where, C, is the specific heat capacity of aqueous media (in our case, was water, $C = 4180 \frac{J}{kg} K$), T, is the temperature (K) and t,is the time (s), respectively.

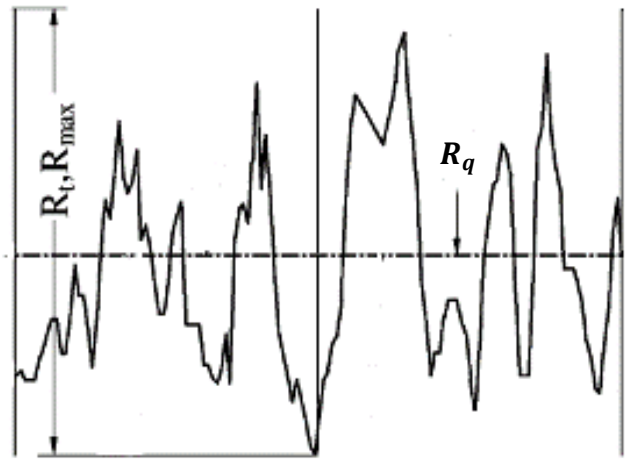
11. Rheology

The rheological measurements were performed on the precursor solutions of the magnetic CA films using a stress-controlled rheometer (Anton Paar MCR 302), equipped with a parallel plate geometry of 20 mm diameter at 25 °C keeping a 1.0 mm gap. The dynamic frequency sweep measurements were conducted in the linear viscoelastic regime of the CA solutions, as determined by previous strain sweep measurements. All measurements were performed on the same day in which the precursor solutions of the CA films were prepared to avoid solvent evaporation and during the measurements a used a solvent-trap was used to minimize evaporation loss.

12. Profilometer

The confocal laser optical profilometry results were obtained with a 3D Optical Profiler (Sensofar S. Neox) microscope with a white-light vertical scanning interferometry (VSI) mode and CFI60-2 Nikon objective lens. The topography images of the cellulose microfibers and CA films were obtained using objective lenses of 10x and 50x and the images were processed using the SensoMap software. Roughness parameters R_q, R_t, R_{sk} and R_{ku} were calculated by the instrument from multiple measures in each area [2]. Figure A1 shows the distribution of the different roughness parameters.

(a)



USC UNIVERSIDADE DE SANTIAGO DE COMPOSTELA

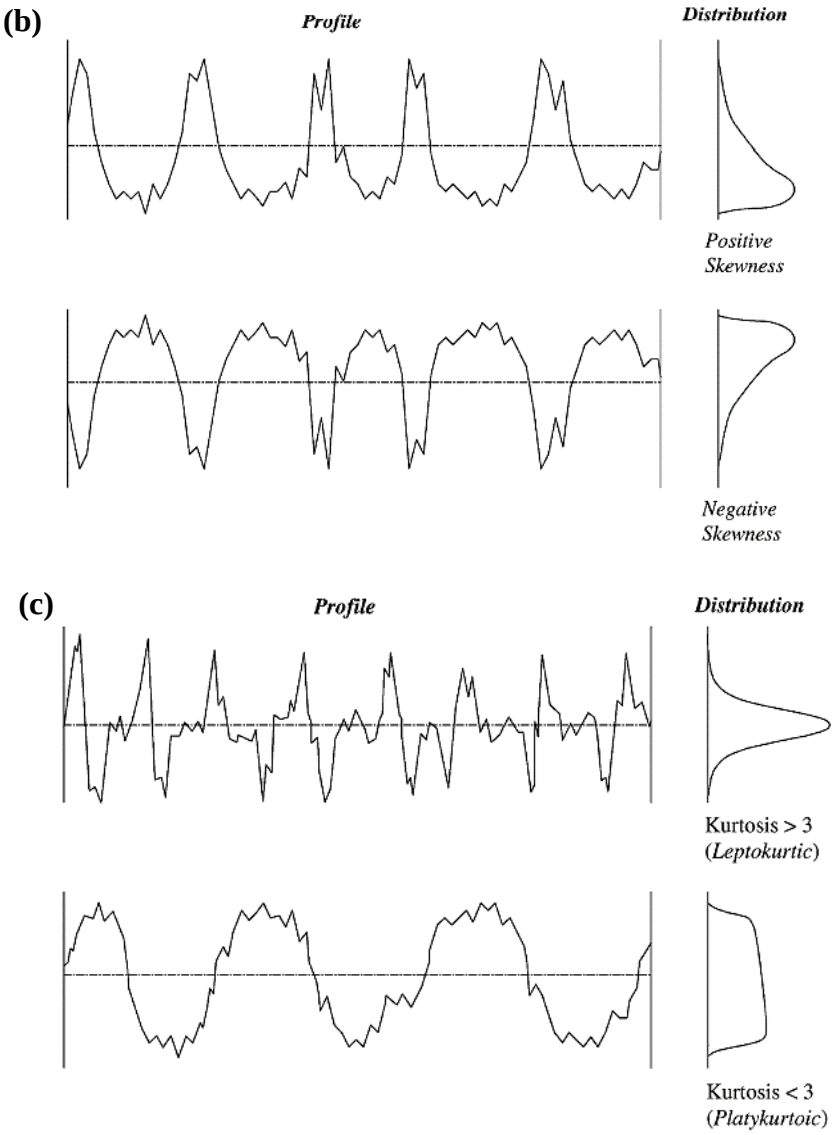


Figure A1. Distribution of the roughness parameters, R_t and R_a (a), R_{sk} and R_{ku} (b) (Adapted with permission from reference [2]. Copyright (2022) *Elsevier*).

- **Root mean square roughness** (R_q), represents the root mean square of the height distribution along a surface.
- **Total height of profile (R_t)**, is defined as the vertical distance between the highest and lowest peak along a surface profile.
- **Skewness (R_{sk})** this parameter is used to evaluate the height distribution (steep valleys or high peaks). If, $R_{sk} > 0$, surface contains more high peaks; $R_{sk} < 0$, surface with scratches or deep valleys; $R_{sk} = 0$, the surface has a symmetrical distribution.
- **Kurtosis (R_{ku})** this parameter describes the geometry of the peaks and valleys. If, $R_{ku} > 3$, the peak distribution is shaper with low valleys and is called leptokurtic; $R_{ku} < 3$, the peak distribution is even and is said to be platykurtic; $R_{ku} = 3$, the surface is normal distributed,

13. Mechanical properties

The mechanical strength of both magnetic microfibers (core@shell and core) and respective reference microfibers was determined through an Instron 5944 Single Column Tabletop Universal Testing System operated in tensile mode. Before testing, all microfibers were conditioned at 23 °C in 50 % humidity overnight. The load cell was 100 N, gauge length was set to 10 mm with an elongation rate of 0.5 mm/min. The microfiber diameter was achieved using a micrometre (Ironside, graduation 0.001 mm) and at least 7 replicates of one sample were measured. The mechanical strength of both control and magnetic CA films were determined using a Shimadzu AGX-V with a load cell of 500 N and an elongation rate of 50 mm/min. It was prepared at least 4 replicates per film sample with 2 x 7 cm, as seen in the Figure A1.1. The thickness of the films was recorded by an electronic micrometre (Schutt, graduation 0.001 mm).



Figure A1.1. Film allocated on the equipment before the mechanical testing.

14. Colorimetry

Colorimetric analyses of the magnetic CA films were done with a CR-400 Chroma Metre (Konica Minolta), as shown in Figure A1.2. The instrument was calibrated before the experiment with the standard white and black tiles. The colour coordinates L*, a*, and b* values are given by the colorimeter hardware device which is equipped with a light-emitting diode (LED) as light source. Values were obtained in different areas at least three times in the same film.

USC
UNIVERSIDADE DE SANTIAGO DE COMPOSTELA



Figure A1.2. On-going measurement of one magnetic film.

15. Brunauer-Emmett-Teller (BET) surface area analysis

The BET specific surface area and the pore size distribution of the magnetic beads (L3 and L13) and respective precursors (SBA-15, CMK-3 and commercial AC) were determined under N_2 adsorption-desorption isotherms at 77 K using Micromeritics ASAP 2020. Before starting the measurements, the samples were previously degasified in vacuum for 12 h at 30 °C.

16. X-ray photoelectron spectroscopy (XPS)

The XPS analysis of the magnetic beads (L3, L13, L13T and L16) and the precursors (CMK-3 (B,T) and commercial AC) before and after adsorption of metal ions was performed using a Thermo Scientific K-Alpha ESCA instrument equipped with aluminium Kα monochromatized radiation at 1486.6 eV X-ray source. Photoelectrons were collected from a take-off angle of 90º relative to the sample surface. The measurement was done in a Constant Analyser Energy mode (CAE) with a 100 eV pass energy for survey spectra and 20 eV pass energy for high resolution spectra. Charge referencing was done by setting the lower binding energy C1s photo peak at 284.8.0 eV C1s hydrocarbon peak. Surface elemental composition was determined using the standard Scofield photoemission cross sections.

17. Inductively coupled plasma optical emission spectrophotometry (ICP-OES)

The metal solutions were measured by inductively coupled plasma optical emission spectrophotometry (ICP-OES) using an emission spectrometer PerkinElmer Model Optima 3300 DV. The equipment requires gas Ar 99.99 %, N_2 99.99 % (both from Nippon Gases, Madrid) and compressed air produced on site by means of a compressor. Table A1 shows the conditions of the measurements. Whenever possible the dilution of the samples was avoided. In cases where the concentration exceeded the linear range of the calibration. The samples were diluted with 1 % HNO_3 in triplicate and the same dilution was performed in the entire series of samples.

Table A1. Experimental parameters used in the metal's determination by ICP-OES.

Parameter	Type/Value
Radio frequency power	1300 W
Nebulizer	Cross Flow GemTip
Plasma gas flow	16.0 L/min
Auxiliary gas flow	0.5 L/min
Nebulization flow	0.80 L/min
Sampling speed	1.5 mL/min
Integration time	5 s
Replica per sample	5
Working mode	Axial
Wavelengths	Ca= 393.36 nm Cd= 214.44 nm and 361.05 nm (2º less sensitive, avoid dilution) Hg= 194.16 nm Ni= 231.60 nm
Calibration HNO_3 (1%)	0.05/ 0.1/ 0.5/ 1/ 2.5/ 5/ 10/ 25/ 50 mg/L

USC UNIVERSIDADE DE SANTIAGO DE COMPOSTELA

6.2. Chapter 2: Appendix

6.2.1. Magnetic beads composition and data related with their magnetic behaviour and particle size

Table A1.1. Composition (wt%) of the distinct beads used on the adsorption studies

Particles	Fe_3O_4 (%)	$NaC_6H_7O_6$ (%)	HA (%)	Na_2SO_3 (%)	AC_comm. (%)	Pec_est (%)	Pectin (%)	$Na_2S_2O_5$ (%)	TOCNF (%)	CMK-3 (%)	GO (%)	CRG (%)	CS (%)
L1	45.2	54.8	-	-	-	-	-	-	-	-	-	-	-
L2	24.3	51.7	-	-	-	-	-	-	-	-	-	12	12
L3	20	45.8	-	-	34.3	-	-	-	-	-	-	-	-
L4	28.8	37	-	34.2	-	-	-	-	-	-	-	-	-
L5	36.3	53	-	10.7	-	-	-	-	-	-	-	-	-
L6	23.3	25.6	-	-	-	-	-	-	-	-	51.1	-	-
L7	30.9	34.4	-	-	-	-	34.7	-	-	-	-	-	-
L8	46.4	35.7	-	-	-	-	-	17.9	-	-	-	-	-
L9	40.4	36.7	22.9	-	-	-	-	-	-	-	-	-	-
L10	30	35	-	-	20	15	-	-	-	-	-	-	-
L11	30	24	-	-	17	26	-	-	-	-	-	-	-
L12	30	20	-	-	27	23	-	-	-	-	-	-	-
L13	34.6	57.7	-	-	-	-	-	-	-	7.69	-	-	-
L14	25.7	40.5	-	-	-	-	-	-	33.8	-	-	-	-
L15	17.8	54.2	-	-	-	-	-	-	22.6	5.42	-	-	-
L16	33.6	66.4	-	-	-	-	-	-	-	-	-	-	-

USC UNIVERSIDADE DE SANTIAGO DE COMPOSTELA

USC UNIVERSIDADE DE SANTIAGO DE COMPOSTELA

Table A1.2 DLS and Zeta Potential values of all particles of chapter 2.

Particles	DLS size number (nm)	PDI	Zeta Potential (mV)
Fe_3O_4	18	0.218	13.6
Fe_3O_4_com	138	0.433	-26.1
L1	131	0.329	-50.5
L2	443	0.222	-75.0
L3	346.9	0.150	-63.3
L4	465.8	0.458	-50.4
L5	638.3	0.578	-43.9
L6	335.2	0.714	-58
L7	435.9	0.103	-61.5
L8	609.1	0.586	-37.9
L9	122.2	0.235	-53.9
L10	873.6	0.342	-36.8
L11	241.6	0.409	-61.2
L12	178.6	0.344	-56.2
L13	420.7	0.288	-91.1
L14	1200	0.370	-32.0
L15	656.0	0.059	-35.9
L16	465.3	0.238	-76.2

Table A1.3. Calculated magnetization constants and respective mass percentage of magnetic content in all particles (beads and Fe_3O_4 NPs).

Particles	Magnetic solid content (%)	M_s (emu/g_{Fe3O4})	M_R (emu/g_{Fe3O4})	H_C (Oe)
Fe_3O_4	86.40	59.29	3.73	25.81
Fe_3O_4_com	89.80	7.57	0.889	91.57
L1	39.88	46.52	1.34	15.9
L2	22.03	18.44	0.274	6.79
L3	23.25	38.02	0.777	8.77
L4	33.64	37.95	1.10	15.21
L5	37.45	46.18	1.09	12.08
L6	26.52	44.69	0.736	7.364
L7	33.71	22.01	1.01	20.70
L8	40.42	91.43	5.345	51.08
L9	38.28	40.30	0.307	4.194
L10	46.69	19.87	0.597	15.91
L11	44.85	22.27	0.808	18.28
L12	50.24	17.17	0.636	17.92
L13	40.22	29.53	1.57	36.29
L14	30.81	40.47	0.415	4.77
L15	32.01	6.375	0.097	7.18
L16	26.38	57.94	2.38	23.36

Statistical error functions

The adsorption models (linear and nonlinear) were validated using six statistical error functions namely:

1. Sum of the Square of the Errors (ERRSQ):

$$\sum_{i=1}^{p}(q_{e.exp}-q_{e.calc})_i^2$$

2. Composite Fractional Error Function (HYBRID):

$$\sum_{i=1}^{p}\left[\frac{(q_{e.exp}-q_{e.calc})^2}{q_{e.exp}}\right]_i$$

3. Derivative of Marquardt's Percent Standard Deviation (MPSD):

$$\sum_{i=1}^{p}\left(\frac{q_{e.exp}-q_{e.calc}}{q_{e.exp}}\right)_i^2$$

4. Sum of the Absolute Errors (EABS):

$$\sum_{i=1}^{p}\left|q_{e.exp}-q_{e.calc}\right|_i$$

5. The Average Relative Error (ARE):

$$\sum_{i=1}^{p}\left|\frac{q_{e.exp}-q_{e.calc}}{q_{e.exp}}\right|_i$$

6. The Chi-square test (χ^2):

$$\sum_{i=1}^{n}\frac{(q_{e.exp}-q_{e.calc})^2}{q_{e.calc}}$$

USC UNIVERSIDADE DE SANTIAGO DE COMPOSTELA

Where, n, corresponds to the number of initial metal concentrations.

Table A1.4 Chi-square Distribution table [3].

Chi-square Distribution Table

d.f.	.995	.99	.975	.95	.9	.1	.05	.025	.01
1	0.00	0.00	0.00	0.00	0.02	2.71	3.84	5.02	6.63
2	0.01	0.02	0.05	0.10	0.21	4.61	5.99	7.38	9.21
3	0.07	0.11	0.22	0.35	0.58	6.25	7.81	9.35	11.34
4	0.21	0.30	0.48	0.71	1.06	7.78	9.49	11.14	13.28
5	0.41	0.55	0.83	1.15	1.61	9.24	11.07	12.83	15.09
6	0.68	0.87	1.24	1.64	2.20	10.64	12.59	14.45	16.81
7	0.99	1.24	1.69	2.17	2.83	12.02	14.07	16.01	18.48
8	1.34	1.65	2.18	2.73	3.49	13.36	15.51	17.53	20.09
9	1.73	2.09	2.70	3.33	4.17	14.68	16.92	19.02	21.67
10	2.16	2.56	3.25	3.94	4.87	15.99	18.31	20.48	23.21
11	2.60	3.05	3.82	4.57	5.58	17.28	19.68	21.92	24.72
12	3.07	3.57	4.40	5.23	6.30	18.55	21.03	23.34	26.22
13	3.57	4.11	5.01	5.89	7.04	19.81	22.36	24.74	27.69
14	4.07	4.66	5.63	6.57	7.79	21.06	23.68	26.12	29.14
15	4.60	5.23	6.26	7.26	8.55	22.31	25.00	27.49	30.58
16	5.14	5.81	6.91	7.96	9.31	23.54	26.30	28.85	32.00
17	5.70	6.41	7.56	8.67	10.09	24.77	27.59	30.19	33.41
18	6.26	7.01	8.23	9.39	10.86	25.99	28.87	31.53	34.81
19	6.84	7.63	8.91	10.12	11.65	27.20	30.14	32.85	36.19
20	7.43	8.26	9.59	10.85	12.44	28.41	31.41	34.17	37.57
22	8.64	9.54	10.98	12.34	14.04	30.81	33.92	36.78	40.29
24	9.89	10.86	12.40	13.85	15.66	33.20	36.42	39.36	42.98
26	11.16	12.20	13.84	15.38	17.29	35.56	38.89	41.92	45.64
28	12.46	13.56	15.31	16.93	18.94	37.92	41.34	44.46	48.28
30	13.79	14.95	16.79	18.49	20.60	40.26	43.77	46.98	50.89
32	15.13	16.36	18.29	20.07	22.27	42.58	46.19	49.48	53.49
34	16.50	17.79	19.81	21.66	23.95	44.90	48.60	51.97	56.06
38	19.29	20.69	22.88	24.88	27.34	49.51	53.38	56.90	61.16
42	22.14	23.65	26.00	28.14	30.77	54.09	58.12	61.78	66.21
46	25.04	26.66	29.16	31.44	34.22	58.64	62.83	66.62	71.20
50	27.99	29.71	32.36	34.76	37.69	63.17	67.50	71.42	76.15
55	31.73	33.57	36.40	38.96	42.06	68.80	73.31	77.38	82.29
60	35.53	37.48	40.48	43.19	46.46	74.40	79.08	83.30	88.38
65	39.38	41.44	44.60	47.45	50.88	79.97	84.82	89.18	94.42
70	43.28	45.44	48.76	51.74	55.33	85.53	90.53	95.02	100.43
75	47.21	49.48	52.94	56.05	59.79	91.06	96.22	100.84	106.39
80	51.17	53.54	57.15	60.39	64.28	96.58	101.88	106.63	112.33
85	55.17	57.63	61.39	64.75	68.78	102.08	107.52	112.39	118.24
90	59.20	61.75	65.65	69.13	73.29	107.57	113.15	118.14	124.12
95	63.25	65.90	69.92	73.52	77.82	113.04	118.75	123.86	129.97
100	67.33	70.06	74.22	77.93	82.36	118.50	124.34	129.56	135.81

USC UNIVERSIDADE DE SANTIAGO DE COMPOSTELA

MATLAB CODING

```
%ALGORITHMS FOR NONLINEAR AND LINEAR ADSORPTION ISOTHERM MODELS:
FREUNDLICH AND LANGMUIR
clear all
MODEL=input('Please type 1 for Freundlich Model,2 for Langmuir Model,3
for Temkin model and 4 for DKR mdoel: ');
%Non-linear least square method
 Xdata = [,]; % Data X
 Ydata =[,]; % Data y
 err = [,]; % Error y
if MODEL==1    %%%%%%%%%Freundlich Model%%%%%%%%%%%%%
   for i=1:2
     xdata=Xdata(i,:);
     ydata=Ydata(i,:);
     %Function for non-linear square method
     disp('Parameters and minimized resnorm:  ')
     [P,resnorm]=lsqcurvefit(@(P,xdata) P(1).*xdata.^P(2),[1
1],xdata,ydata)
     KF=P(1)
     bF=P(2)
     %Error sources
     ERRSQ=0;
     EHYBRD=0;
     EMPSD=0;
     EARE=0;
     EABS=0;
     Rsq1=0;
     ycal= P(1).*xdata.^P(2);
     for k=1:length(ydata)
       ERRSQ=ERRSQ+(ydata(k)-ycal(k))^2;
       EHYBRD=EHYBRD+(ydata(k)-ycal(k))^2/ydata(k);
       EMPSD=EMPSD+((ydata(k)-ycal(k))/ydata(k))^2;
       EARE=EARE+abs((ydata(k)-ycal(k))/ydata(k));
       EABS=EABS+abs(ydata(k)-ycal(k));
       Rsq1 = 1 - sum((ydata - ycal).^2)/sum((ydata-mean(ydata)).^2);
       chi2stat=sum((ydata-ycal).^2 ./ ycal);
     end
     %Displaying errors
     disp('Multiple sources of error: ')
     ERRSQ
     EHYBRD
     EMPSD
     EARE
     EABS
     Rsq1
     chi2stat
   end
elseif MODEL==2 %%%%%%%%%%Langmuir Model%%%%%%%%%%%%%%%% (…)
```

USC UNIVERSIDADE DE SANTIAGO DE COMPOSTELA

MATLAB CODING

```
%ALGORITHMS non-linear or linear ADSORPTION KINETIC MODELS: PFO,PSO,
AND ELOVICH
MODEL=input('Please type 1 for PFO Model, 2 for PSO Model, or 3 for
Elovich Model: ')
%Non-linear least square method
    xdata = [,];      % Data x
    ydata=[,]; % Data y
    err = [,]; % err y
   if MODEL==1    %%%%%%%%%PFO, PSO or Elovich Model%%%%%%%%%%%%%
    conc=input('conc70 or conc150 or conc230: ') %Type for the
different concentration
    if conc==70/150/230
      Ydata=ydata;
      hold on;
    else
      disp('SOMETHING WENT WRONG,PLEASE RUN THE PROGRAM AGAIN')
    end
for i=1:5
ydata=ydata(i,:);
%Function for non-linear square method (Example for PFO model)
disp('Parameters and minimized resnorm:  ')
[P,resnorm]=lsqcurvefit(@(P,xdata)P(1).^(1-exp(-P(2).*xdata)),[1,
1],xdata,ydata) %% type linear or nonlinear eq.
qe=P(1)
k1=P(2)
%Error sources
ERRSQ=0;
EHYBRD=0;
EMPSD=0;
EARE=0;
EABS=0;
ycal=P(1).^(1-exp(-P(2)*xdata));
for k=1:length(ydata)
    ERRSQ=ERRSQ+(ydata(k)-ycal(k))^2;
    EHYBRD=EHYBRD+(ydata(k)-ycal(k))^2/ydata(k);
    EMPSD=EMPSD+((ydata(k)-ycal(k))/ydata(k))^2;
    EARE=EARE+abs((ydata(k)-ycal(k))/ydata(k));
    EABS=EABS+abs(ydata(k)-ycal(k));
end
%Displaying errors
 disp('Error sources: ')
 ERRSQ
 EHYBRD
 EMPSD
 EARE
 EABS
 Rsquared = 1 - sum((ydata - ycal).^2)/sum((ydata - mean(ydata)).^2)
 chi_square = sum((ydata-ycal).^2/ycal
```

USC UNIVERSIDADE DE SANTIAGO DE COMPOSTELA

6.2.2. Results from Mycotoxins adsorption

Table A1.5. Mycotoxins removal efficiency (%) from aqueous solution and adsorption capacity (q_e, ng/g) of various magnetic beads

Particles	Removal efficiency	DON	ZEN	FB1	AFB1	AFB2	AFG1	AFG2	Total
Control	%	0.95 ± 1.07	1.52 ± 0.66	1.10 ± 1.40	3.11 ± 0.41	1.55 ± 3.25	1.39 ± 1.16	1.34 ± 2.21	0.56 ± 2.42
L1	%	10.88 ± 1.57	77.44 ± 1.04	0.34 ± 0.62	85.89 ± 6.19	90.41 ± 0.54	86.34 ± 1.50	82.31 ± 1.06	34.32 ± .41
	Qe	4.9 9± 0.88	158.78 ± 6.54	0.97 ± 1.59	6.18 ± 0.98	5.41 ± 0.28	3.99 ± 0.42	3.61 ± 0.35	189.66 ± 6.98
L2	%	4.59 ± 2.21	7.45 ± 1.75	9.73 ± 1.36	20.30 ± 3.86	17.23 ± 2.25	6.54 ± 0.61	6.25 ± 2.68	8.32 ± 1.61
	Qe	4.15 ± 1.95	30.69 ± 6.08	34.24 ± 6.28	2.49 ± 0.37	2.22 ± 0.29	0.67 ± 0.08	0.73 ± 0.32	75.19 ± 14.19
L3	%	54.34 ± 3.12	70.54 ± 6.86	71.63 ± 6.77	80.28 ± 6.14	82.20 ± 5.54	76.57 ± 6.13	76.57 ± 4.95	69.95 ± 6.23
	Qe	25.03 ± 1.29	145.46 ± 13.00	177.45 ± 13.24	5.07 ± 0.52	4.95 ± 0.51	3.79 ± 0.62	3.55 ± 0.56	598.45 ± 47.53
L4	%	15.42 ± 0.65	15.57 ± 1.59	3.97 ± 0.76	31.16 ± 3.48	30.27 ± 1.51	30.82 ± 2.73	23.42 ± 3.59	11.50 ± 0.62
	Qe	13.81 ± 0.83	59.06 ± 10.05	14.43 ± 2.96	3.71 ± 0.50	3.63 ± 0.40	3.16 ± 0.26	2.59 ± 0.44	100.38 ± 7.42
L5	%	10.78 ± 2.72	18.17 ± 4.48	12.21 ± 2.28	40.05 ± 3.43	45.14 ± 4.50	39.18 ± 4.30	34.85 ± 3.41	15.99 ± 2.42
	Qe	10.98 ± 3.15	76.12 ± 15.73	48.73 ± 7.95	5.54 ± 0.73	6.19 ± 0.52	4.36 ± 0.71	4.23 ± 0.57	156.14 ± 22.57
L6	%	18.53 ± 6.38	47.39 ± 1.25	29.91 ± 2.86	50.70 ± 2.49	54.43 ± 5.28	25.52 ± 6.38	24.86 ± 1.24	37.08 ± 0.91
	Qe	22.01 ± 8.82	226.75 ± 12.37	131.31 ± 14.34	7.66 ± 0.58	8.44 ± 0.79	3.39 ± 0.93	3.51 ± 0.16	407.94 ± 13.63
L7	%	26.23 ± 3.32	20.04 ± 1.23	44.13 ± 4.28	62.39 ± 3.89	69.25 ± 0.32	59.12 ± 0.60	57.53 ± 2.96	36.73 ± 2.82
	Qe	14.13 ± 2.77	24.93 ± 1.14	125.41 ± 25.71	2.92 ± 0.32	4.01 ± 0.16	2.86 ± 0.27	3.39 ± 0.59	177.65 ± 28.43
L8	%	22.29 ± 2.07	6.17 ± 2.27	49.38 ± 2.35	3.33 ± 0.56	0.21 ± 0.79	5.98 ± 0.27	1.13 ± 0.77	34.37 ± 1.43
	Qe	18.96 ± 1.44	13.28 ± 5.97	194.73 ± 34.38	0.20 ± 0.05	0.01 ± 0.07	0.44 ± 0.04	0.09 ± 0.06	284.93 ± 12.22
L9	%	14.40 ± 1.28	54.01 ± 3.47	41.52 ± 6.18	54.53 ± 4.00	47.37 ± 5.76	34.73 ± 4.11	20.56 ± 4.40	44.67 ± 5.75
	Qe	18.00 ± 1.92	165.05 ± 25.20	181.74 ± 82.90	3.69 ± 1.16	5.95 ± 0.60	3.23 ± 0.35	2.21 ± 0.40	495.46 ± 40.25
L10	%	28.54 ± 11.84	95.2 ± 1.13	92.38 ± 1.57	94.14 ± 1.08	94.88 ± 0.986	94.35 ± 1.25	92.69 ± 1.70	388.16 ± 58.41
	Qe	19.12 ± 9.00	174.01 ± 19.81	171.78 ± 24.81	5.81 ± 1.33	6.46 ± 1.48	5.23 ± 1.33	5.75 ± 1.53	85.00 ± 2.50

-Continued on next page-

USC UNIVERSIDADE DE SANTIAGO DE COMPOSTELA

Table A1.5 *Continued*

Particles	Removal efficiency	DON	ZEN	FB1	AFB1	AFB2	AFG1	AFG2	Total
L11	%	26.05 ± 12.74	96.1 ± 0.158	89.52 ± 2.17	94.85 ± 0.816	95.45 ± 0.921	95.46 ± 0.626	94.22 ± 0.91	0.766 ± 0.128
	Qe	0.034 ± 0.0207	0.3479 ± 0.036	0.332 ± 0.063	0.013 ± 0.002	0.014 ± 0.003	0.012 ± 0.002	2.79 ± 2.78	84.72 ± 2.26
L12	%	59.5 ± 7.23	96.09 ± 0.767	93.44 ± 1.29	94.64 ± 0.149	95.36 ± 0.198	94.49 ± 0.386	93.63 ± 0.318	0.838 ± 0.093
	Qe	0.079 ± 0.018	0.354 ± 0.041	0.363 ± 0.0421	0.01 ± 0.0004	0.012 ± 0.0002	0.0093 ± 0.0005	1.73 ± 1.72	89.89 ± 1.72
L13	%	6.29 ± 4.51	94.45 ± 0.785	88.61 ± 3.14	95.66 ± 0.256	95.48 ± 0.294	96.61 ± 0.428	96.61 ± 0.296	79.70 ± 1.47
	Qe	3.90 ± 2.78	160.63 ± 4.50	150.15 ± 11.0	36.14 ± 2.25	6.14 ± 0.105	5.99 ± 0.375	6.11 ± 0.270	338.99 ± 14.94
L14	%	9.31 ± 4.06	39.76 ± 8.18	16.25 ± 4.43	94.96 ± 0.022	30.40 ± 3.19	53.15 ± 1.01	38.54 ± 4.09	25.82 ± 3.06
	Qe	0.012 ± 0.005	0.129 ± 0.025	0.055 ± 0.01	6.04 ±0.105	0.0036 ± 0.0004	0.006 ± 0.0003	0.791 ± 0.787	0.213 ± 0.0207
L15	%	34.59 ± 6.96	92.63 ± 0.472	39.51 ± 11.3	0.004 ± 0.0002	94.20 ± 0.326	95.1 ± 0.397	96.15 ± 0.127	63.45 ± 4.74
	Qe	0.045 ± 0.009	0.327 ± 0.003	0.142 ± 0.05	0.012 ± 0.0001	0.012 ± 0.0003	0.0114 ± 0.0003	1.89 ± 1.88	0.551 ± 0.061

USC UNIVERSIDADE DE SANTIAGO DE COMPOSTELA

Table A1.6 Recovered mycotoxins after desorption (%)

Particles	DON	ZEN	FB1	AFB1	AFB2	AFG1	AFG2	Total
L1	-	12.16 ± 3.45	-	11.03 ± 2.84	13.28 ± 5.39	17.93 ± 8.16	18.77 ± 8.13	22.43 ± 5.83
L2	-	-	-	61.31 ± 23.17	35.22 ± 15.38	-	-	63.90 ± 31.74
L3	105.0± 3.61	66.85 ± 22.95	82.14 ± 33.42	100.95 ± 41.29	79.65 ± 23.02	93.14 ± 23.47	101.10 ± 32.80	77.98 ± 26.85
L4	37.46 ± 13.82	83.18±11.14	-	38.66 ± 10.60	33.21 ± 4.36	41.73 ± 9.79	48.06 ± 4.66	75.09 ± 8.65
L5	46.56 ± 9.19	59.02 ±15.08	45.84 ± 7.91	30.99 ± 15.64	19.09 ± 4.84	37.61 ± 19.09	34.09 ± 12.34	60.06 ± 6.57
L6	19.54 ± 8.71	39.59 ±14.74	20.90 ± 0.98	71.95 ± 39.83	38.66 ± 13.25	29.87 ± 6.75	63.07 ± 28.00	48.89 ±16.96
L7	34.23 ± 6.67	96.36 ± 23.28	45.92 ± 9.77	18.45 ± 2.27	11.32 ± 0.26	18.79 ± 1.71	17.22 ± 2.60	53.15 ± 6.73
L8	29.10 ± 0.32	-	25.96 ±5.45	-	-	-	-	44.51 ± 6.04
L9	35.63 ± 5.15	109.64 ± 4.78	80.42 ± 12.90	100.39 ± 1.62	86.67 ± 7.70	110.70 ± 14.30	96.05 ± 23.78	92.26 ± 5.32
L10	10.75 ± 1.85	13.18 ± 2.18	34.46 ± 3.50	4.99 ± 0.544	4.56 ± 0.544	11.1 ± 1.85	12.34 ± 2.66	23.96 ± 4.44
L11	11.66 ± 1.83	13.68 ± 2.05	48.85 ± 9.48	3.57 ± 0.585	2.95 ± 0.585	6.05 ± 0.864	8.11 ± 1.128	27.05 ± 4.48
L12	11.21 ± 1.74	7.23 ± 1.85	39.92 ± 7.752	1.3 ± 0.018	0.99 ± 0.023	1.66 ± 0.068	2.4 ± 0.187	21.06 ± 4.09
L13	10.37 ± 0.511	8.41 ± 0.142	46.28 ± 0.688	1.81 ± 0.023	2.52 ± 0.061	10.39 ± 0.416	17.19 ± 0.464	27.02 ± 2.93
L14	11 ± 0.477	17.35 ± 0.765	12.6 ± 0.358	11.37 ± 0.348	10.86 ± 0.383	11.7 ± 0.749	11.82 ± 1.19	14.15 ± 0.536
L15	17.71 ± 1.190	4.14 ± 0.464	7.11 ± 2.01	4.71 ± 0.484	5.35 ± 0.865	7.99 ± 1.09	8.16 ± 1.75	7.44 ± 0.953

6.2.3. Results from Cd(II) ions adsorption by L3 beads

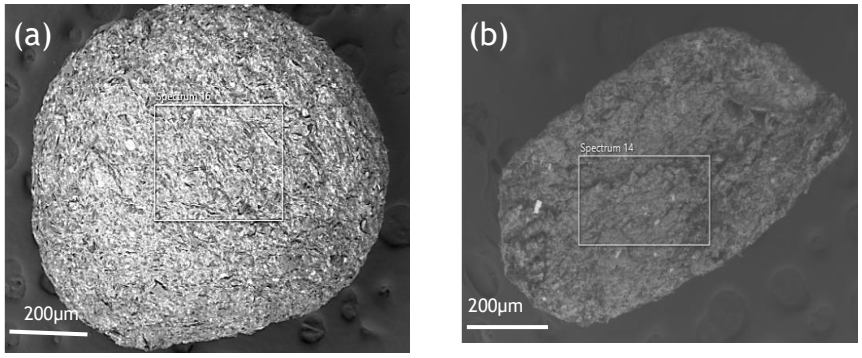


Figure A1.3. SEM micrograph of the L3 beads surface (a) and internally (b) after adsorption of Cd(II) ions

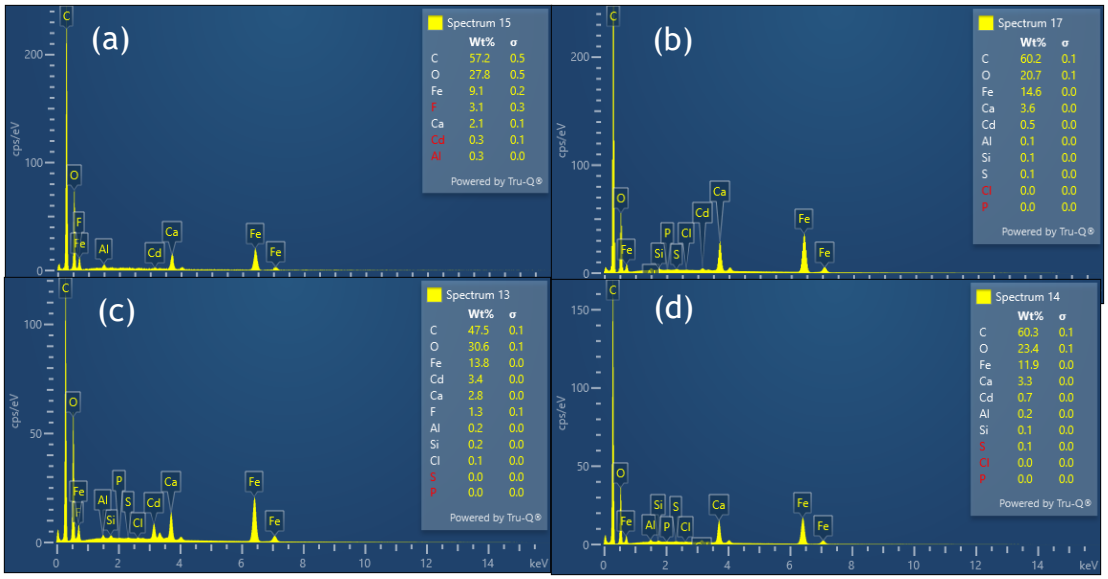


Figure A1.4. Diagrams of the SEM-EDX analysis of the beads surface and internal structure after Cd(II) adsorption at a concentration of 10 mg/L (a, b) and 250 mg/L (c, d). respectively.

USC UNIVERSIDADE DE SANTIAGO DE COMPOSTELA

Table A1.7. Linear and nonlinear parameters of the Kinetic models, PFO, PSO, and Elovich with respective errors of Cd(II) ions adsorption onto L3 beads

PFO Model	**Linear fitting**					**Nonlinear fitting**			
Cd(II) concentration (mg/L)	$qe_{(cal)}$ (mg/g)	k_1 (min^{-1})	R^2	χ^2	$qe_{(exp)}$ (mg/g)	$qe_{(cal)}$ (mg/g)	k_1 (min^{-1})	MSPD	χ^2
70	24.36	0.046	0.918	4.652	16.6	19.28	0.05	0.403	0.204
150	20.96	0.047	0.829	4.752	18.25	16.83	0.08	0.203	0.205
230	11.04	0.038	0.922	24.869	31.01	31.93	0.3	0.043	0.242

PSO Model	**Linear fitting**						**Nonlinear fitting**				
Cd(II) concentration (mg/L)	$qe_{(cal)}$ (mg/g)	k_2 (mg/g min^{-1})	h (mg/g min^{-1})	R^2	χ^2	$qe_{(exp)}$ (mg/g)	$qe_{(cal)}$ (mg/g)	k_2 (mg/g min^{-1})	h (mg/g min^{-1})	MSPD	χ^2
70	27.47	0.001	0.50	0.476	0.714	16.6	47.43	0.002	0.39	0.286	0.190
150	25.32	0.001	0.88	0.899	0.127	18.25	25.89	0.001	0.84	0.072	0.088
230	26.60	0.012	8.39	0.993	0.289	31.01	35.53	0.01	10.73	0.024	0.123

Elovich Model	**Linear fitting**				**Nonlinear fitting**			
Cd(II) concentration (mg/L)	β (g/mg min)	a (mg/g min)	R^2	χ^2	β (g/mg min)	a (mg/g min)	MSPD	χ^2
70	0.124	8.37	0.734	1630.12	0.059	0.423	0.3039	0.198
150	0.185	5.61	0.884	669.48	0.133	1.106	0.0489	0.070
230	0.237	0.0613	0.7037	5413.69	250.76	0.237	0.017	0.087

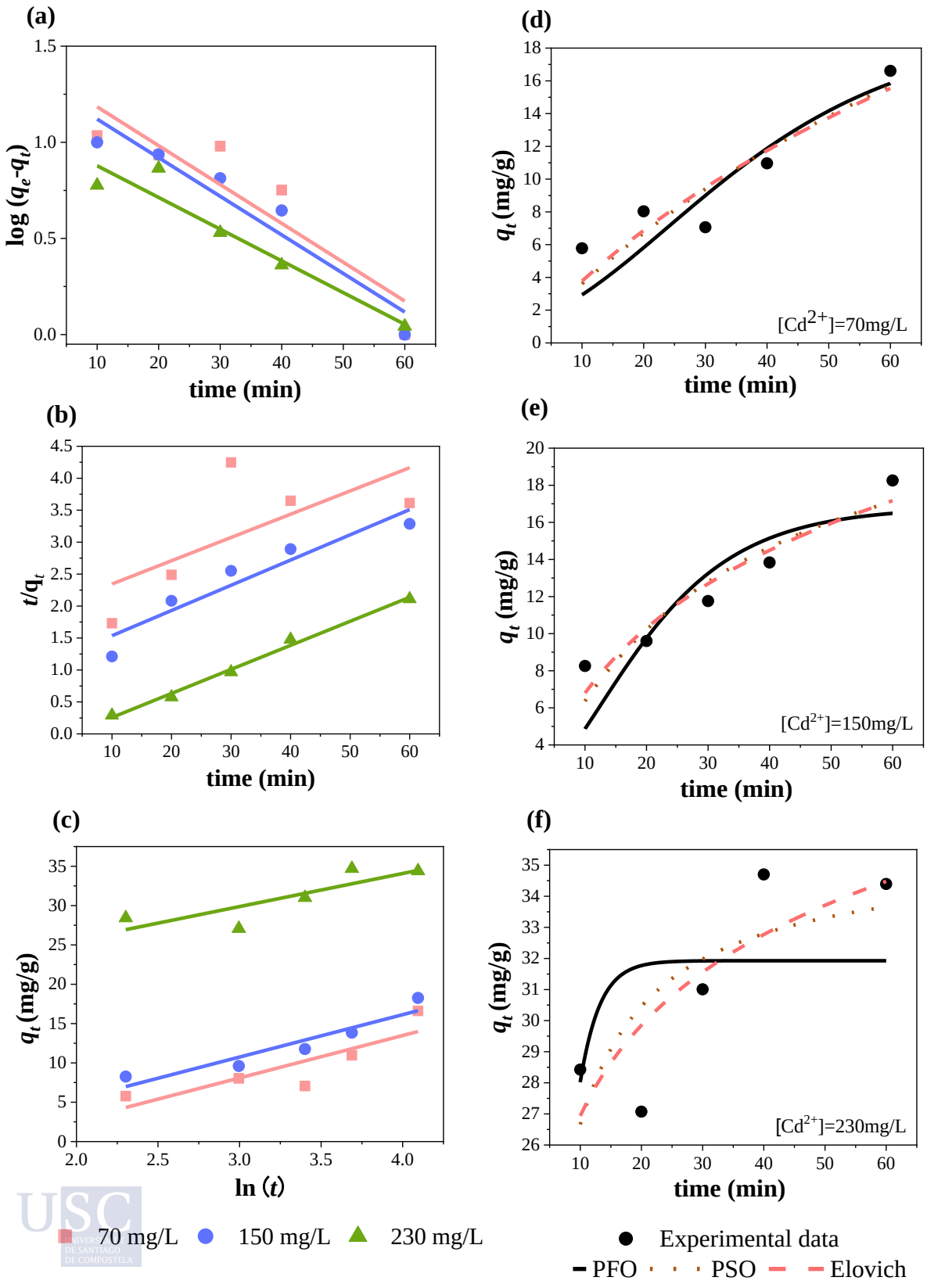


Figure A1.5. Linear Kinetic models: PFO (a); PSO (b); Elovich (c) and nonlinear kinetic models (d, e, f) representing Cd(II) ions adsorption by L3 beads at 70,150, and 230 mg/L.

6.2.4. Results from Binary adsorption by L3, L13 and L16 beads

Synthesis of mesoporous SBA-15 and CMK-3 carbon

Mesoporous silica SBA-15, was prepared according to the procedure described by Zhao et al. [4] with some modifications. By using triblock copolymer poly(ethylene glycol)-block-poly-(propylene glycol)-block-poly (ethylene glycol) (Pluronic P123) as the surfactant and tetraethyl orthosilicate (TEOS 98%) as silica source. Typically, (4.0 g) of P123 were dissolved in 150 mL of HCl (1.6 M) at 35 °C for 3 h. After that, (8.5 g) of TEOS were added to the P123 solution under vigorous stirring for 20 h at 35 °C. The resultant white precipitate was aged at 80 °C for 20 h. The sample was filtered. dried without washing and calcined at a heating rate of 1 °C/min to a temperature of 550 °C for 6 h.

The CMK-3 mesoporous carbon was synthesized by impregnation of the SBA-15 with a solution of sucrose. as a carbon source. The synthesis using the SBA-15 hard template was prepared according to previous work [5]. Briefly, 1.0 g of SBA-15 was added to a previously prepared solution of 1.25 g of sucrose and 0.14 g of H_2SO_4 in 5.0 g of H_2O. The mixture was placed in a drying oven for 6 h at 100 °C and subsequently to 160 °C for 6 h. The sample was treated again at 100 °C and 160 °C after the addition of 0.8 g of sucrose and 0.09 g of H_2SO_4 in 5.0 g of H_2O. The sucrose SBA-15 sample was then carbonized under nitrogen flow at 900 °C. Afterwards, the silica present in the sample was removed using a solution of 10 wt% hydrofluoric acid at room temperature under magnetic agitation. The sample was then filtered. washed with ethanol and dried at 105 °C for 12 h.

USC UNIVERSIDADE DE SANTIAGO DE COMPOSTELA

Table A1.8. Linear and nonlinear fitting of the kinetic models describing the Hg(II) ions adsorption onto the L3 beads (Binary experiment).

PFO Model	Linear fitting					Nonlinear fitting			
Hg(II) concentration (mg/L)	$q_e(calc)$ (mg/g)	k_1 (min^{-1})	R^2	χ^2	$q_e(exp)$ (mg/g)	$q_e(calc)$ (mg/g)	k_1 (min^{-1})	MSPD	χ^2
70	15.21	0.009	0.899	5.41	18.80	18.27	0.021	1.975	0.180
150	40.83	0.022	0.952	17.337	52.58	45.18	0.127	0.146	0.821
230	114.7	0.033	0.809	28.43	41.99	41.70	0.032	0.321	0.477

PSO Model	Linear fitting					Nonlinear fitting					
Hg(II) concentration (mg/L)	$q_e(calc)$ (mg/g)	k_2 (mg/g min^{-1})	h (mg/g min^{-1})	R^2	χ^2	$q_e(exp)$ (mg/g)	$q_e(calc)$ (mg/g)	k_2 (mg/g min^{-1})	h (mg/g min^{-1})	MSPD	χ^2
70	26.46	0.007	4.819	0.569	143.65	18.8	24.23	4.160	2442.3	3.577	0.329
150	55.25	0.051	155.89	0.994	0.865	52.58	51.72	0.002	4.173	0.060	0.340
230	57.80	0.009	29.41	0.882	48.43	41.99	54.98	0.0003	0.662	1.110	0.903

Elovich Model	Linear fitting				Nonlinear fitting			
Hg(II) concentration (mg/L)	β (g/mg min)	α (mg/g min)	R^2	χ^2	β (g/mg min)	α (mg/g min)	MSPD	χ^2
70	0.116	8.57E+09	0.721	2228.96	0.157	0.344	2.55	0.207
150	0.077	2.17E+06	0.841	7508.93	0.148	45.93	0.038	0.214
230	0.034	4.86E+09	0.873	78183.91	0.066	0.838	2.493	1.521

USC UNIVERSIDADE DE SANTIAGO DE COMPOSTELA

Table A1.9. Linear and nonlinear fitting of the kinetic models describing the Hg(II) ions adsorption onto the L13 beads (Binary experiment).

PFO Model	**Linear fitting**					**Nonlinear fitting**			
Hg(II) concentration (mg/L)	$q_e(calc)$ (mg/g)	k_1 (min^{-1})	R^2	χ^2	$q_e(exp.)$ (mg/g)	$q_e(calc)$ (mg/g)	k_1 (min^{-1})	MSPD	χ^2
70	8.53	0.012	0.636	10.21	13.40	12.40	0.036	0.554	0.157
150	5.07	0.007	0.285	7.81	29.90	25.89	0.009	0.283	0.664
230	6.1	0.004	0.534	2.24	22.70	18.56	0.229	0.284	0.456

PSO Model	**Linear fitting**						**Nonlinear fitting**				
Hg(II) concentration (mg/L)	$q_e(calc)$ (mg/g))	k_2 (mg/g min^{-1})	h (mg/g min^{-1})	R^2	χ^2	$q_e(exp)$ (mg/g)	$q_e(calc)$ (mg/g)	k_2 (mg/g min^{-1})	h (mg/g min^{-1})	MSPD	χ^2
70	15.04	0.001	0.308	0.965	3.00	13.4	14.83	0.002	0.347	0.706	0.115
150	29.94	0.003	2.51	0.991	0.389	29.9	27.49	0.009	6.80	0.249	0.554
230	22.73	0.002	1.14	0.976	1.24	22.7	19.26	0.003	8.34	0.281	0.441

Elovich Model	**Linear fitting**				**Nonlinear fitting**			
Hg(II) concentration (mg/L)	β (g/mg min)	α (mg/g min)	R^2	χ^2	β (g/mg min)	α (mg/g min)	MSPD	χ^2
70	0.297	1071.10	0.8354	162.77	0.320	0.693	0.79	0.135
150	0.061	4.19	0.296	3453.46	0.473	4842	0.198	0.440
230	0.076	0.84	0.1894	1140.84	0.832	71308	0.247	0.372

Table A2.0 Linear and nonlinear fitting of the kinetic models describing the Hg(II) ions adsorption onto the L16 beads (Binary experiment).

PFO Model	Linear fitting					Nonlinear fitting			
Hg(II) concentration (mg/L)	$q_e(calc)$ (mg/g)	k_1 (min^{-1})	R^2	χ^2	$q_e(exp)$ (mg/g)	$q_e(calc)$ (mg/g)	k_1 (min^{-1})	MSPD	χ^2
70	5.14	0.004	0.564	2.31	9.71	8.21	0.04	1.909	0.229
150	5.23	0.006	0.690	4.53	18.62	17.30	0.08	0.108	0.104
230	4.6	0.004	0.086	5.69	14.91	12.54	0.07	0.764	0.442

PSO Model	Linear fitting						Nonlinear fitting				
Hg(II) concentration (mg/L)	$q_e(calc)$ (mg/g))	k_2 (mg/g min^{-1})	h (mg/g min^{-1})	R^2	χ^2	$q_e(exp)$ (mg/g)	$q_e(calc)$ (mg/g)	k_2 (mg/g min^{-1})	h (mg/g min^{-1})	MSPD	χ^2
70	9.40	0.002	0.203	0.884	14.35	9.71	9.55	0.003	0.262	2.537	0.242
150	19.27	0.004	1.31	0.991	0.083	18.62	19.31	0.004	1.316	0.035	0.038
230	10.25	0.006	0.59	0.816	7.92	14.91	13.65	0.005	0.915	1.576	0.650

Elovich Model	Linear fitting				Nonlinear fitting			
Hg(II) concentration (mg/L)	β (g/mg min)	α (mg/g min)	R^2	χ^2	β (g/mg min)	α (mg/g min)	MSPD	χ^2
70	0.535	63,563	0.645	23.28	0.527	0.591	2.81	0.282
150	0.253	47,9	0.859	151.07	0.384	1.72	0.050	0.074
230	0.330	11,45	0.267	47.36	0.570	10.279	2.337	0.868

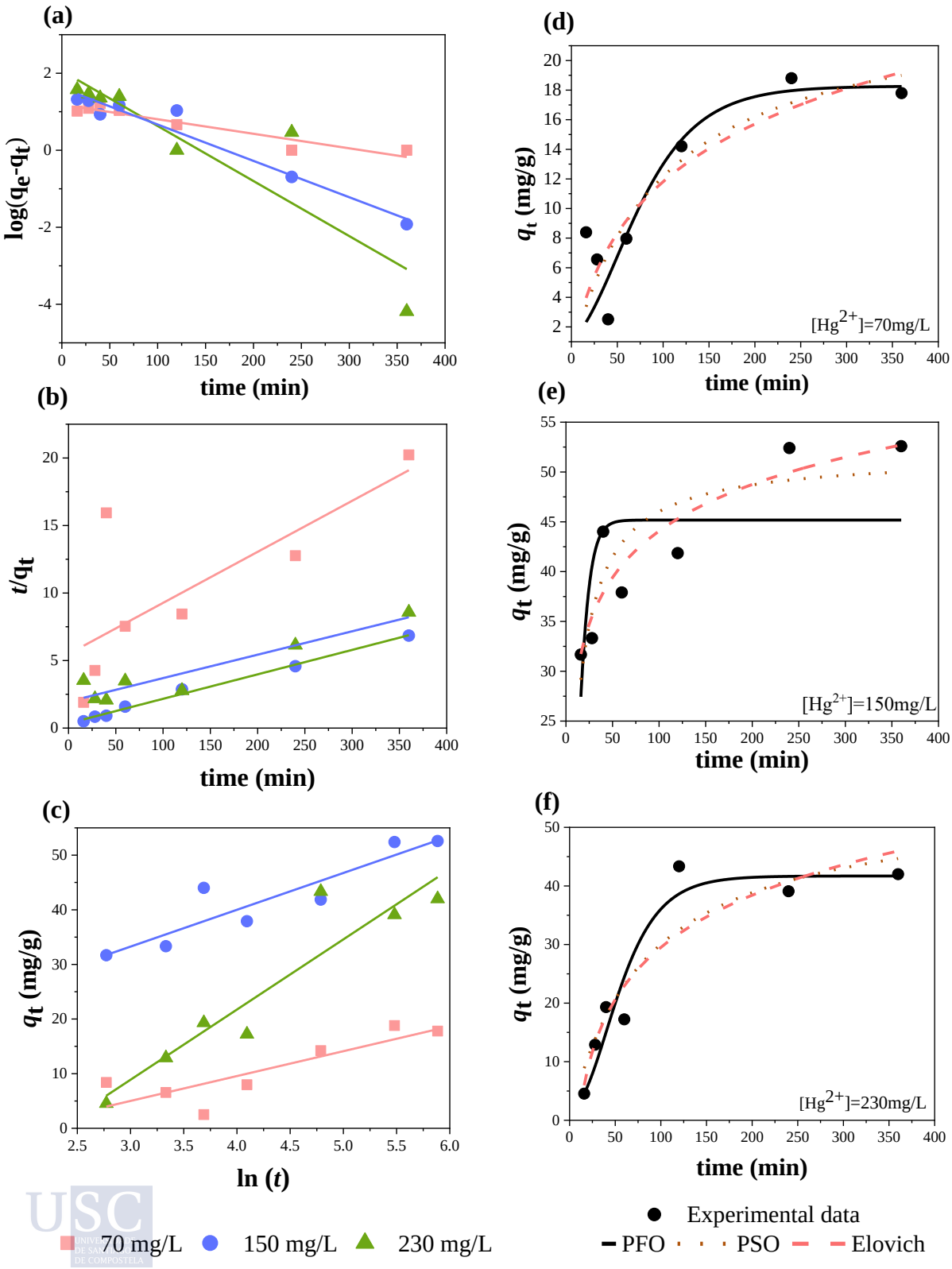


Figure A1.6. Linear Isotherm models: PFO (a); PSO (b) and Elovich (c) and the nonlinear models (d, e, f) describing Hg(II) ions adsorption onto L3 beads.

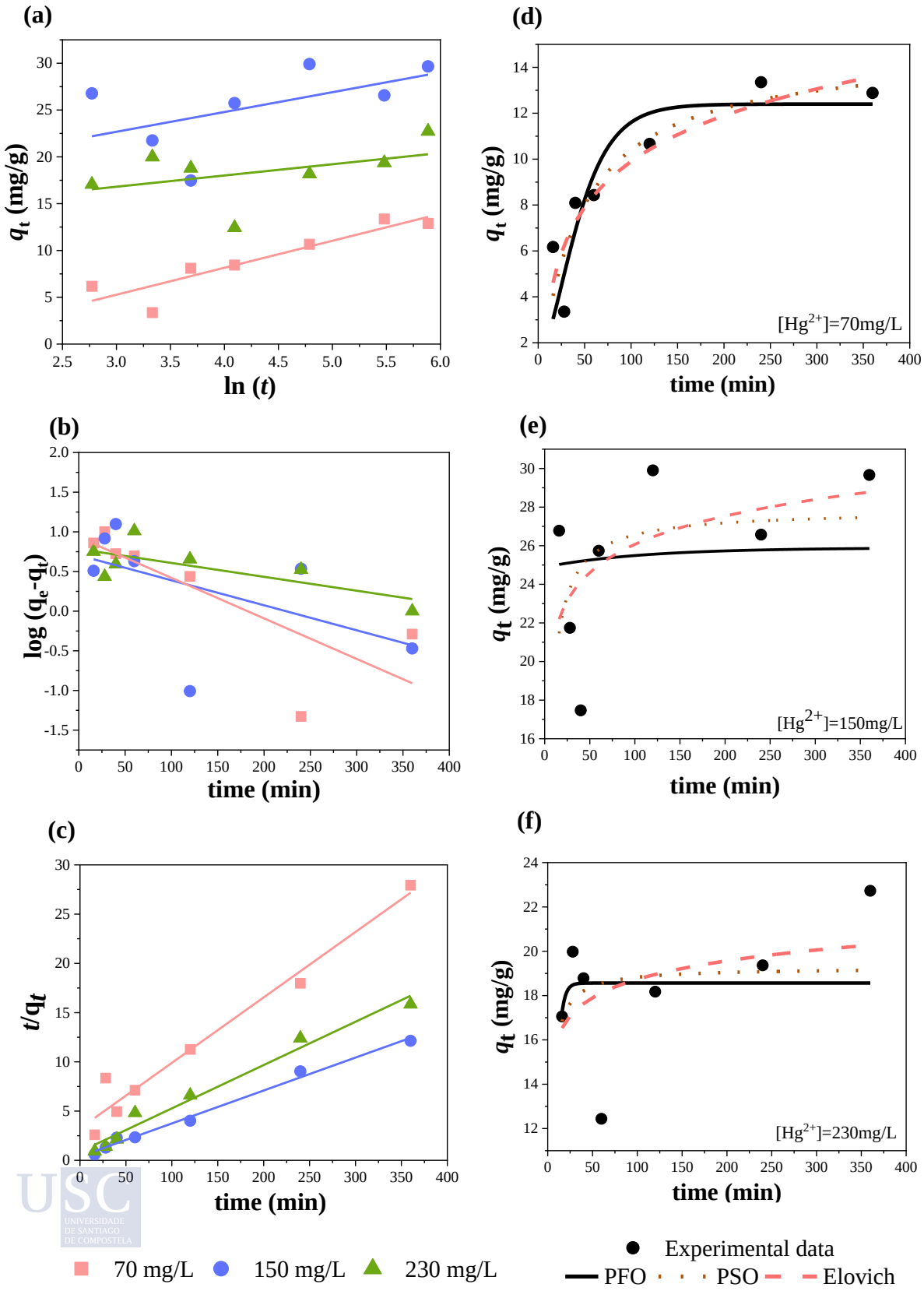


Figure A1.7. Linear Isotherm models: PFO (a); PSO (b) and Elovich (c) and the nonlinear models (d, e, f) describing Hg(II) ions adsorption onto L13 beads.

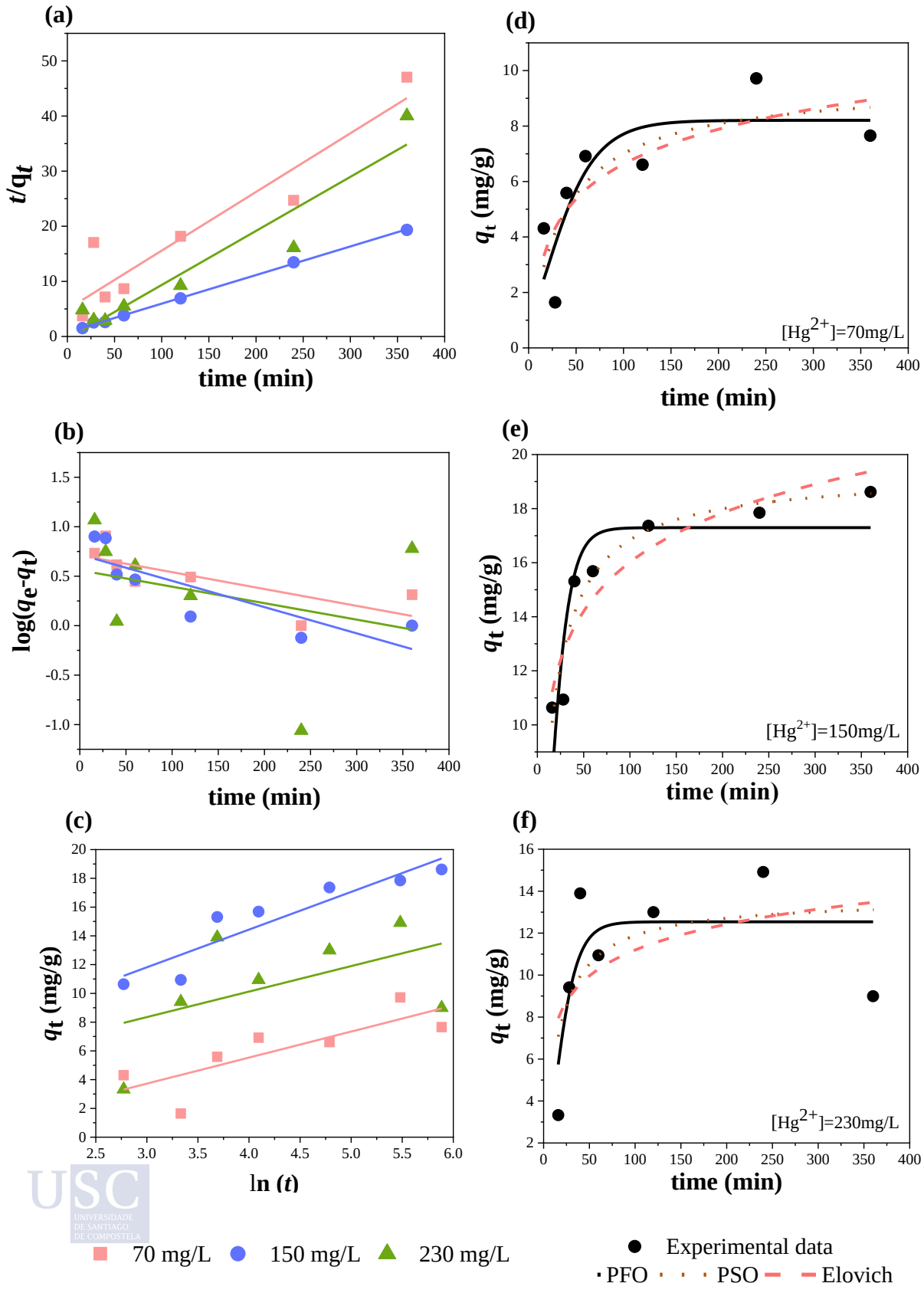


Figure A1.8. Linear Isotherm models: PFO (a); PSO (b) and Elovich (c) and the nonlinear models (d, e, f) describing Hg(II) ions adsorption onto L16 beads.

Table A2.0 High-resolution XPS scan of the beads L3, L13 (binary), and L13T (used in the ternary experiment) before adsorption.

Chemical bond	L3		L13		L13T	
	BE (eV)	Rel. (%)	BE (eV)	Rel. (%)	BE (eV)	Rel (%)
C1s C-OH/ C-O-C/ Cl-C, C-N	286.43	38.77	286.55	52.94	286.36	34.69
C1s O=C-/ O=C-O/N-C=O	288.13	26.86	288.3	19.79	289.65	17.71
C1s C=O					288	40.73
C1s CF2-CF2						
O1s metal oxides	Powder 529.79	Powder 8.24	Powder 529.88	Powder 10.35	530.8	4.37
O1s O=C/ O=C-O	531.2	14.66	531.16	23.31	532.79	42.03
O1s C-O-C/ C-OH	532.83	55.08	532.54	46.24	534.37	53.6
F1s CF2-CF2			Powder 689.25	Powder 74.88	Powder 689.7	Powder 100
F1s metal fluorides			684.13	100		
N1s R2C=NR imine	400.06	75.12	399.98	100	401.19	100
N1s RC(=O)NR'R"	402.93	24.88				
S2p^3-S2p (organic disulphide)	163.53	54.16	163.58	30.44		
S2p (metal sulfate)	168.52	45.84	168.62	69.56		

USC UNIVERSIDADE DE SANTIAGO DE COMPOSTELA

Table A2.1. High-resolution XPS scan of the beads L3 and L13 (binary) after adsorption.

Chemical bonds	Adsorption system	L3		L13	
		BE (eV)	Rel. (%)	BE (eV)	Rel. (%)
C1s C-OH/ C-O-C/ Cl-C/ C-N	Hg	286.5	34.15	286.43	48.15
	Hg-Cd	286.54	39.3	286.54	48.22
	Hg-Ni	287	70.51	286.64	54.64
C1s O=C-/ O=C-O/N-C=O	Hg	288.08	25.82	288.58	12.16
	Hg-Cd	288.28	23.79	288.52	16.13
	Hg-Ni	289.32	11.64	288.63	15.96
C1s CF2-CF2	Hg	292.31	1.06		
	Hg-Cd	292.43	1.32		
	Hg-Ni	292.36	1.91		
O1s metal oxides	Hg	530.08	2.88	530.85	17.32
	Hg-Cd	530.06	3.33	530.16	11.55
	Hg-Ni			530.7	22.73
O1s O=C/ O=C-O	Hg	531.92	37.42	532.4	53.14
	Hg-Cd	531.68	30.13	531.72	35.12
	Hg-Ni	531.6	16.41	532.18	26.79
O1s C-O-C/ C-OH	Hg	533.24	49.49	533.63	29.54
	Hg-Cd	533.12	60.56	532.99	49.45
	Hg-Ni	533.01	52.48	533.36	50.47
F1s CF2-CF2	Hg	689.65	100	689.04	100
	Hg-Cd	698.71	100	689.05	100
	Hg-Ni	690.12	100	689.33	100
N1s	Hg	400.24	100	399.9	100
	Hg-Cd	400.13	100	399.78	100
	Hg-Ni	400.68	100	400.05	100
S2p3-S2p (organic disulphide)	Hg	163.61	100	163.48	35.67
	Hg-Cd	163.72	31.24	163.64	33.3
	Hg-Ni	164.39	16.61	163.93	56.7
S2p (metal sulfate)	Hg			169.05	64.33
	Hg-Cd	168.98	68.76	168.86	66.7
	Hg-Ni	169.15	83.39	169.02	43.3

USC UNIVERSIDADE DE SANTIAGO DE COMPOSTELA

Table A2.2. Elemental composition of Ca(II) (At%.) ions before and after mono/binary adsorption at the L3 and L13 surface.

Adsorption system	L3	L13
Before adsorption	2.93	2.91
Hg(II)	1.95	2.41
Hg(II)-Cd(II)	1.42	1.3
Hg(II)-Ni(II)	1.54	1.45

Table A2.3. Values of calcium initial and final concentration with pH variation after mercury adsorption by L3 and L13 (Binary experiment).

L3 beads

Hg(II) initial concentrations (mg/L)	Initial solution pH	Ca(II) initial concentration in solution (mg/L)	After Hg(II) adsorption		
			Hg(II) q_e(mg/g)	Ca(II) final conc. (mg/L)	Final solution pH
10	4.5	0.105	3.37	0.110	6.11
70	4.5	0.110	17.80	0.295	5.96
150	4.5	0.120	52.59	0.399	5.78
200	4.5	0.278	5.50	0.299	5.87
230	4.5	0.116	42.00	0.612	5.8

L13 beads

Hg(II) initial concentrations (mg/L)	Initial solution pH	Ca(II) initial concentration in solution (mg/L)	After Hg(II) adsorption		
			Hg(II) q_e(mg/g)	Ca(II) final conc. (mg/L)	Final solution pH
10	4.5	0.104	0.84	0.425	6.05
70	4.5	0.136	12.89	1.677	5.64
150	4.5	0.151	29.66	1.812	5.52
200	4.5	0.273	5.94	1.154	5.73
230	4.5	0.136	22.73	1.703	5.59

USC UNIVERSIDADE DE SANTIAGO DE COMPOSTELA

Table A2.4. Linear and nonlinear parameters of the Isothermal models, Langmuir and Freundlich with respective errors of L3 beads at the mono and ternary system.

Langmuir Model	Linear fitting				Nonlinear fitting			
L3 bead	q_m (mg/g)	K_L (L/mg)	R^2	χ^2	q_m (mg/g)	K_L (L/mg)	MSPD	χ^2
Mono-Cd(II)	59.17	0.048	0.981	0.131	59.18	0.040	0.291	5.512
Mono-Hg(II)	7.937	0.041	0.860	16.454	12.55	0.370	0.630	6.761
Mono-Ni(II)	37.04	0.031	0.945	0.596	42.70	0.015	0.629	18.60
Tern-Cd(II)	25.19	0.713	0.758	2.505	31.97	0.165	0.783	19.37
Tern-Hg(II)	7.949	0.089	0.486	27.231	14.87	0.047	9.544	30.69
Tern-Ni(II)	7.396	0.047	0.771	20.143	16.16	0.225	3.520	34.37

Freundlich Model	Linear fitting					Nonlinear fitting				
L3 bead	1/*n*	n	K_F ($mg^{1-}{}_{(1/n)}L^{1/n}g^{-1}$)	R^2	χ^2	1/*n*	n	K_F ($mg^{1-}{}_{(1/n)}L^{1/n}g^{-1}$)	MSPD	χ^2
Mono-Cd(II)	0.397	2.521	7.086	0.983	0.006	0.333	3.000	9.500	0.153	1.482
Mono-Hg(II)	0.036	28.09	9.425	0.018	0.096	0.047	21.50	9.520	0.639	7.405
Mono-Ni(II)	0.358	2.794	4.816	0.995	0.027	0.391	2.560	4.120	0.024	0.333
Tern-Cd(II)	0.264	3.784	7.822	0.580	0.090	0.201	4.980	11.24	1.006	23.40
Tern-Hg(II)	0.632	1.581	0.453	0.511	0.567	0.260	3.840	3.380	17.92	36.31
Tern-Ni(II)	0.104	9.588	7.158	0.058	0.331	0.101	9.874	9.078	3.535	38.86

Table A2.5. Linear and nonlinear parameters of the Isothermal models, Langmuir and Freundlich with respective errors of L13T beads at the mono and ternary system.

Langmuir Model	Linear fitting				Nonlinear fitting			
L13-T bead	q_m (mg/g)	K_L (L/mg)	R^2	χ^2	q_m (mg/g)	K_L (L/mg)	MSPD	χ^2
Mono-Cd(II)	53.19	0.127	0.997	0.013	53.58	0.126	0.023	0.332
Mono-Hg(II)	39.841	0.020	0.685	2.358	46.11	0.016	0.980	13.915
Mono-Ni(II)	45.66	0.114	0.997	0.072	46.55	0.078	0.389	8.53
Tern-Cd(II)	27.32	0.684	0.940	0.399	28.154	0.542	0.072	1.46
Tern-Hg(II)	1.271	0.022	0.446	139.349	1.42	0.030	1.567	0.75
Tern-Ni(II)	9.579	0.057	0.911	8.559	13.05	1.335	0.283	2.80

Freundlich Model	Linear fitting					Nonlinear fitting				
L13-T bead	$1/n$	n	K_F ($mg^{1-}{}_{(1/n)}L^{1/n}g^{-1}$)	R^2	χ^2	$1/n$	n	K_F ($mg^{1-}{}_{(1/n)}L^{1/n}g^{-1}$)	MSPD	χ^2
Mono-Cd(II)	0.372	2.690	8.255	0.911	0.027	0.246	4.070	14.800	0.895	7.247
Mono-Hg(II)	0.431	2.32	3.513	0.724	0.069	0.405	2.47	4.196	0.741	12.080
Mono-Ni(II)	0.320	3.125	8.867	0.982	0.005	0.261	3.825	11.610	0.156	1.496
Tern-Cd(II)	0.186	5.376	11.151	0.831	0.017	0.153	6.552	13.06	0.175	3.18
Tern-Hg(II)	0.429	2.330	0.123	0.554	28.763	0.379	2.640	0.171	1.55	0.80
Tern-Ni(II)	0.046	21.834	8.453	0.997	0.073	0.043	23.210	10.290	0.315	3.33

Table A2.6. Linear and nonlinear parameters of the Isothermal models, Temkin and DKR with respective errors of L3 beads at the mono and ternary system.

Temkin Model	**Linear fitting**				**Nonlinear fitting**				
L3 bead	b_T (J mol)	K_T (L/g)	R^2	χ^2	b_T (J mol)	K_T (L/g)	R^2	MSPD	χ^2
Mono-Cd(II)	258.62	1.282	0.984	4959.8	2.27	1.195	0.392	0.017	0.532
Mono-Hg(II)	4101.940	3198879.8	0.030	395414.7	0.604	3.182	0.030	0.65	7.33
Mono-Ni(II)	436.19	1.102	0.922	8731.9	5.68	1.102	0.896	0.10	1.72
Tern-Cd(II)	503.57	3.694	0.345	12960.9	4.921	3.692	0.127	0.83	21.08
Tern-Hg(II)	750.779	0.346	0.162	11838.4	3.29586	0.346	0.162	7.5	32.39
Tern-Ni(II)	1492.513	69.379	0.050	62228.4	1.66	69.129	0.050	3.6	37.66

DKR Model	**Linear fitting**					**Nonlinear fitting**					
L3 bead	E (kJ/mol)	β (mol^2/kJ^2)	q_m (mg/g)	R^2	χ^2	E (kJ/mol)	β (mol^2/kJ^2)	q_m (mg/g)	R^2	MSPD	χ^2
Mono-Cd(II)	0.71	-1.00E-06	46.89	0.957	1.80	0.0121	0.003	47.55	0.793	0.13	4.77
Mono-Hg(II)	0.408	-3.00E-06	11.59	0.096	0.307	0.0076	0.009	12.35	0.100	0.61	6.65
Mono-Ni(II)	0.50	-2.00E-06	26.95	0.892	2.01	0.01	0.004	27.62	0.63	0.24	4.99
Tern-Cd(II)	0.71	-1.00E-06	27.83	0.627	1.10	0.0117	0.004	30.09	0.17	0.78	19.71
Tern-Hg(II)	0.158	-2.00E-05	10.25	0.662	4.40	0.002552	0.077	13.09	0.24	4.4	27.22
Tern-Ni(II)	0.500	-2.00E-06	12.42	0.145	1.17	0.007071	0.010	15.68	0.11	3.5	33.81

USC UNIVERSIDADE DE SANTIAGO DE COMPOSTELA

Table A2.7. Linear and nonlinear parameters of the Isothermal models, Temkin and DKR with respective errors of L13T beads at the mono and ternary system.

Temkin Model	**Linear fitting**				**Nonlinear fitting**				
L13-T bead	b_T (J mol)	K_T (L/g)	R^2	χ^2	b_T (J mol)	K_T (L/g)	R^2	MSPD	χ^2
Mono-Cd(II)	274.07	1.957	0.940	5846.3	9.0436	1.956	0.920	0.124	2.34
Mono-Hg(II)	298.863	0.315	0.593	4358.5	8.29	0.315	0.457	1.059	12.41
Mono-Ni(II)	362.75	3.553	0.991	8775.4	6.83	3.553	0.987	0.01	0.209
Tern-Cd(II)	741.79	30.859	0.765	26698	3.34	30.860	0.687	0.12	2.40
Tern-Hg(II)	8018.032	0.285	0.395	125430.9	0.3086	0.280	0.193	1.52	0.747
Tern-Ni(II)	4432.150	60558891.110	0.101	485798.8	0.558	60600000.000	0.101	0.31	3.28

DKR Model	**Linear fitting**					**Nonlinear fitting**				
L13-T bead	E (kJ/mol)	β (mol^2/kJ^2)	q_m (mg/g)	R^2	χ^2	E (KJ/mol)	β (mol^2/kJ^2)	q_m (mg/g)	R^2	MSPD	χ^2
Mono-Cd(II)	0.50	-2.00E-06	49.353	0.995	2.54	0.011516	0.004	49.430	0.974	0.8558	75.11
Mono-Hg(II)	0.224	-1.00E-05	27.325	0.526	1.22	0.000654	1.170	39.260	0.552	1.9842	15.65
Mono-Ni(II)	1.00	-5.00E-07	40.557	0.970	1.95	0.00	0.242	44.570	0.90	0.0734	2.17
Tern-Cd(II)	1.12	-4.00E-07	27.470	0.925	0.852	0.000224	9.931	27.660	0.81	0.0675	1.41
Tern-Hg(II)	1.291	-3.00E-07	1.042	0.590	46.58	0.002724	0.067	1.147	0.18	1.519	0.766
Tern-Ni(II)	0.158	-2.00E-05	12.632	0.243	19.00	0.025126	0.001	12.990	0.23	0.2788	2.75

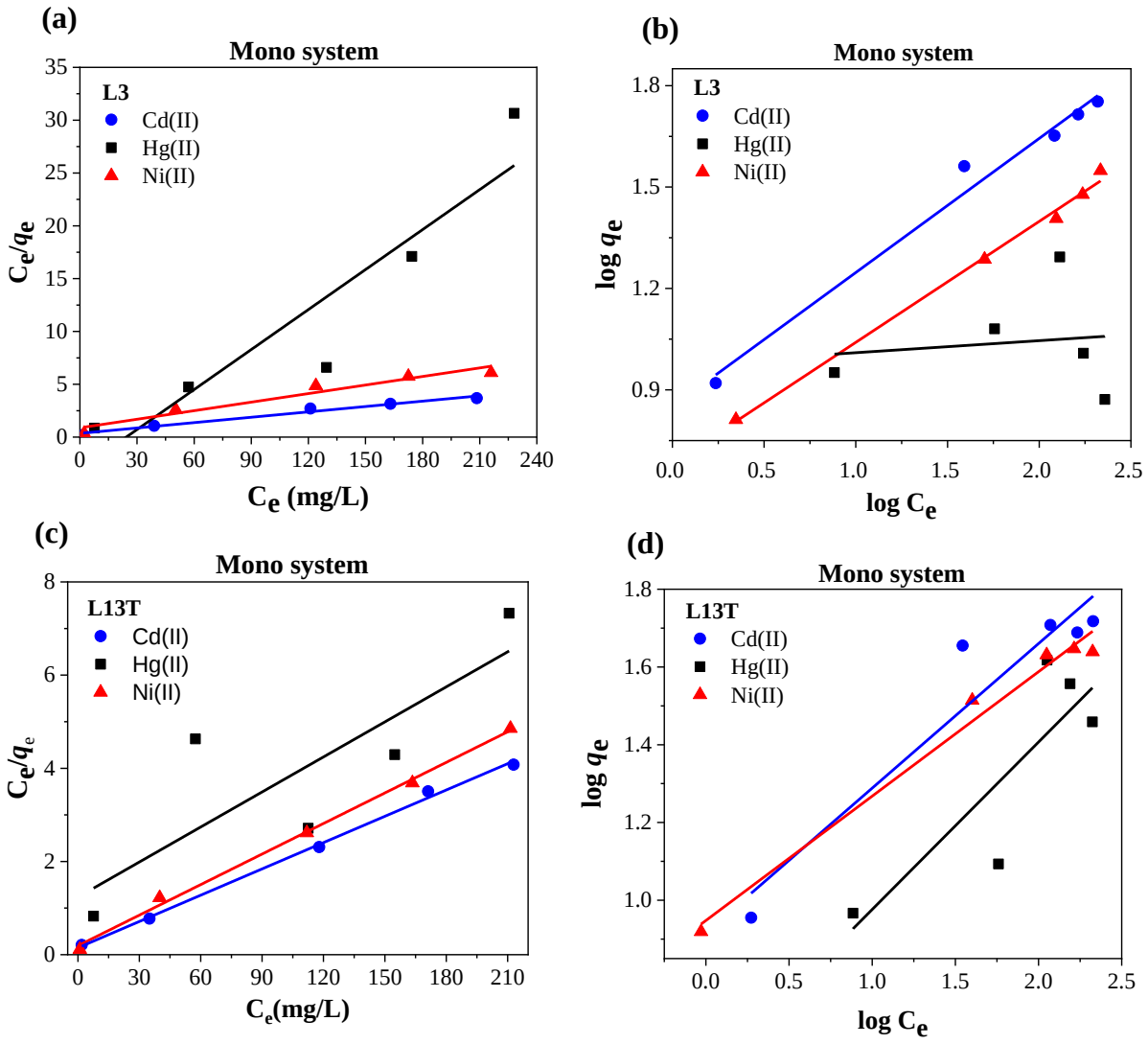


Figure A1.9. Langmuir (a, c) and Freundlich (b, d) linear models of the mono adsorption system by the beads, L3 and L13T, respectively.

USC
UNIVERSIDADE DE SANTIAGO DE COMPOSTELA

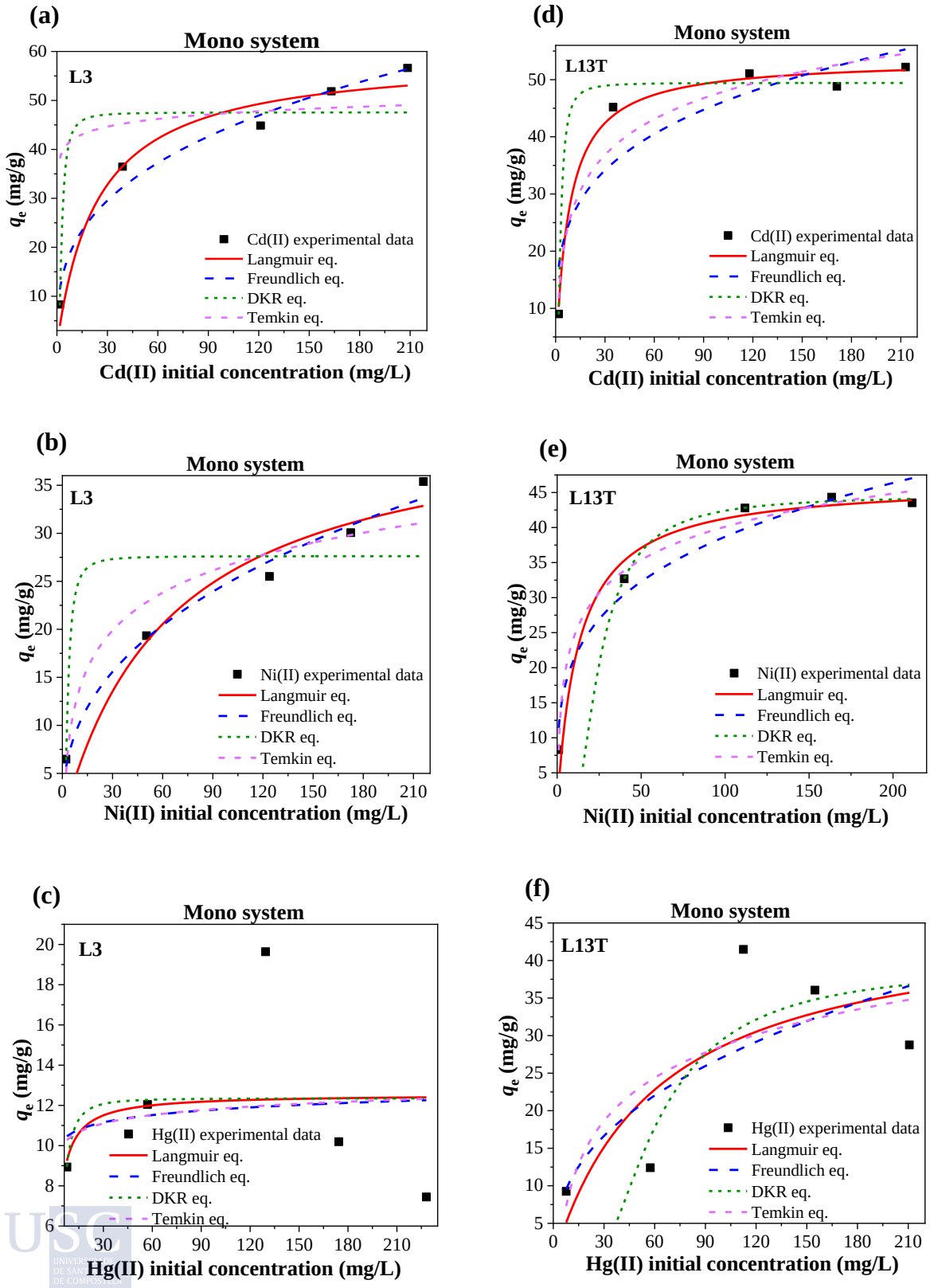


Figure A2.0. Nonlinear isotherm models and experimental data representation of Cd(II), Ni(II), and Hg(II) adsorption capacity, $q_e(mg/g)$, at the mono system against the initial Cd(II) initial concentration, $C_e(mg/L)$ for bead L3 and L13T

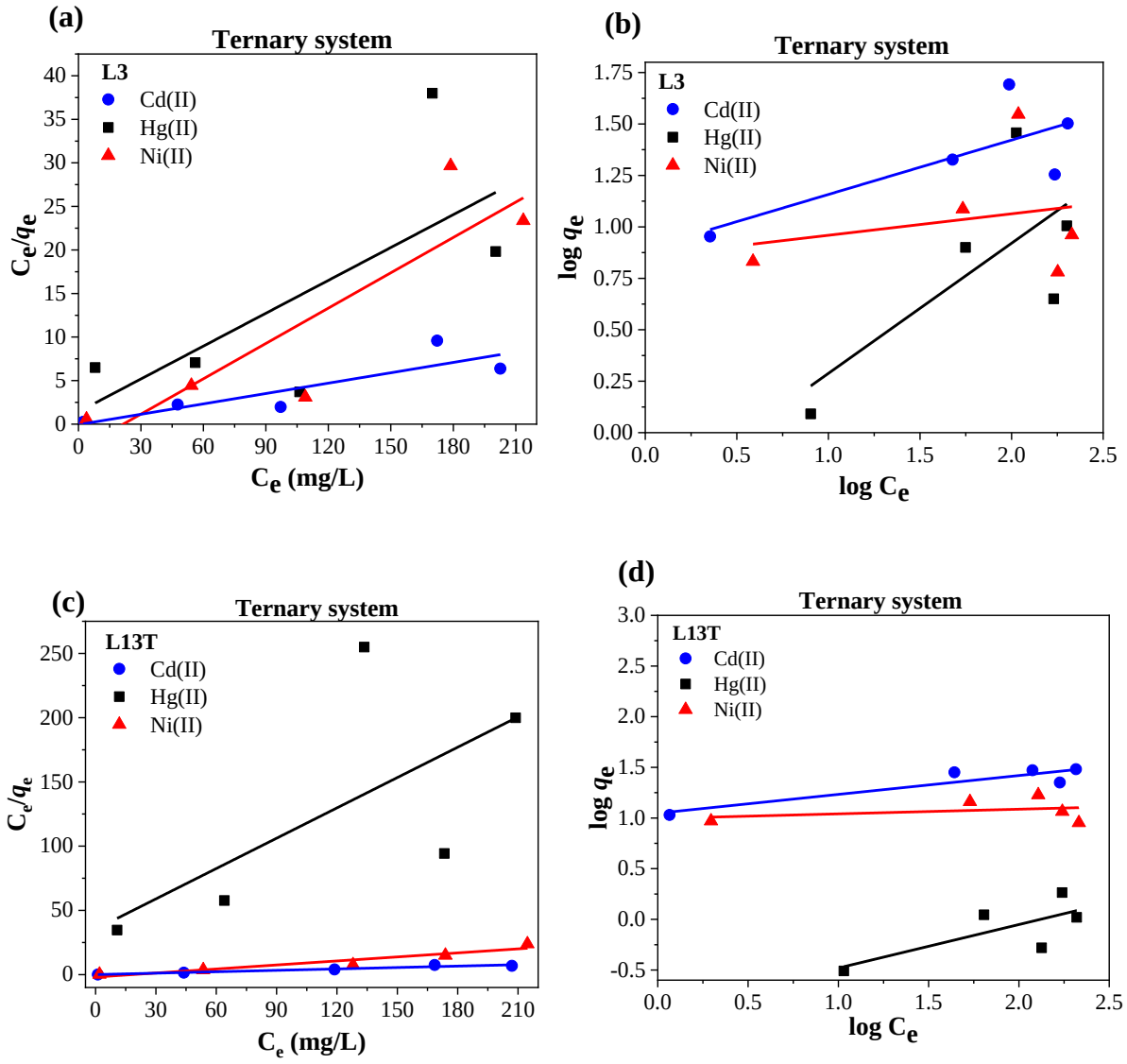


Figure A2.1. Langmuir (a, c) and Freundlich (b, d) linear models of the ternary adsorption system by the beads, L3, and L13T, respectively.

USC
UNIVERSIDADE DE SANTIAGO DE COMPOSTELA

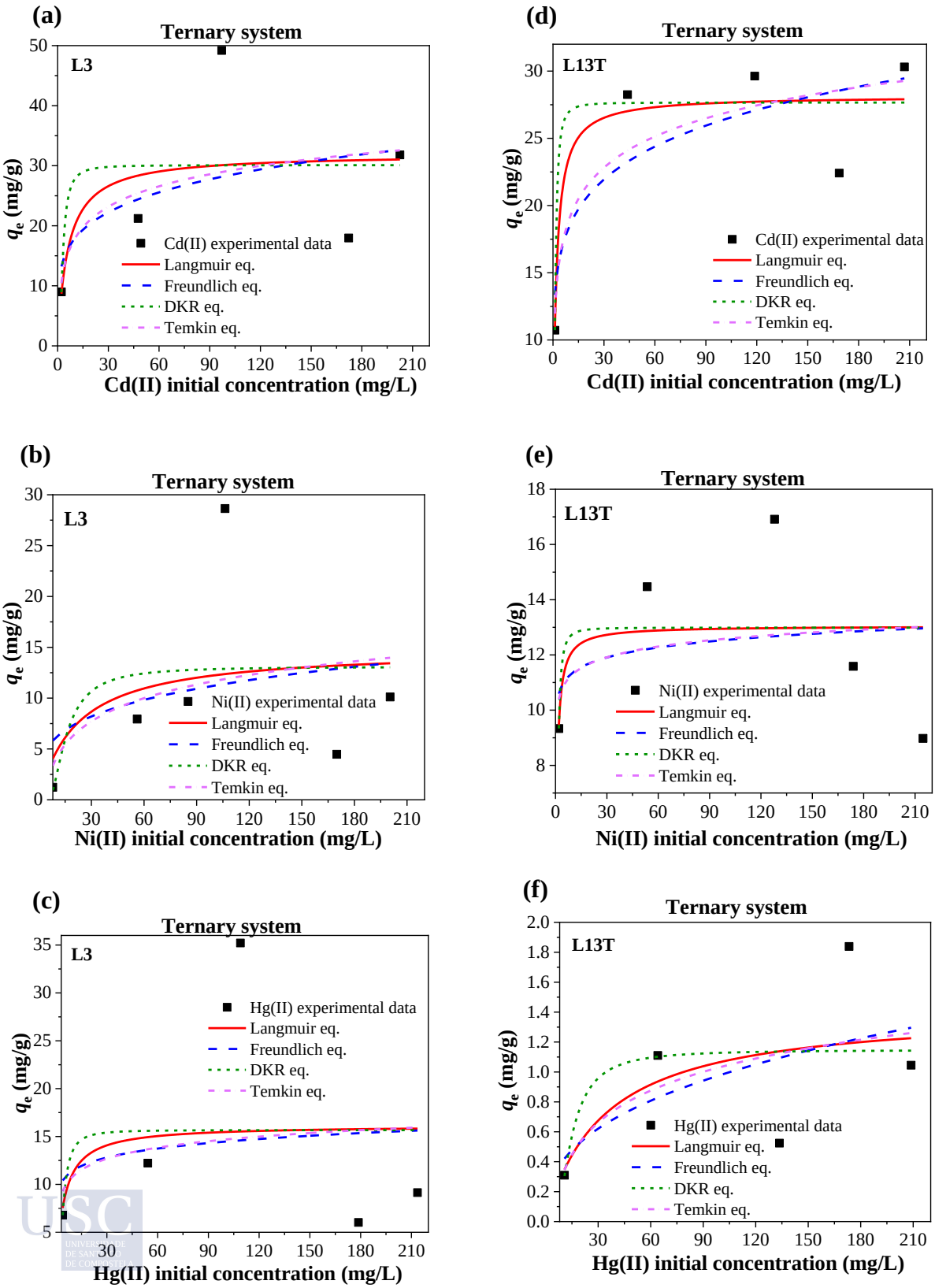


Figure A2.2. Nonlinear isotherm models and experimental data representation of Cd(II), Ni(II), and Hg(II) adsorption capacity, $q_e(mg/g)$, at the ternary system against the initial Cd(II) initial concentration, $C_e(mg/L)$ for bead L3 and L13T.

Table A2.8. High-resolution XPS scan of the beads L3 and L13T at the mono system (ternary experiment).

Chemical bonds	Adsorption system	L3		L13T	
		BE (eV)	Rel. (%)	BE (eV)	Rel. (%)
C1s C-OH/ C-O-C/ Cl-C/ C-N	Cd	286.64	45.16	286.15	22.56
	Hg	286.49	36.25	286.76	55.41
	Ni	286.67	47.07	286.55	17.97
C1s O=C-/ O=C-O/N-C=O	Cd	288.4	24.45	287.7	38.9
	Hg	288.12	28.8	288.74	20.8
	Ni	288.58	17.95	288	47.46
C1s CF2-CF2	Cd	689.74	100	689.59	100
	Hg	689.49	100	689.74	100
	Ni	689.64	100	689.94	100
O1s metal oxides	Cd	530.33	10.87	530.76	7.22
	Hg	530.3	10.29	530.5	3.22
	Ni	530.4	14.57	530.68	7.43
O1s O=C/ O=C-O	Cd	531.8	29.07	532.27	26.13
	Hg	531.54	26.99	531.79	25.67
	Ni	532.01	32.51	532.26	27.85
O1s C-O-C/ C-OH	Cd	533.11	57.58	533.83	66.65
	Hg	532.93	60.93	533.22	66.24
	Ni	533.29	51.04	533.8	50.3
F1s CF2-CF2	Cd	689.74	100	689.59	100
	Hg	689.39	100	689.74	100
	Ni	689.64	100	689.94	100
N1s	Cd	400	100	400.55	100
	Hg	399.98	100	400.39	100
	Ni	400.14	100	401.06	100
$S2p_3$-S2p (organic disulphide)	Cd	-	-	-	-
	Hg	163.44	53.8	163.62	29.74
	Ni	163.51	39.85	-	-
S2p (metal sulfate)	Cd	-	-	169.05	100
	Hg	169.07	46.2	169.52	70.26
	Ni	168.69	60.15	-	-

USC UNIVERSIDADE DE SANTIAGO DE COMPOSTELA

6.3. Chapter 3: Appendix

6.3.1. Magnetic behaviour and particle size of cellulose materials (microfibers, films and capsules)

Table A2.9. Size distribution (DLS and Zeta Potential values of all particles of chapter 3).

Particles	DLS size number (nm)	PDI	Zeta Potential (mV)
SA/T/Fe25	363.6	0.629	-68.7
SA/Fe25	397.3	0.237	-63.3
SA/T/Fe25N	826.4	0.253	-78.8
SA/F/Fe10	840.2	0.649	-68.2
SA/T/Fe5	856.9	0.898	-65.4
M1 (Fe_5C_2)	235.7	1.000	3.14
M2 (Fe_5C_2)	73.26	1.000	-7.77
M3 (*h*-Fe_3O_4)	397.2	0.393	-1.29
M4 (*m*-Fe_3O_4)	1318	0.261	-48.5
F6 (Fe_3O_4@PAA)	113.4	0.190	-60.7

USC UNIVERSIDADE DE SANTIAGO DE COMPOSTELA

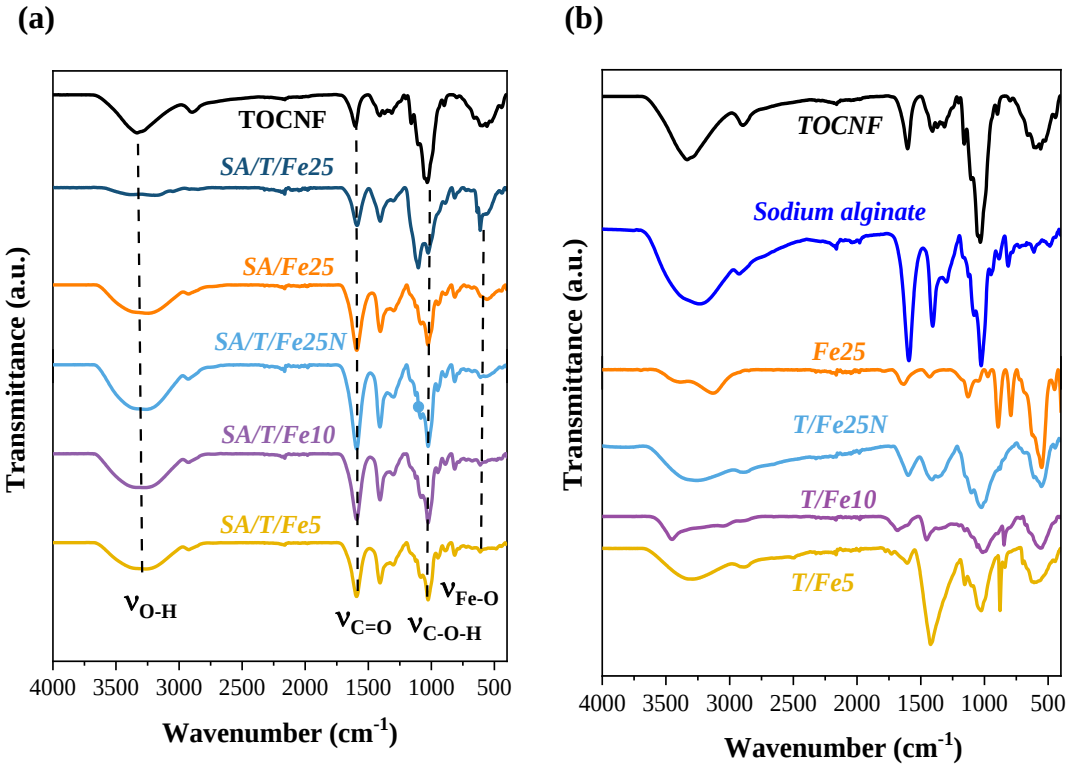


Figure A2.3. FTIR spectra of the magnetic solutions with (a) and without (b) sodium alginate.

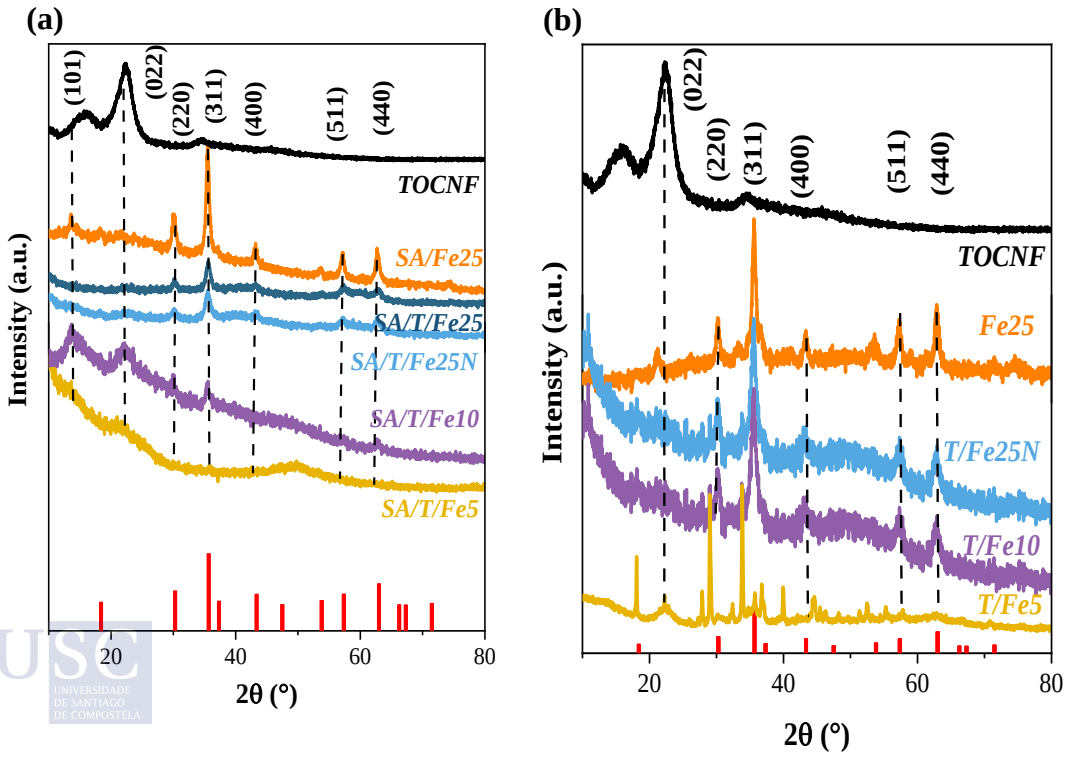


Figure A2.4. XRD diffraction pattern of the magnetic solutions with (a) and without (b) sodium alginate with standard Fe_3O_4 diffraction pattern (red columns).

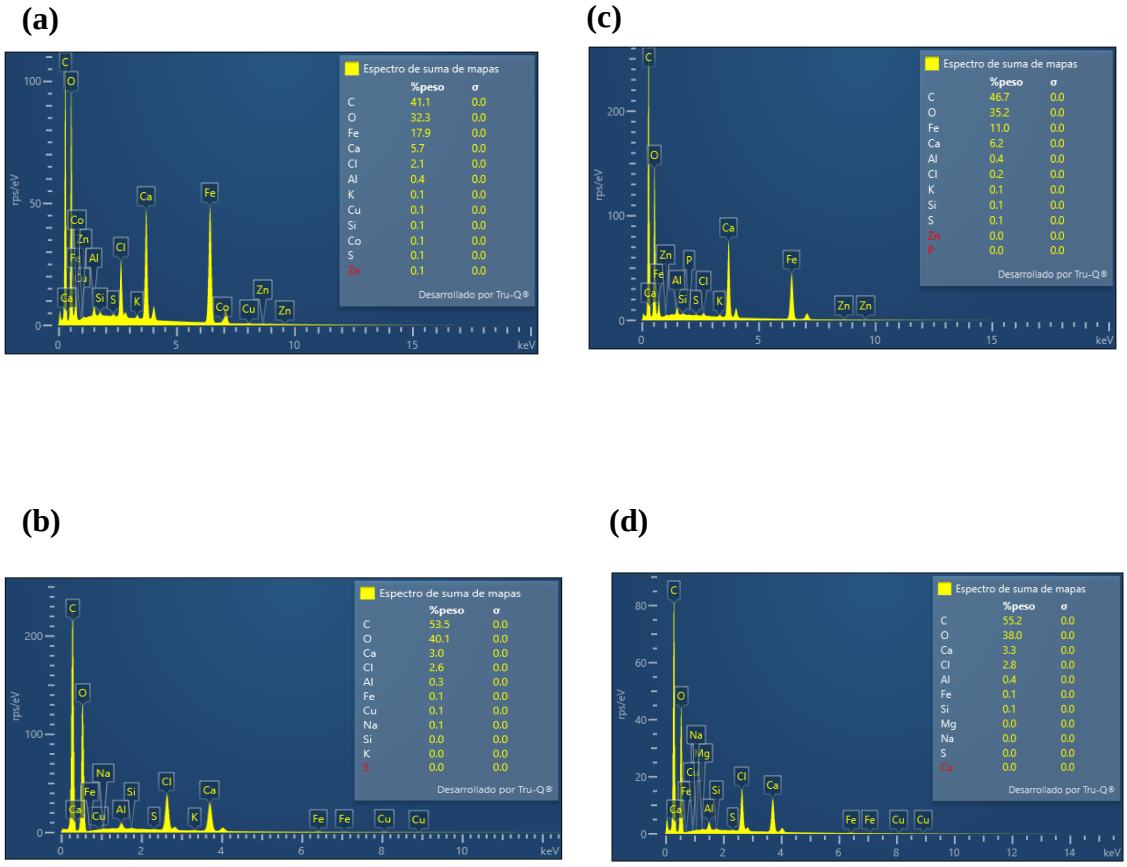
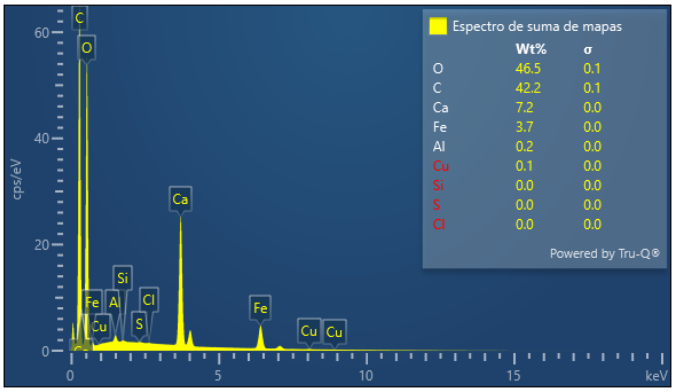


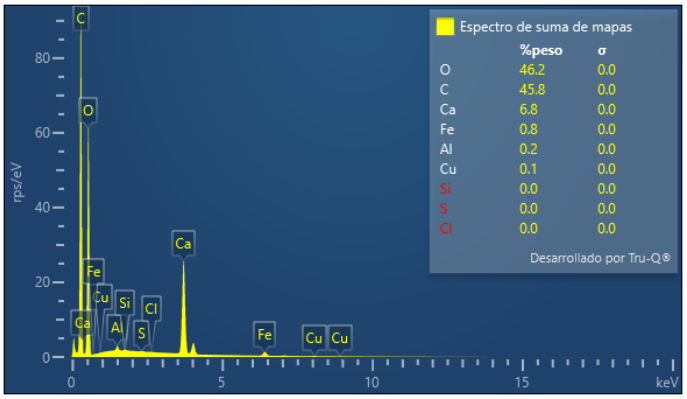
Figure A2.5. EDX analysis of the microfiber F1N (a), F1@TS (b), F2N (c) and F2@TS (d) surface.

USC
UNIVERSIDADE DE SANTIAGO DE COMPOSTELA

(a)



(b)



(c)

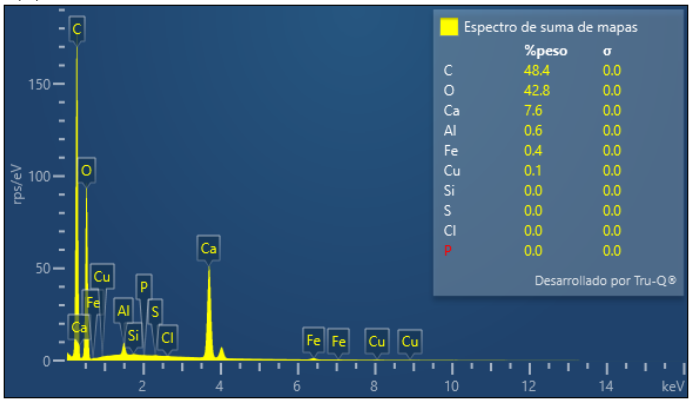


Figure A2.6. EDX analysis of the microfibers F3N (a), F4N (b) and F5N (c) surface.

USC UNIVERSIDADE DE SANTIAGO DE COMPOSTELA

Table A3.0. Magnetization properties of both dopes and microfibers normalized with the respective magnetic solid content (%).

Particles	Magnetic solid content (%)	M_s (emu/g_{Fe3O4})	M_R (emu/g_{Fe3O4})	H_C (Oe)
SA/T/Fe25	45.1	45.89	0.83	6.48
SA/Fe25	42.1	59.65	3.94	12.51
F1N	35.8	56.77	0.96	8.49
F1@TS	15.7	57.87	1.71	9.52
F2N	23.45	56.27	2.01	21.38
F2@TS	16.69	28.40	0.71	15.26

USC UNIVERSIDADE DE SANTIAGO DE COMPOSTELA

Table A3.1. Magnetization properties of both milled dopes and microfibers normalized with the respective magnetic solid content (%).

Particles	Magnetic solid content (%)	M_s (emu/g_{Fe3O4})	M_R (emu/g_{Fe3O4})	H_C (Oe)
SA/T/Fe25	41.40	49.88	0.901	6.46
SA/Fe25	38.5	62.46	2.25	12.97
F1N	59.76	33.25	0.563	8.50
F1@TS	42.84	20.27	0.597	9.56
F2N	49.58	26.61	1.91	21.37
F2@TS	33.24	14.26	0.358	15.24
F3N	25.45	19.4	0.184	5.27
F4N	13.38	11.3	0.068	3.67
F5N	23.65	1.60	0.015	4.59

USC UNIVERSIDADE DE SANTIAGO DE COMPOSTELA

Table A3.2. Mechanical properties of the microfibers and respective reference microfibers (±SD).

Micofibers	Tensile stress σ (MPa)	Strain ε (%)	Young's modulus E(GPa)	Toughness
*RF1	229±38	6±1	12±2	10±3
*RF1@TS	255±30	7±2	13±2	12±4
F1N	118±13	6±2	8±1	6±2
F1@TS	148±12	7±3	9±1	9±4
*RF2	212±22	19±6	9±2	32±9
*RF2@TS	222±34	7±2	11±1	12±4
F2N	216±20	17±5	10±1	27±7
F2@TS	171±45	9±1	9±3	11±4
F3N	182±28.19	8±1.3	9±1.5	15±2.8
F4N	194±11.05	10±2.4	11±0.45	16±2.2
F5N	201±19.24	15±3.6	14±1.5	23±7.1

*(R) reference microfibers without nanoparticles

USC UNIVERSIDADE DE SANTIAGO DE COMPOSTELA

Table A3.3. Magnetic properties of the CA films (F) and respective nanoparticles.

Nanoparticles and Films	Magnetic solid content (%)	M_s (emu/g_{Fe3O4})	M_R (emu/g_{Fe3O4})	H_C (Oe)
M1 (Fe_5C_2)	82.25	104.3	29.0	307.6
M2 (Fe_5C_2)	82.0	109.0	18.8	280.4
M3 (*h*-Fe_3O_4)	95.1	85.0	12.0	84.0
M4 (*m*-Fe_3O_4)	90.0	93.9	9.3	46.6
FM1Fe0.02	0.021	90.6	22.1	323.2
FM1Fe0.1	0.081	97.7	20.1	343.8
FM2Fe0.005	0.004	44.1	14.8	422.5
FM2Fe0.02	0.018	92.9	15.6	342.2
FM2Fe0.1	0.043	96.1	14.0	327.4
FM2Fe0.2	0.21	109.8	13.6	297.5
FM3Fe0.02	0.038	80.8	9.0	163.5
FM3Fe0.1	0.085	86.2	7.3	148.5
FM4Fe0.02	0.021	88.0	4.9	56.4
FM4Fe0.1	0.081	89.9	5.0	62.5

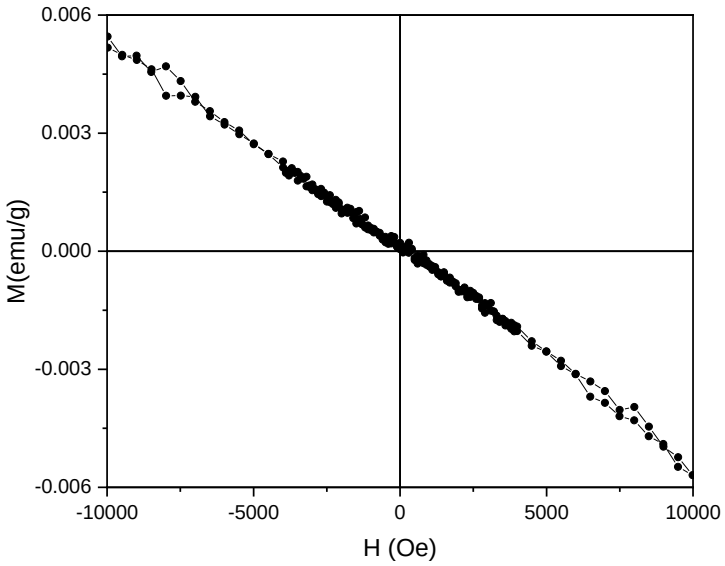


Figure A2.7. Magnetization cycle of cellulose acetate film without magnetic nanoparticles revealing a diamagnetic behaviour

USC UNIVERSIDADE DE SANTIAGO DE COMPOSTELA

Table A3.4. Magnetic properties of magnetic BNC capsules and respective nanoparticle.

Particles	Magnetic solid content (%)	M_s (emu/g_{Fe3O4})	M_R (emu/g_{Fe3O4})	H_C (Oe)
F6 NPs (Fe_3O_4@PAA)	83.12	58.39	1.63	10.7
CF6 (0h)	91.1	57.0	2.94	20.93
CF6 (2y)	88.83	54.43	2.75	23.62

References

1. Shubitidze, F., Kekalo, K., Stigliano, R., and Baker, I. Magnetic nanoparticles with high specific absorption rate of electromagnetic energy at low field strength for hyperthermia therapy. *Journal of applied physics* **117**, 094302 (2015).
2. E.S. Gadelmawla, M.M. Koura, T.M.A. Maksoud, I.M. Elewa, H.H. Soliman Roughness parameters. *J. Mater. Process. Technol*. **123,** pp. 133-145 (2002).
3. Edwin B. Wilson, Margaret M. Hilferty. **17**, 684-688 (1931). DOI: https://doi.org/10.1073/pnas.17.12.684
4. D. Y. Zhao, J. L. Feng, Q. S. Huo, N. Melosh, G. H. Fredrickson, B. F. Chmelka, G. D. Stucky, Triblock copolymer syntheses of mesoporous silica with periodic 50 to 300 angstrom pores. *Science* **279**, 548–552 (1998).
5. Ponomarenko, I.V., Parfenov, V.A., Zaitseva, Y.N. *et al.* Template synthesis of CMK-3 nanostructured carbon material and study of its properties. *Glass Phys Chem* **40**, 79–87 (2014).

USC UNIVERSIDADE DE SANTIAGO DE COMPOSTELA

6.4. Figures Rights and Permissions

6.4.1. Chapter 1 (General Introduction)

Figures	Right and Permissions
1.1	Re: [EXTERNAL] Copyright image VG Visual Identity System Help Desk, GS-O <visual_id@usgs.gov> 02/09/2021 16:48 To: DE CASTRO ALVES LISANDRA CRISTINA Image is fine to use. Thank you for asking. **From:** DE CASTRO ALVES LISANDRA CRISTINA <lisandracristina.decastro@usc.es> **Sent:** Thursday, August 26, 2021 1:11 PM **To:** Visual Identity System Help Desk, GS-O <visual_id@usgs.gov> **Subject:** [EXTERNAL] Copyright image This email has been received from outside of DOI - Use caution before clicking on links, opening attachments, or responding. Dear Sir or madam, Iam a PhD student writing currently my thesis, and I would like to use the image below. Do you know if i need a specific licence to be able to use it in my thesis? Or is just fine to mention the author? https://pubs.usgs.gov/circ/circ1133/heavy-metals.html
1.2 a) b) c) d) e) f) g) h) i) j)	 "Fusarium spore" by Oregon State University is licensed under CC BY-SA 2.0 "Aspergillus niger" by Cornell Fungi is licensed under CC BY-NC-SA 2.0 "Penicillium wm Carolina 02" by clare_and_ben is licensed under CC BY-NC-ND 2.0 "Alternaria alternata - Champignon" by Philippe Garcelon is licensed under CC BY 2.0 "Cladosporium berbarum Link." is licensed under CC BY-NC-SA 4.0 "Fusarium head blight on wheat spike" by CIMMYT is licensed under CC BY-NC-SA 2.0 "Grapefruit: Penicillium mold, rot of fruit" by Plant pests and diseases is marked with CC0 1.0 "Pineapple (Ananas comosus): Fruit decay" by Plant pests and diseases is marked with CC0 1.0 "Mountain naupaka (Scaevola gaudichaudiana): Alternaria leaf spot" by Plant pests and diseases is marked with CC0 1.0 "Taro: Cladosporium leaf spot" by Plant pests and diseases is marked with CC0 1.0.

USC UNIVERSIDADE DE SANTIAGO DE COMPOSTELA

1.4

License Number	5142000423731
License date	Sep 04, 2021
Licensed Content Publisher	Springer Nature
Licensed Content Publication	Springer eBook
Licensed Content Title	Fungi Contamination of Drinking Water
Licensed Content Author	Hamid Mohammad Al-Gabr, Tianling Zheng, Xin Yu
Licensed Content Date	Jan 1, 2014
Type of Use	Thesis/Dissertation
Requestor type	non-commercial (non-profit)
Format	print and electronic
Portion	figures/tables/illustrations
Number of figures/tables/illustrations	1
Will you be translating?	no
Circulation/distribution	1 - 29
Author of this Springer Nature content	no
Title	Magnetic nanomaterials based on sustainable polymers for circular bioeconomy
Institution name	Universidade de Santiago de Compostela
Expected presentation date	Apr 2022
Portions	Figure 4, diagram use

1.5

License Number	5138280543028
License date	Aug 29, 2021
Licensed Content Publisher	Elsevier
Licensed Content Publication	Coordination Chemistry Reviews
Licensed Content Title	Insight on water remediation application using magnetic nanomaterials and biosorbents
Licensed Content Author	M.I.A. Abdel Maksoud,Ahmed M. Elgarahy,Charlie Farrell,Ala'a H. Al-Muhtaseb,David W. Rooney,Ahmed I. Osman
Licensed Content Date	Jan 15, 2020
Licensed Content Volume	403
Licensed Content Issue	n/a
Licensed Content Pages	1
Type of Use	reuse in a thesis/dissertation
Portion	figures/tables/illustrations
Number of figures/tables/illustrations	1
Format	both print and electronic
Are you the author of this Elsevier article?	No
Will you be translating?	No
Title	Magnetic nanomaterials based on sustainable polymers for circular bioeconomy
Institution name	Universidade de Santiago de Compostela
Expected presentation date	Apr 2022
Portions	Figure of mechanims of biosorption

1.6

Advances in porous and nanoscale catalysts for viable biomass conversion

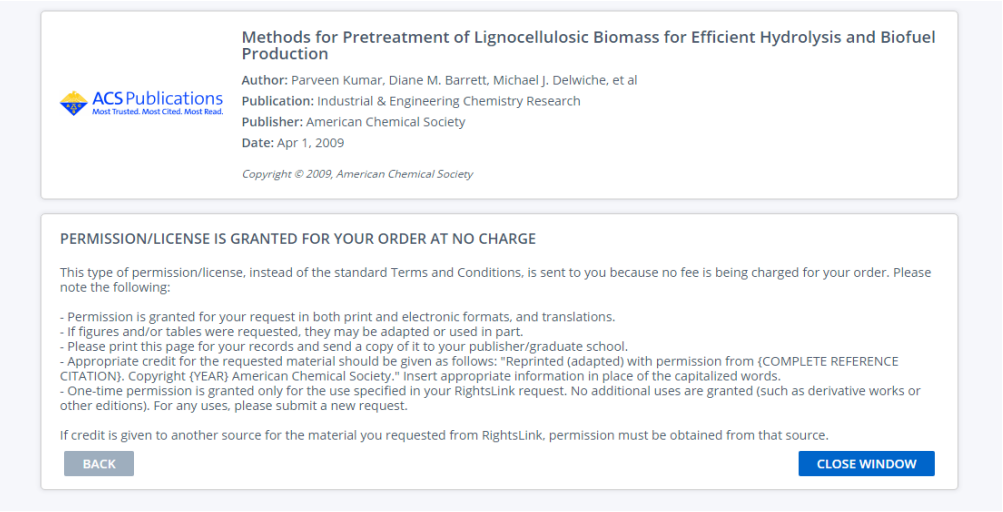
P. Sudarsanam, E. Peeters, E. V. Makshina, V. I. Parvulescu and B. F. Sels, *Chem. Soc. Rev.*, 2019, **48**, 2366 **DOI:** 10.1039/C8CS00452H

This article is licensed under a Creative Commons Attribution-NonCommercial 3.0 Unported Licence. **You can use material from this article in other publications, without requesting further permission** from the RSC, provided that the correct acknowledgement is given and it is not used for commercial purposes.

To request permission **to reproduce material from this article in a commercial publication**, please go to the Copyright Clearance Center request page.

USC UNIVERSIDADE DE SANTIAGO DE COMPOSTELA

1.7



Methods for Pretreatment of Lignocellulosic Biomass for Efficient Hydrolysis and Biofuel Production

Author: Parveen Kumar, Diane M. Barrett, Michael J. Delwiche, et al
Publication: Industrial & Engineering Chemistry Research
Publisher: American Chemical Society
Date: Apr 1, 2009

Copyright © 2009, American Chemical Society

PERMISSION/LICENSE IS GRANTED FOR YOUR ORDER AT NO CHARGE

This type of permission/license, instead of the standard Terms and Conditions, is sent to you because no fee is being charged for your order. Please note the following:

- Permission is granted for your request in both print and electronic formats, and translations.
- If figures and/or tables were requested, they may be adapted or used in part.
- Please print this page for your records and send a copy of it to your publisher/graduate school.
- Appropriate credit for the requested material should be given as follows: "Reprinted (adapted) with permission from {COMPLETE REFERENCE CITATION}. Copyright {YEAR} American Chemical Society." Insert appropriate information in place of the capitalized words.
- One-time permission is granted only for the use specified in your RightsLink request. No additional uses are granted (such as derivative works or other editions). For any uses, please submit a new request.

If credit is given to another source for the material you requested from RightsLink, permission must be obtained from that source.

BACK CLOSE WINDOW

1.8

License Number	5138280020261
License date	Aug 29, 2021
Licensed Content Publisher	Springer Nature
Licensed Content Publication	Biomass Conversion and Biorefinery
Licensed Content Title	Pretreatment methods of lignocellulosic wastes into value-added products: recent advances and possibilities
Licensed Content Author	Diego Batista Meneses et al
Licensed Content Date	Apr 22, 2020
Type of Use	Thesis/Dissertation
Requestor type	academic/university or research institute
Format	print and electronic
Portion	figures/tables/illustrations
Number of figures/tables/illustrations	1
Will you be translating?	no
Circulation/distribution	30 - 99
Author of this Springer Nature content	no
Title	Magnetic nanomaterials based on sustainable polymers for circular bioeconomy
Institution name	Universidade de Santiago de Compostela
Expected presentation date	Apr 2022
Portions	Diagram of main treatments

1.9

License Number	5137690250662
License date	Aug 28, 2021
Licensed Content Publisher	Elsevier
Licensed Content Publication	Journal of Environmental Management
Licensed Content Title	Valorization of pelagic sargassum biomass into sustainable applications: Current trends and challenges
Licensed Content Author	Fernando Amador-Castro,Tomás García-Cayuela,Hal S. Alper,Verônica Rodriguez-Martinez,Danay Carrillo-Nieves
Licensed Content Date	Apr 1, 2021
Licensed Content Volume	283
Licensed Content Issue	n/a
Licensed Content Pages	1
Type of Use	reuse in a thesis/dissertation
Portion	figures/tables/illustrations
Number of figures/tables/illustrations	1
Format	both print and electronic
Are you the author of this Elsevier article?	No
Will you be translating?	No
Title	Magnetic nanomaterials based on sustainable polymers for circular bioeconomy
Institution name	Universidade de Santiago de Compostela
Expected presentation date	Apr 2022
Portions	Figure 2 Environmental effects of Sargassum tides in near-shore coral and seagrass communities.

USC UNIVERSIDADE DE SANTIAGO DE COMPOSTELA

1.11	License Number: 5144290191955 License date: Sep 08, 2021 Licensed Content Publisher: Elsevier Licensed Content Publication: Journal of Cleaner Production Licensed Content Title: Circular bioeconomy strategies: From scientific research to commercially viable products Licensed Content Author: Ana Sofia Brandão,Artur Gonçalves,José M.R.C.A. Santos Licensed Content Date: 1 May 2021 Licensed Content Volume: 295 Licensed Content Issue: n/a Licensed Content Pages: 1 Type of Use: reuse in a thesis/dissertation Portion: figures/tables/illustrations Number of figures/tables/illustrations: 1 Format: both print and electronic Are you the author of this Elsevier article?: No Will you be translating?: No Title: Magnetic nanomaterials based on sustainable polymers for circular bioeconomy Institution name: Universidade de Santiago de Compostela Expected presentation date: Apr 2022 Portions: Adaptation of figure 4
1.14	• "Illustration of DNA" by DennisM2 is marked with CC0 1.0 • "Human blood with red blood cells, T cells (orange) and platelets (green)" by ZEISS Microscopy is licensed under CC BY-NC-ND 2.0 • "atom" is marked with CC0 1.0 • "Ultrastructural morphology shown by coronavirus. Original image sourced from US Government department: Public Health Image Library, Centers for Disease Control and Prevention. Under US law this image is copyright free, please credit the government department whenever you canandrdquo;." by Centers for Disease Control and Prevention is marked with CC0 1.0 • "Ant,-side_2012-07-26-16.09.36-ZS-PMax" by Sam Droege is marked with CC PDM 1.0 • "umbrella woman" is marked with CC0 1.0
1.15	SPRINGER NATURE Inhaled nanomaterials and the respiratory microbiome: clinical, immunological and toxicological perspectives **Author:** Tuang Yeow Poh et al **Publication:** Particle and Fibre Toxicology **Publisher:** Springer Nature **Date:** Nov 20, 2018 *Copyright © 2018, The Author(s).* **Creative Commons** This is an open access article distributed under the terms of the Creative Commons CC BY license, which permits unrestricted use, distribution, and reproduction in any medium, provided the original work is properly cited. You are not required to obtain permission to reuse this article. CC0 applies for supplementary material related to this article and attribution is not required.
1.16	License Number: 5152540268545 License date: Sep 19, 2021 Licensed Content Publisher: Elsevier Licensed Content Publication: Elsevier Books Licensed Content Title: Nanofinishing of Textile Materials Licensed Content Author: Majid Montazer,Tina Harifi Licensed Content Date: Jan 1, 2018 Licensed Content Pages: 16 Type of Use: reuse in a thesis/dissertation Portion: figures/tables/illustrations Number of figures/tables/illustrations: 1 Format: both print and electronic Are you the author of this Elsevier chapter?: No Will you be translating?: No Title: Magnetic nanomaterials based on sustainable polymers for circular bioeconomy Institution name: Universidade de Santiago de Compostela Expected presentation date: Apr 2022 Portions: Figure 16.1

1.17	License Number: 5151971159901 License date: Sep 18, 2021 Licensed Content Publisher: Elsevier Licensed Content Publication: Elsevier Books Licensed Content Title: Nanofinishing of Textile Materials Licensed Content Author: Majid Montazer,Tina Harifi Licensed Content Date: Jan 1, 2018 Licensed Content Pages: 16 Type of Use: reuse in a thesis/dissertation Portion: figures/tables/illustrations Number of figures/tables/illustrations: 1 Format: both print and electronic Are you the author of this Elsevier chapter?: No Will you be translating?: No Title: Magnetic nanomaterials based on sustainable polymers for circular bioeconomy Institution name: Universidade de Santiago de Compostela Expected presentation date: Apr 2022 Portions: Figure 16.2 hysteresis curve
1.18	License Number: 5153180996313 License date: Sep 20, 2021 Licensed Content Publisher: Elsevier Licensed Content Publication: Elsevier Books Licensed Content Title: Handbook of Magnetic Materials Licensed Content Author: Jeotikanta Mohapatra,Jia Ping Liu Licensed Content Date: Jan 1, 2018 Licensed Content Pages: 57 Type of Use: reuse in a thesis/dissertation Portion: figures/tables/illustrations Number of figures/tables/illustrations: 1 Format: both print and electronic Are you the author of this Elsevier chapter?: No Will you be translating?: No Title: Magnetic nanomaterials based on sustainable polymers for circular bioeconomy Institution name: Universidade de Santiago de Compostela Expected presentation date: Apr 2022 Portions: Figure 3

USC UNIVERSIDADE DE SANTIAGO DE COMPOSTELA

6.4.2. Chapter 2 (Materials based on Blue economy concept for contaminants adsorption: magnetic beads)

<table>
<tr><th>Figure</th><th>Right and Permissions</th></tr>
<tr><td>2.1</td><td>
<table>
<tr><td>License Number</td><td>5333001507953</td></tr>
<tr><td>License date</td><td>Jun 20, 2022</td></tr>
<tr><td>Licensed Content Publisher</td><td>Elsevier</td></tr>
<tr><td>Licensed Content Publication</td><td>Journal of Hazardous Materials</td></tr>
<tr><td>Licensed Content Title</td><td>Adsorption kinetic models: Physical meanings, applications, and solving met</td></tr>
<tr><td>Licensed Content Author</td><td>Jianlong Wang,Xuan Guo</td></tr>
<tr><td>Licensed Content Date</td><td>May 15, 2020</td></tr>
<tr><td>Licensed Content Volume</td><td>390</td></tr>
<tr><td>Licensed Content Issue</td><td>n/a</td></tr>
<tr><td>Licensed Content Pages</td><td>1</td></tr>
<tr><td>Type of Use</td><td>reuse in a thesis/dissertation</td></tr>
<tr><td>Portion</td><td>figures/tables/illustrations</td></tr>
<tr><td>Number of figures/tables/illustrations</td><td>1</td></tr>
<tr><td>Format</td><td>both print and electronic</td></tr>
<tr><td>Are you the author of this Elsevier article?</td><td>No</td></tr>
<tr><td>Will you be translating?</td><td>No</td></tr>
<tr><td>Title</td><td>Magnetic nanomaterials based on sustainable polymers for circular bioecono</td></tr>
<tr><td>Institution name</td><td>Universidade de Santiago de Compostela</td></tr>
<tr><td>Expected presentation date</td><td>Oct 2022</td></tr>
<tr><td>Portions</td><td>Figure 1. Adsorption mass transfer steps.</td></tr>
</table>
</td></tr>
<tr><td>2.8</td><td>
SPRINGER NATURE
Graphene and graphene oxide as nanomaterials for medicine and biology application
Author: Subhashree Priyadarsini et al
Publication: Journal of Nanostructure in Chemistry
Publisher: Springer Nature
Date: Jun 7, 2018
Copyright © 2018, The Author(s)
Creative Commons
This is an open access article distributed under the terms of the Creative Commons CC BY license, which permits unrestricted use, distribution, and reproduction in any medium, provided the original work is properly cited.
You are not required to obtain permission to reuse this article.
To request permission for a type of use not listed, please contact Springer Nature
</td></tr>
</table>

USC UNIVERSIDADE DE SANTIAGO DE COMPOSTELA

2.11



The Dietary Fiber Pectin: Health Benefits and Potential for the Treatment of Allergies by Modulation of Gut Microbiota

Author: Frank Blanco-Pérez et al
Publication: Current Allergy and Asthma Reports
Publisher: Springer Nature
Date: Sep 10, 2021

Copyright © 2021, The Author(s)

Creative Commons

This is an open access article distributed under the terms of the Creative Commons CC BY license, which permits unrestricted use, distribution, and reproduction in any medium, provided the original work is properly cited.

You are not required to obtain permission to reuse this article.
To request permission for a type of use not listed, please contact Springer Nature

License Number	5330261183590
License date	Jun 15, 2022
Licensed Content Publisher	Springer Nature
Licensed Content Publication	Journal of Materials Science: Materials in Electronics
Licensed Content Title	Sodium alginate incorporated with magnesium nitrate as a novel solid biopolymer electrolyte for magnesium-ion batteries
Licensed Content Author	R. Tamilisai et al
Licensed Content Date	Aug 3, 2021
Type of Use	Thesis/Dissertation
Requestor type	academic/university or research institute
Format	print and electronic
Portion	figures/tables/illustrations
Number of figures/tables/illustrations	1
Will you be translating?	no
Circulation/distribution	1 - 29
Author of this Springer Nature content	no
Title	Magnetic nanomaterials based on sustainable polymers for circular bioeconomy
Institution name	Universidade de Santiago de Compostela
Expected presentation date	Oct 2022
Portions	Figure 1 - molecular structure of sodium alginate

2.38

License Number	5330720853150
License date	Jun 16, 2022
Licensed Content Publisher	Elsevier
Licensed Content Publication	International Journal of Biological Macromolecules
Licensed Content Title	Alginate-based adsorbents for removal of metal ions and radionuclides from aqueous solutions: A review
Licensed Content Author	Zetty Azalea Sutirman,Mohd Marsin Sanagi,Wan Ibrahim Wan Aini
Licensed Content Date	Mar 31, 2021
Licensed Content Volume	174
Licensed Content Issue	n/a
Licensed Content Pages	13
Type of Use	reuse in a thesis/dissertation
Portion	figures/tables/illustrations
Number of figures/tables/illustrations	1
Format	both print and electronic
Are you the author of this Elsevier article?	No
Will you be translating?	No
Title	Magnetic nanomaterials based on sustainable polymers for circular bioeconomy
Institution name	Universidade de Santiago de Compostela
Expected presentation date	Oct 2022
Portions	Figure 2. egg box structure

USC UNIVERSIDADE DE SANTIAGO DE COMPOSTELA

6.4.3. Chapter 3 (Future materials from forest-based bioeconomy: magnetic microfibers, films and capsules)

Figure	Right and Permissions	
3.1	License Number	5221920826645
	License date	Jan 04, 2022
	Licensed Content Publisher	Springer Nature
	Licensed Content Publication	Nature
	Licensed Content Title	Developing fibrillated cellulose as a sustainable technological material
	Licensed Content Author	Tian Li et al
	Licensed Content Date	Feb 3, 2021
	Type of Use	Thesis/Dissertation
	Requestor type	academic/university or research institute
	Format	print and electronic
	Portion	figures/tables/illustrations
	Number of figures/tables/illustrations	1
	High-res required	no
	Will you be translating?	no
	Circulation/distribution	1 - 29
	Author of this Springer Nature content	no
	Title	Magnetic nanomaterials based on sustainable polymers for circular bioeconomy
	Institution name	Universidade de Santiago de Compostela
	Expected presentation date	May 2022
	Portions	Use of figure 1 : An overview of fibrillated cellulose

6.4.4. Characterization methods

Figure	Right and Permissions	
A1	License Number	5222370092541
	License date	Jan 05, 2022
	Licensed Content Publisher	Elsevier
	Licensed Content Publication	Journal of Materials Processing Technology
	Licensed Content Title	Roughness parameters
	Licensed Content Author	E.S. Gadelmawla,M.M. Koura,T.M.A. Maksoud,I.M. Elewa,H.H. Soliman
	Licensed Content Date	Apr 10, 2002
	Licensed Content Volume	123
	Licensed Content Issue	1
	Licensed Content Pages	13
	Type of Use	reuse in a thesis/dissertation
	Portion	figures/tables/illustrations
	Number of figures/tables/illustrations	4
	Format	both print and electronic
	Are you the author of this Elsevier article?	No
	Will you be translating?	No
	Title	Magnetic nanomaterials based on sustainable polymers for circular bioeconomy
	Institution name	Universidade de Santiago de Compostela
	Expected presentation date	May 2022
	Portions	Figure 1, 3, 6 and 7: Roughness parameters Ra, Rt, Rsk and Rsku

Published content (chapter 2)

nanomaterials

MDPI

Article

Novel Magnetic Nanostructured Beads for Cadmium(II) Removal

Lisandra de Castro Alves, Susana Yáñez-Vilar *, Yolanda Piñeiro-Redondo and José Rivas

Applied Physic Department, NANOMAG Laboratory, Research Technological Institute, Universidade de Santiago de Compostela (USC), 15782 Santiago de Compostela, Spain; lisandracristina.decastro@usc.es (L.d.C.A.); yolanda.fayoly@gmail.com (Y.P.-R.); jose.rivas@usc.es (J.R.)

* Correspondence: susana.yanez@usc.es; Tel.: +34-8818-140-0018

Received: 31 January 2019; Accepted: 21 February 2019; Published: 4 March 2019

check for updates

(This article belongs to the Special Issue **Low Dimensional Materials for Environmental and Biomedical Applications**)

Quality index:

- **Journal Rank (2019):** SNIP: 1.129; SJR: 0.919; CiteScore: Q1.
- **Impact factor (2019):** 4.324
- **Number of citations (publication):** 25

USC UNIVERSIDADE DE SANTIAGO DE COMPOSTELA

© 2019 by the authors. Licensee MDPI. Basel. Switzerland. This article is an open access article distributed under the terms and conditions of the Creative Commons Attribution (CC BY) license (http://creativecommons.org/licenses/by/4.0/).

Contents lists available at ScienceDirect

Food Chemistry

journal homepage: www.elsevier.com/locate/foodchem

Detoxification agents based on magnetic nanostructured particles as a novel strategy for mycotoxin mitigation in food

Jesús M. González-Jartín[a], Lisandra de Castro Alves[b], Amparo Alfonso[a], Y. Piñeiro[b], Susana Yáñez Vilar[b], Manuel González Gomez[b], Zulema Vargas Osorio[b], María J. Sainz[c], Mercedes R. Vieytes[d], J. Rivas[b,*], Luis M. Botana[a,*]

[a] Departamento de Farmacología, Facultad de Veterinaria, Universidade de Santiago de Compostela, 27002 Lugo, Spain
[b] Departamento de Física Aplicada, Universidad de Santiago de Compostela, Facultad de Física, 15782 Santiago de Compostela, Spain
[c] Departamento de Producción Vegetal y Proyectos de Ingeniería, Facultad de Veterinaria, Universidade de Santiago de Compostela, 27002 Lugo, Spain
[d] Departamento de Fisiología, Facultad de Veterinaria, Universidade de Santiago de Compostela, 27002 Lugo, Spain

Quality index:

- **Journal Rank (2019):** SNIP: 2.372; SJR: 1.775; CiteScore: Q1.
- **Impact factor (2019):** 6.5
- **Number of citations (publication):** 28

Detoxification agents based on magnetic nanostructured particles as a novel strategy for mycotoxin mitigation in food

Author:
Jesús M. González-Jartín,Lisandra de Castro Alves,Amparo Alfonso,Y. Piñeiro,Susana Yáñez Vilar,Manuel González Gomez,Zulema Vargas Osorio,María J. Sainz,Mercedes R. Vieytes,J. Rivas,Luis M. Botana

Publication: Food Chemistry
Publisher: Elsevier
Date: 1 October 2019

© 2019 Elsevier Ltd. All rights reserved.

Journal Author Rights

Please note that, as the author of this Elsevier article, you retain the right to include it in a thesis or dissertation, provided it is not published commercially. Permission is not required, but please ensure that you reference the journal as the original source. For more information on this and on your other retained rights, please visit: https://www.elsevier.com/about/our-business/policies/copyright#Author-rights

BACK CLOSE WINDOW

inorganics

MDPI

Article

Efficient Separation of Heavy Metals by Magnetic Nanostructured Beads

Lisandra de Castro Alves, Susana Yáñez-Vilar *, Yolanda Piñeiro-Redondo and José Rivas

Applied Physic Department, NANOMAG Laboratory, Research Technological Institute, Universidade de Santiago de Compostela (USC), 15782 Santiago de Compostela, Spain; lisandracristina.decastro@usc.es (L.d.C.A.); yolanda.fayoly@gmail.com (Y.P.-R.); jose.rivas@usc.es (J.R.)

* Correspondence: susana.yanez@usc.es

Received: 9 April 2020; Accepted: 24 June 2020; Published: 26 June 2020

check for updates

(This article belongs to the Special Issue **Smart Tools for Smart Applications: New Insights into Inorganic Magnetic Systems and Materials**)

Quality index:

- **Journal Rank:** SNIP: 0.666; SJR: 0.650; CiteScore: Q2.
- **Impact factor (2020):** 4.4
- **Number of citations (publication):** 3

© 2020 by the authors. Licensee MDPI. Basel. Switzerland. This article is an open access article distributed under the terms and conditions of the Creative Commons Attribution (CC BY) license (http://creativecommons.org/licenses/by/4.0/).





The present thesis is focused on the development of biocompatible nanostructured materials with magnetic properties, combining biopolymers of algae orgin (e.g., alginate), plant origin (e.g., pectin, cellulose, pectin) and animal origin (e.g., chitosan). The main idea was to design magnetic materials with different morphology (beads, microfibers, films and capsules) and study their biocompatability, reusability and magnetic properties for posterior use in future and environmental applications.